A 3D molecular simulation showing a liquid interface. The interface is represented by a layer of water molecules (red and white spheres) and lipid molecules (red and grey spheres). Above the interface, a layer of silica nanoparticles (red and grey spheres) is adsorbed. The background is a gradient from yellow to blue. The text is centered in the upper half of the image.

***In situ* investigation of the particle adsorption layer
properties of positively and negatively charged
silica nanoparticles adsorbed to pristine and
aminolipid-laden liquid interfaces**

***In situ* investigation of the particle adsorption layer
properties of positively and negatively charged silica
nanoparticles adsorbed to pristine and aminolipid-laden
liquid interfaces**

Vom Fachbereich Produktionstechnik

der

UNIVERSITÄT BREMEN

Zur Erlangung des Grades
Doktor der Ingenieurwissenschaften (Dr.-Ing.)
genehmigte

Dissertation

Von

M.Sc. Joeri Smits

Gutachter:

Prof. Dr.-Ing. Kurosch Rezwan, Universität Bremen

Prof. Dr. Sc. ETH Tobias Kraus, Universität des Saarlandes

Tag der mündlichen Prüfung: 02 November 2022

“Logic will get you from A to Z; imagination will get you everywhere.”

- Albert Einstein

Table of contents

Table of contents	v
Acknowledgments	ix
Kurzfassung	xi
Abstract	xvii
List of abbreviations and symbols	xxiii
1 Introduction	1
2 Fundamentals of colloid and interface science	5
2.1 Surface tension and surfactants	6
2.1.1 Surface tension and surface free energy.....	6
2.1.2 Mechanism of surfactant adsorption.....	8
2.2 Wetting of substrates and particles adsorbed to liquid interfaces	11
2.2.1 Three-phase contact angle.....	12
2.3 Free energy of detachment for a spherical particle	17
2.4 Interaction forces between colloidal particles in solution	19
2.4.1 DLVO interactions: attractive and repulsive contributions in a continuous medium	19
2.5 Particle interactions at the liquid surface	21
2.5.1 van der Waals interactions.....	22
2.5.2 Electrostatic interactions	23
2.5.3 Capillary interactions.....	25
2.5.4 Other types of interactions	26
2.5.5 Interactions induced by external influences	27
3 State-of-the-art	29
3.1 Determination of particle adsorption layer properties at liquid interfaces	30
3.1.1 Visualization methods	30
3.1.2 Indirect methods	34
3.2 Macroscopic observable adsorption of nanoparticles to liquid interfaces	38
3.2.1 The surface tension response to the accumulation of nanoparticles	38
3.2.2 Quantitative thermodynamic description including particle-particle interactions.....	42
3.2.3 Particle adsorption does not always result in a measurable change in surface tension.....	45
3.2.4 Interfacial rheology	47
3.2.5 Interfacial dilational rheology for particle-laden interfaces.....	49
3.2.6 Interfacial shear rheology for particle-laden interfaces.....	51
3.3 Mixed adsorption of hydrophilic, inorganic nanoparticles and surfactants to liquid interfaces	54
3.3.1 Surface-active polar lipids	55
3.3.2 Synergistic and competitive adsorption.....	56
3.3.3 (Semi-)quantitative description of particle-surfactant adsorption layers.....	60
3.3.4 Interfacial dilational rheology for particle-surfactant-laden interfaces.....	61
3.3.5 Interfacial shear rheology for particle-surfactant-laden interfaces	65
3.4 Aim and approach	67

4	<i>Methodology</i>	71
4.1	Principles	71
4.1.1	Sol-gel process, silanization, and functional group quantification.....	71
4.1.2	Characterizing particle size and zeta potential for colloids and planar substrates	83
4.1.3	Surface wetting characterization of colloids and macroscopic substrates: Contact angle, interfacial tension and rheology, and X-ray reflectivity.....	94
5	<i>Reversible adsorption of nanoparticles at surfactant-laden liquid-liquid interfaces</i> ..	113
5.1	Theoretical approach: Additivity of interfacial free energy contributions of particles and surfactants	114
5.2	Materials	116
5.3	Methods	116
5.4	Scientific outcome	121
5.4.1	Scanning electron microscopy of lipids and particles	121
5.4.2	Interfacial shear rheology for rigid particle-lipid films	122
5.4.3	Tensiometry and dilational rheology for liquid-like particle-lipid films	124
5.4.4	Oil/water contact angle in the presence of lipids	125
5.5	Discussion	127
5.6	Conclusions	131
5.7	Acknowledgements	131
6	<i>Synergistic and competitive adsorption of hydrophilic nanoparticles and oil-soluble surfactants at the oil-water interface</i>	133
6.1	Materials	134
6.2	Methods	134
6.3	Scientific outcome	138
6.3.1	Size and zeta potential characterization	138
6.3.2	X-ray reflectivity of particles at liquid interfaces	139
6.3.3	X-ray reflectivity of particles and lipids at the oil/water interface	141
6.3.4	Physical parameters of particle adsorption.....	142
6.3.5	Tensiometry and dilation rheology of particles/lipids at the oil/water interface	144
6.4	Discussion	145
6.4.1	Adsorption of negatively charged silica nanoparticles in the presence of a cationic amino-lipid	145
6.4.2	Adsorption of positively charged silica nanoparticles in the presence of a cationic amino-lipid .	146
6.4.3	Interfacial interaction between nanoparticles and cationic amino-lipid	148
6.5	Conclusions	151
6.6	Acknowledgments	152
7	<i>Assessment of nanoparticle immersion depth at liquid interfaces from chemically equivalent macroscopic surfaces</i>	153
7.1	Materials	155
7.2	Methods	155
7.3	Scientific outcome	160
7.3.1	Mimicking the nanoparticle surface on smooth and rough planar substrates	160

7.3.2	Analogous electrokinetic potentials between nanoparticles and macroscopic substrates	161
7.3.3	<i>In situ</i> observation of self-assembled nanoparticles at liquid interfaces	163
7.3.4	Air/water and oil/water macroscopic contact angle measurements.....	164
7.4	Discussion.....	167
7.4.1	Comparing contact angles at the nano- and macroscale	167
7.4.2	APTES-coated silica.....	169
7.4.3	Silica	171
7.5	Conclusions.....	172
7.6	Acknowledgments.....	173
8	<i>Conclusion and outlook</i>	175
9	<i>Appendix</i>.....	179
A.1	Young-Laplace equation in axisymmetric drop shape analysis	179
A.2	Procedure column chromatography.....	181
A.3	Supplementary content to Chapter 5	183
A.4	Supplementary content to Chapter 6	187
A.5	Supplementary content to Chapter 7	195
10	<i>References</i>	213
	<i>List of publications and oral presentations</i>	247
	<i>Author contributions for the presented publications</i>.....	249
	<i>List of student projects</i>.....	250

Acknowledgments

I am very grateful for the support given by my supervisors, colleagues, collaboration partners, friends, and family.

First and foremost, I like to thank Prof. Dr.-Ing. Kurosch Rezwan for his guidance and the opportunity to pursue my Ph.D. studies at the Advanced Ceramics institute. I am grateful to him and my supervisor PD Dr. Michael Maas, for the invested time, scientific input, and advice over the past few years. Finally, I want to thank Prof. Dr. Sc. ETH Tobias Kraus for supporting me as the second examiner of the presented work.

Besides the scientific work, I am grateful that I have met many different kinds of people during my time at the institute. I thank every person for our brief or long encounter, as it showed me that kindness and a smile could make your life easier and bring more joy to others. To name everyone would be too long, but I like to express my sincerest gratitude to a few. First of all, I like to thank the technical staff (Tina Kühn, Cristian Nuortila, Jürgen Horvath, and Christian Ellenberg) for their expertise and willingness to assist us during stressful times. Especially Tina and Cristian N. hold a special place in my heart, and I truly miss our conversations.

I owe my sincerest gratitude to my partners in crime, my fellow Ph.D. and postdoc colleagues. Thanks to Marieke M. Hoog Antink, Jéssica C. Mainardi, Thamires Canuto, Reshma Kadam, Natalia Fontão, and Pedro H.d.R Braun for the nice daily breaks filled with positive and funny conversations. It was nice to feel supported, appreciated and cared for during this important milestone in our lives. Additionally, I want to give additional thanks to Rafael K. Nishihora, Renato Almeida, and Daniel Carmona for throwing an unforgettable bachelor party for my wedding.

Most importantly, I owe special thanks to my family, especially to my husband Keith. Without him, I would have never moved to Bremen, and none of this would have been possible. Not having our close relatives around made us highly dependent on each other for everything, a situation that makes or breaks the relationship. His perseverance and unconditional love (and patience!) in life undoubtedly made things easier for me. I thank my parents, siblings, and closest ‘Belgian’ friends for attempting to listen to my “science jibber-jabber” and support all my choices.

Thank you all from the bottom of my heart!

Joeri

Kurzfassung

Teile dieser Kurzfassung wurden in *Langmuir*, 2019, DOI: [10.1021/acs.langmuir.9b01568](https://doi.org/10.1021/acs.langmuir.9b01568), *Langmuir*, 2021, DOI: [10.1021/acs.langmuir.1c00559](https://doi.org/10.1021/acs.langmuir.1c00559) and *Journal of Colloid and Interface Science*, 2021, DOI: [10.1016/j.jcis.2021.12.113](https://doi.org/10.1016/j.jcis.2021.12.113) veröffentlicht und werden mit Genehmigung der Herausgeber *American Chemical Society* und *Elsevier* adaptiert.

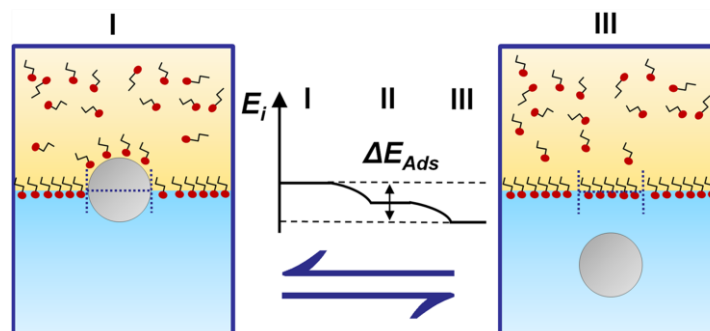
Selbstorganisation und Einschluss von Partikeln an Gas-Flüssigkeit- und Flüssigkeit-Flüssigkeit-Grenzflächen kann zu komplexen zwei- und dreidimensionalen Konfigurationen führen, die in vielen verschiedenen natürlichen und industriellen Prozessen vorkommen. Ein grundlegendes Verständnis der physikalisch-chemischen Aspekte bezüglich Dynamik, Adsorption und Gleichgewicht von partikelbeladenen Grenzflächen sind für die Herstellung oder Destabilisierung dispergierter Systeme und rekonfigurierbarer Geräte unerlässlich. Beispiele hierfür sind die hohe Desorptionsenergie für eingeschlossene Partikel, grenzflächenspezifische Wechselwirkungen zwischen den Partikeln aufgrund der Asymmetrie der Flüssigphasengrenzfläche und das rheologische Verhalten bei mechanischer Verformung der Adsorptionsschicht. Kugelförmige Partikel, die an der Öl/Wasser-Grenzfläche adsorbieren und eine Gleichgewichtsposition auf halbem Weg entlang der Phasengrenze einnehmen, gelten als intermediär benetzbar und weisen sehr hohe Adsorptionsenergien auf, die ihre Desorption zurück in ihr jeweiliges Dispersionsmedium verhindern. Bei genau gleichmäßiger Benetzbarkeit der Partikel beträgt der Dreiphasenkontaktwinkel (CA) an der Feststoff-Wasser-Öl-Grenzfläche mit beiden Lösungsmitteln 90° . Eine vollständige Monoschicht, die durch Adsorption kugelförmiger Partikel mit mittlerer Benetzbarkeit gebildet wird, deckt etwa 91 % der gesamten Grenzfläche ab, was die Destabilisierungsmechanismen in Schäumen und Emulsionen, wie Koaleszenz und Ostwald-Reifung, stark hemmt. Die durch die Adsorption der Teilchen verursachte Verringerung der Flüssigkeitsgrenzfläche, die der Fläche eines Kreises mit dem Radius des betreffenden Teilchens entspricht, geht mit einer Änderung der Grenzflächenenergie einher. Die Fläche und die Energie einer Flüssigkeitsgrenzfläche sind wiederum thermodynamisch mit der Grenzflächenspannung (IFT) verbunden, die an Flüssigkeitsgrenzflächen gemessen wird. Die IFT kann experimentell an zweidimensionalen Flüssigkeitsgrenzflächen gemessen werden, und eine Abnahme der Spannung kann mit der Grenzflächenkonzentration von Proteinen, Polymeren, Tensiden und (Nano-)Partikeln in Verbindung gebracht werden, sofern ein geeignetes thermodynamisches Adsorptionsmodell existiert.

Niedermolekulare Tenside senken die IFT aufgrund ihrer amphiphilen Natur erheblich. Wechselwirkungen zwischen Partikeln und Tensiden können die Affinität der Partikel für die Flüssigkeitsgrenzfläche verändern, wodurch die Grenzflächenbedeckung erhöht oder verringert wird. Folglich wird die Beziehung zwischen der Abnahme der Grenzflächenspannung und der Grenzflächenkonzentration, die mit mehreren Adsorbentien bedeckt ist, oft durch deren kombinierte Oberflächenaktivität und potenzielle Wechselwirkungen überlagert. Die erhöhte Komplexität bei der adäquaten Bestimmung der physikalisch-chemischen Eigenschaften des Grenzflächensystems in gemischten Partikel-Tensid-Filmen stellt Experimentatoren und Theoretiker vor die Herausforderung, grundlegende Ansätze zu entwerfen oder zu erweitern, die auf die Adsorption von mehreren Komponenten anwendbar sind. Wenn sich mehrere Komponenten gleichzeitig selbst anordnen können, hängt ihre individuelle Grenzflächenbedeckung von der relativen Stärke ihrer synergistischen oder konkurrierenden Wechselwirkungen ab, was im Allgemeinen zu einer Packung der Grenzflächen bzw. einer Destabilisierung der partikelbeladenen Grenzflächen führt. Beide Adsorptionsmechanismen können anhand eines Systems aus polaren Lipiden in Kombination mit stark hydrophilen (Wasserkontaktwinkel $\ll 90^\circ$) Nanopartikeln (NPs ≤ 100 nm) untersucht werden. In Abwesenheit von Additiven, die die Benetzbarkeit der Partikel beeinflussen, hat das hydrophile Nanomaterial eine hohe Wahrscheinlichkeit, als Folge der thermischen Bewegung von der Flüssigkeitsgrenzfläche zu desorbieren, und es wird erwartet, dass die IFT der reinen Öl/Wasser-Grenzfläche ähnelt (d. h. keine Adsorption). Diese grundlegenden Erkenntnisse über das Zusammenspiel und die Selbstorganisation von NPs und oberflächenaktiven Stoffen an der Flüssig-Flüssig-Grenzfläche spielen eine entscheidende Rolle bei der Interpretation der weitverbreiteten kolloidalen Systeme, die in unserer natürlichen Umgebung, einschließlich Lebensmitteln und Gewässern, sowie in der Industrie zur Emulsionsstabilisierung, Medikamentenabgabe oder verbesserten Ölgewinnung vorkommen. Darüber hinaus ermöglichen gut kontrollierte Modellsysteme für die gemischte Grenzflächenadsorption von NPs und Tensiden beispiellose Einblicke in nicht-ideale oder kontaminierte partikelstabilisierte Emulsionen.

Daher besteht der erste Eckpfeiler dieser Arbeit darin, ein einfaches theoretisches Modell zu testen, welches die Anzahl der adsorbierten Partikel an der mit Tensiden beladenen Flüssig-Flüssig-Grenzfläche abschätzt. Sowohl die Partikel als auch die Lipide tragen positive Ladungen und sind in getrennten, nicht mischbaren Phasen aufgelöst. Letzteres stellt sicher, dass die Wechselwirkungen auf den Grenzflächenbereich beschränkt sind, während ersteres davon ausgeht, dass es keine direkten Wechselwirkungen zwischen Teilchen und Tensid gibt.

Die Grenzflächenadsorption von aminierten Siliziumdioxidpartikeln (80 nm) mit oder ohne Octadecylamin (ODA) an der Dekan/Wasser-Grenzfläche wird durch IFT-Messungen beobachtet, ergänzt durch die Grenzflächenrheologie der adsorbierten Grenzflächenfilme, REM-Aufnahmen von Langmuir-Blodgett-Filmen und Messungen der dreiphasigen CA auf einem makroskopischen, planaren Substrat, das die NP-Oberfläche nachahmt.

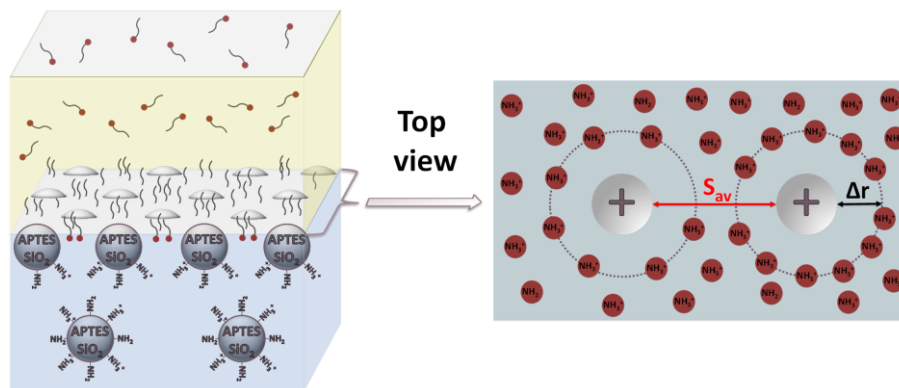
Die Messungen zeigen, dass die Partikel bei allen untersuchten Tensidkonzentrationen an der mit Tensiden beladenen Grenzfläche adsorbieren und mit den Tensiden um die Grenzflächenbedeckung konkurrieren. Außerdem ändert sich die Benetzbarkeit der hydrophilen Partikel in Gegenwart der Lipide nicht, außer bei der höchsten untersuchten Lipidkonzentration. Der Vergleich der Adsorptionsenergien eines Partikels und der Lipide in Abhängigkeit der Partikel-CA liefert einen Schätzwert für die Tendenz zur Adsorption der Partikel an der Grenzfläche, anhand dessen die Partikelbedeckung beurteilt werden kann (ΔE_{ads}). Auf der Grundlage dieser Ergebnisse zeigen gleich geladene Partikel und Lipide ein Konkurrenzverhalten an der Grenzfläche, das durch die Tensidkonzentration und die Bindungsenergien der Partikel an der Grenzfläche gesteuert wird. Daraus ergibt sich ein einfaches mechanistisches Modell (Graphische Kurzfassung 1), das beschreibt, dass Partikel aufgrund der direkten Verdrängung durch Tenside, die auf der dem Öl zugewandten Partikelseite lose adsorbiert sind, leicht von der Grenzfläche desorbieren können. Dieser Mechanismus senkt die normalerweise hohe Grenzflächenenergiebarriere gegen die Partikeldesorption entscheidend, die andernfalls zu einer praktisch irreversiblen Partikelanhaftung an der Grenzfläche führen würde.



Graphische Kurzfassung 1 Partikel adsorbieren reversibel in Gegenwart von gleich geladenen öllöslichen Tensiden. Folglich konkurrieren beide Komponenten um die Grenzflächenbedeckung, die von der Tensidkonzentration abhängt.

Um die theoretischen Ergebnisse zu untermauern, wird die Adsorption zwischen kleineren negativ oder positiv geladenen Siliziumdioxid-NP mit ODA mit hochauflösender, in situ Synchrotron-basierter Röntgenreflektometrie (XRR) untersucht, die zusammen mit dynamischer Grenzflächentensiometrie analysiert und diskutiert wird. Die Ergebnisse zeigen,

dass negativ geladene Silica NPs nur adsorbieren, wenn die Öl/Wasser-Grenzfläche mit dem positiv geladenen Lipid bedeckt ist. Dies deutet auf eine synergistische Adsorption hin, die durch die gegenseitige elektrostatische Anziehung stimuliert wird. Umgekehrt adsorbieren die positiv geladenen NPs eher unabhängig voneinander, konkurrieren aber mit ODA und desorbieren reversibel mit zunehmender Lipidkonzentration. Darüber hinaus zeigt das zuvor vorgeschlagene analytische Modell, dass bei konkurrierender Adsorption eine elektrostatische Ausschlusszone (Δr) um die adsorbierten Partikel herum existiert (Graphische Kurzfassung 2). Diese Zone verhindert die Adsorption von Lipidmolekülen in diesem Bereich, was zu einer geringeren Oberflächenüberschusskonzentration von Tensiden, einer unerwartet hohen IFT und einer entsprechend geringeren Viskoelastizität bei nicht zu hohen Lipidkonzentrationen führt.



Graphische Kurzfassung 2 Um die positiv geladenen Teilchen herum bildet sich eine elektrostatische Ausschlusszone (Δr), die die Adsorption von gleich geladenen Lipiden in diesem Bereich verhindert. Die Stabilität partikelbeladener Grenzflächen ist mit der Benetzbarkeit der Partikel verknüpft, die durch ihren CA oder Wassereindringtiefe charakterisiert ist, und wird im Allgemeinen aus makroskopischen Kontaktwinkeln (mCAs) extrapoliert, die von liegenden Tropfen auf ebenen Substraten abgeleitet wurden. Aufgrund der nanoskopischen Auflösung, die XRR in Bezug auf die Lage der NPs relativ zur Flüssigkeitsgrenzfläche und ihre Grenzflächenbedeckung bietet, wird ein Ansatz getestet, um zu untersuchen, ob liegende Tropfen die Benetzbarkeit von NPs, die sich an einer Flüssigkeitsgrenzfläche befinden, angemessen beschreiben können. Dafür wird angenommen, dass die NPs und die makroskopischen Substrate chemisch äquivalent sind, wenn beide Oberflächen das gleiche elektrokinetische (ζ) Potenzial aufweisen (Graphische Kurzfassung 3), was durch eine physikalische topographische Analyse untermauert wird. Dieses Konzept wird an Partikeln getestet, die an einer reinen Luft/Wasser-Oberfläche oder einer Öl/Wasser-Grenzfläche ohne Tenside adsorbieren. Kieselsäure und aminoterminierte Kieselsäure-NP werden mit makroskopischen Oberflächen mit extrem geringer Rauheit (root mean square [RMS] Rauheit ≤ 2 nm) oder einer Rauheit, die durch eine dicht gepackte Schicht

von NPs bestimmt wird (RMS-Rauheit ~ 35 nm), verglichen. Die Gleichwertigkeit der Oberflächenchemie wird durch den Vergleich der elektrokinetischen Potenziale der NPs mittels elektrophoretischer Lichtstreuung und der makroskopischen Substrate mittels Strömungspotentialanalyse bewertet. Die Benetzbarkeit der makroskopischen Substrate wird anhand fortschreitender (ACAs) und zurückweichender Kontaktwinkel (RCAs) ermittelt. Im Allgemeinen liefert der RCA auf glatten Oberflächen eine angemessene Schätzung der Benetzungseigenschaften von Nanopartikeln. Die mCAs allein können jedoch keine Adsorptionsbarrieren vorhersagen, die eine Entmischung der NP an der Grenzfläche verhindern, wie es bei den nativen SiO_2 -Nanopartikeln der Fall ist. Die vorgestellte Strategie erleichtert die Bewertung der Benetzungseigenschaften von NPs für Anwendungen wie Emulsionsformulierung, Flotation oder Wasseraufbereitung.



Grafische Kurzfassung 3 Die Benetzbarkeit von Nanopartikeln, die an einer Flüssigkeit haften, lässt sich auf makroskopischer Ebene genauer vorhersagen, wenn beide Oberflächen chemisch gleichwertig sind, was durch das Zeta-Potenzial (ζ) gemessen wird.

Abstract

Parts of the abstract have been published in *Langmuir*, 2019, DOI: [10.1021/acs.langmuir.9b01568](https://doi.org/10.1021/acs.langmuir.9b01568), *Langmuir*, 2021, DOI: [10.1021/acs.langmuir.1c00559](https://doi.org/10.1021/acs.langmuir.1c00559) and *Journal of Colloid and Interface Science*, 2021, DOI: [10.1016/j.jcis.2021.12.113](https://doi.org/10.1016/j.jcis.2021.12.113) and are adapted with permission of the publishers *American Chemical Society* and *Elsevier*.

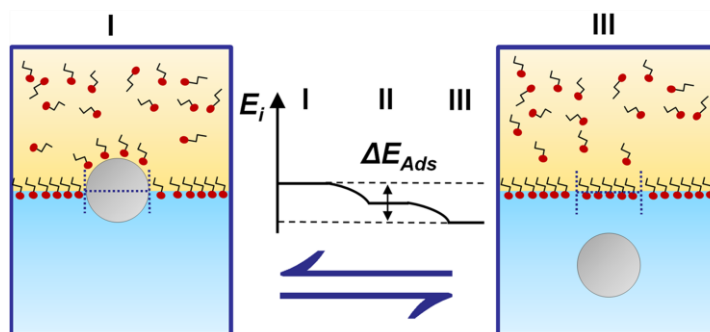
The self-assembly and confinement of particles to gas-liquid and liquid-liquid interfaces can result in complex, two- and three-dimensional configurations commonly found in various natural and industrial processes. A fundamental understanding into the physicochemical aspects related to the dynamics of adsorption and equilibration of particle-laden interfaces, such as the high desorption energy for trapped particles, interface-specific interparticle interactions due to the asymmetry of the liquid phase boundary plane, and the rheological response after mechanical deformation of the adsorption layer, are essential for the fabrication or destabilization of dispersed systems and reconfigurable devices. Spherical particles that adsorb at the oil/water interface and occupy an equilibrium position halfway along the phase boundary are considered to have intermediate wettability with very high adsorption energies that prevent their desorption back into their respective dispersion medium. In the case of exactly equal wettability of the particles, the three-phase contact angle (CA) at the solid-water-oil intersection with both solvents is 90° . A complete monolayer formed by adsorption of spherical particles with intermediate wettability covers roughly 91% of the total interfacial area, which greatly inhibits the destabilization mechanisms in foams and emulsions, such as coalescence and Ostwald ripening. The decrease in liquid interfacial area induced by particle adsorption, equal to the area of a circle having a radius of the relevant particle, is accompanied by a change in interfacial energy. In turn, the area and energy of a liquid interface are thermodynamically related to the interfacial tension (IFT) measured at liquid interfaces. The IFT can be measured experimentally at two-dimensional liquid interfaces and a decrease in the tension can be associated to the interfacial concentration of proteins, polymers, surfactants, and (nano)particles, provided that a suitable thermodynamic adsorption model exists.

Small-molecule surfactants significantly lower the IFT due to their amphiphilic nature. Particle-surfactant interactions may alter the particles' affinity for the liquid interface, thereby increasing or decreasing interfacial coverage. Consequently, the relationship between the decrease in IFT and interfacial concentration covered with multiple adsorbents is often obscured by their combined surface-activity and potential interactions. The increased complexity in

adequately determining the physicochemical properties of the interfacial system in mixed particle-surfactant films challenges experimentalists and theoreticians to design or extend fundamental frameworks applicable to multicomponent adsorption. When multiple components are allowed to self-assemble simultaneously, their individual interfacial coverage will depend on the relative strength of their synergistic or competitive interactions, which generally leads to interfacial packing or destabilization of the particle-laden interfaces, respectively. Both adsorption mechanisms can be explored using a system of polar lipids combined with highly hydrophilic (contact angles $\ll 90^\circ$) nanoparticles (NPs ≤ 100 nm). In the absence of additives affecting the wettability of the particles, hydrophilic nanomaterial has a high probability of desorbing as a consequence of thermal agitation of the liquid interface and the IFT is expected to resemble that of the pure oil/water interface (i.e., no adsorption). These fundamental insights into the interplay and self-assembly of NPs and surface-active agents at the liquid-liquid interface play a pivotal role in interpreting the universal colloidal systems present in our natural surroundings, including foods and aquatic life, and in the industry for emulsion stabilization, drug delivery, or enhanced oil recovery. Moreover, well-controlled model systems for mixed interfacial adsorption of NPs and surfactants allow unprecedented insights into nonideal or contaminated particle-stabilized emulsions.

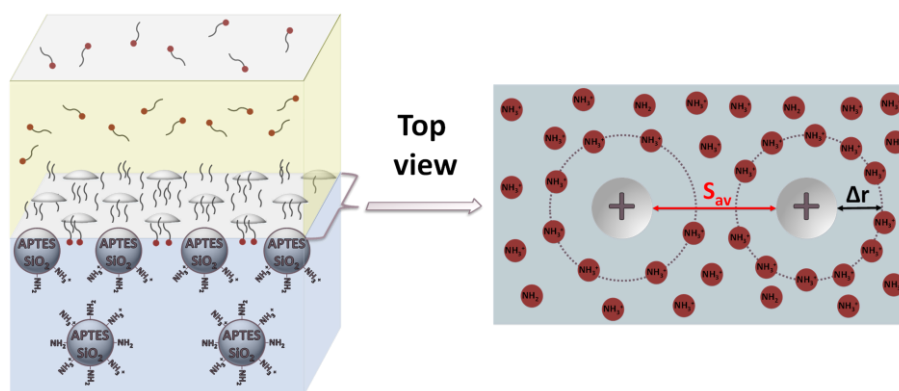
Therefore, the first cornerstone of this work is to test a simple theoretical model to assess the number of adsorbed particles at the surfactant-laden liquid-liquid interface. The particles and lipids both bear positive charges and are dissolved in separate immiscible phases. The latter ensures interactions are limited to the interfacial region, while the former assumes direct particle/surfactant interactions are absent. The interfacial adsorption of aminated silica particles (80 nm) with or without octadecyl amine (ODA) to the decane/water interface is monitored by IFT measurements, supplemented by interfacial rheology of the adsorbed interfacial films, SEM-micrographs of Langmuir-Blodgett films, and measurements of the three-phase CA on a macroscopic, planar substrate mimicking the NP surface. The measurements show that particles adsorb at the surfactant-laden interface at all investigated surfactant concentrations and compete with the surfactants for interfacial coverage. Additionally, the wettability of the hydrophilic particles does not change in the presence of the lipids, except for the highest investigated lipid concentration. Comparing the adsorption energies of one particle and the lipids as a function of the particle CA provides an estimate of the tendency for interfacial particle adsorption to occur from which the particle coverage can be assessed (ΔE_{ads}). Based on these findings, equally charged particles and lipids show a competitive behavior at the interface regulated by the bulk surfactant concentration and the

attachment energies of the particles at the interface. This leads to a simple mechanistic model ([Graphical abstract 1](#)) demonstrating that particles can readily desorb from the interface due to direct displacement by surfactants, which are loosely adsorbed at the oil-facing particle side. This mechanism critically lowers the normally high interfacial energy barrier against particle desorption, which otherwise would lead to virtually irreversible particle attachment at the interface.



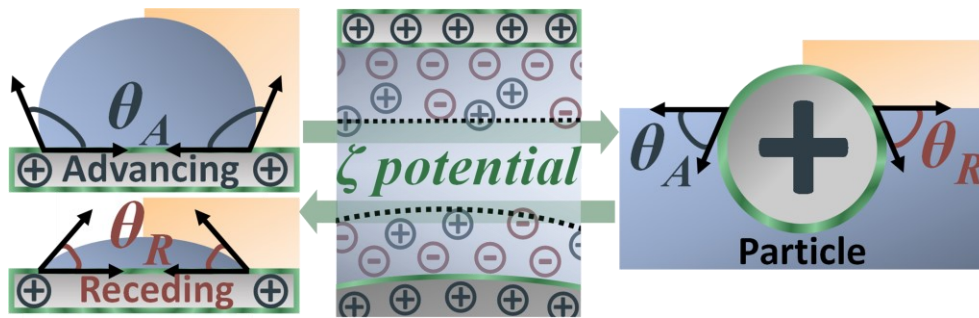
Graphical abstract 1 Particles reversibly adsorb in the presence of equally charged oil-soluble surfactants. Consequently, both components compete for interfacial coverage that depends on the surfactant concentration.

To substantiate the theoretical outcome, adsorption between smaller negatively or positively charged silica NPs with ODA is studied with high-resolution, *in situ* synchrotron-based X-ray reflectometry (XRR), which is analyzed and discussed jointly with dynamic interfacial tensiometry. The results indicate that negatively charged silica NPs only adsorb if the oil/water interface is covered with the positively charged lipid, indicating synergistic adsorption stimulated by the mutual electrostatic attraction. Conversely, the positively charged NPs readily adsorb independently but compete with ODA and reversibly desorb with increasing lipid concentrations. Furthermore, the analytical model proposed earlier indicates that an electrostatic exclusion zone (Δr) exists around the adsorbed particles that experience competitive adsorption ([Graphical abstract 2](#)). This zone prevents the adsorption of lipid molecules in this area leading to a decreased surface excess concentration of surfactants, unexpectedly high IFT, and accordingly decreased viscoelasticity for not too high lipid concentrations.



Graphical abstract 2 An electrostatic exclusion zone (Δr) is formed around the positively charged particles and prevents adsorption of equally charged lipids in this region.

The stability of particle-laden interfaces is linked to the wettability of the particles, characterized through their CA or water immersion depth, and is generally extrapolated from sessile drop-derived macroscopic contact angles (mCAs) on planar substrates. Owing to the nanoscopic resolution provided by XRR regarding the location of the NPs relative to the liquid interface and their interfacial coverage, an approach is tested to investigate whether sessile drops can adequately describe the wettability of NPs straddling at a liquid interface. The assumption that the NPs and macroscopic substrates are chemical equivalents is hypothesized when both surfaces feature the same electrokinetic (ζ) potential (Graphical abstract 3), substantiated with physical topographic analysis. This concept is tested on particles adsorbing to a pure air/water surface or oil/water interface without surfactants. Silica and amino-terminated silica NPs are compared to macroscopic surfaces with extremely low roughness (root mean square [RMS] roughness ≤ 2 nm) or a roughness determined by a close-packed layer of NPs (RMS roughness ~ 35 nm). Equivalence of the surface chemistry is assessed by comparing the electrokinetic potentials of the NPs *via* electrophoretic light scattering and of the macroscopic substrates *via* streaming current analysis. The wettability of the macroscopic substrates is obtained from advancing (ACAs) and receding contact angles (RCAs). Generally, the RCA on smooth surfaces provides a reasonable estimate of NP wetting properties. However, mCAs alone cannot predict adsorption barriers that prevent NP segregation to the interface, as is the case with the native SiO₂ nanoparticles. This strategy facilitates assessing the wetting properties of NPs for applications such as emulsion formulation, flotation, or water remediation.



Graphical abstract 3 The wettability of nanoparticles adhering to a liquid is predicted with greater accuracy on a macroscopic scale when both surfaces are chemically equivalent, measured through the zeta (ζ) potential.

List of abbreviations and symbols

<i>Symbol/ Abbreviation</i>	Description
A	Surface area
a	Radius of a sphere
A_c	Area of the oil/water interface occupied by the particle attached to the liquid interface
ACA	Advancing contact angle
AFM	Atomic force microscope
A_i	Total interfacial area
A_m	Area per molecule
A_P	Area per particle
APTES	(3-aminopropyl)triethoxysilane
A_{SF}	Area occupied by surfactant molecules
$A_{surface}$	Area of the liquid interface
A/W	Air/water
Å	Angstrom
ΔA	Change in area
A_0	Mean droplet area
b	Sessile drop base radius
b	Lateral particle radius
B_0	Bond number
C	Concentration
CA	Contact angle
C_N	Bulk particle concentration
c	Proportionality constant
c^0	Ionic concentration
CAH	Contact angle hysteresis
CTAB	Cetyltrimethylammonium bromide
D	Diffusion coefficient
d	Diameter
d_{eff}	Effective diameter of correlated domains within a particle
d_h	Hydrodynamic diameter
d_{layer}	Film thickness
DLS	Dynamic light scattering
DLVO	Derjaguin, Landau, Verwey, Overbeek
E	Electric field
e	Elementary charge
ECA	Equilibrium contact angle
ED	Electron density
E_i	Total free energy of the interface
ELS	Electrophoretic light scattering
E_m	Scaled electrophoretic mobility
EOS	Equation of state
E_{SF}	Energy contribution of the surfactant-covered interface
E_P	Energy contribution of one adsorbed particle
ΔE_{Ads}	Energy difference between surfactants and one adsorbed nanoparticle that occupy the same interfacial area
E_0	Dilational surface elasticity/Gibbs elasticity

$E^*(i\omega)$	Complex dilational viscoelasticity
E'	Elastic component dilation
E''	Viscous component dilation
F	Force
\mathcal{F}	Fourier transform
F_c	Faraday constant
FFR	Fast field reversal
FreeSCa	Freeze-fracture shadow-casting
G	Elastic modulus
g	Gravitational acceleration
GISAXS	Grazing-incidence small-angle scattering
GTT	Gel-trapping technique
ΔG_a	The free energy of particle attachment
ΔG_d	The free energy of particle detachment
G_s	The surface free energy of the system
G_γ	Gibbs free energy
G^*	Complex shear modulus
G'	Elastic shear modulus / Storage modulus
G''	Viscous shear modulus / Loss modulus
H	Hamaker constant
h	Drop height
h_{av}	Average immersion depth adsorbed particle
HCP	Hexagonal close-packing
HLB	Hydrophilic-lipophilic-balance
I	Ionic strength
IEP	Isoelectric point
I_i	Incident intensity
IFT	Interfacial tension
iQd	Interquartile distance
$I(Q_z)$	Reflected intensity
I_{str}	Streaming current
J	Joule
K	A function of the deformation amplitude of the interface
K_c	Particle-particle interaction constant
k	Boltzmann constant
k_i	Incoming wavevector
k_n	Wavenumber
k_r	Outgoing wavevector
kT	Thermal energy
kT/e	Thermal voltage
L	Characteristic length
l	Length
l_c	Capillary length
l_s	Long-range surface interactions
N	Newton
n	Number of molecules/particles
N_A	Avogadro's constant
$n_1/n_1/n_2/$	Refractive index of any phase/medium 1/medium 2
NG-ELS	Next generation electrophoretic light scattering
nm	Nanometer

N_{Max}	Number of particles for a hexagonally close-packed monolayer
N_P	Total number of particles adsorbed at the interface
NP	Nanoparticle
n_γ	Factor in the Gibbs equation
m	Meter
m/\bar{m}	Scaled ionic drag coefficients
mCA	Macroscopic contact angle
M3-PALS	Mixed mode-Phase Analysis Light Scattering
ODA	Octadecyl amine
-OH	Hydroxyl group
OHW	Ohshima, Healy, White
-OR	Alkoxy group
O/W	Oil/water
PBE	Poisson-Boltzmann equation
PDI	Polydispersity index
PF	Particle-covered film
$\Delta p^{Laplace}$	Young-Laplace pressure
Q	Total charge
q	Bragg wavevector dynamic light scattering
Q_c	Critical wave vector transfer
Q_{eff}	Effective electric charge
Q_z	Scattering vector X-ray reflectivity
R	Gas constant
-R	Alkyl group
RCA	Receding contact angle
r_e	Classical electron radius
$R_F(Q_z)$	Fresnel reflectivity
RMS	Root mean square
$R(Q_z)$	Reflectivity intensity
$R_{w/s}$	Water/TEOS ratio
R_0	Radius of curvature of the droplet at its apex
R_1/R_2	Radii of curvature
-R'	Functional group
Δr	Electrostatic exclusion zone
s_{av}	Average interparticle spacing
SC	Streaming current
SD	Standard deviation
SDS	Sodium dodecyl sulfate
SEM	Scanning electron microscopy
SF	Smooth film
SFR	Slow field reversal
SFT	Surface tension
SHG	Second harmonic generation
Si-OH	Silanol
Si-O-Si	Siloxane bond
SLC	Stagnant layer conduction
T	Temperature
TEM	Transmission electron microscopy
TEOS	Tetraethyl orthosilicate
TMOS	Tetramethyl orthosilicate

$U_{Capillary}(a)$	Capillary interactions
U_{EDL}	Electric double layer repulsive interaction potential
$U_{Electro}$	The total electrostatic interaction potential
U_{vdW}	van der Waals attractive interaction potential
$U(x)$	Total interaction potential
V	Volume
v	Velocity
$v/v\%$	Volume/volume percent
W	Work
W_a	Work of adhesion
W_c	Work of cohesion
W_s	Work of spreading
$w/w\%$	Weight/weight percent
$w/v\%$	Weight/volume percent
x	Separation distance between two objects
XRR	X-ray reflectivity
z	Direction perpendicular to the interface
z_i	Valence of ion i

<i>Greek letters</i>	Meaning or description
α	Phase α
α_a	Variation of drop area
α_c	Critical angle
α_i	Angle of incidence
α_r	Angle of refraction
β	Phase β
β_{XR}	Imaginary part refractive index
Γ_i	Surface concentration/interfacial excess
Γ_∞	Surface excess for saturated layer
γ	(true) Surface/interfacial tension
γ_{ij}	Surface stress tensor
γ_{lg}	Liquid-gas interfacial tension
γ_{lo}	Oil-water interfacial tension
γ_m	Mean surface tension
γ_{SF}	Equilibrium tension after adsorption surfactant
γ_{sg}	Solid-gas interfacial tension
γ_{sg}^{Av}	Average apparent surface free energy
γ_{sg}^{CAH}	Apparent surface free energy from contact angle hysteresis
γ_{sg}^{EOS}	Apparent surface free energy from equation of state
γ_{sl}	Solid-liquid interfacial tension
γ_{so}	Solid-oil interfacial tension
$\gamma(t)$	Dynamic surface tension
γ^*	(apparent) Surface tension after adsorption of species
γ_{12}	Surface tension between phases 1 and 2
γ_0	Initial surface tension
Δ	Finite variation or change of a quantity
δ_A	Phase angle of area change
δ_{ij}	Surface unit tensor
δ_{XR}	Real part refractive index

δ_γ	Phase shift of surface tension
$\dot{\epsilon}$	Strain rate tensor
ϵ_r	Dielectric constant/relative permittivity
ϵ_{xy}	Strain tensor
ϵ_0	Permittivity of vacuum
ζ potential	Zeta potential
$\bar{\zeta}$ potential	Scaled zeta potential
η	Viscosity
η_d	Dilational viscosity
η_{rel}	Viscosity ratio of the particle-laden interface to the clean interface
η_s	Dynamic viscosity
Θ	Interfacial particle coverage or density
Θ_{app}	Apparent particle coverage
Θ_{max}	Maximum 2D packing
Θ_C	Critical packing density
θ	Angle
θ_A	Advancing contact angle
θ_E	Equilibrium contact angle
θ_i	Line tension-corrected contact angle
θ_{io}	Contact angle oil-water
θ_P	Particle contact angle
θ_R	Receding contact angle
$\Delta\theta\%$	Contact angle hysteresis percentage
κ	Debye parameter
κ^{-1}	Debye length
A^0	Limiting conductance ions
λ	Wavelength
λ_{idc}	Ionic drag coefficients
λ_{XR}	X-ray wavelength
λ_0	Laser wavelength
μ	Electrophoretic mobility
μ_a	Linear absorption coefficient
μ_i	Chemical potential
μ_b	Chemical potential particles in bulk
μ_e	Entropic contribution
μ_{int}	Chemical potential particles at interface
μ_s	Shear strain
$\dot{\mu}_s$	Shear strain rate
Π	Surface pressure
Π_{coh}	Cohesion pressure
ρ	Material density
ρ_e	Electron density
ρ_w	Bulk water electron density
ρ_p	Bulk particle electron density
ρ_d	Bulk decane electron density
$\rho(z)$	Average electron density
$\rho_i(z)$	Electron density liquid interface
$\rho_{NP}(z)$	Electron density adsorbed particles

ζ	Detection angle dynamic light scattering
σ	Surface charge density
σ_i	Interfacial roughness
σ_{xy}	Stress tensor
σ_ζ	Electrokinetic charge density
τ	Line tension
τ_D	Delay time
τ_{el}	Elastic stress contribution
τ_{des}	Characteristic timescale of particle desorption
τ_{ij}	Surface extra stress
τ_s	Shear stress
τ_v	Viscous stress contribution
τ_0	Stress amplitude
τ^*	Yield stress
Φ	Volume fraction of particles in the bulk
ω	Angular frequency
ω_0	Available surface area of the solvent

1 Introduction

Parts of Chapter 1 have been published in *Langmuir*, 2019, DOI: [10.1021/acs.langmuir.9b01568](https://doi.org/10.1021/acs.langmuir.9b01568), *Langmuir*, 2021, DOI: [10.1021/acs.langmuir.1c00559](https://doi.org/10.1021/acs.langmuir.1c00559) and *Journal of Colloid and Interface Science*, 2021, DOI: [10.1016/j.jcis.2021.12.113](https://doi.org/10.1016/j.jcis.2021.12.113) and have been adapted with permission of the publishers *American Chemical Society* and *Elsevier*.

The ubiquitous occurrence of liquid interfaces covered with single and multiple adsorbents in a wide array of industries, ranging from oil^{1,2} and mineral³ processing to food technology,⁴ cosmetics,⁵ and drug delivery^{6,7} evolved into an impressive gallery of scientific findings with the goal of better grasping the underlying principles of particle adsorption in order to optimize the formulation design of long-lived particle-stabilized foams and emulsions,^{8–10} i.e., Ramsden-Pickering emulsions,^{11,12} or transient stabilization as found in froth flotation.^{13,14} A plethora of (responsive) particle-coated drop types and intricate three-dimensional shapes can be created by playing with a large number of variables, such as tuning the particle properties (e.g., size, shape, ‘soft’ or ‘hard’ surface, and wetting properties),^{15–20} adding constituents (e.g., salts, surfactants, proteins, and polymers)^{7,21–25} in varying volume fractions or concentrations, and manipulating environmental factors (e.g., solvent, temperature, pH, ionic strength, electromagnetic radiation, and liquid flow conditions).^{23,26–31} Thereby, the liquid interface acts as a versatile template for the self-assembly or removal of surface-active materials. The equilibrium composition (or interfacial concentration) is determined by their respective adsorption energies and the interactions between the adsorbents. The mechanism responsible for segregation of materials to the liquid interface can be clarified using adsorption thermodynamics and is practically relevant for industries.

The adsorption mechanism of a particular duo, namely small-molecule surfactants and solid particles, has received much attention owing to their prevalent use. Surfactants and solid particles differ in that the latter material does not need to be amphiphilic to adsorb, while the former has a high tendency to occupy the interface and continuously adsorb and desorb due to their low adsorption energy associated with their molecular size.^{32,33} Contrarily, the origin for strong particle attachment to the interface depends primarily on their wettability with the liquid(s), particle size, and interfacial tension. Particle entrapment causes a significant reduction in the interfacial free energy as more particles occupy the interface. Consequently, extremely small nanoparticles (< 5 nm) and/or very hydrophilic/hydrophobic particles remain mainly concentrated in the bulk phase.^{34,35} In this case, adding surfactants to tailor the properties of the liquid interface and/or of the particles can promote their adsorption, thereby inducing

(quasi-)irreversible interfacial particle entrapment.^{32,33} Alternatively, surfactants can destabilize the particle monolayer by forming cracks on the interface covered with close-packed particles and potentially cause particle redispersion into the bulk.³⁶⁻³⁹

Novel insights into the theoretical basis of (generalized) adsorption and equilibrium phenomena for multicomponent adsorption are conventionally gained from ‘simplified’ two-dimensional interfaces using surface-sensitive methods, such as measuring the interfacial tension or its variation before and after adsorption (i.e., surface pressure). Surveilling the interfacial properties of bulk phases with known composition makes it possible to elucidate each particular component’s role and combinations thereof. Direct application of this unprocessed data into theoretical (thermodynamic) models are highly desirable to predict the particle adsorption layer properties (i.e., interfacial concentration, contact angle or immersion depth, and lateral interactions).⁴⁰⁻⁴³ However, nanoparticles adsorbing at a quiescent liquid interface are presented with a highly complex energetical and topographical landscape that often convolutes such model formulation, owing to the superposition of the surface tension,⁴⁴ thermally-activated capillary waves,⁴⁵ viscoelasticity,⁴⁶ inhomogeneities of the particle surface,^{47,48} and lateral particle-particle interactions.⁴⁹⁻⁵² Moreover, it becomes experimentally more challenging to predict the monolayer properties when the particle size decreases, and sophisticated methods are necessary to provide sufficient detail. Consequently, only a handful of (semi-)quantitative surface pressure models for multiple adsorbents have been designed, as they are characterized by a complicated relationship between surface pressure and particle coverage. Additionally, the effective interactions between the adsorbents become harder to predict or validate at smaller length scales and a complete physiochemical picture of the particle-laden interface is missing, especially for multiple ‘surface-active’ adsorbents.⁵³⁻⁵⁵

This thesis contributes to the colloid and interface sciences and offers a fundamental understanding of the adsorption mechanisms between inorganic hydrophilic nanoparticles and oil-soluble surfactants at the oil/water interface. First, the difference in interfacial tension in the absence and presence of particles while varying the lipid concentration is used in an analytical model to estimate particle density at the liquid interface. Assuming that potential particle-surfactant interactions only occur at the liquid interface and are (electrostatically) unfavorable, the principle of additivity is applied to the theoretical construct. In other words, the total change in surface free energy induced by mixed particle-surfactant adsorption is divided into an individual contribution of the adsorbed lipids and the adsorbed particles. These observations are substantiated with high-resolution X-ray reflectometry, which further provides nanoparticle wettability by fitting a physically realistic model to the electron density

plot obtained by simulating the reflectivity curve. Finally, the wetting properties of nanoparticles adsorbed at the pristine air/water and oil/water interface are estimated using the conventional sessile drop method on macroscopic substrates, which are considered to be chemically equivalent to the particles when their electrokinetic properties are identical. The possible influence of surface roughness is accounted for by preparing surfaces with extremely low and higher roughness.

The content of this thesis is organized into 8 chapters, starting with the introduction in Chapter 1. Chapter 2 recaps the fundamental principles of colloid and interface science necessary to comprehend the relevant scientific background presented in Chapter 3. Several methods are discussed in Chapter 3 to determine particle wettability at liquid interfaces (section 3.1), followed by the macroscopic change particle adsorption may induce (section 3.2). Section 3.3 discusses the possible interactions inorganic particles and surfactants may experience at the liquid interface, followed by the aim and approach (section 3.4). Chapter 4 describes the methodology regarding material design (section 4.1.1), particle size and zeta potential characterization (section 4.1.2), and concluded with surface wetting characterization of colloidal particles and planar substrates (section 4.1.3). Chapters 5 to 7 include a brief introduction, experimental details, scientific outcome, and discussion that form the main results of this project. An analytical model is designed in Chapter 5 to estimate the number of adsorbed nanoparticles in the presence of surface-active lipids based on the surface pressure. A competitive adsorption mechanism between the two adsorbents is proposed, indicating that the particles reversibly adsorb. Subsequently, the model is validated using complementary X-ray reflectometry with nanoscopic resolution in Chapter 6. Here, negatively or positively charged particles with the positively charged lipid absorb either synergistically to form a close-packed monolayer or competitively by forming a surfactant-exclusion zone around the particles. Chapter 7 discusses how similar zeta potentials between colloids and substrates provide better overall control in estimating contact angles of nanoparticles adsorbed at an air/water surface or oil/water interface. A general conclusion of the presented work and outlook are given in Chapter 8.

2 Fundamentals of colloid and interface science

Parts of Chapter 2 have been published in *Langmuir*, 2019, DOI: [10.1021/acs.langmuir.9b01568](https://doi.org/10.1021/acs.langmuir.9b01568), *Langmuir*, 2021, DOI: [10.1021/acs.langmuir.1c00559](https://doi.org/10.1021/acs.langmuir.1c00559) and *Journal of Colloid and Interface Science*, 2021, DOI: [10.1016/j.jcis.2021.12.113](https://doi.org/10.1016/j.jcis.2021.12.113) and have been adapted with permission of the publishers *American Chemical Society* and *Elsevier*.

Systematic research on emulsion stabilization by combining particles and surfactants is simplified by studying adsorption phenomena of two-dimensional (mostly planar) interfaces formed by immiscible bulk phases. Surfactants reduce the interfacial tension and prevent flocculation and coalescence in emulsions combined with steric and/or electrostatic repulsion between surfactant films at droplet interfaces. Surfactants allow tailoring the final structure,⁸ stability,⁹ or flow behavior¹⁰ of emulsions/foams decorated with particles, and such additives are necessary to direct adsorption for particles exhibiting low affinity to the liquid interface. Although surfactant molecules readily diffuse to the interface, thermal energy fluctuations efficiently expel them towards the bulk phase and kinetic stabilization of droplets can only be achieved at surfactant concentrations close to the critical micelle concentration. In effect, a dynamic adsorption and desorption process of surfactants exists without a strong attachment to the interface (section 2.1).⁵⁶

Contrarily, spherical particles can become irreversibly trapped at the liquid interface which depends mainly on the interfacial tension (γ), particle size (radius a) and particle wettability. The wetting properties of the particles strongly influence their affinity to adsorb and are theoretically described by the three-phase contact angle (θ), which was first developed for an ideal smooth, planar substrate (i.e., zero roughness).⁵⁷ However, very large⁵⁸ or small^{59–64} particles deform the liquid interface due to gravitational and line tension effects, respectively. Most material surfaces have some degree of physical and/or chemical heterogeneity that induces contact line pinning due to capillary interactions.^{47,51,65} Additionally, particle wettability can be described by their immersion depth in the aqueous phase relative to the liquid interface (section 2.2).^{32,66} Adsorption of one particle in an equilibrium position is described by the change in interfacial free energy (G_γ) due to the decrease in surface area of the interface (A) upon particle adsorption and is thermodynamically related to the interfacial tension (γ) (section 2.3).^{15,17}

Based on this, one might expect that particle adsorption to a liquid interface is a clearly predictable process by tuning particle wettability and size. However, even particles with optimal properties can show cracks and voids in the monolayer, leading to coalescing droplets and phase

separation, i.e., unstable emulsions or foams. Therefore, the two-dimensional lateral interactions cannot be neglected. While the particle-laden interface bears some resemblance to the interaction forces between particles in the bulk (section 2.4), the phase boundary gives rise to surface-specific particle-particle and particle-surface interactions that help understand the complex behavior of particle-covered films on a deeper level (section 2.5).

2.1 Surface tension and surfactants

This first section covers the micro- (section 2.1.1.1) and macroscopic (section 2.1.1.2) description of a pure liquid surface followed by the mechanism of surfactant adsorption (section 2.1.2) and the Gibbs adsorption equation (section 2.1.2.1).

2.1.1 Surface tension and surface free energy

2.1.1.1 Microscopic origin of surface tension

Every liquid molecule experiences cohesive forces shared equally with its neighbors in a bulk liquid, where no net force exists. A bulk liquid adjoining a gaseous phase or immiscible liquid creates a boundary because the liquid molecules at the surface lack some binding partners above them due to adhesion. This region is referred to as the liquid surface or interface, respectively (Fig. 2.1A). Compared to the bulk state, an excess free energy is formed by the lack of binding partners. The arising net inward force tends to pull the water molecules into the bulk to minimize the number of molecules at the surface that virtually contracts the surface layer and puts it under tension. A considerable barrier is formed that resists deformation as the increase in the surface area requires energy because more molecules will be present in the unbalanced situation. This boundary layer is termed the surface tension at air/water surfaces or interfacial tension at immiscible oil/water interfaces.^{67,68} The enhanced lateral hydrogen bond interactions between pairs of water molecules at the surface cause minimization of the surface free energy.⁶⁹ Generally, liquids of higher polarity (stronger dipole, stronger Coulomb forces) exhibit stronger attractive forces and thus higher cohesive energy, boiling point, and surface tension.^{67,68}

The surface tension is not strictly located at the surface but arises within the first few molecular layers and is highly dynamic due to thermal motion (e.g., collision events, diffusion, and evaporation from and to the surface region). Thermal agitation and discreteness of the surface molecules consequently create in reality an unsharpened liquid surface, meaning that the density of molecules smears out over a small, finite region (Fig. 2.1B).^{67,68} For instance, the thermally activated capillary waves (height fluctuations of the liquid interface) carry the

entropy of the liquid surface with an amplitude not more than a molecular diameter ($d \sim 2.8 \text{ \AA}$ for water)⁷⁰ and define the interfacial thickness ($\sim 1 \text{ nm}$ wide for the air/water surface).⁷¹ This density decrease helps understand that surface energies act as tensions, i.e., tensile forces tangential to the surface. In the bulk, the minimum interaction potential $U(x)$ gives the average distance between molecules related to the bulk liquid's density (Fig. 2.1C). The molecules repeatedly bump into the repulsive potential barrier since liquids are very dense. In the surface region, a gradual increase in the average distance between adjacent molecules occurs. For separations slightly larger than d , adjacent molecules experience attractive forces. Averaged over the entire surface region leads to a net tensile force within the range of the density gradient that tries to reduce the surface area.

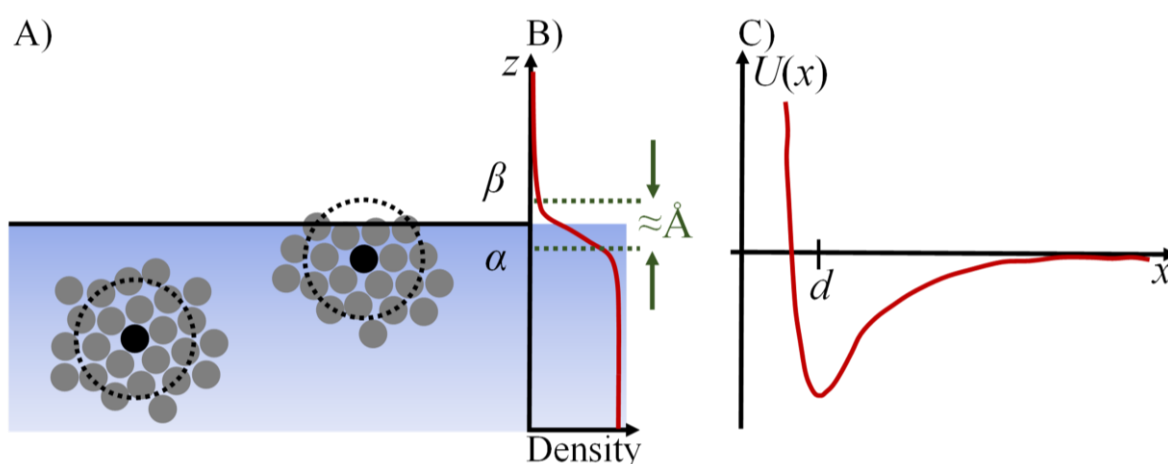


Fig. 2.1 A) Microscopic schematic of one specific liquid molecule (black dot) in phase α with the interaction range of the molecular forces surrounding it (dotted circle). The interacting neighbors (grey dots) for the bulk and surface molecule are different since no cohesive interactions are possible with molecules in phase β . B) The molecule density profile gradually decreases from phase α to phase β . The thickness of the surface/interfacial region is generally only a few angstroms wide. C) A generic molecular interaction potential, $U(x)$, when two molecules of diameter d come closer together (intermolecular distance x becomes smaller). Reproduced with kind permission by *John Wiley and Sons* from Mugele.⁶⁷

The water molecules' orientation at and near the air/water surface is well-ordered up to a 1 - 2 nm distance towards the bulk^{67,68} and insensitive to temperature variations measured between $\sim 7 \text{ }^\circ\text{C} - 57 \text{ }^\circ\text{C}$.⁷² However, higher temperatures increase the kinetic energy that enhances excitation of the capillary waves causing an increase in interfacial thickness that leads to a decrease in surface tension.⁷² In the case of replacing the gas phase with an immiscible oil, the same reasoning applies that the nonpolar oil and polar water molecules lack binding partners and are more strongly attracted to their own species.^{67,68} The interaction between oil and water molecules stems primarily from London dispersion forces (induced dipole-induced dipole),⁷³ and the thickness for alkane-water interfaces is about 4 - 6 \AA .⁷⁴

2.1.1.2 Macroscopic definition of surface energy and surface tension

The surface or interfacial layer can also be expressed in terms of a geometrical surface of uniform tension whose location is dependent on the distribution of the stress tensor within that layer. Contrarily to planar surfaces, this is especially true for curved surfaces where the surface tension is not uniquely defined because bending and torsion moments are involved.⁷⁵ Hence, emphasis is placed on planar/slightly curved surfaces characterized by a sharp boundary for simplicity. The surface tension is the mechanical force per unit length of the contour limiting the interface between two (or more) phases ($\gamma = F/2l$, N m⁻¹) or the work required to create an interface unit ($\gamma = \delta W/dA$, J m⁻²), where N m⁻¹ = J m⁻². While the first definition may seem unintuitive, the second energy term is easily understandable from a microscopic view. As all surface molecules exhibit an energy excess compared to the bulk ones, creating more surface area (A) while keeping the number of molecules (and density) constant implies a transfer of bulk molecules to the surface. Work needs to be performed against the molecular interaction forces and is stored as additional surface energy in the total Gibbs free energy G_γ of the system.^{67,68} It can be defined as a product with the thermodynamic conjugate variable, A , and as a partial derivative:^{67,68,76-78}

$$G_\gamma = \gamma A, \quad \gamma = \left(\frac{\partial G_\gamma}{\partial A} \right)_{T,P,V,n} \quad \text{Eq. 2.1}$$

Thus, the surface tension is the increase in Gibbs free energy per increase in surface area at constant temperature (T), pressure (P), volume (V), and the number of molecules (n). The book chapter written by Moradi⁷⁹ provides a complete thermodynamic description of liquid interfaces. Eq. 2.1 provides a convenient relation between γ and G_γ in an equilibrium state since the natural variables pressure and temperature are constant in most applications. The energetic cost due to the existence of a liquid surface/interface, G_γ , means the system drives to minimize the amount of surface area. Liquids will minimize the surface area to volume ratio by adopting the lowest geometrical energy state, which is why liquid drops form spheres. This is what happens during coalescence, where multiple tiny spherical droplets merge into larger ones and are governed by the Young-Laplace equation for capillarity (see section 4.1.4.1).^{67,68,76,78}

2.1.2 Mechanism of surfactant adsorption

Vigorous mixing of water with air or oil to form bubbles or droplets quickly leads to phase separation, based on their polarity difference quantified by the dielectric constant (ϵ_r), e.g., highly polar water ($\epsilon_r^{20^\circ\text{C}} = 80.4$) and nonpolar gas ($\epsilon_r^{20^\circ\text{C}} = 1$) or oil ($\epsilon_r^{20^\circ\text{C}} = 2 - 3$).⁸⁰

Stable mixtures can be achieved by the addition of surfactants. A surfactant molecule derives its name from “surface-active agent” and is usually an organic, amphiphilic compound containing two distinct regions in its chemical structure. The lipophilic ‘tail’ and hydrophilic ‘head’ of opposite polarity will orient their corresponding ‘body parts’ in the preferred continuous phase. Their preference to adsorb at the gas/liquid, oil/liquid, and solid/liquid interface originates from their amphiphilicity. Adsorption of surfactant to the gas/liquid and oil/liquid interface replaces some surface water molecules (i.e., creates a unit of area). This action reduces the tensile force of the liquid surface because the attractive forces between two water molecules are stronger than between a surfactant and a water molecule. Hence, they are sometimes referred to as tensides. Contrarily, adsorption to a solid/liquid interface does not replace surface molecules. Adsorption generally occurs through physisorption *via* weak electrostatic van der Waals forces or hydrogen bonding, chemisorption *via* covalent or ionic interactions, or combinations of them. The structure of the hydrophobic and hydrophilic moieties varies widely in chemical groups, chain length, or bulkiness, and are conventionally categorized based on their charge characteristics as anionic, cationic, zwitterionic, or nonionic.⁵⁶ Furthermore, each can be classified numerically on the hydrophilic-lipophilic-balance (HLB) scale (non-ionic⁸¹ and ionic surfactants⁸²) to determine their preferred oil or water solubility.

A general surfactant adsorption mechanism occurs as follows.⁸³ A freshly formed surface or interface is initially surfactant-free and characterized by the pure air/water or oil/water tension since a finite time is required to establish equilibrium.⁸⁴ The bulk surfactant molecules need time to migrate towards the subsurface region by Brownian diffusion.⁸⁵ This subsurface region is a geometrical plane that can act as a potential barrier to adsorption. For example, the electric double layer of the liquid surface influences approaching ionic species⁸⁶ or possibly due to the hydrophobic effect in the case of nonionic species.^{87,88} Subsequently, the surfactant molecules penetrate the adsorption layer and arrange themselves at the interface. Relaxation mechanisms, such as reorientation and solvation/desolvation, start taking place at the surface.⁸⁹ During these surface enrichment and relaxation stages, the surface tension is ‘dynamic’ and continuous to decrease until achieving a ‘stable’ plateau value. The surface free energy reduces to a minimum as a function of interfacial coverage (i.e., related to the bulk surfactant concentration). When achieving equilibrium, simultaneous ad- and desorption of surfactant molecules into the bulk and/or mass transfer into the opposite phase will continue.⁸³ The formation of a surfactant monolayer may exceed 10^3 s when convective transport in the liquid is absent.⁸⁵ Beyond monolayer formation, surfactants exhibit

a minimum in lowering the surface tension when plotted on a surface tension versus log concentration curve, despite further increases in concentration (Fig. 2.2). This point is the ‘critical micelle concentration’ (CMC) and the monomers in solution assemble into a supramolecular structure, orienting their hydrophobic/hydrophilic parts outwards to form inverse/normal-phase micelles if they are soluble in a nonpolar/polar solvent.⁸³ The CMC corresponds to a single concentration with a narrow transition region where micelles start to form below CMC and the monomer concentration reaches its maximum above CMC.⁹⁰ When surfactant solutions contain impurities, a significant minimum appears on the plot that gradually disappears as the impurity dissolves in the micelles above CMC. This is the case for technical-grade nonionic surfactants, which show a broader molecular weight distribution owing to their degree of ethoxylation,⁹¹ and with ionic surfactants that are partially hydrolyzed.^{92–94}

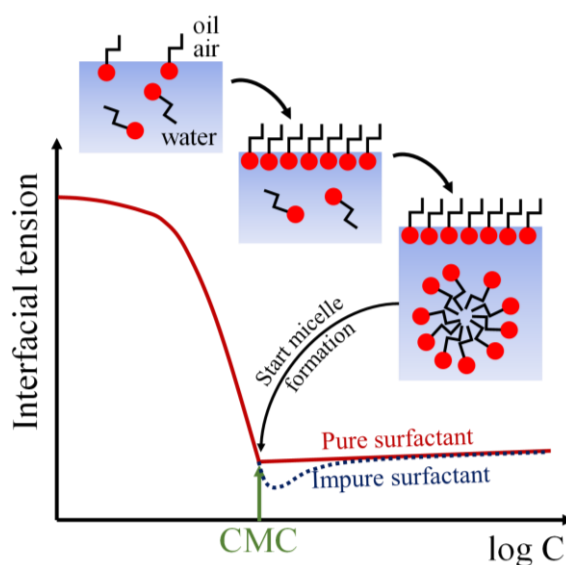


Fig. 2.2 Surface tension versus log concentration (C) plot. The surface tension decreases when more surfactant is added to the system and organizes itself at the interface. The most significant decrease indicates the critical micelle concentration (CMC). This point is where micelles begin to form, and the interfacial tension remains relatively constant for pure surfactant solutions (full line). Conversely, when the surfactant contains impurities (dotted line), a liquid tension minimum exists that normalizes to its pure form as the impurities are incorporated in the growing number of micelles.

2.1.2.1 The Gibbs adsorption isotherm

As early as 1878, Gibbs⁹⁵ derived a differential equation to estimate the area a surface-active adsorbent occupies at the interface from the relation between the surface tension, the number of molecules, and the chemical potentials (μ_i) of the i -th solute at the liquid surface:⁹⁵

$$d\gamma = - \sum_i \Gamma_i d\mu_i \quad \text{Eq. 2.2}$$

where Γ_i is the surface excess concentration and is approximated by the number of molecules per unit area ($\Gamma_i = n/A$). A quick glance at Fig. 2.1B shows that the interface has a nonzero thickness, meaning that Γ_i depends on the location of the dividing surface which is a mathematical plane of zero thickness. The relative surface excess quantity is invariant to the reference plane, but its derivation and adaptations lie beyond the scope of this work.^{68,79,96–98} The Gibbs equation (Eq. 2.2) allows calculating the concentration of molecules at the interface to extract the area one molecule occupies at the interface from measuring the surface tension, as in Fig. 2.2. For ideal systems where the chemical potential obeys the relationship $\mu_i = RT \ln C_i$ (bulk concentrations (C) of the order ~ 1 mM), the Gibbs adsorption isotherm for one adsorbent is:⁹⁵

$$\Gamma_i = - \frac{1}{n_\gamma RT} \frac{d\gamma}{d \ln C_i} \quad \text{Eq. 2.3}$$

where R is the universal gas constant, and n_γ is 1 for nonionic surfactants and 2 for ionic surfactants in the absence of electrolyte. Polynomials of the best fit before CMC are used to calculate the surface excess. However, an accurate fit implies measuring many different concentrations and can be a time-consuming process. A recent study by Martinez-Balbuena et al.⁹⁸ confirmed the applicability of Eq. 2.3 for several ionic and nonionic surfactants after some authors cast doubt on using this method to estimate the surface excess concentration. The slope from the plot in Fig. 2.2 is used to calculate the area per molecule (A_m) in \AA^2 and is only valid for saturated surface layers:^{99,100}

$$A_m = \frac{10^{20}}{N_A \Gamma_i} \quad \text{Eq. 2.4}$$

where N_A is Avogadro's constant. Exceptions exist, so additional methods are recommended when high accuracy is required, such as very sensitive neutron reflectivity experiments. Many detailed extensions of the Gibbs equation are still in development. Similarly, a wide variety of published work related to the branch of surfactant adsorption kinetics (non-equilibrium conditions) is not discussed in depth.^{101–103}

2.2 Wetting of substrates and particles adsorbed to liquid interfaces

Per definition, wetting involves the intermolecular interactions between contacting liquids and solids described by the three-phase contact angle and surface free energy of the solid (section 2.2.1).

2.2.1 Three-phase contact angle

Interfacial phenomena arise when the different states of matter (i.e., solid, liquid, gas, or immiscible oil) touch each other. They meet at the three-phase contact line and are motionless for a system in equilibrium. The tangential forces are balanced because of the interfacial tensions between each boundary (Fig. 2.3). With the formation of the triple line, wettability is conventionally assessed by measuring the angle through the more polar liquid phase, which can be liquid droplets placed on a solid substrate (section 2.2.1.1) or, for smaller objects, by determining their position relative to the liquid surface upon adsorption (section 2.2.1.2).

2.2.1.1 Young's equation for sessile drops on a planar solid surface

In 1805, Young⁵⁷ quantitatively related the most stable or equilibrium contact angle (θ_E) of a sessile drop deposited on an ideal, planar surface by vectorial summation of the three interfacial tensions that intersect at the three-phase point, namely the solid-gas (γ_{sg}), solid-liquid (γ_{sl}), and liquid-gas (γ_{lg}) interfacial tensions (Fig. 2.3A):^{104,105}

$$\cos \theta_E = \frac{\gamma_{sg} - \gamma_{sl}}{\gamma_{lg}} \quad \text{Eq. 2.5}$$

An important implication of measuring the contact angle is determining the surface free energy of the solid, defined as the excess energy at the surface compared to the bulk material or the energy required to create new surface area and is considered the surface tension of a solid. The surface free energy of the solid-gas interface, γ_{sg} , dictates how liquids will wet the surface, γ_{sl} . Depending on the surface energy of the surface, different models are preferred, such as Zisman,¹⁰⁶ Owens-Wendt-Rabel-Kaelble (OWRK),¹⁰⁷⁻¹⁰⁹ Oss-Good,¹¹⁰ and Wu.¹¹¹ The Neumann equation of state uses only one solvent by ignoring the different (polar and nonpolar) interaction components and gives approximate energies compared to the other models.^{112,113} If $\gamma_{sg} > (\gamma_{sl} + \gamma_{lg})$, this is characteristic of a solid with high surface energy. Suppose Young's equation indicates $\cos \theta_E = 1$ and $\theta_E = 0^\circ$. In that case, complete spreading of the hydrophilic liquid occurs and is termed as a superhydrophilic solid. Conversely, complete dewetting occurs when the hydrophilic liquid touches a superhydrophobic solid in a single point with a corresponding contact angle of 180° . Solids with contact angles of 90° using a hydrophilic liquid are termed intermediately wetting.^{104,105}

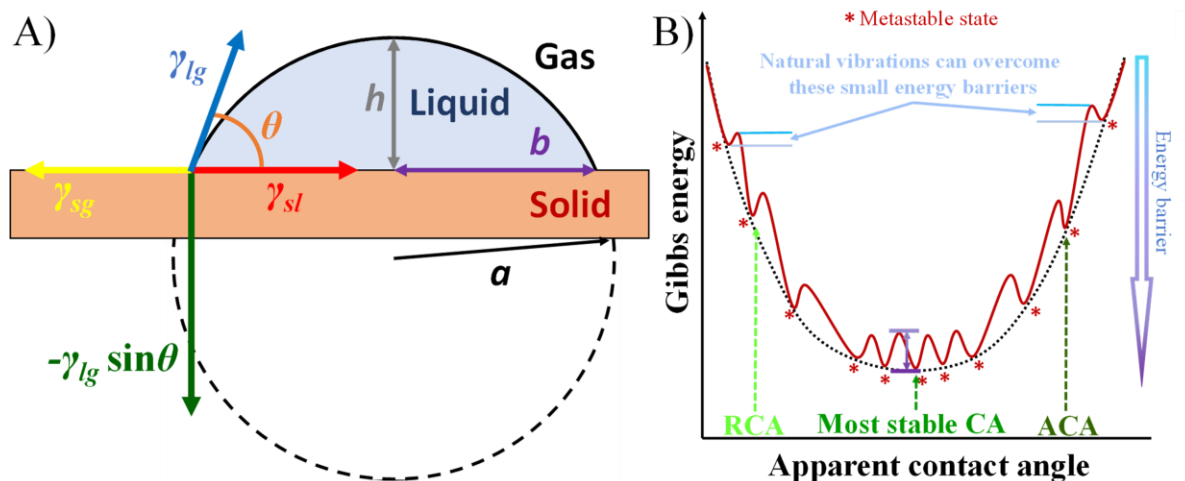


Fig. 2.3 A) An equilibrated, liquid sessile drop on a substrate allows the acquisition of the contact angle (θ). Other parameters are h for drop height, b is the drop base radius, a is the radius of the sphere, γ_{sg} , γ_{sl} , and γ_{lg} are the solid-gas, solid-liquid, and liquid-gas interfacial tensions. Reproduced with kind permission of *Elsevier* from Erbil.¹⁰⁵ B) The apparent contact angle as a function of the Gibbs free energies of ideal (black dotted line) and real (red line) wetting at the solid-gas-liquid intersection. In the ideal case, the most stable contact angle or equilibrium contact angle is measured as the system has only one free energy minimum. The most stable contact angle is located at the global minimum free energy for real surfaces. Still, it has several local free energy minima corresponding to metastable contact angles with increasing energy barriers. A deposited 'static' drop can be trapped in any of these free energy minima within the hysteresis range owing to the energy barrier between the local free energy minima. As it cannot be directly determined at which minima a static drop is located, the method of advancing (ACA) and receding contact angles (RCA) is preferred. Reproduced with kind permission of *Elsevier* from Drelich.¹¹⁴

However, the definition of the contact angle and the one measured on solid surfaces are likely not the same. The former assumes that the liquid wets an ideal surface that is rigid, atomically smooth, and chemically homogenous with zero contact angle hysteresis. In other words, in the ideal case, only one thermodynamically stable contact angle exists for a specific liquid (Fig. 2.3B, most stable contact angle). The irregularities on real surfaces, such as surface defects, impurities, adsorption, coating defects, etc., cause contact line pinning. This generally leads to varying solid-gas interfacial tensions, γ_{sg} , under equilibrium conditions that consequently affect the force balance at the triple line in Young's equation.¹¹⁵ Therefore, more than one equilibrium contact angle exists on every surface, which are non-equilibrium or 'apparent' contact angles that reflect different local free energy minima (Fig. 2.3B, red line). Stringent control of well-documented experimental parameters and conditions is necessary.^{116–118} In practice, measuring the advancing and receding contact angles is an established method to improve reproducibility (section 4.1.3.1).^{104,105,117,118} Consequently, calculated surface free energies of the solid based on the static or advancing/receding contact angle method are also apparent ones,¹¹⁹ especially since other experimental techniques and theoretical models measure approximately tenfold higher surface energies.¹²⁰ Contact angles also show a drop size

dependency, especially for extremely small droplets where gravity effects are neglected.^{121,122} This dependency is explained by the existence of line tension (τ), which arises from an imbalance of the intermolecular forces within the three-phase contact line and results in excess free energy of the molecules located at or close to this contact line. Gibbs¹²³ already pointed out that in submicron-sized systems, an additional force term may distort the macroscopic contact angle due to the increased curvature of the contact line. For a spherical droplet on an ideal surface, Eq. 2.5 can be rewritten as:^{124,125}

$$\cos \theta_i = \cos \theta_E - \frac{\tau}{\gamma_{lg} b} \quad \text{Eq. 2.6}$$

where θ_i is the actual contact angle, and b is the drop base radius. Theoretically, calculated line tension values lie in the range of 10^{-11} and 10^{-12} N and can be positive or negative in sign, but disagree with experimentally derived numbers that lie around 10^{-6} N.^{61,126,127} Two length scales play a prominent role here, namely the capillary length (l_c) and the long-range surface interactions (l_s):¹²⁸

$$l_c = \sqrt{\frac{\gamma_{lg}}{\Delta\rho g}} \quad \text{Eq. 2.7}$$

$$l_s = \theta_E^2 \sqrt{\frac{H}{6\pi\gamma_{lg}}} \quad \text{Eq. 2.8}$$

where $\Delta\rho$ is the density difference, and g is the gravitational acceleration. The capillary length of water is around 2.71 mm in air/water and is closely related to the Bond number:¹²⁹

$$Bo = \frac{\Delta\rho g L^2}{\gamma_{lg}} \quad \text{Eq. 2.9}$$

This dimensionless parameter, where L is a characteristic length, indicates if gravitational forces ($Bo > 1$) or surface tension forces ($Bo < 1$) dominate. This number determines droplet shape, i.e., a puddle forms in the center of the drop with decreased drop height or drops exhibit a spherical cap shape, respectively, and consequently the contact angle.¹³⁰ The long-range forces operate at a length scale below $\sim 1 - 10$ nm and can be ignored in conventional sessile drop experiments using microliter volumes.¹²⁸

To account for surface roughness, Wenzel¹³¹ and Cassie-Baxter¹³² originally developed theories by incorporating the interfacial area within the contact perimeter in case liquid penetrates the surface grooves or creates air pockets underneath the liquid, respectively. However, the solid and liquid interactions at the three-phase contact angle alone determine the

advancing and receding contact angles (and hysteresis) measured on rough and chemically heterogeneous surfaces.^{104,133,134} The main reason for inadequate use of the Wenzel and Cassie equations is that, unlike liquid molecules, solid molecules at the surface are immobile and cannot contract spontaneously to minimize their surface area, which leads to a non-equilibrium surface structure. Therefore, surface tension and surface free energy of solids are not equal and prohibit the applicability of the laws of capillarity for liquids to solids.^{135,136} Currently, no adequate theory exists on the effect of the length, density, and shape of the three-phase contact line concerning apparent contact angles. The community awaits the contribution of experimentalists and theoreticians in this area.^{104,105} In the absence of improved theoretical considerations for actual surfaces, concise protocols were (recently) designed for the uniform application of sessile drops based on Young's equation (Eq. 4.13).^{117,118}

2.2.1.2 Immersion depth for a spherical particle trapped at the liquid surface

A similar triple point is generated at the solid-liquid-gas intersection when a solid, spherical particle adsorbs at the air/water surface or is trapped at the interface between two immiscible liquids. Young's equation (Eq. 2.5) is equally valid for an ideal solid surface equilibrated at a planar, liquid interface (Fig. 2.4A) and a particle adsorbs when the right-hand term of Eq. 2.5 has a magnitude of less than one, in order for the contact angle to exist (or $|\gamma_{sl}-\gamma_{sg}| < \gamma_{lg}$). Alternatively, the contact angle of a spherical particle can be determined from the water immersion depth (h) of the particle relative to the liquid surface.^{32,66}

$$\cos \theta_p = \left(\frac{h}{a}\right) - 1 \quad \text{Eq. 2.10}$$

where θ_p is the particle contact angle, and a the radius of the spherical particle. Eq. 2.10 requires exact knowledge of the position of the particles and becomes experimentally more challenging for smaller nanoparticles. Using Eq. 2.5, hydrophilic particles ($\theta < 90^\circ$) tend to stabilize oil-in-water emulsions, while hydrophobic particles ($\theta > 90^\circ$) stabilize water-in-oil emulsions. When the volume fraction of the continuous phase (Φ_1 , phase 1) is equal to or smaller than the dispersed phase (i.e., containing the particles; Φ_2 , phase 2), hydrophilic particles stabilize oil-in-water emulsions and hydrophobic particles stabilize water-in-oil emulsions. When $\Phi_2 > \Phi_1$, flocculation or destabilization occurs. Catastrophic phase inversion depends on the volume fraction and theoretically occurs when $\Phi_2 = \Phi_1$, thereby abruptly altering the type of energetically favorable emulsion.¹³⁷ Experimentally, for hydrophilic and hydrophobic silica nanoparticles ≤ 100 nm in diameter and a number of different oils, phase inversion from oil-in-water to water-in-oil is observed at higher Φ_1 , e.g., $\Phi_1 = 0.7$.¹³⁸

Similar concerns exist in describing the wetting behavior of an adsorbed particle based on Young's equation in real systems. Gravitational forces can be neglected for particles smaller than $\sim 5 \mu\text{m}$, and the liquid interface can be considered flat but only up to the three-phase contact angle (Fig. 2.4B).¹³⁹ Rather than a single equilibrium contact angle for a collection of particles, a distribution of apparent particle contact angles is generally observed.^{140–142} Additionally, line tension effects seem to affect the adsorption of particles $\leq 100 \text{ nm}$ and these forces become very prominent for spherical particles smaller than 20 to 40 nm in diameter. The corrected contact angle can be estimated from Eq. 2.6 (where b corresponds to the lateral particle radius), assuming that the particle-laden liquid interface is in mechanical and thermal equilibrium.^{59–64} For intermediately wetting particles (i.e., 90°), Eq. 2.5 and Eq. 2.6 provide similar results as the line tension is almost perpendicular to the liquid interface since the tangential component of τ is very small.^{143,144} The tangential component of τ is relatively high for particles with contact angles further away from 90° . It achieves a maximum contribution at the wetting extremes, where particle adsorption is promoted or opposed (i.e., adsorption barrier) for negative or positive line tension, respectively.^{61,62} However, the sign's origin and the actual magnitude of line tension (estimated 1 – 100 pN) are not fully elucidated, similar to sessile drops.⁶¹ Line tension increases for particle shapes that deviate from spheres as this contributes to the contact line length in relation to the particle volume.⁶⁰

The contact line on the surface of porous and rough particles can attain an asymmetric shape compared to smooth, nonporous particles. This causes irregular wetting and can alter the particle contact angle due to different pinning/depinning phenomena of the contact line on the surface of adsorbed particles.⁷⁷ Chemical heterogeneities and/or surface roughness can cause significant pinning of the contact line reflected as large contact angle hysteresis. Pinning due to the surface roughness of adsorbed microparticles arrests their adsorption in long-lived metastable states. When the surface roughness is high, particle wettability can be inverted irrespective of their chemical nature due to the large hysteresis. Rough particles can stabilize oil-in-water and water-in-oil emulsions for intermediate pinning without modifying their wettability.¹⁴⁵ Particle wetting is likely determined by the particle radius and shape, the area fraction of their surface in contact with the liquid phases, and the interfacial tension between the solid and liquid phases.¹⁴⁶

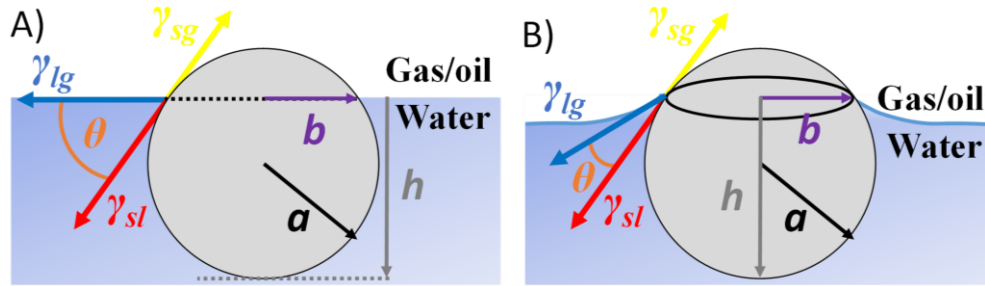


Fig. 2.4 A) Schematic view of an ideal solid particle adsorbed at a planar, liquid surface showing the balance of the vectorial interfacial forces that determine the contact angle (θ) in equilibrium, where a is the particle radius, h the immersion depth in the aqueous phase, and b the lateral radius of the adsorbed particle. B) Interacting particles adsorbed at the liquid interface have physical and/or chemical inhomogeneities on their exterior, causing nonuniform wetting and deformations of the liquid surface in the vicinity of the three-phase contact line.

2.3 Free energy of detachment for a spherical particle

Ramsden¹¹ and Pickering¹² were the first to study spontaneous, strong particle attachment to a liquid surface. Particles adsorbing spontaneously to an air/water surface or oil/water interface are surface-active, but not necessarily due to their amphiphilic nature like surfactants (i.e., Janus particles).¹⁴⁷ Pieranski¹⁴⁸ observed irreversible adsorption of 245 nm-sized spherical polystyrene particles at the air/water surface and proposed they are trapped in a deep surface energy well. The theory was extended by Levine et al.³⁴ and the following paragraph has been described in the book by Binks.³² The adsorption behavior of particles at the air/water surface is mainly determined by their wettability, which is influenced by the surface tension of the liquid. At oil/water interfaces, adsorption is determined by their partial wetting with both liquid phases. For simplicity, a hypothetical small particle sits in equilibrium (i.e., to obey Young's equation, the θ is a constant value) at the undeformed, planar oil/water interface and the surface free energy of the system (G_s) is at its minimum (Fig. 2.4A):³²

$$G_s = \gamma_{lo}A_{lo} + \gamma_{pl}A_{pl} + \gamma_{po}A_{po} \quad \text{Eq. 2.11}$$

where γ and A are the interfacial tension and the area of the oil/water (lo), particle/water (pl), and particle/oil (po) interfaces. The sum of the latter two areas equals the particle's total surface area (A_p). Measuring the change in surface free energy ΔG is quickly done by determining the surface free energy after its detachment from the interface and complete immersion into the nonpolar phase (G_o):

$$G_o = \gamma_{lo}A_{lo} + \gamma_{po}A_{po} \quad \text{Eq. 2.12}$$

where A_{lo} is the area of the flat oil/water interface after detachment and A_{po} is the total particle surface area, in this case. Subtracting Eq. 2.11 from Eq. 2.12 and taking into account Eq. 2.5

and that $A_P = A_{pl} + A_{po}$, the free energy of particle detachment into the oil (ΔG_{do}) and aqueous phase (ΔG_{dl}) are:

$$\Delta G_{do} = \gamma_{lo}(A_c + A_{pl}\cos\theta) \quad \text{Eq. 2.13}$$

$$\Delta G_{dl} = \gamma_{lo}(A_c - A_{po}\cos\theta) \quad \text{Eq. 2.14}$$

where A_c is the area of the oil/water interface occupied by the particle attached to the liquid interface. The relationship between the two free energies of particle detachment is expressed as:

$$\Delta G_{do} = \Delta G_{dl} + \gamma_{lo}A_P\cos\theta \quad \text{Eq. 2.15}$$

Consequently, the energetic cost to detach a hydrophilic particle ($\cos\theta > 0$) into the oil is higher than into the water phase ($\Delta G_{do} > \Delta G_{dl}$) and is opposite for a hydrophobic particle. When $\theta = 90^\circ$, both energies are equal to each other and help understand the stabilization of emulsions by adsorbed solid particles. The free energy of particle detachment (ΔG_d) is the minimum energy required for particle detachment irrespective into which bulk phase, i.e., ΔG_{dl} for $0^\circ \leq \theta \leq 90^\circ$ and ΔG_{do} for $90^\circ \leq \theta \leq 180^\circ$. Particle attachment (ΔG_a) is governed by the same equations with opposite signs. The general form of the equations stated above is valid for any particle shape if the liquid interface is considered flat up to the particle surface. For a spherical particle, the three-phase contact line is a circle with radius $a_c = a\sin\theta$ dividing the particle surface (with area $A_P = 4\pi a^2$) into two spherical caps. Therefore, $A_c = \pi(a\sin\theta)^2$ and $A_{pl} = 2\pi a^2(1 + \cos\theta)$ and substituting into Eq. 2.13 and Eq. 2.14 give:

$$\Delta G_{do} = \pi a^2 \gamma_{lo} (1 + \cos\theta)^2 \quad \text{Eq. 2.16}$$

$$\Delta G_{dl} = \pi a^2 \gamma_{lo} (1 - \cos\theta)^2 \quad \text{Eq. 2.17}$$

And combined:

$$\Delta G_d = \pi a^2 \gamma_{lo} (1 - |\cos\theta|)^2 \quad \text{Eq. 2.18}$$

It is common to replace ΔG_d with ΔE_P for adsorption energy. For particles with homogeneous surface chemistry, the reduction in interfacial energy associated by replacing the oil/water interface with a single particle in its equilibrium position is calculated by considering geometry and surface tension alone. Typical values range from $1 - 10^3 kT$ (k is the Boltzmann constant, T is the absolute temperature, and kT is the thermal energy) for nanometer-sized particles^{149,150} up to $10^6 kT$ for microspheres¹⁵¹ due to the quadratic dependence of the particle size on the adsorption energy. Microparticles are considered irreversibly adsorbed even at interfaces with extremely low surface tension (Fig. 2.5).^{152,153} This is in stark contrast with surfactant molecules, which continuously ad- and desorb due to their small adsorption energies

in the range of $1 - 20 kT$.^{32,33} This reversible attachment-detachment behavior can also occur for nanoparticles, and the transition lies around $20 - 50 kT$ ¹⁶ up to $100 kT$.^{45,154,155} Since the energy of particle attachment to a liquid interface is negative ($\Delta G_d = -\Delta G_a$), particle adherence is thermodynamically favorable for sufficiently large particles (≥ 20 nm, smooth, and chemically homogenous) to ignore line tension safely.^{32,52,156} This is the main reason why chemically homogenous particles can spontaneously adsorb to the liquid surface and obtain their surface activity since part of the liquid interface with area A_c is removed upon their adsorption (Eq. 2.13 and Eq. 2.14).

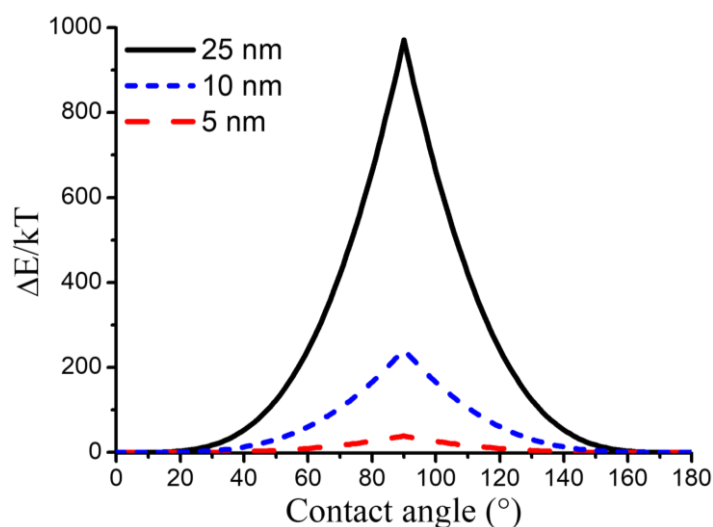


Fig. 2.5 Minimum free energy of detachment for 5, 10, and 25 nm spherical particles plotted against the three-phase contact angle with a surface tension of 50 mN m^{-1} .

2.4 Interaction forces between colloidal particles in solution

A brief discussion is given on the interaction forces arising between colloidal particles dispersed in a liquid medium based on the DLVO theory named after its inventors Derjaguin B., Landau L., Verwey E., and Overbeek T.

2.4.1 DLVO interactions: attractive and repulsive contributions in a continuous medium

The original DLVO theory provides a simplistic and unobscured explanation for the stability of colloids based on several assumptions. It deals with long-range forces only and its essential physics was designed in actuality for lyophobic colloids. Many ‘non-DLVO’ forces contradict the original theory because of the development of sophisticated technologies to study interaction forces for all kinds of systems. Nevertheless, its foundation is solid to demonstrate aggregation of suspensions. It describes the force between charged surfaces interacting through a liquid medium (e.g., assuming that the bulk properties of the liquid extend to the solid

surface). The approximate free energy per unit area can be modeled by the additive contributions of the van der Waals attraction (U_{vdW}) and the electric double layer repulsion (U_{EDL}) between planar substrates, spheres, and a combination of them:^{157–159}

$$U(x) = U_{vdW}(x) + U_{EDL}(x) \quad \text{Eq. 2.19}$$

Van der Waals forces result from the interactions of the fluctuating or rotating dipoles of atoms and molecules resulting in an attractive force and are almost always present in all states of matter. For small separation distances between two spheres with smooth surfaces and radius (a), the nonretarded van der Waals interaction can be modeled in its simplified form as:^{160,161}

$$U_{vdW}(x) = -\frac{Ha}{12(x-2a)} \quad \text{for } (x-2a) \quad \text{Eq. 2.20}$$

When the spheres are separated at larger distances, more time is required for the light-induced fluctuations to travel from one atom to the other and is thus retarded. The retardation effect is a correction factor that lowers the estimated van der Waals interaction potential. The interaction decays rapidly at larger separation until it reaches a certain limit:^{160,161}

$$U_{vdW}(x) = -\frac{H2a^2}{3x^2} \quad \text{for } (x \gg 2a) \quad \text{Eq. 2.21}$$

where H is the Hamaker constant that defines the strength of the interaction in the range of $10^{-21} - 10^{-19}$ J and is in most cases positive reflecting its attractive character. With the addition of increasing electrolytes, these values may slightly decrease. At smaller distances, enhanced surface roughness may lower the interaction potential.^{157–159}

Electric double layer interactions are essential for charged surfaces, especially at low salt concentrations. The unscreened solid surface can establish significant surface charge densities (σ), ranging from 0.1 to 1 $e \text{ nm}^{-2}$. Ions in the polar phase are attracted to the charged particle surface bearing the opposite sign, thereby reducing or screening the particles' surrounding effective charge. The interaction-free energy from the double layer interactions between two identical spherical particles bearing the same charge can be expressed as:^{162,163}

$$U_{EDL}(x) = \frac{Q^2}{4\pi\epsilon_0\epsilon_r(1+\kappa a)^2} \frac{e^{-\kappa(x-2a)}}{x} \quad \text{Eq. 2.22}$$

where Q is the total charge on the particle surface, ϵ_0 the permittivity of vacuum, ϵ_r the relative permittivity, and κ the inverse Debye length, defined as:¹⁶³

$$\kappa^{-1} = \sqrt{\frac{\epsilon_0\epsilon_r RT}{2c^0 z_i^2 F_c^2}} \quad \text{Eq. 2.23}$$

where R is the gas constant, T is the absolute temperature, c^0 is the ionic concentration, z_i^2 the valency of the ion type, and F_c^2 the Faraday constant. The electric double layer free energy formula is valid when the surface charge density is low and for sufficiently large surface separations. The interaction energies can be calculated by applying the Debye-Hückel theory. For higher surface charge densities, the Poisson-Boltzmann theory is applicable.¹⁶³ Fig. 2.6 summarizes the various interactions described above and the effect variations in electrolyte concentration and/or pH have on the potential.

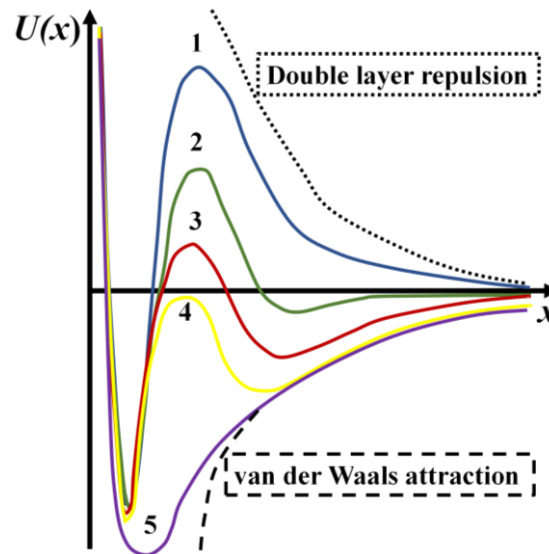


Fig. 2.6 Schematic DLVO plot for the additive effect of the van der Waals attraction and the double layer repulsion on the total interaction potential, $U(x)$, between two charged surfaces in an aqueous solution with increasing electrolyte concentration (1 to 5). Changing the pH and/or electrolyte concentration influences the surface charge density (σ) on the solids between highly charged (1) and very low charge or uncharged (5).

2.5 Particle interactions at the liquid surface

The adsorption process itself is more complex since the particles must overcome an adsorption barrier, which originates from the total interaction potential (e.g., van der Waals and electrostatic interactions) between the particles and liquid interface and controls the organization and dynamics of the particles within the interface. Interfacially trapped particles can act as a (physical) barrier to suspended particles as the probability of occupying some free interfacial area decreases when increases in coverage. However, confined particles experience several interface-specific forces giving rise to particle-particle interactions that can be attractive or repulsive.^{20,164,165}

Particle-particle interactions at the liquid surface differ from bulk interparticle interactions. However, they show similar behavior to a 2D system, governed by the areal density (i.e., particle-particle distance) and interaction potentials of the particles. The particle

ensembles are restrained to a fluctuating boundary separated by two phases that generally differ significantly in density, ionic strength, and permittivity.^{76,77} Such phase anisotropy creates various effects that are difficult to quantify because several physicochemical aspects such as particle size, shape, wettability, surface chemistry, and electrical potential, each show a unique behavior.^{76,77,166–169} A detailed quantitative description of these effects^{32,59,164,167,169} is beyond the scope, and a general overview of particle-particle interactions is addressed here. Garbin et al.¹⁶⁴ describes that the adsorption and desorption balance is dependent on the particle's chemical potential differences of adsorbed particles (μ_{int}) and those that are freely moving in the bulk (μ_b).¹⁶⁴

$$\Delta\mu = \mu_{int} - \mu_b \quad \text{Eq. 2.24}$$

Therefore, adsorption occurs when $\Delta\mu < 0$ and desorption in the opposite case. The chemical potentials of the particles in the bulk and interface include entropic, enthalpic, and wetting contributions:¹⁶⁴

$$\Delta\mu(\Phi, \Theta) = \Delta E_P + \mu_i(\Phi, \Theta) + \mu_e(\Phi, \Theta) \quad \text{Eq. 2.25}$$

where ΔE_P , μ_i , and μ_e define the particle wettability, particle interactions, and entropic contribution, respectively. Φ is the bulk particle volume fraction, and Θ is the particle coverage at the interface. By introducing ΔE_P (Eq. 2.18), the influence of the contact angle on the energetic landscape is taken into account. Particles trapped at a liquid interface reduce their translational degrees of freedom, representing the unfavorable entropic contribution represented by μ_e . All interactions occurring between particles at the interface are captured by μ_i (e.g., van der Waals, electrostatic, capillary) and originate from the interparticle coupling.¹⁶⁴

2.5.1 van der Waals interactions

Contrarily to the van der Waals interactions for particles in the bulk, particles adsorbed at the interface are surrounded by two media that can differ significantly in physicochemical properties. By taking into account the volume fraction of the particle in either phase, an apparent Hamaker constant is defined, which thus depends on the particle wettability.^{76,77} The average nonretarded van der Waals interaction between two particles adsorbed at the liquid interface is approximated as:^{59,168,170,171}

$$U_{vdW} = -\frac{H}{12} \left(\frac{2x}{a-2x} \right) \quad \text{Eq. 2.26}$$

where x is the interparticle distance. The van der Waals interaction energy between a spherical particle and a flat surface can be expressed as:

$$U_{vdW} = -\frac{Ha}{6x} \quad \text{Eq. 2.27}$$

where x is the distance between the particle edge and the surface and is a valid expression irrespective of the theoretical approach used to determine H . The corresponding Hamaker constant is positive in bulk, and therefore, van der Waals interactions are attractive. At the liquid interface, van der Waals attraction and repulsion are possible depending on the dielectric properties of the three media.^{165,171} In general, the van der Waals interactions have minimal influence ($0.1 - 1 kT$) and play only a role when interparticle distances become very small.⁵⁹ This is uncommon due to the prevalent repulsive contributions, but van der Waals interactions appear stronger for interfacial particles than particles dispersed in the bulk.^{20,59,172}

2.5.2 Electrostatic interactions

2.5.2.1 Charge of the liquid interface

Electrostatic interactions between a suspended particle and the liquid interface emerge since the latter also accumulates excess counterions that build an electric double layer. Several experimental studies indicated that the charge of the air/water and oil/water interface is negative, but the existence and origin of this charge remain controversial. For instance, electrophoretic mobility (μ) measurements in pure, surfactant-free oil drops dispersed in water bear a negative charge that is neutralized when the pH decreases. Water molecules preferentially orient their oxygen atoms toward the oil phase. This directional ordering causes the exposed hydrogen atoms of interfacial water molecules to selectively adsorb hydroxide ions.¹⁷³⁻¹⁷⁷ The air/water and oil/water interface for respective air bubbles and oil droplets is mobile, contributing to surface conduction, especially at low ionic strength. A significant underestimation in calculating the ζ potential occurs when using the Smoluchowski¹⁷⁸ approximation. The conduction-corrected surface complexation model developed by Leroy et al.¹⁷⁹ showed more negative ζ potentials for air bubbles of older reports but had similar trends as a function of pH and ionic strength. Specifically, adding inorganic electrolytes to water lowers the ζ potential of the air/water interface with an isoelectric point at pH 3-4 independent of bubble size.^{177,180}

Alternatively, a second theory for the origin of the negative charge stems from charge transfer along hydrogen bonds and asymmetries in the hydrogen bond network due to topological defects both at air/water and oil/water interfaces.^{181,182} Computed surface charge densities at both interfaces are approximately $-0.016 e \text{ nm}^{-2}$, similar to electrophoretic mobility measurements. Contrarily to the air/water surface, the oil side attains a negative charge due to

some spillage of electron density, which makes the water phase right below the interface positively charged.¹⁸² Nevertheless, Larson-Smith et al.¹⁸³ observed that adsorption of positively charged particles is favored over negatively charged particles to the oil/water interface. This preference further supports the idea that the charge of the native liquid interface is negative. Moreover, the addition of cationic or anionic surfactants can render the surface charge of the liquid surface positive or negative, respectively.¹⁸⁴

2.5.2.2 Electrostatic interactions between particles at the liquid interface

Charged colloids floating in the polar phase with typical surface charge densities of 0.1 to 1 $e \text{ nm}^{-2}$ attract oppositely charged ions on their surface to renormalize the effective charge surrounding the particles.^{162,163} Upon breaching the particle through the liquid interface and exposing part of its solid exterior to the nonpolar gas or oil phase, the consequent asymmetric charge distribution forms strong electrostatic dipoles (Fig. 2.7A).¹⁸⁵ These interparticle dipole-dipole interactions operate over long distances ($1/x^3$) and are strongly repulsive that can induce 2D colloidal crystal formation with separation distances of several particle diameters.¹⁴⁸ The nature and origin of this interaction force are still a source of controversy, specifically what happens to the charges on the particle surface facing the nonpolar phase. The system follows the expected behavior at the air/water surface. Here, ion pairs in low dielectric media recombine to neutralize any bare charges since these are energetically very expensive (Fig. 2.7B). It remains unclear if some charges remain trapped on the low dielectric particle surface adsorbed to the oil/water interface.^{76,186–190}

Throughout the aqueous phase, a short-ranged exponentially decaying repulsive force exists ($1/x$) due to the overlap of the asymmetric, diffuse ion clouds (Coulomb force) and raises the adsorption barrier against suspended particles (Fig. 2.7A).^{186,190} The total electrostatic interaction potential ($U_{Electro}$) for two hard spherical particles at the oil/water interface combines the long-ranged dipole-dipole interactions and the short-ranged screened Coulomb interaction:¹⁹¹

$$U_{Electro} = \frac{v_1 kT}{3x} e^{-\kappa x} + \frac{v_2 kT}{x^3} \quad \text{Eq. 2.28}$$

where x is the center-to-center interparticle distance, and v_1 and v_2 are parameters that determine the role of the screened Coulomb potential and the dipolar interaction, respectively. The dipolar interaction predominates at sufficiently large interparticle distances ($\kappa x \gg 10$). The relative strength of the dipole-dipole and Coulomb forces depends on their actual immersion depth, surface charge densities, and electrolyte in the water, which in turn controls the 2D colloidal

aggregation state.^{76,77} For example, more hydrophobic particles confined at the liquid surface experience a weaker electrolyte dependency. They can form well-ordered monolayers in the presence of 100 mM salt in the aqueous phase. In contrast, more hydrophilic particles form disordered, aggregated monolayers even in the absence of salt.^{192–195} Adding electrolyte^{28,30,196} or altering the pH to lower the surface charge densities^{28,197,198} can promote particle adsorption from suspension by electrostatic screening. Interestingly, the water immersion depth of negatively/positively charged particles trapped at the air/water surface increases/decreases for higher salt concentrations, respectively.^{199,200}

2.5.3 Capillary interactions

Of all interactions due to particle confinement to the interface, capillary ones most likely have the most decisive impact on the energetic landscape.⁷⁷ Adsorbing particles may deform the liquid surface by their attachment or from contact line pinning and the interaction strength depends on the relative particle orientation and interparticle distance.⁴⁷ From a thermodynamic point of view, long-ranged capillary interactions arise due to the formation of a meniscus because the system tends to minimize its surface area.⁷⁶ A vertical force on the liquid interface imposed by an adsorbed isotropic particle is required to form a meniscus around it, which can occur when the interface and particle are charged or when they have distinct material densities.^{51,201,202} In the first case, capillary interactions are negligible for weak electrostatic interactions or in the second case for small particles.^{76,77} When big particles are used ($> 5 - 10 \mu\text{m}$), flotation forces arise due to significant deformations induced by gravity and buoyancy forces combined with the particle wetting properties (Fig. 2.7C).⁵⁸ For particles smaller than the capillary length of the liquid surface (Eq. 2.7) or $Bo \ll 1$ (Eq. 2.9), flotation forces can be safely ignored. The weight of particles below $5 - 10 \mu\text{m}$ is too light to induce significant deformation of the liquid interface.⁷⁷ Still, capillary interactions play a substantial role in smaller particles because of the physical and/or chemical anisotropy present on most applied material surfaces.^{47,51,65} For example, even a 1% deviation from sphericity causes dendritic or hexagonal-lattice type micron-sized particle aggregation because of the nonuniform contact lines.²⁰³ In this smaller size regime ($< 5 \mu\text{m}$), the wetting properties of the particles mainly determine the immersion forces. The capillary forces exist due to a nonuniform contact line, i.e., undulation along the contact line or other irregular shapes around a particle's perimeter (Fig. 2.7D).^{47,51,65} Overlapping of the respective interface deformations from a collection of adsorbed particles determines if neighboring particles are attracted or repelled,

which in turn is dependent on the local curvature of the interface. For sufficiently large interparticle distances ($\gg a$), $U_{Capillary}(a)$ can be expressed as:⁴⁷

$$U_{Capillary}(a) = -12\pi\gamma K^2 \zeta \frac{x^4}{a^4} \quad \text{Eq. 2.29}$$

where K corresponds to the amplitude of deformation, ζ is a term that depends on the relative particle orientation, and x is the distance between particle centers. For separation distances on the order of the particle radius, higher multipole order effects come into play.⁵²

Charged colloids segregated to the interface can experience direct electric repulsions, electrocapillary forces, and electro-dipping forces originating from the different permittivities of the two surrounding phases.⁶⁴ When the liquid interface around an adsorbed colloid is deformed by the electrostatic force of its neighboring particles, electrocapillary forces induce long-range capillary attraction.^{49,185} Electro-dipping forces arise on single particles as the dielectric constant differences of the surrounding phases create an electrostatic pressure that deforms the liquid surrounding the particles and is balanced on the charged particle towards the higher dielectric constant medium.⁵⁰ These interactions may induce interfacial deformation comparable to that resulting from the flotation forces in bigger particles.^{167,204}

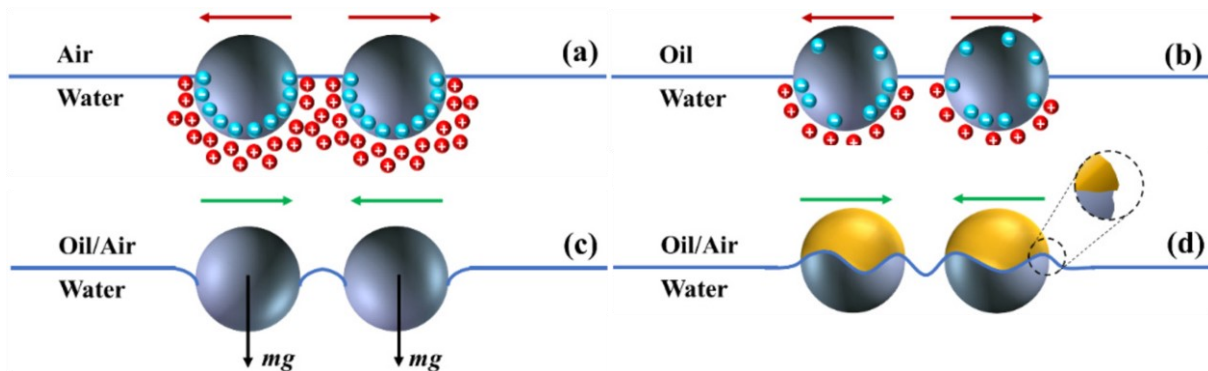


Fig. 2.7 Possible interparticle interaction forces at the liquid interface. A) Repulsive dipole-dipole interactions arise due to the dissociation of surface groups; B) Long-ranged repulsive interactions may arise from trapped water on the particle surface in the oil phase; C) Gravitational forces deform the liquid interface for heavy particles and generate attractive capillary interactions; D) Surface roughness and/or chemical surface heterogeneity can cause contact line undulations that result in capillary interactions. Figure reused with kind permission of the *Multidisciplinary Digital Publishing Institute* from Correia et al.²⁰⁵

2.5.4 Other types of interactions

Hydrophobic interactions appear to minimize the unfavorable particle-solvent contacts and become essential when the particle size approaches the length scales of the solvent.^{77,206,207}

Steric interactions, e.g. stemming from polymer additives adsorbed or grafted to the surface, occur when overlapping polymer chains between two particles cause an increase in osmotic

pressure that leads to enhanced repulsion. Particle aggregation is prevented in this way because compression of the solvated chains is entropically unfavorable. Depending on the nature of the polymer, particle monolayers can be obtained with tunable interactions.^{77,164,208} The chains of water-soluble polymer particles protruding from the interface will stretch out throughout the subsurface region to minimize the energetic cost. Depending on the length of the polymer chain, significant separation distances can be created between particle centers.²⁰⁹ Alternatively, soft and deformable particles, such as microgels, can significantly alter their shape upon adsorption, dependent on their areal density²⁰ or the tension of the liquid interface,²¹⁰ and present a special class that will not be discussed further.

2.5.5 Interactions induced by external influences

When particles are trapped at the liquid interface, this does not implicate they remain in the same interfacial location. Instead, diffusive motion occurs predominantly parallel to the liquid interface. This in-plane diffusion tends to become slower when their wettability increases. Simulations of trapped particles show a significant slowing down of their rotational diffusion when contact line fluctuations occur due to partial wetting dynamics (i.e., pinning/depinning phenomena).^{211–213} Furthermore, a reduction in the detachment force is predicted when there is a finite contact angle hysteresis between the particle and the liquid.²¹⁴ At high particle coverage and the emergence of hexagonal structures, the diffusion also decreases because of caging effects.²¹⁵ Experimental observations of nanoparticles trapped at the oil/water interface indicate a slowing down of their in-plane diffusion, mostly evident for liquids with identical viscosities (e.g., decane/water).^{216,217} Their interfacial mobility allows manipulations of the interfacial plane by mechanical deformation to induce 2D phase transitions. Examples are expansion/compression cycles to change the interfacial area (i.e., dilational deformation) or its shape (i.e., shear deformations).^{218–222} Furthermore, adjusting environmental conditions (e.g., pH, ionic strength, or temperature) or applying external magnetic/electric fields modifies the assemblies and interactions of responsive particles.^{76,77}

3 State-of-the-art

Parts of Chapter 3 have been published in *Langmuir*, 2019, DOI: [10.1021/acs.langmuir.9b01568](https://doi.org/10.1021/acs.langmuir.9b01568), *Langmuir*, 2021, DOI: [10.1021/acs.langmuir.1c00559](https://doi.org/10.1021/acs.langmuir.1c00559) and *Journal of Colloid and Interface Science*, 2021, DOI: [10.1016/j.jcis.2021.12.113](https://doi.org/10.1016/j.jcis.2021.12.113) and have been adapted with permission of the publishers *American Chemical Society* and *Elsevier*.

The previous chapter elaborated on the underlying principles of the adsorption of surfactant and particles to a liquid interface, indicating that particles can be stuck at the interface owing to their high adsorption energy, which depends on the interfacial tension, the particle size, and their wetting properties. This latter property may be deduced from contact angle measurements using large droplets on planar substrates, i.e., the sessile drop method. However, this method operates at larger length scales and does not provide information on specific particle-particle and particle-surface effects. Determination of particle contact angles at the liquid interface is therefore preferred. Depending on the method, it may capture extra information on the physicochemical foundations of particle-laden interfaces (section 3.1).

As the particle size decreases, the sophistication required to measure the particle properties at the interface increases. Fortunately, particle adsorption can also be measured with a more affordable and feasible scientific apparatus by monitoring macroscopic variables such as interfacial area (A) and liquid tension (γ). The measurement provides “mean-field” data that averages over the whole interface from which the behavior of single particles can be inferred, providing insights into the physical foundations of particle adsorption and rheological properties of the interface. However, nearly close-packed particle-laden interfaces tend to form a viscoelastic surface layer, giving rise to additional stresses other than surface tension and, in most cases, deviating from the thermodynamic predictions.^{223–225} Such interfaces contribute to droplets' bulk stability and rheology by two additional mechanisms. The first is mechanical protection from coalescence by forming a protective shell. Its strength and ability to mitigate coalescence depend on the particle contact angle.²²⁶ Hence, interfacially trapped particles can stabilize these emulsions at relatively low particle concentrations and possess enhanced long-term stability compared to exclusively surfactant-covered interfaces.³³ Secondly, the capability of the interfacial microstructure to resist deformation is dictated by interparticle forces^{215,227} that depends highly on the overall physicochemical properties of the particle-laden interfaces (section 3.2).

Binary or multicomponent mixtures of surfactants, particles, and/or other additives are ubiquitous in the academic and industrial setting and a thorough understanding of their

interactions and psychochemical characteristics has received increased attention in the last few decades. However, accurate determination of these properties on the nanoscale is complicated by the limited available experimental and computational approaches along with considerable variability in particle materials (e.g., size, shape, wettability, etc.),¹⁵⁻¹⁹ the spectrum of environmental conditions (e.g., solvent,^{23,26,27} pH,^{28,29} ion concentration^{28,30} or the presence of surface-active impurities⁹³), and the often unique interplay between sets of surfactants and particles.^{7,21-23} Combinations of water-soluble and/or -insoluble particles and surfactants provide a diverse array of well-defined systems to scrutinize mixed adsorption behavior, which can alter the rheological properties of the interface significantly (section 3.3). Following this literature review, the aim and approach of this thesis are given in section 3.4.

3.1 Determination of particle adsorption layer properties at liquid interfaces

The most studied properties of particles assembled at the liquid interface are their structure formation and immersion depth relative to the interface or three-phase contact angle. Particle-laden interfaces are often studied after reaching equilibrium, as it is not easy to study adsorption kinetics in detail. Estimating particle wettability, i.e., the particle contact angle is pivotal in unraveling the intricate factors that harness particle adsorption to a liquid interface. However, the colloid and interface science community has no standardized approaches, and the exact determination of particle dynamics and contact angles is challenging.^{76,77} The current techniques can be divided into visualization (section 3.1.1) and indirect methods (section 3.1.2).

3.1.1 Visualization methods

Visualization methods include techniques that are capable of directly determining the contact angle of particles confined at the liquid surface. A handful of different microscopy techniques are available to study single-particle interfacial properties by determining the absolute position of the particles and their immersion depth in order to retrieve the contact angle (section 3.1.1.1). Physically trapping the particles and subsequent microscopy investigation of a relatively large fraction of the interface allows for studying the wetting properties of individual particles and as an ensemble (section 3.1.1.2).

3.1.1.1 Microscopy techniques to study individual particle properties

In recent years, real-space imaging to map each particle's spatial and temporal position is on the rise to study both the structure and dynamics of particle assemblies in localized regions.

The individual wetting properties of single particles adsorbed to the liquid surface can be obtained by assorted noninvasive *in situ* microscopy techniques by determining the particle protrusion distance relative to the interface and has the benefit of directly observing the dynamic nature of the particle-interface interactions on a quiescent liquid surface with realistic contact angle distributions. The minimum particle size that can be studied depends on the resolution of the applied method. In digital holographic microscopy, trajectories of nonfluorescent microspheres dispersed in the water or oil phase are recorded using two lasers as they approach and breach the oil/water interface, which generates a hologram that captures the particle position in three dimensions. Equilibrium contact angles were extracted from an equation of motion for the height of the particle that reproduces a logarithmic trajectory. After adsorption, a logarithmic relaxation time was observed for all particle materials exhibiting different sizes and surface chemistry. They related to transient contact line pinning/depinning originating from topographical features inherent to colloidal particles, such as surface roughness. This out-of-equilibrium behavior is the most prominent in aqueous polymer particles (100 s or more), while lipophilic polymeric particles and hydrophilic silica equilibrate much faster (approximately < 0.1 s).^{228,229} Bessel beam microscopy provides nanometer-scale resolution for 10 nm to a few micrometer-sized nonfluorescent particles to their 3D position. Thousands of adsorbed particles can be visualized simultaneously. The method's dynamic nature showed that 1 μm polystyrene latex particles have contact angles following a normal distribution with a relatively large standard deviation of 19.3° . This more significant than previously observed distribution has severe ramifications for particle-laden interfaces as they are typically 2D in their interactions. However, the height variations observed here ($\sim 20\%$ of particle diameter) suggest otherwise, i.e., the nonmonotonic contact angle creates a 3D system on the interface. Suppose such a distribution range is present in Pickering emulsions. It will influence the interfacial rheology and the mechanical protection against coalescence and requires a fundamental reconsideration regarding the interparticle and particle-interfacial forces.¹⁴⁰ Interface point accumulation for imaging in nanoscale topography (iPAINT) exploits noncovalent and continuous labeling of all present interfaces with photoactivatable fluorescent probes. Gas/liquid/solid interface coloring allows simultaneous visualization of adsorbed nanoparticles while reconstructing the liquid interface.^{198,230,231} A nonnegligible contact angle dependency ascribed to the particle size dispersity ($\sim 330 \pm 19$ nm) and possible chemical heterogeneities were observed for both hydrophilic ($59.5^\circ \pm 6.9^\circ$) and hydrophobic ($111.5^\circ \pm 7.0^\circ$) silica particles.²³¹ Only a modest contact angle distribution was observed, compared to the study above by Snoeyink et al.¹⁴⁰ An effective line tension of 10^{-9} N was

inferred with the iPAINT approach that agrees with other experimental studies on single colloids adsorbed at liquid interfaces,^{39,62,142,229,232–234} and no significant aging of the contact line was noticed over four hours.^{198,230,231} Additionally, the method allowed to capture interfacial deformations upon adsorption of anisotropic particles²³¹ and examine the effect of environmental changes (e.g., pH) on the particle wettability.¹⁹⁸ However, the possible influence of the dyes on the wetting properties must be considered.⁷⁷

Electron microscopy techniques are very suitable for studying structural aspects of particle dynamics in the nanometer range, such as *in situ* transmission electron microscopy (TEM). The dispersion is encapsulated in a liquid cell and liquid evaporation under the high vacuum imaging conditions is avoided by utilizing silicon nitride windows.^{235,236} Nanoparticle attachment, rearrangement, and reorientation to nanodroplets (10 – 15 nm) dispersed in solution and coalescence of those particle-covered nanodroplets could be resolved in this manner.²³⁷ Cryo-TEM allows studying the spatial distribution of particles adsorbed to emulsified droplets.²³⁸ One has to consider that beam damage to organic matter and particle-cell wall interactions may influence the dynamics. Alternatively, *in situ* SEM allows single-particle imaging without interfacial perturbations using nonvolatile ionic liquids.⁷⁶ The high spatial and temporal resolution allowed visualization of particle positions and their lateral movement at the liquid surface for differently shaped particles and/or various surface chemistries.²³⁹

Recently, *in situ* AFM of particles adsorbed at the oil/water interface provides high lateral resolution in real space for topographical evaluation of the assemblies and time-resolved dynamics of adsorption. The technique remains challenging since liquids do not support shear forces (i.e., the liquid flows or deforms with minimal shear, easily caused by the cantilever) and imaging requires the presence of an interfacial thin film. Due to the widespread applicability of the AFM, these developments are promising in extracting accurate particle contact angles, distribution, and areal density as well as adsorption dynamics aiding in the design and fabrication of responsive assemblies.^{30,240–242}

3.1.1.2 Trapping techniques to study particle ensembles

Historically, the structure of particles assembled into monolayers studied by *ex situ* electron microscopies involved transferring the particles to a substrate at constant surface pressure (i.e., Langmuir-Blodgett films). The disadvantage is that significant alterations in the structure occur at low particle coverage due to capillary forces during sampling and solvent drying, and disruption of close-packed monolayers during transfer.^{243,244} This issue can be

tackled by solidifying one of the liquid phases and trapping the adsorbed particles. Consequently, part of the particle surface protrudes the interface and this height can be measured afterward from simple geometrical considerations and their topography investigated with scanning electron microscopy (SEM) and/or atomic force microscopy (AFM).⁷⁷ In the gel trapping technique (GTT), the aqueous phase (50 °C) is enriched with a not surface-active gelling polysaccharide. The particles are dispersed in a spreading agent, which aids in their transfer to the air/water surface. Upon cooling down to room temperature, the aqueous phase solidifies and adsorbed particles remain trapped at the gelled surface. A replica is formed by adding polydimethylsiloxane (PDMS) on top and subsequently visualized with SEM/AFM. The GTT applies to both air/water and oil/water interfaces.^{233,234,245,246} The increased temperature of the liquids (related to the boiling point of hydrocarbons and adsorption dynamics), possible interactions between particles and gelling agent due to comparable molecular length scales for small nanoparticles, and significant perturbations of the liquid interface may modify the position of the particles and influence particle adsorption/desorption.

Alternatively, introducing *n*-butyl cyanoacrylate via the gas phase entraps particles spread at the air/water interface (tested for particle sizes between 225 nm – 4890 nm) due to anionic monomer polymerization initiated by contact with water. Nucleophilic surface groups can also initiate polymerization to form a thin membrane, such as hydroxyl and amino groups. The temporal evolution of the polymer film grows exclusively towards the aqueous phase and does not influence the lateral particle arrangement or contact angle.¹⁴¹ Deposition of a metal film by a reducing agent, initiated by the aqueous phase, on spread colloids at the air/water and oil/water interface allows tracing the three-phase contact line of the grown nanofilm. The particles are transferred to a substrate, visualized with SEM, and the contact angle is calculated from geometrical relations. This method is applicable with different coatings as long as the deposited nanofilm/nanoparticles on the adsorbed colloids provide sufficient contrast in the SEM and for not too small adsorbing nanoparticles.²⁴⁷ The minimum particle size that can be investigated in these methods has not been studied but is limited to particle sizes not too close to the thickness of the coating.

Spreading of particles on a liquid surface using a volatile solvent shows a contact angle dependency because the solvent adsorbs between the nano-/micropores of the particle surface. Volatile solvents significantly alter the wettability of the particulate material and can even make hydrophilic particles hydrophobic.^{233,248,249} Freeze-fracture shadow casting (FreSCa), only applicable to oil/water interfaces, can measure contact angles for self-assembled particles down to 10 nm in size. The liquid interface is formed in a cell, clamped and instantly frozen by

a jet freezer ≤ 1 ms), fractured and unidirectional metal-coated with roughly 4 nm thick tungsten at a specified oblique angle. The contact angles are calculated from the particle diameter, projected particle height, and shadow length during observation in the cryo-SEM. The accuracy has been cross-compared with other techniques. However, concerns exist regarding the perturbation of the liquid interface before jet freezing, and the freezing itself could change the vertical position of the particles from their original location. Also, contact angles of very hydrophilic particles cannot be determined since the lowest accessible casting angle is 30° . While it is a time-consuming process, analyzing large sample regions allows evaluating the heterogeneity of the contact angle distribution and consequently the particle packing density (Θ).^{18,39,142,145,250–252}

3.1.2 Indirect methods

Indirect methods generally give average values of all adsorbed particles by relating a theory to the particle contact angle. The most common approach to estimate the wettability of particles adsorbed to a liquid interface is with the sessile drop method on planar, macroscopic substrates having the same physical and chemical composition as the particles. A liquid droplet is deposited on a flat substrate and the contact angle is measured with a goniometer.¹¹⁷ As discussed in section 2.2.1.1, the nonideal nature of most surfaces mandates researchers to rely on measuring the advancing and receding contact angles. In the case of a hydrophilic particle, the advancing and receding angles correspond to the particle approaching the interface from the air/oil phase and when the particle adsorbs from the aqueous phase, respectively.^{128,253} Attempts were made to directly measure the wetting properties of particles assembled on planar substrates via spin coating, dip coating, or Langmuir-Blodgett type transfer of particles assembled at the liquid interface.^{254–258} The liquid interface acts as a template for single or multicomponent colloids to self-assemble into organized patterns on relatively large scales.^{64,259–261} However, the sessile drop approach neglects the role of surface roughness,¹⁴⁵ curvature,²⁶² particle rotation,²¹⁴ and line tension⁶¹ on the particle contact angle. In the case of hydrophilic surfaces, surface contamination by airborne organics, moisture, and dust is often neglected which has severe implications on the wettability.²⁶³ For instance, water spreads on native silver and gold films with very high surface-free energies, but contact angles as high as 90° are generally observed.^{264,265} During 3 – 4 days of storage in ambient conditions in laboratory air, contact angles of silica increased from complete water-wet to $35 - 38^\circ$.²⁶⁶ Takeda et al.^{266,267} noticed that organic contaminants are attracted to the surface -OH groups and found a correlation between the -OH group density and the amount of adsorbed

contaminants from the atmosphere. These contaminants can even penetrate several water layers adsorbed from the moisture. Therefore, it is recommended to place these reactive surfaces immersed in water until needed if this does not alter the chemistry of the surface and/or rinse with appropriate solvents. All the above-stated considerations warrant caution when relating macroscopic contact angles to particle wetting at the liquid interface, despite its convenient use.²⁶³

Alternatively, a wettability profile was constructed on reservoir rock particles to evaluate their tolerance and interaction with inhibitors by measuring the colloidal system's ζ potential. While these qualitative results do not allow exact determination of the particle contact angle, they provide predictions to study the effect of reservoir conditions on particle wettability, making it an appealing approach for real-life applications without the need for sophisticated equipment.²⁶⁸ Fixating microspheres on an AFM tip allows determining their advancing/receding contact angles (and line tension) at air/water and oil/water interfaces from the force-distance curves.^{269–271} Alternatively, the local surface hydrophobicity of immobilized nanoparticles submerged in a liquid can be obtained from the scanning probe method by measuring the adhesion forces between (functionalized) AFM tips and the particle surface.²⁷² Enthalpy of immersion measured by heat flow microcalorimetry was used to evaluate contact angles of fumed silica particles at air/water, air/oil, and oil/water derived from thermodynamic principles.²⁷³ Mixing particles with water vapor and placing them into the size analyzing nuclei counter (SANC) gives a well-defined and uniform supersaturated vapor by adiabatic expansion. The formation of aerosols is related to the vapor-to-liquid nucleation process and scanning of the vapor saturation from zero to complete. The number of activated particles can be measured relative to the total amount of particles. This yields heterogeneous nucleation probabilities of water drops on the nanoparticles and using appropriate theories plus geometrical considerations of nucleation, microscopic contact angles were calculated. The calculated microscopic angles of the droplets on 4.8 nm silver particles lie around 15° , while macroscopic contact angles of silver substrates are around 90° .²⁶⁵ These smaller angles have been attributed to negative line tensions in the order of 10^{-10} J m⁻¹ and become increasingly dominant when the contact line curvature enhances.²⁷⁴ Line tension of similar magnitudes was found using FreSCa for 20 nm amidine latex particles at the hexane/water interface,¹⁴² with AFM for hydrophobized silica particles (~ 66 nm)⁶² and in accord with theoretical predictions.^{59,125}

Employing a Wilhelmy plate or Langmuir balance, one can obtain the two-dimensional surface pressure (Π), which is equal to the surface tension difference before (γ_o) and after (γ') adsorption of surface-active species: ($\Pi = \gamma_o - \gamma'$).²⁷⁵ Evaluating interfacial pressure-area (Π - A)

isotherms of particle-laden interfaces gives the contact angle by analyzing the area exclusion effects or evaluating the collapse pressure. In the former, contact angles are calculated from area shifts in the Π - A isotherm that are assumed to occur when colloidal particles adsorb while displacing the insoluble surfactant, as it cannot occupy the liquid interface anymore.^{248,276,277} In the second approach, the interfacial area is continuously decreased, forcing the particles into a close-packed configuration before collapsing. The collapse pressure and area where this occurs allow for estimating the particle contact angle based on geometrical factors. Advancing and receding contact angles correspond to the movement of the particles during the collapse, which is when a hydrophilic particle is forced into the aqueous phase or the oil phase, respectively.^{278–281} The traditional film balance method has been combined with many other methods (e.g., Brewster angle microscopy [BAM],^{281–283} ellipsometry,^{284–286} and specular X-ray reflectometry [XRR] or grazing-incidence small-angle X-ray scattering [GISAXS],^{49,282,287–294}) to provide further insights into the complex adsorption behavior of particles because particle contact angles are generally overestimated when relying on Langmuir trough experiments alone. BAM allows studying the morphology of an adsorbed layer over time and needs to be combined with other methods to obtain more details on interfacial characteristics.^{281–283}

A practical approach to studying quiescent interfaces is to utilize the scattering properties of light. With light extinction, contact angles of 1 μm polystyrene particles adsorbed at a planar liquid surface were determined by comparing the transmittance spectra of a particle monolayer and particles dispersed in a homogenous media. The difference is explained in terms of a phase shift parameter used to determine the particle's position relative to the interface.²⁹⁵ Multiple angle of incidence ellipsometry has been successfully employed at air/water and oil/water interfaces to determine contact angles of nanoparticles by dividing the interfacial plane into an upper and lower region that each contains a fraction of adsorbed particles and surrounding phase. Modeling the response of the interface with the effective medium approach allows for establishing a relationship between the thickness of the two layers and the contact angle of the particles.^{284–286,296,297} One study compared the sessile drop-derived contact angles on planar substrates with 18 nm gold nanoparticles and found good agreement between the macroscopic equilibrium contact angles at toluene/water. In contrast, the advancing contact angle better described the particles adsorbed at the air/water surface.²⁹⁷ Second harmonic generation (SHG) is a surface-sensitive second-order nonlinear spectroscopic technique able to study adsorption dynamics of molecules at various interfaces by monitoring the change in amplitude of the SHG signal. The increased/decreased SHG emission upon adsorption of

negatively/positively charged polystyrene nanoparticles, similar to the adsorption of ionic surfactants to oil/water interfaces, allowed to determine adsorption free energies using the Langmuir adsorption model. Interestingly, adsorption energies around $-15 \text{ kcal mol}^{-1}$ ($\sim 23^\circ$) were found for the 20 nm oppositely charged latex beads showing that the major driving force to interfacial adsorption is the van der Waals interaction instead of charge-charge interactions.²⁹⁸ For comparison, the contact angles of 20 nm amidine particles at the decane/water interface observed with FreSCa show much higher contact angles ($\sim 116^\circ$).¹⁴²

Unprecedented nanoscopic resolution to measure the *in situ* structure of surfaces and thin films covered with surfactants or small nanoparticles is realized using X-rays or neutrons as the scattering probe. It even allows to detect the accumulation of surfactant impurities at the oil/water interface.²⁹⁹ A finely collimated beam impinges at small angles ($0^\circ - 1.5^\circ$) on the horizontal liquid interface and the intensity of the scattered rays is subsequently collected. In reflectometry (XRR with X-rays and NR with neutrons), the reflected beam is analyzed in the specular direction (i.e., reflected and incident angles are equal, similar to ellipsometry), and the exact shape of the reflectivity profile contains structural information such as thickness, density, and roughness to estimate particle coverage and differentiate between mono- or multilayers.^{27,196,289,291,293,294,300-303} An electron density profile can be constructed by simulating the reflectivity curve calculated from Parratt's recursive formalism³⁰⁴ or Abelès matrix formalism,³⁰⁵ and a solution is found by minimizing the fitness function. The average particle immersion depth at buried oil/water interfaces has been determined by fitting a physically realistic model to the electron density curve^{38,209} or the reflectivity profile.³⁰⁶ XRR modeling does not guarantee the uniqueness of the solution and biased results can be supplemented using GISAXS experiments (or GISANS using neutrons). Here, the X-rays are incident onto the interface close to the critical angle ($0.05^\circ - 0.50^\circ$) and an area detector collects the diffuse scattering in all directions over the footprint of the beam to provide information on the vertical and lateral arrangement, the symmetry and interparticle spacing of particle/surfactant assemblies.^{49,196,217,289,291,300,301,303} SAXS and SANS, employing larger angles of $0.1^\circ - 5^\circ$, help study more complex fluids and colloids, and the scattering signal contains information about the size and shape of individual objects and their interactions. An elaborate model applicable to Pickering emulsions quantitatively determines the total area fraction of particles adsorbed to the 3D oil/water interface.^{183,307} Furthermore, X-ray photon correlation spectroscopy (XPCS), analogous to dynamic light scattering while using X-rays, allowed obtaining the in-plane dynamics of interfacially assembled nanoparticles

(and phospholipids) by evaluating the time dependence of the X-ray speckle pattern formed by the coherent scattering of the incident rays.^{292,308}

3.2 Macroscopic observable adsorption of nanoparticles to liquid interfaces

Adsorbing nanomaterial to a liquid interface can influence macroscopic variables, such as reducing the interfacial tension and resisting interfacial deformation due to enhanced surface elasticity. The variation in these observable quantities allows researchers to extract the physicochemical characteristics of individual particles, but these results do not always agree with the nanoscale resolution methods discussed above. Nevertheless, the ability to monitor a macroscopic variable and its response to various external stimuli (e.g., pH, electrolyte and particle concentration, temperature) allow for rational design and formulation of complex 3D structures.^{76,77} This section provides the potential effect of particle adsorption on the interfacial tension and a quantitative description thereof in sections 3.2.1 to 3.2.3, followed by the measurable viscoelastic parameters (section 3.2.3 to 3.2.6).

3.2.1 The surface tension response to the accumulation of nanoparticles

The most widely used techniques to monitor the air/water surface tension or oil/water interfacial tension are the vertical Wilhelmy plate, combined with a Langmuir trough to influence the 2D surface pressure, and the pendant drop tensiometry. In general, for the former, when a vertically suspended plate contacts a liquid surface, a force acts on this plate that correlates to the interfacial tension and contact angle of the liquid with the plate. During barrier compression, the decrease in surface area is simultaneously recorded with increased surface pressure.²⁷⁵ In the second case, a small liquid drop is formed at the end of a capillary in air or an immiscible liquid, and gravity and surface stresses determine the droplet shape. The surface tension is calculated from the Young-Laplace equation for capillarity (Eq. 4.13).³⁰⁹⁻³¹¹

It is noteworthy to mention the difference between ‘apparent’ (γ') and ‘actual’ (γ) surface/interfacial tension, which correspond to the macroscopic and microscopic tensions introduced in section 2.1.1, respectively. The microscopic surface tension acts at the free liquid surface between adsorbed solutes (i.e., a local value), while the macroscopic surface tension is operating at distances much larger than the average separation distance of the adsorbed solutes (i.e., a global area-averaged value). Particles adsorbing to the liquid interface reduce the interfacial area of the liquid interface by πa^2 per particle (Eq. 2.18), which lowers the surface free energy of the system. Unlike surfactant-covered interfaces, the surface tension decrease

has no microscopic origin because particle adsorption to the liquid interface results in regions where the tension remains unchanged, even for close-packed films. From a macroscopic perspective, the reduction in surface free energy arises from lateral particle-particle and entropic interactions, which produces a 2D lateral surface pressure (Π) that opposes the interfacial area contraction induced by the action of the interfacial tension. This pressure is the 2D equivalent of the osmotic pressure. The surface tension of a particle-laden interface can be defined as the difference between that of a clean liquid interface and the interfacial pressure ($\gamma' = \gamma_0 - \Pi$). Therefore, the apparent surface tension obtained with standard experimental methods (e.g., pendant drop tensiometry) allows monitoring of the increase in particle packing at the interface. In contrast, the actual surface tension is helpful for computational simulations (e.g., to explain the shape of the microscopic meniscus around a colloid in a gravitational field).^{34,35,40}

It is possible to derive the concentration of particles adsorbed at the interface (surface excess concentration: Γ) considering that the particle-laden interface is a closed system where the particles can freely exchange between the bulk and interface (i.e., small and reversibly bound particles).^{76,164} The areal surface excess concentration itself depends on the total number of particles present in the whole system (n):^{15,17}

$$\gamma' = \left(\frac{\partial G_\gamma}{\partial A} \right)_\Gamma = \left(\frac{\partial G_\gamma}{\partial A} \right)_{T,P,V,n} \quad \text{Eq. 3.1}$$

Whenever a particle adsorbs to the liquid interface, γ' reduces theoretically by $\Delta E_P/A$ per particle, which is monitored during pendant drop tensiometry. When interparticle interactions are negligible, i.e., Γ is small:⁷⁶

$$\Pi(\Gamma) = \Gamma |\Delta E_P| \quad \text{Eq. 3.2}$$

$$\gamma' = \gamma_0 - \Gamma \Delta E_P \quad \text{Eq. 3.3}$$

where γ_0 is the interfacial tension of the clean liquid interface prior to adsorption. Accordingly, differences in interfacial tension allow calculating the number of reversibly adsorbed particles. This particle adsorption reversibility is reflected in the surface pressure curve for repeated compressions of the interfacial area. If the pressure-area curves differ between the cycles, this is indicative of nonequilibrium microstructures at the interface, such as aggregates and networks. In this case, the surface pressure upon compression is not equal to the equilibrium thermodynamic quantity $\Pi(\Gamma)$ stated above.¹⁶⁴ Under specified conditions, these equations apply to many particle-laden interfaces. For example, 500 nm spherical particles segregated to the interface of Pickering emulsion droplets ‘hop’ between neighboring droplets through a

bridging mechanism. The droplets share particles before exchanging them or, to a lesser extent, are reabsorbed after interfacial expulsion into the bulk phase. No significant change in droplet size was observed for several months with continuing particle exchange. This phenomenon occurs more likely for particles with a lower tendency to adsorb (i.e., contact angle further away from 90°) and in the absence of electrolyte.³¹² Du et al.¹⁷ monitored the reduction of the oil/water interfacial tension of several spherical micro- and nanoparticles and found reasonable adsorption energies using Eq. 3.2, which does not account for interparticle interactions directly. They assumed a hexagonal close-packed monolayer was formed ($\Theta = \pi a^2(n/A) = \pi a^2\Gamma \approx 0.91$) if the interfacial tension did not reduce further while increasing the bulk particle concentration (n). Rearranging Eq. 3.3 then allows to estimate particle binding energies without needing prior knowledge about particle wettability:

$$|\Delta E| = \frac{\gamma_0 - \gamma'}{\Theta} \pi a^2 \quad \text{Eq. 3.4}$$

Zhang et al.¹⁵ determined the actual particle coverage on a polymerized pendant drop using SEM to elucidate further the validity of neglecting interparticle interactions. A direct relation for the packing density of adsorbed particles was determined by combining the energy of particle attachment (Eq. 2.18) and Eq. 3.2:

$$\gamma' = \gamma_0 [1 - \Theta(1 - \cos \theta)^2] \quad \text{Eq. 3.5}$$

Their theoretically predicted and experimentally estimated results correlated surprisingly well when two out of three parameters were known (interfacial tension, particle coverage, and contact angle). The calculated particle coverage using Eq. 3.2 and tensiometry was approximately within 15% of the coverage measured with SEM. Secondly, it showed to be valid when packing densities are below a close-packed monolayer (e.g., $\Theta = 0.60$ of cellulose nanoparticles and contact angle of $\sim 90^\circ$ at the oil/water interface). This suggests that particle-particle interactions contribute little to the interfacial tension decrease in many cases.¹⁵

Thus far, adsorption properties for particles have been derived based on thermally and mechanically equilibrated interfaces, mainly by comparing the difference in surface tension between a clean and particle-covered surface. Dynamic surface/interfacial tension can be applied to measure the kinetics of nanoparticle adsorption, provided that a suitable model exists that relates the time-dependent tension to the transient particle coverage at the interface. The classical diffusion model developed by Ward and Tordai³¹³ for surfactants forms the basis to describe the time-dependent interfacial characteristics. In most cases using surfactants, diffusional transport is the primary process governing the entire formation of surfactant layers

at the interface.^{102,103} Asymptotic derivation of these equations³¹⁴ has been used to interpret the early ($t \rightarrow 0$) and late ($t \rightarrow \infty$) stages of particle adsorption to a liquid interface.^{28,315–320} Bizmark et al.¹⁶ described the adsorption process as diffusion-limited in the short-timescale (~ 10 s) with an adjustment to incorporate particle wetting and agreed well with the experimental dynamic tension data:

$$\gamma' = \gamma_0 - 2C_N \Delta E \sqrt{\frac{Dt}{\pi}} \quad \text{Eq. 3.6}$$

where C_N is the bulk particle concentration (number per unit volume), and D is the diffusion coefficient or the adsorption rate to the interface. There is no adsorption barrier at this early onset of adsorption as the interface is entirely unoccupied, and therefore, D equals the diffusion coefficient given by the Stokes-Einstein relation (Eq. 4.1). In the long-time limit, they assumed that adsorption was no longer diffusion-limited and irreversible, thereby devising an asymptotic expression based on random sequential adsorption (RSA),¹⁶ which in essence is a blocking function that quantifies the effect of already adsorbed particles.³²¹ If their measurements were actually in the diffusion-limited regime was not determined, but the model allowed to extract an energy barrier against adsorption.¹⁶ In later experiments, they combined Eq. 3.3 with the energy of particle attachment (Eq. 2.18) to estimate the surface coverage from the dynamic interfacial tension $[\gamma(t)]$ values and contact angles from sessile drops:³²²

$$\Theta(t) = \frac{1 - \gamma(t)/\gamma_0}{(1 - |\cos \theta|)^2} \quad \text{Eq. 3.7}$$

Utilizing Eq. 3.7, the likely formation of a steady-state close-packed hexagonal monolayer was confirmed, which validates their initial estimate of $\Theta \approx 0.91$.¹⁶ Because nanoparticles have relatively larger sizes than surfactants, they have smaller diffusivities that decelerate adsorption. This dimension difference makes the dynamic tension measurements with particles more susceptible to convection and contamination. Despite achieving similar equilibrium coverage, dispersions of higher polydispersity adsorb faster than less polydisperse samples. Similar equilibrium tension is likely because the larger particles replace the smaller ones at longer timescales.^{53,150,323}

The discussed approaches cannot be generalized as they are limited to particles exhibiting intermediate wetting (i.e., contact angle not too far away from 90°), ideally having no adsorption barrier and liquid interfaces with not too low tension. Otherwise, the tension drop upon particle adsorption will be too small to be accurately measured, translating into high uncertainties in the calculated parameters.^{76,77}

3.2.2 Quantitative thermodynamic description including particle-particle interactions

Calculated adsorption energies and kinetics based on surface tension or pressure rely on the tentative assumption that a close-packed, densely populated particle film has formed when further increasing the bulk particle concentration results in constant interfacial tension.^{16,17,30,315,320} Surprisingly, Eq. 3.2 seems valid in many cases, even when particle coverage is close to a monolayer, based on the assumption that no significant particle-particle interactions exist that affect the interfacial tension. However, the spatial confinement of the particles at the interface along with the long-range repulsive electrostatic forces and attractive capillary interactions between adsorbed particles and between adsorbed particles with those in the bulk must be considered. This sets up an energy barrier for further adsorption and densification, which limits particle coverage well below what might be expected from a hexagonally close-packed monolayer.^{15,49,186} Computational studies have shown that when particle-particle repulsion is large (i.e., occurring when the particle coverage increases), the interfacial tension decreases more strongly which requires a more physically relevant equation of state that relates the surface pressure (Π) to the particle concentration at the interface (Γ) and in the bulk (C_N).^{324,325} In order to do so, the particle-particle interactions, the energetic cost associated with the formation of the three-phase contact at the interface (i.e., wetting), and the chemical potentials of the adsorbed and bulk particles have to be incorporated simultaneously.^{76,77} Several types of these surface isotherms exist based on surfactant or protein adsorption. The Henry equation is the 2D analog of an ideal gas and the simplest equation of state [$\Pi = \Gamma kT$], similar to Eq. 3.2. Corrections regarding the excluded volume are introduced in the Langmuir and Volmer equations and further extended by Frumkin and Van der Waals by adding a cohesive pressure term, respectively.^{42,326} Adsorption of particles smaller than 10 nm is often described by the Frumkin and Van der Waals equations of state.³³ However, the surface pressure for a given area fraction is generally independent of particle radius, whereas a strong particle size-dependency is predicted with the equations above.⁴² For larger particle monolayers, a thermodynamic description regarding Π - A isotherms was derived by Fainerman et al.^{40,41} from a model applicable to a protein-laden interface. They treat the particles as inert hard spheres with a long-range attraction giving rise to a surface pressure that is independent of particle size. The interfacial pressure for a particle-laden interface can be defined as:^{40,41}

$$\Pi = -\frac{kT}{\omega_0} \left[\ln \left(1 - \frac{\omega}{A} \right) + \left(\frac{\omega}{A} \right) \right] - \Pi_{\text{coh}} \quad \text{Eq. 3.8}$$

where ω_0 is the particle area, ω/A is the particle coverage, and Π_{coh} the cohesive pressure (accounting for particle-particle interactions) thereby eliminating the particle size dependency. The term ω/A in Eq. 3.8 can refer to the individual particles and to that of several particles in a larger interfacial area. Their results provided a realistic picture of the thermodynamic behavior of particle-laden interfaces (7.5 nm – 75 μm) for particle coverages below close-packing and independent of particle size or chemical nature. Their calculations also produced reasonable numbers for the area of solvent molecules in the range of 0.12 – 0.18 nm².^{40,41} Recently, Verwijlen et al.⁴³ showed by performing Langmuir trough compressions of elastic interfaces that the resulting surface pressure in the Π - A isotherms is a combination of rheological contributions and compressibility in the absence of relaxation mechanisms. Proper separation of those two effects, including corrections of the trough geometry, allowed a rationalization of experimental data indicating that the surface pressure is indeed a fixed value when surface coverage and ambient conditions are constant. Any deviations indicate the presence of rheological contributions to the surface pressure, and the more elastic an interface is, the more deformation-dependent the surface pressure becomes. Seemingly, the viscoelasticity of particle-laden interfaces plays an essential element when designing generalized thermodynamic expressions tested against experimental Π - A isotherms.^{43,327}

In an attempt to overcome these limitations, Groot et al.⁴² developed a simulation model to describe the adsorption and desorption of soft gel particles from liquid interfaces by accounting for the particle-particle interactions that depend on the particle coverage:

$$\Pi \approx \frac{4kT}{\pi d_{\text{eff}}^2} \left[\frac{byZ(\lambda y)}{\lambda} - b_2 y^2 \right] \quad \text{Eq. 3.9}$$

where d_{eff} is the effective diameter of correlated domains within a particle and generally larger than the actual diameter d , b and b_2 account for interparticle interactions, $y = \pi\Gamma d^2/4$ is the area fraction covered with particles, Z accounts for the compressibility factor, and $(\lambda)^{1/2}$ is the effective hard disk diameter. They concluded that the surface pressure is related to all internal degrees of freedom within the particles and not just the pressure exerted by the particles. Therefore, the surface pressure of a particle monolayer is not simply proportional to kT/d^2 . For gel particles, $\Pi = kT/d_m^2$, and for glass beads, $\Pi = kT/d_{\text{eff}}^2$, where d_m is the size of the molecular building blocks and $d_{\text{eff}} > d_m$. The surface coverage was varied, and with the inclusion of short- and long-range interactions, “a power-law dependence was found for the surface pressure ($\Pi \approx \Gamma^{10 \pm 0.5}$) related to the (fractal) structure of the adsorbed particle network that is consistent with surface percolation.”⁴² The model has been tested using polymeric

microgel particles and accurately describes the adsorption process of these particles before interfacial buckling occurs, making it a promising expression for future developments.³²⁸

Alternatively, a thermodynamic model was constructed in an experimental-based single and multicomponent study by Hua et al.,^{53,329} considering that the interfacial tension reduction originates from simultaneous particle adsorption and interparticle interactions. First, a nanoparticle adsorption isotherm provided the number of gold particles adsorbed to the oil/water interface, as determined from the decrease in the UV-vis absorbance signal of the bulk dispersions before and after creating the oil/water interface. Second, assuming that the total surface pressure originates from the linear additivity of single nanoparticle wetting and the surface pressure of particle-particle interactions at the liquid interface provided the surface pressure isotherm from tensiometry. There is good agreement between the particle concentration and surface pressure (Eq. 3.2) at low area fractions ($\Theta \approx 0.2$). Furthermore, since the areal particle densities were known for all bulk concentrations, the influence of the interparticle interactions on the surface pressure for those interfaces with more adsorbed particles could be directly estimated. Finally, additional physical parameters were determined using the Frumkin adsorption model (i.e., accounting for nonideal attractive/repulsive interactions). The interfacial pressure under assumed thermodynamic equilibrium is written as:

$$\Pi = -kT\Gamma_{\infty} [\ln(1-\Theta) - 0.5K_c\Theta^2] \quad \text{Eq. 3.10}$$

where Γ_{∞} is the maximum interfacial excess concentration, K_c is the particle-particle interaction factor, and $\Theta = \Gamma / \Gamma_{\infty}$ is the fraction of the interface covered with particles. Their data also suggests that the interfacial tension reduction due to particle-particle interactions is of minor influence.^{53,329} This claim is substantiated by the Π - A isotherms complemented with *in situ* GISAXS experiments from forced compression of 126 nm spherical polystyrene particles spread at the air/water interface. The most considerable increase in surface pressure arises before forming a close-packed layer. Moreover, data modeling of X-ray scattering shows a contact angle dependency with interparticle distances.⁴⁹ Furthermore, combining the Ward-Tordai equations with a Frumkin adsorption isotherm incorporating a wetting equation of state can model the diffusion-limited adsorption of nanoparticles to a liquid interface for particle area fractions < 0.3 . Slower dynamics are observed at broader particle coverages, possibly originating from particle size polydispersity or reorganization at the interface.^{53,54,150,323} A thermodynamic characterization of particle-laden interfaces based on surface pressure is challenging, and no generalized consensus has been formulated yet. Developing realistic models that accurately capture the effect of both particle-particle

interactions and their wettability is necessary before other effects, such as morphological and structural properties of the particle-covered interface can be studied on a thermodynamic basis.³³⁰

3.2.3 Particle adsorption does not always result in a measurable change in surface tension

Large enough, surface-active particles with adequate wetting (i.e., contact angles not too close to 0° or 180°) should adsorb to a liquid interface and thus reduce the free energy per unit area on macroscopic length scales. Therefore, a significant free energy reduction is generally explained by the considerable adsorption energy of these particles straddling the interface. However, an interfacial tension reduction may not be observed even when these conditions are satisfied. These particles are then declared as “not surface-active”^{15,29,331–335} even though particle adsorption is likely to occur.³²⁵ In the experiment of Wang et al.³³⁶ microparticles seem to have negligible influence on the macroscopic surface tension. They modified the sessile bubble method for microparticle-coated bubbles by considering the interaction force between an air/water interface and adsorbed microparticles. The classical sessile bubble method overestimates the surface tension of microparticle-decorated bubbles and is corrected by accounting for particle size and contact angle that also influence the droplet's shape. The presence of a close-packed microparticle layer does not alter the surface tension of these immobile bubbles as they are in static equilibrium, i.e., the interparticle forces do not generate any surface pressure.³³⁶

This situation is different for nanoparticle-laden interfaces. Absent interfacial tension changes for sufficiently high bulk concentrations of particles can be attributed to low surface coverage and/or weak particle-particle interactions. For example, Okubo et al.³³⁷ noticed a substantial interfacial tension reduction when adsorbed nanoparticles experienced strong repulsive particle-particle interactions to form crystalline structures and not otherwise.^{331,337} A molecular dynamics study of pendant drops covered with a monolayer of colloidal particles having purely repulsive interparticle interactions indicated that particle properties and coverage determine the surface pressure. The surface stress was homogenous and isotropic when droplet pinch-off was not observed, i.e., for coverages < 0.5 of charged particles, a single value exists for the surface tension. Extra and deviatoric contributions to the surface stress for such repulsive particles become only significant close to maximum packing. A larger surface pressure stems from increased coverage or interaction strength, and the minimum surface coverage necessary to produce a finite surface pressure (Θ_{\min}) can be estimated based on the electrostatic screening

length κa . An average particle-particle distance can be estimated for a hexagonal close-packed layer according to:³²⁴

$$x = \sqrt{\frac{2\pi a^2}{\sqrt{3}\Theta_{min}}} \quad \text{Eq. 3.11}$$

Moreover, an estimate for the finite pressure can be obtained when assuming $x = \kappa^{-1}$:

$$\Theta_{min} = \frac{2\pi}{\sqrt{3}} (\kappa a)^2 \quad \text{Eq. 3.12}$$

Therefore, larger κa values, i.e., larger particles and/or lower electrostatic charge, require higher particle coverages at the interface to reduce the surface tension. Polydispersity and clustering also affect the surface pressure, which can be studied using their method. Expulsion or ejection of particles can occur, but only when surface coverage is extensive and/or particle adsorption is relatively weak.³²⁴

The interfacial activity of weakly surface-active and highly charged colloids can be enhanced by adding electrolyte^{28,338–342} or altering the pH^{28,29,341,343} to effectively screen the repulsive particle-interface charges. However, this strategy does not always ensure a measurable tension reduction.¹⁵ Whether weakly surface-active particles occupy the interface is often inferred from their ability to stabilize emulsions. Turbulent eddies may facilitate adsorption, which is primarily absent during tension monitoring, but not surface-active particles can still stabilize emulsions under certain circumstances.^{187,331,335,344,345} Noteworthy, Marina et al.³⁴⁵ dispersed hydrophilic silica nanoparticles in the nonconventional oil phase, showing that the particles are strongly attracted to the oil/water interface (theoretically calculated contact angle $\sim 90^\circ$) with exceptional pH-independent, long-term stability at low particle concentrations. Unfortunately, no interfacial tension measurements were conducted to monitor adsorption of these particles which would have shed light on the likely increase in surface pressure and to validate their estimated contact angle.³⁴⁵

One crucial key challenge remains to know with certainty whether particles have adsorbed at all to the liquid interface. For many particle materials, an energy barrier against adsorption exists from already adsorbed particles, the charge of the air/water and oil/water interface, and/or image charge effects. Supposedly, this latter electrostatic repulsive effect occurs at the liquid interface having different bulk phase permittivity. Its sign and magnitude are the same as the actual particle approaching the interface but positioned in the opposite medium at an equal distance from the interface. The closer the real particle approaches the interface, the stronger the repulsive force of the imaginary particle is felt if the actual particle

is dispersed in the medium with a higher dielectric constant. The opposite effect occurs (i.e., attraction) when the real particle is dispersed in the lower dielectric constant medium. Therefore, the repulsive or attractive force is felt the strongest in the subsurface region right below the interface just before the particle adsorbs to the liquid interface, and systems containing highly charged particles will show extremely slow adsorption kinetics.^{340,346–348} Other types of interaction forces (i.e., van der Waals, hydrodynamic, and hydration forces) can also act as a barrier and the full-scale interplay of all these effects needs to be clarified further.^{349,350}

For example, it has been reported that hydrophobic interactions can overpower electrostatic repulsion with the liquid interface and stimulate adsorption of ionic species.^{351,352} It is advisable to augment surface tension measurements with complementary techniques (section 3.1) to further elucidate the effect nanoparticle adsorption may have on the macroscopic properties of the liquid interface.

3.2.4 Interfacial rheology

Interfacial rheology studies the deformation of solid-like materials and flow behavior of liquid-like materials upon applying external stresses and is a critical parameter in establishing the stability of bijels (bicontinuous Pickering emulsions), foams, and emulsions. It provides information on the thermodynamic and hydrodynamic interactions between adsorbed material and the surrounding liquids, but only when the mechanical response of the interfacial layer is dominant in relation to the bulk liquids. Additionally, adsorption mechanisms can be unraveled by studying the kinetics of relaxation processes. It is clear from the previous paragraphs that the surface tension always tends to minimize the interfacial area to lower the energetic cost. When particles adsorb to the interface, a lateral surface pressure arises that acts in the opposite direction of the tension. This pressure in turn gives rise to in-plane deformations (i.e., dilation and shear) due to coupling between the bulk and interfacial flows, meaning that the flow of the interfacial region is not independent of the bulk flow. The main difference between bulk and interfacial rheology is that interfaces are compressible. Interfacial rheology is also suited to study several out-of-plane deformations, e.g., removal of adsorbed particles into the bulk, buckling, or multilayers, which occur under particular mechanical stress conditions.^{20,77,353} Deformation of a liquid interface alters the amount (i.e., dilation) or shape (i.e., shear) of the interface, which deforms the adsorbed material. A certain amount of energy is required and the different stresses that can arise are defined as:^{223–225}

$$\gamma_{ij} = \gamma'(\Gamma, T)\delta_{ij} + \tau_{ij} \quad \text{Eq. 3.13}$$

where γ_{ij} is the surface stress tensor, $\gamma'(\Gamma, T)$ is the surface/interfacial tension, and is a state variable that depends only on the surface excess concentration Γ and the temperature T , δ_{ij} is the surface unit tensor, and τ_{ij} is the surface extra stress tensor. The surface stress tensor can be broken down into two contributions: the isotropic, scalar, surface energy term ($\gamma'\delta_{ij}$) and an anisotropic, tensor term (τ_{ij}). The former represents the energetic cost for liquid interface deformations, adsorption/desorption effects of surface-active components have on the surface tension upon changes in the interfacial area, and Marangoni stresses due to concentration gradients in surface tension. In contrast, the deviatoric stress describes the response to deform adsorbed material present at the interface.^{223,224,309} Taking the derivative of Eq. 3.13 concerning the appropriate strain determines the elastic moduli of the interface. The surface stress equals the experimentally measured air/water or oil/water interfacial tension when $\tau_{ij} = 0$, namely in the case of pure liquids or with reversibly adsorbing components. When the adsorbing material binds quasi-irreversibly, τ_{ij} quickly becomes significant and solidifies the interface. In that case, enhanced deformations lead to complex shapes where the stress response and strain input behave nonlinearly, complicating the analysis, particularly for industrial processes where such conditions are often prevalent.³⁵⁴⁻³⁵⁶ The theoretical foundations of bulk rheology can adequately describe viscoelastic interfaces in the (small) linear regime, i.e., to identify if the populated interfaces behave more elastic or viscous under low strain input to explain the stability of emulsions and foams.

Interfacial shear rheology allows directly probing the interface's mechanical properties since $\gamma'\delta_{ij}$ does not change during shear, unlike interfacial dilational rheology. Therefore, both can act in complementary ways where interfacial dilational rheology is accessible for (a dilute) liquid-like viscoelastic interfaces. Furthermore, the existence of a shear modulus is characteristic of a quasi-irreversible adsorption layer, and interfacial shear rheology is suitable for (a saturated) solid-like viscoelastic interfaces.²²³⁻²²⁵ Note that several experimental methods exist to measure these interfacial properties with their specific benefits, disadvantages, and reliable working range, which will not be discussed separately.³⁵⁷⁻³⁵⁹

Interfacial rheology thus provides information on the microstructure of the particle-laden interface, which depends on the interparticle forces. These forces are generally influenced by particle shape,³⁶⁰⁻³⁶³ size,³⁶⁴ wettability,³⁶⁵⁻³⁶⁷ presence of electrolyte and/or surfactant,^{170,368,369} and the surface coverage (Eq. 3.14):^{193,194,205,370}

$$\Theta = \frac{\sum_{i=1}^n A_P}{A_{surface}} \quad \text{Eq. 3.14}$$

where n is the number of adsorbed particles, A_P is the area of the particle cross-section, and $A_{surface}$ is the interface area. Depending on the coverage, particle-laden interfaces show different phase behavior ranging from liquid-like at low coverage to solid-like at high coverage. In the intermediate region (i.e., the hexatic phase), particle monolayers organize themselves into crystal-order percolated networks or aggregated domains, which depend on the relative strength of the interparticle forces. Crystal-ordered monolayers occur when $\Theta \geq 0.3$, typically observed for electrolyte-free systems with highly hydrophobic particles^{193,194,205,370} or when the lipophilicity of the particles is enhanced,^{368,369} up to $\Theta \approx 0.91$ where the spherical particles form a close-packed, jammed monolayer.

3.2.5 Interfacial dilational rheology for particle-laden interfaces

Briefly, dilational rheology modifies the interfacial area and provides information on the changes induced on the surface tension, and applies to Langmuir troughs and pendant drops, for example. Therefore, uniaxial stress creates an infinitesimal change of the interfacial area, $dA(t)$, that leads to a time-dependent change in the surface tension, $d\gamma(t)$. A complex interfacial dilational modulus (E^*) is obtained with small amplitude oscillatory deformations at a specified frequency that contains a real elastic (E') and imaginary viscous (E'') modulus. These are quantified accordingly by the time lag between the area deformation and tension response. Details on the oscillating pendant drop can be found in section 4.1.3.3.1.

Such external deformations on particle-laden interfaces influence their adsorption state and structure due to the induced stress response.^{281,371} Low amplitude surface area perturbations provide viscoelastic information about the interfacial structure. In contrast, large deformations provide information on the particle-particle (or particle-surfactant) interactions and regarding the macroscopic structures of particulate monolayers formed at the interface.³⁷² As a response to the perturbation, one can also determine the relaxation dynamics that are strongly dependent on the studied timescale.^{281,371} However, the response of a ‘simple’ particle-laden interface to dilational stress is far from clear when comparing experiment to theory or necessitates many parameters that cannot be easily accessed.^{40,281}

Nevertheless, varying experimental parameters and subsequent qualitative viscoelasticity analysis is helpful towards practical applications. For example, adsorption of fumed silica nanoparticles with varying hydrophobicity at the air/water interface measured in the low-frequency range (0.016 – 0.1 Hz) was employed to study the relaxation process.

This particle-laden interface exhibited long timescales (~ 1000 s) assigned to interfacial reorganization being faster when the particle hydrophobicity decreased. A possible reason for this could be the lower particle coverage when exhibiting less affinity to adsorb, which reduces the steric hindrance and enhances their lateral mobility.³⁷³ The high-frequency range (200 – 990 kHz) showed a strong correlation between elasticity and particle wettability. The elastic component increases when the particle affinity for the interface becomes more favorable and with increasing interfacial coverage. At the same time, the viscous part always remains close to that of pure water ($E' > E''$). Changing the particle hydrophobicity from completely lyophobic to completely lyophilic increases E' twofold.^{365–367} In the low surface pressure range, the correlation between the elastic modulus and particle wettability may originate from the repulsive particle-particle interactions of electrostatic origin. An increase in E' to high values (~ 300 mN m⁻¹) is due to the formation of a close-packed layer, as confirmed with BAM, and this maximum occurs for particles with intermediate wettability.³⁶⁷ Such high elasticity values indicate that the interface is stiff, making it fragile and it easily fractures during small expansion/compression cycles.³⁷⁴ Fracturing can be observed as a drop in the moduli after reaching a maximum and results from out-of-plane deformations of the monolayer.³⁷⁵ It is typical for irreversibly bound particles to exhibit relatively simple phase behavior (i.e., isotropic liquid, hexatic, and solid phase) and remain a monolayer upon compression.^{376–378} However, when the monolayer solidifies, the particle assembly buckles out of plane to form wrinkles rather than multilayers^{377,379} unless a depletion pressure is exerted on the particle monolayer.³⁸⁰ When particles of equal wettability decrease in size, their elastic modulus increases, likely due to more efficient interfacial packing of the smaller ones.³⁶⁴

During interfacial dilational experiments of particle-laden pendant drops (section 4.1.3.3.1), one of the main difficulties is that drop deformations are not always purely dilational. The local deformation can depend on the particle position on the drop surface, resulting in shear stresses that determine the drop shape and hence provide obscured viscoelasticity values.²²¹ This effect is usually negligible for conventional surfactants and charge-stabilized repulsive particles with coverages < 0.5 .³²⁴ When significant particle adsorption forms a rigid interface, further droplet compressions can show wrinkles, and the Young-Laplace equation (Eq. 4.13) needs to be modified.^{372,381,382} For pendant drops, the anisotropic stresses are mainly localized in the neck region. The non-uniform curvature redistributes the particles on the surface to satisfy the condition of zero tangential forces on the particles after surface stress relaxation.^{324,382,383} This might explain the significant differences

in particle coverage ($\sim 20\%$ between lowest and highest Θ) at different positions of an equilibrated pendant drop, i.e., constant interfacial tension.¹⁵

Large area compressions of equilibrated drops are a valuable indication of whether the measured tension and viscoelastic moduli can be trusted, i.e., in the case of reversibly adsorbed particles at high coverage.^{154,374} Additionally, Clint et al.²⁷⁸ found that particles can be expelled from the interface above a critical surface pressure, which increases with the particle wettability and is maximum when the contact angle is 90° . Particles can only desorb from the interface if the mechanical work done upon compression exceeds their desorption energy.¹⁶⁴ The mechanical properties of simple particle-based systems under compression depend on the compression rate (i.e., strain rate $\dot{\epsilon} = \frac{dA/A}{dt}$) and characteristic timescale of particle desorption τ_{des} .⁷⁶ For irreversibly bound particles, wrinkles remain visible indefinitely long after compression has been completed.³⁸⁴ In some cases, buckling occurs during compression due to particle aggregation at the interface, and the wrinkling relaxes on the timescale of particle desorption ($\dot{\epsilon} = \tau_{des}^{-1}$).³⁸⁵ In case $\dot{\epsilon} \gg \tau_{des}^{-1}$, the Young-Laplace equation accurately describes the interface during compression,^{154,155} and reversibly adsorbed particles are preferably ejected from the interface at regions with high curvature, i.e., drop apex.^{324,386}

3.2.6 Interfacial shear rheology for particle-laden interfaces

The shear properties of an in-plane deformation reflect the resistance of the interface to changes in shape rather than area because shear deformations are decoupled to the rest of the interfacial modes, contrarily to dilational deformations that may contain shear contributions. The shear elasticity corresponds to an in-plane deformation as the proportionality constant that relates the measured stress (τ_s) to the applied strain (μ_s), and their ratio defines the elastic modulus (G) (section 4.1.3.3.2).⁷⁷ Small-amplitude shear deformations provide the complex interfacial shear modulus (G^*) with a real elastic (G') and imaginary viscous (G'') component that will be termed as storage and loss modulus, respectively, to differentiate them from the dilational parameters. The storage modulus describes solid-like behavior, which is often the case for particle assemblies as they resist deformation. In contrast, the loss modulus dominates for liquid-like films that flow under the applied strain, as for lipids.³⁸⁷ By contrast, soluble surfactants usually possess negligible shear viscosity.³⁸⁸

After forming the liquid interface, the time-dependent evolution of the moduli at fixed frequency and strain provide information about the adsorption dynamics of self-assembled particle monolayers³⁸⁹ or when increasing the surface pressure with a strong dependence on

surface coverage.^{390–392} The interfacial shear moduli for equilibrated particle-laden interfaces at low coverages show a mainly viscous character, $G'' > G'$, as the particles can move freely in the 2D plane due to repulsive interactions. Both viscoelastic moduli tend to have higher values with denser particle coverage by increasing the bulk concentration, the surface pressure, or electrolyte concentration. A transition point is reached at intermediate coverage where the storage and loss moduli are equivalent, $G'' = G'$, and occurs faster when the ionic strength increases due to electrostatic screening and enhanced particle aggregation. Higher coverages lead to strong elastic-like interfacial films, $G' > G''$.^{393,394}

The spherical particle (0.2 μm sulfate polystyrene) ordering of the microstructure and coverage strongly influences the shear moduli when the strain or frequency is varied. Increasing the strain at low coverage ($\Theta \approx 0.6$) shows shear thinning behavior related to disintegrating particle clusters because these smaller clusters show reduced resistance to deformation, whereas higher coverages ($\Theta \approx 0.7$) show yielding behavior due to the generation of macro slip planes on the particle-laden interface. Increasing shear rates increases the particle ordering at the interface away from the slip plane, i.e., higher shear rates induce hexagonal packing, and occurs well below the maximum coverage as long as the attractive interparticle forces are strong enough.³⁹⁵ Furthermore, the storage modulus and the yield stress increase by a factor of ten when the interfacial coverage of 820 nm polystyrene-polyvinylpyrrolidone spheres goes from 0.47 to 0.88, showing that the mesostructural organization of the local microstructure regulates the elasticity and yield. Elastic interfaces are formed by large domains of aligned hexagonal-packed particle assemblies.^{360,396} Interestingly, the rheological properties of 2D particle aggregates display similarities to their 3D counterparts, including “an elastic response with small linearity limits, a power-law dependence on surface coverage, and a dependence on the strength of attraction.”^{368,390–392,397,398} Power-law behavior under shear experiments is used to quantitatively describe the bulk and interfacial rheological behavior using constitutive models.³⁹⁹ For example, adsorption of silver nanoparticles to the oil/water interface is reminiscent of a 2D glassy material.³⁸⁹ At the air/water interface, gold nanoparticles form a gel-like structure characterized by strain-induced softening.^{390–392}

The magnitude of the interfacial viscoelastic moduli is determined locally by the degree of restricted particle motion. This is related to the interparticle capillary attraction and the amount of caging induced by the microstructure, i.e., particles trapped by their neighbors.³⁹⁶ Crystalline-ordered isolated islands behave primarily viscous above moderate frequencies and strains characterizing very small viscoelastic moduli between 10^{-6} to 10^{-4} N m^{-1} for coverages between 0.4 to 0.89, respectively.^{394,400,401} The moduli for percolated networks increase up to

10^{-2} N m^{-1} for higher surface concentrations and are primarily elastic at moderate frequencies and strains.³⁶⁸ Interfaces with aggregated 2D particle clusters show high moduli around 10 N m^{-1} .³⁹⁶ The Krieger-Dougherty relationship for 2D systems can be used to determine the apparent particle coverage (Θ_{app}) from shear experiments:⁴⁰²

$$\eta_{rel} = \left(1 - \frac{\Theta_{app}}{\Theta_{max}}\right)^{-[\eta]\Theta_{max}} \quad \text{Eq. 3.15}$$

where η_{rel} is the viscosity ratio of the particle-laden interface to the clean interface, Θ_{max} is the maximum 2D packing, and the product $[\eta]\Theta_{max}$ is 1.9. A modified version allows determining the apparent aggregate size as the relative viscosity decreases with the increase in particle size and polydispersity.^{403,404}

The dipolar repulsive interparticle interaction is present in both dilute and concentrated monolayers.⁴⁰⁵ Electric double layer screening by adding electrolyte leads to an increase in the shear moduli and lower yield strain, evidencing larger aggregates at the interface.^{406,407} When the particle size increases, the resistance to fracturing increases, but these surfaces behave more brittle, i.e., have lower yield strain.⁴⁰⁸ Mixing of small and large particle size distributions generally leads to weaker and more brittle layers, despite having higher packing density than a monomodal monolayer.⁴⁰⁸ This is reminiscent of 3D polydisperse systems that show reduced yield stress, viscosity, and shear moduli compared to monodisperse systems.⁴⁰⁹

The effect of particle wettability for spread monolayers of fumed silica nanoparticles (100% to 20% SiOH) with equal surface concentrations increases both storage and loss modulus as the particles become more lyophilic. A transition from mainly elastic to viscous behavior occurred as the hydrophobicity increased.^{283,365} Silica particles with intermediate wetting ($\theta = 90^\circ$) portrayed a maximum storage modulus due to their high binding energy. At low strain amplitudes and fixed frequency, no dependency on G' was found and is almost two orders of magnitude larger than the loss modulus. A melting transition occurs at higher strain amplitudes above the yield stress, showing a decrease in storage modulus and a maximum in G'' indicative of a fractured monolayer.^{283,373,403} The particle-laden interfaces behave mainly viscous at low shear rates and small deformations. In contrast, the opposite occurs when the strain rate amplitude increases due to a decrease in structural relaxation time^{283,373} and shows similar behavior to that found in 3D soft solids.⁴¹⁰ Under small amplitude deformations, a quasi-linear relationship was discovered between the inverse of the shear rate and relaxation time that was scalable onto a single master curve (i.e., a composite graph formed by a superposition process to separate two main variables upon which the viscoelastic properties depend). Large strain deformations of these particle-laden interfaces that induce fracturing showed repeatedly rapid

recovery and self-healing (< 1 s) of the monolayer when the stress is released, followed by slow disappearance of defects initially created during the healing process. This behavior depends on the coverage and particle wettability and also influences the yield and melt stresses, which attain their maximum values for particles with contact angles close to 90° .^{403,411}

Particle roughness influences the shear response of particle-covered interfaces, and the surface roughness is strongly correlated to the particle coverage. When the surface roughness increases, the shear viscosity reduces at low coverage. When the monolayer gets close to the jamming state, increased surface roughness causes the opposite effect on the viscosity. This turnover is ascribed to differences in the friction between the particles present at the interface and explains the shear thickening behavior of particle-laden interfaces.^{412–415}

3.3 Mixed adsorption of hydrophilic, inorganic nanoparticles and surfactants to liquid interfaces

In the previous sections, most of the referenced literature studied particle-laden interfaces where the material inherently possesses adequate wettability, was spread on top of the liquid interface or was coated with firmly bound ligands in a separate modification step to stimulate adsorption.⁴¹⁶ They represent a relatively simple platform to study their physicochemical aspects and interpret 3D shapes. However, the industrial and natural habitats are recurrently encountered with multicomponent adsorption. In this case, at least two different components are allowed to adsorb to the interface (e.g., surfactants, proteins, different particle sizes). Their fractional coverage is determined by the net energy balance of their interfacial activities and molecular interplay. Surfactants significantly lower the interfacial tension and enhance the rheological properties of the interface. Therefore, they are commonly used as additives when the particle material has a low affinity for the liquid interface, such as inorganic oxide particles (e.g., silica, titania, zinc oxide).⁴¹⁷ Depending on the solubility, surfactants can be added to the same or opposite phase as the colloidal particles. Long-chain polar lipids are mainly water-insoluble surfactants and typical features, specifically for octadecyl amine, are briefly discussed in section 3.3.1. The presented literature in section 3.3.2 for the ‘mixed’ particle-surfactant systems is commonly studied on qualitative grounds by measuring the response of a clean liquid interface, adsorption of single components, followed by the binary system. Particles and surfactants can interact cooperatively or unfavorably, classifying adsorption as synergistic or competitive, respectively. Furthermore, surfactants strongly influence the interface's surface pressure and rheological properties, making it harder to separate the individual contributions on surface pressure and rheology when designing thermodynamic

models for mixed films.^{42,43,327} Nevertheless, some progress has been made in the last few years (section 3.3.3). Consequently, the viscoelastic rheological response of the interface against dilation (section 3.3.4) and shear (section 3.3.5) for mixed films have been studied mainly on a semi-quantitative experimental basis.

3.3.1 Surface-active polar lipids

When surfactants adsorb and orient preferentially to the phase of equal polarity, the polar head-water and hydrophobic tail-oil interactions affect the interfacial tension.^{418–420} Polar lipids (e.g., fatty acids and fatty amines) consist of an aliphatic chain with an ionizable polar headgroup. Lipids with longer chains ($C_n \geq 12$) form insoluble monolayers (i.e., Langmuir monolayers) at the air/water interface, and a rich range of phase behavior is observed when forced area compressions increase their density. The monolayer collapses into a 3D structure, such as multilamellar, once a critical coverage is reached.⁴²¹ When the material easily dissolves in an organic solvent, these lipids form soluble monolayers (i.e., Gibbs monolayers) that are in an exchange equilibrium with the bulk. During area compression of soluble monolayers, they easily desorb owing to their low adsorption energies ($1-20 kT$).²⁰⁸

Since the local environment of the liquid interface differs from the bulk, the bulk pKa values (an expression of acidity) for many surfactants deviate from the experimentally-derived surface methods. Interfacial pressure or surface potential versus pH curves resemble bulk phase titration curves. However, an apparent shift occurs in the pKa of several pH units with the largest impact in the absence of electrolyte.^{422–424} For example, octadecyl amine with a bulk pKa of 10.6⁴²⁵ is estimated to be 8.5 at the interface.⁴²² The same reasoning applies regarding the pH of a neat liquid interface, i.e., that there is an effective pH at the surface that differs from the bulk pH.^{426,427}

The elemental intermolecular forces in a monolayer of long-chain polar molecules originate from the van der Waals interaction between the hydrocarbon chains and the attraction or repulsion between the polar heads.⁴²⁸ In the absence of electrolyte, unionized and partly ionized films experience low repulsion and the monolayer condenses, while an expansion occurs at high degrees of ionization showing increased interfacial activity.^{419,428,429} With the addition of electrolyte, counterion adsorption (partially) neutralizes the electrostatic repulsion between ionic surfactants, causing the monolayer to condense and generally increases their interfacial activity visible as a more substantial decrease in interfacial tension and enhanced viscoelasticity.^{430–433} For nonionic surfactants, the opposite effect is observed and they can form stable films through steric stabilization only at high surface coverage.^{432,434}

The aliphatic amino lipid octadecyl amine (ODA, Fig. 3.1) forms an insoluble monolayer at aqueous pH > 5.7. Its water solubility increases with a maximum around a pH of 3.5 due to the protonation of the amine groups.^{435,436} The unfavorable free energy cost to transfer one CH₂ group into the water phase is roughly 0.8 kcal mol⁻¹. However, it gets overthrown by the dipole-dipole or ion-dipole interactions between the surfactant head and the water molecules.⁸³ Significant phase transfer into the aqueous phase typically increases the time-dependent interfacial tension.^{83,437}

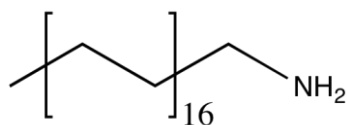


Fig. 3.1 Chemical structure of octadecyl amine (C₁₈H₃₇NH₂).

Liggieri et al.⁴³⁸ monitored the hexane/water (aqueous pH 7.5) interfacial tension of different ODA concentrations (0.1 – 5 mM). Between 0.5 and 1 mM, the tension declines sharply (~ 20 mN m⁻¹) with longer equilibration time. The constructed adsorption isotherm shows a discontinuity in the concentration-dependent interfacial tension reminiscent of systems undergoing interfacial phase transitions. A thermodynamic model describing interfacial aggregation^{439,440} showed a good fit with the equilibrium tension data, suggesting that adsorbed ODA forms interfacial aggregates starting at concentrations of 1 mM, likely due to enhanced hydrocarbon tail interactions. As stated above, phase transfer of ODA should not occur under the investigated conditions here and was confirmed by evaluating the fluorescence spectra of the oil-soluble Nile red. A shift in the absorbance occurs with solvent polarity⁴⁴¹ and shows an excitation wavelength-dependent fluorescence emission when it is incorporated into micelles,⁴⁴² which was observed starting at 1 mM ODA.⁴³⁸ They also estimated ODA has a cross-sectional area of 20 Å², typical for alkylamines adsorbed at the oil/water interface.⁴⁴³

3.3.2 Synergistic and competitive adsorption

As has been established above, adsorbing nanoparticles reduce the free interfacial area that creates a 2D surface pressure,^{34,35,40} while surfactants reduce the tension by disrupting the molecular interactions at the clean liquid interface.⁴¹⁸⁻⁴²⁰ Several studies investigated mixtures of hydrophilic particles and water-soluble surfactants, either nonionic⁴⁴⁴⁻⁴⁴⁷ or ionic with equal^{21,23,94,445,448-450} and opposing charge^{21-23,372,444,445,450,451}. Dispersing hydrophilic nanoparticles with nonionic or oppositely charged surfactants in the same liquid medium generally modifies the particle hydrophobicity through hydrogen bonding and electrostatic interactions that form synergistic particle-surfactant complexes.^{446,452} Consequently, less free

surfactant molecules are available to lower the interfacial tension and adsorbed complexes, which are initially hydrophilic particles, reduce the tension to a lower extent at low to moderate surfactant concentrations. A general observation from these particle-surfactant studies is that with high surfactant coverage of the interface, the equilibrium interfacial tension is unaffected by the presence of particles. At the same time, surfactant adsorption to the nanoparticle surface can change particle wettability in a surfactant concentration-dependent manner. This dependency may lead to different surfactant structures assembled on the particle surface, which in turn yields particles with varying surface activity and consequently differing stabilization efficiency. Similarly, mixing oppositely charged particles of equal composition stabilizes emulsion droplets as the average charge on the clusters is effectively neutralized.^{453,454} Direct observations of the liquid-liquid interface using X-ray scattering³⁸ or FreSCa cryo-SEM³⁹ showed that higher particle coverages were obtained at low surfactant concentrations due to partially hydrophobized particles. In contrast, high surfactant concentrations reversed particle wettability back to hydrophilic resulting in less particle adsorption. In principle, particle-surfactant complexation explains differences in the tension of mixed interfaces compared to particle-free interfaces, which are highly dependent on the concentration of each component.^{21,22,334,372,444,447,455} A recent study by Vialetto et al.⁴⁵⁶ showed that micromolar concentrations of a cationic surfactant (dodecyltrimethylammonium bromide, DTAB) allow self-assembly of micro- and nanoparticles (down to 100 nm) into highly ordered polycrystalline domains at the air/water surface using the ‘flipping method’. Here, the mixed particle-surfactant dispersion is turned upside down in a narrow cylindrical cell and the particles migrate to the concave air/water surface over a period of 2 hours. The cell is flipped back into its original position, left overnight and only adsorbed particles will remain attached that concentrate in the center of the interface. They argued that for surfactant concentrations of 1 μM to 100 μM most of the particle’s surface charge is retained, which induces sufficient electrostatic repulsion to form organized structures with remarkable optical properties. For surfactant concentrations in the millimolar range, amorphous structures result from significant surface charge neutralization of the particles. This effect was reproducible for different material compositions (gold, silver, and silica) and particle shapes (spheres and cubes).⁴⁵⁶ By using photosensitive surfactants (e.g., AzoTAB, a cationic surfactant with an azobenzene moiety that isomerizes from *trans* to *cis* with adequate irradiation), new kinds of reconfigurable photonic devices can be designed when using very small amounts of surfactants. Micrometer-sized polystyrene particles with AzoTAB showed a fast crystallization time of ~ 10 s upon light irradiation and slower disassembly in the dark phase of ~ 1 min.⁴⁵⁷

In the case of equally charged surfactants and nanoparticles dispersed in water, interactions are expected to be repulsive, but the exact mechanism determining the adsorption balance remains poorly understood. For example, the interfacial tension and dilational moduli for silica nanoparticles in the presence of negatively charged surfactants at the heptane-water interface were attributed to the electrostatic repulsion between both materials.⁹⁴ At the same time, a recent study ascribes this difference to an increase in the surfactant's surface activity induced by dissociation of the surface groups of the silica nanoparticles, which raises the ionic strength of the bulk.⁴⁵⁸ Increasing the particle concentration with fixed surfactant concentration causes a more potent interfacial tension reduction and shows a particle size-dependency for constant particle mass fractions.^{94,448,458} Stable oil-in-water emulsions were formed using very low particle (10^{-4} w/w%) and surfactant concentrations (10^{-5} M) bearing equal charges. The surfactant molecules lower the interfacial tension and endow droplets with charge stabilization, whereas the charged particles are dispersed in the aqueous films between droplets retaining thick lamellae that reduce water drainage and hinder flocculation and droplet coalescence.⁴⁴⁹ Laser scanning confocal microscopy analysis indicates that the non-adsorbed particles impart stability primarily via entropic forces caused by the accumulation of silica particles in the coherent phase between dispersed oil drops.⁴⁵⁹ At high surfactant concentrations, the particles are removed from the interface showing that the process is reversible and suggests that larger quasi-irreversibly bound particles can be dislodged from the interface as well.⁴⁶⁰

When particles and surfactants of opposite polarity are dispersed in different immiscible phases, their synergistic interactions are limited to the interfacial region. Santini et al.⁴⁶¹ studied hydrophilic silica and palmitic acid's emulsion stability and interfacial tension at the hexane/water interface. Phase transfer of palmitic acid from hexane to water with subsequent electrostatic and hydrogen bond interactions formed particle-surfactant complexes. They accumulate at the interface with emulsions showing very long shelf-life stability arising from steric stabilization. This enhanced stability was only the case when a surfactant monolayer was present on the particle surface, as excess surfactant redispersed the particles into the aqueous phase.⁴⁶¹ Stable oil-in-water Pickering emulsions were obtained when hydrophilic laponite dispersions at basic pH were mixed with the cationic lipid ODA. Here, Whitby et al.⁴⁶² explained this behavior as a consequence of the synergistic interactions that arise at the interface between the oppositely charged constituents as indicated by the significant difference in interfacial tension. They observed similar interactions between hydrophilic silica nanoparticles and ODA only when sufficient surfactant was adsorbed at the interface, in agreement with dilational rheology as indicated by an overall raising of the elasticity compared to the absence

of nanoparticles.⁴³⁸ *In situ* infrared spectra of silica submerged in carbon tetrachloride showed that ODA interacts strongly with silanol groups and chemisorbs to a certain extent⁴⁶³ with a thickness around 1.5 nm.⁴⁶⁴ Bulkier lipids and mixtures thereof (e.g., 1,2-dipalmitoyl-sn-glycerol-3-phosphocholine (DPPC), 1,2-dioleoyl-sn-glycero-3-phosphocholine (DOPC), and cholesterol) also interact with negatively charged inorganic particles due to electrostatic attraction or hydrogen bonds, which depend on the nature of the lipids. The particles penetrate the Langmuir monolayer and distort the interfacial packing of the lipid monolayer, thereby hindering their organization. The disorder in the monolayer increases, and a shift in the surface pressure isotherm for the mixed monolayer is caused by excluded area-like effects of the penetrated particles.^{330,465–467} Ramazani et al.⁴⁶⁸ performed coarse-grained molecular dynamics simulations to model DPPC lipid interactions and organizations with inorganic nanoparticles of varying hydrophobicity (contact angle between 17.26° - 114.42°). The lipids form a corona around the particles when their contact angle is higher than ~ 60°, while less hydrophobic particles have a micelle structure attached to their surface. This transition from tails coating the particle surface to hemicelle coating as the contact angle changes is abrupt, suggesting a first-order-like transition.⁴⁶⁸

A final group involves particles and surfactants of equal charge dispersed in opposite, immiscible liquid phases. Emulsification of hydrophilic nanoparticles and oil-soluble surfactants bearing equal charges allowed synthesizing hollow, submicron-sized colloidal capsules. Deflated capsules were retrieved when the sign of the charged materials was opposite, argued by charge normalization.^{469–472} Pichot et al.^{334,473} investigated the influence of surfactant type and concentration on Pickering emulsions' stability and noticed that interfacial nanoparticle displacement was evident at high surfactant concentrations but only when both components were dissolved in the same phase. Interestingly, when lecithin was added to the oil phase, interfacial tension values with and without particles were similar, and particle adsorption at the interface was independent of lipid concentration. All these studies show how distinctly the interfacial tension responds in each different particle/surfactant system, making quantification via a general analytical approach challenging. The great number of adsorption isotherms and equations of state for surfactants alone demonstrate the divergent behavior of interfacial tension to adsorption.^{474–476}

3.3.3 (Semi-)quantitative description of particle-surfactant adsorption layers

Despite the complexity associated with providing a thermodynamic description of particle-surfactant-laden interfaces, estimating particle coverage or adsorption energies for mixed films has not been without success. Katepalli et al.³⁷ discussed that interfacial particle displacement occurs from a drop surface upon adding surfactant if the surfactant-stabilized drop of equal radius has higher surface free energy than the particle-stabilized drop according to:

$$\frac{\gamma_{lo} - \gamma_{SF}}{\gamma_{lo}} > \Theta \left[\frac{(1 - |\cos\theta|)}{\sin\theta} \right]^2 \quad \text{Eq. 3.16}$$

where γ_{lo} and γ_{SF} are the interfacial tension of the pure oil/water and of the surfactant-laden interface, respectively. In other words, the fractional change in interfacial tension upon adding surfactant must be more significant than the area fraction of the surface covered by particles. This model does not account for additional effects caused by direct particle-surfactant interactions. Adsorption of hydrophilic, negatively charged carbon black particles was studied at the oil/water interface with anionic, cationic, and nonionic surfactants with concentrations between 0.1 mM and just above their CMC. A significant decrease in interfacial tension by surfactant alone (e.g., 94% with Triton X-100 from 51 to 3 mN m⁻¹) displaces the particles from the interface and not otherwise (e.g., 67% decrease with sodium octyl sulfate). Particle clustering and intermittent release into the bulk were observed with the cationic surfactant at low surfactant concentrations which changes to a steady release at higher concentrations. The interactions between the particles with the anionic and nonionic surfactants occur through hydrophobic binding and particles were released continuously from the droplets.³⁷

Utilizing pendant drop tensiometry complemented with small amplitude dilational rheology, Vatanparast et al.³⁷² monitored the surface pressure and standard deviations from Laplacian drop shape fitting during large-amplitude surface area compression/expansion cycles of synergistic surfactant-decorated nanoparticles. The deviation from Laplacian shape under large amplitude deformations (~ 70% initial drop surface area) shows a characteristic onset and dimple representative of a close-packed and collapsed monolayer, respectively. These features are absent for compressed drops of pure liquid or coated solely with surfactant. They observed a stronger reduction in the interfacial tension when the particle concentration increased, despite having fewer physisorbed cationic surfactant molecules per particle, as this was fixed to 0.1 CMC for all particle concentrations. E' increases significantly for the lowest concentration of

particles and is virtually independent of particle concentration. The number of adsorbed particle-surfactant complexes was calculated by assessing the drop surface area at close-packing by assuming $\Theta \approx 0.91$. Roughly 1.5 times more complexes adsorbed when the particle concentration increased from 0.5 w/w% to 2.0 w/w%. This slight increase in adsorbed complexes suggests minor alterations in particle hydrophobicity under these conditions, and the amount of adsorbed particle-surfactant complexes influences the macroscopic interfacial tension. Estimating the concentration of adsorbed particles/complexes at the liquid interface using large compression/expansion cycles does require them to adsorb (quasi-)irreversibly and is thus limited in their use.⁹⁴

To the best of my knowledge, Hua et al.⁵³ are the first to comprehensively characterize adsorption in a hybrid nanoparticle/surfactant system using surface-active ions and ultra-small gold nanoparticles coated with the same ionic ligand. They formulated a competitive adsorption model that relates the change in interfacial tension to both adsorbents' surface activity and the particles' wetting properties by treating the two contributions as additive (section 3.2.2).

Following Hua et al.,⁵³ Olayiwola et al.⁵⁵ developed a physicochemical model using the Gibbs isotherm for a dividing surface to calculate the surface/interfacial tension. Accounted for are the lateral cohesive interaction energy of the surfactant's CH₂ groups, the electric double layer effect of ions in the system coming from nanoparticles, electrolytes, and surfactants, and also the dipole-dipole interaction between the ions of the nanoparticles and electrolytes. A set of model equations were developed, e.g., particles with surfactants bearing equal or opposite charges, or no charges in the case of nonionic surfactants, and the absence and presence of symmetric electrolytes. Fitting the model equations to published surface/interfacial tension data for the various combinations showed significantly good predictions below CMC. These results indicate that the dipole-dipole interactions of the ions, the electric double layer effect, and the cohesive energy contribute to the interfacial free energy reduction and provide new insights into the stability of multicomponent Pickering emulsions.⁵⁵ Such derivations contribute to the fundamental understanding of multicomponent adsorption at interfaces based on only a few experimental parameters from a very well-defined experimental approach. This lays the groundwork for potential extensions that use larger particles exhibiting more significant adsorption energies as well as other particle-surfactant mixtures.

3.3.4 Interfacial dilational rheology for particle-surfactant-laden interfaces

The most often studied synergistically interacting particle-surfactant complexes regarding interfacial dilational rheology were executed using silica particles and the water-

soluble surfactant cetyltrimethylammonium bromide (CTAB, $[(C_{16}H_{33})N(CH_3)_3]Br$, CMC \approx 0.9 mM).⁴⁷⁷ Electrostatic attraction between the surface silanols of the particles and surfactant cationic head group, and surfactant tail-tail hydrophobic attractions are responsible for the surface-specific adsorption behavior that is reminiscent of aggregation in the bulk.^{38,296,452,478} Depending on the number of surfactant molecules present (and thus dependent on the particle size), a dispersion-flocculation-redispersion sequence can be observed that influences their packing density and wettability. For a low number of adsorbed CTAB on the particle surface, aggregates and single surfactant molecules are present and their contact angle and packing start to increase.^{296,452} Hemimicelles form at intermediate concentrations and form dense, particle-covered interfaces with the highest hydrophobicity. Whether particles are more immersed in the water ($\theta < 90^\circ$) or oil phase ($\theta > 90^\circ$) seems to depend on the particle size, i.e., when the size dimensions of the particles and surfactant become comparable, the particles become more hydrophobic.^{38,296,452} The length of CTAB is estimated to be 1 – 2 nm.^{479,480} The particle wettability reverses back to hydrophilic at higher surfactant concentrations as micelles start to form on the surface, redispersing the particles in the bulk. A large excess of free surfactant can also occupy the liquid interface, thereby preventing particles to adsorb. Consequently, fewer particles will occupy the interface.^{38,296,452}

While the interfacial tension of the complexes is higher than pure CTAB, the complex dilational modulus tends to increase for these mixed films compared to the single components. Moreover, the modulus demonstrates a dependency of the viscoelastic response at low frequencies (0.005 – 0.2 Hz).^{22,481–484} The rheological properties of the mixed film were enhanced at the oil/water interface compared to the air/water surface.⁴⁸³ The linearity limits for the oscillation frequency in classical pendant drop rheology⁴⁸⁵ required additional methods (capillary pressure tensiometer and electrocapillary wave device) to monitor the dilational response for a broader frequency spectrum (10^{-3} – 10^3 Hz).^{281,482,484} The dilational stress at varying frequencies indicated two distinct relaxation processes operate in this system. The first relaxation process occurs at low frequencies and corresponds to diffusion-limited adsorption of surfactant-decorated particles migrating toward the interface. The second relaxation occurs at high frequency involving the ad- and desorption of unbound surfactant molecules since adsorbed hydrophobized particles are expected to remain irreversibly attached. Theoretical models accounting for the physical origin of the two processes indicated a transition from purely diffusive transport to mixed diffusion and reorganization of the adsorbed layer as the hydrophobicity of the particles increased. Large area compressions indicate the presence of

other processes active over long timescales, which could be related to particle or multilayer reorganization under solid-like conditions.^{281,482,484,486}

The dilational response of the interface is strongly dependent on the depletion of CTAB from the solution onto the particle surface (i.e., particle-surfactant ratio), which in turn modulates the particle wettability and particle-particle interactions at the interface and bulk.^{281,296,486} Kirby et al.²² studied the effect of the hydrocarbon tail length on the dynamic surface properties of concentrated dispersions of silica nanoparticles and alkyltrimethylammonium bromides (C_n TAB, where $n = 14, 16, 18$) at the air/water surface. All dispersions had a ratio of approximately 8 C_n TAB molecules per particle. The equilibrium surface pressure increases with tail length, while E' changes only slightly, meaning it has little influence on interfacial particle coverage. A substantial increase in surface pressure occurred at 33% area compression independent of the surfactant tail length. When the particle-surfactant dispersion was exchanged with pure water, the surface pressure decreased almost back to the pure air/water value. Subsequent 33% area compression led to a similar abrupt increase in surface pressure indicative of irreversible particle adsorption, while the surfactant can desorb. Subphase replacement with increasing amounts of electrolyte led to enhanced hysteresis of the surface pressure isotherms, and the enhanced electric double layer screening formed a fully rigid interface at low particle coverage.²²

Synergistic adsorption of hydrophilic particles and oil-soluble surfactants have been studied to a smaller extent but show similarly enhanced frequency-dependent viscoelastic properties. Since phase transfer of each substance is unlikely to occur under the investigated conditions, differences are ascribed to particle incorporation into the liquid interface. Adsorption of carboxylic acid-modified silica nanoparticles in different electrolyte concentrations (0 – 500 mM) to the toluene/water interface in the presence of an oil-soluble amine-terminated PDMS surfactant has been explored. Droplet compressions and the associated decrease in tension as the particles' areal density increases show similar profiles for all electrolyte concentrations, which merge into a single plot. Normalization of the data to the surface area of the droplet when wrinkling is first observed showed overlap for all salt concentrations, allowing to estimate the gas-liquid-solid regimes. The different slopes of each region allowed to extract the quasi-equilibrium surface elasticity outside the jammed state, which was 15 mN m^{-1} for a monolayer resembling the gaseous state and 55 mN m^{-1} for a liquid-like monolayer. Higher compression ratios resulted in a solid-like structure and wrinkling of the monolayer at very high ionic strengths.³⁰ Another example that leads to the formation of an elastic film and stable emulsions is the set of water-soluble carboxylated

fullerene combined with a number of toluene-soluble poly(styrene-*b*-2-vinylpyridine) polymer-derivatives. Their interactions are essentially determined by the dissociation and protonation of the amine group. At low pH, the interfacial tension could not be trusted due to the formation of a rigid, solid-like film. A fast development of wrinkles was observed at small area compressions and neutral pH that prevented droplet coalescence under forced contact. The time evolution and frequency sweep of E' was always larger than E'' . At highly basic conditions, droplets coalesced and showed no sign of wrinkling.⁴⁸⁷ Stearic acid dissolved in decane mainly shows viscous behavior at the interface at low deformation frequencies and transitions to a dominantly elastic interface at 0.01 Hz while E'' continuous to decrease at higher frequencies. Both moduli increase when water-soluble carbon graphite particles are present, indicating interfacial particle adsorption. The elastic modulus increases with almost a factor of two, but the shape of both moduli and viscous-to-elastic transition points are identical to the pure surfactant solution. This indicates that the strength of the moduli is determined by the presence of particles, while the dynamic properties of the interface are determined by the surfactant.³⁶⁴ ODA dissolved in hexane attracts the negatively charged silica particles to the oil/water interface based on electrostatic attraction and hydrogen bonding. At low ODA concentrations, the magnitude of E' in the absence and presence of particles is quite similar. Noticeably higher elasticity values for the mixed adsorption layer arise in association with a significant drop in the interfacial tension. A nonlinear response to droplet dilation was observed at very high surfactant concentrations, irrespective of the presence of particles, while wrinkling was only observed in the silica/surfactant system. Also, only the magnitude of E' is influenced by adsorbed particles without apparent differences in their shape.⁴³⁸ In the case of binary adsorption of particles and bulkier lipids (e.g., DPPC, DOPC), particle/lipid monolayers show higher elastic moduli than the pure lipid monolayer with no significant differences in their shape.^{330,465–467}

A limited amount of research on interfacial dilational rheology is available in the case of equally charged surfactants and particles. For instance, Sun et al.⁴⁸⁸ studied adsorption between silica nanoparticles in the presence of the water-soluble sodium dodecyl sulfate (SDS) surfactant. There exists a competitive adsorption behavior, and the presence of particles lowers the adsorption rate. These hybrid systems enhance the dilational elasticity with almost constant dilational viscosity. Despite competing for occupancy at the interface, the silica-SDS system exhibits synergy on foam stability, although the foam volume is less with added particles to the system.⁴⁸⁸ This contrasts with earlier studies, showing that the foam volume increases when particles are added⁴⁴⁸ with similar interfacial elasticities as the pure surfactant-coated bubbles.

The bubble elasticity decreases slightly when more particles are added, accompanied by stronger interfacial tension reductions.^{448,458} Adsorption rates in the presence of particles are much faster and not retarded both at the air/water and oil/water interface.^{94,448} The reason for this discrepancy is unclear but can either be due to impurities stemming from SDS hydrolysis to dodecanol, which occurs in aged SDS solutions. In the latter case, the surface tension response between fresh and aged SDS solutions in absence and presence of particles shows an opposite adsorption behavior⁹⁴ that is consistent with the results from Sun et al.⁴⁸⁸

A final remark to consider is the aging phenomenon of the interfacial layer. While the mechanical stiffness of the interface increases over time, the surface tension of particle-laden interfaces shows hardly any changes. This can be explained based on the irreversible attachment of the particles that forms a solid-like layer associated with a densification process,^{76,77} where the exchange of particles between the bulk and interface is negligible or present at very slow dynamics.^{481,484,489}

3.3.5 Interfacial shear rheology for particle-surfactant-laden interfaces

Unlike dilational rheology studies, only a limited amount of work is available that is focused on the shear response of particle-surfactant systems. Some general observations were made with silica-CTAB complexes at the air/water interface. Oscillatory shear experiments supplemented with surface tension, imaging ellipsometry, and BAM allowed rheological modeling of the particle coverage at the air/water surface. Below the CMC of CTAB, a liquid behavior is observed at low particle coverage, while higher coverages form an interconnected CTAB/particle network that ultimately percolates into a solid-like surface, occurring at a packing fraction of 0.86 (i.e., random close packing). Further compressions lead to a buckled interface that recovers after relaxation of the interface. Shear strain sweeps of the CTAB/silica-laden interfaces show a power-law dependence for small strains on the particle coverage (Θ) and the elastic interface shows a plastic flow beyond the yield point.²¹⁸ The elastic shear modulus lies in the range of $0.1 - 1 \text{ N m}^{-1}$, similar to other reports.^{365,373,411,490} A good power-law fit as in the percolation theory is found for the elasticity values by introducing a critical packing density (Θ_C) parameter, which is the particle concentration obtained from the Π - Θ isotherms where the liquid to solid transition is expected:²¹⁸

$$G' \sim \left(\frac{\Theta}{\Theta_C} - 1 \right)^\beta \quad \text{Eq. 3.17}$$

Below Θ_C , the shear modulus is small and snowballs as the system approaches a jammed state.²¹⁸ In many particle-based systems, the monolayer assembles into polycrystalline^{491,492}

and/or amorphous³⁹⁴ 2D structures with identical shear rheological properties. Namely, particle monolayers respond to the shear deformation under low strains as elastic solids whereas larger strains induce microstructural rearrangements that become irreversible beyond the yield point and show a plastic flow behavior.⁴⁹¹ In a follow-up study, Maestro et al.²²⁰ proposed a theoretical model to explain both the linear and nonlinear stress-strain relation for the deformation of the mixed particle-surfactant system under shear strain. The total stress (τ_s) is the sum of the elastic (τ_{el}) and viscous stress (τ_v) contributions and includes all relevant particle-level physics such as the interaction potential, nonaffine displacements (i.e., additional work required to maintain mechanical equilibrium in a disordered lattice that is being transmitted through the nearest particle neighbors), shear-induced modifications in the local particle network, the thermally activated cage distortion, and the viscous dissipation caused by microscopic friction. Two non-trivial parameters are required, the relaxation time of the particle cage and the viscous relaxation time, that provide a very good fit between theory and experiment below and above the yield point. Silica particles adsorbing at the air/water interface form a 2D amorphous solid with characteristics of a colloidal glass and the authors' framework provides a template for quantitative tuning and design regarding the mechanical response of particle assemblies adsorbed to the liquid surface.²²⁰ The yield stress (τ^*) of these mixed monolayers also shows power-law behavior dependent on the interfacial coverage, i.e., $\tau^* \sim \Theta^\alpha$.²¹⁸ Similar trends are observed using attractive, micrometer-sized particles³⁶⁸ and computer simulations, where α was estimated to vary between 4 and 8.4.^{493,494} A frequency-dependent power-law behavior on both G' and G'' corresponds to the soft glassy rheology model.^{220,495} Silica-electrolyte systems under small- and large-amplitude oscillatory shear show reminiscent behavior.⁴⁰⁷

Maas et al.⁴⁹⁶ followed the dynamic film evolution of silica nanoparticles and differently charged lipids, showing that the film evolution follows a two-stage increase in both G' and G'' until reaching a plateau. The initial increase in moduli is evidence for adsorption and continued adsorption of particles after long times is indicated by the slow increase in G' . Due to the polar headgroups of the lipids, they are responsive to pH changes allowing to tune the mechanical strength of the interface and relate this to emulsion stability. Faster adsorption kinetics and higher moduli are achieved when the charges of the particles and lipids are opposite, while equally charged components tend to form weaker films showing lower moduli and require longer equilibration times.^{470,471,496} Similar behavior is found using positively charged γ -Fe₂O₃ nanoparticles combined with water-soluble⁴⁹⁷ and oil-soluble surfactants.²⁹⁴ When describing particle-laden interfaces, the term monolayer is readily used to assume that multilayers are

absent once the interface reaches maximum packing. Surprisingly, G' values for particle sizes from 14 nm to 3 μm all lie within the $0.1 - 1 \text{ N m}^{-1}$ range.⁷⁶ At the same time, one would expect that G' correlates to the thickness of the monolayer, i.e., particle diameter ($G' \sim d$).^{368,373,394,411,490} Therefore, the continuum mechanics approach, which basically models the monolayer behavior as a continuous mass rather than discrete particles, has limited applicability in evaluating their deformation modes. This is beyond the scope of this work, and some compelling arguments have been stated elsewhere.^{76,77}

3.4 Aim and approach

In recent decades, the fundamental driving force behind particle adsorption at liquid interfaces and their interparticle interactions has been described by a well-developed theoretical framework (Chapter 2) that forms the basis of many single and multicomponent adsorption studies (Chapter 3). Owing to the expansion in technological development, several methods have been designed to extract the contact angle of (small) particles adsorbed at liquid interfaces, each with their specific benefits and limitations (section 3.1). The observed particle adsorption layer properties (i.e., interfacial coverage and immersion depth) obtained in those experiments are then related to the fundamental principles underlying adsorption, which in turn can be determined from adsorption studies by monitoring macroscopic variables such as interfacial tension (IFT) and surface elasticity (section 3.2). While the results between the nanoscale-resolution ‘contact angle (CA) methods’ and adsorption studies do not always agree, in many instances the experimental surface pressure term for equilibrated single-particle correlates surprisingly well with the thermodynamics of particles at liquid interfaces. For multiple adsorbents (e.g., particles and surfactants), the resulting surface pressure is governed by the interactions between the various components, and a clear distinction between their individual contributions to the IFT is not always obvious (section 3.3). Also, the properties of the adsorption layer formed by particles may be altered by the interacting surfactant, necessitating the use of sophisticated methods to make accurate predictions on particle adsorption layer properties (section 3.1). Nevertheless, such findings will aid scientists active in the colloid and interface sciences to understand and predict the interactions between particles and surfactants at two- and three-dimensional liquid interfaces, both at an academic and practical industrial level.

Therefore, the aim of this work is to unravel fundamental questions about synergistic particle-surfactant adsorption and can be addressed by selecting a suitable system, where particle-surfactant interactions at the oil/water interface are expected to be minimal.

This allows dividing the two-dimensional interfacial pressure into individual contributions of the nanoparticles (NPs) and surfactant using an analytical model based on the principle of additivity in an attempt to predict the nanoparticle coverage, which can only uphold if the CA of the NPs remains unaffected by the surfactant (Chapter 5). Particularly, aminated silica nanoparticles coated with (3-aminopropyl)triethoxysilane (APTES) and equally charged octadecyl amine (ODA) are tested in a water/decane system. Because the polar heads of the surfactant are similar to the particle's surface groups and dissolved in an immiscible nonpolar medium, interactions can be assumed to be limited to the interfacial phase and repulsive through the aqueous phase. Therefore, it can be expected that the lipids prefer to adsorb at the oil-water interface while leaving the particles unaffected. Consequently, the decrease in interfacial free energy caused by the particles and by the surfactants should behave additively in this particular experimental system. The validity of this assumption is tested via CA measurements on APTES-coated substrates that simulate the NP surface in the presence of varying amounts of lipids. In IFT measurements using a pendant drop setup, various concentrations of ODA are dissolved in decane and examined against a fixed concentration of 1 w/w% APTES-coated silica NPs dispersed in water at a pH that protonates the amine groups on the surface of the particles and of the interfacially adsorbed surfactants. The results of the CA and IFT measurements are discussed in light of an additivity continuum model explained in Chapter 5. Furthermore, the population of adsorbed particles at the liquid-liquid interface is visualized with scanning electron microscopy (SEM) after Langmuir-Blodgett-type transfer of the interfacial film. In addition, the viscoelastic properties of the interface are examined via dilational and shear rheological measurements. These techniques provide additional semi-quantitative evidence of the validity of the presented approach.

Because the possibility exists that the particle immersion depth is still affected in a surfactant concentration-dependent manner at the nanoscale when their charges are equal and that changes in interfacial tension can be superimposed for multiple adsorbents, a detailed *in situ* representation of the mixed adsorption layer for positively and negatively charged NPs in presence of positively charged surfactants at the oil/water interface can be acquired using synchrotron-based X-ray reflectivity (XRR) (Chapter 6). To this purpose, negatively charged silica NPs and positively charged APTES-coated silica NPs dispersed in the aqueous phase at pH 5.8 at a fixed concentration of 0.1 w/w% are studied. The XRR data are analyzed via a physical model that realistically describes the adsorption of spherical particles to a liquid interface and fits the electron densities (EDs). NP coverage and CA obtained through modeling of the EDs are compared to and discussed with the previously reported continuum-based

analytical model using the surface pressure difference in the presence and absence of APTES-coated silica NPs.

Furthermore, CAs of particles adsorbed to liquid interfaces are generally extrapolated from macroscopic sessile drops on planar substrates, which are assumed to be topographical and chemical equivalents to the NP surface. However, both assumptions are rarely verified simultaneously and could be part of the strong discrepancy found in the literature between sessile drops and adsorbed particles. Since the CA of the silica and APTES-coated silica NPs adsorbed at the liquid interface using XRR are measurable with high-precision, a versatile approach is tested where the particle contact angles at the surfactant-free liquid interface are compared to macroscopic CAs of sessile droplets on corresponding planar substrates in an identical environment (Chapter 7). The synthesis and functionalization procedures are adjusted to ensure that both surfaces have comparable surface chemistry, which is assumed to be the case when the zeta (ζ) potentials of the dispersed NPs measured with electrophoretic light scattering and the coated planar substrates obtained through streaming current overlap. Additionally, to understand the possible influence of surface roughness of the macroscopic substrate on the adsorption behavior of the particles, smooth (SFs) and particle-covered films (PFs) are evaluated concurrently.

4 Methodology

This chapter elaborates on the fundamental principles behind the applied experimental methods and techniques. Experimental details are provided in the Materials and Methods section of Chapters 5 to 7. Parts of Chapter 4 have been published in *Langmuir*, 2019, DOI: [10.1021/acs.langmuir.9b01568](https://doi.org/10.1021/acs.langmuir.9b01568), *Langmuir*, 2021, DOI: [10.1021/acs.langmuir.1c00559](https://doi.org/10.1021/acs.langmuir.1c00559) and *Journal of Colloid and Interface Science*, 2021, DOI: [10.1016/j.jcis.2021.12.113](https://doi.org/10.1016/j.jcis.2021.12.113) and have been adapted with permission of the publishers *American Chemical Society* and *Elsevier*.

4.1 Principles

This part describes the principles behind the established inorganic silica nanoparticles and silica thin films with subsequent surface modification and ligand density quantification (Chapter 4.1.1). Subsequently, light scattering, zeta potential, and streaming current techniques are revised (Chapter 4.1.2), concluding with complementary methods to study surface wetting of colloidal particles and planar substrates (Chapter 4.1.3).

4.1.1 Sol-gel process, silanization, and functional group quantification

4.1.1.1 Sol-gel: hydrolysis and condensation of silicon alkoxides

The sol-gel process is a wet-chemical technique to create polysiloxanes from hydrolyzing silicate precursors, or mixtures thereof, that agglomerate into particle-like polymer coils dispersed in a solution (sol) and eventually link together into a coherent network (gel) of amorphous material.^{498,499} Common silicon alkoxides are tetramethyl orthosilicate (TMOS, $\text{Si}(\text{OCH}_3)_4$) and tetraethyl orthosilicate (TEOS, $\text{Si}(\text{OC}_2\text{H}_5)_4$) having four methoxy or ethoxy chains, respectively, which are covalently bound to a central Si atom.^{498–500} These alkoxy silane precursors provide the backbone in designing various materials such as particles,^{501,502} fibers,⁵⁰³ monoliths,⁵⁰⁴ thin films,⁵⁰⁵ and fine powders,⁵⁰⁶ with applications including colloid synthesis,⁴⁹⁸ semiconductors,⁵⁰⁷ coatings,⁵⁰⁸ *etc.* This diversity is ascribed to the specific reaction kinetics controlled by adjusting experimental variables. The kinetics are primarily affected by the type of (in)organic catalyst, water/silane ratio, pH, and organo-functional groups, along with secondary factors such as temperature, solvent, ionic strength, leaving group, and silane concentration.⁴⁹⁹ The polymerization mechanism of alkoxy silanes and organoalkoxy silanes is complex and is generally simplified in three major steps:^{498–500}

- 1) Hydrolysis: the alkyl groups (-R) are substituted by the hydroxyl group (-OH), forming silanols (Si-OH) in presence of acidic, alkaline, or neutral medium, and possibly

homogenizing solvents (usually the parent alcohol to prevent alcoholysis)⁵⁰⁹ since most alkoxysilanes are immiscible with water (Fig. 4.1A).

- 2) Condensation: siloxane bridges (Si-O-Si) are formed by removal of an alcohol or water molecule from two alkoxysilanes (dimerization) through dehydration or dealcoholation, depending on the water content (Fig. 4.1B). Linear oligomers further crosslink into cyclic and highly crosslinked structures by maximizing 'internal' siloxane bonds and minimizing terminal hydroxyl groups to form nuclei (Fig. 4.1C).
- 3) Phase separation: the reaction medium becomes more heterogeneous as the nuclei undergo successive condensation. As a result, other assemblies form chains and networks constituting a liquid in a continuous solid (gel) or a solid (e.g., precipitate or particles) in a continuous liquid (sol) (Fig. 4.1D).

Hydrolysis and condensation are quite sensitive to steric hindrance (i.e., the complexity of alkyl chain) and inductive effects (i.e., increases in electron-withdrawing effect to the Si atom from basic alkyl (-R) substitution to acidic alkoxy (-OR)).⁴⁹⁸⁻⁵⁰⁰ Polymerization is generally very slow in the absence of a catalyst, but there are exceptions like (3-amino)propyltriethoxy silane (APTES) where the amino group acts as an intramolecular catalyst.⁵¹⁰ Common catalysts are mineral (e.g., HCl, KOH) or organic (e.g., acetic acid, L-arginine) acids and bases. The type and nature of catalysts significantly influence the final properties.⁵¹¹ The reacting hydrolysis species of TEOS depend on the pH of the solution. Below pH 7 water is the nucleophile attacking the protonated (electrophilic) alkoxysilane (acid catalysis), while above pH 7 hydroxide ions react with the alkoxysilane (base catalysis). The polymerization process can be divided into three pH domains: < pH 2, pH 2 – 7, and pH > 7. The isoelectric point (IEP) of silica is around 1 - 3 and at this pH, the electric mobility of silica is zero and reaction rates are extremely low. Growth and aggregation occur simultaneously and growth stops when the particles reach 2 – 4 nm because the solubility of silica is low at the IEP. At or above pH 7, the silica solubility and dissolution rates are maximized and the silica particles become highly ionized, which allows discrete particle growth without aggregation or gelation. Between pH 2 – 7, it is assumed that above the IEP of silica the condensation rate is proportional to the hydroxide concentration because the gel times decrease steadily from pH 2 to pH 6. The final structures in this pH range shape into chains and networks rather than discrete particles. Below pH 2, gel times are relatively long and represent a metastable region also capable to form chains and networks. A general polymerization scheme is shown in Fig. 4.1D.⁴⁹⁸

Orthosilicic acid ($\text{Si}(\text{OH})_4$) is a weakly acidic (pK_a 9.2,⁵¹² 9.8⁵¹³), water-soluble form of silica that is stable in water at room temperature when its concentration remains below ~ 1 mM. At higher concentrations, autopolycondensation initiates to keep its solution concentration low. At neutral pH, roughly 0.18 % orthosilicic acid molecules are ionized and readily react with the unionized ones to form oligomers. Although the silanol groups in the monomer are mildly basic, small oligomers can have pK_a values between 9.5 and 10.7. The composite pK_a for surface silanol groups of nuclei 1 nm in diameter is 6.8, meaning they behave like a weak acid and their acidity increases with the degree of crystallinity (i.e., from amorphous to crystalline).⁵¹³ This likely explains the scatter in the literature for the point of zero charge and isoelectric point of silica in the absence of specific ion adsorption, which lies between pH 1 - 4.^{514,515} An earlier SHG study at the aqueous-fused silica (crystalline quartz) interface for the same interface indicated 19% of silanols have a pK_a of 4.5 and 81% a pK_a of 8.5.⁵¹⁶ Simulations for the same interface provided a pK_a of 5.6 for the more acidic out-of-plane silanols with strong hydrogen bonding to water and 8.5 for the less-acidic in-plane silanols with weak hydrogen bonds to water.^{512,517}

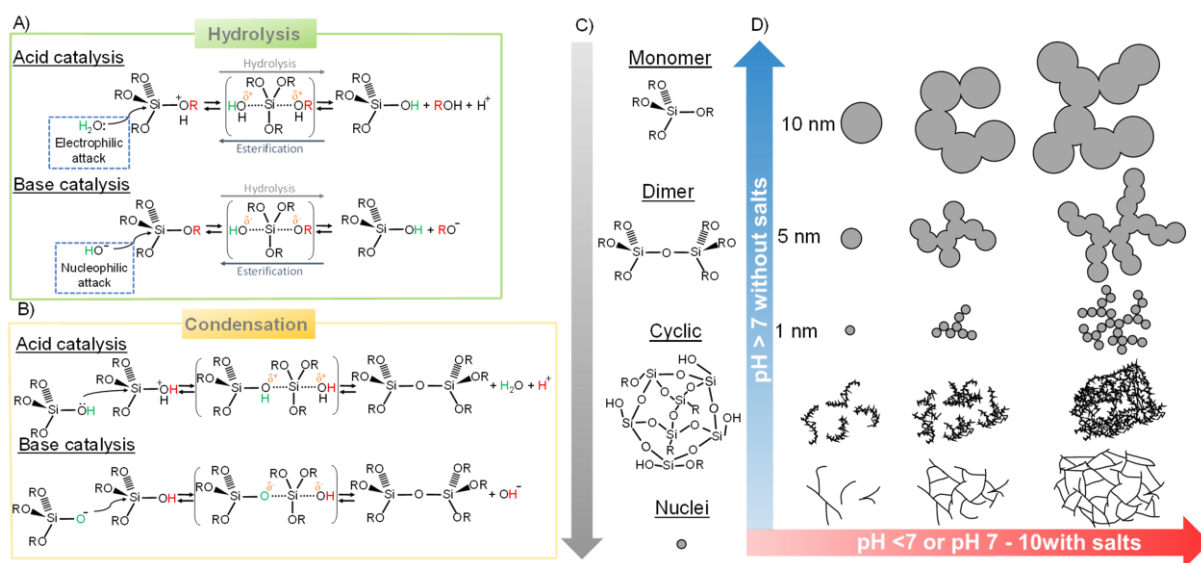


Fig. 4.1 A) Reaction mechanism of acid- and base-catalyzed hydrolysis and B) condensation with the intermediate molecule between brackets. For TEOS, the -R group is C_2H_5 . C) Step-wise addition of new monomers forms condensed nuclei. D) Depending on sol conditions, such as pH and electrolyte, a weakly branched polymer solution is formed, or highly condensed particles increase in size over time. Figure adapted with kind permission by Elsevier from Brinker et al.⁴⁹⁸

4.1.1.2 Base-catalyzed TEOS sol-gel: amorphous silica particles

On a molecular level in alkaline media ($\text{pH} > 7$), the nucleophilic hydroxyl anion initiates hydrolysis by attacking the silicon atom to form a pentacoordinate transition state before displacing the alkoxide anion. The hydrolysis rate is stimulated or hindered by electron-withdrawing ($-\text{OH}$) and providing ($-\text{OR}$) substituents, respectively, meaning that

successive hydrolysis becomes progressively faster under basic conditions (Fig. 4.1A). In turn, the condensation rate depends on the extent of hydrolysis. The silanols easily donate a proton to the hydroxyl anions in the basic medium, thereby acquiring a negative charge and becoming mutually repulsive to like-charged species with a preference to react with neutral silanols by attacking the silicon center. The polymerization is thus proportional to the hydroxyl concentration (Fig. 4.1B). The result is that multiple condensation steps form small, highly branched agglomerates, and after reaching a critical size, this repulsion prevents fast gelation (Fig. 4.1C & D).⁴⁹⁸⁻⁵⁰⁰ The number of silanol groups per unit surface area varies, but a completely hydroxylated surface is considered to have $4.6 - 4.9 \text{ OH nm}^{-2}$, i.e., the Kiselev-Zhuravlev constant. The silanol number decreases significantly by drying in vacuo from $\sim 4.6 \text{ OH nm}^{-2}$ at $200 \text{ }^\circ\text{C}$ to $\sim 2.5 \text{ OH nm}^{-2}$ at $400 \text{ }^\circ\text{C}$ and continuously drops to zero around $1000 - 1200 \text{ }^\circ\text{C}$. Up to $400 \text{ }^\circ\text{C}$ in vacuo, rehydroxylation by adding excess water is entirely reversible at room temperature. In comparison, above $1200 \text{ }^\circ\text{C}$ only siloxane bridges are present on the surface, making the particle very hydrophobic.⁵¹⁸

Stöber et al.⁵⁰¹ are considered pioneers in producing amorphous silica spheres in a size range of 50 nm to $2 \text{ }\mu\text{m}$ (Fig. 4.2A). The general Stöber method employs an alcoholic solution at high pH (pH 11-13) from alkoxide precursors catalyzed by ammonium hydroxide.⁵⁰¹ Amorphous or non-crystalline means that the atoms do not possess long-range order. As prepared, they are readily suspended in polar solvents, acquire a negative charge under neutral conditions from the silanolate surface groups, and have a bulk density of approximately 2 g cm^{-3} that depends on the degree of condensation.¹ Several mechanistic studies aimed to explain or control the size and size distribution of Stöber silica particles. The consecutive growth of silica particles is argued by two contrasting mechanisms: the LaMer ‘nucleation burst’,⁵¹⁹⁻⁵²¹ and the controlled aggregation model.^{522,523} In the former, an initial burst of nucleation leads to a supersaturated solution, and growth occurs due to the diffusion of hydrolyzed monomers binding on the nuclei’s (primary particle) surface. This model explains the high particle size uniformity due to the constant number of growing particles plus a self-sharpening growth mechanism, which stipulates a faster growth rate for smaller particles. Yet, it fails to explain the origin of micropores on the particle surface since growth through the molecular addition of monomers cannot form porous structures.⁵¹⁹⁻⁵²¹ The major growth pathway for the second model is due to a continuous nucleation process that aggregates into larger (secondary) particles, and colloidal stability plays a prominent role in the final particle size and uniformity.^{522,523} This model does explain the granular appearance of Stöber particles, corroborated with bulk density measurements, small-angle X-ray scattering, transmission

electron microscopy, and nuclear magnetic resonance.⁵²⁴⁻⁵²⁷ A third model incorporates both monomer-addition and aggregation processes and provides a more comprehensive description of the Stöber process. The major contribution to particle growth is during the aggregation process, forming nanopores inside the silica particles. Later, when the monomer concentration decreases and nucleation ceases, the addition of monomers or small oligomers becomes the dominant process, and a pore-clogging effect blocks the entrance of inner micropores.⁵²⁸⁻⁵³⁰ Aging of the colloidal dispersion in the reaction mixture enables efficient pore closing leading to better monodispersity.^{522,531} Specifically, shorter reaction times, post-synthesis washing step with water instead of ethanol, and drying at moderate temperatures results in microporous Stöber silica particles with large specific surface area.⁵³²

However, attempts to synthesize particles smaller than 50 nm adversely influence their monodispersity under conditions of the Stöber process. Alternatively, the microemulsion method generates low polydisperse silica nanoparticles below 50 nm, but the use of organic solvents and surfactants along with the associated cost, purification, and particle recovery can be disadvantageous for large-scale productions.^{500,533} Highly monodisperse silica ‘seeds’ in the 10 – 40 nm range can be prepared without alcohol and under weakly basic conditions (pH 9 - 10) using basic amino acids such as lysine^{502,534,535} and arginine⁵³⁶ (Fig. 4.2B). Their isoelectric points are approximately 9.50 and 10.80, respectively.⁵³⁷ The immiscibility between water and TEOS forms a liquid/oil biphasic system with less contact area available for hydrolysis than homogenization with alcohols. Especially in weakly basic conditions, the reaction time becomes significant before completion. For example, aqueous n-butylamine solutions with initial pH of 9.5 take ten days to complete the polymerization process due to significant pH lowering during polymerization since acidic silanols neutralize the solution.^{498,538} The amphoteric buffering capacity of amino acids dampens pH fluctuations and finishes TEOS consumption quickly. For example, lysine-catalyzed hydrolysis with an initial pH of 9.8 is completed in one day.⁵³⁸ One-step⁵³⁹ or multi-step^{536,540} protocols based on controlled seed regrowth extend this size range from 12 nm up to 550 nm. Further size control is achieved by adjusting pH,⁵³⁸ temperature,⁵³⁰ stirring conditions,^{534,541} reaction time,⁵³⁴ precursor concentration,⁵³⁰ and use of organic solvents.^{539,542}

The seed dispersions have many reactive hydroxyl groups forming a gel-type hydration layer on their surface. Subsequent heating of the dispersion (90 °C) does not cause the dissolution of the particles. However, it enhances the intraparticle siloxane bond formation to improve their stability upon storage.^{543,544} After the synthesis process, purification of the sol is done either by (ultra)centrifugation, centrifugal ultrafiltration, or dialysis.^{545,546} In the case

that particle pellets formed in ethanol are exchanged with water, sonication must be executed quickly since permanent aggregation occurs due to solvent exchange and osmotic pressure.⁵⁴⁷ In order to preserve the monodispersity, dialysis is preferred since the centrifugal forces press the particles together. In addition, the attraction between the reactive surface groups can cause irreversible aggregation between the particles (Fig. 4.2C).⁵⁴⁶ For this reason, smaller-sized colloids (< 50 nm) are commercially available as sols, while larger spheres are obtainable as powders.

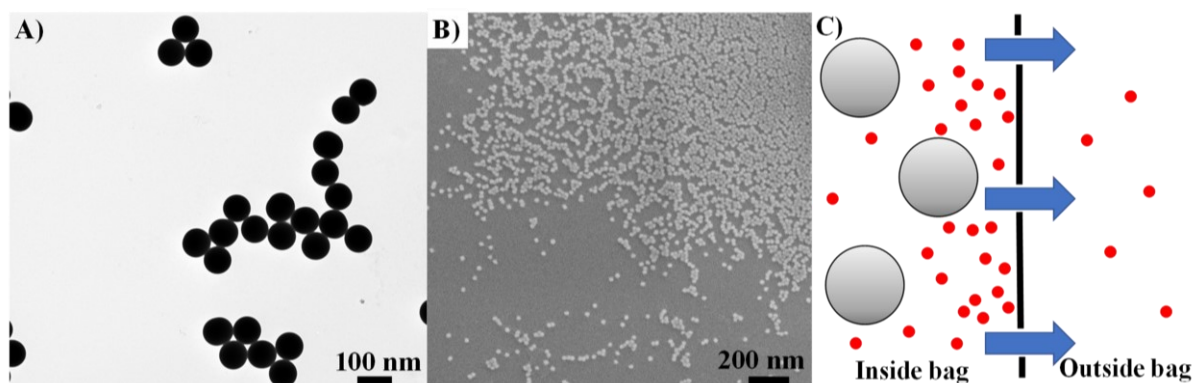


Fig. 4.2 A) Transmission electron microscopy image of 80 nm silica nanoparticles commercially available in powder form. B) Scanning electron microscopy image of 17.8 nm silica nanoparticles synthesized with L-arginine as the catalyst. C) Principle of dialysis. The nanoparticles (large spheres) cannot pass through the membrane pores contrarily to smaller molecules, such as the amino acid. Surrounding the dialysate in pure (alcoholic) aqueous solutions draws the smaller molecules outside the bag based on osmosis. Repeated cycles of adding fresh solvent purify the particle dispersion without affecting the particle monodispersity.

4.1.1.3 Acid-catalyzed TEOS sol-gel: porous silica network

In acidic media ($\text{pH} < 7$) at the molecular level, the alkoxide gets protonated first and withdraws electron density from the silicon atom, increasing its electrophilicity. The oxygen from a water molecule attacks the silicon from the rear and acquires a partial positive charge, which lowers that of the protonated alkoxide to make the alcohol a better leaving group (intermediate). The first hydrolysis step is typically the fastest, forming various intermediate species containing silanols that progressively slow this process. Condensation is initiated before hydrolysis is completed (Fig. 4.1A). The formed silanols get protonated again, causing an increase in the silicon's electrophilicity and making it susceptible to react with a terminal (neutral) silanol (Fig. 4.1B). The polymerization rate is proportional to the proton concentration below $\text{pH} 2$ and the hydroxide concentration between $\text{pH} 2 - 7$. The solubility of silica below $\text{pH} 2$ is low and does not contain many highly ionized species, which results in the formation of chain-like structures in the sol and network-like structures in the gel (Fig. 4.1 D, bottom two rows).^{498–500} Below $\text{pH} 2$ and low water/TEOS ratio ($R_{w/s} \leq 2$), a weakly branched microporous structure is formed with pore sizes < 2 nm, while a particle gel forms having larger pores at

pH > 2 and $R_{w/s} \geq 2$. The water content thus determines the final structure of the solids, which has no noticeable effect in neutral or basic medium.^{498,548} Theoretically, an $R_{w/s} = 2$ is sufficient to complete the hydrolysis and condensation, but this is generally not the case due to the formation of intermediate species, and an alcoholic co-solvent is necessary to speed up the process.^{498,505}

4.1.1.4 Surface coating methods to produce silica thin films

Thin-film deposition methods can either be physical (evaporation and sputtering) or chemical (sol-gel, chemical vapor deposition, spray pyrolysis). Films with good quality can be produced in the first group but are relatively expensive and often require large amounts of material. Contrarily, chemical deposition techniques produce good quality films without high costs.^{549,550} An important prerequisite in achieving homogeneous coatings is that the surface of the substrates is clean. The (aged) sol is preferably deposited on a substrate prior to gelation, which otherwise leads to unstable coatings.⁵⁵¹ After forming a porous silica network under acidic conditions, the sol is deposited on a macroscopic substrate to produce a coating. In the sol, hydrolysis/condensation reactions may overlap with the deposition stage leading to simultaneous drying and gelling.⁵⁰⁵ Coatings derived from sol-gels are usually obtained via spin or dip coating. The main difference between these two is that in spin coating, the deposited film thins by evaporation and centrifugal draining at high speed, while a dip-coated sample is withdrawn vertically from the sol. Spin coating applies to small disks and lenses, while large surfaces can be prepared from the dip coat process.^{549,550} Obtaining a homogenous coating becomes more challenging as the surface tension of the solvent is high (e.g., water), which is why alcohols are often employed (e.g., ethanol). With porous substrates, infiltration of solutes modifies their initial properties.⁵⁵¹ An overview of the fundamental aspects of dip coating is shown in Fig. 4.3. It shows the relation between the chemical and processing parameters (A), and the driving forces that influence the final thickness (B). The equation for film thickness (C) bridges the final dry film thickness (h_0) to two elements: the evaporation rate divided by the speed (Eu^{-1}) and physicochemical constants multiplied by the speed ($Du^{2/3}$). The first term describes the capillary regime where the combined influence of continuous evaporation at the meniscus and the capillary rise at the drying line determine the final thickness (D, red, low speed). The second term corresponds to the viscous drag regime (F, blue, high speed) and an intermediate region (E, green, intermediate speed).⁵⁵²

Dip coating can fabricate transparent oxide layers on a (transparent) substrate with high surface quality and degree of planarity, thicker than 20 nm and up to 1 μm .^{553,554}

For silica-derived sols, a critical thickness of 300 ± 30 nm was determined, below which the film remains crack-free.⁵⁵⁵ The drying and/or consolidation process gives rise to lateral tensile stresses that cause the films to crack.^{553–555} Contrarily, organosilicon materials exhibit much larger critical thicknesses above 1 μm film thickness.⁵⁵⁵ Thicker silica films are obtained when prolonging the aging, proportional to the solution viscosity⁵⁵⁶ and increasing $R_{w/s}$.⁵⁰⁵ Dip coated films with $R_{w/s} = 2$ contain many unreacted monomers, and polymerization continues during drying enacted by atmospheric moisture in room temperature conditions and leads to films with higher hydrophobicity.⁵⁰⁵ To improve the hydrophilicity of silica, alkoxide residue can be decomposed by 30 min exposure to 350 °C. At higher temperatures of 400 °C, major pore structure modifications lead to densification of the surface.^{557,558}

Highly ordered monolayers of particles on large, planar substrates impart new functionalities to surfaces by modifying their wettability, optical reflectivity, tribological properties, hardness, conductivity, etc.²⁵⁵ Organized particle assemblies on planar substrates are mainly created with spin coating,⁵⁵⁹ dip coating,^{255,560} and Langmuir-Blodgett monolayers.^{257,561} In most cases, particles are dispersed in water and/or alcohol, and the solvent evaporates. The particle rearrangement (e.g., hexagonal close-packing for spheres) and their wetting properties are commonly determined. Unless the particles or substrate are modified to strengthen their connection, they are easily removed and often serve as a template for subsequent processing.^{254,255,562,563} Adding the particles to a hardening medium, such as resins, binders, and sol-gels, traps the particles after solidification of the medium and protrude through the surface.^{564–568} For example, coatings with embedded titania anatase particles are transparent and show high photocatalytic effects for self-cleaning applications.⁵⁶⁷ Adding silica particles to a sol-gel prior to the coating procedure provides a degree of substrate roughness. Trapping of the particles allows subsequent wet chemical surface modification as it prevents redispersion of particles in the liquid medium or when a liquid shears over the surface.

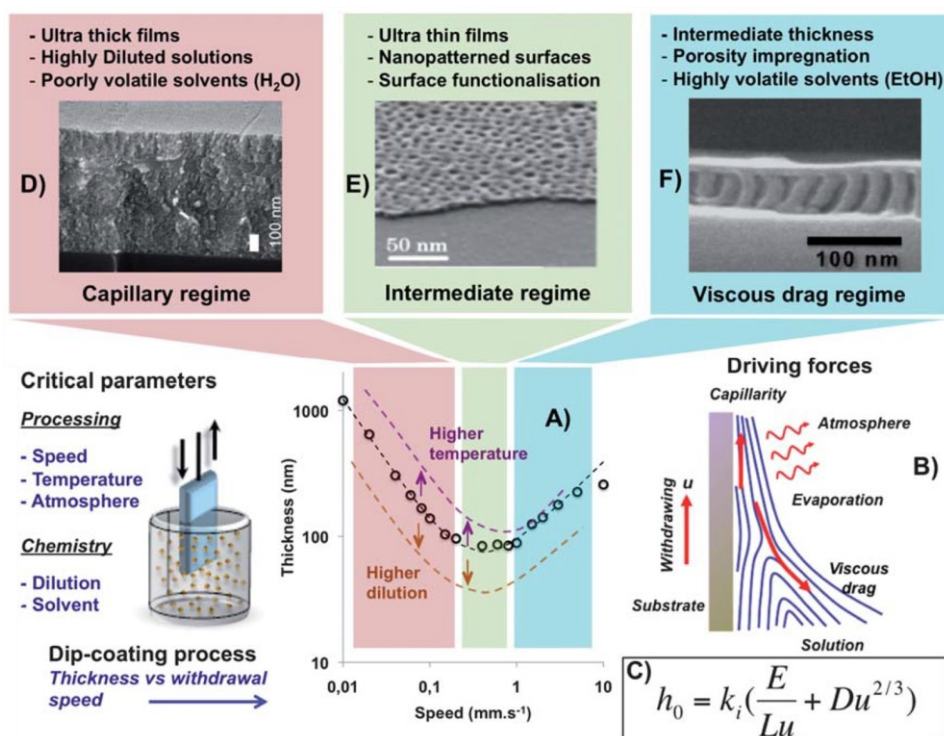


Fig. 4.3 A) Withdrawal speed versus thickness plot is divided into three regions with the corresponding scanning electron microscopy images in D), E), and F). The effects of temperature and dilution on final film thickness are extrapolated from the experimentally derived thickness of mesoporous silica (open circles). B) Scheme of the driving forces during dip coating. C) The equation governing the final thickness h_0 versus the solution composition constant k_i , withdrawal speed u , evaporation rate E , substrate width L , and physicochemical solution characteristics D . Reused with kind permission of *The Royal Society of Chemistry* from Grosso.⁵⁵¹

4.1.1.5 Organosilanization: primary amino-alkoxysilanes

Organosilanes impart additional properties to the surface such as adhesion, temperature resistance, crosslinking, adjustable wettability, abrasion resistance, and corrosion protection for applications in paints, inks, composites, and adhesives.⁵⁶⁹ Organosilanes are monomeric silicone-based hybrid molecules with at least one hydrolyzable alkoxy group at one end and an organic functionality at the other side having at least one direct bond via carbon to the silicon atom. The general formula is $-R'-Si(OR)_3$, where $-R'$ corresponds to the main chain and the functionality. The $-OR$ groups are susceptible to the same catalysis-induced hydrolysis/condensation steps as the silicon alkoxides described above, allowing these molecules to covalently bond to the surface. In general, silanes having a single ethoxy moiety are more easily controllable compared to multiple reactive sites since various orientations on the substrate are possible (Fig. 4.4, not shown is multilayer formation due to covalent bonding).⁵⁷⁰ The number of silanes commercially available is impressive, and only a particular class will be discussed: the aminosilanes.

The amine moiety on the alkyl chain is basic because of nitrogen's lone electron pair. Consequently, it is easily protonated, and minute amounts of water rapidly autocatalyze the silane, such as moisture in the air.⁵⁰⁹ Primary amines are also susceptible to CO₂ contamination.^{571,572} This uncontrolled self-condensation can form multilayers on the substrate, limiting its reactivity due to the embedded amine groups.⁵⁷³ Paradoxically, such reactions can be better controlled in an aqueous solution by setting the pH to influence the kinetics of the reaction, which is generally acidic to promote hydrolysis and constrains the amount of condensation.^{509,571,574–576} Many publications exist on achieving stable aminosilanes grafted on a substrate both in anhydrous nonpolar solvents and in pure or mixtures of aqueous and alcoholic solutions.

Focus is placed on solution-phase-deposition with the primary aliphatic amine (3-aminopropyl)triethoxysilane (APTES; pK_a ~ 9.6).⁵⁷⁷ APTES surface modification of silica particles and silica coatings occurs through the same mechanism, but the hydrolytic stability of the coatings is generally much weaker than the particles. In general, anhydrous solvents with trace amounts of water (or from adsorbed water on the substrate surface, about 1.5 ppm)⁵⁷⁸ and low silane concentration (≤ 2 v/v%) in an inert atmosphere is desirable, though multilayer formation is hard to avoid. Stringent solvent rinsing or sonication are often employed to remove physisorbed APTES.^{573,579–588} In 100% anhydrous conditions, the reaction kinetics are much slower since the amine moiety needs to catalyze the hydroxyls on the target surface.⁵⁷⁸ Silanization in water is possible due to the high solubility of APTES. In water, APTES exists mainly in its monomeric form below 0.25 w/w% with many hydrolyzed groups where the monomer-oligomer transition lies around 0.15 w/w%.^{571,589} It has been suggested that the amine groups of monomers can coordinate with the silicon atom and form a stable five-membered cyclic intermediate for intramolecular catalysis. Stable, pre-hydrolyzed stock solutions of APTES prepared as dilute aqueous solutions^{571,580,590} and concentrated in alcohol⁵⁹⁰ bypass the multilayer formation issue.⁵⁸⁹ Thinner and more stable APTES coatings are also formed when the reaction medium itself is aqueous.^{583,591,592} One of the most accessible strategies in promoting horizontal polymerization (i.e., covalent bonding parallel to the substrate compared to vertical, multilayer formation) is proceeding the reaction at temperatures ≥ 70 °C to disrupt the intra- and intermolecular hydrogen bonds. In addition, heating during the reaction significantly improves film quality and hydrolytic stability.^{579,583,591,593} Post-curing temperatures between 90 °C to 150 °C on substrates do not increase film density but improve hydrolytic stability. In the case of room temperature silanization, post-curing increases the amount of available amino groups because it releases amines that were hydrogen-bonded to the

substrates back into primary amines.^{573,578,579,582,592} When APTES-coated substrates are allowed to age in an aqueous environment at neutral pH, siloxane hydrolysis occurs by nucleophilic attack of the amine group catalyzed by water^{580,581,593,594} with slower kinetics for bulky or long-chain amines.^{579,580,595,596} The same issue occurs with APTES-coated nanoparticle dispersions on longer timescales, ranging from several weeks to months. Virtually all APTES molecules can be preserved bound to the surface when stored in a polar solvent under very acidic conditions (0.10 M HCl).⁵⁸¹ The protonated amino group is inactive towards surface silanols. This strategy has been employed to decelerate the polymerization reaction at any given moment during the functionalization. These solutions have to be handled with great care for safety.⁵⁴⁵ Alternatively, acetic acid, a weak acid, is more attractive for several reasons. Equivalent amounts of acetic acid to APTES also inhibit the polycondensation reaction, albeit at higher pH. Substrate rinsing or dialyzing with acetic acid diluted in alcohol eliminates weakly bonded APTES molecules.^{545,588,597} Acetic acid can act both as a solvent and catalyst,⁵⁹⁸ and participates during hydrolysis. The acetyl groups are consumed in the reaction with alcohol, forming ethyl acetate as a byproduct and leaving behind a hydroxyl group.⁵¹¹

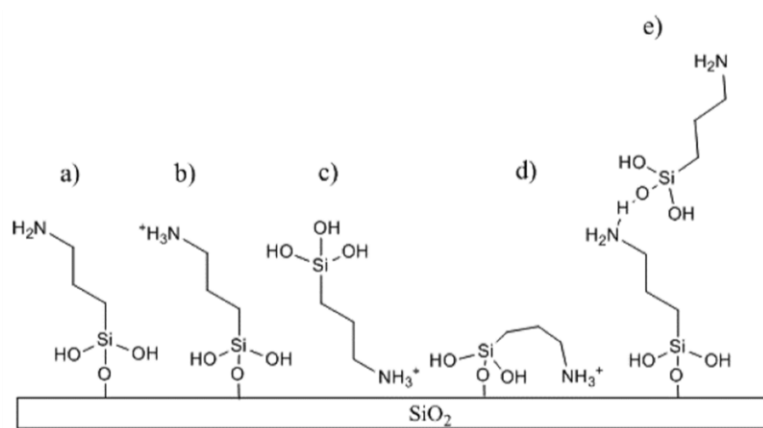


Fig. 4.4 Possible orientations of APTES A) monodentate primary amine, B) monodentate protonated amine, C) hydrogen-bonded protonated amine to the silica surface, D) monodentate protonated amine forming a hydrogen bond to the surface, and E) multilayer (vertical) formation due to hydrogen bonding between a surface amine and a hydrolyzed silane. Reproduced with kind permission of the *American Chemical Society* from Okhrimenko et al.⁵⁸²

4.1.1.6 Primary amine quantification: ninhydrin spectrophotometric assay

Several approaches exist to quantify ligand density both on planar surfaces and nanoparticles listed by Smith et al.,⁵⁹⁹ such as thermogravimetric analysis, optical, atomic, vibrational, and nuclear magnetic resonance spectroscopies, pH-based methods, electrospray-differential mobility analysis, and X-ray photoelectron spectroscopy. Since each method has limitations, careful sample preparation and measurement facilitate general agreement in ligand densities between different methods. This is primarily based on the particle/substrate properties,

for example, if the ligand and/or substrate is optically active. One major obstacle with quantifying surface-bound chemical groups on nanoparticles is their polydispersity in size and shape.⁵⁹⁹ Effortless determination of the exact particle concentration is highly desirable and has recently been demonstrated by single particle inductively coupled plasma mass spectrometry (spICP-MS) using the dynamic mass flow (DMF) approach. No reference nanomaterial is required, only a very dilute suspension to avoid multiple particles reaching the plasma simultaneously. The plasma atomizes and ionizes the particle's constituents that are quantified with the mass spectrometer. Several particle characteristics can be measured with this method such as particle number concentration, total and individual particle mass concentration, and the particle diameter (including number-size distribution) if the particle geometry is known. Their results were in good agreement compared to confirmatory methods (e.g., particle frequency approach and particle tracking analysis) and are also suitable for more complex-shaped particles.⁶⁰⁰

In this work, quantification of primary amino groups on APTES-coated nanoparticles was obtained by the reaction of ninhydrin (2,2-dihydroxyindane-1,3-dione) to form the colored ninhydrin chromophore called Ruhemann's purple ($\lambda_{max} \sim 570$ nm, Fig. 4.5). It is essentially a redox reaction where ninhydrin, the oxidizing agent, is reduced. Initially, ninhydrin is dehydrated and reacts with an amine to form a Schiff base, followed by decarboxylation and releasing CO₂. Next, an aldehyde is released from the imino-intermediate due to an attack from water and forms diketohydrindamine. Finally, this primary amine molecule condenses again with ninhydrin to form the final dimeric imino-derivative Ruhemann's purple (diketohydrindylidene-diketohydrindamine).^{601,602} Generally, an optimum pH of around 5.5 provides the highest color yield.^{603,604} The reaction is unique in that it forms the same soluble chromophore amongst primary amines, be it amines, amino acids, peptides, proteins, or ammonia.

Consequently, L-arginine in solution or entrapped in the silica shell could also be detected. Since the chromophore does not bind to the substrate, the insoluble target material can be centrifuged or filtered out after the reaction without the loss of the chromophore.⁶⁰² Recent comparative studies using solution proton nuclear magnetic resonance (¹H-NMR) routinely measure higher total amine contents than assays, like ninhydrin and 4-nitrobenzaldehyde, as APTES-modified particles can have inaccessible amines due to various surface orientations and multilayer formation (see Fig. 4.4) or from particle agglomeration.^{595,605} Conversely, Hristov et al.⁵⁹¹ found agreeable numbers (NH₂ nm⁻²) between

the two methods, possibly by increasing the reaction temperature (90 °C) after addition of APTES, which promotes horizontal polymerization as discussed above.^{579,583,591,593}

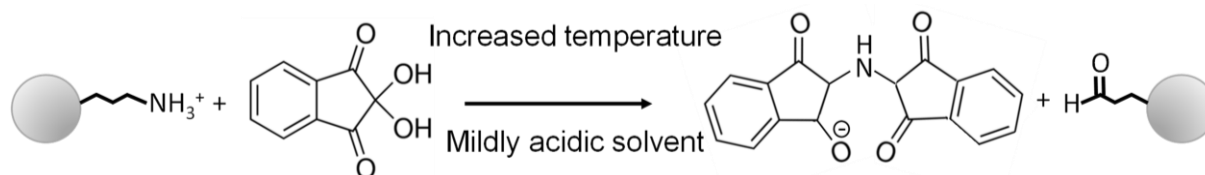


Fig. 4.5 General ninhydrin reaction scheme with primary amino groups on silica particles coated with APTES to form Ruhemann's purple. Reused with kind permission of *The Royal Society of Chemistry* from Sun et al.⁶⁰⁵

4.1.2 Characterizing particle size and zeta potential for colloids and planar substrates

Information on particle sizing using dynamic light scattering (4.1.2.1) and the electrokinetic potential (4.1.2.2) of colloidal dispersions and macroscopic planar substrates characterized with electrophoretic light scattering (4.1.2.3) and streaming current (4.1.2.4), respectively, are provided below.

4.1.2.1 Dynamic light scattering for colloidal dispersions

Dynamic light scattering (DLS), also known as photon correlation spectroscopy, studies the diffusion behavior of macromolecules in solution with sizes between 0.3 nm to 10 μm based on the principle of light scattering. Rayleigh's theory applies to particles with diameters less than 1/10th of the laser wavelength (e.g., He-Ne: $\lambda_0 = 633$ nm) since their produced scattering is isotropic with an intensity proportional to a^6 . For particles larger than $a \sim 30$ nm, the isotropic scattering is distorted and shows a larger component of scattered light in the forward direction than in the reverse direction. This asymmetric scattering shows several maxima and minima on a polar scattering plot as the particle size increases. According to Mie theory, which describes how spheres of all sizes and optical properties scatter light, the scattered intensity becomes a complex function of the scattering angle.^{606,607} Fig. 4.6 shows how the light scatters with different particle sizes. Mie's theory is used by default to convert intensity size distributions (a^6) into volume (a^3) and number (a) for all sizes of particles, which requires exact knowledge of the viscosity, refractive index, and absorption coefficient. This transformation assumes all particles are spherical and have homogenous and equivalent densities.^{606,607}

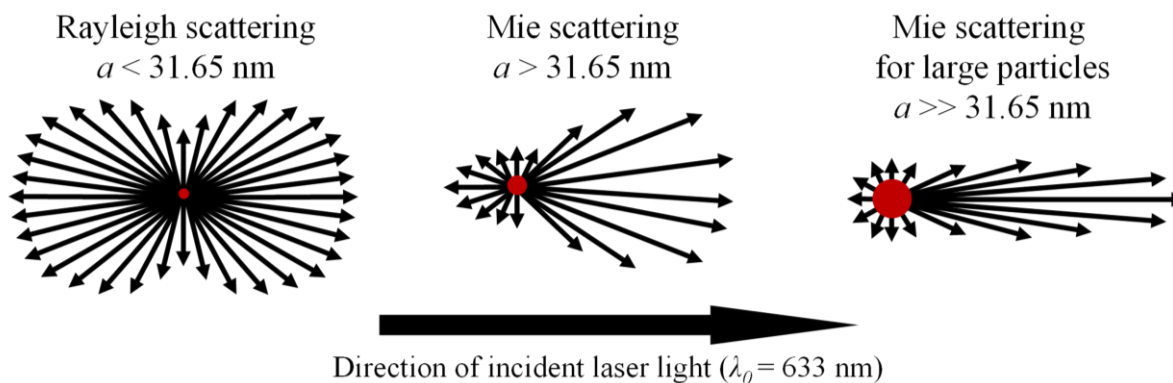


Fig. 4.6 For particle sizes below $1/10^{\text{th}}$ of the laser wavelength, scattering is predominantly Rayleigh (elastic) scattering. Mie (inelastic) scattering dominates for particles larger than the wavelength showing a stronger forward scattering. This effect enhances with larger particle sizes and can produce scattering with many maxima and minima (not shown here). Adapted with kind permission of *Elsevier* from Bhattacharjee.⁶⁰⁶

In DLS, a monochromatic laser is polarized, and the incident light scatters in all directions when it encounters randomly moving macromolecules (Brownian motion). Detectors are usually placed at an angle of 173° to detect backscattering and exclude excess scattered light (Fig. 4.7A). Larger contaminants, such as dust, mainly scatter in the forward direction, meaning that collecting the backscatter greatly reduces the effect of dust. Brownian motion of particles originates from the energy transfer during the constant collisions with solvent molecules, resulting in the faster movement for smaller particles than larger ones. The scattered light results in either mutually destructive phase relationships that cancel each other out or mutually constructive ones that enhance the scattering signal. These ‘noisy’ intensity fluctuations of scattered light are autocorrelated to extract the time dependence and produce a function (Fig. 4.7B). This autocorrelation function plotted on a correlogram contains features about sample quality. For example, an intercept close to 1 and a flat baseline indicate good quality. Large deviations from the former indicate too low or high particle concentrations. For the latter, peaks at large decay times can indicate non-random motion due to sedimentation. The autocorrelation function is modeled with an exponential function for monodisperse particles containing the translational diffusion coefficient or diffusivity (D), i.e., the velocity of Brownian motion (Fig. 4.7). The diffusion coefficients are obtained by fitting the correlation function with suitable algorithms, resulting in the cumulant particle size (Z-average, gives one overall size) and an overall polydispersity index (PDI) or the distribution particle size that gives a mean size and a width for each size peak of the distribution. The Z-average is the intensity-weighted mean diameter and is very sensitive to the presence of aggregates or larger contaminants, which is why dispersions are generally filtered prior to the measurement. PDI values between 0.08 – 0.7 are where the distribution algorithms operate the best.

Generally, a low polydisperse sample ($PDI \leq 0.3$) is suitable for most applications. Finally, the translational diffusion coefficient (D) can be converted into the hydrodynamic diameter (d_h) via the Stokes-Einstein equation:

$$d_h = \frac{kT}{3\pi\eta D} \quad \text{Eq. 4.1}$$

where k is the Boltzmann's constant, T is the absolute temperature, and η is the viscosity. The speed of Brownian motion depends, besides size, in large on the viscosity and temperature of the medium, and temperature drift should be avoided at all times. The hydrodynamic diameter depends on the 'core' or hard-sphere, the structure of the surface (e.g., roughness, ligands), and the type and concentration of any ions in the medium (i.e., electric double layer). At ionic concentrations < 10 mM, the extended double layer will reduce the diffusion speed and result in a larger, apparent hydrodynamic diameter. Therefore, measuring particle size (and electrophoretic mobility, see section 4.1.2.3) with ≥ 10 mM salt is recommended. Concentrated dispersions suffer from multiple scattering and electric double layer overlap leading to smaller hydrodynamic radii.^{606,607} Recently, Malm et al.⁶⁰⁸ improved the precision and accuracy of the particle size information by correlating a set of sub-measurements of 1 s each. It allows to differentiate between steady-state (aggregate) and transient (dust) size fractions and is thus more representative of the sample whether they are monomodal, multimodal, or polydisperse.

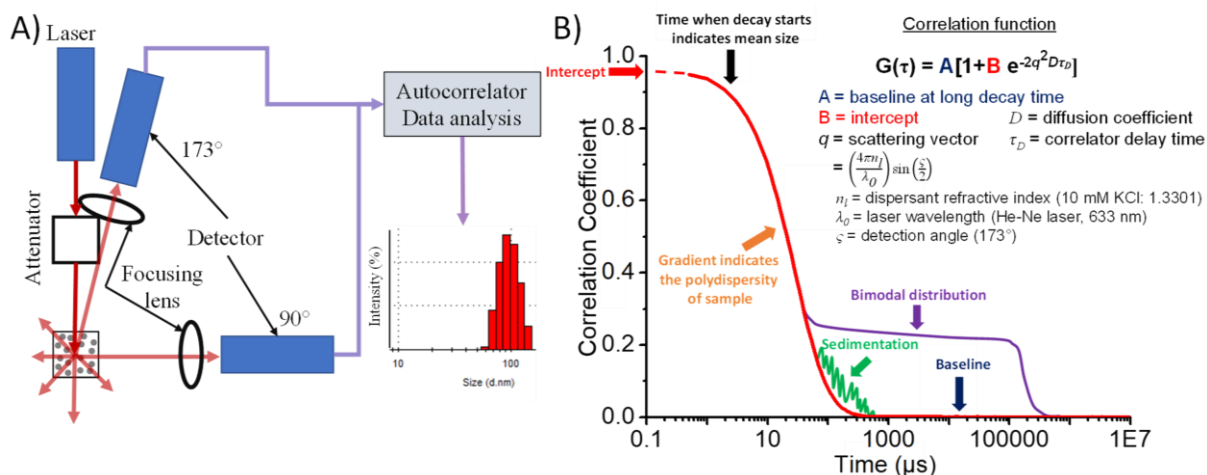


Fig. 4.7 A) Schematic of the dynamic light scattering method with detectors at 90° and 173° . Adapted with kind permission by Elsevier from Bhattacharjee.⁶⁰⁶ B) Correlogram of a monomodal (red), bimodal (purple), and multimodal (green) sample. The raw correlation function is plotted against delay time (τ_D). The mono-exponential correlation function on the right is applicable for purely monodisperse samples. For polydisperse samples, the equation can be written as $G(\tau_D) = A[1 + B g_I(\tau_D)^2]$, where $g_I(\tau_D)$ is the sum of all the exponential decays contained in the correlation function.

4.1.2.2 Zeta potential

When a solid material is dispersed in an aqueous liquid, surface charge formation occurs either from adsorption of charged molecules or ions on the solid surface and/or from dissociation/protonation of functional surface groups in contact with the liquid to form the electric double layer (EDL, Fig. 4.8A). The inner layer (Stern layer) predominantly consists of counterions, with a charge opposite to the dispersed solid, and is hydrodynamically immobile. Beyond this layer, the electrostatic effects originating from the surface charge on the solid are electrically screened by a factor of $1/e$ with the distance of each Debye length (κ^{-1}). This outer layer is the diffuse layer consisting of co- and counterions. It is very variable, i.e., influenced by pH, ionic strength, and type of ion, and the ion distribution is determined by the balance of electrostatic forces and random thermal motion. In this diffuse layer, there is an abstract plane (slipping/shear plane) in the vicinity of the solid/liquid interface where liquid starts to slide relative to the surface under the influence of shear stress. The zeta (ζ) potential, also termed electrokinetic potential, is the potential at the slipping/shear plane. It reflects the potential difference between the stationary layer and the surrounding dispersion medium. Its magnitude and sign are established through an appropriate theory and help establish stable regions for certain suspensions. When the ζ potential is zero, the number of protonated and deprotonated surface groups are equal and it is defined as the isoelectric point (IEP) which is assessed by variation of the pH (Fig. 4.8B). Both the IEP and shape of the ζ potential pH-titration curve provide valuable information on the nature of the material. For nonspecific adsorption (physical and chemical) of counterions on the solid, the IEP is the same as the point of zero charge (PZC).^{606,609,610}

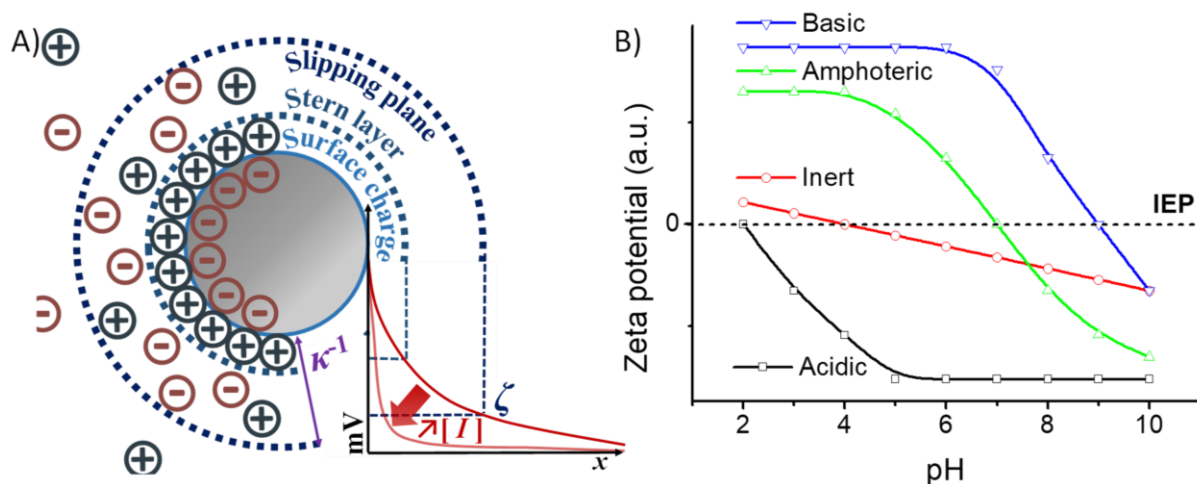


Fig. 4.8 A) A simplified model of a solid particle bearing a negative charge on its surface when dispersed in a liquid medium. The electrochemical double layer models divide the solid/liquid interface into two layers: a firmly adhering layer of oppositely charged counter-ions that remain stagnant under particle movement (Stern layer). Beyond lies the diffuse layer comprising of surface-charge compensating ions. During electrophoresis, the negatively charged particle with its stationary layer will move as an entity to the electrode of opposite charge, creating an interface (slipping/shear plane) between the charged particle and the surrounding layer of dispersant that corresponds to the ζ potential. The electric double layer has a thickness equal to the Debye length (κ^{-1}). If the ionic concentration ($[I]$) increases, enhanced screening of the electric double layer shifts the curve to lower zeta potentials when keeping all other parameters constant. B) Typical pH-dependent ζ potential curves for different classes of surfaces.

4.1.2.3 Electrophoretic light scattering for colloids

Applying an electric field (E) to a colloidal (electrolyte) dispersion will migrate the charged ‘double layer’ particles at a certain velocity (v) to the oppositely charged electrode in a stationary liquid to retrieve the electrophoretic mobility (μ):

$$\mu = \frac{v}{E} \quad \text{Eq. 4.2}$$

The electric field is the ratio of the applied voltage to the distance between the electrodes (V/d). The particle movement is opposed by viscous forces acting on the particles and will move at constant velocity when reaching equilibrium between the two opposing forces. The mobility depends on the viscosity and dielectric constant of the medium, the strength of the electric field or voltage gradient, and the ζ potential.^{606,610} The same laser as for DLS is divided into a reference and incident beam, the latter being scattered by the sample and detected at an angle of 12.8° . Recombination of the two beams causes a shift in the signal due to particle migration. A sophisticated laser doppler velocimetry method called M3-PALS (Mixed mode-Phase Analysis Light Scattering) significantly improves the accuracy of the measured mobilities and is employed in the ZetaSizer NanoZSP (Malvern, United Kingdom) (Fig. 4.9). The M3 mode performs fast (FFR ~ 20 Hz) and slow (SFR ~ 1 Hz) alternating fields to extract the contribution of electroosmotic flow. PALS differs from conventional laser Doppler

electrophoresis in that it employs signal processing of the time domain phase information of all particles within the scattered light instead of analyzing its frequency domain. This allows the usage of smaller electric fields to avoid Joule heating and increases accuracy for small particle displacements. The mean mobility is obtained from FFR in conjunction with PALS (phase analysis), while the full mobility spectrum is determined from SFR using Fourier analysis (frequency analysis).⁶¹¹⁻⁶¹³ Recently, the inventor of PALS, J.F. Miller, developed the next-generation electrophoretic light scattering (NG-ELS) devices, showing that M3-PALS technology can only accurately determine μ up to 10 mM KCl. When further increasing the salt concentration, current M3-PALS devices suffer from electrode polarization, Joule heating, and convection that significantly underestimates μ .⁶¹⁴

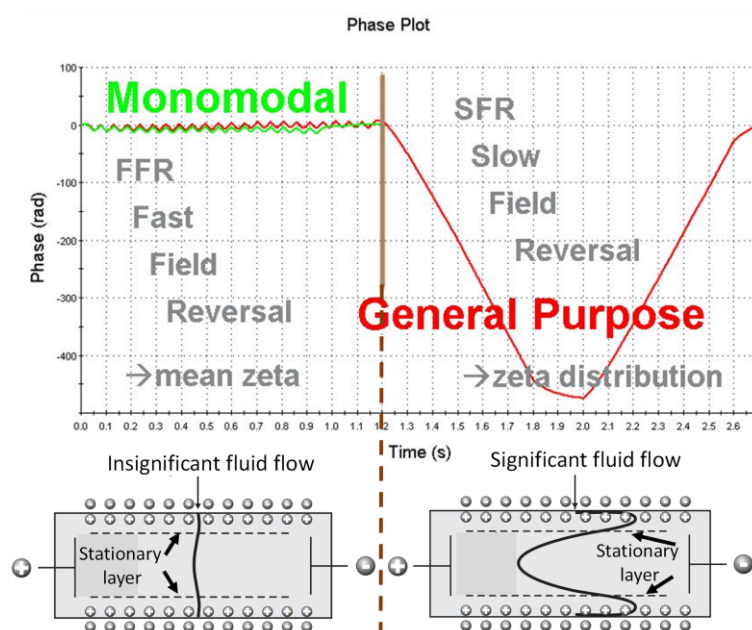


Fig. 4.9 Current zeta potential analysis with the M3-PALS technique can extract effects for ζ potential normalization from FFR and SFR, which provide more accurate estimates in case of low mobilities and avoids Joule heating at high conductivities (> 150 mM salt). Adapted with kind permission from *Malvern Instruments*.⁶¹¹

After the measurement, the proper electrokinetic model that converts μ into ζ potential needs to be selected. Electrokinetic analyzers employ standardized models to calculate the ζ potentials which, however, only provide accurate results under specified conditions. The criteria depend strongly on the particle volume fraction and the κa value, where a is the 'hard' particle radius and κ the Debye parameter. The Debye screening length (κ^{-1}) is mainly related to the ionic strength of the solution and represents the extent of immobile surface charge screening. For an aqueous symmetric monovalent electrolyte (1:1) of valence z and bulk concentration n^∞ :

$$\kappa^{-1} = \left(\frac{\varepsilon_r \varepsilon_0 kT}{2n^\infty z^2 e^2} \right)^{1/2} \quad \text{Eq. 4.3}$$

Smoluchowski's mobility formula is the most widely used μ versus ζ potential relationship for a spherical colloidal particle:¹⁷⁸

$$\mu = \frac{\varepsilon_r \varepsilon_0 \zeta}{\eta} \quad (\kappa a \gg 1, |\zeta| < 2kT e^{-1}) \quad \text{Eq. 4.4}$$

where ε_r is the dielectric constant of the liquid, ε_0 the permittivity of vacuum, η the electrolyte viscosity, kT the thermal energy at 25 °C and e the fundamental charge. $kT e^{-1}$ is equal to 25.7 mV at 25°C. Eq. 4.4 is only valid assuming that the electric double layer thickness is much thinner than the particles themselves characterized by a large κa , namely for micrometer-sized particles. For very small particles, high salt concentrations and/or nonpolar solvents, κa becomes much smaller than 1 and Hückel established the following relationship:⁶¹⁵

$$\mu = \frac{2}{3} \frac{\varepsilon_r \varepsilon_0 \zeta}{\eta} \quad (\kappa a \ll 1, |\zeta| < kT e^{-1}) \quad \text{Eq. 4.5}$$

Two limiting cases can be described when κa is much smaller or larger than 1, while many colloidal dispersions fall somewhere between these two extremes. Introducing the Henry function [$f(\kappa a)$] monotonically bridges the Hückel [$f(\kappa a) = 1$] and Smoluchowski [$f(\kappa a) = 1.5$] limits for any value of κa :⁶¹⁶

$$\mu = \frac{2}{3} \frac{\varepsilon_r \varepsilon_0 \zeta}{\eta} f(\kappa a) \quad (|\zeta| < kT e^{-1}) \quad \text{Eq. 4.6}$$

Where $f(\kappa a)$ was approximated with negligible errors by Ohshima:⁶¹⁷

$$f(\kappa a) = 1 + \frac{1}{2[1 + 2.5/\{\kappa a(1 + 2e^{-\kappa a})\}]^3} \quad \text{Eq. 4.7}$$

These models (Eq. 4.4 - Eq. 4.7) are implemented in most electrokinetic analyzers and describe a linear relation between μ and ζ potential. However, Eq. 4.4 is only applicable when $|\zeta| < 2kT e^{-1}$, while the remaining equations are accurate for $|\zeta| < kT e^{-1}$. They account for the retardation effect but not the relaxation effect. The ionic atmosphere and the surrounding fluid of the charged particle oppose particle movement and thus retard it. Relaxation effects, i.e., double-layer polarization, stem from the asymmetry in the ion cloud during particle motion where an accumulation of excess charge occurs on one side of the particle and depletion on the other, which becomes significant at long Debye lengths.^{618,619} Thus μ becomes a complicated function of κa and ζ potential because of the relaxation effect as indicated by O'Brien and White.⁶¹⁹ They performed exact numerical calculations of the mobility of a spherical particle for κa ranging between zero (Hückel) and infinity (Smoluchowski) for a symmetrical

1:1 electrolyte (Fig. 4.10). Taken from Wiersema et al.,⁶²⁰ the authors plotted their results as the scaled mobility (E_m) and scaled zeta potential ($\bar{\zeta}$):

$$E_m = \frac{3\eta ze}{2\varepsilon_r \varepsilon_0 kT} \mu \quad \text{Eq. 4.8}$$

$$\bar{\zeta} = \frac{e\zeta}{kT} \quad \text{Eq. 4.9}$$

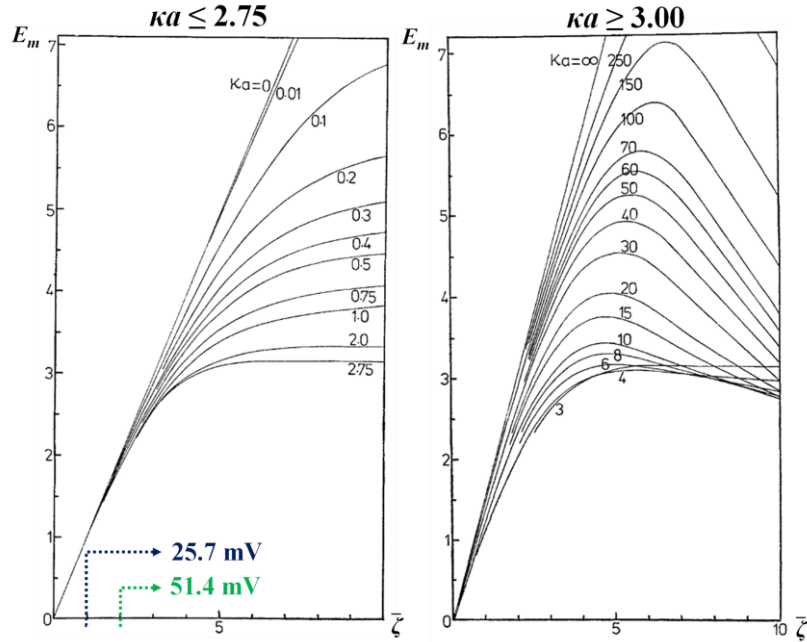


Fig. 4.10 Scaled electrophoretic mobility (E_m) of a positively charged spherical particle in a KCl solution at 25 °C as a function of scaled ζ potential for $\kappa a \leq 2.75$ (left) and $\kappa a \geq 3.00$ (right) from the numerical results from O'Brien and White.⁶¹⁹ On the left, the mobility is a monotonic increasing function of the ζ potential and all converge to Hückel at low ζ potentials irrespective of κa . On the right, a maximum mobility exists that becomes more pronounced and shifts to higher ζ potential with increasing κa . These maxima exist due to the relaxation effect⁶²¹ and tend to non-zero limiting mobility as only co-ions contribute to the mobility.⁶²² Adapted with kind permission of the *Faraday Division of Chemical Society* from O'Brien and White.⁶¹⁹

Efforts were conducted to develop analytical expressions to find agreement with the numerical results from O'Brien and White.⁶¹⁹ The approximate analytical expression designed by Ohshima, Healy, and White (OHW, Eq. 4.10) is consistent with the numerical results from O'Brien and White⁶¹⁹ to the order $(\kappa a)^{-1}$ (the first two terms of Eq. 4.10 are expressed as an asymptotic series in powers of $(\kappa a)^{-1}$, i.e., the first term is independent of $(\kappa a)^{-1}$ and the second term is linear in $(\kappa a)^{-1}$ as it is present in the denominator and divisor). Their semi-empirical formula has relative errors $< 1\%$ for all ζ potentials when $\kappa a \geq 10$:⁶²³

$$E_m = \frac{3}{2} \bar{\zeta} - \frac{3F}{1+F} H + \frac{1}{\kappa a} \left[-18 \left(t + \frac{t^3}{9} \right) K + \frac{15F}{1+F} \left(t + \frac{7t^2}{20} + \frac{t^3}{9} \right) - 6(1+3\bar{m})(1-e^{-\bar{\zeta}/2}) G \right] \quad \text{Eq. 4.10}$$

$$+ \frac{12F}{(1+F)^2} H + \frac{9\bar{\zeta}}{1+F} (\bar{m}G + mH) - \frac{36F}{1+F} \left(\bar{m}G^2 + \frac{m}{1+F} H^2 \right) \Big]$$

$$F = \frac{2}{\kappa a} (1+3m)(e^{\bar{\zeta}/2} - 1) \quad \text{Eq. 4.10a}$$

$$G = \ln \left(\frac{1+e^{-\bar{\zeta}/2}}{2} \right) \quad \text{Eq. 4.10b}$$

$$H = \ln \left(\frac{1+e^{\bar{\zeta}/2}}{2} \right) \quad \text{Eq. 4.10c}$$

$$K = 1 - \frac{25}{3(\kappa a + 10)} \exp \left[-\frac{\kappa a}{6(\kappa a - 6)} \bar{\zeta} \right] \quad \text{Eq. 4.10d}$$

$$t = \tanh(\bar{\zeta}/4) \quad \text{Eq. 4.10e}$$

$$m = \frac{2\varepsilon_r \varepsilon_0 kT}{3\eta z^2 e^2} \lambda_{idc} \quad \text{Eq. 4.10f}$$

$$\bar{m} = \frac{2\varepsilon_r \varepsilon_0 kT}{3\eta z^2 e^2} \bar{\lambda}_{idc} \quad \text{Eq. 4.10g}$$

$$\lambda_{idc} = \frac{N_A e^2 z}{A^0} \quad \text{Eq. 4.10h}$$

where F corresponds to Dukhin's number,⁶²⁴ m and \bar{m} are the scaled ionic drag coefficients (λ_{idc}) of counterions and co-ions, respectively, N_A is Avogadro's number, and A^0 is the limiting conductance for the anions or cations. For a 10 mM KCl dispersion, ε_r is 78.53, η is $8.854 \cdot 10^{-4}$ Pa, m is 0.176 and \bar{m} is 0.169. Dukhin's number is related to surface conductivity, i.e., stagnant layer conductivity in the inner region of the electric double layer, caused by an excess of electrical charge on the solid surface from hydroxide and hydronium ions and appears on both hydrophilic and hydrophobic surfaces. This lowers experimentally measured μ because of increased counterion adsorption compared to the bulk solution. Surface conductivity is likely significant when a maximum is found in μ (or apparent ζ potential) when plotted against different electrolyte concentrations.⁶²⁴⁻⁶²⁶ No maximum in μ has been observed with silica nanoparticles and KCl,^{627,628} although surface conductivity starts to dominate at salt concentrations < 10 mM salt from insufficient screening.^{629,630} ζ potentials for dilute colloid systems when $\kappa a \geq 10$ can be accurately determined with Eq. 4.10, but the asymptotic expansion of the mobility in powers of $(\kappa a)^{-1}$ becomes inappropriate for $\kappa a < 10$.

Based on the (complicated) results from Overbeek⁶³¹ and Booth⁶³², which takes into account the double-layer polarization effect, Ohshima⁶³³ derived a convenient interpolation

formula for μ expressed in powers of ζ potential (i.e., first term) with corrections to the third power of ζ potential (i.e., in the double brackets) in Henry's mobility formula:⁶¹⁶

$$\mu = \frac{2\varepsilon_r\varepsilon_0\zeta}{3\eta} \left[f_1(\kappa a) - \left(\frac{e\zeta}{kT} \right)^2 \left\{ f_3(\kappa a) + \left(\frac{\bar{m}+m}{2} \right) f_4(\kappa a) \right\} \right] \quad \text{Eq. 4.11}$$

Jalil et al.⁶²⁹ modified Eq. 4.11 where only the dimensionless drag coefficient of the counterion (m) is considered when electrolytes containing monovalent cations and anions differ primarily in their μ . The first term on the right-hand side of Eq. 4.11 is Henry's formula while f_1 , f_3 , and f_4 are a function of κa (note that $f_1(\kappa a)$ is Eq. 4.7 and is given below for clarity as Eq. 4.11a):

$$f_1(\kappa a) = 1 + \frac{1}{2 \left[1 + \frac{2.5}{\{\kappa a(1+2e^{-\kappa a})\}} \right]^3} \quad \text{Eq. 4.11a}$$

$$f_3(\kappa a) = \frac{\kappa a(\kappa a + 1.3e^{-0.18\kappa a} + 2.5)}{2(\kappa a + 1.2e^{-7.4\kappa a} + 4.8)^3} \quad \text{Eq. 4.11b}$$

$$f_4(\kappa a) = \frac{9\kappa a(\kappa a + 5.2e^{-3.9\kappa a} + 5.6)}{8(\kappa a + 1.55e^{-0.32\kappa a} + 6.02)^3} \quad \text{Eq. 4.11c}$$

Excellent agreement is found with an error of less than 1% for $\bar{\zeta} \leq 3$ at $\kappa a = 1$ and for $\bar{\zeta} \leq 7$ with $\kappa a = 0.1$. Errors can become very large for $1 < \kappa a < 10$ and $\bar{\zeta} > 4$. Eq. 4.11 is also applicable when $\kappa a > 10$ but Eq. 4.10 is more appropriate since it incorporates Dukhin's number to account for possible ionic surface conduction behind the slipping plane.⁶²⁴

4.1.2.4 Streaming current for planar substrates

Evaluating the ζ potential of macroscopic, planar surfaces can be done by the streaming potential or streaming current electrokinetic phenomena. Focus is placed on the latter since the former is susceptible to surface conductance and generally underestimates the ζ potential.^{634,635} Contrarily to electrophoretic light scattering, the solid is stationary. A laminar, tangential electrolyte flow is pushed through a slit channel at varying pressure in both directions (Fig. 4.11A). The liquid shears off the diffuse counterions compensating for the surface charge of the solid and transporting them towards the electrode at the outlet of the slit channel. By directly measuring the electrical current between two positions up- and downstream via nonpolarizable electrodes, the streaming current is obtained due to the ion-electrode charge transfer. The low internal resistance electrometer justifies the neglect of the back current through the channel (electroosmosis), whereas high internal resistance allows measuring the electrical potential. The ζ potential for solid materials with a planar surface using the streaming current method is determined with the Helmholtz-Smoluchowski equation (Eq. 4.12). The

electrolyte concentration and geometry of the capillary channel need to be known for correct ζ potential calculations.⁶³⁶

$$\zeta = \frac{dI_{str}}{d\Delta p} \frac{\eta}{\varepsilon_r \varepsilon_0} \frac{L}{A} \quad (\kappa a \gg 1) \quad \text{Eq. 4.12}$$

The measured streaming current coefficient ($dI_{str}/d\Delta p$, the slope of streaming current versus differential pressure, Fig. 4.11B) is related to the gap between adjacent samples (H) or the cell constant (L/A) where the cross-section (A) is the product of the channel width and gap height ($W \times H$), and L is the length of the streaming channel. To ensure laminar flow conditions, a channel height of $\sim 90 - 120 \mu\text{m}$ must correspond to a flow of $50 - 150 \text{ ml min}^{-1}$ at $200 - 400 \text{ mbar}$.⁶³⁶ A similar boundary condition as the Smoluchowski equation in electrophoretic light scattering is that $\kappa a \gg 1$ where a corresponds to half the channel gap ($H/2 = a$) for a nonconducting surface. Generally, surface conduction is negligible above 1 mM for a 1:1 electrolyte and lies around $1 - 2 \text{ nS}$. However, several solid materials exhibit an intrinsic material conductance that is higher than the surface conductance, hence in the case of semiconducting amorphous silica, a silicon-oxide, 10 mM KCl was chosen to suppress any additional currents that would predict lower (apparent) ζ potentials.⁶³⁴⁻⁶³⁹

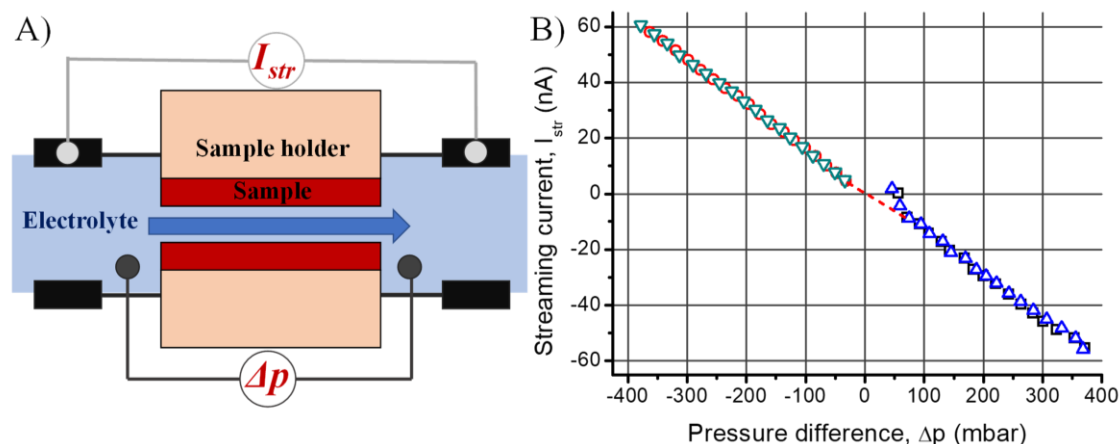


Fig. 4.11 A) Scheme of the microslit electrokinetic setup between adjacent solid samples. The electrolyte is pumped through the slit at varying pressure and measured twice in each direction. B) The pressure difference (Δp) is continuously increased/decreased while monitoring the streaming current (I_{str}), showing that the relationship between the two is linear with the slope ($dI_{str}/d\Delta p$) being proportional to the ζ potential (Eq. 4.12). The few outliers are excluded as the linear portion extrapolates to zero current at zero pressure.

4.1.3 Surface wetting characterization of colloids and macroscopic substrates: Contact angle, interfacial tension and rheology, and X-ray reflectivity

Information to determine contact angles from the sessile drop method (4.1.3.1), measuring the surface and interfacial tension of pendant drops (4.1.3.2), interfacial dilational rheology for oscillating pendant drops, oscillatory shear rheology with the Du Noüy ring (4.1.3.3), and X-ray scattering and reflectivity of a liquid surface (4.1.3.4) are given below.

4.1.3.1 Contact angle goniometry of sessile drops

The wetting behavior of solid surfaces is conventionally estimated from contact angle measurements of sessile drops using drop shape analysis. Contact angle measurements are typically executed by optical goniometers/tensiometers equipped with a tilting stage on a non-vibrating table (Fig. 4.12A). The OCA25 (DataPhysics, Germany) has LED lighting with an automatic temperature drift compensation to ensure stable and continuous illumination. The high-performance camera allows recording up to 3250 frames s⁻¹ with a 6-fold zoom lens and focus. The automatic dosing needle system accurately provides small volumes at the end of the cannula, and the deposited droplet is illuminated from behind. The contour of the shadow image and the solid/liquid interface baseline are recognized by the image processing software SCA, which is based on a specific algorithm to determine the droplet contour (Fig. 4.12B). Contact angles are obtained by automatic curve fitting with software modules such as Young-Laplace, circle, ellipse, tangent, and polynomial. Their suitability depends on the sample and drop type. The Young-Laplace method, or axisymmetric drop shape analysis (ADSA),^{640–642} is the sole method with a physical basis by employing the Young-Laplace equation of capillarity. It describes the pressure inside a droplet ($\Delta p^{Laplace}$) based on the radii of curvature (R_1 and R_2) and surface tension between phases α and β ($\gamma_{\alpha,\beta}$):¹¹⁷

$$\Delta p^{Laplace} = \gamma_{\alpha,\beta} \left(\frac{1}{R_1} + \frac{1}{R_2} \right) = \Delta p_0 - \Delta \rho g z \quad \text{Eq. 4.13}$$

where Δp_0 is the pressure difference at reference plane $z = 0$, $\Delta \rho g z$ is the hydrostatic pressure where $\Delta \rho$ is the density difference between phase α (drop) and β (surrounding matrix), g is the gravitational acceleration, and z is the vertical height of the given point on the drop surface, measured from the reference plane. The right-hand side term of Eq. 4.13 applies when other external forces, besides gravity, are absent.^{104,640} The boundaries that confine the system are shown in Appendix A.1. Eq. 4.13 is satisfactory for symmetrical drops with angles between

20° - 180°, while the purely geometrical circular/elliptical fit applies to drops on the order of the capillary length ($\sim l_c$), i.e., very hydrophilic surfaces.^{104,643,644}

Experimentally retrieving contact angles seems relatively straightforward. However, the (generalized) Young equation is only valid for ‘ideal’ surfaces that are atomically flat, isotropic, chemically non-reactive, and rigid. Generally, real solid surfaces are heterogenous and rough on the micro- and nanoscale, and mechanical thermodynamic equilibrium conditions cannot be guaranteed. Therefore, under normal circumstances one measures the apparent static or dynamic contact angles, depending on whether the contact line remains constant (Fig. 4.12C; a-b-d-f) or when the contact line is in motion (Fig. 4.12C; c-e). Static contact angles can be measured by gently moving the sample stage towards a small drop formed at the capillary since falling drops will inject additional kinetic energy into the system to simulate an increased wetting effect. The equilibrium or Young’s contact angle, which represents the lowest energy shape for a drop on a surface, is sometimes chosen when the contact angle remains stable over a range of different drop volumes (\sim advancing contact angle).^{104,645} However, since real solid surfaces deviate from ideal, the most reliable and reproducible manner is to calculate the equilibrium contact angle with the advancing/receding contact angle method (further below). In short, the droplet volume is initially increased (advancing) and subsequently decreased (receding) in such a way that the speed of the moving contact line is slow enough to suppress any dynamic effects, e.g., convection (Fig. 4.12C). The difference between the advancing and receding contact angle is referred to as hysteresis.^{104,118} For liquids with a dynamic viscosity well below 10 cP, no dependence on the advancing/receding contact angle is found for contact lines moving up to $\sim 12 \text{ mm min}^{-1}$.⁶⁴⁶ In practical terms, a pumping speed up to $0.05 \mu\text{L s}^{-1}$ is used and requires adjustments to very low speeds when liquids significantly wet the surface (i.e., spreading). Korhonen et al.¹¹⁸ formulated a model to estimate the minimum required advancing drop volume from the receding drop volume. Their results indicate that higher drop volumes are necessary as the contact angle hysteresis increases. The contact angles of interest are the most stable during this dynamic movement and can be considered quasi-static.^{104,118} A detailed procedure can be found in Huhtamäki et al.¹¹⁷ Generally, this procedure requires droplets with a contact radius $b > 1.5 - 2.5 \text{ mm}$ to overcome the highly system-dependent surface heterogeneity.^{104,645,647,648} Excessively large drop volumes (Bond number: $Bo \gg 1$) lead to significant shape distortion with large fitting errors, especially for larger contact angles.^{104,117,118,642} Conventional goniometers fail to recognize the drop contour for very low contact angles ($\leq 5^\circ$) and are preferably done using the capillary bridge contact angle method.⁶⁴⁹

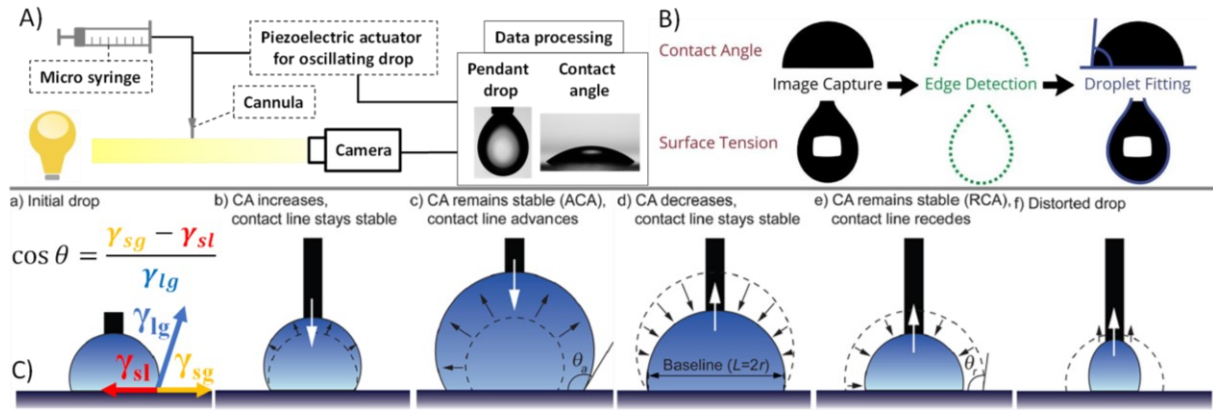


Fig. 4.12 A) Schematic setup of the optical contact angle (OCA) and contour analysis system. B) The high-performance camera records an image of the sessile or pendant drop and evaluates its contour by Axisymmetric Drop Shape Analysis (ADSA) to obtain the contact angle or surface tension, respectively. C) From left to right shows the method for the advancing (ACA) and receding contact angle (RCA). The Young equation with the interfacial tensions solid-gas (γ_{sg}), solid-liquid (γ_{sl}), and liquid-gas (γ_{lg}) that make up the three-phase contact angle are shown for clarity. Adapted with kind permission by the *American Chemical Society* from Korhonen et al.¹¹⁸

In the case of an ideal surface, the difference between the advancing and receding contact angle or contact angle hysteresis is zero and thus corresponds to the equilibrium contact angle. On the other hand, for an actual, smooth (finitely rigid) surface, Tadmor et al.⁶⁵⁰ implemented the contact line energy into the Young-Laplace equation to derive the equilibrium contact angle (θ_E) from advancing (θ_A) and receding contact angles (θ_R):

$$\theta_E = \cos^{-1} \left(\frac{\Gamma_A \cos \theta_A + \Gamma_R \cos \theta_R}{\Gamma_A + \Gamma_R} \right) \quad \text{Eq. 4.14}$$

where

$$\Gamma_A = \left(\frac{\sin^3 \theta_A}{2 - 3 \cos \theta_A + \cos^3 \theta_A} \right)^{\frac{1}{3}} \quad \text{Eq. 4.15}$$

$$\Gamma_R = \left(\frac{\sin^3 \theta_R}{2 - 3 \cos \theta_R + \cos^3 \theta_R} \right)^{\frac{1}{3}} \quad \text{Eq. 4.16}$$

The goniometer cannot measure CAs $\leq 5.00^\circ$ accurately, and when no RCA can be measured due to vanishing drop contour and significant spreading of the liquid (i.e., virtually zero contact angle), a value of 0.10° or 5.00° could be chosen to approximate the contact angle distribution for these calculations.

The difference between θ_A and θ_R is the contact angle hysteresis ($\Delta\theta$) and can be expressed as a percentage to describe the degree of hysteresis, where 0% means no hysteresis and 100% maximum hysteresis:¹¹⁸

$$\Delta\theta_{\%} = \left(\frac{\cos\theta_R - \cos\theta_A}{2} \right) 100 \quad \text{Eq. 4.17}$$

The work of adhesion (W_a) is linearly proportional to $\Delta\theta_{\%}$, allowing to directly compare hysteresis values between surfaces regarding how the movement of the contact line is facilitated.

Because it is an established and quick method, the sessile drop approach is preferred in research and industry to determine the surface free energy of a solid surface despite its probable inaccuracy compared to other experimental and theoretical approaches.¹²⁰ A minimum of two liquids with different polarities are deposited on the sample surface, usually highly polar water and nonpolar diiodomethane. First, the purpose is to determine the solid-gas interfacial tension (γ_{sg}) from Young's equation to establish the solid-gas-liquid interactions that describe the adhesion between the solid and liquid (γ_{sl}). Chibowski^{651,652} proposed a method to determine the total apparent surface free energy of a smooth, solid material (γ_{sg}) based on the contact angle hysteresis (CAH) with one test liquid:

$$\gamma_{sg}^{CAH} = \frac{\gamma_{lg}(1 + \cos\theta_A)^2}{2 + \cos\theta_R + \cos\theta_A} \quad \text{Eq. 4.18}$$

The air/water surface tension (γ_{lg}) value is 0.0722 N m^{-1} . Additionally, γ_{sg} can also be estimated from Neumann's equation of state (EOS) approach from the advancing or the equilibrium contact angle determined from Eq. 4.14.⁶⁵³

$$\cos\theta_Y = -1 + 2 \frac{\sqrt{\gamma_{sg}^{EOS}}}{\gamma_{lg}} e^{-\beta(\gamma_{lg} - \gamma_{sg}^{EOS})^2} \quad \text{Eq. 4.19}$$

where the constant $\beta = 1.25 \times 10^{-4} (\text{m}^2 \text{ mJ}^{-1})^2$. Eq. 4.19 is obtained by combining Young's equation with the EOS for the interfacial tensions to calculate the solid-liquid interfacial tension γ_{sl} :

$$\gamma_{sl} = \gamma_{lg} + \gamma_{sg} - 2 \sqrt{\gamma_{lg}\gamma_{sg}} e^{-\beta(\gamma_{lg} - \gamma_{sg})^2} \quad \text{Eq. 4.20}$$

Stammitti-Scarpone et al.⁶⁵⁴ obtained reasonable predictions for the solid-oil interfacial tension (γ_{so}) using an extended-EOS (e-EOS) for aqueous droplets on a sample immersed in oil to determine the solid-liquid-liquid surface free energy (i.e., at oil/water):

$$\gamma_{so} = \gamma_{lo} + \gamma_{sl} - 2 \sqrt{\gamma_{lo}\gamma_{sl}} e^{-\beta(\gamma_{lo} - \gamma_{sl})^2} \quad \text{Eq. 4.21}$$

where γ_{lo} is the oil/water interfacial tension (decane/water = 0.0522 N m^{-1}). Modifying the Young equation allows to predict the contact angle of a solid in the presence of an immiscible oil and water (θ_{lo}):

$$\cos\theta_{lo} = \frac{\gamma_{so} - \gamma_{sl}}{\gamma_{lo}} \quad \text{Eq. 4.22}$$

4.1.3.2 Pendant drop tensiometry

The surface/interfacial tension of liquid systems is preferably measured with the pendant drop tensiometry method compared to other methods such as Wilhelmy plate, maximum bubble pressure method, and the drop weight/volume method. It requires only small sample volumes ($\sim 10 - 100 \mu\text{L}$), is capable of measuring both the gas/liquid surface tension and oil/liquid interfacial tension, allows time-resolved (dynamic) measurements, and can measure low surface/interfacial tensions ($< 1 \text{ mN m}^{-1}$). Additionally, diffusive equilibration is relatively fast due to the small length scales of the drop, making this geometry very well-suited for studying complex interfacial assembly processes.³¹¹ Briefly, a droplet is formed at the end of a capillary using the same OCA25 device (DataPhysics, Germany, Fig. 4.12A) for sessile drops along with the ADSA ‘curve fitting’ principle that is numerically fit to a theoretical Laplacian curve with known surface tension values (Eq. 4.13, Fig. 4.12B). The existence of a single, isotropic surface tension is implied in Eq. 4.13. Care must be taken when anisotropic surface stresses are present, i.e., solidified interface. Integration of a pressure sensor on the droplet-side allows direct measurement of the Laplace pressure, accounting for these effects in complex interfaces.³⁸² Monitoring correct surface/interfacial tensions require non-creeping, axisymmetric drops with dimensions larger than the capillary length l_c for gravity to distort the drop from its spherical shape. At the same time, too large drops are unstable, give blurry images from drop vibrations, and detach from the capillary.⁶⁵⁵ The shape parameter quantifies the deformation of the drop from sphericity and corresponds to the fraction of the droplet outside of a circle with radius R_0 , i.e., the radius of curvature of the droplet at its apex (Appendix A.1).^{311,656,657} Other dimensionless evaluation parameters, such as the Bond, Worthington and Neumann numbers, have recently been evaluated for their suitability to predict the interfacial tension.^{658,659} For limited available liquid volumes or minor interfacial density differences, the non-gradient-based Nelder-Mead algorithm accurately measures surface tensions for drops with $Bo \geq 0.01$, which is at least a factor of 10 smaller than the current ADSA limit.⁶⁶⁰

Except during initial droplet formation ($\sim 1 - 10 \text{ s}$), the dynamic surface tension can be monitored for weeks until the adsorption of surface-active molecules reaches a stable equilibrium or plateau. It is an attractive approach to use the mean-field experimental interfacial tension/pressure data in unison with theoretical equilibrium or dynamic models

(section 3.2.1 and 3.2.2). An essential prerequisite for such quantitative studies is to ensure that the liquids and dispersed solutes are of high purity. Minute concentrations of surface-active impurities decrease the (equilibrium) interfacial tension that interferes with and/or masks the adsorption of the components of interest. Phenomena caused by impurities are Marangoni convection due to concentration gradients,⁶⁶¹ slow interfacial tension equilibrium,^{93,662} and present barriers to adsorption.⁶⁶³ By careful design and validating the purity of all components, Okur et al.^{664,665} recently showed that the surface tension minimum occurring at low salt concentrations of 2 ± 1 mM (i.e., the Jones-Ray effect) followed by an increase in tension at higher electrolyte concentrations exists because of ion-induced structural changes to the hydrogen-bond network of water, instead of the generally accepted idea that the surface tension decrease is due to presence of surface-active impurities.⁶⁶⁶

Certain commercial organic solvents with purity $\geq 99\%$ can still contain polar surface-active impurities⁶⁶⁷ which must be removed by column chromatography packed with alumina powder, i.e., decane from Sigma Aldrich (see Appendix A.2 for a detailed procedure). After chromatography, the solvent remained impurity-free during storage under vacuum and was used in Chapter 5. Fig. 4.13A clearly shows this approach is recommended for as-received solvents showing adsorption of surface-active impurities to the pure oil/water interface. The as-received decane from Honeywell (purity $\geq 99.7 - 99.8\%$) remained stable for 2 - 3 months when stored in the atmosphere and sealed with PTFE tape. This decane was used without further purification in Chapters 6 and 7 and routinely checked for impurities after opening a bottle.

The commercial as-received silica powders (and sols) also show minor surface activity (Fig. 4.13B). The particles in powder form were washed three times with pure water using repeated centrifugation/redispersion cycles and subsequently air-dried under a cover. Redispersion of these purified powders using bath sonication showed no significant changes in the interfacial tension (Fig. 4.13B). Probe-type sonication was avoided since wear particles ablated from the tip contaminate the dispersion.⁶⁶⁸

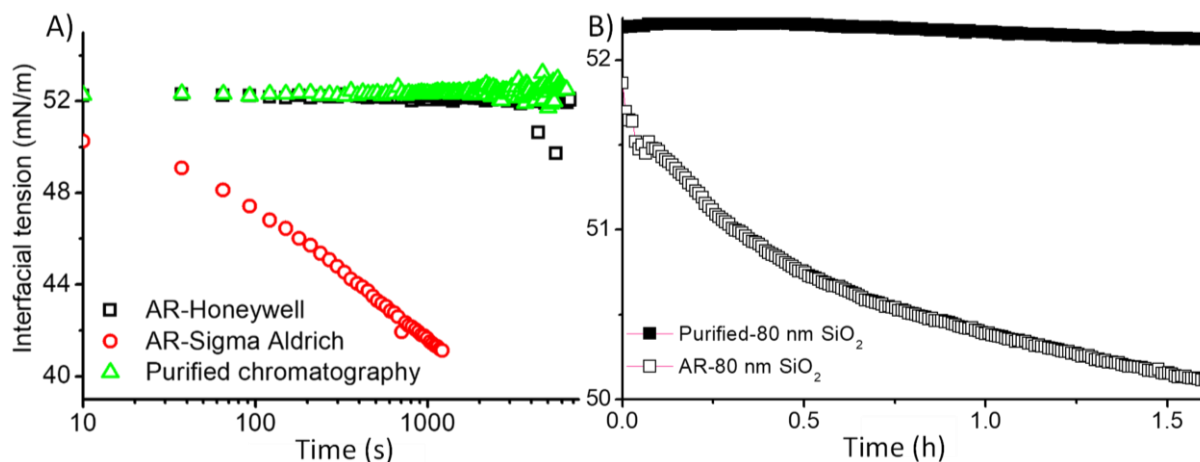


Fig. 4.13 A) Decane-water interfacial tension of as-received (AR) decane from Sigma Aldrich (red circles) and Honeywell (black squares) compared to column chromatography-purified decane (green triangles). B) Decane-water interfacial tension of 1 w/w% 80 nm silica (SiO₂) nanoparticles dispersed in water (pH ~ 5.8) before (open symbols) and after (closed symbols) the centrifugation/redispersion cycles.

4.1.3.3 Interfacial rheology

Boussinesq's⁶⁶⁹ proposal to treat the 2D interfacial rheology as analogous to the 3D bulk rheology allows to discuss the interfacial layers in terms of combined springs and dashpots (viscoelastic) of ideal elastic Hookean (Eq. 4.23) and viscous Newtonian behavior (Eq. 4.24), respectively (Fig. 4.14A):

$$\sigma_{xy} = c\varepsilon_{xy} \quad \text{Eq. 4.23}$$

$$\sigma_{xy} = \eta \left(\frac{d\varepsilon_{xy}}{dt} \right) = \eta \dot{\varepsilon} \quad \text{Eq. 4.24}$$

where σ_{xy} is the stress tensor, ε_{xy} the strain tensor, c a proportionality constant, η the viscosity, and $\dot{\varepsilon}$ the strain rate tensor. At complex interfaces, stresses arise through the simultaneously imposed area and shear variations. However, a decomposition of the strain type is required for quantification. In pendant drop dilational rheology, repeated expansion/compression cycles cause a change in the area without changing the shape of the interface (Fig. 4.14B). In contrast, the area is kept constant during shear and induces changes in the interfacial shape (Fig. 4.14C). Dilational rheology provides information on the composition of mixed interfacial layers, while shear rheology allows identifying structure formation at the interface.⁶⁷⁰ However, the existing theory is only applicable in the linear viscoelastic regime where the stress response equals the strain input, which is typical for small-amplitude oscillatory tests. Non-linear behavior at larger strain/strain rate distorts the sinusoidal stress response, and analysis is not straight-forward even though stresses occurring during emulsification and foaming behave nonlinearly.^{354,355} In this work, interfacial rheology has solely been studied in the linear viscoelastic range.

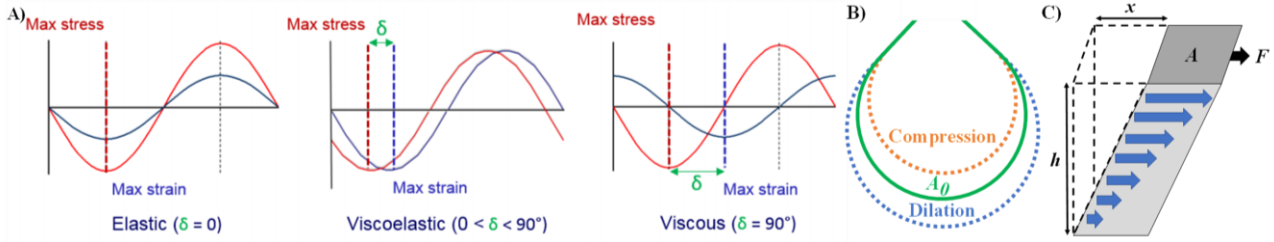


Fig. 4.14 A) Stress-strain curves from left to right for a 2D liquid surface with ideal elastic, viscoelastic, and ideal viscous behavior determined by the phase angle δ . Reproduced with kind permission of *Malvern Instruments*.⁶⁷¹ B) Compression/expansion of a pendant droplet with original area A_0 . C) Displacement (x) of a specific surface area (A) induced by force (F) shears the adjacent liquid layers with different velocities. The displacement is the largest for the topmost layer, while the bottom layer stays stagnant and creates a gradient.

4.1.3.3.1 Interfacial dilational rheology

In general, the drop area (A) is compressed and expanded in a sinusoidal manner that leads to a surface stress response by varying the surface tension ($d\gamma = \gamma(t) - \gamma_0$) from its initial value γ_0 to a generic one at time t . For purely elastic dilational behavior where interactions between adsorbed material and mass transfer between the interface and bulk can be neglected, the sinusoidal surface stress is in phase with the relative variation of the drop area ($\alpha_a = \Delta A/A_0 = (A(t) - A_0)/A_0$):⁶⁷²

$$E_0 = \frac{d\gamma}{d \ln \alpha_a} \quad \text{Eq. 4.25}$$

where E_0 is the dilational surface elasticity, also known as Gibbs elasticity. For purely dilational viscous behavior (η_d):⁶⁷²

$$\eta_d = \frac{d\gamma}{d \ln \dot{\alpha}_a} \quad \text{Eq. 4.26}$$

where $\dot{\alpha}_a = d\alpha/dt$. Generally, a particular time delay of γ occurs when the area is periodically changed due to various relaxation processes within the interfacial layer and between the adjoining bulk phases (mass transfer). Assuming that all perturbations are small (i.e., $\Delta A \ll A_0$; $\Delta\gamma \ll \gamma_m$, the latter parameter is the mean surface tension value) the interfacial area can be subjected to harmonic oscillations:⁶⁷²

$$A(t) = A_0 + \Delta A(t) = A_0 + \Delta A \sin(\omega t + \delta_A) \quad \text{Eq. 4.27}$$

where A_0 , ΔA , δ_A are the mean reference, the amplitude, and phase angle of area change, respectively, and ω is the angular oscillation frequency. For linear systems, it follows that changes of interfacial tension are also harmonic with a specific amplitude and possible phase shift:

$$\gamma(t) = \gamma_0 + \Delta\gamma \sin(\omega t + \delta_\gamma) \quad \text{Eq. 4.28}$$

with γ_0 , $\Delta\gamma$, δ_γ the mean surface tension value, the amplitude and phase shift of surface tension changes, respectively. In general, the sinusoidal parameters of Eq. 4.27 and Eq. 4.28 are processed separately via the discrete Fourier transform. This gives the most general definition for the complex viscoelasticity ($E^*(i\omega)$) of a systems' response relative to the perturbation by the Fourier transform operator (\mathcal{F}):⁶⁷²

$$E^*(i\omega) = \frac{\mathcal{F}\{d\gamma\}}{\mathcal{F}\{\ln(dA)\}} = A_0 \frac{\mathcal{F}\{d\gamma\}}{\mathcal{F}\{dA\}} \quad \text{Eq. 4.29}$$

The discrete Fourier transform is an algorithm that fits a number of sinusoidal functions of discrete frequencies (i.e., multiple integers of the fundamental frequency) to a finite amount of experimental data (i.e., a certain number of periodic droplet oscillations). In other words, the frequency content for each discrete frequency in the original (time domain) signal is determined by expressing the original signal in terms of constituent sinusoids. Because the transform contains a complex exponential, the real values in the time domain are transformed into complex numbers in the frequency domain. The amplitude and phase of the sinusoid at a specific frequency are given by the complex number and can be represented on a complex plane. In most cases, the oscillation corresponds to a single harmonic (i.e., sine wave), which is the fundamental frequency.⁶⁷³ The complex viscoelasticity, $E^*(i\omega)$, carries all information about the oscillations' change in amplitude and phase shift for the surface tension response to the area deformation at varying rates of deformation. The complex functions can be represented in vector (Eq. 4.30 and Eq. 4.31) or exponential form (Eq. 4.32) as:⁶⁷²

$$E^*(i\omega) = E' + iE'' = E_0 + i2\pi\nu\eta_d \quad \text{Eq. 4.30}$$

$$E' = |E^*(i\omega)| \cos \delta, \quad E'' = |E^*(i\omega)| \sin \delta \quad \text{Eq. 4.31}$$

$$E^*(i\omega) = |E_0| e^{i\delta} = \frac{\Delta\gamma}{\Delta A/A_0} e^{i\delta} \quad \text{Eq. 4.32}$$

where ν is the oscillation frequency, η_d is the dilational viscosity with the real elastic ($E' \equiv E_0$) and imaginary viscous ($E'' = 2\pi\nu\eta$) surface contributions, and $2\pi\nu$ is equal to the angular frequency (ω). The form of $E^*(i\omega)$ in Eq. 4.30 is in Cartesian representation, while Eq. 4.32 is in the polar form and both can be related to each other by the equations shown in Fig. 4.15B. Eq. 4.32 expresses $E^*(i\omega)$ in quantities that can be determined experimentally as frequency functions where $\delta = \delta_\gamma - \delta_A$ (Fig. 4.15A).⁶⁷⁴⁻⁶⁷⁹ Therefore, oscillatory experiments must fulfill the conditions of mechanical equilibrium when increasing the perturbation frequency, i.e., linear system response. Above a certain threshold, viscous forces cause nonideal oscillation behavior of the drop leading to an apparent elasticity and viscosity.⁶⁸⁰

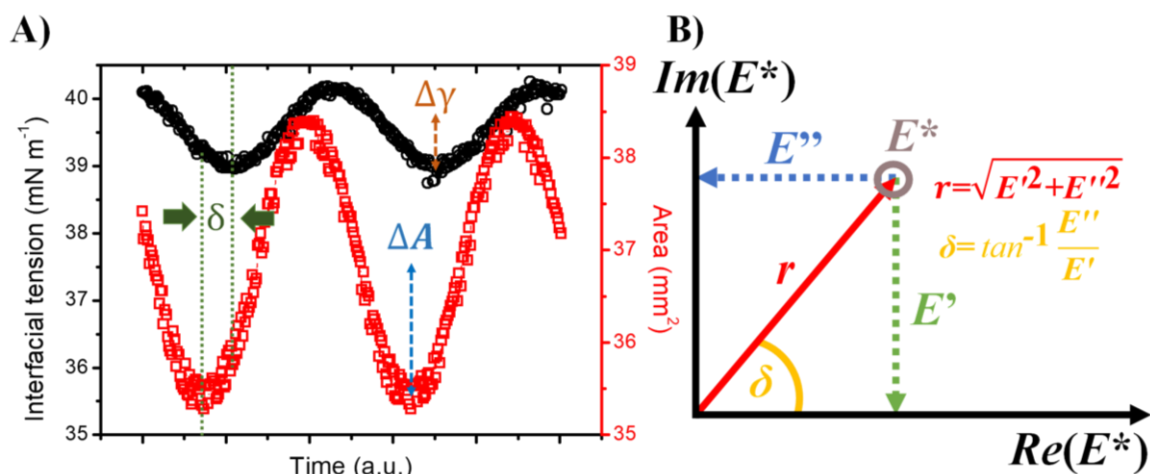


Fig. 4.15 A) An example of the surface tension (γ) response to a sinusoidal surface area (A) deformation for two periods with a delay quantified by the phase shift (δ). B) An Argand diagram that can be used in Cartesian or polar coordinates, which apply for addition and subtraction or multiplication and division of complex numbers, respectively. In both cases, the real (Re) and imaginary (Im) components of the complex number (E^*) can be plotted. The Cartesian form ($E^* = E' + iE''$) works well for Eq. 4.30, while the polar form in Euler notation ($E^* = r e^{i\delta}$) is suitable for Eq. 4.32.

Interfacial dilational rheology can be determined from oscillating pendant drops (Oscillating Drop Generator, ODG 20, DataPhysics, Germany) and analyzed with drop shape analysis as discussed above (section 4.1.3.1). The oscillating drop can be performed during dynamic adsorption or after reaching the equilibrium of an aqueous drop formed at the end of the capillary. A voltage-driven piezo-electric transducer ensures precise control for standard periodic waveforms of surface deformation through volume oscillations without altering the shape of the interface. The system's linearity can be defined by fixing either the frequency (0.001 Hz – 20 Hz) or area deformation (a few μm to mm) and varying the other, an amplitude or frequency sweep can be performed.⁶⁸¹ For non-highly viscous liquids, frequencies above 1 Hz for pure air/water and 0.2 Hz for pure oil/water interfaces show an apparent dilational elasticity and need to be determined for simple and complex interfaces.⁴⁸⁵ The percentage of deformation ($\Delta A/A_0$) varies between 1 – 15%, and the linearity can be evaluated from the total harmonic distortion (THD) of the surface tension and drop area, i.e., the non-harmonic contribution of the interfacial response.⁶⁸² It should be mentioned that the implemented theories are developed for planar interfaces. For physical relevance to surfactant adsorption, corrections are needed for the curvature of the geometry, drop size, and depletion effects (that are absent for bubbles/aqueous drops with surfactant dissolved in the surrounding phase).^{103,675,683–685} For solid-like membranes characterized by anisotropic elastic stresses, a pendant capsule elastometry model extends its applicability beyond the traditional dilational modulus based on the ‘purely liquid interface model.’ A series of images analyzed using nonlinear Hookean elasticity provides information on aging, viscoelastic effects,

and layer thickness.³⁸¹ The capillary pressure tensiometry method can be used for liquids with slight density differences to determine the dilational rheology. However, it has the disadvantage of requiring relatively complex and time-consuming calibration procedures.⁶⁸¹

4.1.3.3.2 Oscillatory interfacial shear rheology

In interfacial shear deformation experiments, the shape of the interfacial layer is changed at a constant area and its results reflect the resistance of the interfacial layer against deformation. The shear stress (τ_s), shear strain (μ_s), and shear rate ($\dot{\mu}_s$) are defined based on a 3D two-plate model of layers of liquid sliding (shearing) over one another (Fig. 4.14C).⁶⁸⁶

$$\tau_s = \frac{F}{A} \quad \text{Eq. 4.33}$$

$$\mu_s = \frac{x}{h} \quad \text{Eq. 4.34}$$

$$\dot{\mu}_s = \frac{d\mu_s}{dt} \quad \text{Eq. 4.35}$$

where F is the force acting over a unit area A . In response to this, the upper fluid layer will move a certain distance x , while the bottom layer remains stagnant resulting in a displacement gradient (dx/dh) across the sample. Unlike a solid where no flow is possible, the constituents can move relative to one another, causing the shear strain to continue to increase for the time during which stress is applied. This creates a velocity gradient $\dot{\mu}_s$ defined as the rate of strain change with time ($d\mu_s/dt$). Applying shear stress to a liquid transfers an equivalent momentum flux to the upper liquid layer, which is transferred through the liquid by collisions and interactions with other liquid components that lower the liquids' velocity and kinetic energy. The shear stress and shear rate proportionality constant is the shear/dynamic viscosity (η_s). This quantity is a measure of the internal fluid friction and is related to damping or loss of kinetic energy in the system. The 2D shear stress in line with Hooke's and Newton's law is, respectively:⁶⁸⁶

$$G = \frac{\tau_s}{\mu_s} \quad \text{Eq. 4.36}$$

$$\tau_s = \eta_s \dot{\mu}_s \quad \text{Eq. 4.37}$$

where the proportionality constant G is the elastic modulus, a measure of the stiffness or resistance to deformation, similar as viscosity is a measure of resistance to flow. Newtonian liquids, such as water, simple hydrocarbons, and dilute colloidal dispersions show a linear relationship between shear stress and shear rate. Hence, the viscosity is invariable with

the shear rate or shear stress. For oscillatory testing according to the harmonic law, sinusoidal shear deformation (or strain μ_s) applied to a surface change with time t .⁶⁸⁶

$$\mu_s(t) = \mu_o \sin(\omega t) \quad \text{Eq. 4.38}$$

The surface responds to a harmonic deformation with harmonic shear stress delayed in-phase (δ) relative to the generating deformation:⁶⁸⁶

$$\tau_s(t) = \tau_o \sin(\omega t + \delta) \quad \text{Eq. 4.39}$$

Where μ_o and τ_o are the amplitudes of deformation and stress, respectively, and ω is the angular frequency. The complex 2D shear modulus ($|G^*|$) is the ratio of τ_o/μ_o and can thus be divided between a real elastic (G') and imaginary loss (G'') modulus, representing the energy stored during stress and dissipated, respectively.⁶⁸⁶

$$G^*(i\omega) = \frac{\tau_o e^{i\delta}}{\mu_o} = G' + iG'' = G' + i\omega\eta_s \quad \text{Eq. 4.40}$$

$$G' = |G^*(i\omega)| \cos \delta, \quad G'' = |G^*(i\omega)| \sin \delta \quad \text{Eq. 4.41}$$

Oscillatory shear measurements performed in the linear viscoelastic regime offer direct information about inter- and intramolecular interactions at interfaces with moduli (G' , G'') independent of the strain amplitude.⁶⁸⁶

In the present study, an oscillatory rotational rheometer (DHR-3, TA instruments, Germany) equipped with a round Pt/Ir Du Noüy ring (RI0111, Krüss, Germany) was used with a Delrin trough having a double-wall circular channel placed on a Peltier plate (Fig. 4.16A). According to the current imposed on the motor, the torque is set and measured, whereas a high-resolution optical encoder measures the angular displacement. A low friction bearing supports the motor, and the built-in normal force sensor allows accurate positioning of the measurement geometry (possible only if the gap was defined prior to attaching the ring). Several calibrations and mapping procedures need to be performed. For example, geometry inertia, friction calibration, and rotational mapping were executed to avoid inaccuracies prior to every measurement. A step formed inside the Delrin trough's circular channel pins the aqueous subphase's meniscus.^{357,687} Subsequently, the Du Noüy ring needs to be positioned precisely at the liquid interface after being wetted before the less dense oil phase is carefully placed on top to ensure the oil does not slip under the ring. The precise placement of the ring in the interfacial layer and the wetting conditions and adhesion (also governed by cleanliness) at the ring have a tremendous influence in rheological applications. The Pt/Ir alloy is chemically inert, easy to clean, and wettable. The light construction of the Du Noüy ring permits the characterization of very fragile interfaces without the inertia dominating the

experiment. Precise determination of interfacial shear properties requires coupling of the interfacial flow with that of the adjacent bulk liquids, and the contribution of the former has to be more significant. The drag suffered is the sum of the force caused by the interfacial shear stress from the response of the complex liquid interface and by the bulk phases due to velocity gradients.^{357,688} The dimensionless Boussinesq number (B_0) quantifies the total drag on the probe geometry as the ratio of interfacial to bulk drag, which acts on the perimeter of the probe ($P = 4\pi R$) and the contact area ($A = 2\pi^2 RD$), respectively. A Boussinesq number $\gg 1$ is desired to ensure the interfacial rheology dominates the measured stress. For the Pt/Ir Du Noüy ring, the equation for a liquid/oil interface is:

$$B_0^{DNR} = \frac{\eta_i P}{\eta_{b12} A} = \frac{\eta_i (4\pi R)}{\eta_{b12} 2\pi^2 RD} = \frac{2\eta_i}{\eta_{b12} D\pi} \quad \text{Eq. 4.42}$$

where η_i is the viscosity of the interface, η_{b12} the viscosity of both immiscible bulk phases, R is the probe radius (10 mm) and D the diameter of the wire (0.36 mm). Since the contact area of the ring is small, subphase contributions can be generally neglected unless interfacial viscosities below 1×10^{-4} Pa.s.m are measured. The reader is referred to the study by Renggli et al.,³⁵⁷ which provides a comprehensive summary to accurately measure oscillatory interfacial shear rheological of thin and fragile interfaces.

A strain-controlled time test monitors the evolution of G' and G'' until reaching equilibrium. Frequency and/or strain sweeps are subsequently performed to evaluate the limits of the linear viscoelastic range to evaluate the presence of instrument inertia and structural breakdown (yielding) of the film, respectively (Fig. 4.16B). In general, when $G' > G''$ the interface has a gel- or solid-like structure ($\delta < 45^\circ$) and can be described as a viscoelastic solid material. In the reverse situation, $G' < G''$, the interface has a liquid-like dominant behavior ($\delta > 45^\circ$) and is a viscoelastic liquid under the preset angular frequency. Furthermore, the data should be evaluated by looking at the stress-strain curves and the Lissajous plots (Fig. 4.16C). Lissajous curves are closed-loop plots of stress vs. strain or stress vs. strain rate that allow a rapid qualitative analysis of the measurement and the type of interface (Fig. 4.16D).³⁵⁵ In the present study, adsorption time tests were performed in the linear viscoelastic region and evaluated by the quality of the stress-strain plots.

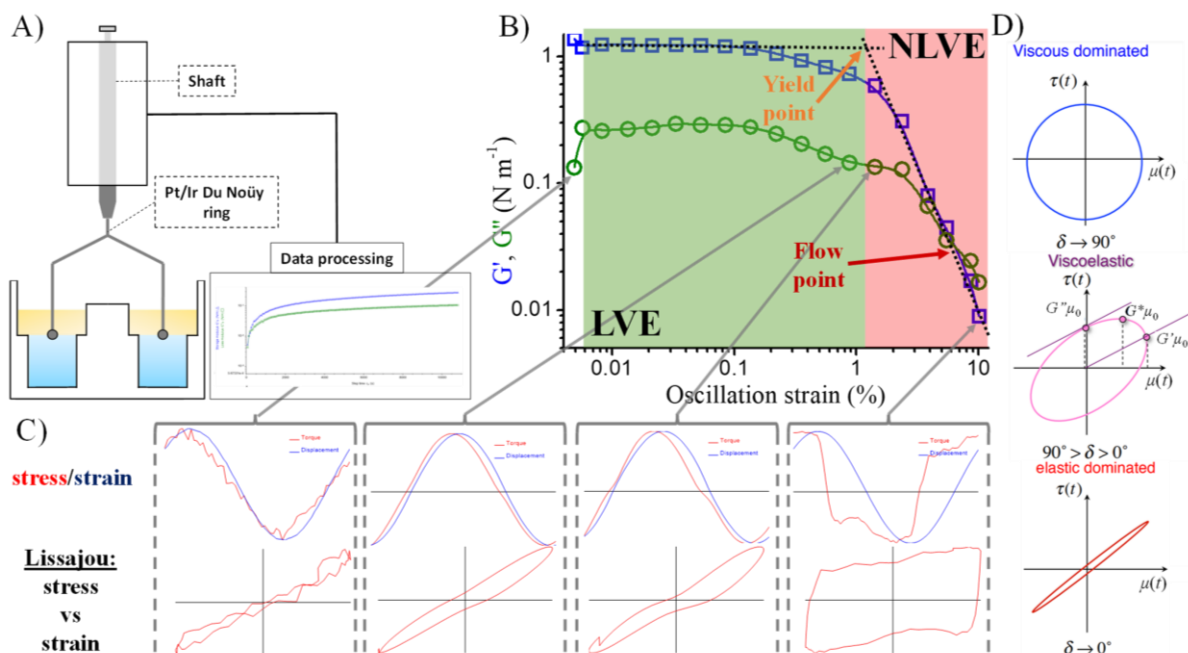


Fig. 4.16 A) Schematic overview of the rotational interfacial shear rheometer equipped with a Du Noüy ring placed at the decane/water interface and data output. B) Amplitude/strain sweep of an equilibrated decane/water interface with 1 mM oil-soluble octadecyl amine. The blue squares are G' and the green circles are G'' . The linear viscoelastic region (LVE) is indicated up to the yield point (intersection dotted lines) where the interface starts to flow under the applied strain and deformation is irreversible. In the nonlinear viscoelastic region (NVLE), the crossover/flow point is the transition point where $G'' > G'$. C) The stress/strain or torque/angular displacement curves of some points in the strain sweep are shown (grey arrows). At the lowest oscillation strain, a sinusoidal signal can be detected. However, the Lissajous plot (stress vs. strain) is noisy, meaning that the interface's response is nonlinear at this strain (and frequency). Up to the yield point, the stress behaves linearly (sinusoidal) even though the moduli start to decrease, i.e., the microstructure fractures but is still reversible. After the yield point, the stress-strain curves become increasingly nonlinear. D) Three examples of how the Lissajous plots can be used to evaluate the dominant behavior of an interface in the LVE region. Figure adapted with kind permission of *Springer Nature* from Fardin et al.⁶⁸⁹

4.1.3.4 Specular X-ray reflectivity

Specular X-ray reflectivity probes at very small angles the electron density profile $\rho(z)$ along the z -direction perpendicular to the liquid interface, with all in-plane detail averaged to determine its structure beyond molecular-length scales (z -resolution < 0.1 nm). The penetration depth of the X-rays is low due to the small angles of incidence, and only structural information of the top surface is obtained. The optical effects of an X-ray impinging on a solid or liquid surface are considered similar to the optics with visible light, i.e., the refractive index n_i is relevant (Fig. 4.18A). Snell-Descartes' law describes that refraction, i.e., bending of the incident beam path, occurs when it passes from one medium to another having different refractive indices.⁶⁹⁰

$$\frac{\cos \alpha_i}{\cos \alpha_r} = \frac{n_2}{n_1} \quad \text{Eq. 4.43}$$

where α_i and α_r are the angles of incidence and refraction, n_1 and n_2 are the refractive indices of the upper media (1) and the lower media (2). As X-rays are incident electromagnetic waves, the complex refractive index in media is only slightly smaller than unity and contains a real dispersive part (δ_{XR} , related to chemical composition and density) and an imaginary dissipative part (β_{XR} , related to absorption effects).^{690,691}

$$n_l = 1 - \delta_{XR} + i\beta_{XR} \quad \text{Eq. 4.44}$$

with

$$\delta_{XR} = \frac{\lambda_{XR}^2 r_e}{2\pi} \rho_e \quad \text{Eq. 4.45}$$

$$\beta_{XR} = \frac{\lambda_{XR}}{4\pi} \mu_a \quad \text{Eq. 4.46}$$

where λ_{XR} is the X-ray wavelength, r_e the classical electron radius (2.818×10^{-15} m), ρ_e the electron density, and μ_a the linear absorption coefficient. Typical values of the dispersive part δ_{XR} are in the range of 10^{-6} , and the dissipative part β_{XR} are approximately 10^{-8} . The deviation from unity caused by β_{XR} is so tiny that it is often neglected ($\beta_{XR} = 0$). Although the values for δ_{XR} are relatively small, it determines the reflected intensity. As the refractive index in Eq. 4.44 is less than unity, the X-rays undergo total external reflection for incident angles below the critical angle $\alpha_c = \sqrt{2\delta_{XR}}$ (in radians), which depends on the material's electron density and X-ray wavelength. When $\alpha_c > \alpha_i$, the X-ray wave enters the material as a decaying evanescent wave with reduced penetration depth (~ 100 Å), and the reflectivity is unity.^{690,691} Measuring at low angles projects a large incident beam onto the sample surface with a length $L_{XR} = T / \sin\alpha_i$, where T is the width of the incident beam slit. This is important at and below the critical angle because the incident beam can spill over the sample surface (i.e., footprint effect), which lowers the accuracy to determine the critical angle and roughness. Solutions to this problem are using large samples, a knife edge (in case of a small sample and large beam size), performing footprint correction, or decreasing the width of the slit to lower the vertical beam size although this latter option has its limitations.⁶⁹² When $\alpha_c < \alpha_i$, the penetration depth quickly increases at higher angles which attenuates the reflectivity intensity by mass absorption that diminishes monotonously (Fig. 4.17).^{690,691}

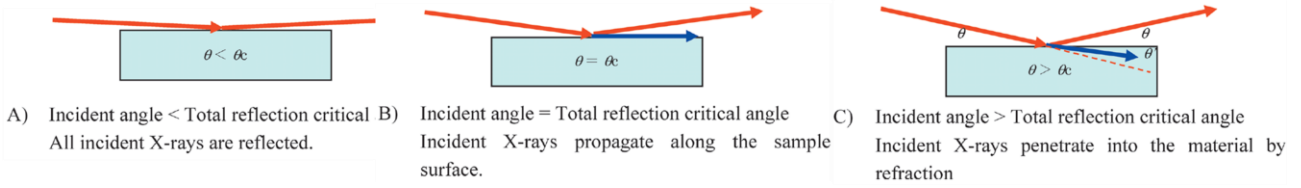


Fig. 4.17 The reflection (red) and refraction (blue) behavior of X-rays at a surface when the grazing angle increases (note that the angle (θ) in the text is represented by (α). Reproduced with kind permission of *Rigaku* from Yasaka.⁶⁹¹

In specular reflectivity experiments, the basic concept is that the X-ray beam is reflected from a perfectly flat surface and the intensity of the reflected X-rays is detected in the specular direction (incident angle α_i equals exit angle α_r). The reflected intensity ($R(Q_z) = I(Q_z)/I_i$, the ratio of the reflected intensity to the incident intensity) is measured as a function of the scattering vector ($Q_z = |\vec{k}_r - \vec{k}_i|$) perpendicular to the direction of the scattered wave given by the incoming and outgoing wavevector k_i and k_r , respectively (Fig. 4.18A). The wave vector is given by the wavenumber $k_n = 2\pi/\lambda_{XR}$ describing the direction and magnitude of the propagating beam (sine wave) along x over 2π with wavelength λ_{XR} . For a given wavelength λ_{XR} , the momentum transfer is:⁶⁹⁰

$$Q_z = \frac{4\pi}{\lambda_{XR}} \sin \alpha_i \quad \text{Eq. 4.47}$$

For an ideal, sharp interface, one obtains the reflected and transmitted intensity from classical optics, including the boundary conditions for electromagnetic waves:⁶⁹⁰

$$R_F(Q_z) = \left| \frac{Q_z - \sqrt{Q_z^2 - Q_c^2}}{Q_z + \sqrt{Q_z^2 - Q_c^2}} \right|^2 \quad \text{Eq. 4.48}$$

where R_F is the Fresnel reflectivity, and the wavelength-independent critical wave vector transfer Q_c has the same form as Eq. 4.47 by exchanging α_i for α_c . For a pure air/water surface $Q_c = 0.0217 \text{ \AA}^{-1}$. For low incident angles ($\alpha_c > \alpha_i$), total external reflection gives $R_F(Q_z) = 1$ since $Q_z < Q_c$. When $Q_z > Q_c$, the total reflected intensity decays because part of the incident beam is reflected and another part is refracted (i.e., bending of light) into the substrate. For a flat surface and $Q_z > 3Q_c$:⁶⁹⁰

$$R_F(Q_z) \approx \left(\frac{Q_c}{2Q_z} \right)^4 \quad \text{Eq. 4.49}$$

However, it is unlikely that the interface between each pair of layers is perfectly smooth. For instance, thermally induced capillary waves for liquids with low surface tension (i.e., $< 100 \text{ mN m}^{-1}$) exhibit height fluctuations corresponding to an interfacial roughness σ_i described by the Debye-Waller factor:^{690,693–695}

$$R(Q_z) = \left| \frac{Q_z - \sqrt{Q_z^2 - Q_c^2}}{Q_z + \sqrt{Q_z^2 - Q_c^2}} \right|^2 e^{-Q_z^2 \sigma_i^2} \quad \text{Eq. 4.50}$$

Roughness causes a decrease in the intensity of the specularly reflected beam because of diffuse scattering. The reflectivity curve decays faster when the substrate's roughness increases. The reflectivity of an interface is described by an electron density profile $\rho(z)$, which is the projection of the electron density $\rho(x,y,z)$ averaged over the xy plane onto a vertical axis perpendicular to the surface.⁶⁹⁰ Parratt's recursive formalism³⁰⁴ provides a theoretical calculation of the reflected intensity from an electron density profile $\rho(z)$. In essence, $\rho(z)$ is modeled as a discretized multistep function where each layer (or slab) has a constant electron density determined from its known bulk value (Fig. 4.18B).

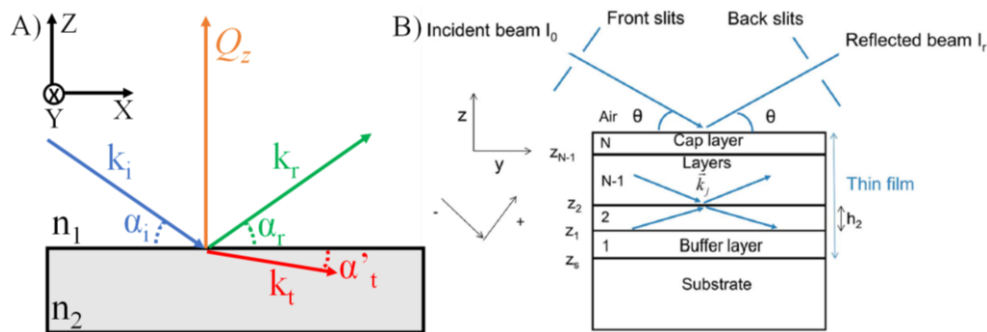


Fig. 4.18 A) Schematic of a specularly reflected X-ray where $\alpha_i = \alpha_r$. Part of the incident beam is transmitted, and the wave vector k_t gives the propagation of the X-rays. B) The plane of incidence for multilayers (defined in the REFLEX software). Reused with kind permission of the *International Union of Crystallography* from Vignaud et al.⁶⁹⁶

When there are multiple interfaces, the reflected X-rays will interfere constructively or destructively due to the incoming angle and depending on the exact path length. This shows in the reflectivity curve as periodic oscillations or Kiessig fringes. The amplitudes of the transmitted and reflected waves from the interfaces separating the slabs are calculated iteratively, starting from the bottom, to yield the reflectivity profile. Since real interfaces have an interfacial roughness, the interfaces in the discretized multistep need to be smeared out which is achieved by convolution with a (Gaussian) error function. One can quickly estimate the thickness of the film from the periodicity in Q_z as $d_{\text{layer}} = 2\pi/\Delta Q_z$, along with surface and interface roughness and material density on a qualitative level (Fig. 4.19).⁶⁹⁰

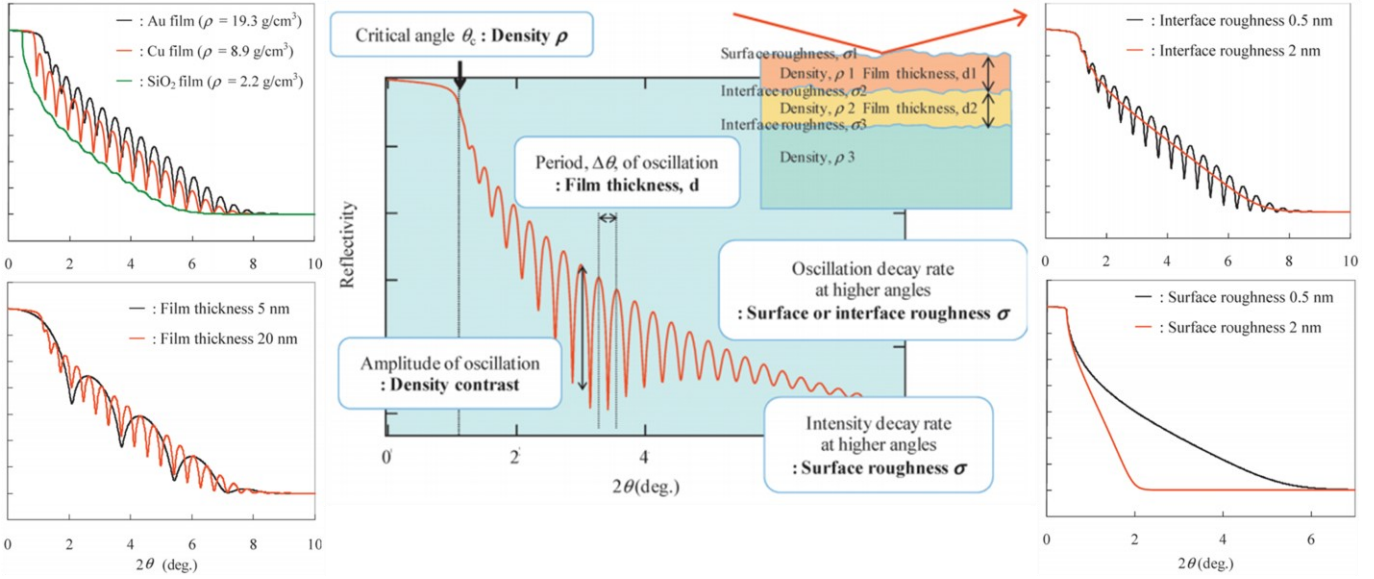


Fig. 4.19 Information in an X-ray reflectivity profile. Only one parameter is changed in the smaller plots, from upper left to bottom right: electron density, interface roughness, film thickness, and surface roughness. Reproduced with kind permission of Rigaku from Yasaka.⁶⁹¹

The obtained electron density profiles (e.g., with *REFLEX* software)⁶⁹⁶ can be computationally fitted to the model developed by Isa et al.²⁰⁹ The symbols in the following equations are shown in Fig. 4.20. A fast Fourier transform is utilized to fit the experimental reflectivity data into an averaged electron density profile $\rho(z)$ within the plane of the reflecting interface to the surface normal. The fast Fourier Transform implemented in *REFLEX* is a computational algorithm for fast and efficient computation of the discrete Fourier transform. Fourier inversion of the reflectivity curve normalized by the Fresnel reflectivity of the substrate provides with good accuracy the layer thicknesses, which is given from the autocorrelation function of the first derivative of the electron density.⁶⁹⁷ The electron density plot can be subsequently fitted to a model that takes the physical parameters of the interface and the shape of the nanoparticles into account:²⁰⁹

$$\rho(z) = \rho_i(z) + \iint [\rho_{NP}(s_{av}, \rho_p; z) - \rho_{NP}(s_{av}, \rho_i(z); z)] G(a_{av}, \sigma_a; a) G(h_{av}, \sigma_h; h) da dh \quad \text{Eq. 4.51}$$

$\rho_i(z)$ describes the plain air/water or decane/water interface with bulk electron densities of water $\rho_w = 0.334 \text{ e } \text{\AA}^{-3}$ and decane $\rho_d = 0.253 \text{ e } \text{\AA}^{-3}$, and an interfacial roughness σ_i described by a Gaussian error function:

$$\rho_i(z) = \rho_w + \frac{\rho_d - \rho_w}{2} \left[1 + \text{erf} \left(\frac{z}{\sigma_i \sqrt{2}} \right) \right] \quad \text{Eq. 4.52}$$

$\rho_{NP}(z)$ represents the contribution of the nanoparticles adsorbed at the interface, modeled as a monolayer of hexagonally packed spheres of radius a , immersion depth h , average interparticle spacing s_{av} , and bulk particle electron density ρ_p :

$$\rho_{NP}(z) = \rho_{NP}(s_{av}, \rho_p; z) = \frac{2\pi\rho_p}{\sqrt{3}(2a + s_{av})^2} [-z^2 + 2(a-h)z + h(2a-h)] \quad \text{Eq. 4.53}$$

when $-h < z < -h + 2a$ and $\rho_{NP}(z) = 0$ otherwise. Liquid displacement due to NP adsorption needs to be accounted for, representing the subtracted term in Eq. 4.51. Normalized Gaussian distributions $G(x_{av}, \sigma_x; x)$ (Eq. 4.51) are introduced to account for size polydispersity (a) and consequently varying immersion depths (h) with their average values x_{av} and their widths σ_x . All parameters were fixed to their known values or constrained except the average separation distance between the nanoparticles (s_{av}) and the average immersion depth (h_{av}). The former determines the average particle coverage associated with the height of $\rho(z)$, while the latter describes the peak particle contact angle by employing Eq. 2.10 and the z -coordinate of the maximum in the electron density profiles.²⁰⁹

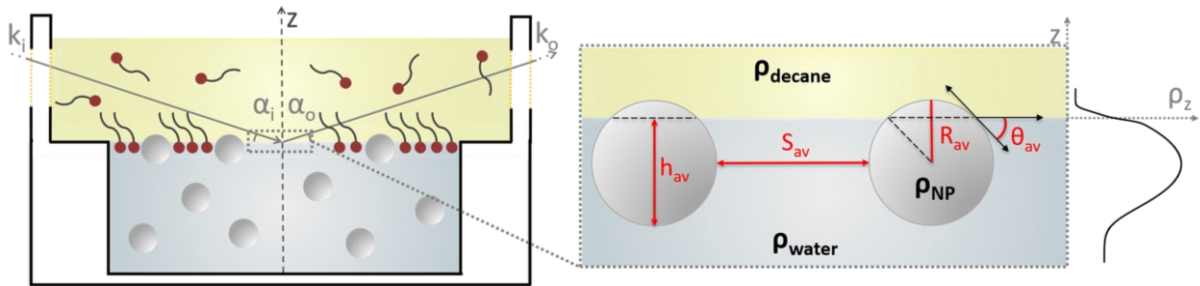


Fig. 4.20 Shown left is a schematic setup of the specular reflectance at the oil-water interface with an amino lipid (ODA) dissolved in the oil phase against 0.1 w/w% silica or amine-coated silica nanoparticles in the aqueous phase (pH ~ 5.8). The pictogram on the right indicates the physical model parameters model derived from the electron density (ED) profiles. Symbols are explained in the text.

5 Reversible adsorption of nanoparticles at surfactant-laden liquid-liquid interfaces

Chapter 5 has been adapted with permission from the *American Chemical Society* and is published in *Langmuir*, 2019, DOI: [10.1021/acs.langmuir.9b01568](https://doi.org/10.1021/acs.langmuir.9b01568).

Systematic research on emulsion stabilization by combining particles and surfactants can be simplified by studying adsorption phenomena of two-dimensional immiscible interfaces. Particularly drop profile analysis tensiometry is a well-established method that measures the macroscopic quantity of interfacial tension (IFT) over time and generates information about steady-state surface tension and adsorption dynamics. A simple theoretical approach is tested by studying the adsorption behavior of hydrophilic particles and oil-soluble surfactants bearing equal charges. Particularly, aminated silica nanoparticles coated with (3-aminopropyl)triethoxysilane (APTES) and octadecyl amine (ODA) are tested in a water/decane system. Because the polar heads of the surfactant are similar to the particle's surface groups and dissolved in an immiscible apolar medium, interactions can be assumed to be limited to the interfacial phase and repulsive through the aqueous phase. Therefore, it can be expected that the lipids prefer to adsorb at the oil-water interface while leaving the particles unaffected. Consequently, the decrease in interfacial free energy caused by the particles and by the surfactants should behave additively in this particular experimental system. The validity of this assumption is tested via contact angle measurements on APTES-coated substrates that simulate the nanoparticle surface in the presence of varying amounts of lipids. In IFT measurements using a pendant drop setup, various concentrations of ODA are dissolved in decane and examined against a fixed concentration of 1 w/w% APTES-coated silica nanoparticles dispersed in water at a pH that protonates the amine groups on the surface of the particles and of the interfacially adsorbed surfactants. The results of the contact angle and IFT measurements are discussed in light of the theoretical continuum approach introduced below. Furthermore, the population of adsorbed particles at the liquid-liquid interface is visualized with SEM after Langmuir-Blodgett-type transfer of the interfacial film. In addition, the viscoelastic properties of the interface are examined via dilational and shear rheological measurements. These techniques provide additional semi-quantitative evidence of the validity of the presented approach.

5.1 Theoretical approach: Additivity of interfacial free energy contributions of particles and surfactants

Based on the approach by Du et al.²⁷ and Zhang et al.,³³ an adapted continuum approach is proposed allowing to estimate the packing density of interfacially adsorbed particles from the change in IFT generated in the absence or presence of surfactants based on assuming additivity of the respective interfacial energy contributions of surfactants and particles:

$$E_i = E_{SF} + N_p \Delta E_p \quad \text{Eq. 5.1}$$

where E_i is the total free energy of the interface as the sum of the energy contribution of the surfactant-covered interface (E_{SF}) and of one particle (Eq. 2.18; ΔE_p) times the total number of particles adsorbed at the interface (N_p). $E_{SF} = \gamma_{SF} A_{SF}$ is defined as the product of the interfacial tension of the interface in the presence of only surfactant molecules (γ_{SF}) and the surfactant-covered fraction of the interface (A_{SF}). This leads to:

$$E_i = \gamma_{SF} A_{SF} + N_p \pi a^2 \gamma_o (1 - \cos \theta)^2 \quad \text{Eq. 5.2}$$

This relation can only uphold when there are no specific interactions between particles and surfactants, such that the three-phase contact angle of the particles at the interface θ remains constant, regardless of surfactant concentration. Integrating the partial derivative of the thermodynamic expression of IFT gives a direct relationship between the measured equilibrium IFT and thus the interfacial free energy E_i of the total interfacial area A_i :

$$\gamma' = \frac{E_i}{A_i} \quad \text{Eq. 5.3}$$

Where γ' is the apparent equilibrium IFT after addition of surfactant (γ_{SF}) or surfactant with particles (γ_{SF+P}). From the above-stated boundary condition and applying Eq. 5.2, the measured IFT difference between surfactant-only and particle-surfactant systems ($\Delta\gamma'$) represents the free energy difference of the interface with and without particles (ΔE_i) which in turn is indirectly related to the number of adsorbed particles, N_p . Contact angle measurements on planar substrates allow calculating how large the area is that one particle occupies at the interface (A_p , see Appendix A.3.1). Particle adsorption decreases the available interfacial area for the non-interacting surfactant, substituting a total area of $N_p A_p$ from A_{SF} . If only the substituted area fraction per particle A_p is taken into account, the difference between ΔE_p and ΔE_{SF} as a function of the particle's contact angle and represents the energy difference per adsorbed nanoparticle (ΔE_{Ads}) which replaces surfactants from the interface per its area A_p . The ratio of the interfacial energy from the collective of adsorbed particles to the interfacial energy of a

single particle for one specific lipid concentration then leads to the total number of adsorbed particles at the interfacial area A_i :

$$\frac{\Delta E_i}{\Delta E_{Ads}} = N_P \quad \text{Eq. 5.4}$$

Taking the ratio of the experimentally derived droplet area and the estimated area occupation of one adsorbed spherical particle gives the number of particles for a fully hexagonally packed monolayer:

$$\frac{A_i}{A_P} 0.91 = N_{Max} \quad \text{Eq. 5.5}$$

This allows the area fraction covered with nanoparticles to be estimated:

$$\frac{N_P}{N_{Max}} = \Theta \quad \text{Eq. 5.6}$$

5.2 Materials

Tetraethyl orthosilicate (TEOS $\geq 99\%$, product no. 86578), (3-aminopropyl) triethoxysilane (APTES 99%, product no. 440140), toluene (anhydrous, $>99.7\%$, product no. 32249-M), citric acid (anhydrous, $\geq 99.5\%$, product no. 27109). and octadecylamine ($\geq 99\%$, product no. 74750) were purchased from Sigma Aldrich (Darmstadt, Germany). Decane ($\geq 99\%$, product no. D901), HCl (0.1 M, product no. 38280; 1 M, product no. 71763) and NaOH (1 M, product no. 71463) solutions were purchased from Honeywell and 0.1 M NaOH (product no. 124200010) from Acros Organics (Nidderau, Germany). 37% HCl (product no. 20252.335), H₂SO₄ (95-97%, product no. 30743-M), acetone (99%, product no. 20063.365) and ethanol absolute ($>99.8\%$, product no. 64-17-5) were obtained from VWR Chemicals (Hannover, Deutschland). Technical grade ethanol (99%, product no. 2211.5000) was sourced from Chemsolute (Hamburg, Germany). Aluminum oxide 90 active basic (mesh size: 0.063-0.2 mm, product no. 1.01076.2000) and pro analysis sea sand (product no. 1.07712.1000) were purchased from Merck Chemicals GmbH (Darmstadt, Germany). Amorphous silica powder with a size of 80 nm was obtained from Fiber Optic Center (New Bedford, USA). All aqueous solutions were made with double deionized water (18.2 M Ω •cm at 25 °C) from a Synergy Water Purification system (Millipore Corp., Massachusetts). Wash-N-Dry coverslip rack (polypropylene, product no. Z688568) was purchased from Sigma Aldrich (Darmstadt, Germany).

5.3 Methods

5.3.1 Cleaning glassware

All glassware (Tradename: amber pressure plus laboratory glass bottles, Duran) was cleaned using hot tap water and soap plus gentle scrubbing, rinsed with DEMI-water, acetone, MilliPore water, and finally ethanol absolute. Cuvettes (Hellma Analytics) were cleaned with acetone, followed by 6% citric acid in MilliPore, and placed for 20 min in a 70 °C oven. Subsequently, the inside walls were rubbed using a soft cotton swab, rinsed with copious amounts of water, and finally with ethanol absolute. Finally, the glassware and cuvettes were covered with a Kimwipe and air-dried. All other materials (e.g., tweezers) that came in contact with samples were cleaned by rinsing with acetone, ethanol, water and dried with a Kimwipe.

5.3.2 APTES functionalization of 80 nm silica particles

The as-received 80 nm silica powders showed some surface activity in pendant drop tensiometry. The particles were washed three times with water using centrifugation and redispersion and subsequently dried in air for 48 h. No influence on the interfacial tension was observed after redispersing them.

Coating the particle surface with amine groups to achieve a positive surface charge at pH 6 was done by a silanization reaction with APTES. Briefly, 1 g of particles was dissolved in a round-bottom flask containing 20 mL of anhydrous toluene and sonicated for 20 min. Water vapor was removed by flushing with nitrogen, and the dispersion was heated to 110 °C with reflux. Once at temperature, 0.5 mL of APTES (2.5 v/v%) was added dropwise and left to react for 6 h. The mixture was cooled down and centrifuged for 10 min at 5000 rpm, followed by redispersion and centrifugation using toluene, ethanol absolute, and water, each three times. The particles were air-dried for 48 h, stored in a desiccator containing silica beads, and used within three months after preparation.

5.3.3 Dispersion preparation

Particle dispersions of 1 w/w% were prepared by adding MilliPore water, and the pH was adjusted in several steps. Ice cooling was necessary during sonication to prevent hydrolysis of the siloxane network of the APTES molecule.⁵⁸⁰ Prior to the measurements, dispersions were sonicated, degassed, and the pH was confirmed (FiveEasy pH-meter, Mettler Toledo, Germany). Dispersions were stored at 4 °C and used for up to three weeks. Also, size and zeta potential measurements (0.1 w/w% in 10 mM KCl; Smoluchowski model) were performed using DLS (ZetaSizer NanoSP, Malvern, United Kingdom). For 10 mM KCl solution, the viscosity is 8.854×10^{-4} Pa s, refractive index 1.3301, and non-significant absorption.^{606,607} The refractive index of synthesized silica is 1.41 with negligible absorption.⁶⁹⁸ Membrane filtering (0.1 – 0.2 μm polyethersulfone) of dispersions prior to light scattering measurements is recommended to remove dust. However, purified particle dispersions were diluted without membrane filtering due to the observed decrease in decane/water interfacial tension, indicating that surface-active material from the PES filter contaminated the dispersion (data not shown). Sub-measurement time per iteration was kept ≥ 10 s, and transient size fractions may influence particle size, size distribution, and PDI.⁶⁰⁸ A pH titration curve was obtained by adjusting the pH of the dispersions one day before measuring and magnetic stirring overnight. Samples were sonicated in ice water, and measurements were done when there was no change in pH between two sonication cycles. The dispersion density at 20 °C was estimated by pipetting 500 μL of the dispersion and noting the weight in triplicate, namely $1.005 (\pm 0.0013)$ g cm^{-3} .

5.3.4 Experimental procedure for decane purification and validation

Inherent surface-active impurities in the as-received decane were removed by running the solvent three times through a gravity column filled with basic alumina. The purity was confirmed using pendant drop tensiometry (OCA25, Dataphysics, Germany) in a temperature-controlled room (20 °C \pm 1 °C). The sensitivity of the device is 0.01 mN m^{-1} .⁶⁹⁹ The density of water and decane at 20 °C are 0.9982 g cm^{-3} and 0.730 g cm^{-3} , respectively, which are implemented in the SCA software.

Right before the measurement, water was degassed, and the system was rinsed at least three times. Solutions were allowed to equilibrate thermally. A water-air surface tension around $72.5 \pm 0.3 \text{ mN m}^{-1}$ indicated no impurities in the tubing system. The purity of decane was checked by generating a 2 μL water drop in the oil phase, discarding it at the bottom of the cuvette, and making a sufficiently large drop of 25 μL . The needle (1.07 mm outer diameter) was gently struck with a metallic object to remove static discharge. The IFT was continuously monitored for 5 min before decreasing the drop volume. The decane was assumed to be pure when the IFT remained constant around 52.2 mN m^{-1} with a systematic error of 0.2 mN m^{-1} .⁷⁰⁰ The purified decane was stored in a stainless steel bottle (Duran group GL45) and placed under vacuum (4 mbar) in a desiccator to significantly slow down the oxidation process that otherwise produces surface-active peroxides.⁶⁶⁷ The purified decane could be stored indefinitely without affecting the IFT of the pristine oil-water interface as long as the vacuum was maintained.

5.3.5 Experimental procedures oscillating drop

The PTFE-coated stainless steel cannula of the pendant drop apparatus was cleaned using acetone, 6% citric acid, ethanol, and water before gently wiping the cannula with a Kimwipe and rinsing the tubing system with MilliPore water. To remove any particles inside the pendant drop tubing, rinsing was done using ethanol, toluene, and acetone three times (0.5 mL per rinsing step), followed by rinsing with water with at least 3 mL.

Surfactant solutions were prepared by dissolving the lipid in purified decane and stirring magnetically (10 x 6 mm) for 24 h at 20 °C. In the case of particles, 75 µL of the dispersion was taken up via the cannula, and the valve was closed to avoid mixing with the water in the tubing system. The cannula was wiped dry with a Kimwipe. When it was possible to dilute the surfactant solutions, 1 mL of pure decane was poured into a cuvette, and a 2 µL drop was discarded. A drop of 15 - 25 µL was formed and allowed to equilibrate for 30 min while monitoring the interfacial tension. Droplet oscillation was started, and 1 mL surfactant solution was added very slowly to minimize disturbance of the droplet while touching the inner wall of the cuvette after the first movie was recorded. Over the long term, there was no significant difference in the IFT profile using this approach or making an aqueous drop in oil initially containing the lipids. For 4 mM ODA, which is close to the solubility limit of the surfactant, the latter procedure could only be executed.

Harmonic oscillations (ODG20, Dataphysics, Germany) by a piezoelectric actuator produced a frequency of 0.1 Hz and area deformations $\Delta A/A_0$ were between 8 - 10%. A movie was recorded with capturing time of 30 s and a time lag of 20 s up to 2 h. Each movie recorded five harmonic area oscillations, which were used afterward for calculation to obtain the average interfacial tension, the complex viscoelastic, elastic, and viscous moduli. All measurements were repeated three times, and the deviation between them was below 0.4 mN m⁻¹.

5.3.6 Experimental procedure sessile drop: TEOS and APTES coating borosilicate glass

Contact angle measurements were conducted on functionalized substrates using the same high-precision optical measuring device (OCA25, Dataphysics, Germany) at 20 °C (± 1 °C) with a standard error of 0.05°. Samples were always handled using tweezers. Squared borosilicate glasses (18 x 18 mm) were cleaned and activated by immersion in 1:1 37% HCl:MeOH for at least 30 min while the solution was magnetically stirred (25 x 8 mm) to ensure both sides of the glass could be functionalized. The samples were rinsed with copious amounts of water and placed in concentrated H₂SO₄ with stirring for 30 min. The samples were rinsed again with water before placing them in gently boiling water for another 30 min. The contact angle of these samples was $\sim 0^\circ$ which indicates a high density of available hydroxyl groups.⁷⁰¹

A thin silica film was deposited on the substrate by sol-gel chemistry to mimic the silica nanoparticle surface. A mixture of 1:2:2 TEOS:water(pH1):ethanol absolute (total volume 45 mL) was magnetically stirred (25 x 8 mm) for 1 h. A hole was punctured in the lid and allowed to evaporate at 70 °C for 5 h and subsequently stored with a closed lid at 20 °C overnight. The following day, activated substrates were dried under a nitrogen stream and dip coated in the sol-gel with a residence time of 120 s, withdrawal speed of 5 mm min⁻¹, and drying for 10 min. The custom-built dip coater is encased with a thick, transparent plastic box to prevent air currents from influencing the drying process. Silica beads were placed inside the casing to slightly control the amount of moisture inside the box, as purging with (inert) gasses was not possible in that laboratory setup. The coated substrates were covered and placed in atmospheric conditions for 24 h to promote further condensation, subsequently stored in a desiccator containing silica beads and used up to three months.⁷⁰²

APTES-coating of the substrates was performed according to the protocol of Yadav et al.⁵⁸⁹ A stock solution of pre-hydrolyzed APTES was made containing 50% MeOH:47.5% APTES: 2.5% water and stored at 4 °C for 1 h prior to use. The solution could be used for several weeks without deterioration. The stored TEOS-coated substrates were cleaned by immersion in 1:1 HCl:MeOH for 30 min, rinsed with water and dried. The APTES stock solution was diluted 1:500 in MeOH (total volume 10 mL), and samples were shaken for 10 min to functionalize both sides. The samples were rinsed with MeOH and cured at 110 °C in air for 25 min.

Afterward, rinsing with 1 mM AcOH in MeOH was necessary to improve the hydrolytic stability of APTES.⁵¹¹ Samples were dried under a gentle nitrogen stream and placed in water at pH 3 for 24 h with shaking. Before use, coated samples were rinsed with fresh water, dried with nitrogen, cut into approximately 0.9 x 0.9 mm pieces, and placed in a cuvette.

Water-in-oil contact angles were obtained by placing a 5 μ L water drop on the functionalized substrate. Then, the decane was carefully added to the cuvette while continuously monitoring for 30 min. Contact angle values reported were retrieved after 30 min equilibration.

5.3.7 Experimental parameters for interfacial shear rheometry

Interfacial shear measurements were performed using an oscillating stress-controlled rheometer (DHR-3, TA instruments, Germany) with a double wall Pt/Ir Du Noüy ring (ring diameter: 20 mm, wire diameter: 0.36 mm) on a vibration-proof table at room temperature. The in-house-made Delrin support was cleaned using acetone, hot tap water and soap plus scrubbing, DEMI-water, 6% citric acid and placed in a 70 °C oven for at least 20 min. The sides were rubbed using a cotton swab followed by rinsing with copious amounts of MilliPore water, ethanol and dried with compressed air (oil-free). The Du Noüy ring was firstly rinsed with ethanol and placed in 6% citric acid solution for 20 min in a sonication bath. Subsequently, the acid was replaced by 1 M NaOH and sonicated for 1.5 h to dissolve any remaining silica on the ring. The ring was flame-cleaned with a propane torch prior to use and checked for any remaining white silica spots.

First, 5.8 mL of the degassed aqueous subphase was loaded into the support until it reached the inner edge to pin the meniscus. Next, the ring was wetted entirely in the water phase and positioned precisely at the interface. Three mL of the oil phase was slowly added on top of the subphase before starting the measurement, and a protective cover was placed in front of the device. Measurements were executed in the linear viscoelastic region where the strain amplitude was set at 0.1% and a frequency of 1 Hz. The raw phase was around 20°, indicating that the measured signal was not caused by instrument inertia.^{703,704} Samples were repeated in triplicate showing similar plateau values, although adsorption kinetics were not as reproducible.

5.3.8 SEM sample preparation of the decane-water interface

Precut silicon wafers (5 x 5 mm, Plano) were sonicated for 15 min each in acetone, water, and ethanol absolute. Samples were placed in a Kimwipe-covered Petri dish. Crystallizing dishes ($a = 4$ cm, Duran) were placed on a vibration-free table at 20 °C, and 24 mL of particle dispersion was added. On top, 7 mL of decane with or without pre-dissolved surfactant was carefully added. After the specific time, most of the oil was carefully removed at the meniscus from the side of the dish but still left a small oil layer on the water phase. An electrically conductive polished silicon wafer was fixed between tweezers and submerged at the periphery of the dish where the oil was removed. The grid was moved to the opposite side and slowly pulled upwards at an angle of 30°. Excess liquid was removed with a Kimwipe by touching the sides and bottom. The wafer was adhered to conductive carbon tape on an alumina sample holder and analyzed with SEM (Supra 40, Carl Zeiss, Germany).

5.3.9 Streaming potential of flat substrates

Zeta potential measurements of planar substrates were measured with a SurPASS apparatus (Anton Paar) at 20 °C. Two functionalized substrates were cut to 10 x 18 mm and attached to the adjustable gap cell with double-sided adhesive tape (tesa®). The electrolyte solution was prepared fresh (1 mM KCl) using degassed water, and the system was rinsed with 100 mL of this solution and subsequently discarded. A 600 mL Duran beaker was filled with 500 mL electrolyte, and the gap distance was adjusted to 100 μ m, ensuring laminar flow (± 75 mL min⁻¹ at 300 mbar). Subsequently,

the system was continuously rinsed for 20 min at a maximum pressure of 500 mbar, and a flow check was performed. The pH was adjusted to basic with 0.1 M NaOH and rinsed for 5 min before starting an acid titration (0.05 M HCl). Afterward, samples were removed, and the system was flushed with 500 mL ethanol absolute followed by 1 L of water. The measurements were repeated thrice with an isoelectric point deviation of ± 0.25 pH units.

5.4 Scientific outcome

The general design of the studied system is based on the interfacial adsorption of particles and surfactants of the same charge to avoid direct particle-surfactant interactions. Therefore, 80 nm-sized silica nanoparticles are coated with a short-chain aminosilane (APTES) with the same terminating functional group as the oil-soluble surfactant octadecyl amine (ODA).⁴³⁸ At mildly acidic conditions, the particles exhibit a significant positive surface charge with good dispersibility in water (Appendix A.3.3, Fig. A.3.1), while the partially positively charged amine head groups of the adsorbed ODA molecules act as a weak base (pK_a ODA: 10.65), thereby alkalifying the pH of the interfacial region⁷⁰⁵ with negligible solubility in the water phase.^{435,436} An overview of the chosen methodology is given in Fig. 5.1.

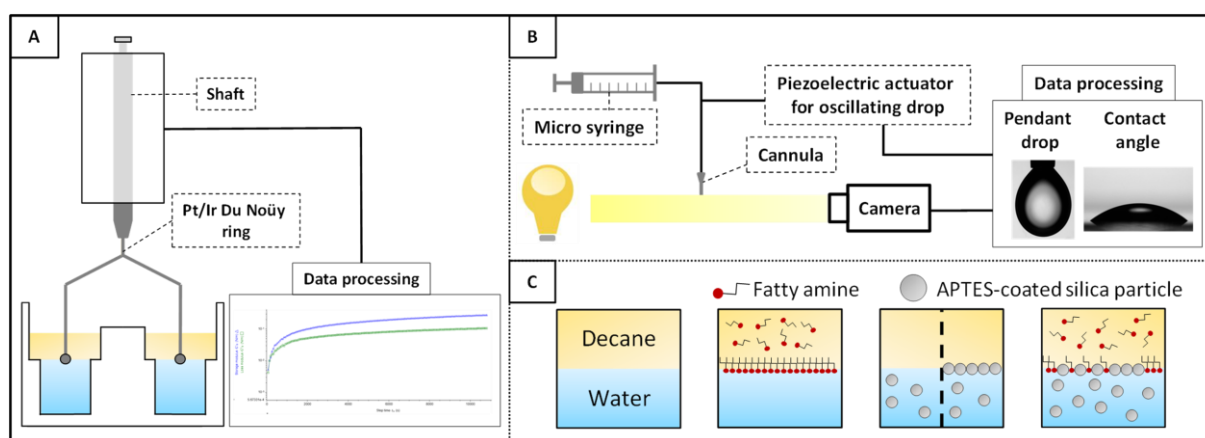


Fig. 5.1 Schematic overview of applied measurement techniques and the systematic study of the decane-water interface. A) The interfacial shear rheometer is equipped with a Du Noüy ring that exhibits low inertia and applies small torques, capable of sensitive interfacial measurements of thin-film formation over time under constant oscillation. B) The camera takes images of a pendant drop hanging from the nozzle or from a sessile water drop on a substrate which is subsequently analyzed via drop shape analysis. The piezoelectric system allows sinusoidal area perturbations of a drop to analyze the dilational rheological behavior. C) Representation of the different interfacial conditions tested in this research. From left to right; the pristine decane-water interface; ODA against water; APTES-coated silica particles against decane (remaining in the bulk, adsorbing at the interface or an intermediate situation); and ODA against APTES-coated silica particles.

5.4.1 Scanning electron microscopy of lipids and particles

In theory, interactions between the two adsorbents are repulsive in nature and arise solely at the interface owing to their phase separation, which raises the question of whether particle adsorption is even preferred.^{15,29,332,448,706} In this regard, SEM examination of Langmuir-Blodgett-type transfers of interfacially adsorbed particles provides a first semi-quantitative assessment of particle adsorption. Interestingly, in the absence of lipids, nanoparticles adsorb at the interface despite their inadequacy to stabilize emulsions (Fig. 5.2). Binks et al.³⁹ observed similar sporadic adsorption behavior of bare silica nanoparticles (contact

angle of around 32°) at the water-decane interface. Adding low surfactant concentrations (0.001 and 0.01 mM) stimulates particle adsorption while increasing the molarity further shows the opposite effect, and fewer particles remain attached to the interface. Similar approximate densities were observed amongst different batches suggesting that surface-active molecules can overpower the high binding energy of adsorbed particles due to interfacial competition. At this point, observations are limited to these simple statements as more sophisticated techniques would be required for accurate microscopical observation of nanoparticles adsorbed at the liquid-liquid interface since artifacts could be introduced by the transfer or by solvent evaporation.^{38,39}

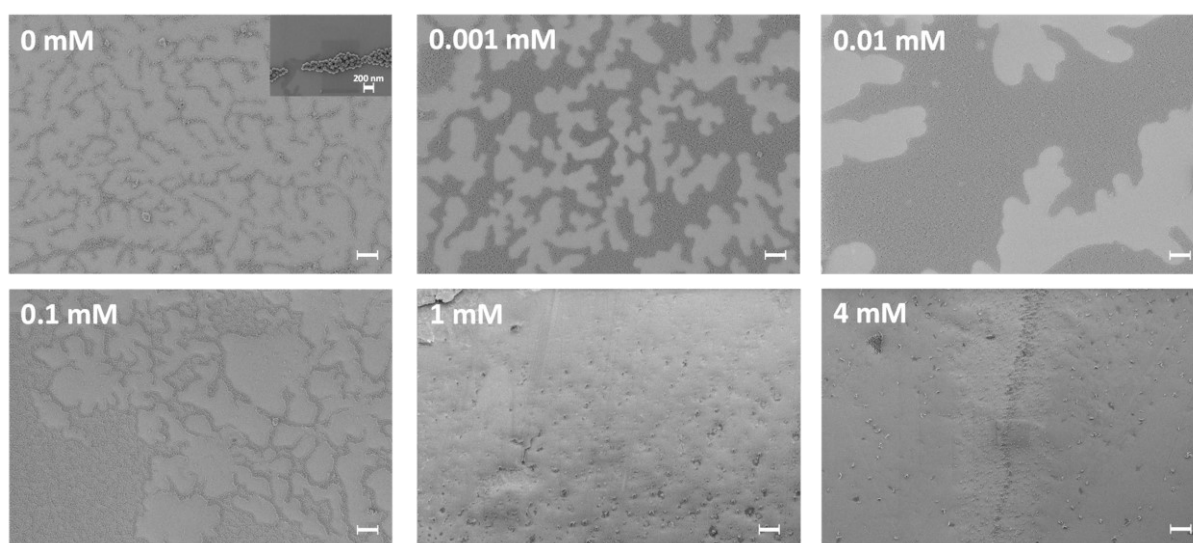


Fig. 5.2 SEM images of particles transferred from the decane-water interface for different concentrations of ODA taken after 1 h equilibration at 20°C . Even without the lipid, some particles adsorb at the interface (darker contrast). The particle density increases when adding 0.001 mM and 0.01 mM ODA while further increments cause a decline in the number of particles. Scale bars are $2\ \mu\text{m}$.

5.4.2 Interfacial shear rheology for rigid particle-lipid films

A more quantitative insight into the structural properties of the interface is obtained by investigating the different interfacial films with interfacial shear rheology. The results with just lipids and combinations of lipids and particles are shown in Fig. 5.3. In the absence of fatty amines, regardless of whether the aqueous subphase contained particles, a noisy signal for the storage modulus (G') was observed due to an insignificant interfacial population and lack of structural ordering. Film growth was detected when a lipid concentration of at least 0.5 mM ODA was used (Appendix A.3.4, Fig. A.3.2). For 1 mM ODA and above, initial interfacial coverage takes place in less than 30 min, followed by a slower increase in G' over time. The steep increase in G' for ODA in decane against pure water indicates the formation of

an elastic solid-like film under low shear strain conditions since G' is larger than G'' (not shown).

Two striking effects occur when replacing pure water with the particle dispersion, which is indicative of competitive adsorption of particles and lipids. The elastic modulus for the mixed system declines compared to the interface covered only with surfactants, while the difference between the plateau values of G' diminishes when the concentration of the amphiphile is increased, namely two orders of magnitude for 1 mM ODA and less than one for the highest fatty amine level. An explanation for the lower G' values in the presence of particles might be that the particles insert into the interface, creating defects in the cohesive lipid layer that weaken the elastic lipid film. Secondly, the difference in magnitude of the moduli with or without particles is primarily determined by the bulk surfactant concentration, indicating a force balance between the two components. Since the pH of the particle dispersion was adjusted using small concentrations of HCl, varying amounts of KCl were dissolved in the absence of particles to study the potential effects of anions on the interfacial films of pure surfactants (Appendix A.3.5, Fig. A.3.3). Increasing the ionic strength indeed leads to a slight decrease in G' ,⁴²⁹ which is however insufficient to explain the distinct shapes and magnitudes of these curves in the presence of particles (Fig. 5.3).

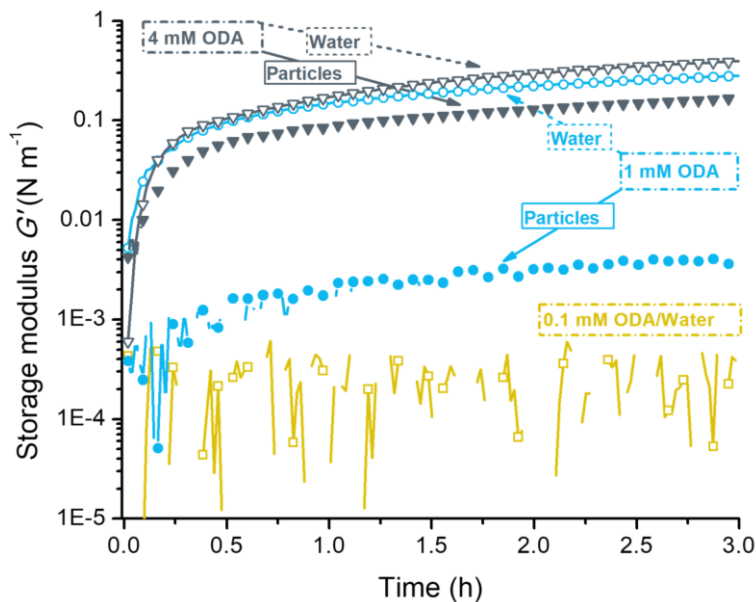


Fig. 5.3 Storage modulus (G') from interfacial shear rheology shows the time-dependent thin film formation of ODA at the decane/water interface, with (full) or without (open) 1 w/w% APTES-coated silica particles at pH 6. Lower moduli are recorded in the presence of particles.

5.4.3 Tensiometry and dilational rheology for liquid-like particle-lipid films

Precisely measuring the IFT between particle-free and particle-covered interfaces in the presence of varying surfactant concentrations is central to the analysis of competitive adsorption (Fig. 5.4A). The IFT of pure water or particle dispersion against pure decane without surfactants shows a constant value around 52.2 mN m^{-1} . This apparent lack of interfacial activity of hydrophilic nanoparticles has been debated in the literature, often leading to a preemptive dismissal of the possibility of particle adsorption to the interface.^{325,444,448} However, even a hexagonally dense packing of (non-interacting) hydrophilic particles at the interface would theoretically (Eq. 2.18; ΔE_P , Eq. 5.1, and Eq. 5.5) change the interfacial tension only by 0.025 mN m^{-1} (assuming a contact angle of 40° , see the discussion below), which is below the precision of pendant drop measurements. Accordingly, the low coverage of particles as observed with SEM (Fig. 5.2) would not lead to significant changes in the IFT. The different lipid concentrations are depicted above the corresponding curves where the dotted lines are pure water-lipid systems, while the full lines represent the IFT for the particle-lipid samples. The equilibrium IFT of pure surfactants follows the expected trend of decreasing IFT with increasing surfactant concentration. For the three lowest lipid concentrations in the absence of particles, the tension decreases exponentially, and the time required for reaching a steady-state IFT increases with concentration. On the other hand, the IFT for 4 mM ODA against water shows an initial minimum followed by an increase in IFT before achieving quasi-stability as a consequence of interfacial rearrangement, since this concentration is above the critical micelle concentration of 3 mM ODA and close to the solubility limit of 4.5 mM ODA in decane. With the addition of particles, the equilibrium IFT significantly changes to higher values compared to pure surfactants. Accordingly, the interfacial free energy of the system is increased in the presence of particles that allows analysis of the newly formed equilibrium of mixed particle-surfactant layers as discussed below. Furthermore, distinct adsorption dynamics and equilibrium IFTs can be observed in the mixed systems. Most notably, at the start of the measurement, the IFT is recorded at lower values with faster equilibration compared to surfactant only. The same phenomenon was also observed for silica-SDS (sodium dodecyl sulfate) systems and attributed to increased surface activity caused by enhanced electrostatic repulsion between the negatively charged nanoparticles and the anionic surfactant.^{94,448} In this case, however, short-range repulsion between the different materials can only arise at the interface, which would oppose adsorption. Instead, the surfactants are introduced to the system after a particle-laden water droplet has been equilibrated in pure decane. Accordingly,

less surfactant is needed to saturate the interface, explaining the faster kinetics. The long-time increase in IFT of 4 mM ODA indicates particle-surfactant interactions, which will be discussed below. Fig. 5.4B shows the dilational elastic (E') moduli for particle-free (open symbols) and particle-laden interfaces (full symbols). The moduli rapidly increase in all cases and achieve a steady-state at around 10 min after starting the measurement. The elastic moduli from 0.01 mM to 1 mM ODA with and without particles are similar in magnitude, while the moduli for 4 mM ODA show differences. Equal moduli indicate that the surfactant purely determines the viscoelastic properties of the interface despite a difference in IFT. For 4 mM ODA, E' is distinctly lower and increases over time in the presence of particles indicating that particles and surfactants interact with each other. This could present a limiting case for the proposed additivity concept due to their intertwined effect on the IFT. However, the extremely high viscoelastic parameters for 4 mM ODA have to be interpreted with care since high ODA concentrations form a solid-like thin film as shown with interfacial shear rheology.

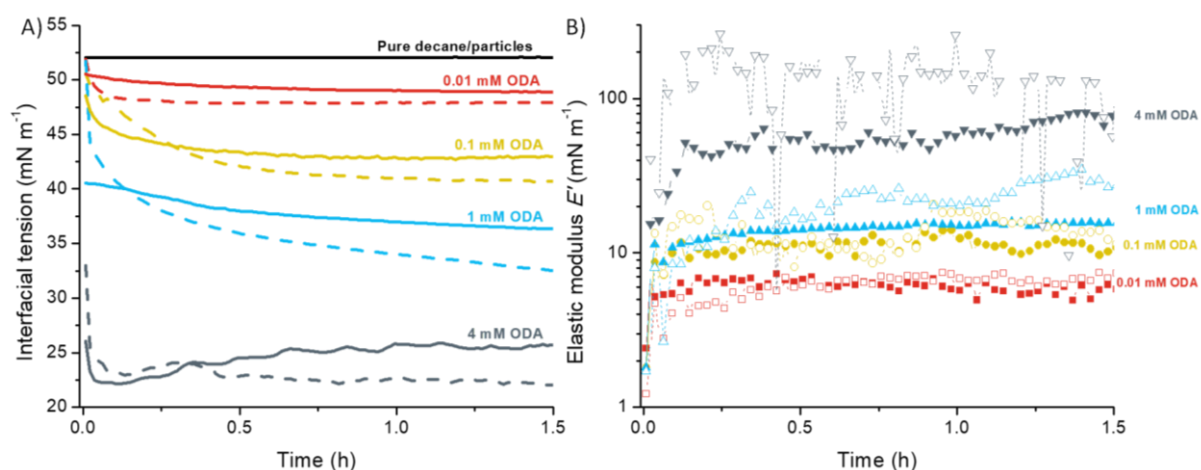


Fig. 5.4 A) Interfacial tension (IFT) measurements while applying continuous droplet oscillations at a frequency of 0.1 Hz and a relative area change $\Delta A/A_0$ between 8-10%. The black line shows a constant IFT in the absence of lipids. The colors represent different ODA concentrations, with (full) or without (dotted) 1 w/w% APTES-coated silica nanoparticles at pH 6. B) Elastic modulus of dilational rheology obtained simultaneously with the IFT measurements, in the absence (open) and presence (closed) of particles.

5.4.4 Oil/water contact angle in the presence of lipids

Particle-surfactant interactions are known to alter the particle's contact angle, which would directly violate the above-defined boundary condition of a constant three-phase contact angle (Eq. 2.5; θ_E) of the particles at the decane/water interface, irrespective of the surfactant concentration. The influence of different ODA concentrations on the water contact angle of functionalized APTES-coated silica substrates provides a reasonable estimate for the wetting behavior of the nanoparticles at the water-decane interface as well as for studying possible interactions between the APTES-coated solid surface and the lipid (Fig. 5.5).

The relative change in contact angle when the surfactant is added, concerning the original contact angle, indicates solid-lipid interactions. To this end, silica substrates that closely resemble the surface structure of APTES-coated Stöber silica particles were prepared. To verify the successful surface functionalization and silanization, streaming potential analysis was employed to obtain the pH-dependent zeta potential, the isoelectric point, and, indirectly, the hydrolytic stability of the surface (Appendix A.3.6, Fig. A.3.4.). The substrates show a strongly positive zeta potential of 37 mV at pH 6 with stable surface coating as evidenced by repeated streaming potential and contact angle measurements. An average contact angle of a water droplet in decane on the APTES-coated silica surface of around $40.05 (\pm 1.43)^\circ$ was measured, which agrees with the literature although slightly varying angles are reported.^{589,707,708} No measurable change in the contact angle was observed with additions of ODA to the decane phase of 1 mM and less. Hence, the deviations shown in Fig. 5.5 represent intersample variation before adding lipids. At 4 mM ODA, the contact angle increased by approximately 5° .

However, the observed lack of change in contact angle at low to intermediate ODA concentrations goes along with a change in surface tension at the oil-water interface as described above (Fig. 5.4). From this follows that, in order to uphold Young's equation (Eq. 2.5; θ_E), the solid-water surface energy must change too. Most likely, lipids accumulate at the solid-water interface and decrease the interfacial energy due to amphiphilic interactions similar to the water-oil interface. In fact, physisorbed water on the silica surfaces might form sites for polar interactions with the lipid head groups.^{443,709} At 4 mM ODA, direct polar interactions between lipid and solid in the proximity of the three-phase contact line become dominant and contract the droplet area with an increase in contact angle. Therefore, the highest fatty amine sample is an explicit limit to the analytical approach discussed below.

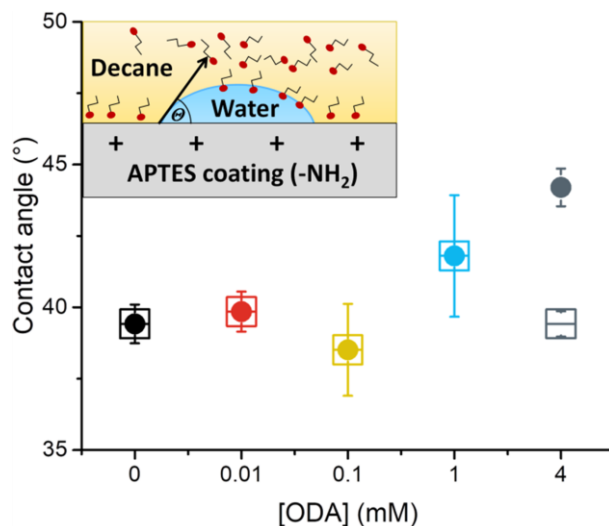


Fig. 5.5 Mean contact angles of a water drop at pH 6 on an APTES-coated silica thin film substrate immersed in decane with varying ODA concentrations, as shown in the inset. The contact angle was measured before (open squares) and after (full circles) addition of lipids to the oil phase.

5.5 Discussion

The theoretical approach presented in section 5.1 is based on a simple continuum approximation of particle adsorption at liquid interfaces and adapted to mixed adsorption between nanoparticles and surfactant molecules. The apparent IFT of the mixed system was obtained with the interfacial area of the droplet A_i and the contact angle measured on the flat substrates was treated as analogous to the particle surface. Based on the measured contact angle, the displaced interfacial area upon particle adsorption A_p is derived through straightforward geometrics for rigid spheres (Fig. 5.6A and Fig. 5.6B, Appendix A.3.1). Fig. 5.6C shows a plot of the free energy difference with particle adsorption of one 80 nm APTES-coated silica particle (ΔE_p) calculated from Eq. 2.18 and the free energy profiles of surfactants occupying the same space as one nanoparticle at a specific contact angle ($\Delta E_{SF} = \gamma_{SF} A_p$). γ_{SF} are the experimentally-derived IFT values of lipids in the absence of particles, obtained at quasi-equilibrium at 30 min. The free energy difference is displayed as a function of the three-phase contact angle of a particle at the decane-water interface. Although the binding energy of a single surfactant molecule is in the thermal energy range, the interfacial energy difference due to surfactant adsorption stems from the surfactants' collective energy contribution at larger occupational areas. In fact, a single particle displaces a number of surfactant molecules on the order of several thousand. This leads to significant changes in interfacial energy, which collectively can surpass the ΔE_p of a single particle, at least at lower contact angles. This effect should be even more apparent at smaller particle sizes but is not plotted here. Hence, the graphical representation in Fig. 5.6 provides a tool to estimate whether particle adsorption is favored over surfactant adsorption at a specific particle contact angle. Put differently, at a specific contact angle,

adsorption might occur when the energy change upon particle adsorption surpasses that of the collective energy changes associated with lipid adsorption at an area equivalent to the particle area ($\Delta E_P > \Delta E_{SF}$) while desorption might be favored if the balance is reversed ($\Delta E_P < \Delta E_{SF}$). The inset in Fig. 5.6C shows the energy difference between ΔE_{SF} and ΔE_P and illustrates how much the energy changes when one particle adsorbs at the interface and displaces surfactants at the particle area and vice-versa (ΔE_{Ads}). For example, one APTES-coated particle with a contact angle of 40° exhibits a rather high binding energy of 3550 kT , which would trap the particles at the interface in the absence of lipids. At 40° , ΔE_P lies between ΔE_{SF} of ODA at 0.01 mM and 0.1 mM , which hints that adsorption of particles to the interface might be preferred for 0.01 mM while desorption would be thermodynamically favored at 0.1 mM , and the equilibrium state between particles and surfactants is defined by the magnitude of the energy difference ΔE_{Ads} . Accordingly, Eq. 5.4 suggests that particle coverage should be higher with smaller positive ΔE_{Ads} in the absence of kinetic constraints against particle adsorption.

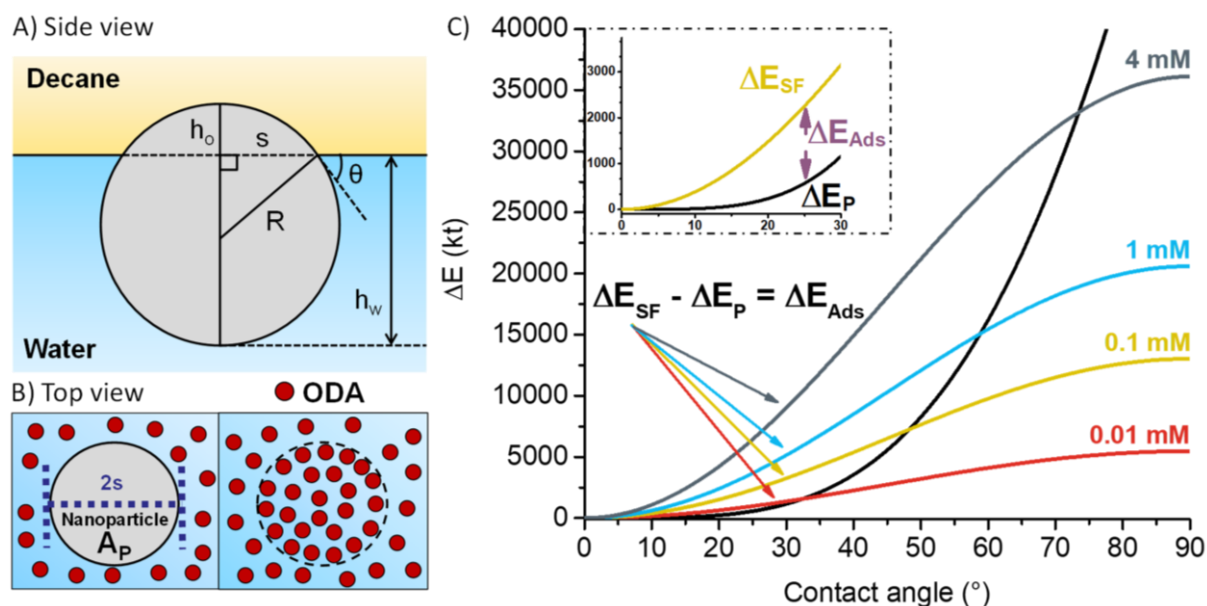


Fig. 5.6 A) Side view of one particle adsorbed at the decane-water interface. The depicted parameters are used to calculate the area of immersion as a function of the contact angle (Appendix A.3.1). B) Top view of the interfacial area. The area occupied by one particle at the surface results in a decreased accessible area for surfactant molecules, which reduces the interfacial energy according to the number of molecules at this area. C) The energy change of desorption for one 80 nm nanoparticle (ΔE_P , black) and the energy of the surfactant-covered interface (ΔE_{SF}) are plotted against the contact angle. The difference between these two thermodynamic quantities gives the energy change per particle adsorbed at the interface (ΔE_{Ads}).

Table 5.1 shows the calculated results from the analytical approach (Eq. 2.18; ΔE_P and Eq. 5.1 to Eq. 5.6) and the experimentally obtained parameters. The particle coverage (Θ) follows the expected trend of stimulating particle adsorption at 0.001 and 0.01 mM ODA, followed by a continuous decrease in particle coverage at 0.1 and 1 mM . The particle coverage

at 4 mM seems reasonably low, but the formation of particle-surfactant complexes as reported above makes this interpretation inaccurate. At very low surfactant concentrations (0.001 mM ODA), the extremely small measured differences in IFT ($\Delta\gamma'$) present the lower limit to interpret the results clearly. Additionally, Eq. A.3.2b and A.3.2c in Appendix A.3.2 allow investigating the additive contributions to the equilibrium IFT by particles and lipids.

Table 5.1 Calculated values for nanoparticle coverage (Θ), interfacial tension difference in absence and presence of particles at 30 min ($\Delta\gamma'$), effect on interfacial tension by lipids ($\Delta\gamma_{SF}$) and particles ($\Delta\gamma_P$) and the number of adsorbed particles at the interface.

Surfactant concentration (mM)	$\Delta\gamma'$ (mN m ⁻¹)	Coverage (Θ)	γ_{SF} (mN m ⁻¹)	γ_P (mN m ⁻¹)	Number of particles (10 ⁹)
0.001	1.42	0.40	0.93	0.65	6.97
0.01	1.51	0.66	1.27	1.63	11.60
0.1	1.60	0.49	5.79	3.10	8.63
1	2.12	0.24	12.94	1.52	4.23
4	1.17	0.05	27.53	0.37	0.63

While the calculated coverages might not be completely accurate due to uncertainties in the contact angle measurements and non-perfect adherence of the system to the assumption of additivity, the experimental and analytical results strongly suggest the existence of a competitive adsorption behavior between surfactants and nonamphiphilic nanoparticles at an interface between the two immiscible liquids. The proposed mechanism for this competitive adsorption behavior is schematically shown in Fig. 5.7. The energy diagram on the right shows the interfacial free energy change during the dynamic adsorption/desorption process, where the total free energy change of the interface during particle adsorption is the sum of the energy contributions of lipids (ΔE_{SF}) and particles (ΔE_P). The top row represents the classical idea that particles remain irreversibly trapped at an interface due to the high energy required to remove them, resulting in a very high activation energy barrier against particle desorption.

The bottom row accounts for the competitive adsorption behavior in a multicomponent system. Here, a dynamic equilibrium (determined by ΔE_{Ads}) is established where particle desorption is accompanied by less sharp free energy changes since the increase in the interfacial area during particle desorption is counteracted by simultaneous adsorption of new lipids. In fact, the contact angle experiments suggest that the particle surface facing the decane phase is already covered by a loosely adsorbed layer of lipids, which are directly available to occupy the interface concurrent to particle desorption. Additionally, accumulated lipids adsorbed at the oil-water interface could displace the particles through increasing surface pressure, similar to

proteins.⁷¹⁰ Readsorption to a surfactant-covered interface is also possible due to the small activation energy barrier of adsorption/desorption. The high propensity of the lipids to adsorb at the oil-water interface explains their concentration-dependent role in the adsorption process, at least at bulk lipid concentrations resulting in densely packed surface coverage. At low surfactant molarities ($\Delta E_p > \Delta E_{SF}$), particle-surfactant interactions are limited since the lipids can be expected to be preferentially located in the free interfacial space.

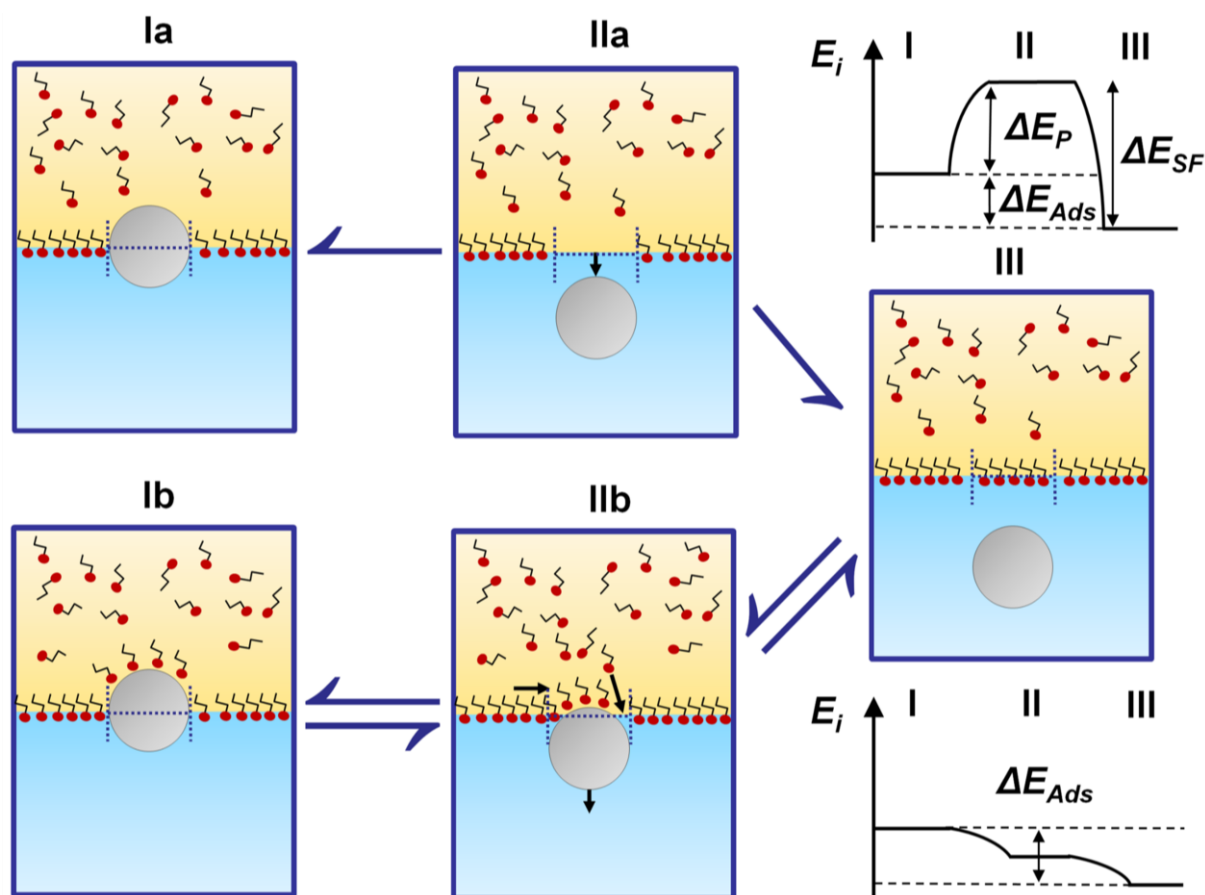


Fig. 5.7 The proposed competitive adsorption behavior between surfactants and nanoparticles with similarly charged groups at the decane-water interface. In the usual model (top row), particles are irreversibly trapped due to high binding energies and transition from stage Ia to stage IIa is not possible. Instead, in the presence of weakly interacting surfactants and particles, desorption of particles from the interface towards the bulk (lower row) is caused by competitive adsorption in a concentration-dependent manner with a transitional state that drastically lowers the energy barrier for particle desorption (Stage IIb). As a result, dynamic ad- and desorption of both species exist at equilibrium which is expressed in the energy diagrams with the interfacial free energy (E_i), the change of interfacial energy by one adsorbed nanoparticle (ΔE_p), the energy change caused by surfactant molecules covering the same area as the particles (ΔE_{SF}) and ($\Delta E_{Ads} = \Delta E_{SF} - \Delta E_p$).

5.6 Conclusions

In summary, a simple continuum-based approach is proposed for analyzing multicomponent adsorption between hydrophilic nanoparticles and surfactants that compete for interfacial adsorption. This approach was experimentally developed by dissolving surfactants and particles with equal charge in separate immiscible liquid phases, which limits particle-surfactant interactions to the interface and allows investigation of their separate and combined effects on the viscoelastic properties of the interface in detail. In these experiments with APTES-coated silica particles and ODA, the dynamic and equilibrium interfacial tension was strongly influenced by the addition of particles. Additionally, interfacial shear rheology showed a distinct difference in elastic moduli of lipid layers with the addition of nanoparticles. Water contact angles on APTES-coated substrates in the presence of lipids in decane demonstrated that the difference in interfacial tension and rheological moduli is caused by particle adsorption without altering the particle's wettability in a wide range of surfactant concentrations. The developed model assumes additivity of the contributions to the total interfacial free energy of lipids and particles, which is substantiated by the contact angle measurements. Furthermore, comparing the contributions to the total interfacial free energy of lipids and particles as a function of the contact angle allows for assessing particle coverage at the interface. The calculated results agree well with the observed trend for competitive adsorption and indicate that reversible adsorption of hydrophilic nanoparticles can occur in the presence of amphiphilic molecules of equal charge. Furthermore, interfacial adsorption of particles is strongly favored with surfactant concentrations that otherwise cause a negligible effect on the IFT and could potentially improve the shelf-life of Pickering emulsions, while high surfactant loadings lead to overpopulation of the interface with possible complex formation between particles and surfactants. Notably, the competitive adsorption behavior suggested here might be a determining factor in many mixed surfactant-particle emulsions which are, for example, found in nutritional products, water remediation, or other complex colloidal systems.

5.7 Acknowledgements

The author thanks Petra Witte for her expertise with the SEM and for the support of the German Research Foundation (DFG MA-4795/5-2).

6 Synergistic and competitive adsorption of hydrophilic nanoparticles and oil-soluble surfactants at the oil-water interface

Chapter 6 has been adapted with permission from the *American Chemical Society* and is published in *Langmuir*, 2021, DOI: [10.1021/acs.langmuir.1c00559](https://doi.org/10.1021/acs.langmuir.1c00559).

In the case of interfacial systems with at least two surface-active adsorbents (e.g., particles and surfactants), the net energy balance between them dictates the final properties of the mixed interfacial film. One major hurdle in estimating particle coverage or adsorption energies of adsorbed nanoparticles (NPs) is to adequately predict their contact angle (CA), especially when surfactants are involved that may alter their hydrophobicity, and are usually derived from sessile droplets on ‘equivalent’ macroscopic substrates. Based on this tentative assumption, the outcome from Chapter 5 indicates that positively charged hydrophilic silica NPs reversibly adsorb in the presence of a cationic oil-soluble surfactant in a competitive fashion. This conclusion is derived from a simple analytical model based on the principle of additivity of the interfacial energy contributions of the different components, used to assess the particle coverage in the absence and presence of NPs from interfacial tension (IFT) measurements. This methodology is valid when particle-surfactant interactions are absent, meaning that the CA does not change upon adding octadecyl amine (ODA).

To validate the approach proposed in Chapter 5, tensiometry of mixed particle/surfactant dispersions needs to be bolstered by additional methods that can more directly obtain NP coverage and/or their three-phase CA at the oil/water interface. Here, X-ray reflectometry (XRR) is utilized in conjunction with tensiometry and dilational rheology to understand the adsorption and self-assembly of hydrophilic NPs in the presence of the cationic, oil-soluble surfactant at the decane/water interface. To this purpose, native negatively charged silica NPs and positively charged APTES-coated silica NPs dispersed in the aqueous phase at pH 5.8 at a fixed concentration of 0.1 w/w% are studied. High purity of all constituents from other surface-active components is strictly observed during these experiments. The XRR data are analyzed via a physical model that realistically describes adsorption of spherical particles to a liquid interface and fitting of the electron densities (EDs), a method adopted from Isa et al.²⁰⁹ (section 4.1.3.4). NP coverage and CA obtained through modeling of the EDs are compared to and discussed with the previously reported continuum-based analytical model using the surface pressure difference in the presence and absence of APTES-coated silica NPs.⁷¹¹

6.1 Materials

Tetraethyl orthosilicate (TEOS $\geq 99.0\%$, product no. 86578), (3-aminopropyl)triethoxysilane (APTES 99.0% , product no. 440140), citric acid (anhydrous, $\geq 99.5\%$, product no. 27109), potassium chloride (KCl $99.0 - 100.5\%$, product no. P3911), L-arginine ($\geq 99.0\%$, product no. 1.01542), octadecyl amine (ODA, $\geq 99.0\%$, product no. 74750) and Hellma® optical glass cuvettes (Volume 3.5 mL, 45 x 12.5 x 12.5 mm, product no. Z600008) were purchased from Sigma Aldrich (Darmstadt, Germany). Decane ($\geq 99.7\%$, product no. D901), HCl (0.1 M, product no. 38280; 1 M, product no. 71763) and NaOH (1 M, product no. 71463) solutions were purchased from Honeywell and 0.1 M NaOH (product no. 124200010) from Acros Organics (Nidderau, Germany). Acetone (99.0% , product no. 20063.365), ethanol absolute ($>99.8\%$, product no. 64-17-5), and glacial acetic acid ($\geq 99.7\%$, product no. 64-19-7) were obtained from VWR Chemicals (Hannover, Deutschland). Technical grade ethanol (99.0% , product no. 2211.5000) was bought from Chemsolute (Hamburg, Germany). Kapton foil (200 x 304 x 0.05 mm, product no. 536-3952) was obtained from RS Components GmbH (Frankfurt am Main, Germany) and ZelluTrans dialysis tubes (MWCO 6-8 kDa, product no. E665.1) from Carl Roth GmbH (Karlsruhe, Germany). Minisart® syringe filter polyethersulfone (PES) with 0.1 μm pore size (product no. 16553-----K) were obtained from Sartorius Stedim Biotech (Germany, Göttingen). All aqueous solutions were made with double deionized water ($18.2 \text{ M}\Omega \text{ cm}^{-1}$ at $25 \text{ }^\circ\text{C}$) from a Synergy Water Purification system (Millipore Corp., Massachusetts).

6.2 Methods

Generally, and well beyond the usual laboratory practice, great care was taken that all chemicals and final particle dispersion were of the highest purity and behaved chemically inert towards the used laboratory materials to ensure that all reported measurements are only caused by the described particles and lipids.^{93,638} All aqueous solutions were degassed before use in Duran pressure plus bottles and sealed with a PTFE coated cap.

6.2.1 Cleaning of material

All glassware was cleaned by rinsing thrice with technical grade ethanol and acetone, water and ethanol absolute, covered with a lint-free wipe, and dried in air. If there was contact with surfactants, the glassware was first rinsed with technical grade ethanol and with a soft brush cleaned in hot tap water with soap followed by copious rinsing with tap water, DEMI water, and Millipore water. Also, after using acetone, the material was rinsed with 6 % citric acid. After the first rinse with citric acid, the glassware was filled with the acidic solution and placed in an oven for 30 min at $70 \text{ }^\circ\text{C}$ before continuing with water and ethanol.

6.2.2 Nanoparticle synthesis

Silica and APTES-coated silica nanoparticles were synthesized and functionalized in a one-pot reaction. A concentrated, alcoholic pre-hydrolyzed solution of APTES (1:0.95:0.05 ethanol absolute:APTES:water, v/v%) was prepared one day in advance and stored at $4 \text{ }^\circ\text{C}$.⁵⁸⁹ First, 300 mg L-arginine was magnetically stirred (40 x 10 mm) with 300 mL water in a 500 mL round-bottom flask at $70 \text{ }^\circ\text{C}$ with reflux for at least 1 h. Afterward, 32 mL of TEOS was added dropwise at 20 mL h^{-1} with a stirring speed of 1000 rpm and this speed was maintained 1 h after the addition of TEOS. The stirring was stopped for 15 min, allowing TEOS to phase separate, and stirring was continued for at least 24 h at 250 rpm. When all TEOS was consumed, the silica particles were heated to $90 \text{ }^\circ\text{C}$ at 750 rpm for 24 h. For coating with APTES, the synthesized particles were cooled down in an ice bath to

approximately 4–6 °C. The pH was lowered to approximately 5 by dropping 100 mM acetic acid diluted in ethanol absolute at 40 mL h⁻¹ with high stirring so the final solution had a concentration of 10 v/v% of ethanol and was continued for 30 min post-addition. The pre-hydrolyzed APTES solution was allowed to thermally equilibrate to room temperature while the particle dispersion was reheated to 40 °C with reflux. Twenty mL of pre-hydrolyzed APTES was added at 10 mL h⁻¹ with stirring at 1000 rpm. Afterward, the temperature was increased to 90 °C for 24 h with stirring at 750 rpm. The final pH increased to 8–9 and another 100 mM acetic acid dissolved in 5 mL ethanol absolute was added dropwise manually until the final pH was 5. Particles were stored at 4 °C or cooled down before purification.

6.2.3 Nanoparticle purification

The silica dispersion was first filtered (PES 0.1 μm), and APTES-coated silica particles were centrifuged at 5000 rpm for 30 min to remove large agglomerates. Two dialysis bags containing 30 mL of the particle dispersion were placed in a 2 L beaker containing 1:0.5:0.007 of water:ethanol absolute:acetic acid for at least 4 h and repeated twice. The particles were 10 times dialyzed against water pH 5.8 with a minimum time interval of 4 h. Upon completion of the dialysis, water was refreshed one final time and stirred for 30 min before collecting the particles in a clean Duran beaker with a PTFE-coated cap. The pH was adjusted to 5.8 if necessary, the solid content was determined in triplicate to be 2.32 ± 0.02 for silica and 1.76 ± 0.04 w/w% for APTES-coated silica and stored at 4 °C. Both dialyzed dispersions remained stable for at least 3 months.

6.2.4 Nanoparticle characterization

Transmission electron microscopy (TEM-EM 900, Carl Zeiss, Germany) was employed to investigate the morphology of the particles by placing a 3 μL water drop of 0.001 w/w% particle dispersion (pH ~ 5.8) onto a copper grid with a carbon Formvar film (Plano GmbH, Wetzlar, Germany). Any additional charge buildup from the electrons by the film is efficiently conducted to the metallic copper network and by carbon, avoiding image drift and allowing high resolution of small nanoparticles.⁷¹² Size and zeta potential were obtained by measuring 0.1 w/w% particle dispersion in 10 mM KCl for conductivity at different pH using the ZetaSizer NanoSP (Malvern, United Kingdom) at 25 °C without membrane filtering and sub-measurement time per iteration for size kept ≥ 10 s, as discussed in section 5.3.3. To remove all organic impurities, 20 g of KCl was dissolved in 200 mL water and heated to 550 °C for 24 h. The pH of the particles was adjusted by adding 0.1 or 1 M KOH and HCl and stirring for 15 min, followed by another pH reading right before measuring the zeta potential. The expression proposed by Ohshima et al.⁶¹⁷ (Eq. 4.7) was used to calculate the Henry function $f(\kappa a)$ by implementing the hydrodynamic radius and electrolyte concentration. The calculated $f(\kappa a)$ values were 1.11 and 1.13 for silica and APTES-coated silica, respectively.

6.2.5 Ninhydrin assay

Primary amine quantification of APTES-coated silica particles was adopted from Hristov et al.⁵⁹¹ A calibration curve was obtained by dissolving 1 mM to 3 mM APTES in 1:0.027 ethanol absolute:acetic acid (Appendix A.4.1, Fig. A.4.1). The purified particles were dialyzed twice against the ethanol absolute:acetic acid mixture and diluted to 0.05 w/w%. Ninhydrin (20 mM) stock solution was prepared fresh in the dark. To a Safe Lock® Eppendorf tube, 0.125 mL ninhydrin was mixed with 0.375 mL of the calibration solution or particle dispersion. A control sample without ninhydrin and particles was also prepared and used as baseline subtraction for the reacted samples. The tubes were incubated in the dark for 45 min at 60 °C, whereafter 200 μL of the suspensions were

pipetted into a 96-well plate. A maximum absorption occurred at a wavelength of 577 nm, and samples were measured in triplicate. For calculating the amine density per nm², assumptions were made that all particles are perfect spheres of the same size (18.8 nm), and their density is equal to 1.9 g cm⁻³.⁶⁹⁸

6.2.6 Preparation of lipids in decane

A stock solution of 4 mM ODA was prepared 4 days in advance of the synchrotron experiments at room temperature to ensure a homogeneous dissolution of the lipid and was also used afterward for the pendant drop experiments.

6.2.7 Pendant drop tensiometry and dilational interfacial rheology

Tensiometry and dilational rheology of the oil-water interface was studied at 20 °C (± 1 °C) using the OCA25 from Dataphysics (Stuttgart, Germany) with a sensitivity of 0.01 mN m⁻¹.⁶⁹⁹ A 20-25 μ L aqueous drop (pH \sim 5.8) was formed from a dosing needle (1.07 mm diameter) in a cuvette filled with 900 μ L pure decane to check the purity if the tension remained constant with a systematic error of 0.2 mN m⁻¹. This is equally true for the aqueous phase regarding the purity of particle dispersions (Appendix A.4.5, Fig. A.4.5A and B). Before adding lipids, the tension was monitored for 30 min after which 900 μ L of the required lipid concentration was slowly added to avoid significant droplet disturbance and measured for 2 h. Dilational viscoelastic properties of the drops were obtained by sinusoidal volume oscillations (ODG20, Dataphysics) at varying frequencies between 0.005 and 0.2 Hz at a fixed area deformation between 9-10 % after the tensiometry test. Each system was measured at least 3 times, and the experimental error was reported (Appendix A.4.5, Fig. A.4.5C).

6.2.8 X-ray reflectivity

The synchrotron reflectivity measurements at the air/water and decane/water interface were performed at the Liquid Interface Scattering Apparatus (LISA) diffractometer at the P08 beamline PETRA III for its delivery of X-rays with high brilliance (DESY, Hamburg, Germany). The 25 keV collimated X-ray beam with a beam size of 0.05 x 0.4 mm² (vertical x horizontal direction) allows penetration through the decane super phase and probes the gas/liquid and buried oil/water interface while varying the incident angles (α_i) using the LISA double crystal beam tilter, without moving the sample, to obtain a reflectivity profile as a function of the momentum transfer (Eq. 4.47) with wavelength $\lambda_{XR} = 0.496$ Å.^{713,714} More information about this setup is provided in Appendix A.4.2.

The sample was prepared in a custom-made cell consisting of an aluminum mounting cell hosting a Delrin cup and mounted on a goniometer for perfect horizontal positioning of the liquid interface (Appendix A.4.2, Fig. A.4.2A-B-C). The cell was first filled with 28 ml of water or 0.1 w/w% particle dispersion (pH \sim 5.8) to pin the meniscus and create a flat interface, followed by a reflectivity measurement (Fig. 4.20). For the decane/water measurements, decane was slowly added from the top by a syringe to a thickness of about 1 cm to avoid decane/air scattering.²⁰⁹ After a clean decane-water interface was established, a calculated amount of decane was removed and replaced with an equal amount of 4 mM ODA stock solution to keep the oil volume constant at 20 mL. The ODA concentration was varied from 0.001 mM to 1 mM for each set of measurements. All reflectivity measurements were initiated after 30 min equilibration time once the liquid surface/interface was formed or lipid was added. Several reflectivity curves were recorded for each concentration, which showed only slight variations and no trend.

Afterward, the background-corrected reflectivity data collected with a Lambda X-ray detector was analyzed using REFLEX software based on Parratt's recursive algorithm with known material electron density (ED) to obtain values for the layer thickness and interfacial roughness (Appendix A.4.4,

Fig. A.4.3.⁶⁹⁶ The ED for silica was kept within physical boundaries determined from a mass density of 1.9 g cm^{-3} ,⁶⁹⁸ although higher densities are reported for macroscopic silica (Appendix A.4.4).^{38,591} Most of the parameters for the particle were highly constrained while allowing the material ED to vary (Appendix A.4.6, Table A.4.1 and Table A.4.2). For clarity, the measured data and their fits were all normalized by the Fresnel reflectivity (R_F) of the corresponding interfaces. The model proposed by Isa et al.²⁰⁹ was used to retrieve information on the particle adsorption layer from the ED plot, which is explained in section 4.1.3.4.

6.3 Scientific outcome

6.3.1 Size and zeta potential characterization

To obtain well-defined and highly pure particles, bare silica NPs were prepared via the Stöber-Watanabe process with the silane tetraethyl orthosilicate (TEOS)⁵⁴⁰ and alternatively coated with the silane (3-aminopropyl)triethoxysilane (APTES) to decorate the particle surface with amino groups, which is similar to the polar head group of ODA. The pK_a of ODA is 10.65, meaning that under the investigated environmental conditions, the protonated form dominates at the interface.⁴³⁵ Fig. 6.1A shows the number distribution of the silica and APTES-coated silica particles with a hydrodynamic diameter of 22.35 ± 6.83 nm and 25.76 ± 5.42 nm, respectively. Both solutions exhibit low polydispersity with a PDI of 0.154 for silica and 0.228 for APTES-coated silica. Their isoelectric points are approximately 2.8 for silica and 7.6 for APTES-coated silica, confirming that both NPs are highly charged at the investigated pH of 5.8 and provide sufficient electrostatic stabilization to prevent particle-particle interactions in the bulk (Fig. 6.1B). Approximately one amine group per nm^2 is present on the particle surface determined with the ninhydrin assay (Appendix A.4.1, Fig. A.4.1).⁵⁹¹ Transmission electron microscopy (TEM) in Fig. 6.1 shows that both silica (C) and APTES-coated silica (D) are nearly spherical with an average diameter of 17.8 ± 2.7 nm and 18.9 ± 2.6 nm, respectively.

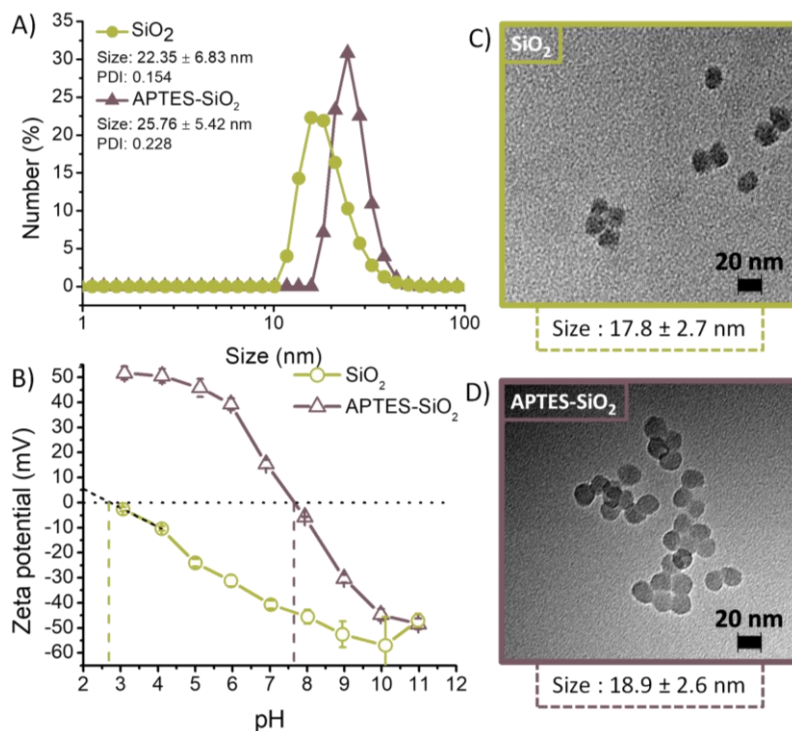


Fig. 6.1 A) The hydrodynamic diameter and polydispersity of silica (circles) and APTES-coated silica (triangles) nanoparticles. B) The zeta potential of 0.1 w/w% silica and APTES-coated silica as a function of pH in 10 mM KCl. The dashed line indicates isoelectric points (IEPs) for clarity. The IEP of silica was extrapolated in OriginPro8. Transmission electron microscopy image of silica (C) and APTES-coated silica (D) showing size and standard deviations.

6.3.2 X-ray reflectivity of particles at liquid interfaces

Adsorption of highly hydrophilic, small NPs to a clean surface or interface is considered unfavorable and unstable due to their low adsorption energies. Particularly XRR provides a highly detailed picture of the liquid interface and adsorbed materials. The upper row of Fig. 6.2 shows the reflectance profiles normalized by the theoretical Fresnel reflectivity R_F of 0.1 w/w% silica (left) and APTES-coated silica particles (right) at the air-water and decane-water interface in the absence of ODA with their corresponding fits obtained with the standalone REFLEX software that simulates the XRR measurements based on Parratt's recursive formalism using a 3-slab model (Fig. A.4.3).⁶⁹⁶ The model parameters can be found in Table A.4.1 (Appendix A.4.6) and further details on the chosen parameters are elaborated in Appendix A.4.4. The bottom row of Fig. 6.2 shows the corresponding EDs, which are fitted using the physical model detailed in the Methods section. In the presence of silica NPs, both air-water and oil-water reflectivity curves are decaying monotonically as a function of Q_z and resemble the Fresnel reflectivity and interfacial roughness of pure water,⁶⁹⁴ indicating the absence of interfacial NP layering at 0.1 w/w%. This situation is clearly different for the APTES-coated silica particles, which are similar in size to the silica NPs but exhibit a positive zeta potential.

Kiessig fringes appear at both air-water and oil-water interfaces from which the thickness (d_{layer}) can be estimated as $d_{layer} = 2\pi/\Delta Q_z$ and is 18.74 ± 1.45 nm, consistent with the particle size determined from TEM (Fig. 6.1D). Subsequent curve fitting of the reflectivity using the 3-slab model confirms the monolayer formation (Fig. 6.2 bottom). The normalized ED profiles for these adsorbing positively charged NPs show that most of their volume remains dispersed in the water phase owing to their hydrophilic character. Besides minimization of the free energy of the interface, the negative charge of a clean surface electrostatically attracts the positively charged NPs to the surface as observed by Larson-Smith et al.,¹⁸³ while it prevents adsorption of the negatively charged NPs.^{38,183} The origin of this negative charge can either be due to selective adsorption and interfacial ordering of hydroxyl ions at the boundary layer^{173,174,715} or from charge transfer between different interfacial water molecules.¹⁸¹

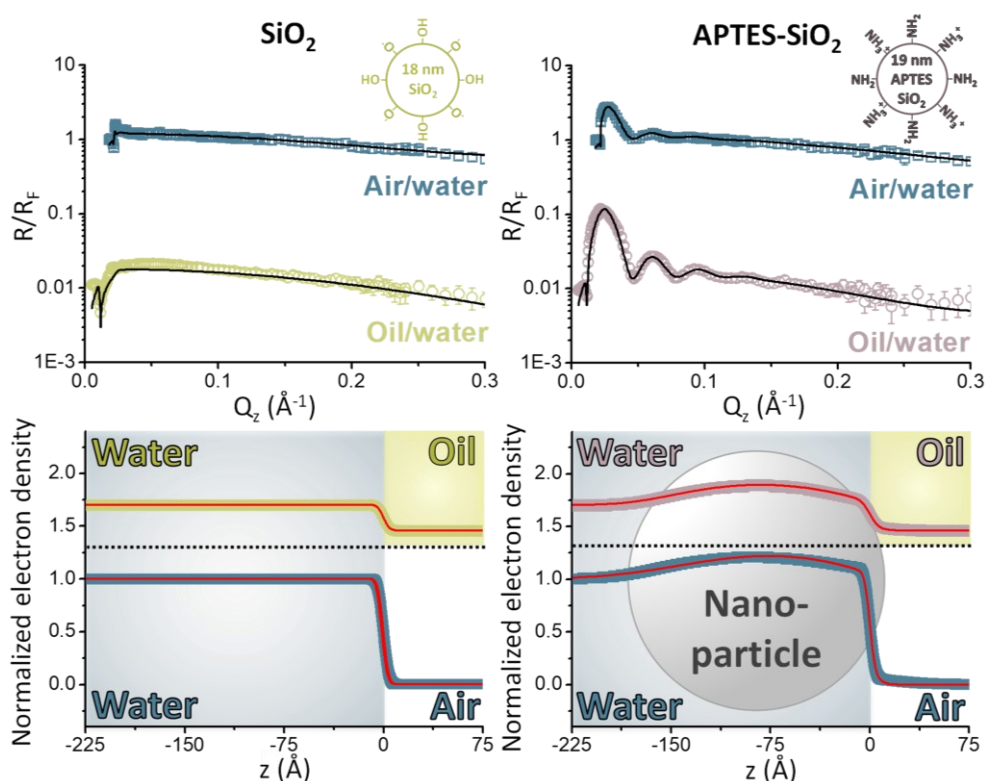


Fig. 6.2 The upper row shows the normalized reflectivity R/R_F data along with the fitted line (black) for 0.1 w/w% silica (left) and APTES-coated silica (right) at the air-water (squares) and decane-water (circles) interface (aqueous pH 5.8). Data is shifted by a factor of 100 for clarity. The bottom row shows the stacked normalized ED curves with the model fits (red) with a corresponding schematic in the background.

6.3.3 X-ray reflectivity of particles and lipids at the oil/water interface

If the charge on the NP surface influences the adsorption based on electrostatics, one can expect that the addition of an ionic surfactant will evoke either synergistic or competitive adsorption due to attractive and repulsive interfacial interactions, respectively. Fig. 6.3 shows the R/R_F data and normalized EDs for both particle types in the presence of diverse quantities of ODA dissolved in the oil phase, and the fit parameters for the reflectivity are shown in Table A.4.2 (Appendix A.4.6). Transitioning of the oil-soluble surfactant ODA across the interface is insignificant at an aqueous subphase pH of 5.8, assuring particle-surfactant interactions occur solely at the phase boundary layer.⁴³⁵ The ED of ODA lies between that of water and decane, and the low scattering contrast makes it difficult to confirm its exact location and structuring, especially in the presence of the stronger scattering NPs. Noticeable oscillations appear for the negatively charged silica NPs when a small amount of 0.01 mM ODA is added to the oil phase, assigned to electrostatic physisorption of the protonated amine group of ODA with the silanol groups on the particle surface similar to (cetyltrimethylammonium bromide) CTAB-silica complexes.³⁸ Furthermore, the surface potential of the interface might change to a positive value upon adsorption of ODA, also facilitating silica adsorption. A maximum in the amplitude of the ED curves is already achieved at 0.1 mM ODA, and a further increase in ODA concentration produces indistinguishable ED profiles. For the APTES-coated NPs, having roughly 1 amine group per nm^2 on their surface (Appendix A.4.1, Fig. A.4.1), a distinct pattern can be observed from the normalized reflectivity and EDs. After adding the lowest concentration (0.01 mM ODA), the oscillations are dampened compared to APTES-coated silica at the pure oil-water interface. A smaller number of NPs at the interface causes this decrease in intensity. This confirms that particles and surfactants carrying a similar charge are competing at the interface for adsorption, and the surfactant molecules can overpower the particles based on the repulsion between like charges, in line with the results of Chapter 5.⁷¹¹

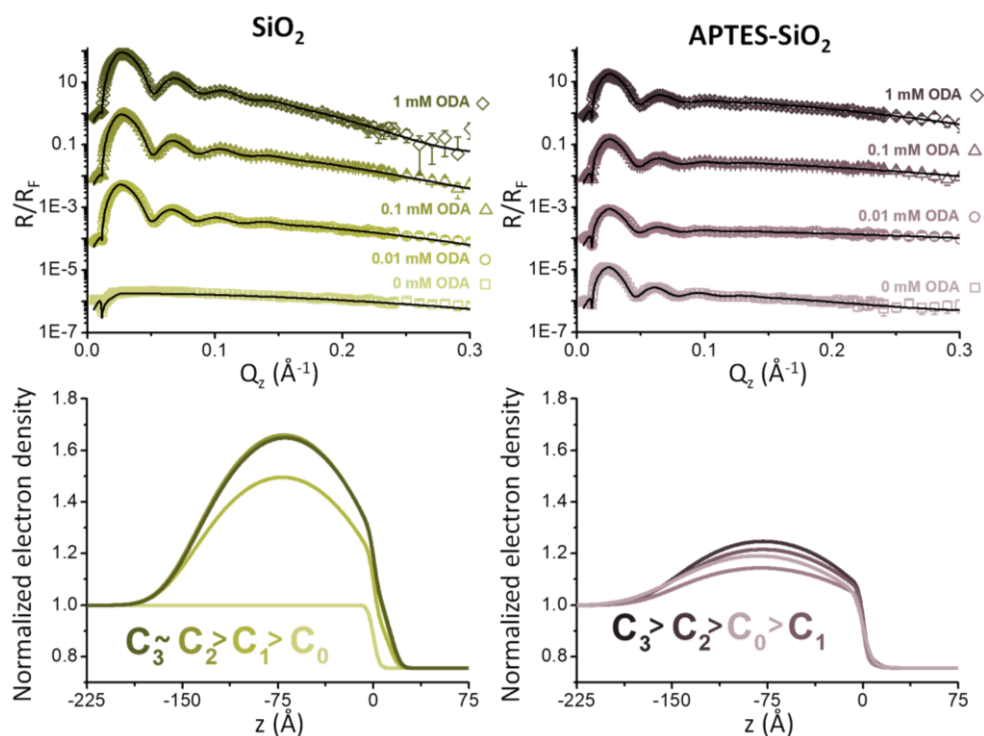


Fig. 6.3 The upper row shows the R/R_F profiles of 0.1 w/w% silica (left) and APTES-coated silica (right) at pH 5.8 for different concentrations of ODA dissolved in the decane phase. Data is shifted by a factor of 100 for clarity. The normalized ED profiles are shown below, where the peak amplitude is indicated in descending order. C_0 means no surfactant is added while the subscripts 1 to 3 correspond to increasing lipid addition from 0.01 mM to 1 mM ODA.

6.3.4 Physical parameters of particle adsorption

Subsequently, the ED profiles are fitted to the physical model, and the simulated parameters for particle diameter, the average separation between neighboring particles, immersion depth, and CA (which is directly calculated from the immersion depth) are shown in Fig. 6.4. The particle size from these fits estimated a diameter of 17.85 ± 0.80 nm for silica and 18.93 ± 1.14 nm for APTES-coated silica, ruling out particle multilayer formation at the interface for all ODA concentrations. The particle coverage was derived from the maximum amplitude of the ED as the ratio of the sample to the maximum silica NP density multiplied by the hexagonal close-packing (HCP) factor ($\varphi = (\rho_{\text{sample}}/\rho_{\text{silica}})90.69$). Fig. 6.4A shows that the spreading distance for 0.1 mM and 1 mM ODA lies around zero. Accordingly, a coverage close to 100 % concerning HCP corresponds to a densely packed particle monolayer. At 0.01 mM ODA, 73.98% of the interface is already covered with silica NPs, and the monolayer is saturated from 0.1 mM ODA onwards. The depth of immersion of the silica particles into the oil phase shows no significant difference between all ODA concentrations, with a CA between 34.9° to 37.1° . The results also suggest that, in the analyzed range, the surfactant concentration has a minor effect on the CA of the NPs irrespective of their coverage.

With the positively charged, aminated NPs and ODA, an opposite behavior can be expected compared to silica, especially since the NPs are spontaneously adsorbing at the pristine oil-water interface. Fig. 6.4A shows an increase in the average particle-to-particle distance with the addition of 0.01 mM ODA. Gradually, the particles come closer when more lipids are added but remain separated from each other by ~ 11 nm at the highest concentration with only 38.75 % coverage in relation to HCP (Fig. 6.4B) and remain more deeply immersed into the water phase compared to the partially-hydrophobized silica particles (Fig. 6.4C). The initial CA of the APTES-coated particles in the absence of lipids ($\sim 22.7^\circ$) acts as a reference to evaluate whether interactions occur between the particles and the equally charged surfactants. The static oil-water CA measurements in Chapter 5 of APTES-coated silica thin films showed no change in CA up to 1 mM ODA despite having a higher initial CA of $40.05^\circ (\pm 1.43^\circ)$ that can be ascribed to the different synthesis process used. Fig. 6.4D shows a gradual increase to $\sim 28.7^\circ$, and the difference of roughly 10° in the wetting angle between the differently charged NPs shows that synergistic adsorption dominates with oppositely charged species. In contrast, similarly charged species compete for interfacial coverage suggesting fewer particle-surfactant interactions occur.

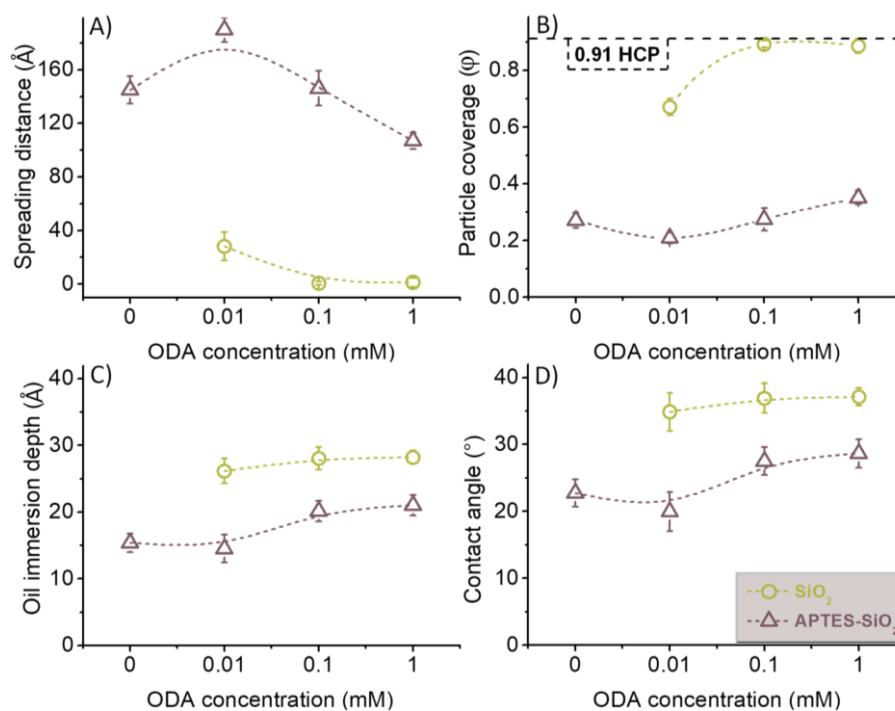


Fig. 6.4 Results of the physical model for 0.1 w/w% silica (circles) and APTES-coated silica (triangles) with or without ODA. Dashed lines are a guide for the eye. From top-left to bottom-right shows (A) the spreading distance between interfacially adsorbed particles, (B) the packing density of adsorbed particles with the straight dashed line corresponding to hexagonal close-packing (HCP), (C) their protrusion distance into the oil phase, and (D) their three-phase contact angle, including standard deviations.

6.3.5 Tensiometry and dilation rheology of particles/lipids at the oil/water interface

Adsorption studies using axisymmetric droplet shape analysis of a quiescent or perturbed oil-water interface provide complementary information to the specular reflectivity data by analyzing the time-resolved IFT in conjunction with frequency-dependent dilational rheology. The IFT of the pristine oil-water interface in the absence of NPs and for both negatively and positively charged NPs is constant, indicating the absence of surface-active impurities (Appendix A.4.5, Fig. A.4.5A). Despite the presence of APTES-coated silica NPs, the elastic modulus of these interfaces is close to zero, as can be expected for a clean interface and surface-inactive molecules (Appendix A.4.5, Fig. A.4.5B). Fig. 6.5 shows the results of different amounts of ODA in the surrounding oil phase on an aqueous pendant drop with or without NPs. For the lowest concentration of 0.01 mM ODA, the IFT decrease is small, with barely any noticeable difference between the three distinct interfaces and minor elastic moduli differences. At 0.1 mM ODA in the absence of NPs, a plateau is not reached for the studied time scale due to relaxation effects at the interface.⁴³⁸ This slower decrease at longer times also occurs for the silica particles associated with a stronger decrease in IFT and equal elasticity values when NPs are absent, showing that the lipid dominates the dilational rheological properties for a silica-covered interface. Contrarily, the adsorption curve with the amine-coated NPs equilibrates within 16 minutes after the onset of lipid addition, and the elastic moduli with these NPs are significantly lower, showing fewer ODA molecules are present at the interface. More complex behavior is observed at 1 mM ODA as both NP dispersions have IFTs lower than pure water with almost identical elastic moduli for the three cases.

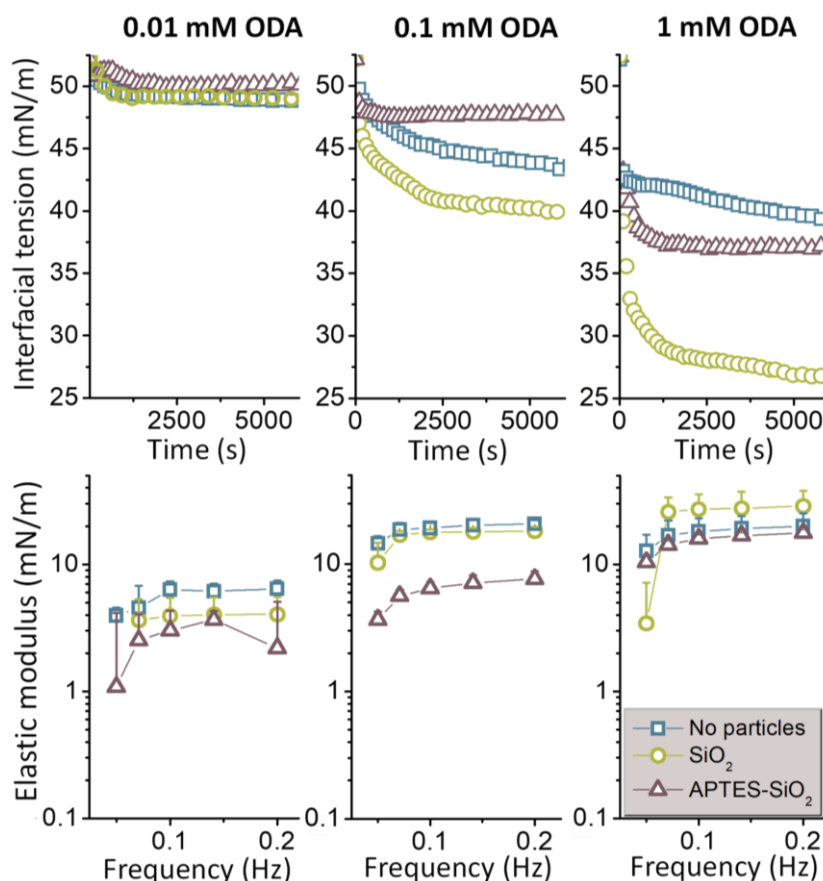


Fig. 6.5 Data for various ODA concentrations measured by adsorption studies using axisymmetric droplet shape analysis. The upper row shows the water-decane interfacial tension without particles (squares) and with 0.1 w/w% silica (circles) or APTES-coated silica (triangles) nanoparticles at pH 5.8 and the lower row the elastic modulus at varying frequencies.

6.4 Discussion

6.4.1 Adsorption of negatively charged silica nanoparticles in the presence of a cationic amino-lipid

Highly charged, strongly hydrophilic particles, like silica, can only adsorb at the interface when the energy barrier against adsorption is sufficiently lowered and can be explained in terms of DLVO interactions, mainly due to van der Waals attraction and screening of electrostatic repulsion.³³⁸ The matching charge between the silica particles and the buried pristine interface is unfavorable as the reflectivity follows the Fresnel line (Fig. 6.2), indicating an adsorbate-free interface, although (brief) adsorption of silica NPs has been previously documented at higher particle concentrations.^{39,301,716} Large amounts of silica NPs at the interface might increase the interfacial roughness due to marginal ordering³⁸ or even cause pronounced dips in the XRR profile due to layer formation at the surface.³⁰¹ When ODA is added, the silica NPs in the subsurface region feel the strong attraction of the protonated surfactant head group and form an electrostatic bond between a silanol and the

amino group that causes partial charge neutralization along with increased lipophilicity, which forces the particles to pack more closely as observed in Fig. 6.5.⁴³⁸ The top view of Fig. 6.6A shows the hexagonal arrangement of the NPs with their contact points below the interface upon dense packing, which is only possible when sufficient double layer screening occurred. A HCP monolayer is already formed at 0.1 mM as derived from the presence of oscillations and model fitting of the ED. Additionally, the stronger decrease in IFT at longer times, whose shape resembles the adsorption curve in absence of NPs, gives strong evidence that these surfactant-particle complexes exert a synergistic effect on the IFT due to the formation of a close-packed interfacial film. However, a further increase in surfactant concentration has no effect on the particle coverage or CA at 0.1 w/w% NPs while the IFT continues to show a significant decrease of more than 10 mN m^{-1} . Information about the lateral particle distribution using grazing-incidence small-angle scattering (GISAXS) experiments with the same synchrotron setup could in principle confirm if a HCP layer is formed, but the weak off-specular signal was too strongly attenuated by the oil-phase. The formation of an adlayer is confirmed by XRR and the constant particle coverage for 0.1 mM and 1 mM ODA strongly suggests that these spherical NPs form a densely packed monolayer. This particle monolayer with a CA of roughly 37° will occupy about $1/3$ of the interfacial area, leaving $2/3$ of the interface free for surfactants to adsorb (Appendix A.4.7). An increase in the effective concentration, where the ionic lipid molecules pack more densely at the interface, explains the observed decrease in IFT at 1 mM ODA without affecting the particle coverage.⁷¹⁷

6.4.2 Adsorption of positively charged silica nanoparticles in the presence of a cationic amino-lipid

When the NPs have a positive charge, they self-assemble at the pristine interface with incomplete coverage (Fig. 6.2). It has been observed that charged colloids trapped at an interface can form highly ordered quasi-crystalline structures through balancing of long- and short-range electrostatic repulsions mediated by the non-polar medium and asymmetric charge dissociation, respectively, against the attractive long-range interactions due to deformation of the interface by the electrostatic force induced by its neighboring particles. As the NPs remain mainly dispersed in the aqueous phase, the dipolar interactions mediated through the oil become less significant compared to the electric double layer repulsion.^[21,22,48,63,190] Despite their adsorption to the pristine oil-water interface, no significant change in IFT is observed owing to their wettability (at HCP coverage without surfactants, the total change in IFT caused by the particles would only be $1.54 \cdot 10^{-4} \text{ mN m}^{-1}$ based on Eq. 2.18; ΔE_P) and additional methods are

required to judge adsorption of hydrophilic NPs (Appendix A.4.5, Fig. A.4.5C). At 0.01 mM ODA, the IFT and elastic moduli are similar to those of silica NPs. However, competition for interfacial coverage is evident from reflectivity data as the lipids desorb some of the initially adsorbed NPs, which can be explained by their small desorption energy of $\sim 21.18 kT$ (Fig. 6.4 and Fig. 6.5). Also, cooperativity between the alkane and low quantities of surfactant molecules that form a mixed adsorption layer might enhance particle expulsion in this particular case.⁷¹⁸ At 0.1 mM ODA, sufficient surfactant is present to monitor IFT changes after particle addition with pendant drop tensiometry. The higher IFT and lower elastic moduli in the presence of APTES-coated NPs compared to the absence of NPs emphasizes that a significant portion of surfactant is prevented from adsorbing. The slight increase in coverage and CA shows that direct particle-surfactant interactions are strongly inhibited as a result of electrostatic repulsion. This trend in coverage and CA continues with 1 mM ODA as well but shows a more substantial IFT decrease and similar elasticity values as droplets without NPs. This also fits with an increase in effective surfactant concentration as observed for very different IFT values of a densely packed silica monolayer.⁷¹⁷ Despite requiring sufficiently high lipid concentrations to monitor changes in IFT, the relatively constant particle coverage and CA support that the same competitive mechanism also occurs at lower ODA concentrations.

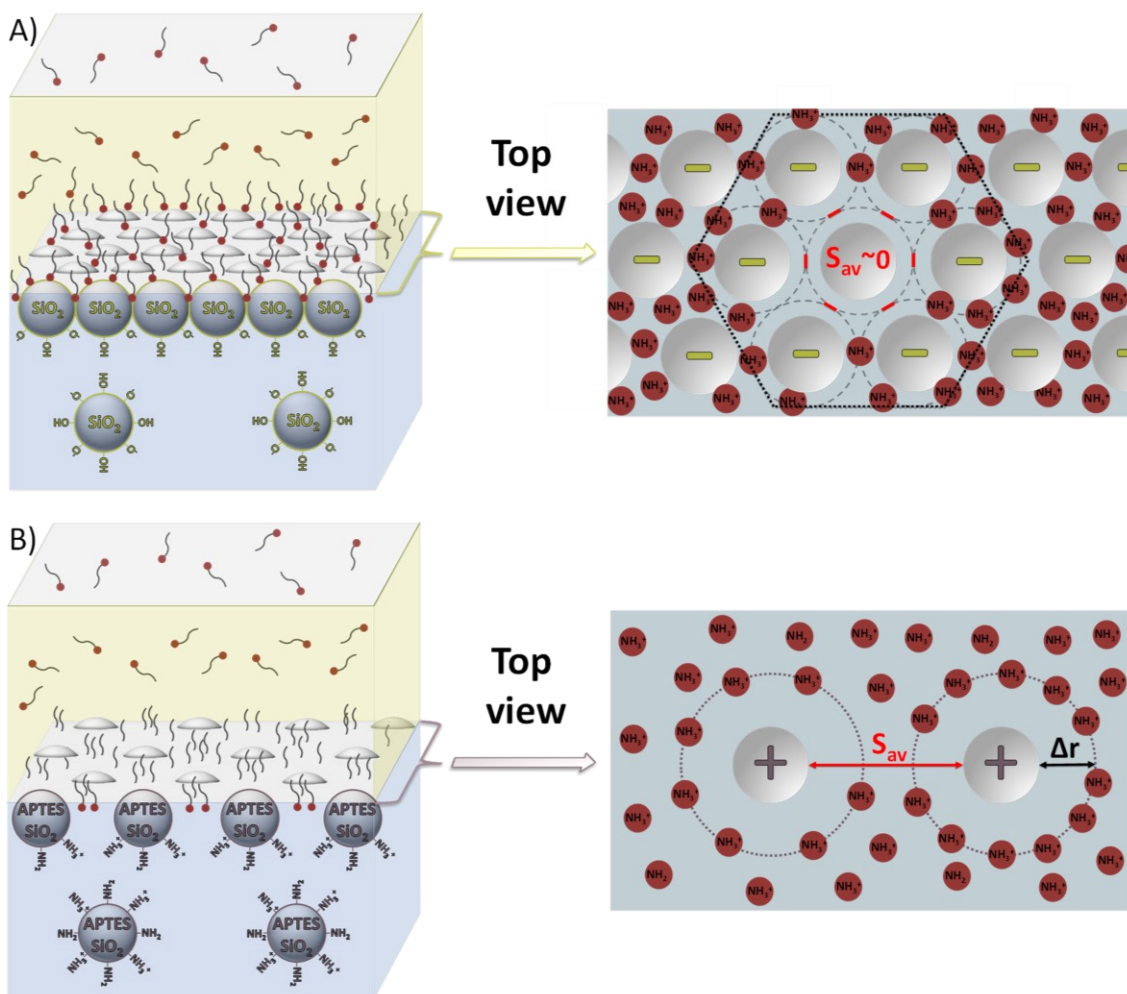


Fig. 6.6 A visual representation of the negatively (A) and positively (B) charged silica nanoparticles adsorbed at the decane-water interface and their interaction with the oil-soluble ODA surfactant molecules at intermediate to high concentrations. In A), the spreading distance s_{av} between particles is highlighted (red lines) and adsorbed ODA molecules have been removed for clarity. A) Negatively charged silica nanoparticles reduce the interfacial energy due to an increase in their CA by interaction with the positively charged amino group of ODA. Local charge neutralization and increased hydrophobicity of the particles favor hexagonal arrangement (black dotted hexagon) at the interface with a center-to-center distance of one particle diameter (grey striped circles). B) In the case of positively charged APTES-coated silica nanoparticles, an electrostatic exclusion zone (Δr , black line) is formed, which rejects the ODA molecules. Their packing is only slightly influenced by an increase in ODA concentration, while the exclusion zone becomes smaller as more ODA molecules adsorb.

6.4.3 Interfacial interaction between nanoparticles and cationic amino-lipid

It is clear that the charge of the surfactant head group and the NPs either promotes or suppresses particle adsorption. Table 6.1 summarizes the CA and particle coverage obtained from the reflectivity data discussed above, as well as the results from the simple analytical model outlined in Chapter 5, Eq. 5.2. The calculations for the coverage based on Eq. 5.2 were determined from the average IFT measurements (Appendix A.4.5, Fig. A.4.5C) and the CA values derived from the XRR data (Fig. 6.4). Even though the model assumes NPs and surfactants are not strongly interacting with each other, as is only the case for APTES-coated

silica and ODA, the analysis for silica is also shown for completeness. At first glance, in both cases, the coverages obtained from Eq. 5.2 using the average CA from XRR disagrees with the scattering data. Since coverage and CA are known from XRR, the coverage was recalculated with varying particle sizes while keeping the other variables constant until both the coverage from XRR and the model matched. This is reported as the corrected diameter in Table 6.1. With increasing ODA concentrations, the expected diameters of the NPs show opposite behavior that increases in the case of synergistic adsorption and decreases for competitive adsorption. As the model cannot account for particle-surfactant interactions in the synergistic case, such as with silica-ODA, no consensus can be formed from these results. This is not the case for the system APTES-coated silica and ODA. Here, due to the repulsive nature between the APTES-coated silica NPs and ODA, the enhanced, corrected diameter might correspond to an exclusion zone with radius Δr in which the lipids are rejected, similar to the recently reported findings by Papavassilou et al.⁷¹⁷ The calculated distances for Δr are generally smaller than the spreading distance obtained from XRR and therefore fit well in between the particles (Fig. 6.6B). The decrease in Δr with increasing surfactant concentration suggests that this exclusion zone is sensitive to the ionic strength at the interface, to which both NPs and surfactants contribute. Inside the exclusion zone, the net repulsive force from the protonated amine groups felt between the NPs and surfactants should be enhanced.^{22,30,94,458}

In comparison to the findings in Chapter 5 using 80 nm NPs, the contribution of such an exclusion zone might be more pronounced for the interfacial system with the smaller NPs. Smaller particles were chosen because of the angular resolution of the XRR diffractometer, which does not allow acceptable resolution of Kiessig fringes of particles $d > 50$ nm. Eq. 5.2, which is simply based on the additivity of all surface energy contributions of the interfacial system, might therefore be only valid if the particle radius is much larger than the radius of the exclusion zone and/or in the presence of moderate concentrations of surfactant at which the exclusion zone is small, and the CA of the particles remains unaffected.

Table 6.1 Experimental values for different concentrations of ODA with 0.1 w/w% silica nanoparticles and APTES-coated silica nanoparticles. Contact angle and particle coverage with their standard deviation were obtained from the specular reflectance data (XRR) analysis and calculated from the analytical model based on Eq. 5.2 using the CA obtained from XRR. In the calculations, the diameter was adjusted until the coverage obtained with XRR was equal to the calculated coverage. Δr represents the difference between the measured and the corrected diameter and might relate to the radius of an electrostatic exclusion zone. The standard error for the parameters calculated with Eq. 5.2 were obtained from the experimental error of the interfacial tension measurements.

Synergistic adsorption SiO ₂ nanoparticles					Competitive adsorption APTES-coated SiO ₂ nanoparticles					
Conc. (mM)	Contact angle XRR (°)	Coverage XRR (Θ)	Calculated coverage (Θ)	Corrected diameter (nm)	Conc. (mM)	Contact angle XRR (°)	Coverage XRR (Θ)	Calculated coverage (Θ)	Corrected diameter (nm)	Δr (nm)
0.01	34.87± 2.86	0.671 ± 0.030	0.328 ± 0.341	15.27 ± 6.18	0.01	19.94± 2.90	0.209 ± 0.019	0.710 ± 0.132	34.67 ± 3.25	7.89 ± 1.63
0.1	36.91± 2.25	0.893 ± 0.012	1.204 ± 0.469	28.07 ± 12.16	0.1	27.49± 2.09	0.275 ± 0.040	0.522 ± 0.266	27.2 ± 5.50	4.15 ± 2.75
1	37.09± 1.31	0.887 ± 0.026	2.388 ± 0.533	41.00 ± 20.37	1	28.65± 2.13	0.352 ± 0.024	0.283 ± 0.098	16.73 ± 3.00	-1.09 ± 1.50

6.5 Conclusions

The adsorption behavior of native negatively charged silica and positively charged APTES-coated silica nanoparticles (NPs) in the presence of an oil-soluble cationic lipid (octadecyl amine, ODA) at the decane-water interface was characterized using specular X-ray reflectometry, tensiometry, and dilational rheology. Fitting of the reflectivity curves and subsequent calculation of the electron densities (EDs) using a physically realistic model was compared to a quantitative analysis of the interfacial tension (IFT) based on a continuum approach substantiated with the contact angles (CAs) derived from the scattering experiments to estimate particle coverage. High-resolution *in situ* X-ray reflectivity data at the pristine air-water surface and oil-water interface showed that silica NPs at 0.1 w/w% do not significantly adsorb at the interface contrary to the APTES-coated silica NPs, which cannot be inferred from oil-water IFT measurements. Bare silica NPs do adsorb at the oil-water interface in the presence of ODA by sufficient surface charge neutralization that forces the NPs to the interface into a hexagonally close-packed (HCP) monolayer with contact angles around 37° , which is consistent with synergistic adsorption. On the other hand, the IFT continues to decrease with increasing ODA concentrations, which stems from the high affinity of the lipids to adsorb at the interface and enhances the effective surfactant concentration between adsorbed NPs. When the charges of the NPs match that of the lipids, competition arises, and NPs are being desorbed at low ODA concentrations indicated by a slight increase in coverage ($\sim 21\%$ to 35%) and CA ($\sim 20^\circ$ to 29°). The dilational elasticity for both particle systems is solely dependent on adsorbed ODA. The deviating behavior when competitive adsorption is at play points to the exclusion of lipid molecules in certain interfacial regions. By introducing an electrostatic exclusion zone around interfacially adsorbed particles in which like-charged surfactants are repelled, the analytical approach to describe the interfacial system as the sum of the individual contributions to interfacial energy from Chapter 5 can be validated with the experimental *in situ* data from X-ray reflectivity. These basic insights underlying the adsorption and interfacial interaction of charged colloids and ionic surfactants have important implications for tailoring particle and surfactant contributions in complex colloidal systems in food, agricultural, cosmetic, and pharmaceutical technologies, as well as in contaminated systems, non-ideal particle-stabilized emulsions, and other valuable applications.

6.6 Acknowledgments

The author thanks P. Witte for her expertise with the SEM and T. Mehrrens for TEM. The author acknowledges DESY (Hamburg, Germany), a member of the Helmholtz Association HGF, for the provision of experimental facilities. Parts of this research were carried out at PETRA III, and the author thanks Dr. M. Lippmann for assistance in using the lab facility. The author acknowledges research grant Verbundforschung BMBF/05KS7FK3/05KS10FK2 and Verbundforschung BMBF/05K16FK1 for financing LISA instrument and the Lambda GaAs detector, respectively. M.M. acknowledges support by DFG (Deutsche Forschungsgemeinschaft) project 278836263. P.H. acknowledges support by the DFG Graduate School GRK2462 “Processes in natural and technical Particle-Fluid-Systems (PintPFS)” (Project number 390794421). This work was also supported by the DFG within the Collaborative Research Initiative SFB 986 “Tailor-Made Multi-Scale Materials Systems” (project number 192346071).

7 Assessment of nanoparticle immersion depth at liquid interfaces from chemically equivalent macroscopic surfaces

Chapter 7 has been adapted with permission from *Elsevier* and is published in the *Journal of Colloid and Interface Science*, 2021, DOI: [10.1016/j.jcis.2021.12.113](https://doi.org/10.1016/j.jcis.2021.12.113).

In the previous chapters, particle wetting at the interfacial contact line is conventionally approximated by macroscopic contact angle (mCA) measurements on a planar substrate according to the Young equation (Eq. 2.5; θ_E). Thereby, the substrates' surface composition and roughness are assumed to mirror that of one adsorbed particle, often without substantial proof.⁵⁷ This assumption implies that wetting with a particular liquid provides a well-defined CA at thermodynamic equilibrium on a perfectly smooth surface. However, this is rarely observed experimentally, giving rise to contact angle hysteresis (CAH) from pinning/depinning phenomena.^{651,719} Additionally, line tension effects (τ) become crucial for nanoscopic drops or particles, which can be positive or negative in sign, and deviate from Young's CA (Eq. 2.6; θ_i).^{61,720} If a spherical particle is trapped at a liquid surface, the particle CA can be estimated directly from its water immersion depth relative to the surface (Eq. 2.10; θ_p).⁶⁶ Applicability of Eq. 2.10 requires exact knowledge about the position of adsorbed particles, which becomes experimentally challenging when their size decreases.

Rather than one equilibrium contact angle, reported literature values of particle CAs and immersion depths show a distribution owing to dynamic adsorption and can vary widely, in part stemming from the large mCA distributions measured between surfaces composed of the same material.^{140,142,228,229,298,721} While advanced alternative methods were developed to measure CAs of adsorbed particles either directly (section 3.1.1) or indirectly (section 3.1.2), accessibility to these fairly sophisticated methods is limited. Since interfacial adsorption of certain particle materials depends on pH²⁸ and ionic strength,^{28,30} which are directly related to the electrokinetic (ζ) potential, efforts have been conducted to construct a wettability profile in relation to the ζ potential without determination of the mCA.²⁶⁸ The exact immersion depth of adsorbed particles cannot be inferred from these studies, but if the ζ potential of particle dispersions determines their preferred wetting state, it also affects the measured mCA on a planar substrate that is a chemical and topographical equivalent of the adsorbed particles.⁷²² A direct association of ζ potential and CA values between particles and flat substrates could provide a platform with better reliability for assessing particle wettability.

Therefore, a versatile approach is tested (Fig. 7.1) where X-ray reflectivity (XRR)-derived CAs of highly charged, hydrophilic silica (SiO₂) nanoparticles (NPs) or SiO₂ NPs coated with

the aminosilane APTES (APTES-SiO₂) adsorbed to the air/water surface and decane/water interface are compared to mCAs of sessile droplets on corresponding planar substrates in an identical environment. The synthesis and functionalization procedures are adjusted to ensure that both surfaces have comparable surface chemistry, which is assumed to be the case when the ζ potentials of the dispersed NPs measured with electrophoretic light scattering and the coated planar substrates obtained through streaming current overlap. Furthermore, to understand the possible influence of surface roughness of the macroscopic substrate on the adsorption behavior of the particles, smooth (SFs) and particle-covered films (PFs) are evaluated concurrently.

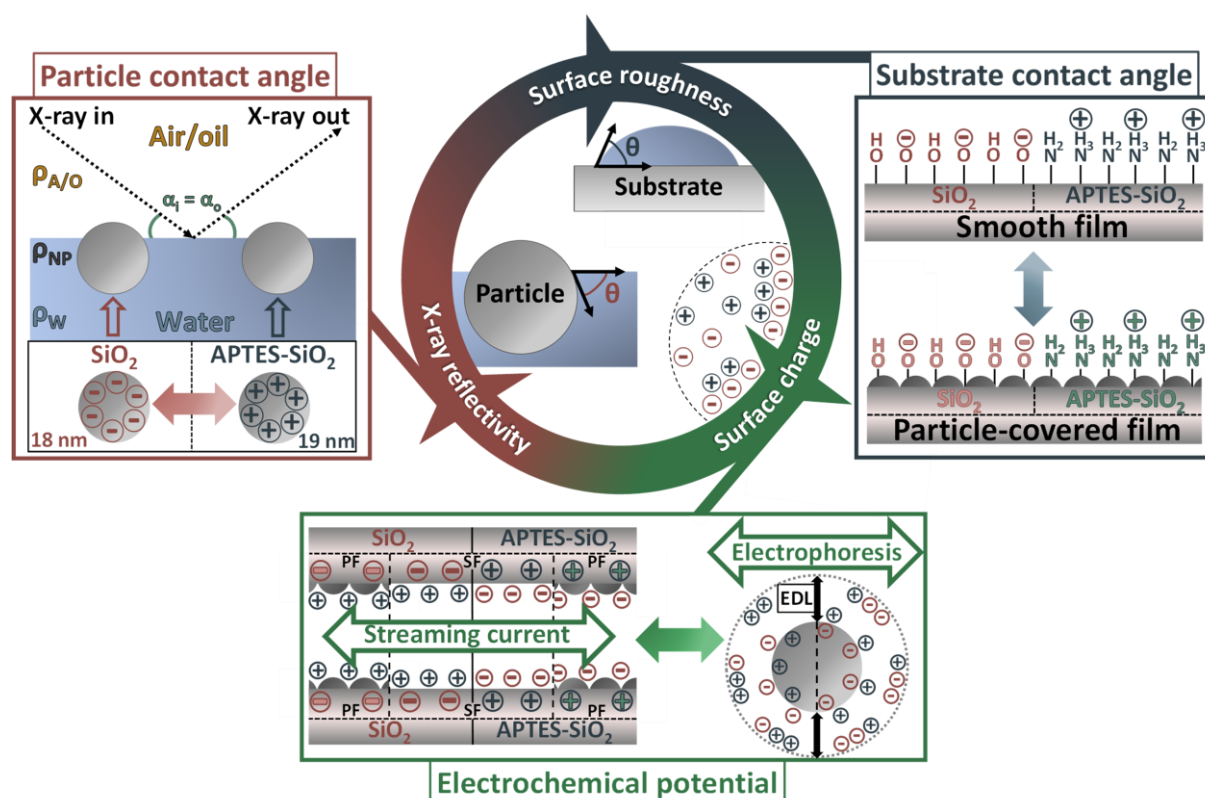


Fig. 7.1 Overview of the methodology to relate the particle contact angle at liquid surfaces to macroscopic contact angles on planar substrates. The particles and planar substrates consist of silica (SiO₂) or are coated with APTES (APTES-SiO₂). The liquid interface in the presence of 18 nm SiO₂ and 19 nm APTES-SiO₂ is analyzed with synchrotron X-ray reflectometry from which the particle contact angle is derived. The zeta potential of particles and planar substrates is measured and compared using electrophoretic light scattering and streaming current, respectively. The effect of surface roughness is investigated by comparing the wettability of a smooth surface (smooth film, SF) with a particle-induced rough surface (particle-covered film, PF).

7.1 Materials

Tetraethyl orthosilicate (TEOS \geq 99.0%, product no. 86578), (3-aminopropyl)triethoxysilane (APTES 99.0%, product no. 440140), L-arginine (\geq 99.0%, product no. 1.01542), potassium chloride powder (KCl 99.0 – 100.5%, product no. P3911) and liquid (MQ 100, 3 M KCl, product no. 60135), sulfuric acid (H₂SO₄ 95.0-98.0%, product no. 258105-M), Wash-N-Dry™ coverslip rack (product no. Z688568), Wheaton Coplin staining jars (product no. S6016), Hellma® optical glass cuvettes (volume 3.5 mL, 45 x 12.5 x 12.5 mm, product no. Z600008) and tweezers (product no. T5540) were purchased from Sigma Aldrich (Darmstadt, Germany). Decane (\geq 99.7%, product no. D901), HCl (0.1 M, product no. 38280; 1 M, product no. 71763), and NaOH (1 M, product no. 71463) solutions were purchased from Honeywell. Ethanol absolute ($>$ 99.8%, product no. 64-17-5), glacial acetic acid (\geq 99.7%, product no. 64-19-7), 37% HCl (product no. 20252.335), methanol ($>$ 99.8%, product no. 20847.295), and amber Duran pressure plus bottles (product no. #215-3267) were obtained from VWR Chemicals (Hannover, Deutschland). Technical grade ethanol (99.0%, product no. 2211.5000) was bought from Chemsolute (Hamburg, Germany). Amorphous silica powders with a size of 80 nm ($>$ 99.9%, SIO2P080-1KG) and 1000 nm ($>$ 99.9%, SIO2P100-01-1KG) were obtained from Fiber Optic Center (New Bedford, USA). Kapton foil (200 x 304 x 0.05 mm, product no. 536-3952) was obtained from RS Components GmbH (Frankfurt am Main, Germany) and ZelluTrans dialysis tubes (MWCO 6-8 kDa, product no. E665.1) from Carl Roth GmbH (Karlsruhe, Germany). Minisart® syringe filter polyethersulfone (PES) with 0.1 μ m pore size (product no. 16553-----K) were obtained from Sartorius Stedim Biotech (Germany, Göttingen). Thermo Scientific Menzel-Gläser coverslips (24 x 24 x 0.13-0.16 mm, product no. 10755315) were obtained from Fisher Scientific (Darmstadt, Germany). Microtip; Tapered, 6.5 mm ¼” for ultrasonication was bought from Terra Universal (Milan, Italy). All aqueous solutions were made with double deionized water (18.2 M Ω •cm at 25 °C) from a Synergy Water Purification system (Millipore Corp., Massachusetts).

7.2 Methods

Similar precautions regarding preparation and handling as in Chapter 6 were taken. In the case of the coated substrates, one side did not come into contact with another surface and was used for the related measurements. All glassware was cleaned thrice by rinsing with technical grade ethanol, acetone, water, and ethanol, followed by covering with a lint-free wipe and further drying in air. An overview of the different silica materials and their application is provided in Table 7.1.

Table 7.1 Overview of the used silica (SiO₂) and APTES-coated silica (APTES-SiO₂) materials and their main purpose. ACA, advancing contact angle; AFM, atomic force microscope; ELS, electrophoretic light scattering; mCA, macroscopic contact angle; PF, particle-covered; RCA, receding contact angle; RMS, root mean square; XRR, X-ray reflectivity.

Material	Size	Main purpose
SiO ₂	17.8 nm	ELS: ζ potential; XRR: air/water and decane/water interfacial adsorption and CA
	80 nm	ELS: ζ potential, dip coating, preparation of PF-substrates
	1000 nm	ELS: ζ potential
	Planar (smooth and particle-covered)	AFM: RMS roughness; mCA: air/water and decane/water ACA/RCA; SC: ζ potential
APTES-SiO ₂	18.9 nm	ELS: ζ potential; XRR: air/water and decane/water interfacial adsorption and CA
	Planar (smooth and particle-covered)	AFM: RMS roughness; mCA: air/water and decane/water ACA/RCA; SC: ζ potential

7.2.1 Cleaning and activation of coverslips

During the whole procedure, coverslips were kept wet. To hydroxylate the coverslips before dip coating, separated coverslips (24 x 24 mm) were placed in a Coplin jar and filled with fresh 1:1 methanol:HCl and gently shaken for at least 30 min. After the first acid wash, the samples were rinsed with copious amounts of water and placed in a second Coplin jar filled with H₂SO₄ with gentle shaking for at least 30 min. The samples were rinsed with water, then with methanol, and stored in a methanol-filled Coplin jar for up to one week. Prior to the dip coating procedure, two glasses were rinsed with water and placed in a 500 mL Duran beaker filled with 100 mL of water, covered with a glass Petri dish, and placed in an oil bath at 140 °C for 45 min to cause gentle boiling.⁷⁰¹ Finally, the glasses were transferred to water at room temperature and dried under a stream of nitrogen before the dip coating procedure.

7.2.2 TEOS sol-gel medium preparation with and without dispersing 80 nm nanopowder

All solutions were prepared in glass vials. The volume ratios used were 1:2:2 of TEOS:ethanol:water to prepare a total of 40 mL. The acidic water was prepared by adding 1 mL of 37% HCl per 10 mL of water (pH < 1). Ethanol absolute was added during magnetic stirring (20 x 6 mm, 500 rpm) followed by dropwise addition of TEOS, and stirring continued for 1 h. Three holes were pierced in the cap, and the sol was placed for 5 h in a 70 °C oven. Afterward, a new cap was placed on the vial, and the sol-gel was subsequently stored overnight at 20 °C.⁵⁰⁵ The next day, cleaned and activated coverslips were dip-coated in the sol-gel medium to obtain smooth thin films. For preparing particle-covered films, 1.33 mL of 3 M KCl was added to 36.667 mL of the TEOS sol-gel medium and magnetically stirred for 1 min. To this, 2 g of 80 nm nanopowder was gently added to the sol-gel medium during bath sonication to end up with a 5 w/v% dispersion. In total, the sol-gel dispersion was sonicated for 1 h and subsequently ultrasonicated (tip 1/4") for 5 min with ice cooling. The particle-sol-gel was left undisturbed at 20 °C for 30 min before the dip coating procedure.

7.2.3 Dip coating of activated coverslips in sol-gel medium with and without 80 nm nanopowder

The nitrogen-dried coverslips were dip coated in the acid-catalyzed TEOS sol-gel using a custom dip coating device. A 50 mL beaker (high form) was filled up to 30 mL with the sol-gel allowing to submerge 80 % of the coverslip and allowing the drying process to take place inside the beaker above the sol-gel surface. Dip coating parameters in the absence of nanopowder were 120 s residence time, 5 mm min⁻¹ withdrawal speed, and 10 min drying (see Appendix A.5.2 for optimization parameters). When the nanopowder was added, the withdrawal speed was set at 50 mm min⁻¹ while keeping the other parameters identical since lower withdrawal speeds caused incomplete particle coverage. Substrates were then placed in Wash-N-Dry™ racks and sealed in a humidified atmosphere for 48 h to complete the condensation reaction.⁵⁰⁵ Finally, the samples were heat-treated at 110 °C for 60 min, stored in an upright position separated from each other in ambient conditions, and protected from dust. The 80 nm nanopowder yielded the best coating results, while the other particle sizes led to incomplete coverage for various tested parameters and were not used in this work.

7.2.4 APTES coating on smooth (SF) and particle-covered (PF) silica films

Only smooth silica films (SF-SiO₂) with an advancing air/water contact angle between 5° - 12° were used for subsequent APTES functionalization and used immediately after preparation. Briefly, a concentrated, pre-hydrolyzed alcoholic solution of APTES (1:0.95:0.05 ethanol absolute:APTES:water) was prepared one day in advance and stored at 4 °C.⁵⁸⁹ A 50 mL glass vial with a plastic cap was filled with 15 mL of 10 v/v% ethanol absolute and 1 mM acetic acid. A hole was pierced in the cap, covered with alumina foil, and placed in a 90 °C water bath for 15 min.⁵⁹³ The APTES stock solution was diluted 0.4:500 (0.04% APTES) in the heated solution, shaken, and SF- or PF-SiO₂ substrates were carefully immersed in the medium for 10 min at 90 °C. The samples were rinsed with 10 v/v% ethanol absolute, dried with nitrogen, and cured at 120 °C in the air for 30 min.⁵⁷³ Samples were allowed to cool down for 15 min before dipping in 4:1 ethanol absolute:acetic acid, dried with nitrogen, and finally stored in 0.1 M HCl for 3 h.⁵⁸¹ Samples were rinsed with copious amounts of water and dried under a stream of nitrogen prior to the measurements.

7.2.5 Preparation of commercial nanopowder

The nanopowders (80 nm and 1000 nm silica) were subjected to 3 redispersion cycles in water. First, 5 g of powder was transferred into a 50 mL falcon tube, and water was added up to 45 mL. The falcon tubes were alternately vortexed and sonicated within 15 min followed by centrifugation of 2 or 10 min at 5000 rpm for 1000 nm and 80 nm silica, respectively. This step was repeated 3 times with fresh water. The particles were placed in a clean, glass Petri dish and covered with a lint-free wipe to air dry. After 72 h, the powders were collected in a glass vial and redispersed to 1 w/w% with alternating sonication/vortexing cycles and pH adjustments before characterization.

7.2.6 Synthesis of silica and APTES-coated silica nanoparticles and purification

Details are provided in Chapter 6, sections 6.2.2 and 6.2.3.

7.2.7 Scanning Electron Microscopy (SEM), Transmission Electron Microscopy (TEM), and Atomic Force Microscopy (AFM)

The smooth (SF) and particle-covered (PF) films were visually examined with SEM (Supra 40, Carl Zeiss, Germany) as well as the 80 nm and 1000 nm silica nanoparticles. Transmission electron microscopy (TEM-EM 900, Carl Zeiss, Germany) to study the morphology of the smaller particles was done by placing a 3 μL drop of 0.001 w/w% particle dispersion (pH \sim 5.8) onto a copper grid (Plano GmbH, Wetzlar, Germany). AFM (JPK Nanowizard III, Berlin, Germany) on the substrates was performed using a cantilever TESP-V2 from Bruker with tip radius 7 nm, nominal frequency of 320 kHz, and nominal spring constant of 37 N m^{-1} in the tapping mode. The line rate was 1 Hz for smooth SF samples and 0.5 Hz for rough PF samples. Gwyddion software was used to determine the root mean square (RMS) roughness and averaged over 4 samples.

7.2.8 Air/water and oil/water contact angle measurements

Contact angle (CA) goniometry of sessile water droplets measured on planar silica and APTES-coated silica substrates formed from a dosing needle (0.55 mm diameter) in air and immersed in decane was done using the OCA25 from Dataphysics (Stuttgart, Germany) at 20 $^{\circ}\text{C}$ (\pm 1 $^{\circ}\text{C}$) with a standard error of 0.05 $^{\circ}$. All samples were rinsed with water and dried with nitrogen before CA measurements. Advancing (ACAs) and receding contact angles (RCAs) were measured with the needle-in sessile drop method according to the procedure proposed by Korhonen et al.¹¹⁸ by simultaneously evaluating CA, drop volume, and base diameter. In general, a 1 μL water drop was formed on the substrate with a 10 s waiting time followed by slowly increasing the droplet volume until the monitored base diameter was at least 5 mm, after which the water was retracted. Air/water and oil/water ACAs/RCAs on all samples were obtained at a dosing speed of 0.025 $\mu\text{L s}^{-1}$, except for SF-APTES where the speed was set at 0.05 $\mu\text{L s}^{-1}$. Samples for air/water CA measurements were prewetted by dropping a larger volume on the surface to bypass stick-slip behavior,⁶⁵³ which was retracted and discarded before placing a fresh 1 μL drop and measuring the ACA/RCA. For oil/water CA measurements, after cutting the samples using a diamond pen (10 x 10 mm), they were rinsed with water and dried with nitrogen before carefully placing them in a cuvette. The cuvette was quickly filled with 900 μL pure decane (purity test see Appendix A.5.7, Fig. A.5.7) and left to equilibrate for 30 min before obtaining the ACA/RCA (Appendix A.5.9, Fig. A.5.8). It was not possible to measure the RCA on all substrates due to the vanishing drop contour, and a total of 50 samples ($n = 50$) were measured for each type of surface (Appendix A.5.10, Table A.5.4).

7.2.9 Electrophoretic light scattering for colloidal nanoparticles

To ensure all organic impurities were removed, 20 g of KCl was dissolved in 200 mL water and heated at 550 $^{\circ}\text{C}$ for 24 h. This purified salt was used to prepare the electrolyte solutions for both electrophoretic light scattering and streaming current measurements. Zeta potentials at different pH levels were obtained by preparing 0.1 w/w% particle dispersions in 10 mM KCl for conductivity at 25 $^{\circ}\text{C}$ and measured using the M3-PALS technology (section 4.1.2.3) available for the ZetaSizer NanoZSP (Malvern, United Kingdom). Samples were measured without membrane filtering. Adjusting pH was done using a maximum of 3 μL doses of 0.1 M or 1 M KOH or HCl. A stock solution of 1 w/w% in pure water was first prepared for the nanopowders and sonicated for 30 min before diluting to 0.1 w/w%. The nanopowder was allowed to equilibrate (rehydroxylation) until the pH was stable, creating a more representative nano-environment of non-dried particles.⁵¹⁸ The pH of the purified nanopowder was adjusted twice per day with magnetic stirring in between until the pH reading after equilibration

time was 0.3 units away from the desired pH. At this point, the pH was slightly adjusted to the desired value and stirred for 1 min before measuring. Conversely, fewer pH fluctuations were observed in the case of the synthesized particles. These particles were magnetically stirred for 15 min after pH adjustment, followed by a final pH reading right before electrophoretic light scattering. A waiting time of 300 s was used to ensure temperature calibration of the samples with an average of 3 samples for each pH value. Electrophoretic mobilities (μ) were used to calculate the zeta potentials, which depend on the Debye parameter (κ) and particle radius (a) (Appendix A.5.3). Hydrodynamic diameters were obtained at a particle concentration of 0.1 w/w% at 25 °C with 3 averaged measurements, containing 10-13 sub-measurements with a duration of 10 s per iteration (Appendix A.5.3, Table A.5.1).

7.2.10 Streaming current for rectangular planar substrates

Zeta potentials of SF- and PF-substrates were obtained via the streaming current method using an electrokinetic analyzer SurPASS 2 (Anton Paar Germany GmbH) at 20 °C (± 1 °C) with an adjustable gap cell for rectangular samples. Before each measurement, the conductivity and pH electrodes were placed in each test liquid for a minimum of 15 min to avoid drift during calibration. Dry, planar substrates were precisely cut (10 x 20 mm) in a homogenous area of the sample, excluding the irregular edges. These slides were attached to the sample holders using double-sided adhesive tape and placed inside the cell. 1 L of fresh 10 mM KCl solution was prepared from degassed water and 100 mL of the solution was transferred to a 600 mL beaker with a stirrer bar (40 x 10 mm) for rinsing and subsequently discarded. The beaker was filled with 500 mL electrolyte, pH, and conductivity electrode rinsed with the remaining electrolyte and the sample cell was rinsed for 20 min at a pressure of 200 mbar while adjusting the gap distance, which was generally around 110 μm . After 20 min, a flow check was performed (corresponding to a flow of 50 - 150 mL min^{-1} at 200 - 400 mbar) and the 0.05 M KOH titration solution was rinsed to remove air bubbles. Titration was performed from pH ~ 5.8 (due to dissolved CO_2) to basic pH 9 at a pressure of 400 mbar and repeated in triplicate. Since measuring from this starting pH to basic does not influence the zeta potential measurements, N_2 purging as suggested by Luxbacher⁷²³ was not implemented in the laboratory setup.

7.2.11 X-ray reflectivity

Experimental details are provided in section 6.2.8 and modeling of the electron density plots is explained in section 4.1.3.4

7.3 Scientific outcome

7.3.1 Mimicking the nanoparticle surface on smooth and rough planar substrates

Comparable nano- and macroscale surfaces were prepared via the sol-gel strategy using the alkoxides tetraethyl orthosilicate (TEOS) and (3-aminopropyl)triethoxysilane (APTES). Stöber-silica (SiO₂) particles were prepared with TEOS at moderate basic pH, while the same alkoxide used at acidic conditions forms a weakly-branched polymeric network and is transferred to a glass substrate by dip coating.⁴⁹⁸ Subsequent drying results in coated substrates with smooth surface films (SF). While different degrees of roughness largely influence the immersion depth of adsorbed microparticles,¹⁴⁵ increased roughness on planar substrates may better represent the wetting behavior of adsorbed NPs compared to smooth coatings. Particle-covered films (PFs) with increased roughness were prepared by adding 80 nm silica particles to the sol-gel medium before the coating (SEM image shown in Appendix A.5.1, Fig. A.5.1). The particles are trapped on the surface and are covered by a thin silane film upon drying, forming a stable surface that can withstand liquid shear forces, e.g., during streaming current experiments (Appendix Fig. A.5.2). In a second step, APTES was covalently attached to the TEOS surface of both NPs and substrates by incubating the materials in the respective sol-gel medium. The experimental procedure described in the Methods section should ensure that multilayer formation of APTES is suppressed due to the short reaction time of pre-hydrolyzed APTES in a diluted alcoholic solvent at elevated temperatures followed by rinsing with acetic acid.^{588,589,592,593} The topographical surface roughness of the dip-coated planar substrates is evaluated using AFM and SEM as shown in Fig. 7.2. The average root mean square (RMS) roughness of the substrate before APTES-coating (SF-SiO₂) is 0.358 nm and very close to that of mica (0.2 nm).⁷²⁴ The average RMS roughness increases to 2.178 nm after APTES functionalization (SF-APTES-SiO₂). This increased roughness is likely a combination of silica-etching⁷²⁵ with possible swelling of APTES at the elevated processing temperature of 90 °C⁵⁸² and low APTES concentration of 0.04% leading to incomplete coverage.⁵⁸⁷ The presence of 80 nm silica NPs confined at the surface before (PF-SiO₂) and after APTES-functionalization (PF-APTES-SiO₂) can be observed with both AFM and SEM in Fig. 7.2. Although not shown, some micron-sized particle aggregates are present on the PF substrates owing to their high stability in the sol-gel medium, which leads to irregular deposition of the NPs.

Subsequent APTES functionalization of PF-SiO₂ shows no difference in RMS roughness, which lies around 35 nm.

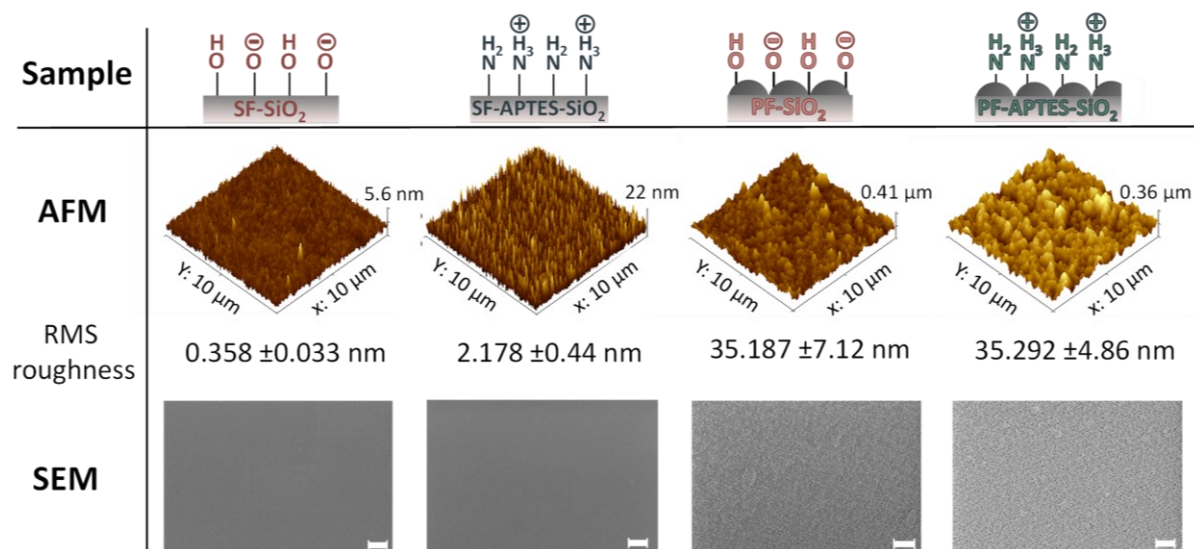


Fig. 7.2 Topographical analysis of planar smooth (SF) and particle-covered films (PF) of silica (SiO₂) and APTES-coated silica (APTES-SiO₂) with AFM and SEM. A 3D surface area of 10 x 10 μm obtained with AFM is shown from which the average root mean square (RMS) roughness per type is determined with standard deviation ($n = 4$). The bottom row depicts SEM images with scale bars of 1 μm.

7.3.2 Analogous electrokinetic potentials between nanoparticles and macroscopic substrates

The reported correlation of particle wettability and electrokinetic (ζ) potential provides a basis to estimate wettability at both the nano- and macroscale.⁷²² At the nanoscale, the ζ potential is measured for differently sized colloids with electrophoretic light scattering, where charged particles migrate to the counter electrode when an external electric field is applied (section 4.1.2.3 for theory; Appendix A.5.3 for practical application). An electric current is evoked for the macroscopic planar substrates when a salt solution is sheared over a stationary surface. The streaming current arises due to charge transfer when the sheared counterions reach the electrode (section 4.1.2.4).

However, comparative ζ potentials between both methods necessitate certain conditions. Briefly, the determination of ζ potentials for smooth and spherical particles based on Smoluchowski's (Eq. 4.4), Hückel's (Eq. 4.5), and Henry's (Eq. 4.6) model shows a linearly varying electrophoretic mobility (μ) with respect to the ζ potential and κa (κ is the Debye parameter [Eq. 4.3] describing the electric double layer thickness κ^{-1} , which is inversely related to the electrolyte concentration, and a the particle radius). Nevertheless, the diffuse double layer cloud around dispersed colloids attains an asymmetric shape for highly charged colloids

($\zeta \geq 25$ mV and $\kappa a \geq 2.75$) that generally underestimates μ and becomes more pronounced with smaller κa such as with decreasing particle size and/or less added electrolyte.⁶¹⁹ Based on the numerical results from O'Brien and White,⁶¹⁹ approximate analytical expressions have been designed to account for this relaxation or double-layer polarization, which describes a non-monotonic relationship between μ and ζ potential. Approximate solutions, such as those by Ohshima, Healy, and White⁶²³ (OHW, Eq. 4.10) and by Ohshima⁶³³ (Eq. 4.11), cover the whole range of possible κa values. Determination of κa for the colloidal silica particles depicted in Fig. 7.3a is discussed in detail in Appendix A.5.4, and model-dependent ζ potentials are visually shown in Fig. A.5.4. Notably, at ζ potentials < 50 mV and electrolyte concentrations ≥ 10 mM, the effects of surface conduction can often be ignored, which would otherwise lower experimental μ due to increased counterion adsorption compared to the bulk by an excess of electrical charge on the solid surface. However, surface conduction becomes increasingly problematic when the particle size decreases, and since it is not accounted for in Ohshima's approximation ($\kappa a < 10$), it could underestimate ζ potentials even below 50 mV.^{625,629,630} This issue is tackled by using very large particles (1000 nm SiO₂) where surface conduction is practically absent, directly determined from Dukhin's number (≤ 0.05) in the OHW equation, and assuming that their surface chemistry is equal to the smaller-sized silica particles.⁵¹⁸ Fig. 7.3a shows the ζ potentials obtained through electrophoresis for the three differently sized silica colloids at a fixed particle concentration of 0.1 w/w% dispersed with a background electrolyte concentration of 10 mM KCl. The ζ potentials are almost identical when pH ≤ 8 , which can be expected for chemically indistinguishable surfaces. Therefore, micrometer-sized spheres can be used as a reference to determine the ζ potential in relation to corresponding particles of smaller sizes. For completeness, the ζ potential values of the 19 nm APTES-coated silica NPs were also calculated with Ohshima's expression.⁶³³

The streaming currents of the smooth (SF) and rough (PF) planar substrates composed of silica (SiO₂) or coated afterward with APTES (APTES-SiO₂) in Fig. 7.3b are calculated using the Helmholtz-Smoluchowski equation (Eq. 4.12) since $\kappa a \gg 1$, and surface conductance above an electrolyte concentration of 1 mM is found to be insignificant for silica during streaming current experiments.^{635,639} PFs for both surface chemistries show slightly weaker ζ potentials than the SFs. The AFM images for the PFs in Fig. 7.2 show a varied landscape with peaks and valleys. Thus, it is very likely that there is no well-defined shear plane within the double layer as presumed by the Helmholtz-Smoluchowski model. The mobile ions inside the

valleys compared to the peaks remain mostly stationary during shearing, and therefore only part of the surface is detected at the electrodes.⁶³⁹

Finally, the ζ potentials of nanoparticles and macroscopic substrates overlap after proper conversion and determination of ζ potentials for dispersed particles with electrophoretic light scattering and thin films with streaming current (Fig. 7.3c, excluded PF data). It should be noted that, although size-dependent ζ potential is accounted for by considering κa , the surface charge density (σ) will increase significantly when the particle size decreases below $a = 5$ nm in comparison to a non-porous, flat surface.^{726,727} However, this effect is still moderate for the smallest particle size used (Appendix A.5.5, Fig. A.5.5). In this case, the direct connection between σ and wettability, both at liquid surfaces⁷²⁸ and on planar substrates,⁷²⁹ could lead to different CAs when working with ultrasmall particles, which pose a limit in relating the mCA to the immersion depth of NPs at liquid interfaces.⁷²² To evaluate the influence of all applied coatings on the ζ potential, Appendix A.5.6, Fig. A.5.6 compares the streaming current results and contact angles of the native SF substrates to the silica-coated substrates with or without APTES.

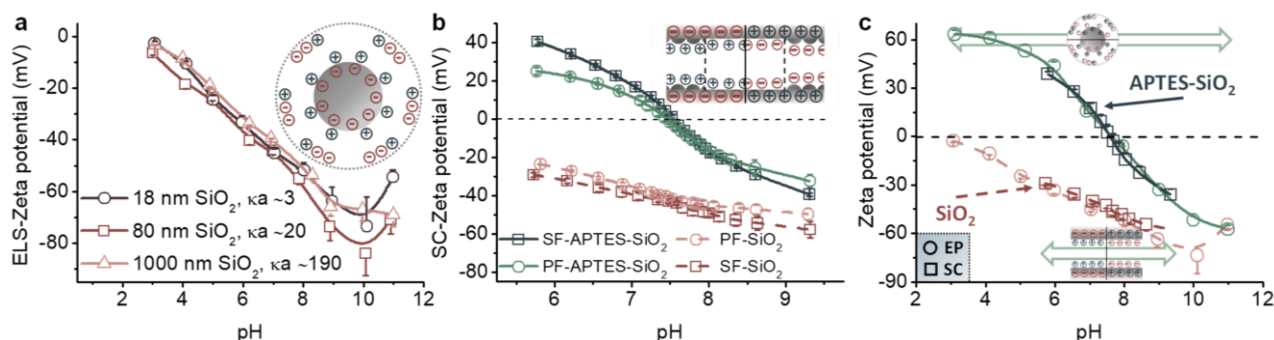


Fig. 7.3 Evaluation of zeta potential with electrophoresis and streaming current at 10 mM KCl. **a**, Zeta potential measurements using electrophoretic light scattering (ELS) for 0.1 w/w% of 1000, 80, and 18 nm silica (SiO_2) particles at different pH with their approximate dimensionless electrokinetic radius κa . **b**, Zeta potential using the streaming current (SC) method for smooth (SF) and particle-covered films (PF) with SiO_2 or coated with APTES (APTES- SiO_2) are measured in a pH range from 5.8 to 9.4. **c**, Comparing the zeta potentials obtained with the ELS and SC method of SiO_2 and APTES- SiO_2 . Only the results of the SF-samples from **3b** are depicted in **c**. The maximum range of the pH titration was different for both methods and is indicated schematically by the broad arrows and experimental standard deviations are provided in all plots ($n = 3$).

7.3.3 *In situ* observation of self-assembled nanoparticles at liquid interfaces

The NPs self-assemble at a quiescent air/water surface and oil/water interface, with an immersion depth that can be determined *in situ* from high-resolution X-ray reflectivity (XRR) data. Before the XRR tests, the purity of the particle dispersions (0.1 w/w% at aqueous pH ~ 5.8) and decane are tested with time-resolved interfacial tension measurements (Appendix A.5.7, Fig. A.5.7). The Fresnel normalized reflectivity profiles (R/R_F) in Fig. 7.4 are

identical to Fig. 6.2, and more details are given in section 6.3.2. The reflectivity curves indicate that when the subphase contains negatively charged silica NPs, adsorption is primarily absent since the reflectivity curve resembles that of a pure air/water surface with a very small negative slope due to the interface roughness.⁶⁹⁴ When particles are positively charged, pronounced Kiessig fringes appear at both liquid interfaces with an estimated thickness ($d_{\text{layer}} \approx 2\pi/\Delta Q_z$) of 18.74 ± 1.45 nm, similar to the particle diameters estimated from TEM (Appendix A.5.1, Fig. A.5.1). The EDs normalized against water (ρ_w) in the insets of Fig. 7.4 indicate that the APTES-coated silica NPs adsorb to both liquid surfaces with a small protrusion distance into the nonpolar gas or liquid. The CA changes from $28.35^\circ \pm 2.52$ to $22.26^\circ \pm 2.68$ when air is replaced by decane, while all other parameters remain constant (Appendix A.5.8, Table A.5.3).

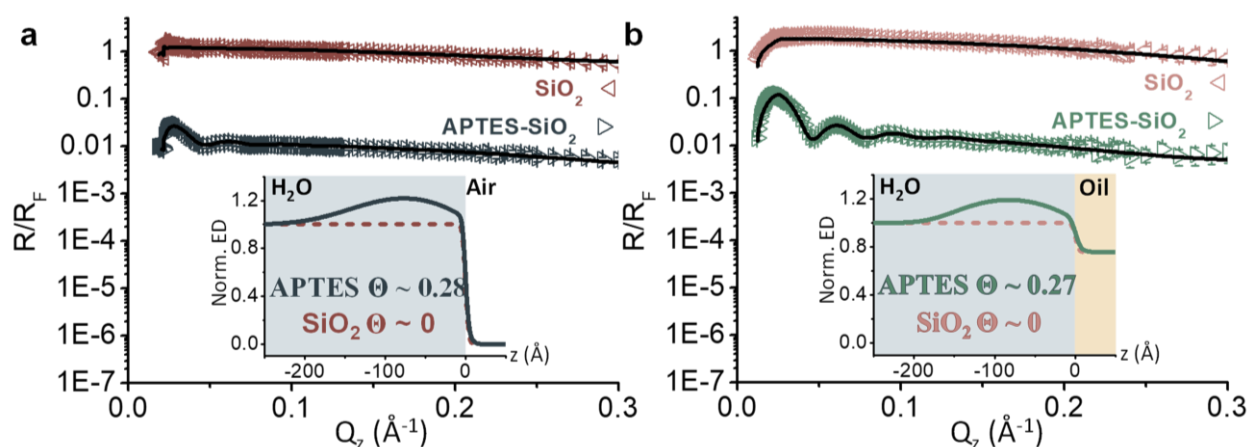


Fig. 7.4 X-ray reflectivity and electron densities of adsorbed particles at the air/water surface and decane/water interface. **a**, Reflectivity curves normalized to the Fresnel reflectivity (R_F) at the air/water interface and **b**, the decane/water interface (aqueous subphase pH ~ 5.8) with 0.1 w/w% 18 nm silica (SiO_2 , left triangles) and 19 nm APTES-coated silica (APTES- SiO_2 , right triangles) with their corresponding fits (black line) and standard deviation ($n = 3$). The insets show the normalized-to-water (ρ_w) electron density plots for SiO_2 (dashed line) and APTES- SiO_2 (solid line) from which the physical parameters, such as particle coverage (Θ), were fitted using the physical model (section 4.1.3.4).

7.3.4 Air/water and oil/water macroscopic contact angle measurements

The mCAs were measured on the planar substrates using the standard sessile drop method (Eq. 2.5; θ_E , Fig. 7.5a) with the techniques of receding (RCA) and advancing contact angle (ACA) at air/water and oil/water interfaces. As expected with the sessile drop method, large CA distributions require sufficient samples ($n = 50$) to represent the CA spread that can be expected for real systems.^{49,229} The mCAs were recorded after prewetting the substrates with larger volumes of water that were subsequently discarded, leaving behind a thin water film that more closely resembles the surface of the water-dispersed NPs. This also allows possible air-borne impurities to dissolve in the discarded liquid, and it minimizes the observed stick-slip behavior on dry substrates.⁶⁵³ Particularly amino-terminated functionalities are prone to quickly

adsorb air- or water-borne impurities that impact the measured ACAs/RCA, complicating the experimental execution in measuring mCAs.⁷³⁰ This pretreatment decreased the air/water ACAs/RCA compared to drops on a dry surface (data not shown).⁷⁰⁸ Sequential ACA/RCA cycles on the same sample immersed in decane provided similar mCAs with less pronounced stick-slip compared to the first cycle, indicated by a semi-stable ACA region that is irrespective of prewetting conditions (Appendix A.5.9, Fig. A.5.8).

Table 7.2 summarizes the mean CAs and hysteresis percentages, and exact numbers of all CAs for substrates and particles are given in Appendix A.5.10, Table A.5.4. At first glance, the wettability enhances for the particle-covered surfaces compared to the smooth surfaces, which agrees with Wenzel's observation under the assumption that the liquid completely penetrates the surface grooves.¹³¹ The RCAs at air/water for all samples are practically zero due to their hydrophilicity. The mean air/water ACA of smooth silica is 9.42° and the oil/water ACA/RCA is $14.12^\circ/8.57^\circ$, while the substrate covered with silica particles shows significant spreading in both environments. The ACA of smooth APTES substrates is 29.02° and decreases to 9.61° on the particle-covered APTES surface. When decane is deposited on top of the smooth substrate, the average oil/water ACA on SF-APTES-SiO₂ increases to 57.01° and the RCA is 21.44° . The oil/water ACA of the particle-covered APTES film showed only a minor increase to 12.19° whereas no RCAs could be measured due to the spreading of the droplet during liquid retraction. Table 7.2 also shows the equilibrium contact angle (ECA, Eq. 4.14), which is the angle defined by the Young-Laplace equation from the far-field equilibrium of the surface forces acting on the triple line, where colloidal interactions are irrelevant, down to length scales of ~ 30 nm. Below this size, the microscopic structure of the contact line is subject to physicochemical properties of the solid and fluids along with van der Waals and electrostatic interactions exerting additional influence on the local contact angle.⁷³¹ Except for SF-APTES in decane/water, the ECA is very hydrophilic ($< 18^\circ$). The contact angle hysteresis (CAH, Eq. 4.17) is given as a percentage to easily compare the different surfaces with each other.¹¹⁸ The roughness-induced wetting for the particle-covered surfaces and smooth silica show very low hysteresis ($\Delta\theta\% < 1\%$), while SF-APTES-SiO₂ shows hysteresis most likely due to topographical (Fig. 7.2) and chemical⁵⁹¹ irregularities or surface defects. The large increase in CAH for smooth APTES when decane is added is proportional to the increase in the work of spreading (Appendix A.5.11).⁷³²

Table 7.3 shows the average apparent surface free energies for the smooth surfaces to assess the solid-oil-water interactions (Eq. 4.22) derived from air/water ACA/RCA and ECAs. Depending on the applied model, at least 2 test liquids are usually necessary to find the solid-

gas interfacial tension (γ_{sg}) to establish the solid-gas-liquid interactions that describe the adhesion between the solid and liquid. Contrarily, the contact angle hysteresis (Eq. 4.18)⁶⁵² or equation of state approaches (EOS, Eq. 4.19)⁶⁵³ roughly estimates γ_{sg} with only one test liquid.¹¹⁹ While more liquids in Eq. 4.18 and Eq. 4.19 improve accuracy in estimating γ_{sg} , similar results to ours are found for silica with extended models (e.g., Wu)¹¹¹ that employed a significant number of solvents.⁷³³ The solid-liquid interfacial tension (γ_{sl}) determined from the EOS (Eq. 4.20) is used to estimate the solid-oil interfacial tension (γ_{so}), which is an extension of the EOS (Eq. 4.21) applicable to a solid surrounded by two immiscible fluids. Similarly, the Young equation (Eq. 2.5, θ_E) was adapted into Eq. 4.22 for oil/water systems. This gives an average oil/water CA of 12.64° for silica and 37.68° for APTES-coated silica when using the ACA/RCA numbers, which are close to the oil/water ECAs determined from Eq. 4.14.⁶⁵⁴ The predicted oil/water/solid CAs determined from the air/water ECAs lie between 5.70° to 10.49° for silica and 14.75° to 24.67° for APTES-coated silica, both regions where the experimental oil/water RCAs fall into. Based on these results, air/water ACA/RCA crudely estimates the oil/water ECA, while air/water ECAs predict the oil/water RCA.

Table 7.2 Advancing (ACA), receding (RCA), equilibrium contact angle (ECA, Eq. 4.14), and contact angle hysteresis (CAH, Eq. 4.17) for the smooth (SF) and particle-covered (PF) surfaces with standard deviation ($n = 50$).

		SF-SiO ₂	SF-APTES-SiO ₂	PF- SiO ₂	PF-APTES-SiO ₂
Air/water	ACA (°)	9.42 ± 1.34	29.02 ± 3.48	0.10* - 5.00**	9.61 ± 2.35
	RCA (°)	0.10* - 5.00**	0.10* - 5.00**	0.10* - 5.00**	0.10* - 5.00**
	ECA (°)	3.99 ± 0.50* - 7.31 ± 0.72**	10.35 ± 1.02* - 17.62 ± 1.75**	0.10* - 5.00**	3.46 ± 0.86 – 7.42 ± 1.26
	CAH (%)	0.67 ± 0.19	6.28 ± 1.47	0.00	0.70 ± 0.35
Decane/ water	ACA (°)	14.12 ± 1.55	57.01 ± 9.49	0.10* - 5.00**	12.19 ± 2.50
	RCA (°)	8.57 ± 1.69	21.44 ± 6.71	0.10* - 5.00**	0.10* - 5.00**
	ECA (°)	11.45 ± 1.60	39.31 ± 7.67	0.10* - 5.00**	4.98 ± 0.88 – 8.81 ± 1.35
	CAH (%)	0.95 ± 0.11	19.32 ± 4.78	0.00	1.13 ± 0.46

Due to the spreading of the droplets, a CA of 0.10° or 5.00°** was chosen to determine the ECA.*

Table 7.3 Surface free energies (mJ m^{-2}) for the smooth silica (SF-SiO₂) and APTES-coated silica (SF-APTES-SiO₂) substrates based on water contact angle measurements (Eq. 4.18 – Eq. 4.21) to predict the contact angle ($^\circ$) for solid-water-oil (Eq. 4.22, θ_{lo}) with standard deviations ($n = 50$).

		$\gamma_{sg}^{CAH} - \gamma_{sg}^{EOS}$	γ_{sg}^{Av}	γ_{sl}	γ_{so}	θ_{lo}
ACA and RCA	SF-SiO ₂	$71.46 \pm 0.21 -$ 71.23 ± 0.27	$71.35 \pm$ 0.25	$1.67 \times 10^{-2} \pm$ 0.95×10^{-2}	$50.93 \pm$ 0.36	$12.64 \pm$ 1.84
	SF-APTES-SiO ₂	$65.42 \pm 1.56 -$ 64.36 ± 1.61	$64.89 \pm$ 1.53	1.14 ± 0.46	$42.37 \pm$ 1.86	$37.68 \pm$ 4.17
		γ_{sg}^{EOS}	γ_{sl}	γ_{so}	θ_{lo}	
ECA (RCA 0.1 $^\circ$)	SF-SiO ₂	72.03 ± 0.05	$6.75 \times 10^{-3} \pm$ 3.40×10^{-3}	51.94 ± 0.07	5.70 ± 0.75	
	SF-APTES-SiO ₂	71.05 ± 0.22	$2.89 \times 10^{-2} \pm$ 1.06×10^{-2}	50.50 ± 0.31	14.75 ± 1.39	
		γ_{sg}^{EOS}	γ_{sl}	γ_{so}	θ_{lo}	
ECA (RCA 5 $^\circ$)	SF-SiO ₂	71.62 ± 0.12	$7.49 \times 10^{-3} \pm$ 2.89×10^{-3}	51.33 ± 0.17	10.49 ± 1.04	
	SF-APTES-SiO ₂	69.01 ± 0.60	0.22 ± 0.08	47.63 ± 0.81	24.67 ± 2.34	

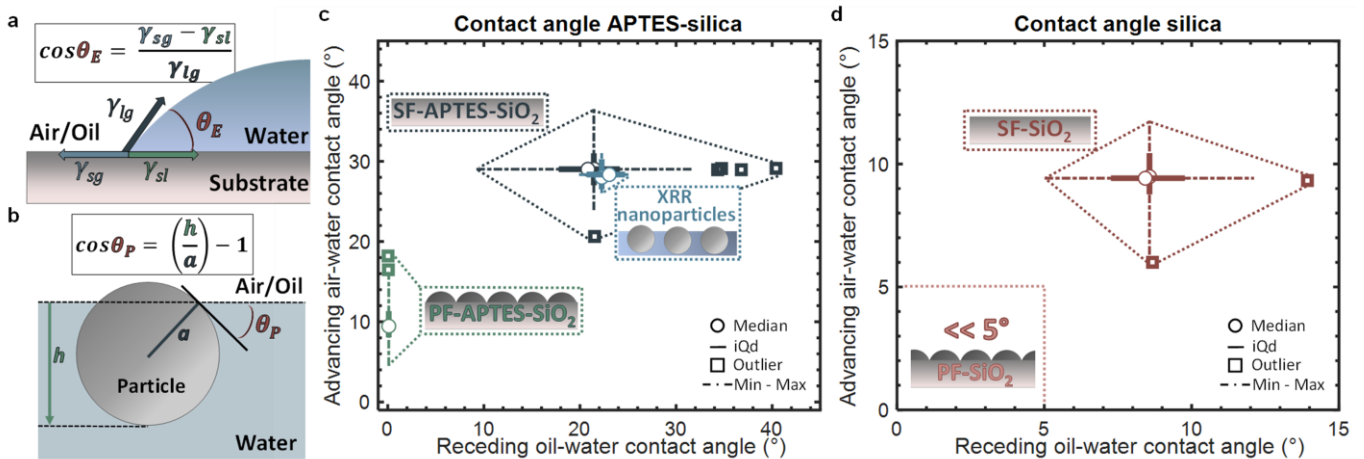


Fig. 7.5 Contact angles of adsorbed nanoparticles and sessile droplets. **a**, The standard Young equation (Eq. 2.5, θ_E) and **b**, relating immersion depth (Eq. 2.10, θ_P) to estimate the contact angle (θ) at the air/water and oil/water interface is applied to macroscopic sessile droplets on planar substrates and interfacially adsorbed nanoparticles resolved with X-ray reflectometry (XRR), respectively. **b,c** A double boxplot of the advancing air/water contact angle against the receding oil/water contact angle for APTES-coated silica (**c**) and bare silica (**d**) visualizes macroscopic contact angles measured on the smooth (SF) and particle-covered films (PF) along with the interfacially adsorbed nanoparticles obtained from XRR (**c**). Circles are the median, ‘iQd’ stands for interquartile distance (middle 50% of the data), the intersection points of air/water and decane/water correspond to the mean, and the dash-dotted line shows the (nonoutlier) minimum and maximum values ($n = 50$).

7.4 Discussion

7.4.1 Comparing contact angles at the nano- and macroscale

The effects of gravity and long-range surface interactions (van der Waals, electrostatic, hydrophobic, and hydration forces) define the theoretical dimensions to properly relate the observed CAs for liquid droplets on planar surfaces and solid particles adsorbing at a liquid

interface. The former is expressed as the capillary length (Eq. 2.7; l_c), which is around 2.71 mm in air/water and 4.44 mm for decane/water, while the latter operates below a characteristic length scale $l_s \approx 1-10$ nm (Eq. 2.8). If the principal radii are smaller than l_c , gravitational forces do not influence the droplet's shape or interface for sessile droplets or adsorbing colloids, respectively.¹²⁸ The sessile drops in this study on the substrates and the NP size are well below l_c and above l_s . While these conditions apply to perfectly smooth and defect-free surfaces, it can be assumed that, beyond the nanometer-scale roughness of the PF substrates (~ 35 nm), the sub-nanometer roughness on the surface between particles and smooth planar thin films are similar. Deviations from perfectly smooth surfaces give rise to greater contact line pinning both at the nano- and macroscale (and thus hysteresis) with additional line tension contributions below a droplet or particle size of 100 nm with size-dependent CAs.¹¹⁵ Line tension is primarily discussed for uncharged fluids, compared to charged solids, with a strong disparity in sign and magnitude.^{61,720} The current approach assumes that equivalent ζ potentials between the NPs and planar substrates improve the predictability of particle wetting as inferred from mCAs of equivalent macroscopic substrates without exact knowledge about pinning or line tension.

It has been proposed that hydrophilic NPs adsorbing from the aqueous phase have CAs that are equivalent to the RCA, while the ACA corresponds to a particle adsorbing from the air/oil phase.^{128,253} Considering the motion of an adsorbing particle towards the interface from either bulk phase, frequent and large surface defects increase the amount of contact line pinning on the particle surface as it protrudes the interface. An advancing particle adsorbing from air/oil to the liquid interface achieves a stable angle after displacement of the contact line, thereby increasing the wetted area of the colloid (higher CA compared to ECA), whereas a lowering of this wetted area occurs for the particle receding the interface (lower CA compared to ECA).¹²⁸ Therefore, one expects that hydrophilic NPs adsorbing at the interface have CAs that more closely correspond to the RCA measured on a flat substrate characterizing similar surface defects, which can be roughly estimated from the CAH. The mCAs, encompassing the ACA, RCA, and ECA, are compared to the CAs of self-assembled NPs at the liquid surface derived from XRR (Appendix A.5.10, Table A.5.4) and calculated using Eq. 2.10 (Fig. 7.5b). Based on the XRR results, only APTES-coated silica NPs adsorb at both liquid interfaces, providing the foundation to compare the NP CAs to the respective mCAs. These corresponding results are summarized as a double boxplot in Fig. 7.5c and Fig. 7.5d for APTES-coated silica and bare silica, respectively, where the mean values lie on the intersection points of each sample.

7.4.2 APTES-coated silica

The obtained mean and median mCAs (air/water ACAs and decane/water RCAs) of smooth APTES-coated planar substrates, comprising similar surface chemistry and ζ potentials as the interfacially adsorbed NPs, coincide nicely with the CA distribution of the NPs measured with XRR. In contrast, the rough, particle-covered surfaces are much more hydrophilic and are unsuitable for judging the CA of adsorbed NPs (Fig. 7.5c). First of all, the oil/water RCA on the flat substrates describes very well the oil/water CAs of the NPs. Based on the air/water ECA and ACA/RCA data of the smooth substrates, the estimated oil/water CAs in Table 7.3 provide an angle of 14.75° and 37.68° , respectively. Surprisingly, the ACA at air/water complements the wetting of the NPs, rather than the expected RCA values. In the literature, the CAs of particles adsorbed at air/water versus oil/water mostly portray an increase in CA for identical particles at the liquid/liquid system, meaning that the choice for estimating wetting at both liquid interfaces stems from either the ACA or the RCA and not a combination of them.^{232,245} However, this trend is not observed for $1\ \mu\text{m}$ APTES-coated silica, with an air/water CA of $\sim 62^\circ$ and $\sim 39^\circ$ at the oil/water interface.²⁴⁷ The exact reason for this prominent difference is unknown. However, its origin can be related to the charge sign since opposite behavior in immersion depth is observed for negatively and positively charged colloids when salt is added to the aqueous phase¹⁹⁹ or simply due to line tension effects as its sign reverses.^{62,720,734} Experimentally, the air/water mCAs measured here and elsewhere^{141,297} do not support the fact that the air/water RCA measured on a planar substrate agrees with the CA of the particles. In contrast, mCA simulations of ultrasmall NPs at air/water⁷³⁵ and oil/water⁷³⁶ do agree with the RCA. Further factors need to be considered, such as the influence of prewetting (which lowers the mCAs), the wettability of the particle material itself (hydrophilic/hydrophobic), and the differences between contact line formation on the macro- and nanoscale (i.e., pinning and line tension effects).

Based on this discussion, a tentative adsorption mechanism is proposed for the positively charged, hydrophilic NPs at the oil/water and air/water interface at a pH ~ 5.8 and absence of electrolyte (Fig. 7.6a and b). Before adsorption, the positively charged hydrophilic NPs are attracted toward the negative charges present at the phase boundary (Ia & Ib).^{38,182,183} Their preferred state after protrusion resembles the RCA as a consequence of particle motion and contact line pinning, experiencing a concave meniscus for the nonpolar phase (IIIa). At air/water, no particles should populate the interface according to the measured RCA (IIb). Still, in this case, the ACA suggests that the meniscus is convex (IVb) and that the air/water

surface wets the particle. To the best of my knowledge, the origin or possibility of such a mechanism has not been explored. Another possibility that occurs only at an air/water surface is enhanced evaporation at the three-phase contact line, causing pinning/depinning effects typically observed for drops on planar substrates exhibiting stick-slip⁷¹⁹ and potentially causing a change in meniscus profile for adsorbed particles. Recently, a fresh insight into the origin of the charge at air/water and oil/water interfaces indicated that both carry a net negative charge of similar magnitude. However, virtually no charges are present in the air, while a large negative charge travels through the oil due to charge transfer of the water, making the latter subsurface region more positive.¹⁸² The possibility of varying effective charges in the vicinity of the air/water and oil/water interfaces might assist in explaining the observed difference in CAs for the same particles.^{232,245,247}

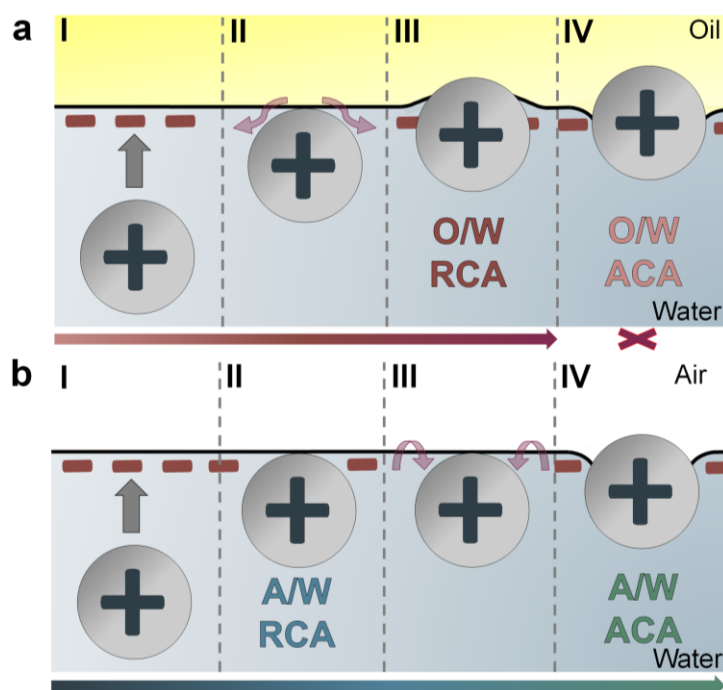


Fig. 7.6 Tentative scheme relating advancing (ACA) and receding contact angle (RCA) of the planar substrates to the adsorbed APTES-coated silica nanoparticles. **I**, For both oil/water (O/W, **a**) and air/water (A/W, **b**), a positively charged nanoparticle is attracted to the interface due to the net negative charges present at the phase boundary. ACAs and RCAs for adsorbing particles create oppositely oriented menisci due to contact line pinning stemming from morphological/chemical imperfections, dragging along part of the liquid. **IIa**, In the case of the O/W interface, the particle and interface interact before breaching through and pinning causes a locally deformed convex meniscus with respect to the water phase, agreeing well with the O/W RCA on smooth planar substrates (**IIIa**). **IVa**, Very high O/W ACAs are energetically unfavorable for these hydrophilic NPs and are not observed. **IIb**, Particle adsorption is not directly observed at the A/W interface, where the A/W RCA is practically zero, while the A/W ACA does correspond to the adsorbed NPs (**IIIb**). This configuration might be possible when the liquid surface wets the particle surface and is attracted toward it. The arrows positioned at the interface indicate how the meniscus pins to the particle surface, in accordance with ACA and RCA, but it remains unclear if such a change in the meniscus is physically possible when the nonpolar phase changes between gas and fluid.

7.4.3 Silica

Since adsorption of the bare silica particles could not be detected with XRR, a direct comparison of the CAs of particles and films cannot be performed, although some studies reported adsorption of these hydrophilic particles at the liquid surface.^{39,141} The monotonic decreasing reflectivity curves for silica in Fig. 7.4 cannot support these observations since a previous study using XRR and grazing-incidence small-angle X-ray scattering (GISAXS) noticed that only subsurface ordering takes place where the particles just touch the air/water surface, and this for very concentrated silica dispersions (40 w/w%).³⁰¹ As no particle adsorption is detected, the measured mCAs on the smooth silica substrates in Fig. 7.5d might represent the inherent wettability of the particle surface since the ζ potentials of the particles and substrates coincide in this case as well. When adsorption of these charged, hydrophilic silica particles is reported, external factors likely play a role, such as perturbations of the liquid surface, contaminations present in the solvents/adsorbed on the particle surface, or use of spreading solvents.²⁴⁸ Appendix A.5.12, Fig. A.5.10 shows a schematic overview of the proposed methodology when a general estimate of particle wettability is required when more sophisticated *in situ* methods are not readily available.

7.5 Conclusions

Assessing the wetting properties of small nanoparticles (NPs) necessitates resource-intensive and sophisticated approaches like synchrotron-based experiments^{38,49,209,301} or other alternative methods.^{142,248,295,297,298} Direct estimation of NP immersion depth at air/water and decane/water interfaces collected from synchrotron-based X-ray reflectivity shows that negatively charged silica (SiO₂) NPs do not adsorb, contrarily to the positively charged APTES-coated silica (APTES-SiO₂) NPs. Since the wettability of particles²⁶⁸ and planar substrates⁷²² have been linked to their surface charge, coupling the pH-dependent ζ potential between chemically and topographically equivalent spherical particles and planar substrates ensures higher accuracy than sessile drop-derived macroscopic contact angles (mCAs) alone. Smooth or particle-covered films with similar coatings as the dispersed particles were prepared to account for possible surface roughness effects. The planar substrates measured with streaming current showed similar ζ potentials as the bulk particle dispersions analyzed through electrophoresis and were almost insensitive to surface roughness. Contrarily, the particle-covered substrates with increased surface roughness showed very hydrophilic behavior determined from the mCAs. In the case of the smooth APTES-coated surface, higher air/water advancing (ACAs) and lower oil/water receding contact angles (RCAs) provided the most realistic description of the NP wetting properties, similar to the observations for microparticles.²⁴⁷ However, it is generally expected that the RCA better describes the wetting of particles adsorbing from the aqueous bulk to the interface and an increase in the particle CA can be expected when gas is exchanged for a denser oil.^{128,141,297,455,735,736} Apparent surface free energies derived from air/water ACAs, RCAs, and equilibrium contact angles (ECAs) provide a range of oil/water mCAs, which conforms with the experimental oil/water RCAs measured on the smooth APTES-coated surfaces.⁶⁵⁰⁻⁶⁵⁴ At the same time, the mCA inherently can only provide approximations of the CAs of straddling particles at a liquid surface. Additionally, the high accuracy of X-ray scattering in this context opens up new possibilities to experimentally investigate line tension contributions of charged particle surfaces⁷²⁰ and CA dependencies by varying particle size, pH, electrolyte concentration in either phase and/or using immiscible oils with different polarities, shedding more light on the applicability of ACAs/RCAs with a variety of particle materials and environmental conditions.

7.6 Acknowledgments

The author thanks P. Witte for her expertise with the SEM and T. Mehrrens for TEM. The author acknowledges DESY (Hamburg, Germany), a member of the Helmholtz Association HGF, for the provision of experimental facilities. Parts of this research were carried out at PETRA III, and the author thanks Dr. M. Lippmann for assistance in using the lab facility. The author acknowledges research grant Verbundforschung BMBF/05KS7FK3/05KS10FK2, Verbundforschung BMBF/05K16FK1/05K19FK2 and 05K19K2 for financing LISA instrument and the Lambda GaAs detector. M.M. acknowledges support by DFG (Deutsche Forschungsgemeinschaft) project 278836263. P.H. acknowledges support by the DFG Graduate School GRK2462 “Processes in natural and technical Particle-Fluid-Systems (PintPFS)” (Project number 390794421). This work was also supported by the DFG within the Collaborative Research Initiative SFB 986 “Tailor-Made Multi-Scale Materials Systems” (project number 192346071).

8 Conclusion and outlook

In this thesis, the adsorption mechanism and the specific adsorption layer properties of nanoparticle-laden liquid interfaces in the absence and presence of an aliphatic aminolipid have been studied on the macro- and nanoscale. For this purpose, dynamic oil/water interfacial tension, dilational rheology, shear rheology, and macroscopic contact angle measurements were supplemented with synchrotron-based *in situ* specular X-ray reflectometry. The latter method and oil/water interfacial tension measurements necessitate the high purity of all solvents and materials, owing to their high susceptibility to surface-active impurities that would otherwise impact the calculations.^{93,299,661–663} Under the investigated electrolyte-free conditions, the charge of the spherical silica nanoparticles is highly negative. It changes to positive after surface modification with an aminosilane, allowing to study the electrostatic charge effect on adsorption to a liquid interface in the absence and presence of the aminolipid.

In the case of binary adsorption with equally charged materials, the results have shown that the 80 nm-sized particles reversibly adsorb and compete for interfacial coverage with the surfactant under the assumption that interactions between both components are negligible. The particles themselves show no surface activity, estimated from the linear time-dependent interfacial tension signal. Since a smaller interfacial tension reduction is observed compared to a particle-free interface, competition between both components at the interface and reversible particle adsorption behavior is plausible. This difference in interfacial tension indicates that the lipids have less space to adsorb at the liquid interface due to the presence of particles. Therefore, their contributions can be treated as additive that form the basis of the proposed analytical model. Subsequent implementation of the experimental interfacial tension into the model gives reasonable estimates of the interfacial particle coverage for not too high surfactant concentrations backed up by electron microscopy imaging of Langmuir-Blodgett samples of the mixed films. Further in-depth analysis obtained with specular X-ray reflectivity and data modeling using 19 nm-sized particles showed that the particle contact angle changes only slightly for different concentrations of added aminolipid, a necessary condition to utilize the additivity model. However, compared to the reflectivity measurements, the model failed to predict the coverage for the smaller particles based on interfacial tension alone likely because the length scale of the electric double layer compared to the solid particle becomes significant.^{458,717} Therefore, larger particle sizes were tested in the additivity model until the particle coverage between the two methods was identical. The estimated particle size became progressively smaller as the lipid concentration increased and suggests an electrostatic

exclusion zone exists, which originates from the asymmetric double layer in the aqueous phase. In the case of small positively charged silica particles and the aminolipid, interactions between the particles and lipids are limited. The nanoparticles physically prevent lipid adsorption by decreasing the amount of interfacial space while simultaneously prohibiting the lipids to adsorb inside the electrostatic exclusion zone.

The full effect particle size has on the interfacial tension is not entirely understood.^{29,315,342,458} The total impact of the electrokinetic radius (κa) in preventing or stimulating adsorption of ionic surfactants can be investigated in future reflectivity and scattering experiments by varying the particle size, changing the pH, and adding different salt concentrations or combinations of them. The unprecedented resolution of synchrotron-based methods^{38,209,306} to study small nanoparticles' (ensemble) monolayer properties and their interactions with other additives might be supplemented by atomic force microscopy at the liquid interface. Its feasible availability plus temporal and spatial nanoscale resolution makes it an appealing approach for continuing this work. Thus far, it is not applicable to very dilute or weakly adsorbing particle-covered interfaces and may not be suitable for the current investigated system.^{30,240–242}

In case the electric charge of the particles and surfactants is opposite, the electrostatic attraction pulls the native silica nanoparticles from the subsurface region to the liquid interface. Their interactions are synergistic since a hexagonal close-packed layer is formed at intermediate lipid concentrations and significantly alters these particles' hydrophobicity. Therefore, inaccurate numbers were obtained using the additivity model and must be modified to account for surfactant-particle interactions. Octadecanoic acid, the acid conjugate of the aminolipid used in this thesis, can be tested with silica and amine-coated silica particles. One would expect a similar competitive adsorption behavior between the equally charged species based on interfacial pressure. However, the silica particles have an additional adsorption barrier to overcome, which is the negative charge of the liquid interface itself.^{173–177,181,182} The fatty acids' surfactant activity, concentration, and amount of headgroup protonation will affect the capacity for the particles to adsorb.^{37,184,422–424}

Additionally, the adsorption dynamics (i.e., adsorption rate, energy barrier, and diffusion coefficient) can be determined for the single and mixed films, preferably using the pendant drop setup. The sorption kinetics can be extracted from the relaxation profile of the interfacial tension and either fitted by an exponential decay function¹⁷ or through (modified) asymptotic equations of the kinetic adsorption theory, initially developed by Ward and Tordai.^{54,315,319} Systematic area compressions at varying frequencies can also extract the

relaxation dynamics.^{281,371,482} Furthermore, the mixed films' shear rheological monolayer properties can be examined more in detail starting from existing approaches, e.g., building master curves,^{403,411} finding power-law behavior,³⁹⁹ and modifying existing equations.⁴⁰²⁻⁴⁰⁴ Simultaneously, the nonlinear response of densely packed and dilute interfaces can be analyzed at larger strain, strain rate, and frequency.^{354,355} Lastly, organized self-assembling monolayers for mixtures of small and large particles are well-established at the two-dimensional air/water surface.⁶⁴ However, the realization into more complex shapes showing nonrandom particle size organization at the oil/water droplet surface awaits advancement. Using hydrophilic particles and oil-soluble surfactants for this purpose is relatively unexplored. The established surface-sensitive methods in this thesis provide a suitable platform to corroborate theories and optimize formulation conditions.

Additionally, another experimentally-derived macroscopic variable with applicability at the nanoscale was evaluated. The macro- and nanoscopic materials' surface electrochemical properties were used as control parameters over the measured macroscopic contact angles. Chemical equivalency between the colloidal dispersions and planar substrates was determined from identical zeta potentials that were calculated by applying appropriate electrokinetic theories. Subsequently, contact angles obtained from specular reflectometry of the positively charged particle monolayer at the pure air/water and oil/water interface were compared to the macroscopic contact angles. A transition is observed from the advancing to the receding contact angle when oil is added on top of the aqueous subphase. The proposed adsorption mechanism for the positively charged particles is unexplored thus far, but the experimental data lies well within the theoretically calculated wettability parameters.⁶⁵⁰⁻⁶⁵⁴ Also, the silica particles show virtually no affinity for the pure liquid interfaces and are poor emulsifiers when highly charged or dispersed in water.^{344,345} The low macroscopic contact angles observed here may represent the inherent wetting properties of the material. The proposed methodology is executable in many laboratories when a general idea about wettability is needed but cannot predict potential adsorption barriers. The framework can be extended using synchrotron-based (or equally sensitive, such as SHG²⁹⁸ and ellipsometry)^{284,296,297} methods using particle materials that exhibit a higher affinity for interfacial adsorption. For example, adsorption of more hydrophobic, negatively or positively charged particles can clarify the abrupt change from advancing to receding when a denser oil phase is added or the role of the adsorption barrier.⁴⁹

A well-thought-out system design and analytical acumen are recommended for future quantitative (thermodynamic) developments for multicomponent adsorption to liquid interfaces. Several complementary methods substantiated with modified theories will be

necessary to sketch a complete and realistic picture of mixed nanoparticle-surfactant monolayer adsorption.^{42,43,53,55,327} The presented strategies provided good predictions concerning the interfacial particle concentration and particle wettability based on experimentally measured macroscopic variables. Furthermore, the approach exemplified the interactions between the binary adsorbing species, indicating its great potential in the field of colloid and interface science. These fundamental results will significantly contribute to researchers in academia and industry involved with designing and formulating complex colloidal systems encountered in nutrition, cosmetics, agriculture, and pharmacy.

9 Appendix

A.1 Young-Laplace equation in axisymmetric drop shape analysis

Hoorfar et al.⁷³⁷ discretized the Young-Laplace equation and a summary is provided here. Fig. A.1.1 shows a schematic of the sessile and pendant drop and all variables are defined there. With the help of geometrical considerations and definition of arc length (s) the radii of curvature ($R_{1,2}$) can be written as:

$$ds = R_1 d\varphi \Leftrightarrow \frac{1}{R_1} = \frac{d\varphi}{ds} \quad \text{Eq. A1.1}$$

$$\sin\varphi = \frac{x}{R_2} \Leftrightarrow \frac{1}{R_2} = \frac{\sin\varphi}{x} \quad \text{Eq. A1.2}$$

Both radii of curvature are the same at the apex and the pressure difference across the interface is equal to the Laplace pressure:

$$\frac{1}{R_1} = \frac{1}{R_2} = \frac{1}{R_0} = b \quad \text{Eq. A1.3}$$

$$\gamma \left(\frac{1}{R_1} + \frac{1}{R_2} \right) = \gamma \frac{2}{R_0} = 2b\gamma = \Delta p_0 \quad \text{Eq. A1.4}$$

Taking into account the hydrostatic pressure at z :

$$\Delta p(z) = \Delta p_0 + \Delta p_g(z) = 2b\gamma + \Delta\rho g z \quad \text{Eq. A1.5}$$

$$\Rightarrow \frac{d\varphi}{ds} = 2b + l_c z - \frac{\sin\varphi}{x} \quad \text{Eq. A1.6}$$

Where c is defined as the capillary constant $l_c \equiv \frac{\Delta\rho g}{\gamma}$. The Young-Laplace equation can be obtained as a coupled set of dimensionless differential equations in terms of arc length measured from the drop apex:

$$\frac{d\varphi}{ds} = 2b + l_c z - \frac{\sin\varphi}{x} \quad \text{Eq. A1.7}$$

$$\frac{dx}{ds} = \cos\varphi \quad \text{Eq. A1.8}$$

$$\frac{dz}{ds} = \sin\varphi \quad \text{Eq. A1.9}$$

This set can be numerically integrated to give the axisymmetric drop profile using the following boundary conditions: $x(0) = z(0) = s(0)$ and $\frac{d\varphi}{ds} = b$ at $s = 0$.

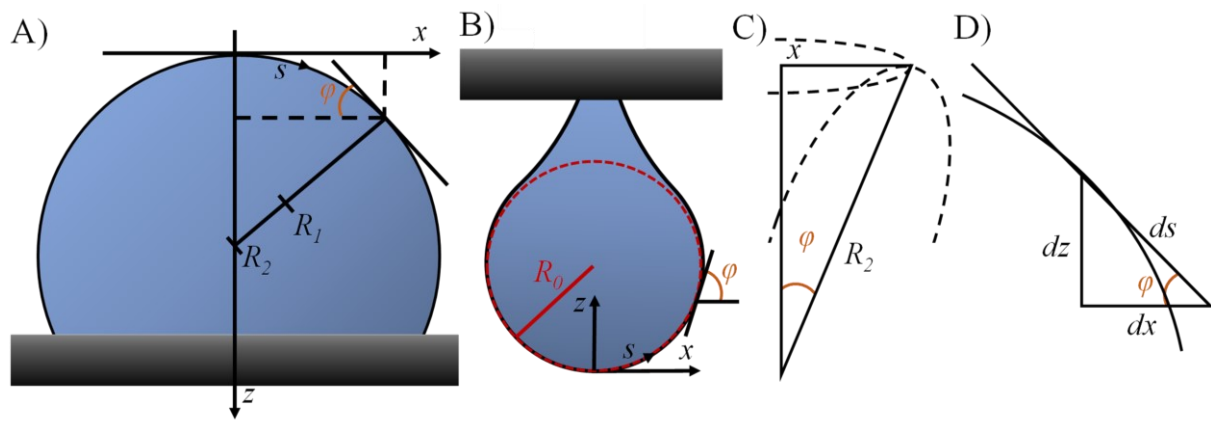


Fig. A.1.1 The applied geometry to formulate the Young-Laplace equation in the axisymmetric case for sessile drops and pendant drops. Figure adapted with kind permission of the *American Chemical Society* from Korhonen et al.¹¹⁸

A.2 Procedure column chromatography

Decane from Honeywell ($\geq 99.7\%$, product no. D901) proved to be of adequate purity and did not require further processing contrarily to decane purchased from Sigma Aldrich ($\geq 99.0\%$, product no. 457116). Confirm the purity of the solvent by measuring the oil/water interfacial tension (as in Fig. 4.13).

A.2.1 Materials

- Acid-washed pro analysis sea sand (product no. 1.07712.1000)
- Active Basic Alumina Oxide 90, Grade I, 0.063-0.200 mm (product no. 1.01076.2000)
Basic alumina particles are chosen as recommended by the manufacturer due to their suitability for the purification of hydrocarbons.
- Stainless steel bottle (Duran group GL45 (product no. DU299016055)
- Separating funnel (product no. SLW2190/08M)

A.2.2 Clean column right before use

- Rinse the column 3x with ethanol absolute and let it completely dry before continuing.
- Stainless steel bottle: rinse with ethanol absolute and let it dry. To be completely sure if all ethanol is removed, perform 3 vacuum cycles in a desiccator.

A.2.3 Pack column and purify decane

- Roll up some cotton wool into a ball and drop in the column. The wool needs to clog the outlet. Turn on the vacuum pump, place your hand (wearing nitrile gloves) on top of the column to seal it and connect the inlet of the pump to the outlet of the column. This creates a vacuum inside. When releasing your hand to allow air inside, the cotton will be pulled deeper. Repeat if necessary.
- Add 0.5-1 cm sea sand. Place a waste beaker below the column and rinse all sides of the column with decane. Close the valve when the column stops dripping.
- Add decane to about $\frac{1}{2}$ of the column.
- The alumina powder sticks to everything so ensure the hood is empty for easy cleaning afterward. Pour the alumina into a separating funnel. Place the funnel on top, open the valve and gently tap the column with a soft stick to remove air bubbles. The alumina should never rise higher than the decane and pour extra if needed. This creates large pores, making the purification process less efficient. In total, the column should be filled about $\frac{2}{3}$ with alumina.
- Add the remaining $\frac{1}{3}$ of decane. Place a clean beaker under the column and open the valve. Once the decane level is at the top of the alumina, close the valve and pour the decane back. Avoid the alumina to make contact with air. This step needs to be repeated at least 12 – 15 times (i.e., 3 times the whole volume of decane).
- After this, the interfacial tension can be tested. More steps may be necessary depending on the number of impurities in the decane and activity of the alumina. Alumina can be

reactivated by dehydration at 360 °C for 5 h or overnight (recommended by manufacturer), and placed under vacuum during cool down.

- If the decane is pure, continue to collect until the dripping stops. Collect this decane in the stainless-steel bottle.
- Place a stopcock on top of the column and connect it to the nitrogen valve. Slowly open the valve and collect the decane that has not been in contact with the nitrogen gas.
- Measure the oil/water tension of this decane before adding it to your stainless-steel bottle to ensure it is pure.
- All the remaining decane in the column can be discarded. Place a waste beaker and let the nitrogen run for 30 min to dry the column.
- Close the stainless-steel bottle and place in the desiccator. Turn on the vacuum pump and close the desiccator when 4 mbar has been reached.
- For the future experiments, pour decane into a clean Duran glass, and subsequently pour this in the cuvette. Extra decane can be recollected in the stainless-steel bottle that can be placed under vacuum as above.

A.2.4 Empty column:

- Turn upside down and tap to remove the alumina.
- Rinse with water to remove any remaining alumina
- Rinse with technical grade ethanol and let it dry.
- If still some alumina is sticking to the sides, pour chloroform followed by ethanol.

A.3 Supplementary content to Chapter 5

This chapter contains the supplementary content of Chapter 5 ‘Reversible adsorption of nanoparticles at surfactant-laden liquid-liquid interfaces,’ and has been adapted with permission from the *American Chemical Society* from the supplementary content of *Langmuir*, 2019, DOI: [10.1021/acs.langmuir.9b01568](https://doi.org/10.1021/acs.langmuir.9b01568).

A.3.1 Calculating the area occupied by one adsorbed particle at the liquid-liquid interface

The area occupied by one nanoparticle with radius a at the interface was calculated via simple geometry (Fig. 5.6A).³² Looking perpendicular at the interface, the depth of particle immersion into the oil (h_o) and water (h_w) phase is calculated as follows:

$$h_o = 2a - h_w \quad \text{A.3.1a}$$

and

$$h_w = a(1 + \cos\theta) \quad \text{A.3.1b}$$

which are dependent on the contact angle (θ) of the adsorbed particle. Using the Pythagorean theorem, the radius of the occupied interface (s) can be derived:

$$a^2 = (h_w - a)^2 + s^2 \quad \text{A.3.1c}$$

and eventually, the replaced interfacial area (A_p) of one adsorbed particle at a specific contact angle is:

$$A_p = \pi s^2 \quad \text{A.3.1d}$$

For example, an APTES-coated silica particle with a contact angle of 40° at the water/decane interface penetrates 10 nm into the decane phase occupying roughly 2100 nm^2 of interfacial space.

A.3.2 Effect of particles and surfactants on the interfacial tension

To find the respective contribution of the surfactants and particles on the interfacial tension (IFT) for the mixed system, Eq. 5.3 becomes:

$$\Delta E_{SF+P} = \Delta \gamma_{SF+P} A_i \quad \text{A.3.2a}$$

where ΔE_{SF+P} and $\Delta \gamma_{SF+P}$ are the difference in free energy and IFT between the pristine oil-water interface and that of the particle-surfactant covered interface, respectively. When the additivity conditions uphold, Eq. 5.2 can be rearranged to find the surfactant's contribution to the IFT:

$$\gamma_{SF} = \frac{\Delta \gamma_{SF+P} A_i - N_P E_P}{A_i} \quad \text{A.3.2b}$$

and subsequently, the effect on the IFT caused by the particles:

$$\gamma_{SF+P} - \gamma_{SF} = \gamma_P \quad \text{A.3.2c}$$

A.3.3 Size and zeta potential of APTES-coated silica between pH 4 and 11

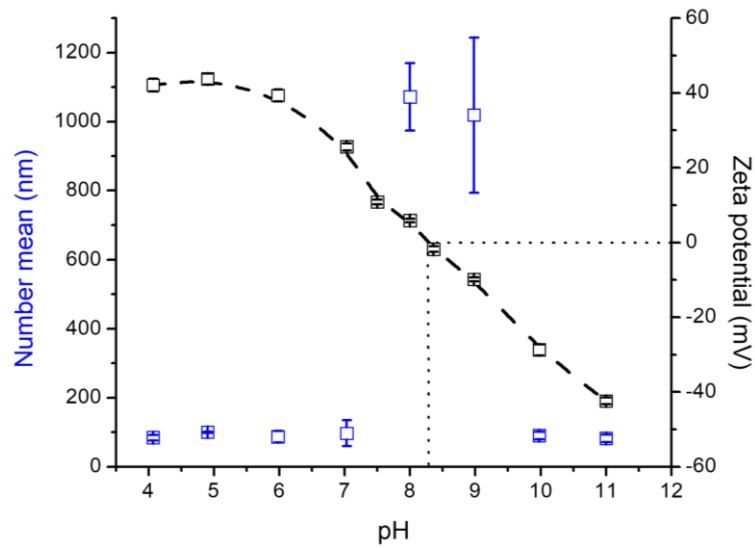


Fig. A.3.1 Size (blue) and zeta potential (black, Smoluchowski model) measurements of 0.1 w/w% APTES-coated silica nanoparticles of 80 nm in 10 mM KCl solution. The isoelectric point lies at a pH of 8.3. At a pH of 6, the particles have a positive potential of +39.3 mV, number mean value of 86.94 (± 16.43) nm, and PDI 0.183 (± 0.003).

A.3.4 The storage modulus of 0.5 mM ODA and 2.5 mM ODA, with and without particles

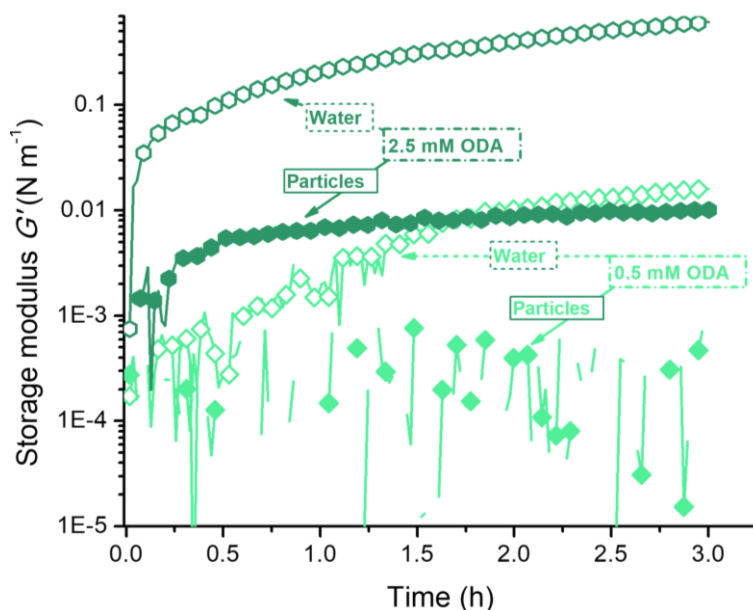


Fig. A.3.2 Storage modulus (G') of 0.5 mM and 2.5 mM ODA, without (open) and with (full) 1 w/w% APTES-coated silica nanoparticles (pH 6). The moduli decrease when particles are present in the subphase. Also, the plateau of 0.5 mM with water lies approximately halfway through the detection window, i.e., between 0.1 mM and 1 mM or above.

A.3.5 The storage modulus of 1 mM ODA and varying amounts of KCl

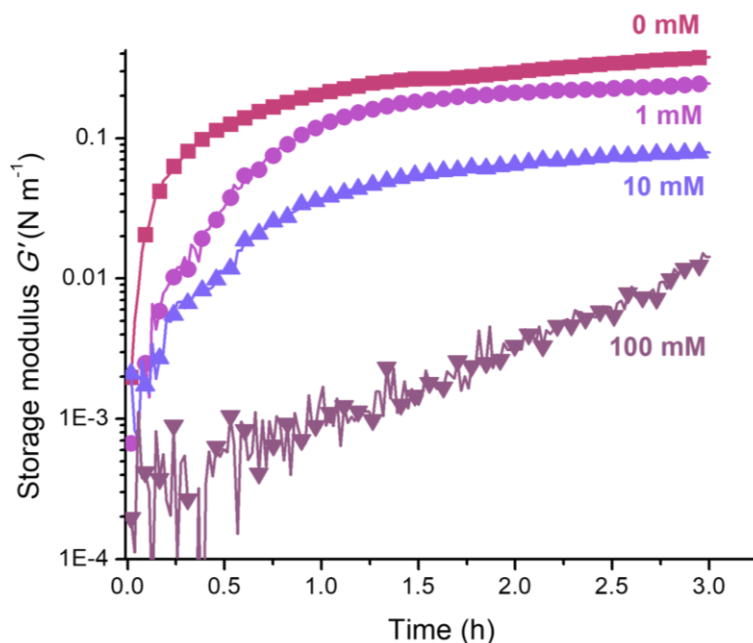


Fig. A.3.3 Storage modulus (G') from interfacial shear rheology of water-decane interfaces at pH 6 and 1 mM ODA. The different concentrations shown in the graph are the amount of KCl added to the subphase. Film formation is impaired, and lower moduli are obtained with increasing ionic strength.

A.3.6 The streaming potential of flat substrates

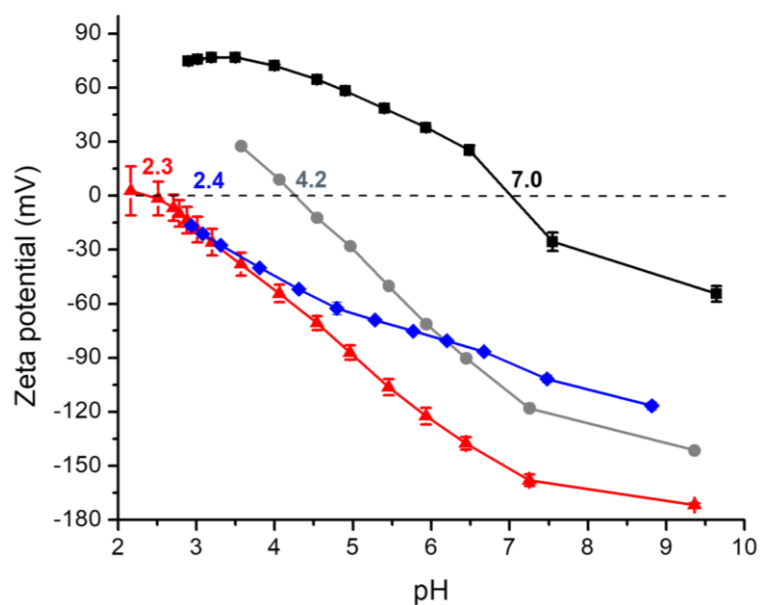


Fig. A.3.4 Streaming potential curves of double-sided adhesive tape (grey circles), activated borosilicate glass (red triangles), TEOS-coated borosilicate glass (blue diamonds), and APTES-coated silica thin film (black squares). The point of zero charge is shown for each sample in the graph with a standard deviation at or below 0.25 pH units.

A.4 Supplementary content to Chapter 6

This chapter contains part of the supplementary content of Chapter 6 ‘Synergistic and competitive adsorption of hydrophilic nanoparticles and oil-soluble surfactants at the oil-water interface’, and has been adapted with permission from the *American Chemical Society* from the supplementary content of *Langmuir*, 2021, DOI: [10.1021/acs.langmuir.1c00559](https://doi.org/10.1021/acs.langmuir.1c00559).

A.4.1 Ninhydrin calibration curve

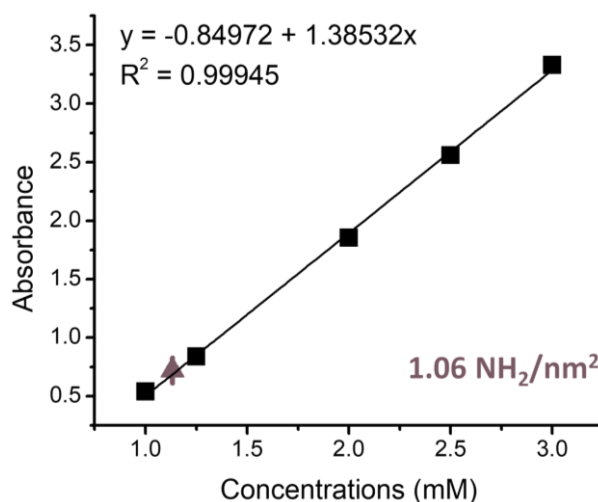


Fig. A.4.1 A calibration curve for the ninhydrin assay was obtained by diluting APTES in ethanol:0.027 v/v% acetic acid. Error bars of the calibration data points are within the symbols. The synthesized APTES-coated silica particles have an amine density of 1.06 groups per nm², calculated for a fixed diameter of 18.9 nm and mass density of 1.9 g cm⁻³.

A.4.2 Experimental considerations for X-ray reflectivity at liquid-liquid interfaces

The intensities provided by laboratory reflectometers are comparatively low ($R \sim 10^{-8}$) to the ones available at insertion device beamlines of third-generation synchrotron facilities ($R \sim 10^{-10}$). In the latter case, this increases the spatial resolution by extending the range of the momentum transfer Q_z , meaning that the penetration depth increases. Also, a significant portion of the X-ray intensity is lost through absorption in the bulk liquid, which necessitates sufficiently high energies (≥ 20 keV). However, in this range the brilliance¹ decays rapidly and needs to be optimized for the specific system (typically 20 – 35 keV).^{713,714} Intensities around

¹ Brilliance is proportional to the emitted flux divided by the angular deviations and beam size. By definition it is the number of photons per second in a given energy range normalized to the size of the source and to the solid angle under which the radiation is emitted (photons s⁻¹ mrad⁻² mm⁻² per 0.1% radiation bandwidth, e.g., 1 eV at 10 keV).⁷⁵⁴

70 keV for studying nanoparticle adsorption at buried^{II} interfaces ensures a sufficient amount of signal is being transmitted through the bulk liquid (i.e., high X-ray penetration power) and enables detection of diffuse scattering at high angles.^{38,209} Higher energies significantly lower the photoelectric adsorption but increase the radiation damage due to Compton scattering that can result in bond breaking and secondary beam damage from free radicals.^{713,714} Studies on biological systems showed that energies in the range of 24 – 34 keV provide an optimum diffraction intensity while minimizing the radiation damage.^{738,739}

The following paragraph includes additional information on the synchrotron diffractometer at DESY specialized to study planar liquid-liquid interfaces. Motor-induced vibrations from the beam-tilter and detector unit can be eliminated as the sample stage for the liquid surface can be mechanically decoupled, which allows faster data collection after motor manipulations. The horizontal direction defines the probed width given by the horizontal beam size, while the vertical beam defines the length probed during measurements (i.e., beam footprint). For solids, the horizontal incoming X-ray beam impinges on the sample and subsequently rotated to vary the incoming angle. Since liquids cannot be tilted, two crystals scattering in Bragg geometry are rotated instead to vary the incident angle from zero to a maximum angle (α_{max}) onto the liquid surface, which is defined by the difference in scattering angles of crystal 1 and crystal 2 ($\alpha_{max} = 2(\theta_2 - \theta_1)$). Both crystals can be aligned independently. A rotating slit system placed after the second crystal is kept vertically oriented (i.e., parallel to the sample surface), which significantly reduces the background signal and allows beam footprint optimization at the sample for low incident angles (i.e., good quality data around the critical angle).^{713,714} A main challenge with reflectivity measurements of liquid surfaces is that a macroscopically curved surface alters the profile of the reflected beam, i.e., reflecting at different angles. Additionally, the incident and reflected beam will interfere if a meniscus is formed at the cell walls. Using large dimensions of the cell wall reduces the curvature and less beam interference can occur for menisci further away from the irradiated area.⁷⁴⁰

The background is usually measured separately (except when area detectors are used that measure the diffuse scattering) as the specular signal also contains background, which can originate from different sources such as detector noise, air/oil scattering, or sample-related diffuse scattering. It is an important step since it influences the roughness parameters and is

^{II} A buried interface is not just between water and an immiscible oil. The cellular membranes in our bodies functioning at physiological conditions and artificially bonded wafers in microelectronics are other examples of buried interfaces.

obtainable by measuring an ‘offset’ scan, where Q_z is measured at a small offset angle with respect to the surface, rather than the case shown in (Fig. 4.18, Q_z is perpendicular to the surface). It is usually obtained by executing several rocking or transverse scans, where the detector is fixed while rocking the sample through the specular ridge at the offset angle. Alternatively, several points on the specular ridge are selected (by changing the incoming angle) and rocking scans are performed on each point. Subsequently, the rocking curves are fitted to a Gaussian curve followed by linear interpolation between the different data points before it is subtracted from the specular scan. This latter method is more accurate because there is no fixed and arbitrary offset angle and more than one point is taken for determination of the background scan.⁶⁹²

A.4.3 X-ray reflectivity cell setup



Fig. A.4.2 Images of the setup for measuring reflectivity at the oil-water interface. A) The outer cell is made out of aluminum with two opposing windows and covered with Kapton. B) The upper part of the cylindrical-shaped Delrin cup was made as thin as possible ($\sim 200 \mu\text{m}$), while the bottom part for the aqueous subphase was thicker to create an inner edge that would pin the meniscus (red stripe-dotted line) with an inner diameter of 60 mm. C) The top part could be closed off hermetically if flushing with inert gas was required but was only used as a cover.

A.4.4 Optimization process of the reflectivity data

After creating the reflectivity curves from the raw data utilizing a Python script by choosing the appropriate region of interest, the standalone *REFLEX*⁶⁹⁶ software was used. The reflectivity was simulated from multilayers by considering the interfacial roughness, slab thickness, and scattering length density. Pure air/water and oil/water scans were used for background correction of the complex liquid interfaces (i.e., with surfactants and particles). In the latter case, a 3-slab model was used (Fig. A.4.3). The scattering length densities of the surrounding media (air = 0, water = $0.9346 \times 10^{-5} \text{ \AA}^{-2}$, decane = $0.7080 \times 10^{-5} \text{ \AA}^{-2}$)⁷⁴¹ were fixed. At the same time, those for silica were kept within physical boundaries. Only the material electron density of silica was allowed to vary, while the roughness and thickness were highly constrained (e.g., roughness not more than half the layer thickness ($\sigma \leq 1/2d_{\text{layer}}$); maintain similar thickness for each specific slab between different measurements). Although higher

densities are reported for macroscopic silica,^{38,591} the choice for a mass density of 1.9 g cm^{-3} for sol-gel synthesized particles⁶⁹⁸ has also been validated in these reflectivity experiments. Under certain circumstances, the formation of a close-packed monolayer of nanospheres was observed at the oil/water interface. In between these tightly packed particles, they are surrounded with liquid or gas due to their curvature, and the material electron density in these slabs is a combination of all scattering components. A maximum electron density would only be physically possible around their contact points. This value has been extracted from the fitting procedure in *REFLEX*,⁶⁹⁶ which agreed with a material density of 1.9 g cm^{-3} and excludes higher mass densities for silica.

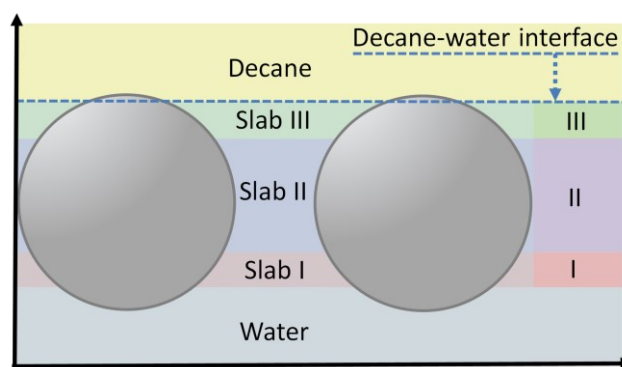


Fig. A.4.3 The particle films at the oil-water interface were approximated by a 3-slab model combined with an error function roughness at each slab interface. This approach has been taken to describe the curvature of the particles adequately. In this respect, the relative thicknesses of the slabs and the transitions between them are arbitrary and cannot be interpreted independently.

One disadvantage with X-ray reflectivity modeling is that it does not guarantee the uniqueness of the solution, meaning that several simulated curves can fit the experimental profile obtained from a different parameter set. This can happen because only the intensity and not the phase of the reflected wave are measured.⁷⁴² It was possible to find a second set of solutions where the particles appeared highly hydrophobic. However, the fit quality determined from the reduced chi-squared value (χ^2) for the hydrophobic particles was lower. Even though silica particles are known to be highly hydrophilic, a stochastic model-independent approach (Stochfit) requiring only a limited amount of input parameters was tested to exclude potential bias.⁷⁴³ The simulated reflectivity and normalized-to-water electron density plots have a numerical instability for unknown reasons (Fig. A.4.4A and B). Nevertheless, the electron density curves for the hydrophilic nanoparticles simulated in Stochfit⁷⁴³ (Fig. A.4.4B) and *REFLEX*⁶⁹⁶ (Fig. A.4.4C, black line) have a similar shape and position at the interface, contrarily to the hydrophobic particles (Fig. A.4.4C, red line). In the latter case, the smaller shoulder centered around the interface could indicate the presence of the lipid ODA. However, the tabulated scattering length density of ODA⁷⁴¹ is $0.8359 \times 10^{-5} \text{ \AA}^{-2}$ and therefore cannot

achieve values higher than unity in the normalized electron density plot of Fig. A.4.4C. Therefore, this second shoulder is unrealistic, and the lipid signal in the hydrophilic case is most likely superimposed by the stronger scattering of silica.

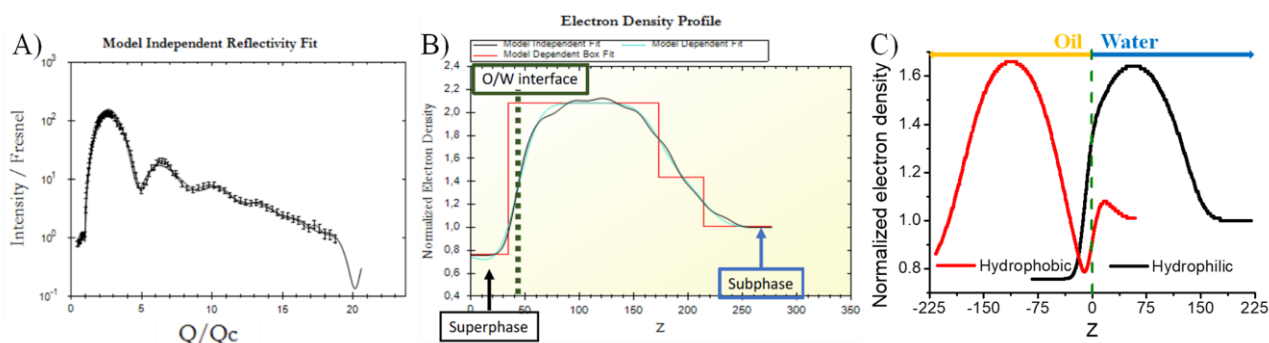


Fig. A.4.4 A) Model-independent fitting of the Fresnel-normalized reflectivity for 0.1 w/w% silica particles and 1 mM ODA using Stochfit.⁷⁴³ There is a good overlap of the experimental data and the fit, except at larger Q/Q_c , which may result in instability (oscillations) in the electron density plot. B) The resulting electron density profile (black) is normalized to water (subphase) with lower electron density for decane (superphase), and the dotted line gives the oil/water interface. C) Normalized electron density of the same sample modeled in *REFLEX*⁶⁹⁶ for hydrophobic (red) and hydrophilic particles (black) adsorbed at the oil/water interface (green dotted line).

A.4.5 Interfacial tension and dilational rheology in absence of lipids and surface pressure at different lipid concentrations.

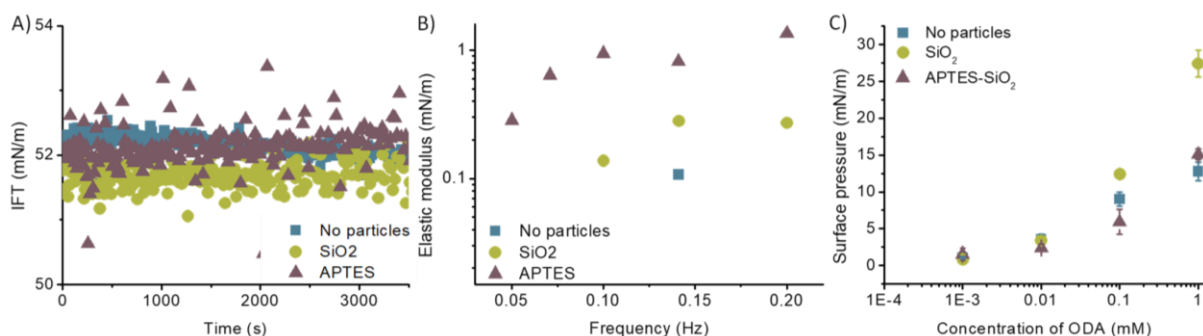


Fig. A.4.5 A) The interfacial tension over time of a drop of water at pH 5.8 (squares), 0.1 w/w% silica (circles), and APTES-coated silica particles (triangles) formed in decane without lipids. B) The corresponding dilational elastic moduli of the three systems in absence of lipids. C) The surface pressure and standard deviation of the measurements shown in Fig. 6.5.

A.4.6 Fitting values *REFLEX*

Table A.4.1 Fitting values from reflectivity fits in Fig. 6.2 for the pure air-water and oil-water interfaces and with the addition of silica or APTES-coated silica nanoparticles in absence of octadecyl amine (ODA). SLD stands for scattering length density, σ represents the roughness between each layer and d is the thickness of the corresponding layers. Colors of each column relate to Fig. A.4.3.

Pristine air-water surface and oil-water interface (no ODA)											
Layer	SLD subphase ($\times 10^{-6} \text{ \AA}^{-2}$)			SLD superphase ($\times 10^{-6} \text{ \AA}^{-2}$)				σ (\AA)			
Air-water	9.346			0				3.21 \pm 0.18			
Decane-water	9.346			7.08				3.57 \pm 0.25			
APTES-coated SiO ₂ nanoparticles at the pristine air-water surface and decane-water interface (no ODA)											
Mono-layer of APTES-coated silica NPs	SLD NP slab I ($\times 10^{-6} \text{ \AA}^{-2}$)	SLD NP slab II ($\times 10^{-6} \text{ \AA}^{-2}$)	SLD NP slab III ($\times 10^{-6} \text{ \AA}^{-2}$)	σ water – NP slab I (\AA)	σ NP slab I – II (\AA)	σ NP slab II – III (\AA)	σ NP slab III – decane (\AA)	d NP slab I (\AA)	d NP slab II (\AA)	d NP slab III (\AA)	d_{total} (\AA)
Air-water	10.89 \pm 0.11	11.27 \pm 0.08	9.65 \pm 0.10	23.35 \pm 0.88	20.85 \pm 1.31	24.10 \pm 1.22	3.46 \pm 0.21	41.11 \pm 1.04	84.55 \pm 1.51	29.53 \pm 0.84	155.19 \pm 0.93
Decane-water	10.69 \pm 0.12	11.28 \pm 0.09	9.41 \pm 0.06	21.99 \pm 0.77	19.17 \pm 0.84	21.42 \pm 0.98	4.81 \pm 0.23	39.99 \pm 1.11	85.14 \pm 1.47	30.74 \pm 0.68	155.87 \pm 1.21

Table A.4.2 Fitting values from reflectivity fits in Fig. 6.3 for the oil-water interface with silica or APTES-coated silica nanoparticles in presence of octadecyl amine (ODA). SLD stands for scattering length density, σ represents the roughness between each layer and d is the thickness of the corresponding layers. Colors of each column relate to Fig. A.4.3.

Synergistic adsorption - SiO ₂ nanoparticles with ODA											
Concentration	SLD NP slab I (x 10 ⁻⁶ Å ⁻²)	SLD NP slab II (x 10 ⁻⁶ Å ⁻²)	SLD NP slab III (x 10 ⁻⁶ Å ⁻²)	σ water – NP slab I (Å)	σ NP slab I – II (Å)	σ NP slab II – III (Å)	σ NP slab III – decane (Å)	d NP slab I (Å)	d NP slab II (Å)	d NP slab III (Å)	d _{total} (Å)
0.01 mM ODA	12.18 ± 0.08	13.98 ± 0.13	11.24 ± 0.09	18.29 ± 0.85	18.88 ± 0.61	20.30 ± 1.12	5.33 ± 0.26	38.10 ± 0.53	85.57 ± 1.20	23.49 ± 0.34	147.16 ± 1.12
0.1 mM ODA	13.23 ± 0.11	15.53 ± 0.06	12.52 ± 0.06	17.87 ± 0.74	18.95 ± 0.57	19.10 ± 0.93	6.57 ± 0.22	38.58 ± 0.57	81.14 ± 1.34	24.35 ± 0.22	144.07 ± 0.89
1 mM ODA	13.24 ± 0.07	15.39 ± 0.10	12.72 ± 0.09	18.71 ± 0.57	18.12 ± 0.55	18.58 ± 0.99	8.57 ± 0.22	36.65 ± 0.53	83.29 ± 0.88	24.33 ± 0.22	144.27 ± 0.87
Competitive adsorption - APTES-coated SiO ₂ nanoparticles with ODA											
Concentration	SLD NP slab I (x 10 ⁻⁶ Å ⁻²)	SLD NP slab II (x 10 ⁻⁶ Å ⁻²)	SLD NP slab III (x 10 ⁻⁶ Å ⁻²)	σ water – NP slab I (Å)	σ NP slab I – II (Å)	σ NP slab II – III (Å)	σ NP slab III – decane (Å)	d NP slab I (Å)	d NP slab II (Å)	d NP slab III (Å)	d _{total} (Å)
0.01 mM ODA	10.32 ± 0.04	10.94 ± 0.12	9.49 ± 0.24	21.05 ± 1.12	18.82 ± 1.19	21.01 ± 1.60	3.84 ± 0.27	39.52 ± 1.11	83.53 ± 1.57	31.23 ± 0.62	154.28 ± 1.66
0.1 mM ODA	10.78 ± 0.24	11.54 ± 0.35	9.90 ± 0.07	22.26 ± 0.57	18.54 ± 0.51	21.66 ± 1.15	4.04 ± 0.20	38.75 ± 0.57	83.75 ± 1.53	30.08 ± 0.58	152.58 ± 1.15
1 mM ODA	11.16 ± 0.06	11.81 ± 0.09	10.09 ± 0.07	22.59 ± 0.60	18.87 ± 0.63	21.26 ± 0.57	5.32 ± 0.23	37.75 ± 0.54	82.21 ± 0.57	30.08 ± 0.58	150.04 ± 1.13

A.4.7 The amount of interfacial area occupied by adsorbed nanoparticles

The average percentage of area occupied by silica ($a = 8.9$ nm) and APTES-coated silica ($a = 9.45$ nm) nanoparticles for different concentrations of octadecyl amine (ODA) is calculated from the water immersion depth (h_w) and particle coverage (Θ_{XRR}) obtained through fitting of the electron density plots. A hexagonal close-packed monolayer occupies 90.69% of the interface and equating this to 100% coverage gives Θ_{100} .

[ODA] (mM)	Silica			APTES-silica		
	h_w (nm)	Θ_{XRR}	Θ_{100}	h_w	Θ_{XRR}	Θ_{100}
0	/	/	/	17.46	0.2726	0.3006
0.01	16.38	0.6709	0.7398	17.55	0.2069	0.2311
0.1	16.20	0.8930	0.9847	16.98	0.2751	0.3034
1	16.18	0.8867	0.9778	16.90	0.3515	0.3875

First, the interfacial area ($A = \pi s^2$) one particle occupies is calculated based on the equations in Appendix A.3.1, where $s = \sqrt{a^2 - (h_w - a)^2}$ is the radius of the occupied interface:

[ODA] (mM)	Silica		APTES-silica	
	s (nm)	A (nm ²)	s (nm)	A (nm ²)
0	/	/	5.01	78.85
0.01	4.82	72.99	4.87	74.51
0.1	5.09	81.39	5.71	102.43
1	5.11	82.03	5.81	106.05

Taking the ratio of the experimental particle area (A) and that of a particle of 90° in the hexagonal close-packed configuration (A_{HCP}) gives the area fraction occupied by particles. Since the exact coverage is known from the reflectivity measurements, the fraction of interfacial area occupied by particles ($A_{100\text{-NP}}$) and free interface ($A_{100\text{-IF}}$) can be estimated from Θ_{100} .

[ODA] (mM)	Silica			APTES-silica		
	A/A_{HCP}	$A_{100\text{-NP}}$	$A_{100\text{-IF}}$	A/A_{HCP}	$A_{100\text{-NP}}$	$A_{100\text{-IF}}$
0	/	/	/	0.2811	0.0845	0.9155
0.01	0.2933	0.2170	0.7830	0.2656	0.0614	0.9386
0.1	0.3270	0.3220	0.6780	0.3651	0.1108	0.8892
1	0.3296	0.3222	0.6778	0.3780	0.1465	0.8535

A.5 Supplementary content to Chapter 7

This chapter contains part of the supplementary content of Chapter 7, ‘Assessment of nanoparticle immersion depth at liquid interfaces from chemically equivalent macroscopic surfaces.’ It has been adapted with permission from *Elsevier* from the supplementary content of *Journal of Colloid and Interface Science*, 2021, DOI: [10.1016/j.jcis.2021.12.113](https://doi.org/10.1016/j.jcis.2021.12.113).

A.5.1 Scanning (SEM) and transmission electron microscopy (TEM)

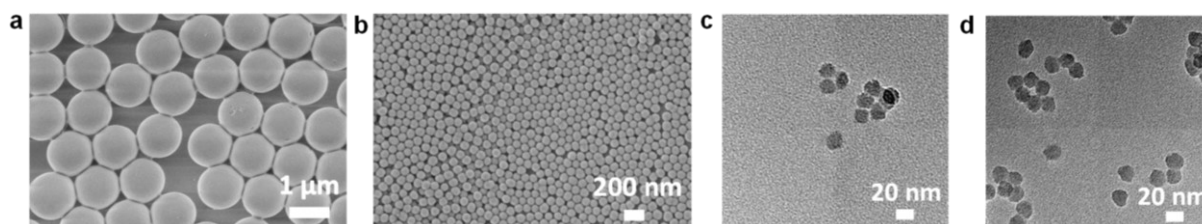


Fig. A.5.1 Electron microscopy images of spherical particles. **a, b** are SEM images of 1154 ± 53 nm and 86.4 ± 9.5 nm silica, respectively. **c, d** are TEM images of 17.8 ± 2.7 nm and 18.9 ± 2.6 nm silica and APTES-coated silica, respectively.

A.5.2 Optimization parameters for dip coating particulate films

Below are SEM images of the particulate (PF) films where 80 nm silica NPs are added to the sol-gel prior to dip coating and shows the influence of particle concentration (Fig. A.5.2a), the effect of adding KCl to the sol-gel (Fig. A.5.2b), varying the withdrawal speed (Fig. A.5.2c), and the presence of the particles after the streaming current experiment (Fig. A.5.2d).

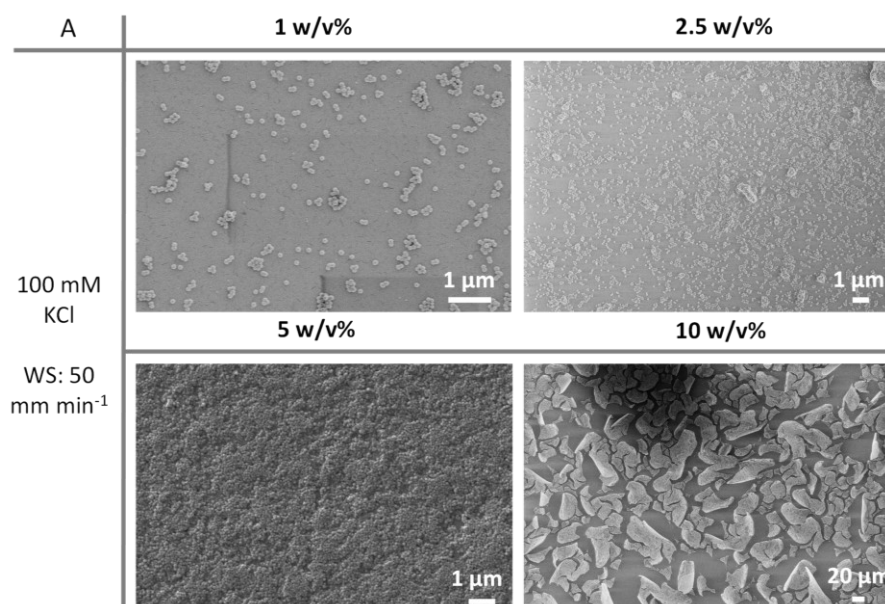


Fig. A.5.2a The effect of particle concentration at fixed 100 mM KCl and withdrawal speed (WS) of 50 mm min^{-1} . Concentrations below 5 w/v% give incomplete surface coverage with the 80 nm silica particles, while higher concentrations lead to film cracking.

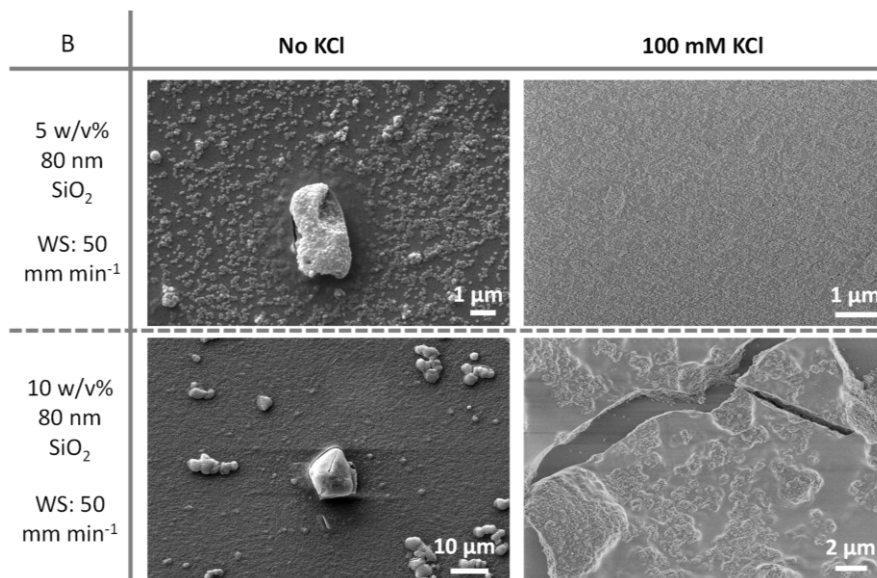


Fig. A.5.2b The influence of KCl at fixed withdrawal speed (WS) of 50 mm min⁻¹. At 5 w/v%, absence or presence of KCl causes the packing density of the 80 nm silica nanopowder at the film surface to be incomplete or complete, respectively. At 10 w/v%, a dense particle layer is obtained without KCl, while the film cracks when KCl is added. Aggregates are also visible in the absence of KCl and with higher particle concentrations, more aggregates are observed.

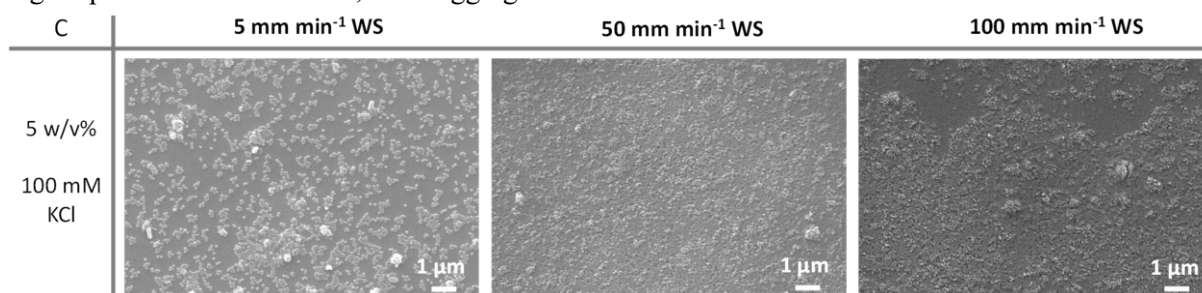


Fig. A.5.2c The effect of withdrawal speed (WS) at fixed particle concentration of 5 w/v% and 100 mM KCl. An incomplete particle coverage is obtained at a WS of 5 mm min⁻¹, while at 100 mm min⁻¹ mixed regions exist of densely packed particles and voids. A dense surface layer is obtained with a WS of 50 mm min⁻¹.

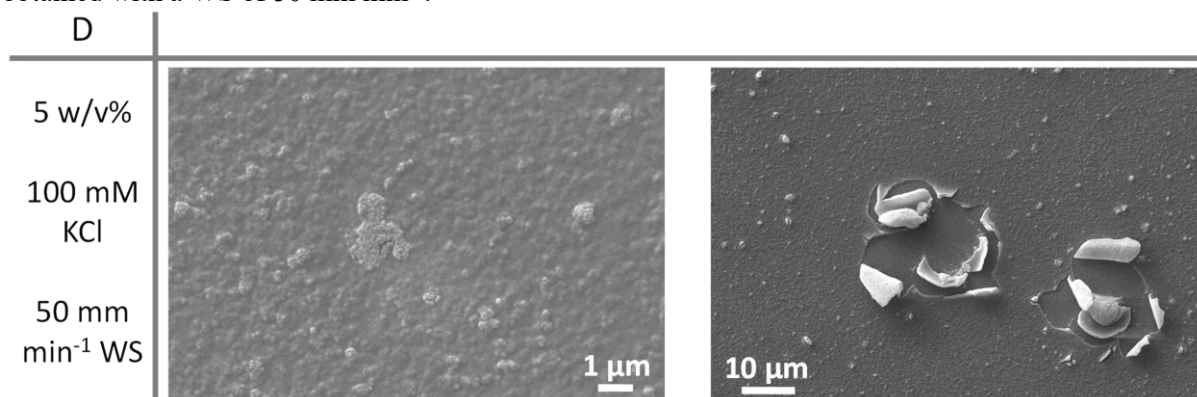


Fig. A.5.2d Images were made after the streaming current experiment. The particles remain present on the surface under liquid shear. However, defects in the coating are visible that likely occur where larger aggregates were initially trapped.

A.5.3 Determination of electrokinetic mobility formula for electrophoresis

The experimental electrophoretic mobilities are given in Table A.5.1.

Table A.5.1 Electrophoretic mobilities for 0.1 w/w% particles in 10 mM KCl at different pH. Units of μ is $\text{m}^2 \text{Vs}^{-1} \times 10^{-8}$.

SiO ₂						APTES-SiO ₂	
1000 nm		80 nm		18 nm		19 nm	
pH	μ	pH	μ	pH	μ	pH	μ
3.08	-0.262 ± 0.004	3.00	-0.445 ± 0.057	3.06	-0.145 ± 0.047	3.10	3.052 ± 0.155
3.99	-0.674 ± 0.021	4.08	-1.297 ± 0.132	4.10	-0.596 ± 0.052	4.11	2.991 ± 0.169
4.89	-1.481 ± 0.061	4.98	-1.654 ± 0.092	5.00	-1.394 ± 0.088	5.13	2.705 ± 0.217
6.20	-2.648 ± 0.060	6.22	-2.728 ± 0.132	5.96	-1.810 ± 0.133	5.96	2.322 ± 0.136
6.93	-3.085 ± 0.579	6.99	-2.968 ± 0.127	7.03	-2.366 ± 0.374	6.90	0.9095 ± 0.093
8.30	-4.209 ± 0.120	7.86	-3.593 ± 0.189	8.01	-2.643 ± 0.269	7.94	-0.337 ± 0.004
8.90	-5.177 ± 0.281	8.88	-4.495 ± 0.432	8.95	-3.052 ± 0.608	8.99	-1.787 ± 0.089
9.97	-5.251 ± 0.364	10.07	-4.875 ± 0.677	10.10	-3.303 ± 0.656	9.98	-2.640 ± 0.137
10.98	-5.418 ± 0.374	10.90	-4.378 ± 0.430	10.97	-2.743 ± 0.154	10.98	-2.857 ± 0.128

Fig. A.5.3 shows the scaled μ vs ζ potential plot (i.e. E_m vs $\bar{\zeta}$) that emphasizes the influence of the relaxation effect (OHW and Ohshima) and stagnant layer conduction (SLC in OHW) based on the particles shown in Table A.5.1. The former influence causes a maximum in the mobility (μ_{max}), while the latter lowers the mobility and shifts μ_{max} to larger $\bar{\zeta}$ when κa increases (for $\kappa a \geq 2.75$).^{619,625} All approximate expressions converge to Smoluchowski (Eq. 4.4) when $\kappa a \rightarrow \infty$ and to Hückel (Eq. 4.5) when $\kappa a = 0$ (black straight lines). These two limiting cases behave linearly by ignoring the additional influences, which can lead to a significant underestimation of μ at intermediate κa values. With $\kappa a = 3$, Ohshima's formula (Eq. 4.10) is only adequate for $\bar{\zeta} < 4$ while the OHW formula (Eq. 4.10) is appropriate for all $\bar{\zeta}$.

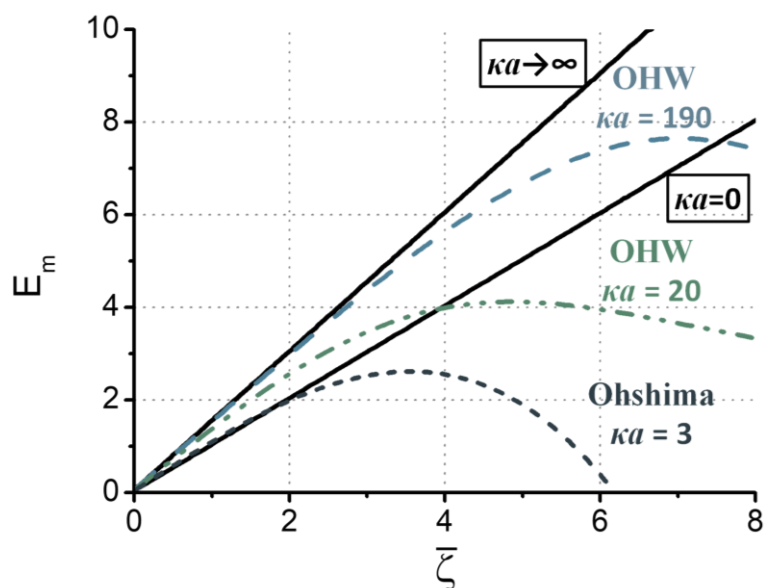


Fig. A.5.3 The scaled electrophoretic mobility (E_m) plotted against the scaled zeta potential ($\bar{\zeta}$). The approximate analytical expressions designed by Ohshima-Healy-White (OHW)⁶²³ and Ohshima⁶³³ are valid for dilute systems when $10 \leq \kappa a \leq \infty$ for all $\bar{\zeta}$ or $1 < \kappa a < 10$ with limits of $\bar{\zeta}$ depending on κa , respectively. When $\kappa a \rightarrow \infty$ or $\kappa a = 0$, approximate solutions converge to the mobility formulas designed by Smoluchowski¹⁷⁸ or Hückel,⁶¹⁵ respectively.

A.5.4 Choosing the appropriate κa

Table A.5.2 summarizes hydrodynamic size from dynamic light scattering (DLS), sonication time, and the chosen particle radius a to obtain κa with the appropriate approximate formula discussed above. Sizes obtained with TEM are generally used to determine a for samples with a low polydispersity index (PDI), which corresponds well to the hydrodynamic sizes obtained with the number distribution in the absence of steady-state size fractions (for 1000 nm, 18 nm, and 19 nm, data not shown).⁶⁰⁸ Fig. A.5.4 shows how the magnitude of the ζ potential varies with different electrophoretic mobility formulas, where the ζ potential of the approximate equations (OHW [Eq. 4.10] and Ohshima [Eq. 4.10]) generally lies between the extremes with infinite (Smoluchowski, red solid line, [Eq. 4.4]) and zero (Hückel, blue dashed line, [Eq. 4.5]) κa . As expected, the ζ potential for the 1000 nm silica can be adequately described by Smoluchowski and only starts to deviate slightly above 50 mV (or $2\bar{\zeta}$) when using the OHW approximation (see Fig. A.5.3). Due to their large size, SLC is negligible at all pH values (≤ 0.05), obtained from F in Eq. 4.10a). The 1000 nm silica particles serve as a reference for the magnitude of the ζ potential for the two smaller particle sizes, considering they all have equal surface chemistry and surface conductance is negligible with sufficient background electrolyte (≥ 10 mM monovalent salt).^{625,629,630} A similar underestimation of the ζ potential above 50 mV also occurs for the 18 nm silica and 19 nm APTES-coated silica NPs using Ohshima when compared to Hückel, despite having non-zero κa values. For the 80 nm

silica particles with a PDI of 0.314 at pH \sim 5.8, choosing $\kappa a = 13.16$ ($a = 40.31$ nm from number distribution) and using OHW or Ohshima's formula gives an unrealistic ζ potential at pH \sim 10 of -104 mV⁷⁴⁴ or falls outside the scaled μ vs ζ potential plot (i.e. no value exists for this μ), respectively. a can be determined from electron microscopy methods such as TEM and SEM, but it is more appropriate to estimate a from the Z-average for polydisperse samples since μ is based on the ensemble of dispersed material. This then gives $\kappa a = 20.44$ with ζ potentials close to the 1000 nm silica.

The proposed equations assume the 'hard sphere' approach with the shear plane localized invariably in the vicinity of the particle surface. However, the silica surface in aqueous suspension develops a gel-type layer that can extend up to a few nanometers in thickness. It is composed of solvent and a loose network of protruding colloidal material characteristic of a thin surface conductance layer.^{544,627} These effects become very pronounced at low electrolyte concentrations (≤ 1 mM)⁶²⁷ and with increasing particle volume fractions (Φ).⁷⁴⁵ The latter parameter is not included in the set of equations and could overestimate μ at high ζ potentials. A minimum silica particle concentration of 0.07 w/w% is necessary to obtain reliable experimental μ values,⁷⁴⁶ which is why the concentrations were fixed at 0.1 w/w% particles dispersed in 10 mM KCl. For an estimated silica particle density of 1.9 to 2.1 g cm⁻³,⁶⁹⁸ Φ is roughly 0.053 to 0.048, respectively. From the numerical results, the volume fraction and intermediate salt concentration used here cause minor hydrodynamic particle-particle interactions (i.e., electric double layer overlap) and increases in conductivity, proving the validity of Eq. 4.10 and Eq. 4.10 with negligible errors.⁷⁴⁷⁻⁷⁴⁹

Table A.5.2 The Z-average, hydrodynamic diameter from number distribution, polydispersity index (PDI), sonication time, a , their estimated radius from TEM* or Z-average** and κa with corresponding electrokinetic model for the different particle types measured at 0.1 w/w% in 10 mM KCl and pH \sim 5.8 at 25 °C. OHW = Ohshima-Healy-White.

Particle type	Z-average (nm)	Number distribution (nm)	PDI	Sonication time	a (nm)	κa	Electrokinetic model
1000 nm silica (powder)	1266 \pm 5.29	1170 \pm 199.40	0.159	30 min	577*	189.78	OHW ⁶²³
80 nm silica (powder)	122.80 \pm 1.30	80.62 \pm 21.05	0.314	60 min	62.15**	20.44	OHW ⁶²³
18 nm silica (Stöber-Watanabe) ⁵³⁴	41.06 \pm 0.58	22.35 \pm 6.83	0.154	0 min	8.90*	2.93	Ohshima ⁶³³
19 nm APTES-coated silica (Stöber-Watanabe) ⁵³⁴	41.31 \pm 0.88	25.76 \pm 5.43	0.228	0 min	9.45*	3.11	Ohshima ⁶³³

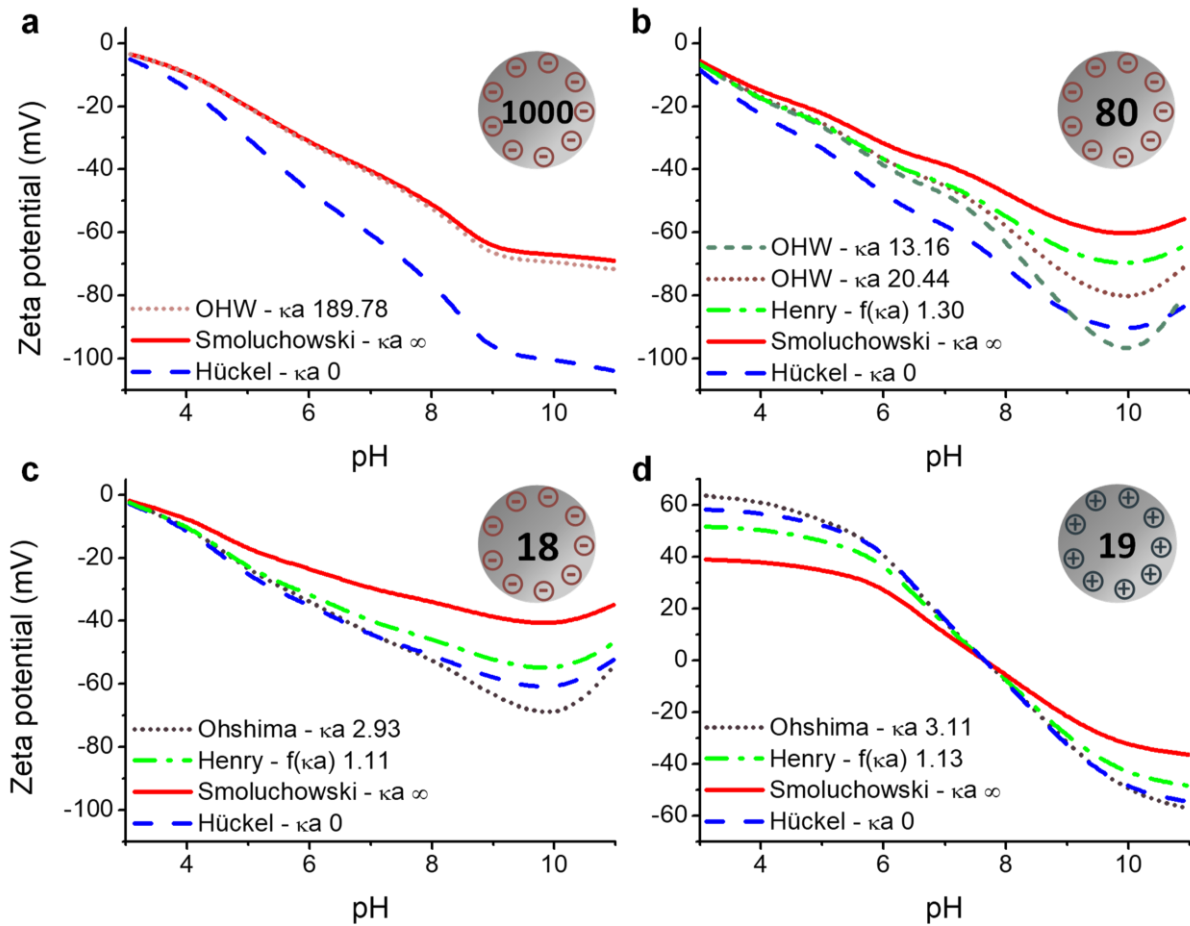


Fig. A.5.4 Influence of electrophoretic mobility conversion on the magnitude of the zeta potential for 0.1 w/w% dispersions measured with ELS of **a**, 1000 nm SiO₂ **b**, 80 nm SiO₂ **c**, 18 nm SiO₂ and **d**, 19 nm APTES-SiO₂ with a background electrolyte solution of 10 mM KCl. Symbols and standard deviations have been removed for clarity. The $f(\kappa a)$ from Henry's function (Eq. 4.7) is determined from the hydrodynamic radius and electrolyte concentration and calculated in the software of the ZetaSizer NanoZSP.

A.5.5 Electrokinetic charge density

With knowledge about the ζ potential and ionic strength for a curved surface, the numerical solution of the Poisson-Boltzmann equation (PBE) allows to determine the electrokinetic charge density (σ_ζ) and can be defined as the effective electric charge (Q_{eff}) normalized on the area of the shear plane (approximated to $4\pi a^2$).⁶²⁰ Loeb et al.⁷⁵⁰ suggested an approximate empirical formula for a 1:1 electrolyte:

$$\sigma_\zeta = \frac{Q_{eff}}{4\pi a^2} = \frac{\varepsilon_r \varepsilon_0 kT}{e} \kappa \left[2 \sinh\left(\frac{e\zeta}{2kT}\right) + \frac{4}{\kappa a} \tanh\left(\frac{e\zeta}{4kT}\right) \right] \quad (\text{A.5.5a})$$

Eq. A.5.5a deviates only by 5% when $\kappa a > 0.5$ and is independent of ζ . Ohshima et al.⁷⁵¹ derived a more accurate analytical expression for a 1:1 electrolyte:

$$\sigma_\zeta = \frac{2\varepsilon_r \varepsilon_0 \kappa kT}{e} \sinh\left(\frac{e\zeta}{2kT}\right) \left[1 + \frac{1}{\kappa a} \left(\frac{2}{\cosh^2\left(\frac{e\zeta}{4kT}\right)} \right) + \frac{1}{(\kappa a)^2} \left(\frac{8 \ln \left\{ \cosh\left(\frac{e\zeta}{4kT}\right) \right\}}{\sinh^2\left(\frac{e\zeta}{2kT}\right)} \right) \right]^{1/2} \quad (\text{A.5.5b})$$

Significant errors also apply here when $\kappa a < 0.5$ and both Eq. A.5.5a and Eq. A.5.5b should give similar outcomes with less than 5% relative error. For the planar limiting case, the PBE can be solved without linearization and gives direct access to the electrokinetic charge density σ_ζ (Grahame equation):⁷⁵²

$$\sigma_\zeta = \frac{2\varepsilon_r \varepsilon_0 \kappa kT}{e} \sinh\left(\frac{e\zeta}{2kT}\right) = \sqrt{8n\varepsilon_r \varepsilon_0 kT} \sinh\left(\frac{e\zeta}{2kT}\right) \quad (\text{A.5.5c})$$

where n is the number density of buffer ions.

Fig. A.5.5 shows the results by applying Eq. A.5.5b and Eq. A.5.5c to estimate the surface charge density of the NPs determined with electrophoretic light scattering and compared to the streaming current results of the SF-substrates. Results did not deviate substantially by using Eq. A.5.5a and Eq. A.5.5b (not shown). The surface charge density of the 1000 nm and 80 nm silica particles is close to that of the smooth planar silica substrate (SF-SiO₂), while larger deviations are observed further away from the iso-electric point when the particle size decreases. This size-dependent surface charge for silica has been attributed to the change in surface concentrations of protons at fixed pH and electrolyte concentration and become significant when the double layer thickness to particle diameter ratio is above 0.2 (the ratio is 0.17 when using a size of 17.8 nm for silica estimated from TEM).⁷²⁶ When pH \geq 9,

the solubility of silica increases, and dissociation of dissolved species causes an apparent surface charge density.⁷⁵³ The particle-covered (PF) substrates have been excluded as I am not aware of any approximate expression that includes surface roughness from experimental ζ .

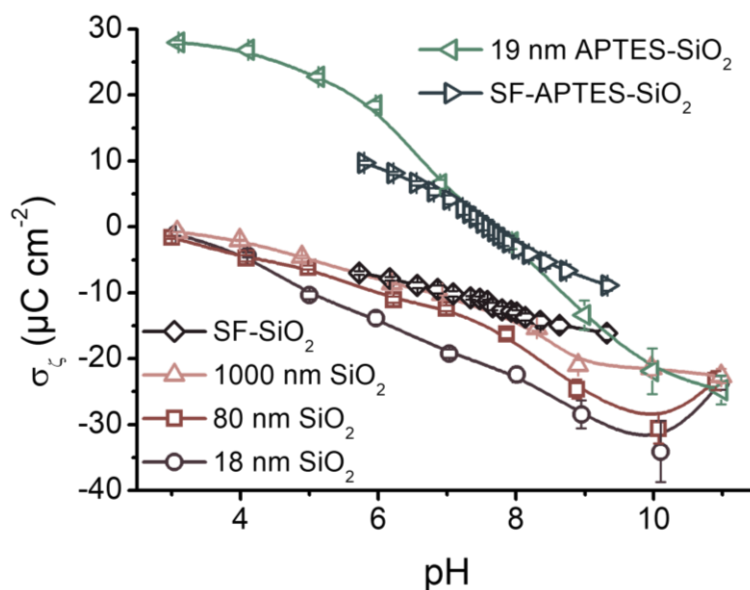


Fig. A.5.5 Electrokinetic charge density at 10 mM KCl of 0.1 w/w% (nano)particles and smooth (SF) rectangular planar substrates made from silica (SiO₂) or coated afterward with APTES (APTES-SiO₂). Error bars are determined from the experimental ζ potential deviation.

A.5.6 Streaming current and contact angle on planar substrates with different surface chemistry

Streaming current (SC, Fig. A.5.6a) and contact angles (CAs, Fig. A.5.6b) of silica coated samples (SF-SiO₂) and subsequently coated with APTES (SF-APTES-SiO₂) are compared to the borosilicate glass (BSG) coverslips, used as template for the dip coating, to validate their use with respect to the ζ potentials of the NPs (not shown here). BSG-1 was cleaned by sonicating the coverslips for 15 min each in acetone, ethanol absolute and water prior to drying with nitrogen, while BSG-2 was cleaned according to the protocol in section 7.2.1. The ζ potentials of BSG-1 are close to SF-SiO₂, with a rather linear dependence of the ζ potential to pH, and shows much larger CAs. The cleaning protocol for BSG-2 ensures maximal hydroxylation, confirmed by the large ζ potentials and zero CAs. The BSG-2 samples were afterwards coated with APTES (BSG-APTES) according to the protocol in section 7.2.4. Interestingly, the ζ potentials of both APTES-coated samples are similar while the mean CA values vary more than 10°.

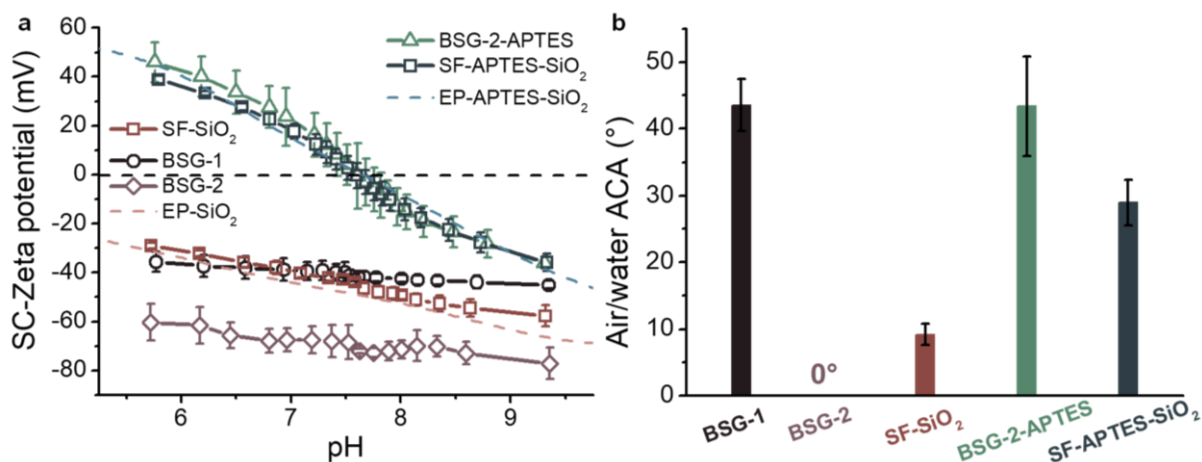


Fig. A.5.6 Comparing streaming current and contact angles for different surfaces. **a**, Zeta potentials measured with streaming current (SC) for different coatings and **b**, their corresponding contact angles and standard deviations ($n = 50$). Abbreviations are explained in the text.

A.5.7 Decane-water interfacial tension in presence and absence of nanoparticles

To validate the purity of all liquids and particle dispersions, the decane/water interfacial tension was monitored. Fig. A.5.7 shows that the interfacial tension (IFT) in the absence and presence of NPs are quasi-linear and indifferent from each other, showing that all liquids and dispersed components are of high purity. The difference in magnitude between the samples is caused by environmental temperature differences of $\pm 1^\circ\text{C}$ as the aqueous drops have been density-corrected. The scatter in the individual samples might also stem from incomplete damping of external disturbances that cause significant drop vibrations.

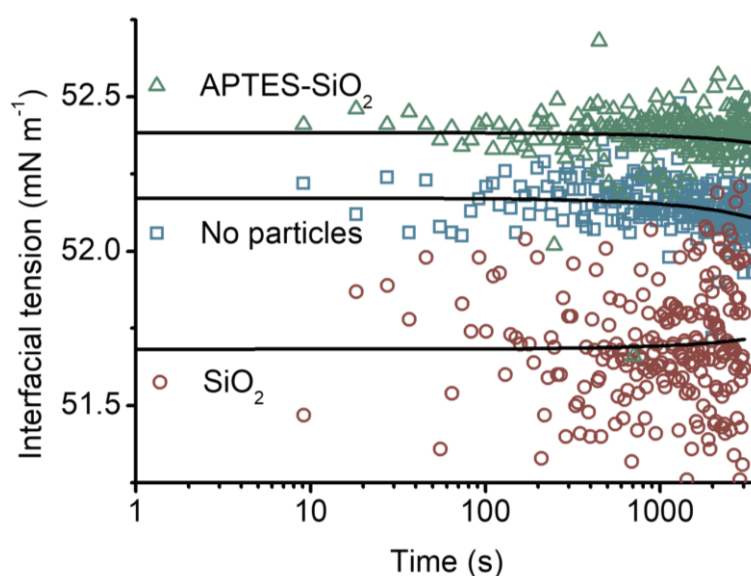


Fig. A.5.7 Time-resolved interfacial tension measurements of the decane/water interface in absence of nanoparticles (squares), silica (circles), and APTES-coated silica nanoparticles (triangles). Black lines are linear fits of the data.

A.5.8 Fitted parameters from the reflectivity plots and physical model applied to X-ray reflectivity data

Part of the parameters in Table A.5.3 come from Fig. 6.4. Contact angles were calculated using Eq. 2.10, θ_p . The adsorption energy was calculated from the decrease in surface free energy (Eq. 2.18; ΔE_p) upon adsorption of a particle with radius a to a liquid surface with surface/interfacial tension (γ_θ) at equilibrium.³⁴

Table A.5.3 Adsorption parameters of APTES-coated silica nanoparticles. Spreading distance, particle coverage, immersion depth, and contact angles are obtained from fitting the electron densities (EDs) derived from simulating the X-ray reflectivity and their standard deviations. Contact angles from ED modeling are used to calculate the adsorption energies and their respective standard deviations. Radius = 9.45 nm, air/water surface tension = 0.0722 N m⁻¹, decane/water interfacial tension = 0.0522 N m⁻¹

<i>Parameter / units</i>	<i>Air/water</i>	<i>Decane/water</i>
<i>Spreading distance (s_{av}) / nm</i>	14.33 ± 1.46	14.49 ± 1.50
<i>Particle coverage (Θ)</i>	27.78 ± 2.24	27.26 ± 2.47
<i>Immersion depth water (h_{av}) / nm</i>	17.08 ± 0.08	17.46 ± 0.10
<i>Contact angle (CA) / °</i>	28.35 ± 2.52	22.26 ± 2.68
<i>Adsorption energy / kcal mol⁻¹</i>	-43.31 ± 15.18	-13.41 ± 5.68

A.5.9 Determination of the advancing and receding contact angle

The protocol of Korhonen et al.¹¹⁸ is used to increase the accuracy of measuring the advancing (ACA) and receding contact angle (RCA) with a real-time example shown in Fig. A.5.8 for the smooth silica (SiO_2) and APTES-coated silica (APTES- SiO_2) substrates immersed in decane. Stable ACAs are obtained when the droplet volume and drop base diameter increase while the mCA remains stable. The stick-slip behavior for APTES- SiO_2 makes it challenging to measure a linear ACA, as shown in Fig. A.5.8b, even for multiple ACA/RCA cycles on the same substrate. In this case, the mCA fluctuates over several degrees, and the average is taken as the semi-stable ACA. Correct RCAs are obtained when a stable mCA is measured while the drop volume and drop base diameter keep decreasing.

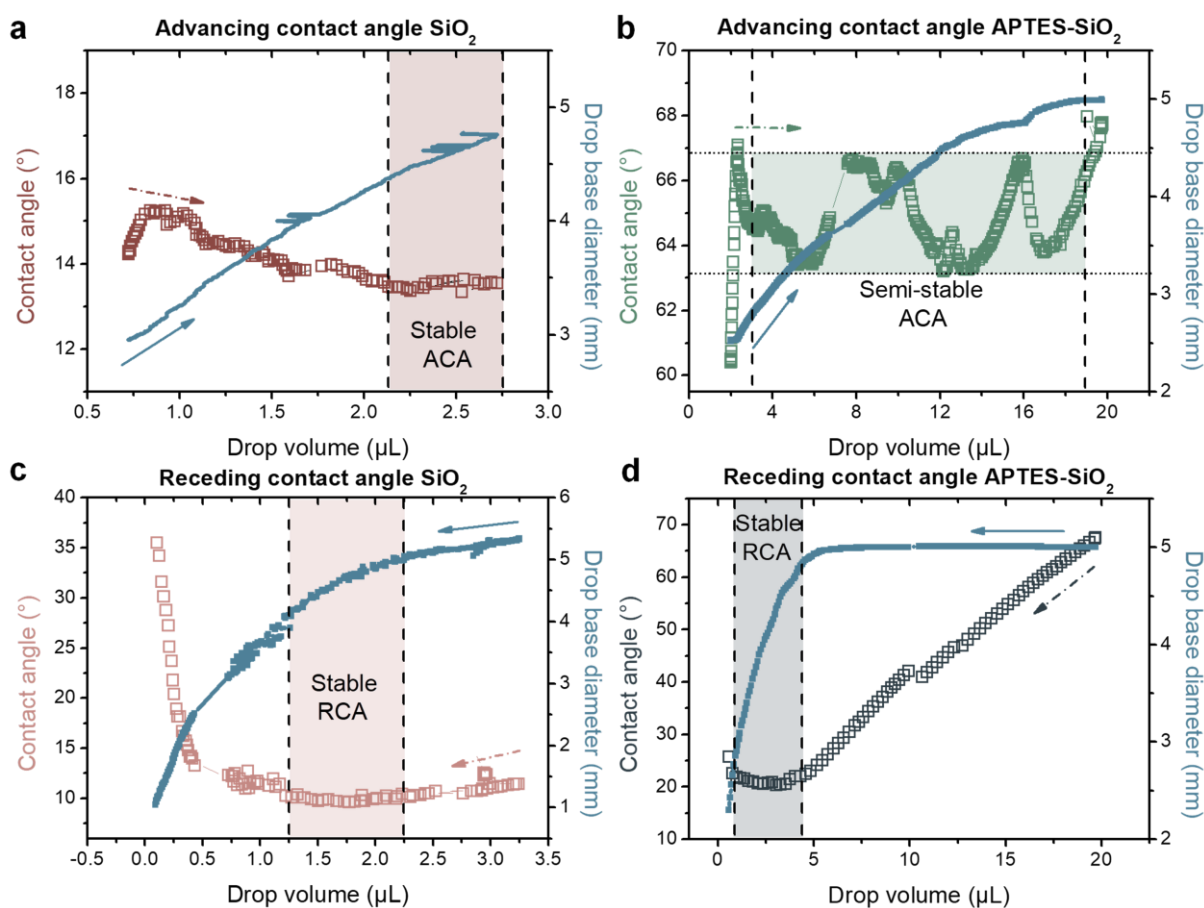


Fig. A.5.8 Advancing (ACA) and receding (RCA) decane/water contact angles of silica (a,c) and coated with APTES (b,d). The arrows indicate the direction of the measurement and the contact angle values inside the highlighted region correspond to (semi-)stable values that are averaged.

A.5.10 Experimental data of contact angles measured on the planar substrates and nanoparticles adsorbed at the liquid surfaces and statistical analysis of the double Boxplot

Table A.5.4 Summarized data of the advancing (ACA), receding (RCA), and equilibrium contact angle (ECA) measurements on smooth (SF) and rough (PF) macroscopic substrates and of the adsorbed nanoparticles from X-ray reflectivity (XRR) at air/water and decane/water. The number of droplets on various planar substrates corresponds to *n*. The mean, median, standard deviation, the interquartile distance between Q1 (25%) - Q3 (75%), and minimum-maximum (including outliers) values are reported here. Although fewer XRR measurements are performed with the adsorbed nanoparticles, making the use of a boxplot obsolete, results are shown for completeness. Note that two columns for the ECA are provided for RCA of 0.1° or 5.00°. Both these numbers were taken when no RCA could be measured ($CA \leq 5.00^\circ$). SD = standard deviation.

Sample	ACA air/water						RCA air/water						ECA 0.10 ° RCA ± SD	ECA 5.00 ° RCA ± SD
	n	Mean (°)	Median (°)	SD. (°)	Q1 – Q3 (°)	Min – Max (°)	n	Mean (°)	Median (°)	SD (°)	Q1 – Q3 (°)	Min – Max (°)		
SF-SiO ₂	50	9.42	9.49	1.34	8.77 – 10.44	6.00 – 11.76	50	< 5°	/	/	/	/	3.99 ± 0.50	7.31 ± 0.72
SF- APTES- SiO ₂	50	29.02	29.04	3.48	27.01 – 31.01	20.63 – 36.61	50	< 5° ¹	/	/	/	/	10.35 ± 1.02	17.62 ± 1.75
PF-SiO ₂	50	< 5°	/	/	/	/	50	< 5°	/	/	/	/	0.10	5.00
PF- APTES- SiO ₂	50	9.61	9.60	2.35	8.05 – 11.33	5.38 – 18.16	50	< 5°	/	/	/	/	3.46 ± 0.86	7.42 ± 1.26
Sample	ACA decane/water						RCA decane/water						ECA 0.10 ° RCA ± SD	ECA 5.00 ° RCA ± SD
	n	Mean (°)	Median (°)	SD (°)	Q1 – Q3 (°)	Min – Max (°)	n	Mean (°)	Median (°)	SD (°)	Q1 – Q3 (°)	Min – Max (°)		
SF-SiO ₂	50	14.12	14.00	1.55	13.05 – 15.40	10.20 – 17.55	50	8.57	8.43	1.69	7.26 – 9.77	5.01 – 13.93	11.45 ± 1.60	/
SF- APTES- SiO ₂	50	57.01	57.24	9.49	50.54 – 63.02	39.40 – 92.47	50	21.44	20.82	6.71	17.79 – 24.15	9.22 – 40.4	39.31 ± 7.67	/
PF-SiO ₂	50	< 5°	/	/	/	/	50	< 5°	/	/	/	/	0.10	5.00
PF- APTES- SiO ₂	50	12.19	12.53	2.50	10.49 – 13.71	6.24 – 19.03	50	< 5°	/	/	/	/	4.98 ± 0.88	8.81 ± 1.35

¹Air/water RCAs on SF-APTES-SiO₂ could only be measured for the highest (outliers) ACAs and are disregarded.

Sample	Particle contact angle air/water						Particle contact angle decane/water						/	/
	n	Mean (°)	Median (°)	SD (°)	Q1 – Q3 (°)	Min – Max (°)	n	Mean (°)	Median (°)	SD (°)	Q1 – Q3 (°)	Min – Max (°)		
XRR- SiO ₂	3	/	/	/	/	/	3	/	/	/	/	/	/	/
XRR- APTES- SiO ₂	3	28.35	28.01	2.52	26.52 – 30.27	26.02 – 31.03	3	22.26	23.04	2.68	20.69 – 24.69	19.90 – 25.24	/	/

With the software program MATLAB, a double boxplot was created to represent a statistical summary for the CA data through their quartiles. The minimum (Q_0) and maximum (Q_4) represent the lowest and largest data points, excluding the outliers. The median (Q_2) is the middle value of the set, while the first (Q_1) and third quartile (Q_3) represent the median of the lower and upper half of the dataset, respectively. The difference between the third and first quartile is the interquartile distance (iQd), which includes 50 % of the data centered around the mean. The data follows a normal distribution since the median lies in the middle and the length of the dash-dotted line toward the minimum or maximum are similar in length. The outliers, which are numerically distant from the rest of the data, are determined when a data point exceeds 1.5 times the iQd above Q_3 and below Q_1 ($Q_1 - 1.5 * iQd$ or $Q_3 + 1.5 * iQd$).

A.5.11 Contact angle hysteresis and work of spreading

The contact angle hysteresis (CAH, $\Delta\theta$) should be related to the work of spreading (W_s) (at the air/water and oil/water interfaces) determined from the work of adhesion (W_a) and the work of cohesion (W_c). Wang et al.⁷³² related CAH to the spreading work on hydrophobic surfaces with different roughness and found that the spreading work increases when the CAH decreases. The work of spreading predicts the tendency of a liquid to spread on a solid surface and depends only on the surface tension of the liquid and the measured ACA. Only the average ACAs from Table 7.2 in Chapter 7 are used here (units mN m^{-1}).

$$W_c = 2\gamma_{lg} \quad (\text{A5.S4})$$

$$W_a = \gamma_{lg} (1 + \cos\theta_A) \quad (\text{A5.S5})$$

$$W_s = W_a - W_c \quad (\text{A5.S6})$$

where γ_{lg} can be exchanged for the oil/water interfacial tension γ_{lo} .

Table A.5.5 Work of cohesion, adhesion, and spreading

	Liquid interface	W_c	W_a	W_s
SF-SiO ₂	A/W	144.4	143.43	-0.97
	O/W	104.4	102.83	-1.57
SF-APTES	A/W	144.4	135.34	-9.06
	O/W	104.4	80.62	-23.78
PF-APTES	A/W	144.4	143.39	-1.01
	O/W	104.4	103.22	-1.18

In all cases, $W_s < 0$ indicates that the spreading is at the partial wetting state. Decane itself spreads completely on all substrates used and $W_s > 0$. Plotting $\Delta\theta\%$ (Eq. 4.14) from Table 7.2 in the manuscript to W_s gives a linear relationship with $R^2 = 0.996$.

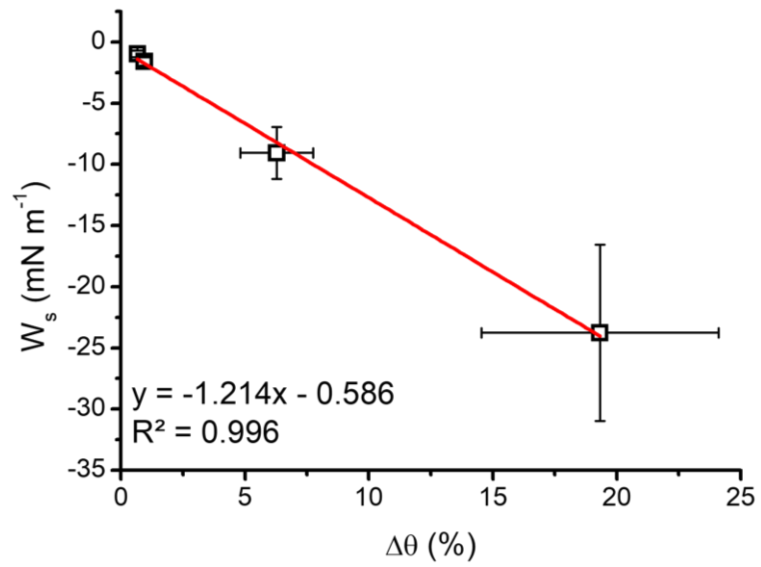


Fig. A.5.9 For the smooth, hydrophilic surfaces, a linear relation between the spreading work (W_s) and contact angle hysteresis percentage ($\Delta\theta\%$) is found. The error bars are determined from the experimental errors in Table 7.2.

A.5.12 Schematic overview of the assessment of nanoparticle wettability

Fig. A.5.10 schematically shows the proposed methodology with the final CA results on the smooth silica and APTES-coated surfaces and adsorbed NPs. The dash-dotted line emphasizes that stringent control of electrokinetic properties between particles and substrates provides better control over the measured mCAs and assists in estimating wettability of NPs adsorbed at a liquid surface.

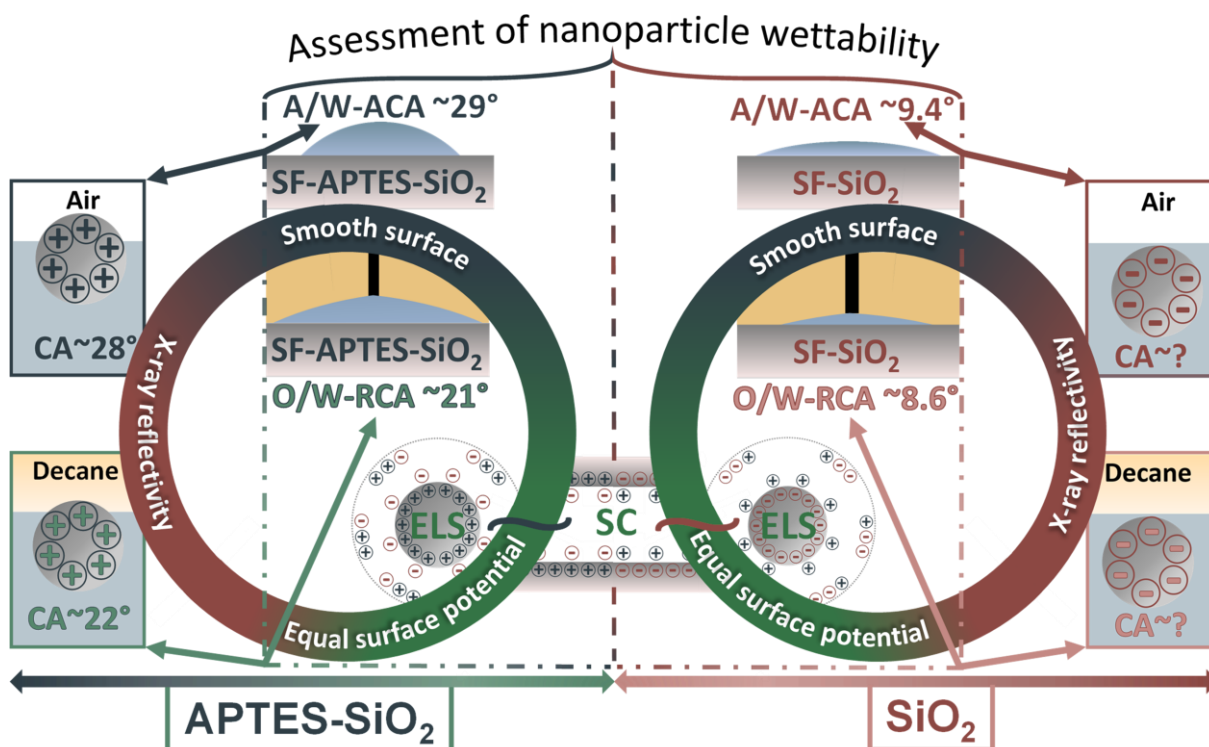


Fig. A.5.10 Determining the wettability of spherical nanoparticles from macroscopic droplets on equivalent substrates. The measured reflectivity of the 18 nm silica (SiO₂) and 19 nm APTES-coated silica (APTES-SiO₂) provides a direct estimation of the immersion depth showing that the negatively charged SiO₂ particles do not adsorb, contrarily to the positively charged APTES-SiO₂. The ζ potentials of the particles and similarly coated smooth planar substrates (SF) analyzed through electrophoresis (ELS) and streaming current (SC) shows good agreement, providing a chemically equivalent surface for contact angle measurements on the SF substrates, as substrates with surface roughness (PF) show very hydrophilic behavior and are not representative in this case. Mean advancing contact angles (ACA) in air/water (A/W) and receding contact angles (RCA) in oil/water (O/W) on the SFs shows excellent agreement with the interfacially adsorbed APTES-SiO₂ nanoparticles. Therefore, evaluating topography, electrokinetic charge, and contact angles on chemically equivalent surfaces provides better control in estimating NP immersion depths with higher accuracy than sessile drop alone.

10 References

- (1) Sircar, A.; Rayavarapu, K.; Bist, N.; Yadav, K.; Singh, S. *Applications of Nanoparticles in Enhanced Oil Recovery*; Elsevier, 2021. <https://doi.org/10.1016/J.PTLRS.2021.08.004>.
- (2) Pereira, M. L. D. O.; Maia, K. C. B.; Silva, W. C.; Leite, A. C.; Francisco, A. D. D. S.; Vasconcelos, T. L.; Nascimento, R. S. V.; Grasseschi, D. Fe₃O₄ Nanoparticles as Surfactant Carriers for Enhanced Oil Recovery and Scale Prevention. *ACS Appl. Nano Mater.* **2020**, *3* (6), 5762–5772. <https://doi.org/10.1021/acsnm.0c00939>.
- (3) Madzokere, T. C.; Rusere, K.; Chiririwa, H. Nano-Silica Based Mineral Flotation Frother: Synthesis and Flotation of Platinum Group Metals (PGMs). *Miner. Eng.* **2021**, *166*, 106881. <https://doi.org/10.1016/J.MINENG.2021.106881>.
- (4) Nile, S. H.; Baskar, V.; Selvaraj, D.; Nile, A.; Xiao, J.; Kai, G. Nanotechnologies in Food Science: Applications, Recent Trends, and Future Perspectives. *Nano-Micro Lett.* **2020**, *12* (1), 1–34. <https://doi.org/10.1007/S40820-020-0383-9>.
- (5) Salvioni, L.; Morelli, L.; Ochoa, E.; Labra, M.; Fiandra, L.; Palugan, L.; Prosperi, D.; Colombo, M. The Emerging Role of Nanotechnology in Skincare. *Adv. Colloid Interface Sci.* **2021**, *293*, 102437. <https://doi.org/10.1016/J.CIS.2021.102437>.
- (6) Yaghmur, A.; Mu, H. Recent Advances in Drug Delivery Applications of Cubosomes, Hexosomes, and Solid Lipid Nanoparticles. *Acta Pharm. Sin. B* **2021**, *11* (4), 871. <https://doi.org/10.1016/J.APSB.2021.02.013>.
- (7) Putro, J. N.; Ismadji, S.; Gunarto, C.; Soetaredjo, F. E.; Ju, Y. H. A Study of Anionic, Cationic, and Nonionic Surfactants Modified Starch Nanoparticles for Hydrophobic Drug Loading and Release. *J. Mol. Liq.* **2020**, *298*, 112034. <https://doi.org/10.1016/j.molliq.2019.112034>.
- (8) Gonzenbach, U. T.; Studart, A. R.; Tervoort, E.; Gauckler, L. J. Tailoring the Microstructure of Particle-Stabilized Wet Foams. *Langmuir* **2007**, *23* (3), 1025–1032. <https://doi.org/10.1021/la0624844>.
- (9) AlYousef, Z.; Almobarky, M.; Schechter, D. Enhancing the Stability of Foam by the Use of Nanoparticles. *Energy and Fuels* **2017**, *31* (10), 10620–10627. <https://doi.org/10.1021/acs.energyfuels.7b01697>.
- (10) Dreja, M.; Heine, K.; Tieke, B.; Junkers, G. Effects of Functionalized Latex Particles and Anionic Surfactants on the Flow Behavior of Aqueous Gelatin Dispersions. *J. Colloid Interface Sci.* **1997**, *191* (1), 131–140. <https://doi.org/10.1006/jcis.1997.4936>.
- (11) Ramsden, W. Separation of Solids in the Surface-Layers of Solutions and “Suspensions.” *Proc. Roy. Soc.* **1903**, *72*, 156–164.
- (12) Pickering, S. U. Emulsions. *J. Chem. Soc. Trans.* **1907**, *91*, 2001–2021.
- (13) Saim, A. Recent Progress in the Application of Nanoparticles in Minerals Flotation. *Chem. Sci. Eng. Res.* **2021**, *3*, 1–7. <https://doi.org/10.36686/Ariviyal.CSER.2021.03.06.027>.
- (14) Micheau, C.; Dedovets, D.; Bauduin, P.; Diat, O.; Girard, L. Nanoparticle Foam Flotation for Caesium Decontamination Using a PH-Sensitive Surfactant. *Environ. Sci. Nano* **2019**, *6* (5), 1576–1584. <https://doi.org/10.1039/c9en00188c>.
- (15) Zhang, Y.; Wang, S.; Zhou, J.; Zhao, R.; Benz, G.; Tcheimou, S.; Meredith, J. C.; Behrens, S. H. Interfacial Activity of Nonamphiphilic Particles in Fluid-Fluid Interfaces. *Langmuir* **2017**, *33* (18), 4511–4519. <https://doi.org/10.1021/acs.langmuir.7b00599>.
- (16) Bizmark, N.; Ioannidis, M. A.; Henneke, D. E. Irreversible Adsorption-Driven Assembly of Nanoparticles at Fluid Interfaces Revealed by a Dynamic Surface Tension Probe. *Langmuir* **2014**, *30* (3), 710–717. <https://doi.org/10.1021/la404357j>.
- (17) Du, K.; Glogowski, E.; Emrick, T.; Russell, T. P.; Dinsmore, A. D. Adsorption Energy of Nano- and Microparticles at Liquid-Liquid Interfaces. *Langmuir* **2010**, *26* (15), 12518–12522. <https://doi.org/10.1021/la100497h>.
- (18) Coertjens, S.; De Dier, R.; Moldenaers, P.; Isa, L.; Vermant, J. Adsorption of Ellipsoidal Particles at Liquid-Liquid Interfaces. *Langmuir* **2017**, *33* (11), 2689–2697. <https://doi.org/10.1021/acs.langmuir.6b03534>.
- (19) Ruhland, T. M.; Gröschel, A. H.; Ballard, N.; Skelhon, T. S.; Walther, A.; Müller, A. H. E.; Bon, S. A. F. Influence of Janus Particle Shape on Their Interfacial Behavior at Liquid-Liquid Interfaces. *Langmuir* **2013**, *29* (5), 1388–1394. <https://doi.org/10.1021/la3048642>.
- (20) Deshmukh, O. S.; van den Ende, D.; Stuart, M.; Mugele, F.; Duits, M. Hard and Soft Colloids at Fluid Interfaces: Adsorption, Interactions, Assembly & Rheology. *Adv. Colloid Interface Sci.* **2015**, *222*, 215–227. <https://doi.org/10.1016/J.CIS.2014.09.003>.
- (21) Jin, J.; Li, X.; Geng, J.; Jing, D. Insights into the Complex Interaction between Hydrophilic Nanoparticles and Ionic Surfactants at the Liquid/Air Interface. *Phys. Chem. Chem. Phys.* **2018**, *20* (22), 15223–15235. <https://doi.org/10.1039/c8cp01838c>.
- (22) Kirby, S. M.; Anna, S. L.; Walker, L. M. Effect of Surfactant Tail Length and Ionic Strength on the

- Interfacial Properties of Nanoparticle-Surfactant Complexes. *Soft Matter* **2017**, *14* (1), 112–123. <https://doi.org/10.1039/c7sm01806a>.
- (23) Hari Krishnan, A. R.; Dhar, P.; Agnihotri, P. K.; Gedupudi, S.; Das, S. K. Effects of Interplay of Nanoparticles, Surfactants and Base Fluid on the Surface Tension of Nanocolloids. *Eur. Phys. J. E* **2017**, *40* (5), 16–23. <https://doi.org/10.1140/epje/i2017-11541-5>.
- (24) Rana, S.; Yu, X.; Patra, D.; Moyano, D. F.; Miranda, O. R.; Hussain, I.; Rotello, V. M. Control of Surface Tension at Liquid-Liquid Interfaces Using Nanoparticles and Nanoparticle-Protein Complexes. *Langmuir* **2012**, *28* (4), 2023–2027. <https://doi.org/10.1021/la204017z>.
- (25) Jiang, Y.; Chakroun, R.; Gu, P.; Gröschel, A. H.; Russell, T. P. Soft Polymer Janus Nanoparticles at Liquid-Liquid Interfaces. *Angew. Chemie - Int. Ed.* **2020**, *59* (31), 12751–12755. <https://doi.org/10.1002/anie.202004162>.
- (26) Sato, N.; Aoyama, Y.; Yamanaka, J.; Toyotama, A.; Okuzono, T. Particle Adsorption on Hydrogel Surfaces in Aqueous Media Due to van Der Waals Attraction. *Sci. Rep.* **2017**, *7* (1), 1–10. <https://doi.org/10.1038/s41598-017-06257-1>.
- (27) Born, P.; Blum, S.; Gerstner, D.; Huber, P.; Kraus, T. Self-Assembly of Gold Nanoparticles at the Oil – Vapor Interface: From Mono- to Multilayers. *Langmuir* **2014**, *30*, 13176–13181. <https://doi.org/10.1021/la503551d>.
- (28) Ferdous, S.; Ioannidis, M. A.; Henneke, D. E. Effects of Temperature, PH, and Ionic Strength on the Adsorption of Nanoparticles at Liquid-Liquid Interfaces. *J. Nanoparticle Res.* **2012**, *14* (5). <https://doi.org/10.1007/s11051-012-0850-4>.
- (29) Manga, M. S.; Hunter, T. N.; Cayre, O. J.; York, D. W.; Reichert, M. D.; Anna, S. L.; Walker, L. M.; Williams, R. A.; Biggs, S. R. Measurements of Submicron Particle Adsorption and Particle Film Elasticity at Oil – Water Interfaces. *Langmuir* **2016**, *32* (17), 4125–4133. <https://doi.org/10.1021/acs.langmuir.5b04586>.
- (30) Chai, Y.; Lukito, A.; Jiang, Y.; Ashby, P. D.; Russell, T. P. Fine-Tuning Nanoparticle Packing at Water-Oil Interfaces Using Ionic Strength. *Nano Lett.* **2017**, *17* (10), 6453–6457. <https://doi.org/10.1021/acs.nanolett.7b03462>.
- (31) Sun, H.; Li, L.; Russell, T. P.; Shi, S. Photoresponsive Structured Liquids Enabled by Molecular Recognition at Liquid-Liquid Interfaces. *J. Am. Chem. Soc.* **2020**, *142* (19), 8591–8595. <https://doi.org/10.1021/jacs.0c02555>.
- (32) Binks, B. P.; Horozov, T. S. Colloidal Particles at Liquid Interfaces: An Introduction. In *Colloidal Particles at Liquid Interfaces*; Binks, B. P., Horozov, T. S., Eds.; Cambridge University Press: New York, 2006; pp 1–76. <https://doi.org/10.1017/CBO9780511536670>.
- (33) Binks, P. Particles as Surfactants—Similarities and Differences. *Curr. Opin. Colloid Interface Sci.* **2002**, *7*, 21–41.
- (34) Levine, S.; Bowen, B. D.; Partridge, S. J. Stabilization of Emulsions by Fine Particles I. Partitioning of Particles between Continuous Phase and Oil/Water Interface. *Colloids and Surfaces* **1989**, *38* (2), 325–343. [https://doi.org/10.1016/0166-6622\(89\)80271-9](https://doi.org/10.1016/0166-6622(89)80271-9).
- (35) Levine, S.; Bowen, B. D.; Partridge, S. J. Stabilization of Emulsions by Fine Particles II. Capillary and van Der Waals Forces between Particles. *Colloids and Surfaces* **1989**, *38* (2), 345–364. [https://doi.org/10.1016/0166-6622\(89\)80272-0](https://doi.org/10.1016/0166-6622(89)80272-0).
- (36) Vella, D.; Kim, H. Y.; Aussillous, P.; Mahadevan, L. Dynamics of Surfactant-Driven Fracture of Particle Rafts. *Phys. Rev. Lett.* **2006**, *96* (17). <https://doi.org/10.1103/PHYSREVLETT.96.178301>.
- (37) Katepalli, H.; John, V. T.; Bose, A. The Response of Carbon Black Stabilized Oil-in-Water Emulsions to the Addition of Surfactant Solutions. *Langmuir* **2013**, *29* (23), 6790–6797. <https://doi.org/10.1021/la400037c>.
- (38) Calzolari, D. C. E.; Pontoni, D.; Deutsch, M.; Reichert, H.; Daillant, J. Nanoscale Structure of Surfactant-Induced Nanoparticle Monolayers at the Oil-Water Interface. *Soft Matter* **2012**, *8* (45), 11478–11483. <https://doi.org/10.1039/c2sm26520f>.
- (39) Binks, B. P.; Isa, L.; Tyowua, A. T. Direct Measurement of Contact Angles of Silica Particles in Relation to Double Inversion of Pickering Emulsions. *Langmuir* **2013**, *29* (16), 4923–4927. <https://doi.org/10.1021/la4006899>.
- (40) Miller, R.; Fainerman, V. B.; Kovalchuk, V. I.; Grigoriev, D. O.; Leser, M. E.; Michel, M. Composite Interfacial Layers Containing Micro-Size and Nano-Size Particles. *Adv. Colloid Interface Sci.* **2006**, *128–130*, 17–26. <https://doi.org/10.1016/j.cis.2006.11.004>.
- (41) Fainerman, V. B.; Kovalchuk, V. I.; Lucassen-Reynders, E. H.; Grigoriev, D. O.; Ferri, J. K.; Leser, M. E.; Michel, M.; Miller, R.; Möhwald, H. Surface-Pressure Isotherms of Monolayers Formed by Microsize and Nanosize Particles. *Langmuir* **2006**, *22* (4), 1701–1705. <https://doi.org/10.1021/LA052407T>.
- (42) Groot, R. D.; Stoyanov, S. D. Equation of State of Surface-Adsorbing Colloids. *Soft Matter* **2011**, *6*, 1682–1692. <https://doi.org/10.1039/B925353J>.

- (43) Verwijlen, T.; Imperiali, L.; Vermant, J. Separating Viscoelastic and Compressibility Contributions in Pressure-Area Isotherm Measurements. *Adv. Colloid Interface Sci.* **2014**, *206*, 428–436. <https://doi.org/10.1016/J.CIS.2013.09.005>.
- (44) Harikrishnan, A. R.; Das, S. K.; Agnihotri, P. K.; Dhar, P. Particle and Surfactant Interactions Effected Polar and Dispersive Components of Interfacial Energy in Nanocolloids. *J. Appl. Phys.* **2017**, *122* (054301), 13. <https://doi.org/10.1063/1.4997123>.
- (45) Cheung, D. L. Molecular Dynamics Study of Nanoparticle Stability at Liquid Interfaces: Effect of Nanoparticle-Solvent Interaction and Capillary Waves. *J. Chem. Phys.* **2011**, *135* (5), 054704. <https://doi.org/10.1063/1.3618553>.
- (46) Shi, X.; Hassanzadeh-Aghdam, M. K.; Ansari, R. Viscoelastic Analysis of Silica Nanoparticle-Polymer Nanocomposites. *Compos. Part B Eng.* **2019**, *158*, 169–178. <https://doi.org/10.1016/J.COMPOSITESB.2018.09.084>.
- (47) Stamou, D.; Duschl, C.; Johannsmann, D. Long-Range Attraction between Colloidal Spheres at the Air-Water Interface: The Consequence of an Irregular Meniscus. *Phys. Rev. E* **2000**, *62* (4), 5263. <https://doi.org/10.1103/PhysRevE.62.5263>.
- (48) Kralchevsky, P. A.; Denkov, N. K.; Krassimir, D. D. Particles with an Undulated Contact Line at a Fluid Interface: Interaction between Capillary Quadrupoles and Rheology of Particulate Monolayers. *Langmuir* **2001**, *17* (24), 7694–7705. <https://doi.org/10.1021/LA0109359>.
- (49) Wu, L.; Wang, X.; Wang, G.; Chen, G. In Situ X-Ray Scattering Observation of Two-Dimensional Interfacial Colloidal Crystallization. *Nat. Commun.* **2018**, *9* (1). <https://doi.org/10.1038/s41467-018-03767-y>.
- (50) Nikolaides, M. G.; Bausch, A. R.; Hsu, M. F.; Dinsmore, A. D.; Brenner, M. P.; Gay, C.; Weitz, D. A. Electric-Field-Induced Capillary Attraction between like-Charged Particles at Liquid Interfaces. *Nature* **2002**, *420* (6913), 299–301. <https://doi.org/10.1038/nature01113>.
- (51) Kralchevsky, P. A.; Danov, K. D. Interactions between Particles at a Fluid Interface. In *Nanoscience: Colloidal and Interfacial Aspects*; Starov, V. M., Ed.; CRC Press: New York, 2010; pp 397–435.
- (52) Danov, K.; Kralchevsky, P. Capillary Forces between Particles at a Liquid Interface: General Theoretical Approach and Interactions between Capillary Multipoles. *Adv. Colloid Interface Sci.* **2010**, *154* (1–2), 91–103. <https://doi.org/10.1016/J.CIS.2010.01.010>.
- (53) Hua, X.; Bevan, M. A.; Frechette, J. Competitive Adsorption between Nanoparticles and Surface Active Ions for the Oil-Water Interface. *Langmuir* **2018**, *34* (16), 4830–4842. <https://doi.org/10.1021/acs.langmuir.8b00053>.
- (54) Hua, X.; Frechette, J.; Bevan, M. A. Nanoparticle Adsorption Dynamics at Fluid Interfaces. *Soft Matter* **2018**, *14* (19), 3818–3828. <https://doi.org/10.1039/c8sm00273h>.
- (55) Olayiwola, S. O.; Dejam, M. Interfacial Energy for Solutions of Nanoparticles, Surfactants, and Electrolytes. *AIChE J.* **2020**, *66* (4). <https://doi.org/10.1002/aic.16891>.
- (56) Rosen, M. J.; Kunjappu, J. T. *Surfactants and Interfacial Phenomena*, 4th ed.; Rosen, M. J., Kunjappu, J. T., Eds.; John Wiley & Sons, Inc., 2012.
- (57) Young, T. III. An Essay on the Cohesion of Fluids. *Phil. Trans. R. Soc* **1805**, *95*, 65–87. <https://doi.org/10.4324/9781315761183-4>.
- (58) Ershov, D.; Sprakel, J.; Appel, J.; Stuart, M. A. C.; Gucht, J. van der. Capillarity-Induced Ordering of Spherical Colloids on an Interface with Anisotropic Curvature. *Proc. Natl. Acad. Sci.* **2013**, *110* (23), 9220–9224. <https://doi.org/10.1073/PNAS.1222196110>.
- (59) Bresme, F.; Oettel, M. Nanoparticles at Fluid Interfaces. *J. Phys. Condens. Matter* **2007**, *19* (41), 413101. <https://doi.org/10.1088/0953-8984/19/41/413101>.
- (60) Dong, L.; Johnson, D. Adsorption of Acicular Particles at Liquid-Fluid Interfaces and the Influence of the Line Tension. *Langmuir* **2005**, *21* (9), 3838–3849. <https://doi.org/10.1021/LA047851V>.
- (61) Law, B. M.; McBride, S. P.; Wang, J. Y.; Wi, H. S.; Paneru, G.; Betelu, S.; Ushijima, B.; Takata, Y.; Flanders, B.; Bresme, F.; Matsubara, H.; Takiue, T.; Aratono, M. Line Tension and Its Influence on Droplets and Particles at Surfaces. *Prog. Surf. Sci.* **2017**, *92* (1), 1–39. <https://doi.org/10.1016/j.progsurf.2016.12.002>.
- (62) McBride, S. P.; Law, B. M. Influence of Line Tension on Spherical Colloidal Particles at Liquid-Vapor Interfaces. *Phys. Rev. Lett.* **2012**, *109* (196101). <https://doi.org/10.1103/PhysRevLett.109.196101>.
- (63) Aveyard, R.; Binks, B. P.; Clint, J. H. Emulsions Stabilised Solely by Colloidal Particles. *Adv. Colloid Interface Sci.* **2003**, *100–102*, 503–546. [https://doi.org/10.1016/S0001-8686\(02\)00069-6](https://doi.org/10.1016/S0001-8686(02)00069-6).
- (64) Lotito, V.; Zambelli, T. Approaches to Self-Assembly of Colloidal Monolayers: A Guide for Nanotechnologists. *Adv. Colloid Interface Sci.* **2017**, *246*, 217–274. <https://doi.org/10.1016/J.CIS.2017.04.003>.
- (65) Danov, K. D.; Kralchevsky, P. A.; Naydenov, B. N.; Brenn, G. Interactions between Particles with an Undulated Contact Line at a Fluid Interface: Capillary Multipoles of Arbitrary Order. *J. Colloid Interface*

- Sci.* **2005**, 287 (1), 121–134. <https://doi.org/10.1016/j.jcis.2005.01.079>.
- (66) Hörvölgyi, Z.; Medveczky, G.; Zrinyi, M. On the Structure Formation of Hydrophobed Particles in the Boundary Layer of Water and Octane Phases. *Colloid Polym. Sci.* **1993**, 271 (4), 396–403. <https://doi.org/10.1007/BF00657421>.
- (67) Mugele, F.; Heikenfeld, J. Introduction to Capillarity and Wetting Phenomena. In *Electrowetting: Fundamental Principles and Practical Applications*; Wiley-VCH Verlag GmbH & Co. KGaA., 2019; pp 1–59.
- (68) Butt, H.; Graf, K.; Kappl, M. *Physics and Chemistry of Interfaces*; WILEY-VCH Verlag GmbH & Co. KGaA, 2003.
- (69) Nihonyanagi, S.; Ishiyama, T.; Lee, T. K.; Yamaguchi, S.; Bonn, M.; Morita, A.; Tahara, T. Unified Molecular View of the Air/Water Interface Based on Experimental and Theoretical $\chi(2)$ Spectra of an Isotopically Diluted Water Surface. *J. Am. Chem. Soc.* **2011**, 133 (42), 16875–16880. <https://doi.org/10.1021/JA2053754>.
- (70) D'Arrigo, J. S. Screening of Membrane Surface Charges by Divalent Cations: An Atomic Representation. *Am J Physiol.* **1978**, 235 (3), 109–117. <https://doi.org/10.1152/ajpcell.1978.235.3.C109>.
- (71) Damodaran, S. Adsorbed Layers Formed from Mixtures of Proteins. *Curr. Opin. Colloid Interface Sci.* **2004**, 9 (5), 328–339. <https://doi.org/10.1016/J.COCIS.2004.09.008>.
- (72) Nagata, Y.; Hasegawa, T.; Backus, E. H. G.; Usui, K.; Yoshimune, S.; Ohto, T.; Bonn, M. The Surface Roughness, but Not the Water Molecular Orientation Varies with Temperature at the Water–Air Interface. *Phys. Chem. Chem. Phys.* **2015**, 17 (36), 23559–23564. <https://doi.org/10.1039/C5CP04022A>.
- (73) Scheiner, S. *Noncovalent Forces*; Springer, 2015. <https://doi.org/10.1007/978-3-319-14163-3>.
- (74) Mitrović, D. M.; Tikhonov, A. M.; Li, M.; Huang, Z.; Schlossman, M. L. Noncapillary-Wave Structure at the Water-Alkane Interface. *Phys. Rev. Lett.* **2000**, 85 (3), 582. <https://doi.org/10.1103/PhysRevLett.85.582>.
- (75) Gurkov, T. D.; Kralchevsky, P. A. Surface Tension and Surface Energy of Curved Interfaces and Membranes. *Colloids and Surfaces* **1990**, 47, 45–68. [https://doi.org/10.1016/0166-6622\(90\)80061-8](https://doi.org/10.1016/0166-6622(90)80061-8).
- (76) Forth, J.; Kim, P. Y.; Xie, G.; Liu, X.; Helms, B. A.; Russell, T. P. Building Reconfigurable Devices Using Complex Liquid–Fluid Interfaces. *Adv. Mater.* **2019**, 31 (18), 1–39. <https://doi.org/10.1002/adma.201806370>.
- (77) Guzmán, E.; Abelenda-Núñez, I.; Maestro, A.; Ortega, F.; Santamaria, A.; Rubio, R. G. Particle-Laden Fluid / Fluid Interfaces : Physico-Chemical Foundations. *J. Phys. Condens. Matter* **2021**, 33, 333001. <https://doi.org/10.1088/1361-648X/ac0938>.
- (78) Tovbin, Y. K. Surface Tension: Mechanics, Thermodynamics, and Relaxation Times. *Russ. J. Phys. Chem. A* **2018**, 92 (6), 853–870. <https://doi.org/10.1134/S0036024418060201>.
- (79) Moradi, O. Thermodynamics of Interfaces. In *Thermodynamics – Interaction Studies – Solids, Liquids and Gases*; Carlos Moreno, J., Ed.; InTech, 2011; pp 201–250.
- (80) Silverstein, T. P. The Real Reason Why Oil and Water Don't Mix. *J. Chem. Educ.* **1998**, 75 (1), 116–118. <https://doi.org/10.1021/ed075p116>.
- (81) Pasquali, R. C.; Taurozzi, M. P.; Bregni, C. Some Considerations about the Hydrophilic-Lipophilic Balance System. *Int. J. Pharm.* **2008**, 356 (1–2), 44–51. <https://doi.org/10.1016/j.ijpharm.2007.12.034>.
- (82) Davies, J. T. A Quantitative Kinetic Theory of Emulsion Type, I. Physical Chemistry of the Emulsifying Agent. In *Gas/Liquid and Liquid/Liquid Interfaces*; 1957; pp 1–13.
- (83) Lowy, D. A. Fatty Acids at Liquid–Liquid Interfaces. In *Encyclopedia of Surface and Colloid Science*; Taylor & Francis, 2015; pp 2662–2673. <https://doi.org/10.1081/e-escs3-120000028>.
- (84) Bonfilln, A.; Sicoli, F.; Langevin, D. Dynamic Surface Tension of Ionic Surfactant Solutions. *J. Colloid Interface Sci.* **1994**, 168 (2), 497–504. <https://doi.org/10.1006/jcis.1994.1447>.
- (85) Couper, A. *Surface Tension and Its Measurement*, 2nd ed.; Rossiter, B. W., Baetzold, R. ., Eds.; J. Wiley & Sons: New York, 1993.
- (86) Borwankar, R. P.; Wasan, D. T. The Effect of Surfactants on Interphase Solute Transport. A Theory of Interfacial Resistance. *Ind. Eng. Chem. Fundam.* **1986**, 25 (4), 662–668. <https://doi.org/10.1021/i100024a031>.
- (87) Moorkanikkara, S. N. Development of Novel Methodologies to Analyze the Adsorption Kinetics of Nonionic Surfactants, Massachusetts Institute of Technology, 2007.
- (88) Danov, K. D.; Valkovska, D. S.; Kralchevsky, P. A. Adsorption Relaxation for Nonionic Surfactants under Mixed Barrier-Diffusion and Micellization-Diffusion Control. *J. Colloid Interface Sci.* **2002**, 251, 18–25. <https://doi.org/10.1006/jcis.2002.8358>.
- (89) Liggieri, L.; Miller, R. Relaxation of Surfactants Adsorption Layers at Liquid Interfaces. *Curr. Opin. Colloid Interface Sci.* **2010**, 15 (4), 256–263. <https://doi.org/10.1016/J.COCIS.2010.02.003>.
- (90) Al-Soufi, W.; Pineiro, L.; Novo, M. A Model for Monomer and Micellar Concentrations in Surfactant Solutions. Application to Conductivity, NMR, Diffusion and Surface Tension Data. *J. Colloid Interface*

- Sci.* **2012**, *370*, 102–110. <https://doi.org/10.1016/j.jcis.2011.12.037>.
- (91) Patist, A.; Bhagwat, S. S.; Penfield, K. W.; Aikens, P.; Shah, D. O. On the Measurement of Critical Micelle Concentrations of Pure and Technical-Grade Nonionic Surfactants. *J. Surfactants Deterg.* **2000**, *31* (1), 53–58. <https://doi.org/10.1007/S11743-000-0113-4>.
- (92) Elhefian, E. Investigation on Some Properties of SDS Solutions. *Aust. J. Basic Appl. Sci.* **2011**, *5* (7), 1221–1227.
- (93) Mysels, K. J.; Florence, A. T. The Effect of Impurities on Dynamic Surface Tension-Basis for a Valid Surface Purity Criterion. *J. Colloid Interface Sci.* **1973**, *43* (3), 577–582. [https://doi.org/10.1016/0021-9797\(73\)90405-0](https://doi.org/10.1016/0021-9797(73)90405-0).
- (94) Vatanparast, H.; Shahabi, F.; Bahramian, A.; Javadi, A.; Miller, R. The Role of Electrostatic Repulsion on Increasing Surface Activity of Anionic Surfactants in the Presence of Hydrophilic Silica Nanoparticles. *Sci. Rep.* **2018**, *8* (1), 1–11. <https://doi.org/10.1038/s41598-018-25493-7>.
- (95) Gibbs, J. W. *The Collected Works of J. W. Gibbs*; Longmans: New York, 1931.
- (96) Marmur, A. Surface Tension and Adsorption without a Dividing Surface. *Langmuir* **2015**, *31* (46), 12653–12657. <https://doi.org/10.1021/acs.langmuir.5b03647>.
- (97) Láng, G. G. Basic Interfacial Thermodynamics and Related Mathematical Background. *ChemTexts* **2015**, *1* (4). <https://doi.org/10.1007/s40828-015-0015-z>.
- (98) Martínez-Balbuena, L.; Arteaga-Jiménez, A.; Hernández-Zapata, E.; Márquez-Beltrán, C. Applicability of the Gibbs Adsorption Isotherm to the Analysis of Experimental Surface-Tension Data for Ionic and Nonionic Surfactants. *Adv. Colloid Interface Sci.* **2017**, *247*, 178–184. <https://doi.org/10.1016/J.CIS.2017.07.018>.
- (99) Menger, F. M.; Shi, L.; Rizvi, S. A. A. Re-Evaluating the Gibbs Analysis of Surface Tension at the Air/Water Interface. *J. Am. Chem. Soc.* **2009**, *131* (30), 10380. <https://doi.org/10.1021/JA9044289>.
- (100) Menger, F. M.; Rizvi, S. A. A. Relationship between Surface Tension and Surface Coverage. *Langmuir* **2011**, *27* (23), 13975–13977. <https://doi.org/10.1021/la203009m>.
- (101) Foo, K. Y.; Hameed, B. H. Insights into the Modeling of Adsorption Isotherm Systems. *Chem. Eng. J.* **2010**, *156* (1), 2–10. <https://doi.org/10.1016/j.cej.2009.09.013>.
- (102) Miller, R.; Aksenenko, E. V.; Fainerman, V. B. Dynamic Interfacial Tension of Surfactant Solutions. *Adv. Colloid Interface Sci.* **2017**, *247*, 115–129. <https://doi.org/10.1016/j.cis.2016.12.007>.
- (103) Kairaliyeva, T.; Aksenenko, E. V.; Mucic, N.; Makievski, A. V.; Fainerman, V. B.; Miller, R. Surface Tension and Adsorption Studies by Drop Profile Analysis Tensiometry. *J. Surfactants Deterg.* **2017**, *20* (6), 1225–1241. <https://doi.org/10.1007/S11743-017-2016-Y>.
- (104) Erbil, H. Y. The Debate on the Dependence of Apparent Contact Angles on Drop Contact Area or Three-Phase Contact Line: A Review. *Surf. Sci. Rep.* **2014**, *69* (4), 325–365. <https://doi.org/10.1016/j.surfrep.2014.09.001>.
- (105) Erbil, Y. H. Dependency of Contact Angles on Three-Phase Contact Line: A Review. *Colloids and Interfaces* **2021**, *5* (1). <https://doi.org/10.3390/colloids5010008>.
- (106) Zisman, W. A. Relation of the Equilibrium Contact Angle to Liquid and Solid Constitution. *Adv. Chem.* **1964**, *43*, 1–51. <https://doi.org/10.1021/ba-1964-0043.ch001>.
- (107) Kaelble, D. H. Dispersion-Polar Surface Tension Properties of Organic Solids. *J. Adhes.* **1970**, *2* (2), 66–81. <https://doi.org/10.1080/0021846708544582>.
- (108) Owens, D. K.; Wendt, R. C. Estimation of the Surface Free Energy of Polymers. *J. Appl. Polym. Sci.* **1969**, *13* (8), 1741–1747. <https://doi.org/10.1002/app.1969.070130815>.
- (109) Rabel, W. Einige Aspekte Der Benetzungstheorie Und Ihre Anwendung Auf Die Untersuchung Und Veränderung Der Oberflächeneigenschaften von Polymeren. *Farbe und Lack* **1971**, *77* (10), 997–1005.
- (110) Good, R. J.; van Oss, C. J. The Modern Theory of Contact Angles and the Hydrogen Bond Components of Surface Energies. In *Modern Approaches to Wettability*; Loeb, G. I., Schrader, M. E., Eds.; Springer, 1992; pp 1–27. https://doi.org/10.1007/978-1-4899-1176-6_1.
- (111) Wu, S. Polar and Nonpolar Interactions in Adhesion. *J. Adhes.* **1973**, *5* (1), 39–55. <https://doi.org/10.1080/00218467308078437>.
- (112) Della Volpe, C.; Maniglio, D.; Brugnara, M.; Siboni, S.; Morra, M. The Solid Surface Free Energy Calculation: I. In Defense of the Multicomponent Approach. *J. Colloid Interface Sci.* **2004**, *271* (2), 434–453. <https://doi.org/10.1016/J.JCIS.2003.09.049>.
- (113) Siboni, S.; Della Volpe, C.; Maniglio, D.; Brugnara, M. The Solid Surface Free Energy Calculation: II. The Limits of the Zisman and of the “Equation-of-State” Approaches. *J. Colloid Interface Sci.* **2004**, *271* (2), 454–472. <https://doi.org/10.1016/J.JCIS.2003.09.050>.
- (114) Drellich, J. W. Contact Angles: From Past Mistakes to New Developments through Liquid-Solid Adhesion Measurements. *Adv. Colloid Interface Sci.* **2019**, *267*, 1–14. <https://doi.org/10.1016/j.cis.2019.02.002>.
- (115) Zhang, H.; Chen, S.; Guo, Z.; Liu, Y.; Bresme, F.; Zhang, X. Contact Line Pinning Effects Influence Determination of the Line Tension of Droplets Adsorbed on Substrates. *J. Phys. Chem. C* **2018**, *122* (30),

- 17184–17189. <https://doi.org/10.1021/acs.jpcc.8b03588>.
- (116) Heib, F.; Schmitt, M. Statistical Contact Angle Analyses with the High-Precision Drop Shape Analysis (HPDSA) Approach: Basic Principles and Applications. *Coatings* **2016**, *6* (4), 57. <https://doi.org/10.3390/coatings6040057>.
- (117) Huhtamäki, T.; Tian, X.; Korhonen, J. T.; Ras, R. H. A. Surface-Wetting Characterization Using Contact-Angle Measurements. *Nat. Protoc.* **2018**, *13* (7), 1521–1538. <https://doi.org/10.1038/s41596-018-0003-z>.
- (118) Korhonen, J. T.; Huhtamäki, T.; Ikkala, O.; Ras, R. H. A. Reliable Measurement of the Receding Contact Angle. *Langmuir* **2013**, *29* (12), 3858–3863. <https://doi.org/10.1021/la400009m>.
- (119) Terpiłowski, K.; Hołysz, L.; Chodkowski, M.; Guinarte, D. C. What Can You Learn about Apparent Surface Free Energy from the Hysteresis Approach? *Colloids and Interfaces* **2021**, *5* (1). <https://doi.org/10.3390/colloids5010004>.
- (120) Bangera, A. E.; Appaiah, K. A Conditional Justification for the Determination of Surface Energy of Solids Using Contact Angle Methods. *Mater. Chem. Phys.* **2019**, *234* (June), 168–171. <https://doi.org/10.1016/j.matchemphys.2019.06.008>.
- (121) Gaydos, J.; Neumann, A. W. The Dependence of Contact Angles on Drop Size and Line Tension. *J. Colloid Interface Sci.* **1987**, *120* (1), 76–86. [https://doi.org/10.1016/0021-9797\(87\)90324-9](https://doi.org/10.1016/0021-9797(87)90324-9).
- (122) Amirfazli, A.; Kwok, D.; Gaydos, J.; Neumann, A. Line Tension Measurements through Drop Size Dependence of Contact Angle. *J. Colloid Interface Sci.* **1998**, *205* (1), 1–11. <https://doi.org/10.1006/JCIS.1998.5562>.
- (123) Gibbs, J. W. *On the Equilibrium of Heterogeneous Substances*; 1878.
- (124) Boruvca, L.; Gaydos, J.; Neumann, A. W. A Novel Strategy for Determining Line Tension from the Shape of a Liquid Meniscus near a Stripwise Heterogeneous Wall. *Colloids and Surfaces* **1990**, *43* (2), 307–326. [https://doi.org/10.1016/0166-6622\(90\)80295-F](https://doi.org/10.1016/0166-6622(90)80295-F).
- (125) Aveyard, R.; Clint, J. H. Particle Wettability and Line Tension. *J. Chem. Soc. Faraday Trans.* **1996**, *92* (1), 85–89. <https://doi.org/10.1039/FT9969200085>.
- (126) Drelich, J.; Miller, J. D. The Effect of Solid Surface Heterogeneity and Roughness on the Contact Angle/Drop (Bubble) Size Relationship. *J. Colloid Interface Sci.* **1994**, *164* (1), 252–259. <https://doi.org/10.1006/JCIS.1994.1164>.
- (127) Drelich, J.; Miller, J. D.; Hupka, J. The Effect of Drop Size on Contact Angle over a Wide Range of Drop Volumes. *J. Colloid Interface Sci.* **1993**, *155* (2), 379–385. <https://doi.org/10.1006/JCIS.1993.1050>.
- (128) Stocco, A.; Nobili, M. A Comparison between Liquid Drops and Solid Particles in Partial Wetting. *Adv. Colloid Interface Sci.* **2017**, *247* (May), 223–233. <https://doi.org/10.1016/j.cis.2017.06.014>.
- (129) Hager, W. H. Wilfrid Noel Bond and the Bond Number. *J. Hydraul. Res.* **2012**, *50* (1), 3–9. <https://doi.org/10.1080/00221686.2011.649839>.
- (130) Zhu, Z.-Q.; Wang, Y.; Liu, Q.-S.; Xie, J.-C. Influence of Bond Number on Behaviors of Liquid Drops Deposited onto Solid Substrates. *Microgravity Sci. Technol.* **2012**, *24* (3), 181–188. <https://doi.org/10.1007/S12217-011-9294-1>.
- (131) Wenzel, R. N. R. N. Resistance of Solid Surfaces to Wetting by Water. *Ind. Eng. Chem.* **1936**, *28* (8), 988–994. <https://doi.org/10.1021/ie50320a024>.
- (132) Cassie, A. B. D.; Baxter, S. Large Contact Angles of Plant and Animal Surfaces. *Nature* **1945**, *155* (3923), 21–22. <https://doi.org/10.1038/155021a0>.
- (133) Extrand, C. W. Contact Angles and Hysteresis on Surfaces with Chemically Heterogeneous Islands. *Langmuir* **2003**, *19* (9), 3793–3796. <https://doi.org/10.1021/LA0268350>.
- (134) Gao, L.; McCarthy, T. J. How Wenzel and Cassie Were Wrong. *Langmuir* **2007**, *23* (7), 3762–3765. <https://doi.org/10.1021/LA062634A>.
- (135) Adamson, A. W.; Ling, I. The Status of Contact Angle as a Thermodynamic Property. *Adv. Chem.* **1964**, *43*, 57–73. <https://doi.org/10.1021/ba-1964-0043.ch003>.
- (136) Herring, C. Some Theorems on the Free Energies of Crystal Surfaces. *Phys. Rev.* **1951**, *82* (1), 87. <https://doi.org/10.1103/PhysRev.82.87>.
- (137) Kralchevsky, P. A.; Ivanov, I. B.; Ananthapadmanabhan, K. P.; Lips, A. On the Thermodynamics of Particle-Stabilized Emulsions: Curvature Effects and Catastrophic Phase Inversion. *Langmuir* **2004**, *21* (1), 50–63. <https://doi.org/10.1021/LA047793D>.
- (138) Binks, B. P.; Lumsdon, S. O. Catastrophic Phase Inversion of Water-in-Oil Emulsions Stabilized by Hydrophobic Silica. *Langmuir* **2000**, *16* (6), 2539–2547. <https://doi.org/10.1021/LA991081J>.
- (139) Kralchevsky, P. A.; Nagayama, K. *Particles at Fluids Interfaces and Membranes: Attachment of Colloid Particles and Proteins to Interfaces and Formation of Two-Dimensional Arrays*; Elsevier, 2001.
- (140) Snoeyink, C.; Barman, S.; Christopher, G. F. Contact Angle Distribution of Particles at Fluid Interfaces. *Langmuir* **2015**, *31* (3), 891–897. <https://doi.org/10.1021/la5040195>.
- (141) Vogel, N.; Ally, J.; Bley, K.; Kappl, M.; Landfester, K.; Weiss, C. K. Direct Visualization of the Interfacial Position of Colloidal Particles and Their Assemblies. *Nanoscale* **2014**, *6* (12), 6879–6885.

- <https://doi.org/10.1039/c4nr00401a>.
- (142) Isa, L.; Lucas, F.; Wepf, R.; Reimhult, E. Measuring Single-Nanoparticle Wetting Properties by Freeze-Fracture Shadow-Casting Cryo-Scanning Electron Microscopy. *Nat. Commun.* **2011**, *2* (1). <https://doi.org/10.1038/ncomms1441>.
- (143) Garbin, V. Colloidal Particles: Surfactants with a Difference. *Phys. Today* **2013**, *66* (10), 68. <https://doi.org/10.1063/PT.3.2158>.
- (144) Ballard, N.; Law, A. D.; Bon, S. A. F. Colloidal Particles at Fluid Interfaces: Behaviour of Isolated Particles. *Soft Matter* **2019**, *15* (6), 1186–1199. <https://doi.org/10.1039/C8SM02048E>.
- (145) Zanini, M.; Marschelke, C.; Anachkov, S. E.; Marini, E.; Synytska, A.; Isa, L. Universal Emulsion Stabilization from the Arrested Adsorption of Rough Particles at Liquid-Liquid Interfaces. *Nat. Commun.* **2017**, *8*, 1–9. <https://doi.org/10.1038/ncomms15701>.
- (146) Nonomura, Y.; Komura, S. Surface Activity of Solid Particles with Extremely Rough Surfaces. *J. Colloid Interface Sci.* **2008**, *317* (2), 501–506. <https://doi.org/10.1016/J.JCIS.2007.09.066>.
- (147) Glaser, N.; Adams, D. J.; Böker, A.; Krausch, G. Janus Particles at Liquid-Liquid Interfaces. *Langmuir* **2006**, *22*, 5227–5229. <https://doi.org/10.1021/la060693i>.
- (148) Pieranski, P. Two-Dimensional Interfacial Colloidal Crystals. *Phys. Rev. Lett.* **1980**, *45* (7), 569–572. <https://doi.org/10.1103/PhysRevLett.45.569>.
- (149) Reeves, M.; Brown, A. T.; Schofield, A. B.; Cates, M. E.; Thijssen, J. H. J. Particle-Size Effects in the Formation of Bicontinuous Pickering Emulsions. *Phys. Rev. E* **2015**, *92* (3), 032308. <https://doi.org/10.1103/PhysRevE.92.032308>.
- (150) Lin, Y.; Skaff, H.; Emrick, T.; Dinsmore, A. D.; Russell, T. P. Nanoparticle Assembly and Transport at Liquid-Liquid Interfaces. *Science* (80-.). **2003**, *299* (5604), 226–229. <https://doi.org/10.1126/SCIENCE.1078616>.
- (151) Clegg, P. S.; Herzig, E. M.; Schofield, A. B.; Egelhaaf, S. U.; Horozov, T. S.; Binks, B. P.; Cates, M. E.; Poon, W. C. K. Emulsification of Partially Miscible Liquids Using Colloidal Particles: Nonspherical and Extended Domain Structures. *Langmuir* **2007**, *23* (11), 5984–5994. <https://doi.org/10.1021/LA063707T>.
- (152) Herzig, E. M.; White, K. A.; Schofield, A. B.; Poon, W. C. K.; Clegg, P. S. Bicontinuous Emulsions Stabilized Solely by Colloidal Particles. *Nat. Mater.* **2007**, *6* (12), 966–971. <https://doi.org/10.1038/nmat2055>.
- (153) Stratford, K.; Adhikari, R.; Pagonabarraga, I.; Desplat, J.; Cates, M. Colloidal Jamming at Interfaces: A Route to Fluid-Bicontinuous Gels. *Science* (80-.). **2005**, *309* (5744), 2198–2201. <https://doi.org/10.1126/SCIENCE.1116589>.
- (154) Garbin, V.; Crocker, J. C.; Stebe, K. J. Forced Desorption of Nanoparticles from an Oil-Water Interface. *Langmuir* **2012**, *28*, 1663–1667. <https://doi.org/10.1021/la202954c>.
- (155) Garbin, V.; Jenkins, I.; Sinno, T.; Crocker, J. C.; Stebe, K. J. Interactions and Stress Relaxation in Monolayers of Soft Nanoparticles at Fluid-Fluid Interfaces. *Phys. Rev. Lett.* **2015**, *114* (10), 108301. <https://doi.org/10.1103/PhysRevLett.114.108301>.
- (156) Wi, H.; Cingarapu, S.; Klabunde, K.; Law, B. Nanoparticle Adsorption at Liquid-Vapor Surfaces: Influence of Nanoparticle Thermodynamics, Wettability, and Line Tension. *Langmuir* **2011**, *27* (16), 9979–9984. <https://doi.org/10.1021/LA201791G>.
- (157) Ninham, B. W. On Progress in Forces since the DLVO Theory. *Adv. Colloid Interface Sci.* **1999**, *83* (1), 1–17. [https://doi.org/10.1016/S0001-8686\(99\)00008-1](https://doi.org/10.1016/S0001-8686(99)00008-1).
- (158) Leite, F. L.; Bueno, C. C.; Da Roz, A. L.; Ziemath, E. C.; Oliveira Jr., O. N. Theoretical Models for Surface Forces and Adhesion and Their Measurement Using Atomic Force Microscopy. *Int. J. Mol. Sci.* **2012**, *13*, 12773–12856. <https://doi.org/10.3390/ijms131012773>.
- (159) Trefalt, G.; Borkovec, M. *Overview of DLVO Theory*; 2014.
- (160) Dörfler, H. D. *Grenzflächen Und Kolloid-Disperse Systeme: Physik Und Chemie*; Springer, 2002.
- (161) Israelachvili, J. *Intermolecular and Surface Forces, with Special Applications to Colloidal and Biological Systems*, 3rd ed.; Academic Press, 2011.
- (162) Belloni, L. Ionic Condensation and Charge Renormalization in Colloidal Suspensions. *Colloids Surfaces A Physicochem. Eng. Asp.* **1998**, *140* (1–3), 227–243. [https://doi.org/10.1016/S0927-7757\(97\)00281-1](https://doi.org/10.1016/S0927-7757(97)00281-1).
- (163) Stolarczyk, J. K.; Deak, A.; Brougham, D. F. Nanoparticle Clusters: Assembly and Control Over Internal Order, Current Capabilities, and Future Potential. *Adv. Mater.* **2016**, *28* (27), 5400–5424. <https://doi.org/10.1002/ADMA.201505350>.
- (164) Garbin, V.; Crocker, J.; Stebe, K. Nanoparticles at Fluid Interfaces: Exploiting Capping Ligands to Control Adsorption, Stability and Dynamics. *J. Colloid Interface Sci.* **2012**, *387* (1), 1–11. <https://doi.org/10.1016/J.JCIS.2012.07.047>.
- (165) Vialeto, J.; Anyfantakis, M. Exploiting Additives for Directing the Adsorption and Organization of Colloid Particles at Fluid Interfaces. *Langmuir* **2021**, *37* (31), 9302–9335. <https://doi.org/10.1021/acs.langmuir.1c01029>.

- (166) Giroto, M.; Dos Santos, A.; Levin, Y. Interaction of Charged Colloidal Particles at the Air-Water Interface. *J. Phys. Chem. B* **2016**, *120* (26), 5817–5822. <https://doi.org/10.1021/ACS.JPCB.5B10105>.
- (167) Oettel, M.; Dietrich, S. Colloidal Interactions at Fluid Interfaces. *Langmuir* **2008**, *24* (4), 1425–1441. <https://doi.org/10.1021/LA702794D>.
- (168) Williams, D. F.; Berg, J. C. The Aggregation of Colloidal Particles at the Air–Water Interface. *J. Colloid Interface Sci.* **1992**, *152* (1), 218–229. [https://doi.org/10.1016/0021-9797\(92\)90021-D](https://doi.org/10.1016/0021-9797(92)90021-D).
- (169) Bresme, F.; Lehle, H.; Oettel, M. Solvent-Mediated Interactions between Nanoparticles at Fluid Interfaces. *J. Chem. Phys.* **2009**, *130* (21), 214711. <https://doi.org/10.1063/1.3148890>.
- (170) Park, B. J.; Pantina, J. P.; Furst, E. M.; Oettel, M.; Reynaert, S.; Vermant, J. Direct Measurements of the Effects of Salt and Surfactant on Interaction Forces between Colloidal Particles at Water–Oil Interfaces. *Langmuir* **2008**, *24* (5), 1686–1694. <https://doi.org/10.1021/LA7008804>.
- (171) Berg, J. C. *An Introduction to Interfaces and Colloids: The Bridge to Nanoscience*; Berg, J. C., Ed.; World Scientific Publishing Co.: Singapore, 2009. <https://doi.org/10.1142/7579>.
- (172) Moncho-Jordá, A.; Martínez-López, F.; González, A. E.; Hidalgo-Álvarez, R. Role of Long-Range Repulsive Interactions in Two-Dimensional Colloidal Aggregation: Experiments and Simulations. *Langmuir* **2002**, *18* (24), 9183–9191. <https://doi.org/10.1021/LA0258805>.
- (173) Marinova, K. G.; Alargova, R. G.; Denkov, N. D.; Velez, O. D.; Petsev, D. N.; Ivanov, I. B.; Borwankar, R. P. Charging of Oil - Water Interfaces Due to Spontaneous Adsorption of Hydroxyl Ions. **1996**, *4* (18), 2045–2051.
- (174) Beattie, J. K.; Djerdjev, A. M. The Pristine Oil/Water Interface: Surfactant-Free Hydroxide-Charged Emulsions. *Angew. Chemie - Int. Ed.* **2004**, *43*, 3568–3571.
- (175) Tanford, C. *The Hydrophobic Effect: Formation of Micelles and Biological Membranes*; Tanford, C., Ed.; Wiley: New York, 1973.
- (176) Gray-Weale, A.; Beattie, J. K. An Explanation for the Charge on Water’s Surface. *Phys. Chem. Chem. Phys.* **2009**, *11* (46), 10994–11005. <https://doi.org/10.1039/b901806a>.
- (177) Takahashi, M. ζ Potential of Microbubbles in Aqueous Solutions: Electrical Properties of the Gas-Water Interface. *J. Phys* **2005**, *109*, 21858–21864. <https://doi.org/10.1021/jp0445270>.
- (178) Smoluchowski, M. *Handbuch Der Elektrizität Und Des Magnetismus.*, L. Greutz.; Leipzig, 1921; Vol. 2. <https://doi.org/https://doi.org/10.1002/bbpc.19210272310>.
- (179) Leroy, P.; Jougnot, D.; Revil, A.; Lassin, A.; Azaroual, M. A Double Layer Model of the Gas Bubble/Water Interface. *J. Colloid Interface Sci.* **2012**, *388* (1), 243–256. <https://doi.org/10.1016/J.JCIS.2012.07.029>.
- (180) Creux, P.; Lachaise, J.; Graciaa, A.; Beattie, J. K. Specific Cation Effects at the Hydroxide-Charged Air/Water Interface. *J. Phys. Chem. C* **2007**, *111* (9), 3753–3755. <https://doi.org/10.1021/JP070060S>.
- (181) Vácha, R.; Rick, S. W.; Jungwirth, P.; Beer, A. G. F. de; Aguiar, H. B. de; Samson, J.-S.; Roke, S. The Orientation and Charge of Water at the Hydrophobic Oil Droplet–Water Interface. *J. Am. Chem. Soc.* **2011**, *133* (26), 10204–10210. <https://doi.org/10.1021/JA202081X>.
- (182) Poli, E.; Jong, K. H.; Hassanali, A. Charge Transfer as a Ubiquitous Mechanism in Determining the Negative Charge at Hydrophobic Interfaces. *Nat. Commun.* **2020**, *11* (1), 1–13. <https://doi.org/10.1038/s41467-020-14659-5>.
- (183) Larson-Smith, K.; Jackson, A.; Pozzo, D. C. SANS and SAXS Analysis of Charged Nanoparticle Adsorption at Oil-Water Interfaces. *Langmuir* **2012**, *28* (5), 2493–2501. <https://doi.org/10.1021/la204513n>.
- (184) Graciaa, A.; Creux, P.; Lachaise, J.; Salager, J. L. ζ Potential at an Air-Water Surface Related to the Critical Micelle Concentration of Aqueous Mixed Surfactant Systems. *Ind. Eng. Chem. Res.* **2000**, *39* (8), 2677–2681. <https://doi.org/10.1021/ie9907977>.
- (185) Danov, K. D.; Kralchevsky, P. A. Interaction between Like-Charged Particles at a Liquid Interface: Electrostatic Repulsion vs. Electrocapillary Attraction. *J. Colloid Interface Sci.* **2010**, *345* (2), 505–514. <https://doi.org/10.1016/j.jcis.2010.02.017>.
- (186) Bossa, G. V.; Roth, J.; Bohinc, K.; May, S. The Apparent Charge of Nanoparticles Trapped at a Water Interface. *Soft Matter* **2016**, *12* (18), 4229–4240. <https://doi.org/10.1039/c6sm00334f>.
- (187) Leunissen, M. E.; van Blaaderen, A.; Hollingsworth, A. D.; Sullivan, M. T.; Chaikin, P. M. Electrostatics at the Oil-Water Interface, Stability, and Order in Emulsions and Colloids. *Proc. Natl. Acad. Sci. U. S. A.* **2007**, *104* (8), 2585–2590. <https://doi.org/10.1073/pnas.0610589104>.
- (188) Aveyard, R.; Clint, J. H.; Nees, D.; Paunov, V. N. Compression and Structure of Monolayers of Charged Latex Particles at Air/Water and Octane/Water Interfaces. *Langmuir* **2000**, *16* (4), 1969–1979. <https://doi.org/10.1021/LA990887G>.
- (189) Kralchevsky, P. A.; Danov, K. D.; Petkov, P. V. Soft Electrostatic Repulsion in Particle Monolayers at Liquid Interfaces: Surface Pressure and Effect of Aggregation. *Philos. Trans. R. Soc. A Math. Phys. Eng. Sci.* **2016**, *374* (2072), 1–18. <https://doi.org/10.1098/rsta.2015.0130>.

- (190) Uppapalli, S.; Zhao, H. The Influence of Particle Size and Residual Charge on Electrostatic Interactions between Charged Colloidal Particles at an Oil-Water Interface. *Soft Matter* **2014**, *10* (25), 4555–4560. <https://doi.org/10.1039/c4sm00527a>.
- (191) Masschaele, K.; Park, B.; Furst, E.; Fransaeer, J.; Vermant, J. Finite Ion-Size Effects Dominate the Interaction between Charged Colloidal Particles at an Oil-Water Interface. *Phys. Rev. Lett.* **2010**, *105* (4), 048303(4). <https://doi.org/10.1103/PHYSREVLETT.105.048303>.
- (192) Wirth, C. L.; Furst, E. M.; Vermant, J. Weak Electrolyte Dependence in the Repulsion of Colloids at an Oil-Water Interface. *Langmuir* **2014**, *30* (10), 2670–2675. <https://doi.org/10.1021/la404538s>.
- (193) Horozov, T.; Aveyard, R.; Binks, B.; Clint, J. Structure and Stability of Silica Particle Monolayers at Horizontal and Vertical Octane-Water Interfaces. *Langmuir* **2005**, *21* (16), 7405–7412. <https://doi.org/10.1021/LA050923D>.
- (194) Horozov, T. S.; Binks, B. P. Particle Behaviour at Horizontal and Vertical Fluid Interfaces. *Colloids Surfaces A Physicochem. Eng. Asp.* **2005**, *267* (1–3), 64–73. <https://doi.org/10.1016/j.colsurfa.2005.06.037>.
- (195) Horozov, T. S.; Binks, B. P. Particle-Stabilized Emulsions: A Bilayer or a Bridging Monolayer? *Angew. Chemie Int. Ed.* **2006**, *45* (5), 773–776. <https://doi.org/10.1002/ANIE.200503131>.
- (196) Velleman, L.; Sikdar, D.; Turek, V. A.; Kucernak, A. R.; Roser, S. J.; Kornyshev, A. A.; Edel, J. B. Tuneable 2D Self-Assembly of Plasmonic Nanoparticles at Liquid|liquid Interfaces. *Nanoscale* **2016**, *8* (46), 19229–19241. <https://doi.org/10.1039/c6nr05081f>.
- (197) Wu, D.; Honciuc, A. Contrasting Mechanisms of Spontaneous Adsorption at Liquid–Liquid Interfaces of Nanoparticles Constituted of and Grafted with PH-Responsive Polymers. *Langmuir* **2018**, *34* (21), 6170–6182. <https://doi.org/10.1021/ACS.LANGMUIR.8B00877>.
- (198) Giakoumatos, E. C.; Aloï, A.; Voets, I. K. Illuminating the Impact of Submicron Particle Size and Surface Chemistry on Interfacial Position and Pickering Emulsion Type. *Nano Lett.* **2020**, *20* (7), 4837–4841. <https://doi.org/10.1021/ACS.NANOLETT.0C00709>.
- (199) Shrestha, A.; Bohinc, K.; May, S. Immersion Depth of Positively versus Negatively Charged Nanoparticles at the Air-Water Interface: A Poisson-Boltzmann Model. *Langmuir* **2012**, *28* (40), 14301–14307. <https://doi.org/10.1021/la303177f>.
- (200) Dhar, P.; Prasad, V.; Weeks, E. R.; Bohlein, T.; Fischer, T. M. Immersion of Charged Nanoparticles in a Salt Solution/Air Interface. *J. Phys. Chem. B* **2008**, *112*, 9565–9567. <https://doi.org/10.1021/jp805042j>.
- (201) Wickman, H. M.; Korley, J. N. Colloid Crystal Self-Organization and Dynamics at the Air/Water Interface. *Nature* **1998**, *393* (6684), 445–447. <https://doi.org/10.1038/30930>.
- (202) Nicolson, M. M.; Evans, R. C. The Interaction between Floating Particles. *Math. Proc. Cambridge Philos. Soc.* **1949**, *45* (2), 288. <https://doi.org/10.1017/S0305004100024841>.
- (203) van Nierop, E. A.; Stijnman, M. A.; Hilgenfeldt, S. Shape-Induced Capillary Interactions of Colloidal Particles. *Europhys. Lett.* **2005**, *72* (4), 671–677. <https://doi.org/10.1209/EPL/I2005-10279-7>.
- (204) Danov, K. D.; Kralchevsky, P. A.; Boneva, M. P. Electrodipping Force Acting on Solid Particles at a Fluid Interface. *Langmuir* **2004**, *20*, 6139–6151. <https://doi.org/10.1021/la0497090>.
- (205) Correia, E. L.; Brown, N.; Razavi, S. Janus Particles at Fluid Interfaces: Stability and Interfacial Rheology. *Nanomaterials* **2021**, *11* (2), 374. <https://doi.org/10.3390/NANO11020374>.
- (206) Wei, B.; Chang, Q.; Yan, C. Wettability Determined by Capillary Rise with Pressure Increase and Hydrostatic Effects. *J. Colloid Interface Sci.* **2012**, *376* (1), 307–311. <https://doi.org/10.1016/J.JCIS.2012.02.072>.
- (207) Frydel, D.; Dietrich, S.; Oettel, M. Charge Renormalization for Effective Interactions of Colloids at Water Interfaces. *Phys. Rev. Lett.* **2007**, *99* (11). <https://doi.org/10.1103/PHYSREVLETT.99.118302>.
- (208) Israelachvili, J. Intermolecular and Surface Forces. In *Intermolecular and Surface Forces*; Elsevier Inc.: Amsterdam, 2011; pp 503–534. <https://doi.org/10.1016/C2009-0-21560-1>.
- (209) Isa, L.; Calzolari, D. C. E.; Pontoni, D.; Gillich, T.; Nelson, A.; Zirbs, R.; Sánchez-Ferrer, A.; Mezzenga, R.; Reimhult, E. Core-Shell Nanoparticle Monolayers at Planar Liquid-Liquid Interfaces: Effects of Polymer Architecture on the Interface Microstructure. *Soft Matter* **2013**, *9* (14), 3789–3797. <https://doi.org/10.1039/c3sm27367a>.
- (210) Vialetto, J.; Nussbaum, N.; Bergfreund, J.; Fischer, P.; Isa, L. Influence of the Interfacial Tension on the Microstructural and Mechanical Properties of Microgels at Fluid Interfaces. *J. Colloid Interface Sci.* **2022**, *608*, 2584–2592. <https://doi.org/10.1016/J.JCIS.2021.10.186>.
- (211) Stocco, A.; Chollet, B.; Wang, X.; Blanc, C.; Nobili, M. Rotational Diffusion of Partially Wetted Colloids at Fluid Interfaces. *J. Colloid Interface Sci.* **2019**, *542*, 363–369. <https://doi.org/10.1016/j.jcis.2019.02.017>.
- (212) Rezvantalab, H.; Drazer, G.; Shojaei-Zadeh, S. Molecular Simulation of Translational and Rotational Diffusion of Janus Nanoparticles at Liquid Interfaces. *J. Chem. Phys.* **2015**, *142* (1). <https://doi.org/10.1063/1.4904549>.

- (213) Dörr, A.; Hardt, S.; Masoud, H.; Stone, H. A. Drag and Diffusion Coefficients of a Spherical Particle Attached to a Fluid–Fluid Interface. *J. Fluid Mech.* **2016**, *790*, 607–618. <https://doi.org/10.1017/JFM.2016.41>.
- (214) Naga, A.; Rgen Butt, H.-J.; Vollmer, D. The Force Required to Detach a Rotating Particle from a Liquid–Fluid Interface. *Langmuir* **2021**, *37* (44), 13012–13017. <https://doi.org/10.1021/ACS.LANGMUIR.1C02085>.
- (215) Luu, X. C.; Yu, J.; Striolo, A. Nanoparticles Adsorbed at the Water/Oil Interface: Coverage and Composition Effects on Structure and Diffusion. *Langmuir* **2013**, *29* (24), 7221–7228. <https://doi.org/10.1021/la304828u>.
- (216) Wang, D.; Yordanov, S.; Paroor, H. M.; Mukhopadhyay, A.; Li, C. Y.; Butt, H. J.; Koynov, K. Probing Diffusion of Single Nanoparticles at Water–Oil Interfaces. *Small* **2011**, *7* (24), 3502–3507. <https://doi.org/10.1002/smll.201101823>.
- (217) Lin, Y.; Böker, A.; Skaff, H.; Cookson, D.; Dinsmore, A. D.; Emrick, T.; Russell, T. P. Nanoparticle Assembly at Fluid Interfaces: Structure and Dynamics. *Langmuir* **2005**, No. 21, 191–194. <https://doi.org/10.1021/la048000q>.
- (218) Maestro, A.; Deshmukh, O. S.; Mugele, F.; Langevin, D. Interfacial Assembly of Surfactant-Decorated Nanoparticles: On the Rheological Description of a Colloidal 2D Glass. *Langmuir* **2015**, *31* (23), 6289–6297. <https://doi.org/10.1021/ACS.LANGMUIR.5B00632>.
- (219) Erni, P. Deformation Modes of Complex Fluid Interfaces. *Soft Matter* **2011**, *7* (17), 7586–7600. <https://doi.org/10.1039/C1SM05263B>.
- (220) Maestro, A.; Zaccone, A. Nonaffine Deformation and Tunable Yielding of Colloidal Assemblies at the Air–Water Interface. *Nanoscale* **2017**, *9* (46), 18343–18351. <https://doi.org/10.1039/C7NR06014A>.
- (221) Thijssen, J. H. J.; Vermant, J. Interfacial Rheology of Model Particles at Liquid Interfaces and Its Relation to (Bicontinuous) Pickering Emulsions. *J. Phys. Condens. Matter* **2017**, *30* (2), 023002. <https://doi.org/10.1088/1361-648X/AA9C74>.
- (222) Noskov, B. A.; Bykov, A. G. Dilational Rheology of Monolayers of Nano- and Microparticles at the Liquid–Fluid Interfaces. *Curr. Opin. Colloid Interface Sci.* **2018**, *37*, 1–12. <https://doi.org/10.1016/J.COCIS.2018.05.001>.
- (223) Hermans, E.; Saad Bhamla, M.; Kao, P.; Fuller, G. G.; Vermant, J. Lung Surfactants and Different Contributions to Thin Film Stability. *Soft Matter* **2015**, *11* (41), 8048–8057. <https://doi.org/10.1039/C5SM01603G>.
- (224) Sagis, L. M. C. Dynamic Properties of Interfaces in Soft Matter: Experiments and Theory. *Rev. Mod. Phys.* **2011**, *83* (4), 1367–1403. <https://doi.org/10.1103/RevModPhys.83.1367>.
- (225) Jaensson, N.; Vermant, J. Tensiometry and Rheology of Complex Interfaces. *Curr. Opin. Colloid Interface Sci.* **2018**, *37* (October), 136–150. <https://doi.org/10.1016/j.cocis.2018.09.005>.
- (226) Stancik, E. J.; Kouhkan, M.; Fuller, G. G. Coalescence of Particle-Laden Fluid Interfaces. *Langmuir* **2003**, *20* (1), 90–94. <https://doi.org/10.1021/LA0356093>.
- (227) Park, B. J.; Furst, E. M. Micromechanics of Colloidal Aggregates at the Oil–Water Interface. *Soft Matter* **2011**, *7* (17), 7683–7688. <https://doi.org/10.1039/C1SM05254C>.
- (228) Wang, A.; McGorty, R.; Kaz, D. M.; Manoharan, V. N. Contact-Line Pinning Controls How Quickly Colloidal Particles Equilibrate with Liquid Interfaces. *Soft Matter* **2016**, *12* (43), 8958–8967. <https://doi.org/10.1039/c6sm01690a>.
- (229) Kaz, D. M.; McGorty, R.; Mani, M.; Brenner, M. P.; Manoharan, V. N. Physical Ageing of the Contact Line on Colloidal Particles at Liquid Interfaces. *Nat. Mater.* **2012**, *11* (2), 138–142. <https://doi.org/10.1038/nmat3190>.
- (230) Aloi, A.; Vilanova, N.; Albertazzi, L.; Voets, I. K. IPAIN: A General Approach Tailored to Image the Topology of Interfaces with Nanometer Resolution. *Nanoscale* **2016**, *8* (16), 8712–8716. <https://doi.org/10.1039/C6NR00445H>.
- (231) Aloi, A.; Vilanova, N.; Isa, L.; Jong, A. M. de; Voets, I. K. Super-Resolution Microscopy on Single Particles at Fluid Interfaces Reveals Their Wetting Properties and Interfacial Deformations. *Nanoscale* **2019**, *11* (14), 6654–6661. <https://doi.org/10.1039/C8NR08633H>.
- (232) Maestro, A.; Guzmán, E.; Ortega, F.; Rubio, R. G. Contact Angle of Micro- and Nanoparticles at Fluid Interfaces. *Curr. Opin. Colloid Interface Sci.* **2014**, *19* (4), 355–367. <https://doi.org/10.1016/j.cocis.2014.04.008>.
- (233) Arnaudov, L. N.; Cayre, O. J.; Cohen Stuart, M. A.; Stoyanov, S. D.; Paunov, V. N. Measuring the Three-Phase Contact Angle of Nanoparticles at Fluid Interfaces. *Phys. Chem. Chem. Phys.* **2010**, *12* (2), 328–331. <https://doi.org/10.1039/b917353f>.
- (234) Paunov, V. N. Novel Method for Determining the Three-Phase Contact Angle of Colloid Particles Adsorbed at Air–Water and Oil–Water Interfaces. *Langmuir* **2003**, *19*, 7970–7976. <https://doi.org/10.1021/la0347509>.

- (235) Zheng, H.; Claridge, S. A.; Minor, A. M.; Alivisatos, A. P.; Dahmen, U. Nanocrystal Diffusion in a Liquid Thin Film Observed by in Situ Transmission Electron Microscopy. *Nano Lett.* **2009**, *9* (6), 2460–2465. <https://doi.org/10.1021/NL9012369>.
- (236) de Jonge, N.; Ross, F. M. Electron Microscopy of Specimens in Liquid. *Nat. Nanotechnol.* **2011**, *6* (11), 695–704. <https://doi.org/10.1038/nnano.2011.161>.
- (237) Lin, G.; Zhu, X.; Anand, U.; Liu, Q.; Lu, J.; Aabdin, Z.; Su, H.; Mirsaidov, U. Nanodroplet-Mediated Assembly of Platinum Nanoparticle Rings in Solution. *Nano Lett.* **2016**, *16* (2), 1092–1096. <https://doi.org/10.1021/ACS.NANOLETT.5B04323>.
- (238) Muller, F.; Dégoussée, T.; Degrouard, J.; Brûlet, A.; Salonen, A. Probing Structure in Submicronic Aqueous Assemblies of Emulsified Microemulsions and Charged Spherical Colloids Using SANS and Cryo-TEM. *J. Colloid Interface Sci.* **2015**, *446*, 114–121. <https://doi.org/10.1016/J.JCIS.2015.01.007>.
- (239) Kim, P. Y.; Ribbe, A. E.; Russell, T. P.; Hoagland, D. A. Visualizing the Dynamics of Nanoparticles in Liquids by Scanning Electron Microscopy. *ACS Nano* **2016**, *10* (6), 6257–6264. <https://doi.org/10.1021/ACSNANO.6B02432>.
- (240) Costa, L.; Li-Destri, G.; Pontoni, D.; Konovalov, O.; Thomson, N. H. Liquid–Liquid Interfacial Imaging Using Atomic Force Microscopy. *Adv. Mater. Interfaces* **2017**, *4* (16). <https://doi.org/10.1002/ADMI.201700203>.
- (241) Costa, L.; Li-Destri, G.; Thomson, N. H.; Konovalov, O.; Pontoni, D. Real Space Imaging of Nanoparticle Assembly at Liquid–Liquid Interfaces with Nanoscale Resolution. *Nano Lett.* **2016**, *16* (9), 5463–5468. <https://doi.org/10.1021/ACS.NANOLETT.6B01877>.
- (242) Chai, Y.; Hasnain, J.; Bahl, K.; Wong, M.; Li, D.; Geissler, P.; Kim, P. Y.; Jiang, Y.; Gu, P.; Li, S.; Lei, D.; Helms, B. A.; Russell, T. P.; Ashby, P. D. Direct Observation of Nanoparticle-Surfactant Assembly and Jamming at the Water–Oil Interface. *Sci. Adv.* **2020**, *6* (48), 1–7. <https://doi.org/10.1126/sciadv.abb8675>.
- (243) Reculosa, S.; Perrier-Cornet, R.; Agricole, B.; Héroguez, V.; Buffeteau, T.; Ravaine, S. Langmuir–Blodgett Films of Micron-Sized Organic and Inorganic Colloids. *Phys. Chem. Chem. Phys.* **2007**, *9* (48), 6385–6390. <https://doi.org/10.1039/B711038N>.
- (244) Li, T.; Lilja, K.; Morris, R. J.; Brandani, G. B. Langmuir–Blodgett Technique for Anisotropic Colloids: Young Investigator Perspective. *J. Colloid Interface Sci.* **2019**, *540*, 420–438. <https://doi.org/10.1016/J.JCIS.2019.01.044>.
- (245) Cayre, O. J.; Paunov, V. N. Contact Angles of Colloid Silica and Gold Particles at Air–Water and Oil–Water Interfaces Determined with the Gel Trapping Technique. *Langmuir*. 2004, pp 9594–9599. <https://doi.org/10.1021/la0489615>.
- (246) Sharp, E. L.; Al-shehri, H.; Horozov, T. S.; Stoyanov, D.; Paunov, V. N. Adsorption of Shape-Anisotropic and Porous Particles at the Air–Water and the Decane–Water Interface Studied by the Gel Trapping Technique. *RSC Adv.* **2014**, *4*, 2205–2213. <https://doi.org/10.1039/c3ra44563a>.
- (247) Sabapathy, M.; Kollabattula, V.; Basavaraj, M. G.; Mani, E. Visualization of the Equilibrium Position of Colloidal Particles at Fluid–Water Interfaces by Deposition of Nanoparticles. *Nanoscale* **2015**, *7* (33), 13868–13876. <https://doi.org/10.1039/c5nr03369a>.
- (248) Maestro, A.; Bonales, L. J.; Ritacco, H.; Rubio, R. G.; Ortega, F. Effect of the Spreading Solvent on the Three-Phase Contact Angle of Microparticles Attached at Fluid Interfaces. *Phys. Chem. Chem. Phys.* **2010**, *12* (42), 14115–14120. <https://doi.org/10.1039/c0cp00570c>.
- (249) Ray, M. A.; Jia, L. Micropatterning by Non-Densely Packed Interfacial Colloidal Crystals†. *Adv. Mater.* **2007**, *19* (15), 2020–2022. <https://doi.org/10.1002/ADMA.200602521>.
- (250) Isa, L. Freeze-Fracture Shadow-Casting (FreSCa) Cryo-Sem as a Tool to Investigate the Wetting of Micro- and Nanoparticles at Liquid–Liquid Interfaces. *Chimia (Aarau)*. **2013**, *67* (4), 231–235. <https://doi.org/10.2533/chimia.2013.231>.
- (251) Sander, J. S.; Isa, L.; Rühls, P. A.; Fischer, P.; Studart, A. R. Stabilization Mechanism of Double Emulsions Made by Microfluidics. *Soft Matter* **2012**, *8* (45), 11471–11477. <https://doi.org/10.1039/C2SM26700D>.
- (252) Geisel, K.; Isa, L.; Richtering, W. Unraveling the 3D Localization and Deformation of Responsive Microgels at Oil/Water Interfaces: A Step Forward in Understanding Soft Emulsion Stabilizers. *Langmuir* **2012**, *28* (45), 15770–15776. <https://doi.org/10.1021/LA302974J>.
- (253) Binks, B. P.; Rodrigues, J. A. Types of Phase Inversion of Silica Particle Stabilized Emulsions Containing Triglyceride Oil. *Langmuir* **2003**, *19* (12), 4905–4912. <https://doi.org/10.1021/la020960u>.
- (254) Hill, D.; Attia, H.; Barron, A. R.; Alexander, S. Size and Morphology Dependent Surface Wetting Based on Hydrocarbon Functionalized Nanoparticles. *J. Colloid Interface Sci.* **2019**, *543*, 328–334. <https://doi.org/10.1016/j.jcis.2019.02.058>.
- (255) Núñez, C. G.; Navaraj, W. T.; Liu, F.; Shakthivel, D.; Dahiya, R. Large-Area Self-Assembly of Silica Microspheres/Nanospheres by Temperature-Assisted Dip-Coating. *ACS Appl. Mater. Interfaces* **2018**, *10* (3), 3058–3068. <https://doi.org/10.1021/acsami.7b15178>.

- (256) Ramiasa-MacGregor, M.; Mierczynska, A.; Sedev, R.; Vasilev, K. Tuning and Predicting the Wetting of Nanoengineered Material Surface. *Nanoscale* **2016**, *8* (8), 4635–4642. <https://doi.org/10.1039/c5nr08329j>.
- (257) Guo, Y.; Tang, D.; Du, Y.; Liu, B. Controlled Fabrication of Hexagonally Close-Packed Langmuir-Blodgett Silica Particulate Monolayers from Binary Surfactant and Solvent Systems. *Langmuir* **2013**, *29* (9), 2849–2858. <https://doi.org/10.1021/la3049218>.
- (258) Munshi, A. M.; Singh, V. N.; Kumar, M.; Singh, J. P. Effect of Nanoparticle Size on Sessile Droplet Contact Angle. *J. Appl. Phys.* **2008**, *103* (8). <https://doi.org/10.1063/1.2912464>.
- (259) Dai, Z.; Li, Y.; Duan, G.; Jia, L.; Cai, W. Phase Diagram, Design of Monolayer Binary Colloidal Crystals, and Their Fabrication Based on Ethanol-Assisted Self-Assembly at the Air/Water Interface. *ACS Nano* **2012**, *6* (8), 6706–6716. <https://doi.org/10.1021/nn3013178>.
- (260) Lotito, V.; Zambelli, T. Self-Assembly of Single-Sized and Binary Colloidal Particles at Air/ Water Interface by Surface Con Finement and Water Discharge. *Langmuir* **2016**, *32*, 9582–9590. <https://doi.org/10.1021/acs.langmuir.6b02157>.
- (261) Vogel, N.; Viguier, L. de; Jonas, U.; Weiss, C. K.; Landfester, K. Wafer-Scale Fabrication of Ordered Binary Colloidal Monolayers with Adjustable Stoichiometries. *Adv. Funct. Mater.* **2011**, *21*, 3064–3073. <https://doi.org/10.1002/adfm.201100414>.
- (262) Drelich, J. W.; Boinovich, L.; Chibowski, E.; Della Volpe, C.; Holysz, L.; Marmur, A.; Siboni, S. Contact Angles: History of over 200 Years of Open Questions. *Surf. Innov.* **2020**, *8* (1–2), 3–27. <https://doi.org/10.1680/JSUIN.19.00007>.
- (263) Drelich, J.; Chibowski, E.; Meng, D. D.; Terpilowski, K. Hydrophilic and Superhydrophilic Surfaces and Materials. *Soft Matter* **2011**, *7* (21), 9804–9828. <https://doi.org/10.1039/c1sm05849e>.
- (264) Burnett, M. K.; Zisman, W. A. Confirmation of Spontaneous Spreading by Water on Pure Gold. *undefined* **1970**, *74* (11), 2309–2312. <https://doi.org/10.1021/J100705A012>.
- (265) Osman, M. A.; Keller, B. A. Wettability of Native Silver Surfaces. *Appl. Surf. Sci.* **1996**, *99* (3), 261–263. [https://doi.org/10.1016/0169-4332\(96\)00101-8](https://doi.org/10.1016/0169-4332(96)00101-8).
- (266) Takeda, S.; Fukawa, M.; Hayashi, Y.; Matsumoto, K. Surface OH Group Governing Adsorption Properties of Metal Oxide Films. *Thin Solid Films* **1999**, *339* (1–2), 220–224. [https://doi.org/10.1016/S0040-6090\(98\)01152-3](https://doi.org/10.1016/S0040-6090(98)01152-3).
- (267) Takeda, S.; Yamamoto, K.; Hayasaka, Y.; Matsumoto, K. Surface OH Group Governing Wettability of Commercial Glasses. *J. Non Cryst Solids* **1999**, *249* (1), 41–46. [https://doi.org/10.1016/S0022-3093\(99\)00297-5](https://doi.org/10.1016/S0022-3093(99)00297-5).
- (268) Taqvi, S.; Bassioni, G. Understanding Wettability through Zeta Potential Measurements. In *Wettability and Interfacial Phenomena - Implications for Material Processing*; 2019; Vol. 1, pp 1–19. <https://doi.org/10.5772/intechopen.84185>.
- (269) Yakubov, G. E.; Vinogradova, O. I.; Butt, H. J. Contact Angles on Hydrophobic Microparticles at Water-Air and Water-Hexadecane Interfaces. *J. Adhes. Sci. Technol.* **2000**, *14* (14), 1783–1799. <https://doi.org/10.1163/156856100743239>.
- (270) Gillies, G.; Büscher, K.; Preuss, M.; Kappl, M.; Butt, H. J.; Graf, K. Contact Angles and Wetting Behaviour of Single Micron-Sized Particles. *J. Phys. Condens. Matter* **2005**, *17* (9). <https://doi.org/10.1088/0953-8984/17/9/011>.
- (271) Preuss, M.; Butt, H. J. Measuring the Contact Angle of Individual Colloidal Particles. *J. Colloid Interface Sci.* **1998**, *208* (2), 468–477. <https://doi.org/10.1006/jcis.1998.5833>.
- (272) Fu, W.; Zhang, W. Measurement of the Surface Hydrophobicity of Engineered Nanoparticles Using an Atomic Force Microscope. *Phys. Chem. Chem. Phys.* **2018**, *20*, 24434. <https://doi.org/10.1039/c8cp04676j>.
- (273) Yan, N.; Maham, Y.; Masliyah, J. H.; Gray, M. R.; Mather, A. E. Measurement of Contact Angles for Fumed Silica Nanospheres Using Enthalpy of Immersion Data. *J. Colloid Interface Sci.* **2000**, *228*, 1–6. <https://doi.org/10.1006/jcis.2000.6856>.
- (274) Winkler, P. M.; McGraw, R. L.; Bauer, P. S.; Rentenberger, C.; Wagner, P. E. Direct Determination of Three-Phase Contact Line Properties on Nearly Molecular Scale. *Sci. Reports 2016 61* **2016**, *6* (1), 1–7. <https://doi.org/10.1038/srep26111>.
- (275) Erbil, H. Y. *Surface Chemistry of Solid and Liquid Interfaces.*; Erbil, H. Y., Ed.; Blackwell Publishing Ltd, 2006; Vol. 9. <https://doi.org/10.1002/cphc.200700726>.
- (276) Grigoriev, D. O.; Krägel, J.; Dutschk, V.; Miller, R.; Möhwald, H. Contact Angle Determination of Micro- and Nanoparticles at Fluid/Fluid Interfaces: The Excluded Area Concept. *Phys. Chem. Chem. Phys.* **2007**, *9*, 6447–6454. <https://doi.org/10.1039/B711732A>.
- (277) Grigoriev, D. O.; Möhwald, H.; Shchukin, D. G. Theoretical Evaluation of Nano- or Microparticulate Contact Angle at Fluid/Fluid Interfaces: Analysis of the Excluded Area Behavior upon Compression. *Phys. Chem. Chem. Phys.* **2008**, *10*, 1975–1982. <https://doi.org/10.1039/b719140e>.
- (278) Clint, J. H.; Taylor, S. E. Particle Size and Interparticle Forces of Overbased Detergents: A Langmuir Trough Study. *Colloids and Surfaces* **1992**, *65* (1), 61–67. [https://doi.org/10.1016/0166-6622\(92\)80175-](https://doi.org/10.1016/0166-6622(92)80175-)

- 2.
- (279) Paunov, V. N.; Binks, B. P.; Ashby, N. P. Adsorption of Charged Colloid Particles to Charged Liquid Surfaces. *Langmuir* **2002**, *18* (18), 6946–6955. <https://doi.org/10.1021/la0203584>.
- (280) Bordács, S.; Agod, A.; Hörvölgyi, Z. Compression of Langmuir Films Composed of Fine Particles: Collapse Mechanism and Wettability. *Langmuir* **2006**, *22* (16), 6944–6950. <https://doi.org/10.1021/la060696v>.
- (281) Santini, E.; Krägel, J.; Ravera, F.; Liggieri, L.; Miller, R. Study of the Monolayer Structure and Wettability Properties of Silica Nanoparticles and CTAB Using the Langmuir Trough Technique. *Colloids Surfaces A Physicochem. Eng. Asp.* **2011**, *382* (1–3), 186–191. <https://doi.org/10.1016/J.COLSURFA.2010.11.042>.
- (282) Deak, A.; Hild, E.; Kovacs, A. L.; Horvölyi, Z. Contact Angle Determination of Nanoparticles: Film Balance and Scanning Angle Reflectometry Studies. *Phys. Chem. Chem. Phys.* **2007**, *9*, 6359–6370. <https://doi.org/10.1039/b702937n>.
- (283) Langevin, D.; Wei, B.; Zang, D.; Binks, B.; Rio, E.; Delon, G. Influence of the Contact Angle of Silica Nanoparticles at the Air–Water Interface on the Mechanical Properties of the Layers Composed of These Particles. *Mol. Phys.* **2011**, *109*:7 (10), 1057–1066. <https://doi.org/10.1080/00268976.2010.542778i>.
- (284) Hunter, T. N.; Jameson, G. J.; Wanless, E. J. Determination of Contact Angles of Nanosized Silica Particles by Multi-Angle Single-Wavelength Ellipsometry. *Aust. J. Chem.* **2007**, *60* (9), 651–655. <https://doi.org/10.1071/CH07133>.
- (285) Zang, D.; Stocco, A.; Langevin, D.; Wei, B.; Binks, B. P. An Ellipsometry Study of Silica Nanoparticle Layers at the Water Surface. *Phys. Chem. Chem. Phys.* **2009**, *11* (41), 9522–9529. <https://doi.org/10.1039/B907903C>.
- (286) Hunter, T. N.; Jameson, G. J.; Wanless, E. J.; Dupin, D.; Armes, S. P. Adsorption of Submicrometer-Sized Cationic Sterically Stabilized Polystyrene Latex at the Air–Water Interface: Contact Angle Determination by Ellipsometry. *Langmuir* **2009**, *25* (6), 3440–3449. <https://doi.org/10.1021/LA803879P>.
- (287) Reitzel, N.; Greve, D. R.; Kjaer, K.; Howes, P. B.; Jayaraman, M.; Savoy, S.; McCullough, R. D.; McDevitt, J. T.; Bjørnholm, T. Self-Assembly of Conjugated Polymers at the Air/Water Interface. Structure and Properties of Langmuir and Langmuir–Blodgett Films of Amphiphilic Regioregular Polythiophenes. *J. Am. Chem. Soc.* **2000**, *122* (24), 5788–5800. <https://doi.org/10.1021/ja9924501>.
- (288) Sanyal, M. K.; Agrawal, V. V.; Bera, M. K.; Kalyanikutty, K. P.; Daillant, J.; Blot, C.; Kubowicz, S.; Konovalov, O.; Rao, C. N. R. Formation and Ordering of Gold Nanoparticles at the Toluene–Water Interface. *J. Phys. Chem. C* **2008**, *112* (6), 1739–1743. <https://doi.org/10.1021/jp710635e>.
- (289) Raveendran, A.; Dewolf, C.; Bu, W.; McWhirter, S.; Meron, M.; Lin, B.; Meli, M. V. Langmuir Films of N-Alkanethiol-Capped Gold Nanoparticles and n-Alkanes: Interfacial Mixing Scenarios Assessed by X-Ray Reflectivity and Grazing Incidence Diffraction. *J. Phys. Chem. C* **2018**, *122* (5), 2975–2982. <https://doi.org/10.1021/acs.jpcc.7b09874>.
- (290) Chen, Y. T.; Su, H. S.; Hung, C. H.; Yang, P. W.; Hu, Y.; Lin, T. L.; Lee, M. T.; Jeng, U. S. X-Ray Reflectivity Studies on the Mixed Langmuir–Blodgett Monolayers of Thiol-Capped Gold Nanoparticles, Dipalmitoylphosphatidylcholine, and Sodium Dodecyl Sulfate. *Langmuir* **2017**, *33* (41), 10886–10897. <https://doi.org/10.1021/acs.langmuir.7b01559>.
- (291) You, S. S.; Heffern, C. T. R.; Dai, Y.; Meron, M.; Henderson, J. M.; Bu, W.; Xie, W.; Lee, K. Y. C.; Lin, B. Liquid Surface X-Ray Studies of Gold Nanoparticle-Phospholipid Films at the Air/Water Interface. *J. Phys. Chem. B* **2016**, *120* (34), 9132–9141. <https://doi.org/10.1021/acs.jpcc.6b03734>.
- (292) Orsi, D.; Rimoldi, T.; Guzmán, E.; Liggieri, L.; Ravera, F.; Ruta, B.; Cristofolini, L. Hydrophobic Silica Nanoparticles Induce Gel Phases in Phospholipid Monolayers. *Langmuir* **2016**, *32* (19), 4868–4876. <https://doi.org/10.1021/acs.langmuir.6b00813>.
- (293) Mouri, E.; Okazaki, Y.; Yoshinaga, K.; Matsuoka, H. X-Ray Reflectometry Confirms Polymer-Grafted Silica Particle Monolayer Formation at the Air–Water Interface. *J. Nanosci. Nanotechnol.* **2009**, *9* (1), 327–333. <https://doi.org/10.1166/jnn.2009.J038>.
- (294) Degen, P.; Paulus, M.; Maas, M.; Kahner, R.; Schmacke, S.; Struth, B.; Tolan, M.; Rehage, H. In Situ Observation of γ -Fe₂O₃ Nanoparticle Adsorption under Different Monolayers at the Air/Water Interface. *Langmuir* **2008**, *24*, 12958–12962. <https://doi.org/10.1021/la802394a>.
- (295) Horváth, I. T.; Colinet, P.; Vetrano, M. R. Measuring Contact Angles of Small Spherical Particles at Planar Fluid Interfaces by Light Extinction. *Appl. Phys. Lett.* **2016**, *108* (20). <https://doi.org/10.1063/1.4950960>.
- (296) Maestro, A.; Guzmán, E.; Santini, E.; Ravera, F.; Liggieri, L.; Ortega, F.; Rubio, R. G. Wettability of Silica Nanoparticle-Surfactant Nanocomposite Interfacial Layers. *Soft Matter* **2012**, *8* (3), 837–843. <https://doi.org/10.1039/c1sm06421e>.
- (297) Stocco, A.; Su, G.; Nobili, M.; In, M.; Wang, D. In Situ Assessment of the Contact Angles of Nanoparticles Adsorbed at Fluid Interfaces by Multiple Angle of Incidence Ellipsometry. *Soft Matter* **2014**, *10* (36), 6999–7007. <https://doi.org/10.1039/c4sm00482e>.
- (298) Wu, W.; Liu, X.; Chen, S. L.; Yuan, Q.; Gan, W. Particle Adsorption at the Oil–Water Interface Studied

- with Second Harmonic Generation. *Soft Matter* **2019**, *15* (38), 7672–7677. <https://doi.org/10.1039/c9sm01125k>.
- (299) Scoppola, E.; Micciulla, S.; Kuhrt, L.; Maestro, A.; Campbell, R. A.; Konovalov, O. V.; Fragneto, G.; Schneck, E. Reflectometry Reveals Accumulation of Surfactant Impurities at Bare Oil/Water Interfaces. *Molecules* **2019**, *24* (22), 1–16. <https://doi.org/10.3390/molecules24224113>.
- (300) Penfold, J.; Staples, E.; Tucker, I.; Cummins, P. Adsorption of Nonionic Surfactants on Silica Sol Particles: The Effects of Sol Type and Concentration, Surfactant Type, Concentration, and Temperature. *J. Phys. Chem.* **1996**, *100* (46), 18133–18137. <https://doi.org/10.1021/jp9611838>.
- (301) Madsen, A.; Konovalov, O.; Robert, A.; Grübel, G. Surface Ordering in a Concentrated Suspension of Colloidal Particles Investigated by X-Ray Scattering Methods. *Phys. Rev. E - Stat. Physics, Plasmas, Fluids, Relat. Interdiscip. Top.* **2001**, *64* (6), 6. <https://doi.org/10.1103/PhysRevE.64.061406>.
- (302) Vaknin, D.; Wang, W.; Islam, F.; Zhang, H. Polyethylene-Glycol-Mediated Self-Assembly of Magnetite Nanoparticles at the Liquid/Vapor Interface. *Adv. Mater. Interfaces* **2018**, *5* (6). <https://doi.org/10.1002/admi.201701149>.
- (303) Wang, W.; Lawrence, J. J.; Bu, W.; Zhang, H.; Vaknin, D. Two-Dimensional Crystallization of Poly(N-Isopropylacrylamide)-Capped Gold Nanoparticles. *Langmuir* **2018**, *34* (28), 8374–8378. <https://doi.org/10.1021/acs.langmuir.8b01042>.
- (304) Parratt, L. G. Surface Studies of Solids by Total Reflection of X-Rays. *Phys. Rev.* **1954**, *95* (2), 359. <https://doi.org/10.1103/PhysRev.95.359>.
- (305) Abelès, F. La Théorie Générale Des Couches Minces. *J. Phys. le Radium* **1950**, *11* (7), 307–309. <https://doi.org/10.1051/JPHYSRAD:01950001107030700>.
- (306) Reguera, J.; Ponomarev, E.; Geue, T.; Stellacci, F.; Bresme, F.; Moglianetti, M. Contact Angle and Adsorption Energies of Nanoparticles at the Air–Liquid Interface Determined by Neutron Reflectivity and Molecular Dynamics. *Nanoscale* **2015**, *7*, 5665–5673. <https://doi.org/10.1039/c5nr00620a>.
- (307) Larson-Smith, K.; Jackson, A.; Pozzo, D. C. Small Angle Scattering Model for Pickering Emulsions and Raspberry Particles. *J. Colloid Interface Sci.* **2010**, *343* (1), 36–41. <https://doi.org/10.1016/j.jcis.2009.11.033>.
- (308) Cui, M.; Miesch, C.; Kosif, I.; Nie, H.; Kim, P. Y.; Kim, H.; Emrick, T.; Russell, T. P. Transition in Dynamics as Nanoparticles Jam at the Liquid/Liquid Interface. *Nano Lett.* **2017**, *17* (11), 6855–6862. <https://doi.org/10.1021/acs.nanolett.7b03159>.
- (309) Nagel, M.; Tervoort, T. A.; Vermant, J. From Drop-Shape Analysis to Stress-Fitting Elastometry. *Adv. Colloid Interface Sci.* **2017**, *247*, 33–51. <https://doi.org/10.1016/J.CIS.2017.07.008>.
- (310) Berry, J. D.; Neeson, M. J.; Dagastine, R. R.; Chan, D. Y. C.; Tabor, R. F. Measurement of Surface and Interfacial Tension Using Pendant Drop Tensiometry. *J. Colloid Interface Sci.* **2015**, *454*, 226–237. <https://doi.org/10.1016/J.JCIS.2015.05.012>.
- (311) Carvajal, D.; Laprade, E. J.; Henderson, K. J.; Shull, K. R. Mechanics of Pendant Drops and Axisymmetric Membranes. *Soft Matter* **2011**, *7* (22), 10508–10519. <https://doi.org/10.1039/c1sm05703k>.
- (312) French, D. J.; Brown, A. T.; Schofield, A. B.; Fowler, J.; Taylor, P.; Clegg, P. S. The Secret Life of Pickering Emulsions: Particle Exchange Revealed Using Two Colours of Particle. *Sci. Rep.* **2016**, *6* (May), 1–9. <https://doi.org/10.1038/srep31401>.
- (313) Ward, A. F. H.; Tordai, L. Time-Dependence of Boundary Tensions of Solutions I. The Role of Diffusion in Time-Effects. *J. Chem. Phys.* **1946**, *14* (7), 453–461. <https://doi.org/10.1063/1.1724167>.
- (314) Fainerman, V. B.; Makievski, A. V.; Miller, R. The Analysis of Dynamic Surface Tension of Sodium Alkyl Sulphate Solutions, Based on Asymptotic Equations of Adsorption Kinetic Theory. *Colloids Surfaces A Physicochem. Eng. Asp.* **1994**, *87* (1), 61–75. [https://doi.org/10.1016/0927-7757\(94\)02747-1](https://doi.org/10.1016/0927-7757(94)02747-1).
- (315) Kutuzov, S.; He, J.; Tangirala, R.; Emrick, T.; Russell, T. P.; Böker, A. On the Kinetics of Nanoparticle Self-Assembly at Liquid/Liquid Interfaces. *Phys. Chem. Chem. Phys.* **2007**, *9* (48), 6351–6351. <https://doi.org/10.1039/b710060b>.
- (316) Ferdous, S.; Ioannidis, M. A.; Henneke, D. Adsorption Kinetics of Alkanethiol-Capped Gold Nanoparticles at the Hexane-Water Interface. *J. Nanoparticle Res.* **2011**, *13* (12), 6579–6589. <https://doi.org/10.1007/S11051-011-0565-Y>.
- (317) Li, Z.; Geisel, K.; Richtering, W.; Ngai, T. Poly(N-Isopropylacrylamide) Microgels at the Oil–Water Interface: Adsorption Kinetics. *Soft Matter* **2013**, *9* (41), 9939–9946. <https://doi.org/10.1039/C3SM52168K>.
- (318) Buchic, C.; Tromp, R. H.; Meinders, M. B. J.; Cohen Stuart, M. A. Harnessing the Advantages of Hard and Soft Colloids by the Use of Core-Shell Particles as Interfacial Stabilizers. *Soft Matter* **2017**, *13* (7), 1326–1334. <https://doi.org/10.1039/c6sm02159j>.
- (319) Moghadam, T. F.; Azizian, S.; Wettig, S. Synergistic Behaviour of ZnO Nanoparticles and Gemini Surfactants on the Dynamic and Equilibrium Oil/Water Interfacial Tension. *Phys. Chem. Chem. Phys.* **2015**, *17* (11), 7122–7129. <https://doi.org/10.1039/c5cp00510h>.

- (320) Nelson, A.; Wang, D.; Koynov, K.; Isa, L. A Multiscale Approach to the Adsorption of Core-Shell Nanoparticles at Fluid Interfaces. *Soft Matter* **2015**, *11* (1), 118–129. <https://doi.org/10.1039/c4sm01881h>.
- (321) Adamczyk, Z. Irreversible Adsorption of Particles. In *Adsorption: Theory, Modeling, and Analysis*; Tóth, J., Ed.; Marcel Dekker Inc.: New York, 2002; pp 251–374.
- (322) Han, Y.; Bizmark, N.; Abukhdeir, N. M.; Ioannidis, M. A. Dynamics of Ethyl Cellulose Nanoparticle Self-Assembly at the Interface of a Nematic Liquid Crystal Droplet. *Phys. Chem. Chem. Phys.* **2017**, *19* (36), 24955–24960. <https://doi.org/10.1039/C7CP04421F>.
- (323) Schwenke, K.; Isa, L.; Gado, E. Del. Assembly of Nanoparticles at Liquid Interfaces: Crowding and Ordering. *Langmuir* **2014**, *30* (11), 3069–3074. <https://doi.org/10.1021/LA404254N>.
- (324) Gu, C.; Botto, L. Direct Calculation of Anisotropic Surface Stresses during Deformation of a Particle-Covered Drop. *Soft Matter* **2016**, *12* (3), 705–716. <https://doi.org/10.1039/C5SM02374B>.
- (325) Fan, H.; Striolo, A. Nanoparticle Effects on the Water-Oil Interfacial Tension. *Phys. Rev. E* **2012**, *86*, 1–11. <https://doi.org/10.1103/PHYSREVE.86.051610>.
- (326) Kralchevsky, P. A.; Danov, K. D.; Broze, G.; Mehreteab, A. Thermodynamics of Ionic Surfactant Adsorption with Account for the Counterion Binding: Effect of Salts of Various Valency. *Langmuir* **1999**, *15* (7), 2351–2365. <https://doi.org/10.1021/LA981127T>.
- (327) Pepicelli, M.; Verwijlen, T.; Tervoort, T. A.; Vermant, J. Characterization and Modelling of Langmuir Interfaces with Finite Elasticity. *Soft Matter* **2017**, *13* (35), 5977–5990. <https://doi.org/10.1039/C7SM01100H>.
- (328) Deshmukh, O. S.; Maestro, A.; Duits, M. H. G.; Ende, D. van den; Stuart, M. C.; Mugele, F. Equation of State and Adsorption Dynamics of Soft Microgel Particles at an Air–Water Interface. *Soft Matter* **2014**, *10* (36), 7045–7050. <https://doi.org/10.1039/C4SM00566J>.
- (329) Hua, X.; Bevan, M. A.; Frechette, J. Reversible Partitioning of Nanoparticles at an Oil-Water Interface. *Langmuir* **2016**, *32* (44), 11341–11352. <https://doi.org/10.1021/acs.langmuir.6b02255>.
- (330) Guzmán, E.; Santini, E.; Ferrari, M.; Liggieri, L.; Ravera, F. Effect of the Incorporation of Nanosized Titanium Dioxide on the Interfacial Properties of 1,2-Dipalmitoyl-Sn-Glycerol-3-Phosphocholine Langmuir Monolayers. *Langmuir* **2017**, *33* (40), 10715–10725. <https://doi.org/10.1021/ACS.LANGMUIR.7B02484>.
- (331) Vignati, E.; Piazza, R.; Lockhart, T. P. Pickering Emulsions: Interfacial Tension, Colloidal Layer Morphology, and Trapped-Particle Motion. *Langmuir* **2003**, *19* (17), 6650–6656. <https://doi.org/10.1021/LA034264L>.
- (332) Fernandez-Rodriguez, M. A.; Ramos, J.; Isa, L.; Rodriguez-Valverde, M. A.; Cabrerizo-Vilchez, M. A.; Hidalgo-Alvarez, R. Interfacial Activity and Contact Angle of Homogeneous, Functionalized, and Janus Nanoparticles at the Water/Decane Interface. *Langmuir* **2015**, *31* (32), 8818–8823. <https://doi.org/10.1021/ACS.LANGMUIR.5B02137>.
- (333) Moghadam, T. F.; Azizian, S. Effect of ZnO Nanoparticle and Hexadecyltrimethylammonium Bromide on the Dynamic and Equilibrium Oil–Water Interfacial Tension. *J. Phys. Chem. B* **2014**, *118* (6), 1527–1534. <https://doi.org/10.1021/JP4106986>.
- (334) Pichot, R.; Spyropoulos, F.; Norton, I. T. Competitive Adsorption of Surfactants and Hydrophilic Silica Particles at the Oil – Water Interface : Interfacial Tension and Contact Angle Studies. *J. Colloid Interface Sci.* **2012**, *377* (1), 396–405. <https://doi.org/10.1016/j.jcis.2012.01.065>.
- (335) Drelich, A.; Gomez, F.; Clausse, D.; Pezron, I. Evolution of Water-in-Oil Emulsions Stabilized with Solid Particles: Influence of Added Emulsifier. *Colloids Surfaces A Physicochem. Eng. Asp.* **2010**, *365* (1–3), 171–177. <https://doi.org/10.1016/J.COLSURFA.2010.01.042>.
- (336) Wang, H.; Brito-Parada, P. The Role of Microparticles on the Shape and Surface Tension of Static Bubbles. *J. Colloid Interface Sci.* **2021**, *587*, 14–23. <https://doi.org/10.1016/j.jcis.2020.11.094>.
- (337) Okubo, T. Surface Tension of Structured Colloidal Suspensions of Polystyrene and Silica Spheres at the Air-Water Interface. *J. Colloid Interface Sci.* **1995**, *171* (1), 55–62. <https://doi.org/10.1006/JCIS.1995.1150>.
- (338) Dugyala, V. R.; Muthukuru, J. S.; Mani, E.; Basavaraj, M. G. Role of Electrostatic Interactions in the Adsorption Kinetics of Nanoparticles at Fluid-Fluid Interfaces. *Phys. Chem. Chem. Phys.* **2016**, *18* (7), 5499–5508. <https://doi.org/10.1039/c5cp05959c>.
- (339) Zhang, H.; Wang, W.; Mallapragada, S.; Travasset, A.; Vaknin, D. Macroscopic and Tunable Nanoparticle Superlattices. *Nanoscale* **2016**, *9* (1), 164–171. <https://doi.org/10.1039/C6NR07136H>.
- (340) Wang, H.; Singh, V.; Behrens, S. H. Image Charge Effects on the Formation of Pickering Emulsions. *J. Phys. Chem. Lett.* **2012**, *3* (20), 2986–2990. <https://doi.org/10.1021/jz300909z>.
- (341) Nayak, S.; Fieg, M.; Wang, W.; Bu, W.; Mallapragada, S.; Vaknin, D. Effect of (Poly)Electrolytes on the Interfacial Assembly of Poly(Ethylene Glycol)-Functionalized Gold Nanoparticles. *Langmuir* **2019**, *35* (6), 2251–2260. <https://doi.org/10.1021/ACS.LANGMUIR.8B03535>.
- (342) Olayiwola, S. O.; Dejam, M. Mathematical Modelling of Surface Tension of Nanoparticles in Electrolyte

- Solutions. *Chem. Eng. Sci.* **2019**, *197*, 345–356. <https://doi.org/10.1016/J.CES.2018.11.047>.
- (343) Luo, M.; Olivier, G. K.; Frechette, J. Electrostatic Interactions to Modulate the Reflective Assembly of Nanoparticles at the Oil–Water Interface. *Soft Matter* **2012**, *8* (47), 11923–11932. <https://doi.org/10.1039/C2SM26890F>.
- (344) Marina, P.; Cheng, C.; Sedev, R.; Stocco, A.; Binks, B.; Wang, D. Van Der Waals Emulsions: Emulsions Stabilized by Surface-Inactive, Hydrophilic Particles via van Der Waals Attraction. *Angew. Chemie* **2018**, *57* (30), 9510–9514. <https://doi.org/10.1002/ANIE.201805410>.
- (345) Marina, P. F.; Xu, J.; Wu, X.; Xu, H. Thinking Outside the Box: Placing Hydrophilic Particles in an Oil Phase for the Formation and Stabilization of Pickering Emulsions. *Chem. Sci.* **2018**, *9*, 4821–4829. <https://doi.org/10.1039/c8sc00678d>.
- (346) Mbamala, E. C.; Grünberg, H. H. von. Effective Interaction of a Charged Particle with an Air–Water Interface. *J. Phys. Condens. Matter* **2002**, *14* (19), 4881. <https://doi.org/10.1088/0953-8984/14/19/313>.
- (347) Von Grünberg, H. H.; Mbamala, E. C. Charged Colloids near Interfaces. *J. Phys. Condens. Matter* **2001**, *13* (21), 4801–4834. <https://doi.org/10.1088/0953-8984/13/21/311>.
- (348) Grünberg, H. H. von; Mbamala, E. C. Colloidal Suspensions at Dielectric Interfaces. *J. Phys. Condens. Matter* **2000**, *12* (50), 10349. <https://doi.org/10.1088/0953-8984/12/50/301>.
- (349) Butt, H. J.; Jaschke, M.; Ducker, W. Measuring Surface Forces in Aqueous Electrolyte Solution with the Atomic Force Microscope. *Bioelectrochemistry Bioenerg.* **1995**, *38* (1), 191–201. [https://doi.org/10.1016/0302-4598\(95\)01800-T](https://doi.org/10.1016/0302-4598(95)01800-T).
- (350) Dagastine, R. R.; White, L. R. Forces between a Rigid Probe Particle and a Liquid Interface: II. The General Case. *J. Colloid Interface Sci.* **2002**, *247* (2), 310–320. <https://doi.org/10.1006/JCIS.2001.8111>.
- (351) Eckenrode, H. M.; Shih-Hui, J.; Han, J.; Yeh, A.-G.; Dai, H.-L. Adsorption of a Cationic Dye Molecule on Polystyrene Microspheres in Colloids: Effect of Surface Charge and Composition Probed by Second Harmonic Generation. *J. Phys. Chem. B* **2005**, *109* (10), 4646–4653. <https://doi.org/10.1021/JP045610Q>.
- (352) Mubarekyan, E.; Santore, M. Characterization of Polystyrene Latex Surfaces by the Adsorption of Rhodamine 6G. *Langmuir* **1998**, *14* (7), 1597–1603. <https://doi.org/10.1021/LA970855Y>.
- (353) Mendoza, A. J.; Guzmán, E.; Martínez-Pedrero, F.; Ritacco, H.; Rubio, R. G.; Ortega, F.; Starov, V. M.; Miller, R. Particle Laden Fluid Interfaces: Dynamics and Interfacial Rheology. *Adv. Colloid Interface Sci.* **2014**, *206*, 303–319. <https://doi.org/10.1016/j.cis.2013.10.010>.
- (354) Erni, P.; Parker, A. Nonlinear Viscoelasticity and Shear Localization at Complex Fluid Interfaces. *Langmuir* **2012**, *28* (20), 7757–7767. <https://doi.org/10.1021/LA301023K>.
- (355) Hyun, K.; Wilhelm, M.; Klein, C. O.; Cho, K. S.; Nam, J. G.; Ahn, K. H.; Lee, S. J.; Ewoldt, R. H.; McKinley, G. H. A Review of Nonlinear Oscillatory Shear Tests: Analysis and Application of Large Amplitude Oscillatory Shear (LAOS). *Prog. Polym. Sci.* **2011**, *36* (12), 1697–1753. <https://doi.org/10.1016/J.PROGPOLYMSCI.2011.02.002>.
- (356) Hilles, H.; Monroy, F.; Bonales, L. J.; Ortega, F.; Rubio, R. G. Fourier-Transform Rheology of Polymer Langmuir Monolayers: Analysis of the Non-Linear and Plastic Behaviors. *Adv. Colloid Interface Sci.* **2006**, *122* (1–3), 67–77. <https://doi.org/10.1016/J.CIS.2006.06.013>.
- (357) Renggli, D.; Alicke, A.; Ewoldt, R. H.; Vermant, J. Operating Windows for Oscillatory Interfacial Shear Rheology. *J. Rheol. (N. Y. N. Y.)* **2020**, *64* (1), 141–160. <https://doi.org/10.1122/1.5130620>.
- (358) Pelipenko, J.; Kristl, J.; Ro, R.; Sa, I. C.; Baumgartner, A.; Kocbek, P. Interfacial Rheology: An Overview of Measuring Techniques and Its Role in Dispersions and Electrospinning. *Acta Pharm* **2012**, *62*, 123–140. <https://doi.org/10.2478/v10007-012-0018-x>.
- (359) Miller, R.; Liggieri, L. *Interfacial Rheology*, 1st ed.; Miller, R., Liggieri, L., Eds.; Brill: Leiden, Boston, 2009.
- (360) Beltramo, P. J.; Gupta, M.; Alicke, A.; Liascukiene, I.; Gunes, D. Z.; Baroud, C. N.; Vermant, J. Arresting Dissolution by Interfacial Rheology Design. *Proc. Natl. Acad. Sci. U. S. A.* **2017**, *114* (39), 10373–10378. <https://doi.org/10.1073/pnas.1705181114>.
- (361) Cavallaro, M.; Botto, L.; Lewandowski, E. P.; Wang, M.; Stebe, K. J. Curvature-Driven Capillary Migration and Assembly of Rod-like Particles. *Proc. Natl. Acad. Sci. U. S. A.* **2011**, *108* (52), 20923–20928. <https://doi.org/10.1073/pnas.1116344108>.
- (362) Madivala, B.; Fransaer, J.; Vermant, J. Self-Assembly and Rheology of Ellipsoidal Particles at Interfaces. *Langmuir* **2009**, *25* (5), 2718–2728. <https://doi.org/10.1021/la803554u>.
- (363) Madivala, B.; Vandebril, S.; Fransaer, J.; Vermant, J. Exploiting Particle Shape in Solid Stabilized Emulsions. *Soft Matter* **2009**, *5* (8), 1717–1727. <https://doi.org/10.1039/B816680C>.
- (364) Tambe, D. E.; Sharma, M. M. The Effect of Colloidal Particles on Fluid–Fluid Interfacial Properties and Emulsion Stability. *Adv. Colloid Interface Sci.* **1994**, *52* (C), 1–63. [https://doi.org/10.1016/0001-8686\(94\)80039-1](https://doi.org/10.1016/0001-8686(94)80039-1).
- (365) Safouane, M.; Langevin, D.; Binks, B. P. Effect of Particle Hydrophobicity on the Properties of Silica Particle Layers at the Air–Water Interface. *Langmuir* **2007**, *23* (23), 11546–11553.

- <https://doi.org/10.1021/LA700800A>.
- (366) Zahn, K.; Wille, A.; Maret, G.; Sengupta, S.; Nielaba, P. Elastic Properties of 2D Colloidal Crystals from Video Microscopy. *Phys. Rev. Lett.* **2003**, *90* (15), 4. <https://doi.org/10.1103/PhysRevLett.90.155506>.
- (367) Zang, D. Y.; Zhang, Y. J.; Hou, Q. W. Effect of Hydrophobicity on Tensile Rheological Properties of Silica Nanoparticle Monolayers at the Air-Water Interface. *Colloids Surfaces A Physicochem. Eng. Asp.* **2012**, *395*, 262–266. <https://doi.org/10.1016/J.COLSURFA.2011.12.047>.
- (368) Reynaert, S.; Moldenaers, P.; Vermant, J. Interfacial Rheology of Stable and Weakly Aggregated Two-Dimensional Suspensions. *Phys. Chem. Chem. Phys.* **2007**, *9* (48), 6463–6475. <https://doi.org/10.1039/B710825G>.
- (369) Reynaert, S.; Moldenaers, P.; Vermant, J. Control over Colloidal Aggregation in Monolayers of Latex Particles at the Oil–Water Interface. *Langmuir* **2006**, *22* (11), 4936–4945. <https://doi.org/10.1021/LA060052N>.
- (370) Horozov, T. S.; Aveyard, R.; Clint, J. H.; Binks, B. P. Order–Disorder Transition in Monolayers of Modified Monodisperse Silica Particles at the Octane–Water Interface. *Langmuir* **2003**, *19* (7), 2822–2829. <https://doi.org/10.1021/LA020858X>.
- (371) Guzmán, E.; Liggieri, L.; Santini, E.; Ferrari, M.; Ravera, F. Influence of Silica Nanoparticles on Dilational Rheology of DPPC–Palmitic Acid Langmuir Monolayers. *Soft Matter* **2012**, *8* (14), 3938–3948. <https://doi.org/10.1039/C2SM07097A>.
- (372) Vatanparast, H.; Javadi, A.; Bahramian, A. Silica Nanoparticles Cationic Surfactants Interaction in Water–Oil System. *Colloids Surfaces A Physicochem. Eng. Asp.* **2017**, *521*, 221–230. <https://doi.org/10.1016/j.colsurfa.2016.10.004>.
- (373) Zang, D. Y.; Rio, E.; Langevin, D.; Wei, B.; Binks, B. P. Viscoelastic Properties of Silica Nanoparticle Monolayers at the Air-Water Interface. *Eur. Phys. J. E* **2010**, *31*, 125–134. <https://doi.org/10.1140/epje/i2010-10565-7>.
- (374) Da, C.; Zhang, X.; Alzobaidi, S.; Hu, D.; Wu, P.; Johnston, K. P. Tuning Surface Chemistry and Ionic Strength to Control Nanoparticle Adsorption and Elastic Dilational Modulus at Air-Brine Interface. *Langmuir* **2021**, *37* (19), 5795–5809. <https://doi.org/10.1021/acs.langmuir.1c00112>.
- (375) Kobayashi, T.; Kawaguchi, M. Surface Dilational Moduli of Latex-Particle Monolayers Spread at Air-Water Interface. *J. Colloid Interface Sci.* **2013**, *390* (1), 147–150. <https://doi.org/10.1016/J.JCIS.2012.09.050>.
- (376) Kelleher, C. P.; Guerra, R. E.; Hollingsworth, A. D.; Chaikin, P. M. Phase Behavior of Charged Colloids at a Fluid Interface. *Phys. Rev. E* **2017**, *95* (2), 022602. <https://doi.org/10.1103/PhysRevE.95.022602>.
- (377) Aveyard, R.; Clint, J. H.; Nees, D.; Quirke, N. Structure and Collapse of Particle Monolayers under Lateral Pressure at the Octane/Aqueous Surfactant Solution Interface. *Langmuir* **2000**, *16* (23), 8820–8828. <https://doi.org/10.1021/LA000060I>.
- (378) Bonales, L. J.; Rubio, J. E. F.; Ritacco, H.; Vega, C.; Rubio, R. G.; Ortega, F. Freezing Transition and Interaction Potential in Monolayers of Microparticles at Fluid Interfaces. *Langmuir* **2011**, *27* (7), 3391–3400. <https://doi.org/10.1021/la104917e>.
- (379) Fenwick, N. I. D.; Bresme, F.; Quirke, N. Computer Simulation of a Langmuir Trough Experiment Carried out on a Nanoparticulate Array. *J. Chem. Phys.* **2001**, *114* (16), 7274. <https://doi.org/10.1063/1.1357795>.
- (380) Kim, K.; Kim, B. Q.; Kim, J. Q.; Choi, S. Q. New Collapse Mechanism of Colloidal Particle Monolayers via Depletion Pressure: Formation of Large-Area Particle Multilayers at the Air–Water Interface. *J. Phys. Chem. C* **2019**, *123* (45), 27862–27867. <https://doi.org/10.1021/acs.jpcc.9b06963>.
- (381) Hegemann, J.; Knoche, S.; Egger, S.; Kott, M.; Demand, S.; Unverfehrt, A.; Rehage, H.; Kierfeld, J. Pendant Capsule Elastometry. *J. Colloid Interface Sci.* **2018**, *513*, 549–565. <https://doi.org/10.1016/j.jcis.2017.11.048>.
- (382) Danov, K. D.; Stanimirova, R. D.; Kralchevsky, P. A.; Marinova, K. G.; Alexandrov, N. A.; Stoyanov, S. D.; Blijdenstein, B. J.; Pelan, E. G. Capillary Meniscus Dynamometry - Method for Determining the Surface Tension of Drops and Bubbles with Isotropic and Anisotropic Surface Stress Distributions. *J. Colloid Interface Sci.* **2015**, *440*, 167–178. <https://doi.org/10.1016/j.jcis.2014.10.067>.
- (383) Knoche, S.; Vella, D.; Aumaitre, E.; Degen, P.; Rehage, H.; Cicuta, P.; Kierfeld, J. Elastometry of Deflated Capsules: Elastic Moduli from Shape and Wrinkle Analysis. *Langmuir* **2013**, *29* (40), 12463–12471. <https://doi.org/10.1021/la402322g>.
- (384) Datta, S. S.; Shum, H. C.; Weitz, D. A. Controlled Buckling and Crumpling of Nanoparticle-Coated Droplets. *Langmuir* **2010**, *26* (24), 18612–18616. <https://doi.org/10.1021/la103874z>.
- (385) Rane, J. P.; Harbottle, D.; Pauchard, V.; Couzis, A.; Banerjee, S. Adsorption Kinetics of Asphaltenes at the Oil-Water Interface and Nanoaggregation in the Bulk. *Langmuir* **2012**, *28* (26), 9986–9995. <https://doi.org/10.1021/la301423c>.
- (386) Tavecchi, J. W.; Katgert, G.; Kim, E. G.; Cates, M. E.; Clegg, P. S. Size Limit for Particle-Stabilized Emulsion Droplets under Gravity. *Phys. Rev. Lett.* **2012**, *108* (26).

- <https://doi.org/10.1103/PHYSREVLETT.108.268306>.
- (387) Fuller, G. G.; Vermant, J. Complex Fluid-Fluid Interfaces: Rheology and Structure. *Annu. Rev. Chem. Biomol. Eng.* **2012**, *3*, 519–543. <https://doi.org/10.1146/ANNUREV-CHEMBIOENG-061010-114202>.
- (388) Zell, Z. A.; Nowbahar, A.; Mansard, V.; Leal, L. G.; Deshmukh, S. S.; Mecca, J. M.; Tucker, C. J.; Squires, T. M. Surface Shear Inviscosity of Soluble Surfactants. *Proc. Natl. Acad. Sci. U. S. A.* **2014**, *111* (10), 3677–3682. <https://doi.org/10.1073/PNAS.1315991111>.
- (389) Krishnaswamy, R.; Majumdar, S.; Ganapathy, R.; Agarwal, V. V.; Sood, A. K.; Rao, C. N. R. Interfacial Rheology of an Ultrathin Nanocrystalline Film Formed at the Liquid/Liquid Interface. *Langmuir* **2007**, *23*, 3084–3087. <https://doi.org/10.1021/la063236a>.
- (390) Orsi, D.; Baldi, G.; Cicutac, P.; Cristofolini, L. On the Relation between Hierarchical Morphology and Mechanical Properties of a Colloidal 2D Gel System. *Colloids Surfaces A Physicochem. Eng. Asp.* **2012**, *413*, 71–77. <https://doi.org/10.1016/J.COLSURFA.2012.01.001>.
- (391) Orsi, D.; Ruta, B.; Chushkin, Y.; Pucci, A.; Ruggeri, G.; Baldi, G.; Rimoldi, T.; Cristofolini, L. Controlling the Dynamics of a Bidimensional Gel above and below Its Percolation Transition. *Phys. Rev. E* **2014**, *89*, 042308. <https://doi.org/10.1103/PhysRevE.89.042308>.
- (392) Orsi, D.; Vezzani, A.; Burioni, R.; Pucci, A.; Ruggeri, G.; Cristofolini, L. Statistical Properties and Morphology of a 2D Gel Network at the Air/Water Interface. *Colloids Surfaces A Physicochem. Eng. Asp.* **2013**, *441*, 912–918. <https://doi.org/10.1016/j.colsurfa.2013.04.020>.
- (393) Yu, K.; Zhang, H.; Biggs, S.; Xu, Z.; Cayre, O. J.; Harbottle, D. The Rheology of Polyvinylpyrrolidone-Coated Silica Nanoparticles Positioned at an Air-Aqueous Interface. *J. Colloid Interface Sci.* **2018**, *527*, 346–355. <https://doi.org/10.1016/J.JCIS.2018.05.035>.
- (394) Cicuta, P.; Stancik, E. J.; Fuller, G. G. Shearing or Compressing a Soft Glass in 2D: Time-Concentration Superposition. *Phys. Rev. Lett.* **2003**, *90* (23), 4. <https://doi.org/10.1103/PhysRevLett.90.236101>.
- (395) Barman, S.; Christopher, G. F. Simultaneous Interfacial Rheology and Microstructure Measurement of Densely Aggregated Particle Laden Interfaces Using a Modified Double Wall Ring Interfacial Rheometer. *Langmuir* **2014**, *30* (32), 9752–9760. <https://doi.org/10.1021/LA502329S>.
- (396) Barman, S.; Christopher, G. F. Role of Capillarity and Microstructure on Interfacial Viscoelasticity of Particle Laden Interfaces. *J. Rheol. (N. Y. N. Y.)* **2015**, *60* (1), 35. <https://doi.org/10.1122/1.4935128>.
- (397) Wijmans, C. M.; Dickinson, E. Simulation of Interfacial Shear and Dilatational Rheology of an Adsorbed Protein Monolayer Modeled as a Network of Spherical Particles. *Langmuir* **1998**, *14* (25), 7278–7286. <https://doi.org/10.1021/LA980687P>.
- (398) Trappe, V.; Weitz, D. A. Scaling of the Viscoelasticity of Weakly Attractive Particles. *Phys. Rev. Lett.* **2000**, *85* (2), 449–452. <https://doi.org/10.1103/PHYSREVLETT.85.449>.
- (399) Jaishankar, A.; McKinley, G. H. Power-Law Rheology in the Bulk and at the Interface: Quasi-Properties and Fractional Constitutive Equations. *Proc R Soc A* **2013**, *469*, 20120284. <https://doi.org/10.1098/rspa.2012.0284>.
- (400) Brugger, B.; Vermant, J.; Richtering, W. Interfacial Layers of Stimuli-Responsive Poly-(N-Isopropylacrylamide-Co-Methacrylicacid) (PNIPAM-Co-MAA) Microgels Characterized by Interfacial Rheology and Compression Isotherms. *Phys. Chem. Chem. Phys.* **2010**, *12* (43), 14573–14578. <https://doi.org/10.1039/C0CP01022G>.
- (401) Keim, N. C.; Arratia, P. E. Yielding and Microstructure in a 2D Jammed Material under Shear Deformation. *Soft Matter* **2013**, *9* (27), 6222–6225. <https://doi.org/10.1039/C3SM51014J>.
- (402) Krieger, I. M.; Dougherty, T. J. A Mechanism for Non-Newtonian Flow in Suspensions of Rigid Spheres. *Trans. Soc. Rheol.* **1959**, *3*, 137–152. <https://doi.org/10.1122/1.548848>.
- (403) Vandebril, S.; Vermant, J.; Moldenaers, P. Efficiently Suppressing Coalescence in Polymer Blends Using Nanoparticles: Role of Interfacial Rheology. *Soft Matter* **2010**, *6*, 3353–3362. <https://doi.org/10.1039/B927299B>.
- (404) Tao, R.; Xu, X. Reducing the Viscosity of Crude Oil by Pulsed Electric or Magnetic Field. *Energy & Fuels* **2006**, *20*, 2046–2051. <https://doi.org/10.1021/ef060072x>.
- (405) Parolini, L.; Law, A. D.; Maestro, A.; Buzza, D. M. A.; Cicuta, P. Interaction between Colloidal Particles on an Oil – Water Interface in Dilute and Dense Phases. *J. Phys. Condens. Matter* **2015**, *27*, 194119. <https://doi.org/10.1088/0953-8984/27/19/194119>.
- (406) Kostakis, T.; Ettelaie, R.; Murray, B. S. Effect of High Salt Concentrations on the Stabilization of Bubbles by Silica Particles. *Langmuir* **2006**, *22* (3), 1273–1280. <https://doi.org/10.1021/la052193f>.
- (407) Zhang, H.; Yu, K.; Cayre, O. J.; Harbottle, D. Interfacial Particle Dynamics: One and Two Step Yielding in Colloidal Glass. *Langmuir* **2016**, *32* (50), 13472–13481. <https://doi.org/10.1021/acs.langmuir.6b03586>.
- (408) Groot, R. D.; Stoyanov, S. D. Close Packing Density and Fracture Strength of Adsorbed Polydisperse Particle Layers. *Soft Matter* **2011**, *7* (10), 4750–4761. <https://doi.org/10.1039/c0sm00859a>.
- (409) Luckham, P. F.; Ukeje, M. A. Effect of Particle Size Distribution on the Rheology of Dispersed Systems. *J. Colloid Interface Sci.* **1999**, *220* (2), 347–356. <https://doi.org/10.1006/JCIS.1999.6515>.

- (410) Wyss, H. M.; Miyazaki, K.; Mattsson, J.; Hu, Z.; Reichman, D. R.; Weitz, D. A. Strain-Rate Frequency Superposition: A Rheological Probe of Structural Relaxation in Soft Materials. *Phys. Rev. Lett.* **2007**, *98* (23), 238303. <https://doi.org/10.1103/PhysRevLett.98.238303>.
- (411) Zang, D.; Langevin, D.; Binks, B. P.; Wei, B. Shearing Particle Monolayers: Strain-Rate Frequency Superposition. *Phys. Rev. E. Stat. Nonlin. Soft Matter Phys.* **2010**, *81* (1 Pt 1). <https://doi.org/10.1103/PHYSREVE.81.011604>.
- (412) Wilson, H. J.; Davis, R. H. Shear Stress of a Monolayer of Rough Spheres. *J. Fluid Mech.* **2002**, *452*, 425–441. <https://doi.org/10.1017/S0022112001006838>.
- (413) San-Miguel, A.; Behrens, S. H. Influence of Nanoscale Particle Roughness on the Stability of Pickering Emulsions. *Langmuir* **2012**, *28* (33), 12038–12043. <https://doi.org/10.1021/la302224v>.
- (414) Brown, E.; Zhang, H.; Forman, N. A.; Maynor, B. W.; Betts, D. E.; Desimone, J. M.; Jaeger, H. M. Shear Thickening and Jamming in Densely Packed Suspensions of Different Particle Shapes. *Phys. Rev. E - Stat. Nonlinear, Soft Matter Phys.* **2011**, *84* (3), 031408. <https://doi.org/10.1103/PhysRevE.84.031408>.
- (415) Keller, D. S.; Jr., D. V. K. The Effect of Particle Size Distribution on the Antithixotropic and Shear Thickening Properties of Coal–Water Dispersions. *J. Rheol. (N. Y. N. Y.)* **1998**, *35* (8), 1583. <https://doi.org/10.1122/1.550246>.
- (416) Binks, B. P.; Lumsdon, S. O. Influence of Particle Wettability on the Type and Stability of Surfactant-Free Emulsions. *Langmuir* **2000**, *16* (23), 8622–8631. <https://doi.org/10.1021/LA000189S>.
- (417) Li, Z.; Mu, Y.; Peng, C.; Lavin, M. F.; Shao, H.; Du, Z. Understanding the Mechanisms of Silica Nanoparticles for Nanomedicine. *Wiley Interdiscip. Rev. Nanomed. Nanobiotechnol.* **2021**, *13* (1). <https://doi.org/10.1002/WNAN.1658>.
- (418) Slavchov, R. I.; Novev, J. K. Surface Tension of Concentrated Electrolyte Solutions. *J. Colloid Interface Sci.* **2012**, *387* (1), 234–243. <https://doi.org/10.1016/J.JCIS.2012.07.020>.
- (419) Reis, P.; Miller, R.; Leser, M.; Watzke, H.; Fainerman, V. B.; Holmberg, K. Adsorption of Polar Lipids at the Water–Oil Interface. *Langmuir* **2008**, *24* (11), 5781–5786. <https://doi.org/10.1021/LA704043G>.
- (420) Vu, T. V.; Papavassiliou, D. V. Oil-Water Interfaces with Surfactants: A Systematic Approach to Determine Coarse-Grained Model Parameters. *J. Chem. Phys.* **2018**, *148* (20). <https://doi.org/10.1063/1.5022798>.
- (421) Baoukina, S.; Monticelli, L.; Risselada, H. J.; Marrink, S. J.; Tieleman, D. P. The Molecular Mechanism of Lipid Monolayer Collapse. *Proc. Natl. Acad. Sci.* **2008**, *105* (31), 10803–10808. <https://doi.org/10.1073/PNAS.0711563105>.
- (422) Betts, J. J.; Pethica, B. A. The Ionization Characteristics of Monolayers of Weak Acids and Bases. *Trans. Faraday Soc.* **1956**, *52*, 1581–1589. <https://doi.org/10.1039/TF9565201581>.
- (423) Glazer, J.; Dogan, M. Z. Ionization of Protein Monolayers and Related Substances. *Trans. Faraday Soc.* **1953**, *49*, 448–455. <https://doi.org/10.1039/TF9534900448>.
- (424) Andersson, . P.; Olsson, M. H. M.; Stipp, S. L. S. Predicting the PKa and Stability of Organic Acids and Bases at an Oil–Water Interface. *Langmuir* **2014**, *30* (22), 6437–6445. <https://doi.org/10.1021/la5008318>.
- (425) Lide, D. R. *CRC Handbook of Chemistry and Physics*; CRC Press: Boca Raton, FL, 1999.
- (426) Beattie, J. K.; Djerdjev, A. M.; Gray-Weale, A.; Kallay, N.; Lützenkirchen, J.; Preocanin, T.; Selmani, A. PH and the Surface Tension of Water. *J. Colloid Interface Sci.* **2014**, *422*, 54–57. <https://doi.org/10.1016/j.jcis.2014.02.003>.
- (427) Goddard, E. D. Ionizing Monolayers and PH Effects. *Adv. Colloid Interface Sci.* **1974**, *4*, 45–78. [https://doi.org/10.1016/0001-8686\(74\)80002-3](https://doi.org/10.1016/0001-8686(74)80002-3).
- (428) Kanicky, J. R.; Shah, D. O. Effect of Degree, Type, and Position of Unsaturation on the PKa of Long-Chain Fatty Acids. *J. Colloid Interface Sci.* **2002**, *256*, 207–207. <https://doi.org/10.1006/jcis.2001.8009>.
- (429) Matthews, R. H.; Cornwell, D. G.; Patil, G. S.; Matthews, R. H.; Cornwell, D. G. Estimation of Surface Area and Counterion Binding Characteristics in Fatty Amine Monolayers from Desorption Kinetics. *J. Lipid Res.* **1976**, *17*, 197–202. [https://doi.org/10.1016/S0022-2275\(20\)36975-3](https://doi.org/10.1016/S0022-2275(20)36975-3).
- (430) Kovalchuk, K.; Masalova, I.; Malkin, A. Y. Influence of Electrolyte on Interfacial and Rheological Properties and Shear Stability of Highly Concentrated W/O Emulsions. *Colloid J.* **2010**, *72* (6), 806–814. <https://doi.org/10.1134/S1061933X10060116>.
- (431) Goodarzi, F.; Zendehboudi, S. Effects of Salt and Surfactant on Interfacial Characteristics of Water/Oil Systems: Molecular Dynamic Simulations and Dissipative Particle Dynamics. *Ind. Eng. Chem. Res.* **2019**, *58* (20), 8817–8834. <https://doi.org/10.1021/ACS.IECR.9B00504>.
- (432) Petkova, B.; Tcholakova, S.; Chenkova, M.; Golemanov, K.; Denkov, N.; Thorley, D.; Stoyanov, S.; Tcholakova, S. Foamability of Aqueous Solutions: Role of Surfactant Type and Concentration. *Adv. Colloid Interface Sci.* **2020**, *276*, 102084. <https://doi.org/10.1016/j.cis.2019.102084>.
- (433) Kumar, M. K.; Mitra, T.; Ghosh, P. Adsorption of Ionic Surfactants at Liquid-Liquid Interfaces in the Presence of Salt: Application in Binary Coalescence of Drops. *Ind. Eng. Chem. Res.* **2006**, *45* (21), 7135–7143. <https://doi.org/10.1021/ie0604066>.

- (434) Opawale, F. O.; Burgess, D. J. Influence of Interfacial Properties of Lipophilic Surfactants on Water- in-Oil Emulsion Stability. *J. Colloid Interface Sci.* **1998**, *197* (1), 142–150. <https://doi.org/10.1006/jcis.1997.5222>.
- (435) Avazbaeva, Z.; Sung, W.; Lee, J.; Phan, M. D.; Shin, K.; Vaknin, D.; Kim, D. Origin of the Instability of Octadecylamine Langmuir Monolayer at Low PH. *Langmuir* **2015**, *31* (51), 13753–13758. <https://doi.org/10.1021/acs.langmuir.5b03947>.
- (436) Albrecht, O.; Matsuda, H.; Eguchi, K. Main and Tilt Transition in Octadecylamine Monolayers. *Colloids Surfaces A Physicochem. Eng. Asp.* **2006**, *284–285*, 166–174. <https://doi.org/10.1016/j.colsurfa.2006.02.044>.
- (437) Demeter-Vodnár, J.; Sălăjan, M.; Lowy, D. A. Kinetic Study of the Diffusion and Adsorption of Fatty Acids at the Benzene-Water Interface. *J. Colloid Interface Sci.* **1996**, *183* (2), 424–430. <https://doi.org/10.1006/jcis.1996.0565>.
- (438) Whitby, C. P.; Fornasiero, D.; Ralston, J.; Liggieri, L.; Ravera, F. Properties of Fatty Amine – Silica Nanoparticle Interfacial Layers at the Hexane – Water Interface. *J. Phys. Chem. C* **2012**, *116*, 3050–3058. <https://doi.org/10.1021/jp210870v>.
- (439) Fainerman, V. B.; Vollhardt, D. Equations of State for Langmuir Monolayers with Two-Dimensional Phase Transitions. *J. Phys. Chem. B* **1999**, No. 2, 145–150. <https://doi.org/10.1021/jp983109q>.
- (440) Fainerman, V. B.; Miller, R. Surface Tension Isotherms for Surfactant Adsorption Layers Including Surface Aggregation. *Langmuir* **1996**, *7463* (11), 6011–6014. <https://doi.org/10.1021/la960457f>.
- (441) Greenspan, P.; Fowler, S. D. Spectrofluorometric Studies of the Lipid Probe, Nile Red. *J Lipid Res* **1985**, *26*, 781–789.
- (442) Stuart, M. C. A.; Pas, J. C. van de; Engberts, J. B. F. N. The Use of Nile Red to Monitor the Aggregation Behavior in Ternary Surfactant-Water-Organic Solvent Systems. *J. Phys. Org. Chem.* **2005**, *18* (9), 929–934. <https://doi.org/10.1002/poc.919>.
- (443) Carre, A.; Malchere, A. Non-Dispersive Interactions at Liquid/Liquid and Liquid/Solid Interfaces. *J. Colloid Interface Sci.* **1992**, *149* (2), 379–391. [https://doi.org/10.1016/0021-9797\(92\)90429-P](https://doi.org/10.1016/0021-9797(92)90429-P).
- (444) Biswal, N. R.; Rangera, N.; Singh, J. K. Effect of Different Surfactants on the Interfacial Behavior of the N-Hexane – Water System in the Presence of Silica Nanoparticles. *J. Phys. Chem. B* **2016**, No. 120, 7265–7274.
- (445) Yekeen, N.; Padmanabhan, E.; Idris, A. K. Synergistic Effects of Nanoparticles and Surfactants on N-Decane-Water Interfacial Tension and Bulk Foam Stability at High Temperature. *J. Pet. Sci. Eng.* **2019**, *179*, 814–830. <https://doi.org/10.1016/j.petrol.2019.04.109>.
- (446) Katiyar, P.; Singh, J. K. A Coarse-Grain Molecular Dynamics Study of Oil-Water Interfaces in the Presence of Silica Nanoparticles and Nonionic Surfactants. *J. Chem. Phys.* **2017**, *146* (20). <https://doi.org/10.1063/1.4984073>.
- (447) Ranatunga, R. J. K. U.; Nguyen, C. T.; Wilson, B. A.; Shinoda, W.; Nielsen, S. O. Molecular Dynamics Study of Nanoparticles and Non-Ionic Surfactant at an Oil-Water Interface. *Soft Matter* **2011**, *7* (15), 6942–6952. <https://doi.org/10.1039/c1sm05145h>.
- (448) Vatanparast, H.; Samiee, A.; Bahramian, A.; Javadi, A. Surface Behavior of Hydrophilic Silica Nanoparticle-SDS Surfactant Solutions : I . Effect of Nanoparticle Concentration on Foamability and Foam Stability. *Colloids Surfaces A Physicochem. Eng. Asp.* **2017**, *513*, 430–441. <https://doi.org/10.1016/j.colsurfa.2016.11.012>.
- (449) Xu, M.; Jiang, J.; Pei, X.; Song, B.; Cui, Z.; Binks, B. P. Novel Oil-in-Water Emulsions Stabilised by Ionic Surfactant and Similarly Charged Nanoparticles at Very Low Concentrations. *Angew. Chemie - Commun.* **2018**, No. 57, 7738–7742. <https://doi.org/10.1002/anie.201802266>.
- (450) Veyskarami, M.; Ghazanfari, M. H. Synergistic Effect of like and Opposite Charged Nanoparticle and Surfactant on Foam Stability and Mobility in the Absence and Presence of Hydrocarbon: A Comparative Study. *J. Pet. Sci. Eng.* **2018**, *166*, 433–444. <https://doi.org/10.1016/j.petrol.2018.03.076>.
- (451) Maestro, A.; Rio, E.; Drenckhan, W.; Langevin, D.; Salonen, A. Foams Stabilised by Mixtures of Nanoparticles and Oppositely Charged Surfactants : Relationship between Bubble Shrinkage and Foam Coarsening. *Soft Matter* **2014**, No. 10, 6975–6983. <https://doi.org/10.1039/C4SM00047A>.
- (452) Jiménez-Ángeles, F.; Khoshnood, A.; Firoozabadi, A. Molecular Dynamics Simulation of the Adsorption and Aggregation of Ionic Surfactants at Liquid-Solid Interfaces. *J. Phys. Chem. C* **2017**, *121* (46), 25908–25920. <https://doi.org/10.1021/acs.jpcc.7b09466>.
- (453) Nallamilli, T.; Mani, E.; Basavaraj, M. G. A Model for the Prediction of Droplet Size in Pickering Emulsions Stabilized by Oppositely Charged Particles. *Langmuir* **2014**, *30* (31), 9336–9345. <https://doi.org/10.1021/la501785y>.
- (454) Nallamilli, T.; Binks, B. P.; Mani, E.; Basavaraj, M. G. Stabilization of Pickering Emulsions with Oppositely Charged Latex Particles: Influence of Various Parameters and Particle Arrangement around Droplets. *Langmuir* **2015**, *31* (41), 11200–11208. <https://doi.org/10.1021/acs.langmuir.5b02443>.

- (455) Binks, B. P.; Rodrigues, J. A.; Frith, W. J. Synergistic Interaction in Emulsions Stabilized by a Mixture of Silica Nanoparticles and Cationic Surfactant. *Langmuir* **2007**, *23* (7), 3626–3636. <https://doi.org/10.1021/la0634600>.
- (456) Vialetto, J.; Rudiuk, S.; Morel, M.; Baigl, D. From Bulk Crystallization of Inorganic Nanoparticles at the Air/Water Interface: Tunable Organization and Intense Structural Colors. *Nanoscale* **2020**, *12* (11), 6279–6284. <https://doi.org/10.1039/c9nr10965j>.
- (457) Vialetto, J.; Anyfantakis, M.; Rudiuk, S.; Morel, M.; Baigl, D. Photoswitchable Dissipative Two-Dimensional Colloidal Crystals. *Angew Chem Int Ed Engl* **2019**, *58* (27), 9145–9149. <https://doi.org/10.1002/anie.201904093>.
- (458) Eftekhari, M.; Schwarzenberger, K.; Javadi, A.; Eckert, K. The Influence of Negatively Charged Silica Nanoparticles on the Surface Properties of Anionic Surfactants: Electrostatic Repulsion or the Effect of Ionic Strength? *Phys. Chem. Chem. Phys.* **2020**, *22* (4), 2238–2248. <https://doi.org/10.1039/c9cp05475h>.
- (459) Pilapil, B. K.; Jahandideh, H.; Bryant, S. L.; Trifkovic, M. Stabilization of Oil-in-Water Emulsions with Noninterfacially Adsorbed Particles. *Langmuir* **2016**, *32* (28), 7109–7116. <https://doi.org/10.1021/acs.langmuir.6b00873>.
- (460) Vashisth, C.; Whitby, C. P.; Fornasiero, D.; Ralston, J. Interfacial Displacement of Nanoparticles by Surfactant Molecules in Emulsions. *J. Colloid Interface Sci.* **2010**, *349* (2), 537–543. <https://doi.org/10.1016/j.jcis.2010.05.089>.
- (461) Santini, E.; Guzmán, E.; Ferrari, M.; Liggieri, L. Emulsions Stabilized by the Interaction of Silica Nanoparticles and Palmitic Acid at the Water-Hexane Interface. *Colloids Surfaces A Physicochem. Eng. Asp.* **2014**, *460*, 333–341. <https://doi.org/10.1016/j.colsurfa.2014.02.054>.
- (462) Whitby, C. P.; Fornasiero, D.; Ralston, J. Effect of Oil Soluble Surfactant in Emulsions Stabilised by Clay Particles. *J. Colloid Interface Sci.* **2008**, *323*, 410–419.
- (463) Hasegawa, M.; Low, M. J. D. Infrared Study of Adsorption in Situ at the Liquid-Solid Interface II. Adsorption of Stearic Acid on Zinc Oxide. *J. Colloid Interface Sci.* **1969**, *29* (4), 593–600. [https://doi.org/10.1016/0021-9797\(69\)90208-2](https://doi.org/10.1016/0021-9797(69)90208-2).
- (464) Campen, S.; Green, J. H.; Lamb, G. D.; Spikes, H. A. In Situ Study of Model Organic Friction Modifiers Using Liquid Cell AFM: Self-Assembly of Octadecylamine. *Tribol. Lett.* **2015**, *58* (3). <https://doi.org/10.1007/s11249-015-0514-5>.
- (465) Guzmán, E.; Ferrari, M.; Santini, E.; Liggieri, L.; Ravera, F. Effect of Silica Nanoparticles on the Interfacial Properties of a Canonical Lipid Mixture. *Colloids Surfaces B Biointerfaces* **2015**, *136*, 971–980. <https://doi.org/10.1016/j.colsurfb.2015.11.001>.
- (466) Guzmán, E.; Liggieri, L.; Santini, E.; Ferrari, M.; Ravera, F. DPPC-DOPC Langmuir Monolayers Modified by Hydrophilic Silica Nanoparticles: Phase Behaviour, Structure and Rheology. *Colloids Surfaces A Physicochem. Eng. Asp.* **2012**, *413*, 174–183. <https://doi.org/10.1016/j.colsurfa.2011.12.059>.
- (467) Guzmán, E.; Liggieri, L.; Santini, E.; Ferrari, M.; Ravera, F. Mixed DPPC-Cholesterol Langmuir Monolayers in Presence of Hydrophilic Silica Nanoparticles. *Colloids Surf. B. Biointerfaces* **2013**, *105*, 284–293. <https://doi.org/10.1016/j.colsurfb.2013.01.020>.
- (468) Ramazani, A.; Mandal, T.; Larson, R. G. Modeling the Hydrophobicity of Nanoparticles and Their Interaction with Lipids and Proteins. *Langmuir* **2016**, *32* (49), 13084–13094. https://doi.org/10.1021/ACS.LANGMUIR.6B01963/SUPPL_FILE/LA6B01963_SI_001.PDF.
- (469) Bollhorst, T.; Grieb, T.; Rosenauer, A.; Fuller, G.; Maas, M. Synthesis Route for the Self-Assembly of Submicrometer-Sized Colloidosomes with Tailorable Nanopores. **2013**.
- (470) Bollhorst, T.; Shahabi, S.; Węrz, K.; Petters, C.; Dringen, R.; Maas, M.; Rezwani, K. Bifunctional Submicron Colloidosomes Coassembled from Fluorescent and Superparamagnetic Nanoparticles. *Angew. Commun.* **2015**, *54*, 118–123. <https://doi.org/10.1002/anie.201408515>.
- (471) Maas, M.; Bollhorst, T.; Zare, R. N.; Rezwani, K. Diamondosomes: Submicron Colloidosomes with Nanodiamond Shells. *Part. Part. Syst. Charact.* **2014**, 1–5. <https://doi.org/10.1002/ppsc.201400022>.
- (472) Sihler, S.; Schrade, A.; Cao, Z.; Ziener, U. Inverse Pickering Emulsions with Droplet Sizes below 500 Nm. *Langmuir* **2015**, *31*, 10392–10401. <https://doi.org/10.1021/acs.langmuir.5b02735>.
- (473) Pichot, R.; Spyropoulos, F.; Norton, I. T. O:W Emulsions Stabilised by Both Low Molecular Weight Surfactants and Colloidal Particles: The Effect of Surfactant Type and Concentration. *J. Colloid Interface Sci.* **2010**, *352* (1), 128–135.
- (474) Fainerman, V. B.; Aksenenko, E. V.; Mucic, N.; Javadi, A.; Miller, R. Thermodynamics of Adsorption of Ionic Surfactants at Water/Alkane Interfaces. *Soft Matter* **2014**, No. 10, 6873–6887.
- (475) Mucic, N.; Javadi, A.; Karbaschi, M.; Sharipova, A. *Surfactant Adsorption Kinetics*; 2013. <https://doi.org/10.1007/978-3-642-20665-8>.
- (476) Bahramian, A.; Zarbakhsh, A. Interfacial Equation of State for Ionized Surfactants at Oil / Water Interfaces. *Soft Matter* **2015**, No. 11, 6482–6491.

- (477) Goronja, J. M.; Janošević Ležaić, A. M.; Dimitrijević, B. M.; Malenović, A. M.; Stanisavljević, D. R.; Pejić, N. D. Determination of Critical Micelle Concentration of Cetyltrimethyl-Ammonium Bromide: Different Procedures for Analysis of Experimental Data. *Hem. Ind* **2016**, *70* (4), 485–492. <https://doi.org/10.2298/HEMIND150622055G>.
- (478) Liu, Y.; Tourbin, M.; Lachaize, S.; Guiraud, P. Silica Nanoparticles Separation from Water: Aggregation by Cetyltrimethylammonium Bromide (CTAB). *Chemosphere* **2013**, *92* (6), 681–687. <https://doi.org/10.1016/J.CHEMOSPHERE.2013.03.048>.
- (479) Hlawacek, G.; Ahmad, I.; Smithers, M. A.; Kooij, E. S. To See or Not to See: Imaging Surfactant Coated Nano-Particles Using HIM and SEM. *Ultramicroscopy* **2013**, *135*, 89–94. <https://doi.org/10.1016/J.ULTRAMIC.2013.07.010>.
- (480) Weidemaier, K.; Tavernier, H. L.; Fayer, M. D. Photoinduced Electron Transfer on the Surfaces of Micelles. *J. Phys. Chem. B* **1997**, *101* (45), 9352–9361. <https://doi.org/10.1021/JP972245C>.
- (481) Yazhgur, P. A.; Noskov, B. A.; Liggieri, L.; Lin, S.; Loglio, G.; Miller, R. Dynamic Properties of Mixed Nanoparticle/Surfactant Adsorption Layers. *Soft Matter* **2013**, *9*, 3305–3314. <https://doi.org/10.1039/c3sm27304k>.
- (482) Liggieri, L.; Santini, E.; Guzman, E.; Maestro, A.; Ravera, F. Wide-Frequency Dilational Rheology Investigation of Mixed Silica Nanoparticle – CTAB Interfacial Layers. *Soft Matter* **2011**, *7*, 7699–7709. <https://doi.org/10.1039/c1sm05257h>.
- (483) Ravera, F.; Santini, E.; Loglio, G.; Ferrari, M.; Liggieri, L. Effect of Nanoparticles on the Interfacial Properties of Liquid/Liquid and Liquid/Air Surface Layers. *J. Phys. Chem. B* **2006**, *110* (39), 19543–19551. <https://doi.org/10.1021/JP0636468>.
- (484) Ravera, F.; Ferrari, M.; Liggieri, L.; Loglio, G.; Santini, E.; Zanobini, A. Liquid–Liquid Interfacial Properties of Mixed Nanoparticle–Surfactant Systems. *Colloids Surfaces A Physicochem. Eng. Asp.* **2008**, *323* (1–3), 99–108. <https://doi.org/10.1016/J.COLSURFA.2007.10.017>.
- (485) Leser, M. E.; Acquistapace, S.; Cagna, A.; Makievski, A. V.; Miller, R. Limits of Oscillation Frequencies in Drop and Bubble Shape Tensiometry. *Colloids Surfaces A Physicochem. Eng. Asp.* **2005**, *261* (1–3), 25–28. <https://doi.org/10.1016/j.colsurfa.2004.11.043>.
- (486) Wang, H.; Gong, Y.; Lu, W.; Chen, B. Influence of Nano-SiO₂ on Dilational Viscoelasticity of Liquid/Air Interface of Cetyltrimethyl Ammonium Bromide. *Appl. Surf. Sci.* **2008**, *254* (11), 3380–3384. <https://doi.org/10.1016/J.APSUSC.2007.11.020>.
- (487) Li, R.; Chai, Y.; Jiang, Y.; Ashby, P. D.; Toor, A.; Russell, T. P. Carboxylated Fullerene at the Oil/Water Interface. *ACS Appl. Mater. Interfaces* **2017**, *9* (39), 34389–34395. <https://doi.org/10.1021/acsami.7b07154>.
- (488) Sun, Q.; Liu, W.; Li, S.; Zhang, N.; Li, Z. Interfacial Rheology of Foam Stabilized by Nanoparticles and Their Retention in Porous Media. *Energy & Fuels* **2021**, *35* (8), 6541–6552. <https://doi.org/10.1021/ACS.ENERGYFUELS.0C03680>.
- (489) Noskov, B. A.; Yazhgur, P. A.; Liggieri, L.; Lin, S. Y.; Loglio, G.; Miller, R.; Ravera, F. Dilational Rheology of Spread and Adsorbed Layers of Silica Nanoparticles at the Liquid-Gas Interface. *Colloid J.* **2014**, *76* (2), 127–138. <https://doi.org/10.1134/S1061933X14020057>.
- (490) Toor, A.; Forth, J.; Bochner De Araujo, S.; Merola, M. C.; Jiang, Y.; Liu, X.; Chai, Y.; Hou, H.; Ashby, P. D.; Fuller, G. G.; Russell, T. P. Mechanical Properties of Solidifying Assemblies of Nanoparticle Surfactants at the Oil-Water Interface. *Langmuir* **2019**, *35* (41), 13340–13350. <https://doi.org/10.1021/acs.langmuir.9b01575>.
- (491) Keim, N. C.; Arratia, P. E. Role of Disorder in Finite-Amplitude Shear of a 2D Jammed Material. *Soft Matter* **2015**, *11* (8), 1539–1546. <https://doi.org/10.1039/C4SM02446J>.
- (492) Buttinoni, I.; Steinacher, M.; Spanke, H. T.; Pokki, J.; Bahmann, S.; Nelson, B.; Foffi, G.; Isa, L. Colloidal Polycrystalline Monolayers under Oscillatory Shear. *Phys. Rev. E* **2017**, *95* (1), 012610. <https://doi.org/10.1103/PhysRevE.95.012610>.
- (493) Roy, S.; Tirumkudulu, M. S. Micro-Mechanical Theory of Shear Yield Stress for Strongly Flocculated Colloidal Gel. *Soft Matter* **2020**, *16* (7), 1801–1809. <https://doi.org/10.1039/C9SM01784D>.
- (494) Roy, S.; Tirumkudulu, M. S. Yielding in a Strongly Aggregated Colloidal Gel. Part II: Theory. *J. Rheol. (N. Y. N. Y.)* **2016**, *60* (4), 575. <https://doi.org/10.1122/1.4948325>.
- (495) Sollich, P.; Lequeux, F.; Hébraud, P.; Cates, M. E. Rheology of Soft Glassy Materials. *Phys. Rev. Lett.* **1997**, *78* (10), 2020. <https://doi.org/10.1103/PhysRevLett.78.2020>.
- (496) Maas, M.; Ooi, C. C.; Fuller, G. G. Thin Film Formation of Silica Nanoparticle/Lipid Composite Films at the Fluid-Fluid Interface. *Langmuir* **2010**, *26* (23), 17867–17873. <https://doi.org/10.1021/LA103492A>.
- (497) Degen, P.; Wieland, D. C. F.; Leick, S.; Paulus, M.; Rehage, H.; Tolan, M. Effect of Magnetic Nanoparticles on the Surface Rheology of Surfactant Films at the Water Surface. *Soft Matter* **2011**, *7* (17), 7655–7662. <https://doi.org/10.1039/C1SM05248A>.
- (498) Brinker, C. J.; Scherer, G. W. *Sol-Gel Science: The Physics and Chemistry of Sol-Gel Processing*; Elsevier,

1990. <https://doi.org/10.1016/C2009-0-22386-5>.
- (499) Issa, A. A.; Luyt, A. S. Kinetics of Alkoxysilanes and Organoalkoxysilanes Polymerization: A Review. *Polymers (Basel)*. **2019**, *11* (3). <https://doi.org/10.3390/polym11030537>.
- (500) Danks, A. E.; Hall, S. R.; Schnepf, Z. The Evolution of “sol-Gel” Chemistry as a Technique for Materials Synthesis. *Mater. Horizons* **2016**, *3* (2), 91–112. <https://doi.org/10.1039/c5mh00260e>.
- (501) Stöber, W.; Fink, A.; Ernst Bohn, D. Controlled Growth of Monodisperse Silica Spheres in the Micron Size Range. *J. Colloid Interface Sci.* **1968**, *26*, 62–69.
- (502) Yokoi, T.; Sakamoto, Y.; Terasaki, O.; Kubota, Y.; Tatsuya Okubo; Tatsumi†, T. Periodic Arrangement of Silica Nanospheres Assisted by Amino Acids. *J. Am. Chem. Soc.* **2006**, *128* (42), 13664–13665. <https://doi.org/10.1021/JA065071Y>.
- (503) Lambilly, H. de; Klein, L. C. Transparent Microporous Silica Fibers by the Sol-Gel Process. *Infrared Opt. Transm. Mater.* **1986**, *0683*, 98–103. <https://doi.org/10.1117/12.936422>.
- (504) Siouffi, A. M. Silica Gel-Based Monoliths Prepared by the Sol-Gel Method: Facts and Figures. *J. Chromatogr. A* **2003**, *1000* (1–2), 801–818. [https://doi.org/10.1016/S0021-9673\(03\)00510-7](https://doi.org/10.1016/S0021-9673(03)00510-7).
- (505) McDonagh, C.; Sheridan, F.; Butler, T.; MacCraith, B. D. Characterisation of Sol-Gel-Derived Silica Films. *J. Non. Cryst. Solids* **1996**, *194* (1–2), 72–77. [https://doi.org/10.1016/0022-3093\(95\)00488-2](https://doi.org/10.1016/0022-3093(95)00488-2).
- (506) Katelnikovas, A.; Barkauskas, J.; Ivanauskas, F.; Beganskiene, A.; Kareiva, A. Aqueous Sol-Gel Synthesis Route for the Preparation of YAG: Evaluation of Sol-Gel Process by Mathematical Regression Model. *J. Sol-Gel Sci. Technol.* **2007**, *41* (3), 193–201. <https://doi.org/10.1007/S10971-006-9002-6>.
- (507) Reisfeld, R. Nanoparticles of Semiconductors in Sol Gel Glasses. In *Functionalized Nanoscale Materials, Devices and Systems*; Vaseashta, A., Mihailescu, I. N., Eds.; Springer, Dordrecht, 2008; pp 257–272. https://doi.org/10.1007/978-1-4020-8903-9_16.
- (508) Emerson, C. *Sol Gel Coatings*; CSA Journal Division, 2009.
- (509) Abel, M. L. Organosilanes: Adhesion Promoters and Primers. In *Handbook of Adhesion Technology: Second Edition*; Da Silva, L., Öchsner, A., Adams, R. D., Eds.; Springer International Publishing, 2018; Vol. 1–2, pp 257–280. https://doi.org/10.1007/978-3-319-55411-2_11.
- (510) Masmoudi, M.; Rahal, C.; Abdelmouleh, M.; Abdelhedi, R. Hydrolysis Process of γ -APS and Characterization of Silane Film Formed on Copper in Different Conditions. *Appl. Surf. Sci.* **2013**, *286*, 71–77. <https://doi.org/10.1016/J.APSUSC.2013.09.018>.
- (511) Pope, E. J. A. J. A.; Mackenzie, J. D. D. Sol-Gel Processing of Silica. II. The Role of the Catalyst. *J. Non. Cryst. Solids* **1986**, *87* (1–2), 185–198. [https://doi.org/10.1016/S0022-3093\(86\)80078-3](https://doi.org/10.1016/S0022-3093(86)80078-3).
- (512) Sulpizi, M.; Gageot, M. P.; Sprik, M. The Silica – Water Interface: How the Silanols Determine the Surface Acidity and Modulate the Water Properties. *J. Chem. Theory Comput.* **2012**, *8*, 1037–1047. <https://doi.org/10.1021/ct2007154>.
- (513) Belton, D. J.; Deschaume, O.; Perry, C. C. An Overview of the Fundamentals of the Chemistry of Silica with Relevance to Biosilicification and Technological Advances. *FEBS J.* **2012**, *279* (10), 1710–1720. <https://doi.org/10.1111/J.1742-4658.2012.08531.X>.
- (514) Papirer, E. *Adsorption on Silica Surfaces*, 1st ed.; CRC Press, 2000.
- (515) Kosmulski, M. The PH Dependent Surface Charging and Points of Zero Charge. VIII. Update. *Adv. Colloid Interface Sci.* **2020**, *275*, 102064. <https://doi.org/10.1016/J.CIS.2019.102064>.
- (516) Ong, S.; Zhao, X.; Eissenthal, K. B. Polarization of Water Molecules at a Charged Interface: Second Harmonic Studies of the Silica/Water Interface. *Chem. Phys. Lett.* **1992**, *191* (3,4), 327–335. [https://doi.org/10.1016/0009-2614\(92\)85309-X](https://doi.org/10.1016/0009-2614(92)85309-X).
- (517) Liu, X.; Cheng, J.; Lu, X.; Wang, R. Surface Acidity of Quartz: Understanding the Crystallographic Control. *Phys. Chem. Chem. Phys.* **2014**, *16* (48), 26909–26916. <https://doi.org/10.1039/C4CP02955K>.
- (518) Zhuravlev, L. T. The Surface Chemistry of Amorphous Silica. Zhuravlev Model. *Colloids Surfaces A Physicochem. Eng. Asp.* **2000**, *173* (1–3), 1–38. [https://doi.org/10.1016/S0927-7757\(00\)00556-2](https://doi.org/10.1016/S0927-7757(00)00556-2).
- (519) LaMer, V. K.; Dinegar, R. H. Theory, Production and Mechanism of Formation of Monodispersed Hydrosols. *J. Am. Chem. Soc.* **2002**, *72* (11), 4847–4854. <https://doi.org/10.1021/JA01167A001>.
- (520) Matsoukas, T.; Gulari, E. Monomer-Addition Growth with a Slow Initiation Step: A Growth Model for Silica Particles from Alkoxides. *J. Colloid Interface Sci.* **1989**, *132* (1), 13–21. [https://doi.org/10.1016/0021-9797\(89\)90210-5](https://doi.org/10.1016/0021-9797(89)90210-5).
- (521) Tan, C. G.; Bowen, B. D.; Epstein, N. Production of Monodisperse Colloidal Silica Spheres: Effect of Temperature. *J. Colloid Interface Sci.* **1987**, *118* (1), 290–293. [https://doi.org/10.1016/0021-9797\(87\)90458-9](https://doi.org/10.1016/0021-9797(87)90458-9).
- (522) Bogush, G. H.; Zukoski IV, C. F. Uniform Silica Particle Precipitation: An Aggregative Growth Model. *J. Colloid Interface Sci.* **1991**, *142* (1), 19–34. [https://doi.org/10.1016/0021-9797\(91\)90030-C](https://doi.org/10.1016/0021-9797(91)90030-C).
- (523) Lee, K.; Sathyagal, A. N.; McCormick, A. V. A Closer Look at an Aggregation Model of the Stöber Process. *Colloids Surfaces A Physicochem. Eng. Asp.* **1998**, *144* (1–3), 115–125. [https://doi.org/10.1016/S0927-7757\(98\)00566-4](https://doi.org/10.1016/S0927-7757(98)00566-4).

- (524) Bogush, G. H.; Tracy, M. A.; Zukoski IV, C. F. Preparation of Monodisperse Silica Particles: Control of Size and Mass Fraction. *J. Non. Cryst. Solids* **1988**, *104* (1), 95–106. [https://doi.org/10.1016/0022-3093\(88\)90187-1](https://doi.org/10.1016/0022-3093(88)90187-1).
- (525) Carcouët, C. C. M. C.; Van De Put, M. W. P.; Mezari, B.; Magusin, P. C. M. M.; Laven, J.; Bomans, P. H. H.; Friedrich, H.; Esteves, A. C. C.; Sommerdijk, N. A. J. M.; Van Benthem, R. A. T. M.; De With, G. Nucleation and Growth of Monodisperse Silica Nanoparticles. *Nano Lett.* **2014**, *14* (3), 1433–1438. <https://doi.org/10.1021/nl404550d>.
- (526) Pontoni, D.; Narayanan, T.; Rennie, A. R. Time-Resolved SAXS Study of Nucleation and Growth of Silica Colloids. *Langmuir* **2002**, *18* (1), 56–59. <https://doi.org/10.1021/la015503c>.
- (527) Green, D. L.; Lin, J. S.; Lam, Y. F.; Hu, M. Z. C.; Schaefer, D. W.; Harris, M. T. Size, Volume Fraction, and Nucleation of Stober Silica Nanoparticles. *J. Colloid Interface Sci.* **2003**, *266* (2), 346–358. [https://doi.org/10.1016/S0021-9797\(03\)00610-6](https://doi.org/10.1016/S0021-9797(03)00610-6).
- (528) Giesche, H. Synthesis of Monodispersed Silica Powders I. Particle Properties and Reaction Kinetics. *J. Eur. Ceram. Soc.* **1994**, *14*, 189–204.
- (529) Van Blaaderen, A.; Van Geest, J.; Vrij, A. Monodisperse Colloidal Silica Spheres from Tetraalkoxysilanes: Particle Formation and Growth Mechanism. *J. Colloid Interface Sci.* **1992**, *154* (2), 481–501. [https://doi.org/10.1016/0021-9797\(92\)90163-G](https://doi.org/10.1016/0021-9797(92)90163-G).
- (530) Huang, Y.; Pemberton, J. E. Synthesis of Uniform, Spherical Sub-100 Nm Silica Particles Using a Conceptual Modification of the Classic LaMer Model. *Colloids Surfaces A Physicochem. Eng. Asp.* **2010**, *360* (1–3), 175–183. <https://doi.org/10.1016/J.COLSURFA.2010.02.031>.
- (531) Filipović, R.; Obrenović, Z.; Stijepović, I.; Nikolić, L. M.; Srdić, V. V. Synthesis of Mesoporous Silica Particles with Controlled Pore Structure. *Ceram. Int.* **2009**, *35* (8), 3347–3353. <https://doi.org/10.1016/J.CERAMINT.2009.05.040>.
- (532) Li, S.; Wan, Q.; Qin, Z.; Fu, Y.; Gu, Y. Understanding Stöber Silicas Pore Characteristics Measured by Gas Adsorption. *Langmuir* **2015**, *31* (2), 824–832. <https://doi.org/10.1021/la5042103>.
- (533) FJ, A.; K, O.-A. Synthesis of Nanosize Silica in a Nonionic Water-in-Oil Microemulsion: Effects of the Water/Surfactant Molar Ratio and Ammonia Concentration. *J. Colloid Interface Sci.* **1999**, *211* (2), 210–220. <https://doi.org/10.1006/JCIS.1998.5985>.
- (534) Yokoi, T.; Wakabayashi, J.; Otsuka, Y.; Fan, W.; Iwama, M.; Watanabe, R.; Aramaki, K.; Shimojima, A.; Tatsumi, T.; Okubo, T. Mechanism of Formation of Uniform-Sized Silica Nanospheres Catalyzed by Basic Amino Acids. *Chem. Mater.* **2009**, *21* (15), 3719–3729. <https://doi.org/10.1021/cm900993b>.
- (535) Davis, T. M.; Snyder, M. A.; Krohn, J. E.; Tsapatsis, M. Nanoparticles in Lysine-Silica Sols. *Chem. Mater.* **2006**, *18* (25), 5814–5816. <https://doi.org/10.1021/CM061982V>.
- (536) Kurtis D. Hartlen; Aristidis P. T. Athanasopoulos, and; Kitaev*, V. Facile Preparation of Highly Monodisperse Small Silica Spheres (15 to >200 Nm) Suitable for Colloidal Templating and Formation of Ordered Arrays. *Langmuir* **2008**, *24* (5), 1714–1720. <https://doi.org/10.1021/LA7025285>.
- (537) Pogliani, L. Molecular Connectivity Model for Determination of Isoelectric Point of Amino Acids. *J. Pharm. Sci.* **1992**, *81* (4), 334–336. <https://doi.org/10.1002/JPS.2600810407>.
- (538) Wang, J.; Sugawara-Narutaki, A.; Fukao, M.; Yokoi, T.; Shimojima, A.; Okubo, T. Two-Phase Synthesis of Monodisperse Silica Nanospheres with Amines or Ammonia Catalyst and Their Controlled Self-Assembly. *ACS Appl. Mater. Interfaces* **2011**, *3* (5), 1538–1544. <https://doi.org/10.1021/am200104m>.
- (539) Hristov, D. R.; Mahon, E.; Dawson, K. A. Controlling Aqueous Silica Nanoparticle Synthesis in the 10–100 Nm Range. *Chem. Commun.* **2015**, *51* (98), 17420–17423. <https://doi.org/10.1039/c5cc06598d>.
- (540) Watanabe, R.; Yokoi, T.; Kobayashi, E.; Otsuka, Y.; Shimojima, A.; Okubo, T.; Tatsumi, T. Extension of Size of Monodisperse Silica Nanospheres and Their Well-Ordered Assembly. *J. Colloid Interface Sci.* **2011**, *360* (1), 1–7. <https://doi.org/10.1016/j.jcis.2010.09.001>.
- (541) Masalov, V. M.; Sukhinina, N. S.; Emel'chenko, G. A. Synthesis of Monodisperse Silica Nanoparticles via Heterogeneous Tetraethoxysilane Hydrolysis Using L-Arginine as a Catalyst. *Inorg. Mater.* **2018**, *54* (2), 156–162. <https://doi.org/10.1134/S0020168518020103>.
- (542) Murray, E.; Born, P.; Weber, A.; Kraus, T. Synthesis of Monodisperse Silica Nanoparticles Dispersible in Non-Polar Solvents. *Adv. Eng. Mater.* **2010**, *12*, 374–378. <https://doi.org/10.1002/adem.201000108>.
- (543) Ding, T.; Yao, L.; Liu, C. Kinetically-Controlled Synthesis of Ultra-Small Silica Nanoparticles and Ultra-Thin Coatings. *Nanoscale* **2016**, *8* (8), 4623–4627. <https://doi.org/10.1039/c5nr08224b>.
- (544) Allison, S. Analysis of the Electrophoretic Mobility and Viscosity of Dilute Ludox Solutions in Terms of a Spherical Gel Layer Model. *J. Colloid Interface Sci.* **2004**, *277* (1), 248–254. <https://doi.org/10.1016/j.jcis.2004.04.050>.
- (545) Pálmai, M.; Nagy, L. N.; Mihály, J.; Varga, Z.; Tárkányi, G.; Mizsei, R.; Szigyártó, I. C.; Kiss, T.; Kremmer, T.; Bóta, A. Preparation, Purification, and Characterization of Aminopropyl-Functionalized Silica Sol. *J. Colloid Interface Sci.* **2013**, *390* (1), 34–40. <https://doi.org/10.1016/j.jcis.2012.09.025>.
- (546) Vauthier, C.; Cabane, B.; Labarre, D. How to Concentrate Nanoparticles and Avoid Aggregation? *Eur. J.*

- Pharm. Biopharm.* **2008**, *69* (2), 466–475. <https://doi.org/10.1016/j.ejpb.2008.01.025>.
- (547) Sigmund, W.; El-Shall, H.; Shah, D. O.; Moudgil, B. M. *Particulate Systems in Nano- and Biotechnologies*, 1st ed.; CRC Press, 2009. <https://doi.org/10.1201/9781420007534>.
- (548) Šefčík, J.; McCormick, A. V. Kinetic and Thermodynamic Issues in the Early Stages of Sol-Gel Processes Using Silicon Alkoxides. *Catal. Today* **1997**, *35* (3), 205–223. [https://doi.org/10.1016/S0920-5861\(96\)00158-7](https://doi.org/10.1016/S0920-5861(96)00158-7).
- (549) Bahuguna, G.; Mishra, N. K.; Chaudhary, P.; Kumar, A.; Singh, R. Thin Film Coating through Sol-Gel Gel Technique. *Res. J. Chem. Sci.* **2016**, *6* (June), 65–72.
- (550) Jilani, A.; Abdel-wahab, M. S.; Hammad, A. H. Advance Deposition Techniques for Thin Film and Coating. In *Modern Technologies for Creating the Thin-film Systems and Coatings*; Nikitenkov, N. N., Ed.; InTechOpen, 2017; pp 137–149. <https://doi.org/10.5772/65702>.
- (551) Grosso, D. How to Exploit the Full Potential of the Dip-Coating Process to Better Control Film Formation. *J. Mater. Chem.* **2011**, *21* (43), 17033–17038. <https://doi.org/10.1039/c1jm12837j>.
- (552) Faustini, M.; Louis, B.; Albouy, P. A.; Kuemmel, M.; Grosso, D. Preparation of Sol-Gel Films by Dip-Coating in Extreme Conditions. *J. Phys. Chem. C* **2010**, *114* (17), 7637–7645. <https://doi.org/10.1021/JP9114755>.
- (553) Kozuka, H. Stress Evolution on Gel-to-Ceramic Thin Film Conversion. *J. Sol-Gel Sci. Technol.* **2006**, *40* (2), 287–297. <https://doi.org/10.1007/S10971-006-9213-X>.
- (554) Kurisu, T.; Kozuka, H. Effects of Heating Rate on Stress Evolution in Alkoxide-Derived Silica Gel-Coating Films. *J. Am. Ceram. Soc.* **2006**, *89* (8), 2453–2458. <https://doi.org/10.1111/J.1551-2916.2006.01107.X>.
- (555) Kappert, E. J.; Pavlenko, D.; Malzbender, J.; Nijmeijer, A.; Benes, N. E.; Tsai, P. A. Formation and Prevention of Fractures in Sol-Gel-Derived Thin Films. *Soft Matter* **2015**, *11* (5), 882–888. <https://doi.org/10.1039/c4sm02085e>.
- (556) Guglielmi, M.; Zenezini, S. The Thickness of Sol-Gel Silica Coatings Obtained by Dipping. *J. Non. Cryst. Solids* **1990**, *121* (1–3), 303–309. [https://doi.org/10.1016/0022-3093\(90\)90148-F](https://doi.org/10.1016/0022-3093(90)90148-F).
- (557) Houmard, M.; Nunes, E. H. M.; Vasconcelos, D. C. L.; Berthomé, G.; Joud, J. C.; Langlet, M.; Vasconcelos, W. L. Correlation between Sol-Gel Reactivity and Wettability of Silica Films Deposited on Stainless Steel. *Appl. Surf. Sci.* **2014**, *289*, 218–223. <https://doi.org/10.1016/j.apsusc.2013.10.137>.
- (558) Yang, X.; Zhu, L.; Chen, Y.; Bao, B.; Xu, J.; Zhou, W. Controlled Hydrophilic/Hydrophobic Property of Silica Films by Manipulating the Hydrolysis and Condensation of Tetraethoxysilane. *Appl. Surf. Sci.* **2016**, *376*, 1–9. <https://doi.org/10.1016/j.apsusc.2016.02.068>.
- (559) Shen, S. J.; Lee, D.; Wu, Y. C.; Liu, S. J. Binary Self-Assembly of Nanocolloidal Arrays Using Concurrent and Sequential Spin Coating Techniques. *Materials (Basel)*. **2021**, *14* (2), 1–10. <https://doi.org/10.3390/MA14020274>.
- (560) Iskandar, F.; Abdullah, M.; Yoden, H.; Okuyama, K. Silica Films Containing Ordered Pores Prepared by Dip Coating of Silica Nanoparticles and Polystyrene Beads Colloidal Mixture. *J. Sol-Gel Sci. Technol.* **2004**, *29* (1), 41–47. <https://doi.org/10.1023/B:JSST.0000016136.39875.24>.
- (561) Isa, L.; Kumar, K.; Müller, M.; Grolig, J.; Textor, M.; Reimhult, E. Particle Lithography from Colloidal Self-Assembly at Liquid-Liquid Interfaces. *ACS Nano* **2010**, *4* (10), 5665–5670. <https://doi.org/10.1021/nn101260f>.
- (562) Poornima, K.; Nadu, T. Cadmium Doped Zinc Oxide Nanoparticles Coated on Glass Substrate by Dip Coating Method. *Int. J. Sci. Res. Rev.* **2019**, *8* (1), 39–43. <https://doi.org/2279-543X>.
- (563) Ten Brink, G. H.; Foley, N.; Zwaan, D.; Kooi, B. J.; Palasantzas, G. Roughness Controlled Superhydrophobicity on Single Nanometer Length Scale with Metal Nanoparticles. *RSC Adv.* **2015**, *5* (36), 28696–28702. <https://doi.org/10.1039/c5ra02348c>.
- (564) Chen, K.; Zhou, S.; Yang, S.; Wu, L. Fabrication of All-Water-Based Self-Repairing Superhydrophobic Coatings Based on UV-Responsive Microcapsules. *Adv. Funct. Mater.* **2015**, *25*, 1035–1041. <https://doi.org/10.1002/adfm.201403496>.
- (565) Cai, S.; Zhang, Y.; Zhang, H.; Yan, H.; Lv, H.; Jiang, B. Sol-Gel Preparation of Hydrophobic Silica Antireflective Coatings with Low Refractive Index by Base/Acid Two-Step Catalysis. *ACS Appl. Mater. Interfaces* **2014**, *6* (14), 11470–11475. <https://doi.org/10.1021/am501972y>.
- (566) Jameel, Z. N.; Haider, A. J.; Taha, S. Y.; Gangopadhyay, S.; Bok, S. Evaluation of Hybrid Sol-Gel Incorporated with Nanoparticles as Nano Paint. In *Technologies and Materials for Renewable Energy, Environment and Sustainability*; 2016; Vol. 1758. <https://doi.org/10.1063/1.4959377>.
- (567) Verhovšek, D.; Veronovski, N.; Lavrenčič Štangar, U.; Kete, M.; Žagar, K.; Čeh, M. The Synthesis of Anatase Nanoparticles and the Preparation of Photocatalytically Active Coatings Based on Wet Chemical Methods for Self-Cleaning Applications. *Int. J. Photoenergy* **2012**, *10*. <https://doi.org/10.1155/2012/329796>.
- (568) Molchan, I. S.; Thompson, G. E.; Skeldon, P.; Hashimoto, T.; Schem, M.; Schmidt, T.; Gerwann, J.;

- Kochanek, W. Sol-Gel-Based Coatings with Incorporated CeO₂ Nanoparticles for Protection of AA2024-T3 Aluminium Alloy. In *Physics, Chemistry and Application of Nanostructures*; 2007; pp 351–355. https://doi.org/10.1142/9789812770950_0078.
- (569) INDUMATHY, B.; Gunasekhar, R.; Sathiyathan, P.; Anand, P. A. Chemistry and Applications of Organosilanes – An Overview <https://spast.org/techrep/article/view/1451>.
- (570) Fadeev, A. Y.; McCarthy, T. J. Self-Assembly Is Not the Only Reaction Possible between Alkyltrichlorosilanes and Surfaces: Monomolecular and Oligomeric Covalently Attached Layers of Dichloro- and Trichloroalkylsilanes on Silicon. *Langmuir* **2000**, *16* (18), 7268–7274. <https://doi.org/10.1021/LA000471Z>.
- (571) Ishida, H.; Naviroj, S.; Tripathy, S. K.; Fitzgerald, J. J.; Koenig, J. L. Structure of an Aminosilane Coupling Agent in Aqueous Solutions and Partially Cured Solids. *J. Polym. Sci. Part A-2, Polym. Phys.* **1982**, *20* (4), 701–718. <https://doi.org/10.1002/pol.1982.180200412>.
- (572) Said, R. Ben; Kolle, J. M.; Essalah, K.; Tangour, B.; Sayari, A. A Unified Approach to CO₂–Amine Reaction Mechanisms. *ACS Omega* **2020**, *5* (40), 26125–26133. <https://doi.org/10.1021/ACSOMEGA.0C03727>.
- (573) Argekar, S. U.; Kirley, T. L.; Schaefer, D. W. Determination of Structure-Property Relationships for 3-Aminopropyltriethoxysilane Films Using x-Ray Reflectivity. *J. Mater. Res.* **2013**, *28* (8), 1118–1128. <https://doi.org/10.1557/jmr.2013.54>.
- (574) Arkles, B.; Steinmetz, J. R.; Zazyczny, J.; Mehta, P. Factors Contributing to the Stability of Alkoxysilanes in Aqueous Solution. *J. Adhes. Sci. Technol.* **1992**, *6* (1), 193–206. <https://doi.org/10.1163/156856192X00133>.
- (575) Vansant, E. F.; Van Der Voort, P.; Vracnken, K. C. *Characterization and Chemical Modification of the Silica Surface*; Elsevier: Amsterdam, 1995.
- (576) Naviroj, S.; Culler, S. R.; Koenig, J. L.; Ishida, H. Structure and Adsorption Characteristics of Silane Coupling Agents on Silica and E-Glass Fiber; Dependence on PH. *J. Colloid Interface Sci.* **1984**, *97* (2), 308–317. [https://doi.org/10.1016/0021-9797\(84\)90301-1](https://doi.org/10.1016/0021-9797(84)90301-1).
- (577) Shyue, J.-J.; Guire, M. R. De; Nakanishi, T.; Masuda, Y.; Koumoto, K.; Sukenik, C. N. Acid–Base Properties and Zeta Potentials of Self-Assembled Monolayers Obtained via in Situ Transformations. *Langmuir* **2004**, *20* (20), 8693–8698. <https://doi.org/10.1021/la049247q>.
- (578) Zhang, F.; Srinivasan, M. P. Self-Assembled Molecular Films of Aminosilanes and Their Immobilization Capacities. *Langmuir* **2004**, *20* (6), 2309–2314. <https://doi.org/10.1021/la0354638>.
- (579) Smith, E. A.; Chen, W. How to Prevent the Loss of Surface Functionality Derived from Aminosilanes. *Langmuir* **2008**, *24* (21), 12405–12409. <https://doi.org/10.1021/la802234x>.
- (580) Zhu, M.; Lerum, M. Z.; Chen, W.; Mojun Zhu, Maria Z. Lerum, and W. C. How to Prepare Reproducible, Homogeneous, and Hydrolytically Stable Aminosilane-Derived Layers on Silica. *Langmuir* **2012**, *28* (1), 416–423. <https://doi.org/10.1021/la203638g>.
- (581) Etienne, M.; Walcarius, A. Analytical Investigation of the Chemical Reactivity and Stability of Aminopropyl-Grafted Silica in Aqueous Medium. *Talanta* **2003**, *59* (6), 1173–1188. [https://doi.org/10.1016/S0039-9140\(03\)00024-9](https://doi.org/10.1016/S0039-9140(03)00024-9).
- (582) Okhrimenko, D. V.; Budi, A.; Ceccato, M.; Cárdenas, M.; Johansson, D. B.; Lybye, D.; Bechgaard, K.; Andersson, M. P.; Stipp, S. L. S. Hydrolytic Stability of 3-Aminopropylsilane Coupling Agent on Silica and Silicate Surfaces at Elevated Temperatures. *ACS Appl. Mater. Interfaces* **2017**, *9* (9), 8344–8353. <https://doi.org/10.1021/acsami.6b14343>.
- (583) Liu, Y.; Li, Y.; Li, X. M.; He, T. Kinetics of (3-Aminopropyl)Triethoxysilane (Aptes) Silanization of Superparamagnetic Iron Oxide Nanoparticles. *Langmuir* **2013**, *29* (49), 15275–15282. <https://doi.org/10.1021/la403269u>.
- (584) Metwalli, E.; Haines, D.; Becker, O.; Conzone, S.; Pantano, C. G. Surface Characterizations of Mono-, Di-, and Tri-Aminosilane Treated Glass Substrates. *J. Colloid Interface Sci.* **2006**, *298* (2), 825–831. <https://doi.org/10.1016/j.jcis.2006.03.045>.
- (585) Chauhan, A. K.; Aswal, D. K.; Koiry, S. P.; Gupta, S. K.; Yakhmi, J. V.; Sürgers, C.; Guerin, D.; Lenfant, S.; Vuillaume, D. Self-Assembly of the 3-Aminopropyltrimethoxysilane Multilayers on Si and Hysteretic Current-Voltage Characteristics. *Appl. Phys. A Mater. Sci. Process.* **2008**, *90* (3), 581–589. <https://doi.org/10.1007/s00339-007-4336-7>.
- (586) Jakša, G.; Štefane, B.; Kovač, J. Influence of Different Solvents on the Morphology of APTMS-Modified Silicon Surfaces. *Appl. Surf. Sci.* **2014**, *315* (1), 516–522. <https://doi.org/10.1016/j.apsusc.2014.05.157>.
- (587) Kim, H.; Kwon, J. Y. Enzyme Immobilization on Metal Oxide Semiconductors Exploiting Amine Functionalized Layer. *RSC Adv.* **2017**, *7* (32), 19656–19661. <https://doi.org/10.1039/c7ra01615h>.
- (588) Miranda, A.; Martínez, L.; De Beule, P. A. A. Facile Synthesis of an Aminopropylsilane Layer on Si/SiO₂ Substrates Using Ethanol as APTEs Solvent. *MethodsX* **2020**, *7* (May). <https://doi.org/10.1016/j.mex.2020.100931>.

- (589) Yadav, A. R.; Sriram, R.; Carter, J. A.; Miller, B. L. Comparative Study of Solution-Phase and Vapor-Phase Deposition of Aminosilanes on Silicon Dioxide Surfaces. *Mater. Sci. Eng. C* **2014**, *35* (1), 283–290. <https://doi.org/10.1016/j.msec.2013.11.017>.
- (590) Chiang, C. H.; Ishida, H.; Koenig, J. L. The Structure of γ -Aminopropyltriethoxysilane on Glass Surfaces. *Journal of Colloid And Interface Science*. 1980, pp 396–404. [https://doi.org/10.1016/0021-9797\(80\)90209-X](https://doi.org/10.1016/0021-9797(80)90209-X).
- (591) Hristov, D. R.; Rocks, L.; Kelly, P. M.; Thomas, S. S.; Pitek, A. S.; Verderio, P.; Mahon, E.; Dawson, K. A. Tuning of Nanoparticle Biological Functionality through Controlled Surface Chemistry and Characterisation at the Bioconjugated Nanoparticle Surface. *Nat. Publ. Gr.* **2015**, No. October, 1–8. <https://doi.org/10.1038/srep17040>.
- (592) Wang, W.; Vaughn, M. W. Morphology and Amine Accessibility of (3-Aminopropyl) Triethoxysilane Films on Glass Surfaces. *Scanning* **2008**, *30* (2), 65–77. <https://doi.org/10.1002/sca.20097>.
- (593) Pasternack, R. M.; Amy, S. R.; Chabal, Y. J. Attachment of 3-(Aminopropyl)Triethoxysilane on Silicon Oxide Surfaces: Dependence on Solution Temperature. *Langmuir* **2008**, *24* (22), 12963–12971. <https://doi.org/10.1021/la8024827>.
- (594) Seitz, O.; Fernandes, P. G.; Tian, R.; Karnik, N.; Wen, H. C.; Stiegler, H.; Chapman, R. A.; Vogel, E. M.; Chabal, Y. J. Control and Stability of Self-Assembled Monolayers under Biosensing Conditions. *J. Mater. Chem.* **2011**, *21* (12), 4384–4392. <https://doi.org/10.1039/c1jm10132c>.
- (595) Kunc, F.; Balhara, V.; Brinkmann, A.; Sun, Y.; Leek, D. M.; Johnston, L. J. Quantification and Stability Determination of Surface Amine Groups on Silica Nanoparticles Using Solution NMR. *Anal. Chem.* **2018**, *90* (22), 13322–13330. <https://doi.org/10.1021/acs.analchem.8b02803>.
- (596) Giraud, L.; Nadarajah, R.; Matar, Y.; Bazin, G.; Sun, J.; Zhu, X. X.; Giasson, S. Amino-Functionalized Monolayers Covalently Grafted to Silica-Based Substrates as a Robust Primer Anchorage in Aqueous Media. *Appl. Surf. Sci.* **2016**, *370*, 476–485. <https://doi.org/10.1016/j.apsusc.2016.02.141>.
- (597) Han, Y.; Mayer, D.; Offenhäusser, A.; Ingebrandt, S. Surface Activation of Thin Silicon Oxides by Wet Cleaning and Silanization. *Thin Solid Films* **2006**, *510* (1–2), 175–180. <https://doi.org/10.1016/j.tsf.2005.11.048>.
- (598) Khimich, N. N.; Venzel', B. I.; Koptelova, L. A.; Drozdova, I. A. Acetic Acid in Sol-Gel Process of Hydrolytic Polycondensation of Tetramethoxysilane. *Russ. J. Appl. Chem.* **2004**, *77* (2), 290–294. <https://doi.org/10.1023/B:RJAC.0000030369.94103.4a>.
- (599) Smith, A. M.; Johnston, K. A.; Crawford, S. E.; Marbella, L. E.; Millstone, J. E. Ligand Density Quantification on Colloidal Inorganic Nanoparticles. *Analyst* **2017**, *142* (1), 11–29. <https://doi.org/10.1039/c6an02206e>.
- (600) Cuello-Nuñez, S.; Abad-Álvaro, I.; Bartczak, D.; Del Castillo Busto, M. E.; Ramsay, D. A.; Pellegrino, F.; Goenaga-Infante, H. The Accurate Determination of Number Concentration of Inorganic Nanoparticles Using SpICP-MS with the Dynamic Mass Flow Approach. *J. Anal. At. Spectrom.* **2020**, *35* (9), 1832–1839. <https://doi.org/10.1039/C9JA00415G>.
- (601) Bottom, C. B.; Hanna, S. S.; Siehr, D. J. Mechanism of the Ninhydrin Reaction. *Biochem. Educ.* **1978**, *6* (1), 4–5. [https://doi.org/10.1016/0307-4412\(78\)90153-X](https://doi.org/10.1016/0307-4412(78)90153-X).
- (602) Friedman, M. Applications of the Ninhydrin Reaction for Analysis of Amino Acids, Peptides, and Proteins to Agricultural and Biomedical Sciences. *J. Agric. Food Chem.* **2004**, *52* (3), 385–406. <https://doi.org/10.1021/jf030490p>.
- (603) Lamothe, P. J.; McCormick, P. G. Influence of Acidity on the Reaction of Ninhydrin with Amino Acids. *Anal. Chem.* **1972**, *44* (4), 821–825. <https://doi.org/10.1021/AC60312A003>.
- (604) Spencer, R. P.; Brody, B. R.; Lutters, B. M. Reaction of Amines and Amino Acids with Aqueous and Nonaqueous Acid-Ninhydrin. *Microchim. Acta* **1964**, *52*, 1144–1150. <https://doi.org/10.1007/BF01224584>.
- (605) Sun, Y.; Kunc, F.; Balhara, V.; Coleman, B.; Kodra, O.; Raza, M.; Chen, M.; Brinkmann, A.; Lopinski, G. P.; Johnston, L. J. Quantification of Amine Functional Groups on Silica Nanoparticles: A Multi-Method Approach. *Nanoscale Adv.* **2019**, *1* (4), 1598–1607. <https://doi.org/10.1039/c9na00016j>.
- (606) Bhattacharjee, S. DLS and Zeta Potential - What They Are and What They Are Not? *J. Control. Release* **2016**, *235*, 337–351. <https://doi.org/10.1016/j.jconrel.2016.06.017>.
- (607) Stetefeld, J.; McKenna, S. A.; Patel, T. R. Dynamic Light Scattering: A Practical Guide and Applications in Biomedical Sciences. *Biophys. Rev.* **2016**, *8* (4), 409. <https://doi.org/10.1007/S12551-016-0218-6>.
- (608) Malm, A. V.; Corbett, J. C. W. Improved Dynamic Light Scattering Using an Adaptive and Statistically Driven Time Resolved Treatment of Correlation Data. *Sci. Rep.* **2019**, *9* (1), 1–11. <https://doi.org/10.1038/s41598-019-50077-4>.
- (609) Hunter, R. J. *Zeta Potential in Colloid Science: Principles and Applications*, 3rd ed.; Ottewill, R. H., Rowel, R. L., Eds.; Academic Press, 1988.
- (610) Doane, T. L.; Chuang, C.; Hill, R. J.; Burda, C. Nanoparticle ζ -Potentials. *Acc. Chem. Res.* **2012**, *45* (3),

- 317–326. <https://doi.org/10.1021/ar200113c>.
- (611) Malvern Instruments Ltd. Size Theory. In *Zetasizer Nano User Manual*; 2013; pp 15.6-15.12.
- (612) McNeil-Watson, F. Electrophoretic Light Scattering. In *Encyclopedia of Biophysics*; Roberts, G. C. K., Ed.; Springer, Berlin, Heidelberg, 2013; pp 648–654. https://doi.org/10.1007/978-3-642-16712-6_288.
- (613) Miller, J. F.; Schätzel, K.; Vincent, B. The Determination of Very Small Electrophoretic Mobilities in Polar and Nonpolar Colloidal Dispersions Using Phase Analysis Light Scattering. *J. Colloid Interface Sci.* **1991**, *143* (2), 532–554. [https://doi.org/10.1016/0021-9797\(91\)90286-H](https://doi.org/10.1016/0021-9797(91)90286-H).
- (614) Miller, J. F. Next Generation Electrophoretic Light Scattering (NG-ELS) Confidence at High Ionic Strength. In *American Chemical Society National Meeting*; 2018; pp 1–13.
- (615) Hückel, E. Die Kataphorese Der Kugel. *Phys. Zeitschrift* **1924**, *25*, 204–210.
- (616) Henry, D. C.; A, P. R. S. L. The Cataphoresis of Suspended Particles. Part I.—The Equation of Cataphoresis. *Proc. R. Soc. London. Ser. A, Contain. Pap. a Math. Phys. Character* **1931**, *133* (821), 106–129. <https://doi.org/10.1098/rspa.1931.0133>.
- (617) Ohshima, H. A Simple Expression for Henry's Function for the Retardation Effect in Electrophoresis of Spherical Colloidal Particles. *J. Colloid Interface Sci.* **1994**, *168* (1), 269–271. <https://doi.org/https://doi.org/10.1006/jcis.1994.1419>.
- (618) Deshiikan, S. R.; Papadopoulos, K. D. Modified Booth Equation for the Calculation of Zeta Potential. *Colloid Polym. Sci.* **1998**, *276* (2), 117–124. <https://doi.org/10.1007/S003960050218>.
- (619) O'Brien, R. W.; White, L. R. Electrophoretic Mobility of a Spherical Colloidal Particle. *J. Chem. Soc., Faraday Trans. 2* **1978**, *74*, 1607–1626. <https://doi.org/https://doi.org/10.1039/F29787401607>.
- (620) Wiersema, P. H.; Loeb, A. L.; Overbeek, J. T. G. Calculation of the Electrophoretic Mobility of a Spherical Colloid Particle. *J. Colloid Interface Sci.* **1966**, *22* (1), 78–99. [https://doi.org/10.1016/0021-9797\(66\)90069-5](https://doi.org/10.1016/0021-9797(66)90069-5).
- (621) Ohshima, H. On the Maximum of the Magnitude of the Electrophoretic Mobility of a Spherical Colloidal Particle in an Electrolyte Solution. *Colloid Polym. Sci.* **2016**, *294* (1), 13–17. <https://doi.org/10.1007/s00396-015-3756-8>.
- (622) Ohshima, H. On the Limiting Electrophoretic Mobility of a Highly Charged Colloidal Particle in an Electrolyte Solution. *J. Colloid Interface Sci.* **2003**, *263* (1), 337–340. [https://doi.org/10.1016/S0021-9797\(03\)00280-7](https://doi.org/10.1016/S0021-9797(03)00280-7).
- (623) Ohshima, H.; Healy, T. W.; White, L. R. Approximate Analytic Expressions for the Electrophoretic Mobility of Spherical Colloidal Particles and the Conductivity of Their Dilute Suspensions. *J. Chem. Soc. Faraday Trans. 2* **1983**, *79*, 1613–1628. <https://doi.org/10.1002/elps.202000339>.
- (624) Dukhin, S. S. Non-Equilibrium Electric Surface Phenomena. *Adv. Colloid Interface Sci.* **1993**, *44* (C), 1–134. [https://doi.org/10.1016/0001-8686\(93\)80021-3](https://doi.org/10.1016/0001-8686(93)80021-3).
- (625) Delgado, A. V.; González-Caballero, F.; Hunter, R. J.; Koopal, L. K.; Lyklema, J. Measurement and Interpretation of Electrokinetic Phenomena. *J. Colloid Interface Sci.* **2007**, *309*, 194–224. <https://doi.org/10.1016/j.jcis.2006.12.075>.
- (626) Lyklema, J. Surface Conduction. *J. Phys. Condens. Matter* **2001**, *13* (21), 5027–5034. <https://doi.org/10.1088/0953-8984/13/21/326>.
- (627) Škvarla, J. Hard versus Soft Particle Electrokinetics of Silica Colloids. *Langmuir* **2007**, *23* (10), 5305–5314. <https://doi.org/10.1021/la0635451>.
- (628) Choi, W.; Mahajan, U.; Lee, S.-M.; Abiade, J.; Singh, R. K. Effect of Slurry Ionic Salts at Dielectric Silica CMP. *J. Electrochem. Soc.* **2004**, *151* (3), G185. <https://doi.org/10.1149/1.1644609>.
- (629) Jalil, A. H.; Pyell, U. Quantification of Zeta-Potential and Electrokinetic Surface Charge Density for Colloidal Silica Nanoparticles Dependent on Type and Concentration of the Counterion: Probing the Outer Helmholtz Plane. *J. Phys. Chem. C* **2018**, *122* (8), 4437–4453. <https://doi.org/10.1021/acs.jpcc.7b12525>.
- (630) Leroy, P.; Devau, N.; Revil, A.; Bizi, M. Influence of Surface Conductivity on the Apparent Zeta Potential of Amorphous Silica Nanoparticles. *J. Colloid Interface Sci.* **2013**, *410*, 81–93. <https://doi.org/10.1016/j.jcis.2013.08.012>.
- (631) Overbeek, J. T. G. Theorie Der Elektrophorese - Der Relaxationseffekt. *Kolloid-Beihfte* **1943**, *54* (7–9), 287–364. <https://doi.org/10.1007/BF02556774>.
- (632) Booth, F. The Cataphoresis of Spherical, Solid Non-Conducting Particles in a Symmetrical Electrolyte. *Proc. R. Soc. London. Ser. A. Math. Phys. Sci.* **1950**, *203* (1075), 514–533. <https://doi.org/10.1098/rspa.1950.0154>.
- (633) Ohshima, H. Approximate Analytic Expression for the Electrophoretic Mobility of a Spherical Colloidal Particle. *J. Colloid Interface Sci.* **2001**, *239* (2), 587–590. <https://doi.org/10.1006/jcis.2001.7608>.
- (634) Werner, C.; Zimmermann, R.; Kratzmüller, T. Streaming Potential and Streaming Current Measurements at Planar Solid/Liquid Interfaces for Simultaneous Determination of Zeta Potential and Surface Conductivity. *Colloids Surfaces A Physicochem. Eng. Asp.* **2001**, *192* (1–3), 205–213. [https://doi.org/10.1016/S0927-7757\(01\)00725-7](https://doi.org/10.1016/S0927-7757(01)00725-7).

- (635) Gallardo-Moreno, A. M.; Vadillo-Rodríguez, V.; Perera-Núñez, J.; Bruque, J. M.; González-Martín, M. L. The Zeta Potential of Extended Dielectrics and Conductors in Terms of Streaming Potential and Streaming Current Measurements. *Phys. Chem. Chem. Phys.* **2012**, *14* (27), 9758–9767. <https://doi.org/10.1039/c2cp40743d>.
- (636) Werner, G.; Körber, H.; Zimmermann, R.; Dukhin, S.; Jacobasch, H. J. Extended Electrokinetic Characterization of Flat Solid Surfaces. *J. Colloid Interface Sci.* **1998**, *208* (1), 329–346. <https://doi.org/10.1006/jcis.1998.5787>.
- (637) Zimmermann, R.; Osaki, T.; Schweiß, R.; Werner, C. Electrokinetic Microslit Experiments to Analyse the Charge Formation at Solid/Liquid Interfaces. *Microfluid. Nanofluidics* **2006**, *2* (5), 367–379. <https://doi.org/10.1007/s10404-006-0087-6>.
- (638) Fernández-Toledano, J. C.; Moncho-Jordá, A.; Martínez-López, F.; Hidalgo-Álvarez, R. Spontaneous Formation of Mesostructures in Colloidal Monolayers Trapped at the Air-Water Interface: A Simple Explanation. *Langmuir* **2004**, *20* (17), 6977–6980. <https://doi.org/10.1021/la0496237>.
- (639) Drechsler, A.; Caspari, A.; Synytska, A. Influence of Roughness and Capillary Size on the Zeta Potential Values Obtained by Streaming Potential Measurements. *Surf. Interface Anal.* **2020**, *52* (12), 991–995. <https://doi.org/10.1002/sia.6792>.
- (640) Bortolotti, M.; Brugnara, M.; Volpe, C. Della; Siboni, S. Numerical Models for the Evaluation of the Contact Angle from Axisymmetric Drop Profiles: A Statistical Comparison. *J. Colloid Interface Sci.* **2009**, *336* (1), 285–297. <https://doi.org/10.1016/J.JCIS.2009.03.055>.
- (641) Fatollahi, A. H.; Hajirahimi, M. *Making Sessile Drops Easier*; 2013.
- (642) Saad, S. M. I.; Neumann, A. W. Axisymmetric Drop Shape Analysis (ADSA): An Outline. *Adv. Colloid Interface Sci.* **2016**, *238*, 62–87. <https://doi.org/10.1016/j.cis.2016.11.001>.
- (643) Krüss. Drop shape analysis <https://www.kruss-scientific.com/en/know-how/glossary/drop-shape-analysis> (accessed Aug 16, 2021).
- (644) Lubarda, V. A.; Talke, K. A. Analysis of the Equilibrium Droplet Shape Based on an Ellipsoidal Droplet Model. **2011**, *27*, 10705–10713. <https://doi.org/10.1021/la202077w>.
- (645) Kwok, D. Y.; Lin, R.; Mui, M.; Neumann, A. W. Low-Rate Dynamic and Static Contact Angles and the Determination of Solid Surface Tensions. *Colloids Surfaces A Physicochem. Eng. Asp.* **1996**, *116* (1–2), 63–77. [https://doi.org/10.1016/0927-7757\(96\)03590-X](https://doi.org/10.1016/0927-7757(96)03590-X).
- (646) Tavana, H.; Neumann, A. W. On the Question of Rate-Dependence of Contact Angles. *Colloids Surfaces A Physicochem. Eng. Asp.* **2006**, *282–283*, 256–262. <https://doi.org/10.1016/J.COLSURFA.2006.01.001>.
- (647) Kwok, D. Y.; Neumann, A. W. Contact Angle Measurement and Contact Angle Interpretation. *Adv. Colloid Interface Sci.* **1999**, *81* (3), 167–249. [https://doi.org/10.1016/S0001-8686\(98\)00087-6](https://doi.org/10.1016/S0001-8686(98)00087-6).
- (648) Drelich, J. The Effect of Drop (Bubble) Size on Contact Angle at Solid Surfaces. *J. Adhes.* **1997**, *63* (1–3), 31–51. <https://doi.org/10.1080/00218469708015212>.
- (649) Nagy, N. Contact Angle Determination on Hydrophilic and Superhydrophilic Surfaces by Using r - θ -Type Capillary Bridges. *Langmuir* **2019**, *35* (15), 5202–5212. <https://doi.org/10.1021/ACS.LANGMUIR.9B00442>.
- (650) Tadmor, R. Line Energy and the Relation between Advancing, Receding, and Young Contact Angles. *Langmuir* **2004**, *20* (18), 7659–7664. <https://doi.org/10.1021/la049410h>.
- (651) Chibowski, E. Contact Angle Hysteresis Due to a Film Present behind the Drop. In *Contact angle, wettability and adhesion*; Mittal, K.L., Ed.; VSP: Utrecht, The Netherlands, 2002; pp 265–288. <https://doi.org/10.1201/b11975>.
- (652) Chibowski, E. Comparison of Apparent Surface Free Energy of Some Solids Determined by Different Approaches. In *Contact angle, wettability and adhesion*; Mittal, K. L., Ed.; VSP: Koninklijke Brill NV, Leiden, The Netherlands, 2009; Vol. 6, pp 283–299. <https://doi.org/10.1201/b12247>.
- (653) Tavana, H.; Yang, G.; Yip, C. M.; Appelhans, D.; Zschoche, S.; Grundke, K.; Hair, M. L.; Neumann, A. W. Stick-Slip of the Three-Phase Line in Measurements of Dynamic Contact Angles. *Langmuir* **2006**, *22* (2), 628–636. <https://doi.org/10.1021/la051715o>.
- (654) Stammitti-Scarpone, A.; Acosta, E. J. Solid-Liquid-Liquid Wettability and Its Prediction with Surface Free Energy Models. *Adv. Colloid Interface Sci.* **2019**, *264*, 28–46. <https://doi.org/10.1016/j.cis.2018.10.003>.
- (655) Parkinson, L. M.; Phan, C. M. Natural Vibration of an Aqueous Pendant Drop. *Exp. Therm. Fluid Sci.* **2018**, *90* (September 2017), 48–54. <https://doi.org/10.1016/j.expthermflusci.2017.09.003>.
- (656) Hoorfar, M.; Neumann, A. W. Axisymmetric Drop Shape Analysis (ADSA) for the Determination of Surface Tension and Contact Angle. *J. Adhes.* **2004**, *80* (8), 727–743. <https://doi.org/10.1080/00218460490477684>.
- (657) Hoorfar, M.; Kurz, M. A.; Neumann, A. W. Evaluation of the Surface Tension Measurement of Axisymmetric Drop Shape Analysis (ADSA) Using a Shape Parameter. *Colloids Surfaces A Physicochem. Eng. Asp.* **2005**, *260*, 277–285. <https://doi.org/10.1016/J.COLSURFA.2004.08.080>.
- (658) Yang, J.; Yu, K.; Zuo, Y. Y. Accuracy of Axisymmetric Drop Shape Analysis in Determining Surface and

- Interfacial Tensions. *Langmuir* **2017**, *33* (36), 8914–8923. <https://doi.org/10.1021/ACS.LANGMUIR.7B01778>.
- (659) Berim, G. O.; Ruckenstein, E. Bond Number Revisited: Axisymmetric Macroscopic Pendant Drop. *Langmuir* **2020**, *36* (23), 6512–6520. <https://doi.org/10.1021/ACS.LANGMUIR.0C00878>.
- (660) Alvarez, N. J.; Walker, L. M.; Anna, S. L. A Non-Gradient Based Algorithm for the Determination of Surface Tension from a Pendant Drop: Application to Low Bond Number Drop Shapes. *J. Colloid Interface Sci.* **2009**, *333* (2), 557–562. <https://doi.org/10.1016/j.jcis.2009.01.074>.
- (661) Ponce-Torres, A.; Vega, E. J. The Effects of Ambient Impurities on the Surface Tension. *EPJ Web Conf.* **2016**, *114*, 2–5. <https://doi.org/10.1051/epjconf/201611402098>.
- (662) Munson, E. A. The Effect of Impurities on the Time Dependence of the Surface Tension of Aqueous Surfactant Systems, 1968.
- (663) Miller, R.; Lunkenheimer, K. On the Importance of the Purity of Surfactant Solutions in Determining Their Adsorption Kinetics. *Colloid Polym. Sci.* **1982**, *260* (12), 1148–1150. <https://doi.org/10.1007/BF01411238>.
- (664) Okur, H. I.; Drexler, C. I.; Tyrode, E.; Cremer, P. S.; Roke, S. The Jones-Ray Effect Is Not Caused by Surface-Active Impurities. *J. Phys. Chem. Lett.* **2018**, *9* (23), 6739–6743. <https://doi.org/10.1021/acs.jpcclett.8b02957>.
- (665) Okur, H. I.; Chen, Y.; Wilkins, D. M.; Roke, S. The Jones-Ray Effect Reinterpreted: Surface Tension Minima of Low Ionic Strength Electrolyte Solutions Are Caused by Electric Field Induced Water-Water Correlations. *Chem. Phys. Lett.* **2017**, *684*, 433–442. <https://doi.org/10.1016/j.cplett.2017.06.018>.
- (666) Uematsu, Y.; Bonthuis, D. J.; Netz, R. R. Charged Surface-Active Impurities at Nanomolar Concentration Induce Jones-Ray Effect. *J. Phys. Chem. Lett.* **2018**, *9* (1), 189–193. <https://doi.org/10.1021/acs.jpcclett.7b02960>.
- (667) Society, T. R.; Cullis, C. F.; Hirschler, M. M.; Rogers, R. L. The Oxidation of Decane in the Liquid and Gaseous Phases. *Proc. R. Soc. London. A. Math. Phys. Sci.* **1981**, *375* (1763), 543–563. <https://doi.org/10.1098/rspa.1981.0067>.
- (668) Retamal Marín, R. R.; Babick, F.; Lindner, G. G.; Wiemann, M.; Stintz, M. Effects of Sample Preparation on Particle Size Distributions of Different Types of Silica in Suspensions. *Nanomaterials* **2018**, *8* (7). <https://doi.org/10.3390/nano8070454>.
- (669) Boussinesq, M. J. The Application of the Formula for Surface Viscosity to the Surface of a Slowly Falling Droplet in the Midst of a Large Unlimited Amount of Fluid Which Is at Rest and Possesses a Smaller Specific Gravity. *Ann. Chim. Phys.* **1913**, *29*, 357–364.
- (670) Miller, R.; Ferri, J. K.; Javadi, A.; Krägel, J.; Mucic, N.; Wüstneck, R. Rheology of Interfacial Layers. *Colloid Polym Sci* **2010**, *288*, 937–950. <https://doi.org/10.1007/s00396-010-2227-5>.
- (671) *A Basic Introduction to Rheology Shear Flow*; 2016.
- (672) Miller, R.; Liggieri, L. Methods to Determine the Rheology Parameters from Interfacial Response Functions. In *Interfacial Rheology (Progress in Colloid and Interface Science)*; CRC Press, 2009; pp 77–102.
- (673) Bracewell, R. *The Fourier Transform & Its Applications*, 3rd ed.; 1999.
- (674) Loglio, G.; Pandolfini, P.; Miller, R.; Makievski, A. V.; Ravera, F.; Ferrari, M.; Liggieri, L. Drop and Bubble Shape Analysis as a Tool for Dilational Rheological Studies of Interfacial Layers. *Stud. Interface Sci.* **2001**, *11* (C), 439–483. [https://doi.org/10.1016/S1383-7303\(01\)80038-7](https://doi.org/10.1016/S1383-7303(01)80038-7).
- (675) Reichert, M. D.; Alvarez, N. J.; Brooks, C. F.; Grillet, A. M.; Mondy, L. A.; Anna, S. L.; Walker, L. M. The Importance of Experimental Design on Measurement of Dynamic Interfacial Tension and Interfacial Rheology in Diffusion-Limited Surfactant Systems. *Colloids Surf. A. Physicochem. Eng. Asp.* **2014**, *467* (C), 135–142. <https://doi.org/10.1016/J.COLSURFA.2014.11.035>.
- (676) Lucassen-Reynders, E. H. Interfacial Viscoelasticity in Emulsions and Foams. *Food Struct.* **1993**, *12* (1), 12.
- (677) Ravera, F.; Loglio, G.; Kovalchuk, V. I. Interfacial Dilational Rheology by Oscillating Bubble/Drop Methods. *Curr. Opin. Colloid Interface Sci.* **2010**, *15* (4), 217–228. <https://doi.org/10.1016/j.cocis.2010.04.001>.
- (678) Ravera, F.; Ferrari, M.; Santini, E.; Liggieri, L. Influence of Surface Processes on the Dilational Visco-Elasticity of Surfactant Solutions. *Adv. Colloid Interface Sci.* **2005**, *117*, 75–100. <https://doi.org/10.1016/j.cis.2005.06.002>.
- (679) Derkach, S. R.; Krägel, J.; Miller, R. Methods of Measuring Rheological Properties of Interfacial Layers (Experimental Methods of 2D Rheology). *Colloid J.* **2009**, *71* (1), 1–17. <https://doi.org/10.1134/S1061933X09010013>.
- (680) Liao, Y. C.; Basaran, O. A.; Franses, E. I. Hydrodynamic Effects on the Oscillations of Supported Bubbles: Implications for Accurate Measurements of Surface Properties. *Colloids Surfaces A Physicochem. Eng. Asp.* **2004**, *250* (1–3), 367–384. <https://doi.org/10.1016/J.COLSURFA.2004.04.101>.

- (681) Russev, S. C.; Alexandrov, N.; Marinova, K. G.; Danov, K. D.; Denkov, N. D.; Lyutov, L.; Vulchev, V.; Bilke-Krause, C. Instrument and Methods for Surface Dilatational Rheology Measurements. *Rev. Sci. Instrum.* **2008**, *79* (10), 104102. <https://doi.org/10.1063/1.3000569>.
- (682) Loglio, G.; Pandolfini, P.; Miller, R.; Makievski, A.; Krägel, J.; Ravera, F. Oscillation of Interfacial Properties in Liquid Systems: Assessment of Harmonic Distortion. *Phys. Chem. Chem. Phys.* **2004**, *6* (7), 1375–1379. <https://doi.org/10.1039/B314592C>.
- (683) Yang, C.; Gu, Y. Modeling of the Adsorption Kinetics of Surfactants at the Liquid–Fluid Interface of a Pendant Drop. *Langmuir* **2004**, *20* (6), 2503–2511. <https://doi.org/10.1021/LA0360097>.
- (684) Jin, F.; Balasubramaniam, R.; Stebe, K. J. Surfactant Adsorption to Spherical Particles: The Intrinsic Length Scale Governing the Shift from Diffusion to Kinetic-Controlled Mass Transfer. *J. Adhes.* **2004**, *80*, 773–796. <https://doi.org/10.1080/00218460490480770>.
- (685) Kairaliyeva, T.; Mucic, N.; Spasojevic, L.; Bucko, S.; Katona, J.; Aksenenko, E.; Aidarova, S.; Fainerman, V.; Makievski, A.; Tarasevich, Y.; Miller, R. Surface Tension Measurements with the Drop Profile Analysis Tensiometry—Consideration of the Surfactant Mass Balance in a Single Drop. *Colloids Interfaces* **2017**, *1*, 1–11. <https://doi.org/10.3390/colloids1010001>.
- (686) Malkin, A. Y.; Isayev, A. I. *Rheology: Concepts, Methods, and Applications*, 2nd ed.; ChemTec Publishing, 2012.
- (687) Vandebriel, S.; Franck, A.; Fuller, G. G.; Moldenaers, P.; Vermant, J. A Double Wall-Ring Geometry for Interfacial Shear Rheometry. *Rheol. Acta* **2010**, *49* (2), 131–144. <https://doi.org/10.1007/s00397-009-0407-3>.
- (688) Franck, A. *Double Wall Ring Geometry to Measure Interfacial Rheological Properties*. [https://doi.org/10.1016/S0924-2244\(97\)01041-8](https://doi.org/10.1016/S0924-2244(97)01041-8).
- (689) Fardin, M. A.; Perge, C.; Casanellas, L.; Hollis, T.; Taberlet, N.; Ortín, J.; Lerouge, S.; Manneville, S. Flow Instabilities in Large Amplitude Oscillatory Shear: A Cautionary Tale. *Rheol. Acta* **2014**, *53* (12), 885–898. <https://doi.org/10.1007/S00397-014-0818-7>.
- (690) Sivia, D. S. *Elementary Scattering Theory: For X-Ray and Neutron Users*; Sivia, D. S., Ed.; Oxford University Press Inc.: New York, 2011.
- (691) Yasaka, M. X-Ray Thin-Film Measurement Techniques V. X-Ray Reflectivity Measurement. *Rigaku J.* **2010**, *26* (2), 9.
- (692) Salah, F.; Harzallah, B.; Van Der Lee, A. Data Reduction Practice in X-Ray Reflectometry. *J. Appl. Crystallogr.* **2007**, *40* (5), 813–819. <https://doi.org/10.1107/S0021889807030403>.
- (693) Schwartz, D. K.; Schlossman, M. L.; Kawamoto, E. H.; Kellogg, G. J.; Pershan, P. S.; Ocko, B. M. Thermal Diffuse X-Ray-Scattering Studies of the Water-Vapor Interface. *Phys. Rev. A, At. Mol. Opt. Phys.* **1990**, *41* (10), 5687–5690. <https://doi.org/10.1103/PHYSREVA.41.5687>.
- (694) Braslau, A.; Pershan, P. S.; Swislow, G.; Ocko, B. M.; Als-Nielsen, J. Capillary Waves on the Surface of Simple Liquids Measured by X-Ray Reflectivity. *Phys. Rev. A* **1988**, *38* (5), 2457–2470. <https://doi.org/10.1103/PhysRevA.38.2457>.
- (695) Sanyal, M. K.; Sinha, S. K.; Huang, K. G.; Ocko, B. M. X-Ray-Scattering Study of Capillary-Wave Fluctuations at a Liquid Surface. *Phys. Rev. Lett.* **1991**, *66* (5), 628–631. <https://doi.org/10.1103/PhysRevLett.66.628>.
- (696) Vignaud, G.; Gibaud, A. REFLEX: A Program for the Analysis of Specular X-Ray and Neutron Reflectivity Data. *J. Appl. Crystallogr.* **2019**, *52*, 201–213. <https://doi.org/10.1107/S1600576718018186>.
- (697) Vignaud, G.; Gibaud, A.; Grübel, G.; Joly, S.; Ausserré, D.; Legrand, J. F.; Gallot, Y. Ordering of Diblock PS-PBMA Thin Films: An X-Ray Reflectivity Study. *Phys. B Condens. Matter* **1998**, *248* (1–4), 250–257. [https://doi.org/10.1016/S0921-4526\(98\)00243-9](https://doi.org/10.1016/S0921-4526(98)00243-9).
- (698) Kimoto, S.; Dick, W. D.; Hunt, B.; Szymanski, W. W.; McMurry, P. H.; Roberts, D. L.; Pui, D. Y. H. Characterization of Nanosized Silica Size Standards. *Aerosol Sci. Technol.* **2017**, *51* (8), 936–945. <https://doi.org/10.1080/02786826.2017.1335388>.
- (699) Goebel, A.; Lunkenheimer, K. Interfacial Tension of the Water/ *n* -Alkane Interface. *Langmuir* **1997**, *13* (2), 369–372. <https://doi.org/10.1021/la960800g>.
- (700) Aveyard, R.; Haydon, D. A. Thermodynamic Properties of Aliphatic Hydrocarbon/Water Interfaces. *Trans. Faraday. Soc.* **1965**, *67*, 2255–2261. <https://doi.org/10.1039/TF9656102255>.
- (701) Cras, J. J.; Rowe-Taitt, C. A.; Nivens, D. A.; Ligler, F. S. Comparison of Chemical Cleaning Methods of Glass in Preparation for Silanization. *Biosens. Bioelectron.* **1999**, *14* (8–9), 683–688. [https://doi.org/10.1016/S0956-5663\(99\)00043-3](https://doi.org/10.1016/S0956-5663(99)00043-3).
- (702) McDonagh, C.; Sheridan, F.; Butler, T.; MacCraith, B. D. Characterisation of Sol-Gel Derived Silica Films. *J. Non. Cryst. Solids* **1996**, *194*, 72–77.
- (703) Velankar, S. S.; Giles, D. Rheology Bulletin Inside : Phase Angle in Oscillatory Testing How Do I Know If My Phase Angles Are Correct ? *Rheol. Bull.* **2007**, *76* (2), 8–20.
- (704) Läger, J.; Stettin, H. Effects of Instrument and Fluid Inertia in Oscillatory Shear in Rotational

- Rheometers. *J. Rheol. (N. Y. N. Y.)* **2016**, *60* (3), 393–406. <https://doi.org/10.1122/1.4944512>.
- (705) Danielli, J. F. The Relations between Surface PH , Ion Concentrations and Interfacial Tension. *R. Soc.* **1937**, No. 827, 155–174. <https://doi.org/10.1098/rspb.1937.0018>.
- (706) Chevalier, Y.; Bolzinger, M. Emulsions Stabilized with Solid Nanoparticles : Pickering Emulsions. *Colloids Surfaces A Physicochem. Eng. Asp.* **2013**, *439*, 23–34. <https://doi.org/10.1016/j.colsurfa.2013.02.054>.
- (707) Maaden, K. Van Der; Sliedregt, K.; Kros, A.; Jiskoot, W.; Bouwstra, J. Fluorescent Nanoparticle Adhesion Assay : A Novel Method for Surface PKa Determination of Self-Assembled Monolayers on Silicon Surfaces. *Langmuir* **2012**, *28*, 3403–3411. <https://doi.org/10.1021/la203560k>.
- (708) Zeng, X.; Xu, G.; Gao, Y.; An, Y. Surface Wettability of (3-Aminopropyl)Triethoxysilane Self-Assembled Monolayers. *J. Phys. Chem. B* **2011**, *115*, 450–454. <https://doi.org/10.1021/jp109259b>.
- (709) Young, G. J. Interaction of Water Vapor with Silica Surfaces. *J. Colloid Sci.* **1958**, *13*, 67–85. [https://doi.org/10.1016/0095-8522\(58\)90010-2](https://doi.org/10.1016/0095-8522(58)90010-2).
- (710) Mackie, A. R.; Gunning, A. P.; Wilde, P. J.; Morris, V. J. Orogenic Displacement of Protein from the Air/Water Interface by Competitive Adsorption. *J. Colloid Interface Sci.* **1999**, *210* (1), 157–166. <https://doi.org/10.1006/JCIS.1998.5941>.
- (711) Smits, J.; Vieira, F.; Bisswurn, B.; Rezwan, K.; Maas, M. Reversible Adsorption of Nanoparticles at Surfactant-Laden Liquid-Liquid Interfaces. *Langmuir* **2019**, *35* (34), 11089–11098. <https://doi.org/10.1021/acs.langmuir.9b01568>.
- (712) Wang, Z. L. Transmission Electron Microscopy of Shape-Controlled Nanocrystals and Their Assemblies. *J. Phys. Chem. B* **2000**, *104* (6), 1153–1175. <https://doi.org/10.1021/JP993593C>.
- (713) Seeck, O. H.; Deiter, C.; Pflaum, K.; Bertam, F.; Beerlink, A.; Franz, H.; Horbach, J.; Schulte-Schrepping, H.; Murphy, B. M.; Greve, M.; Magnussen, O. The High-Resolution Diffraction Beamline P08 at PETRA III. *J. Synchrotron Radiat.* **2012**, *19* (1), 30–38. <https://doi.org/10.1107/S0909049511047236>.
- (714) Murphy, B. M.; Greve, M.; Runge, B.; Koops, C. T.; Elsen, A.; Stettner, J.; Seeck, O. H.; Magnussen, O. M. A Novel X-Ray Diffractometer for Studies of Liquid-Liquid Interfaces. *J. Synchrotron Radiat.* **2014**, *21* (1), 45–56. <https://doi.org/10.1107/S1600577513026192>.
- (715) Stillinger, F. H.; Ben-Naim, A. Liquid-Vapor Interface Potential for Water. *J. Chem. Phys.* **1967**, *47* (11), 4431–4437. <https://doi.org/10.1063/1.1701649>.
- (716) Beloqui Redondo, A.; Jordan, I.; Ziazadeh, I.; Kleibert, A.; Giorgi, J. B.; Wörner, H. J.; May, S.; Abbas, Z.; Brown, M. A. Nanoparticle-Induced Charge Redistribution of the Air-Water Interface. *J. Phys. Chem. C* **2015**, *119* (5), 2661–2668. <https://doi.org/10.1021/jp511915b>.
- (717) Vu, T. V.; Papavassiliou, D. V. Synergistic Effects of Surfactants and Heterogeneous Nanoparticles at Oil-Water Interface: Insights from Computations. *J. Colloid Interface Sci.* **2019**, *553*, 50–58. <https://doi.org/10.1016/j.jcis.2019.05.102>.
- (718) Fainerman, V. B.; Aksenenko, E. V.; Kovalchuk, V. I.; Mucic, N.; Javadi, A.; Liggieri, L.; Ravera, F.; Loglio, G.; Makievski, A. V.; Schneck, E.; Miller, R. New View of the Adsorption of Surfactants at Water/Alkane Interfaces – Competitive and Cooperative Effects of Surfactant and Alkane Molecules. *Adv. Colloid Interface Sci.* **2020**, *279*, 102143. <https://doi.org/10.1016/j.cis.2020.102143>.
- (719) Shanahan, M. E. R.; Sefiane, K. Kinetics of Triple Line Motion during Evaporation. In *Contact angle, wettability and adhesion*; Kash L. Mittal, Ed.; 2009; pp 19–31. <https://doi.org/10.1201/b12247>.
- (720) Dörr, A.; Hardt, S. Line Tension and Reduction of Apparent Contact Angle Associated with Electric Double Layers. *Phys. Fluids* **2014**, *26* (8). <https://doi.org/10.1063/1.4892621>.
- (721) Iglauer, S.; Salamah, A.; Sarmadivaleh, M.; Liu, K.; Phan, C. Contamination of Silica Surfaces : Impact on Water – CO₂ – Quartz and Glass Contact Angle Measurements. *Int. J. Greenh. Gas Control* **2014**, *22*, 325–328. <https://doi.org/10.1016/j.ijggc.2014.01.006>.
- (722) Horiuchi, H.; Nikolov, A.; Wasan, D. T. Calculation of the Surface Potential and Surface Charge Density by Measurement of the Three-Phase Contact Angle. *J. Colloid Interface Sci.* **2012**, *385* (1), 218–224. <https://doi.org/10.1016/j.jcis.2012.06.078>.
- (723) Luxbacher, T. *How Does Carbon Dioxide Affect the Surface Zeta Potential?*; 2020.
- (724) Lu, Q.; Wang, J.; Faghijnejad, A.; Zeng, H.; Liu, Y. Understanding the Molecular Interactions of Lipopolysaccharides during E. Coli Initial Adhesion with a Surface Forces Apparatus. *Soft Matter* **2011**, *7* (19), 9366–9379. <https://doi.org/10.1039/c1sm05554b>.
- (725) Zhu, Z.; Zhang, S.; Li, C.; Zhang, J.; Yu, J.; Du, X.; He, L.; Zhang, X. A Mechanistic Study of Silica-Etching by Hot Water. *Phys. Chem. Chem. Phys.* **2018**, *20* (3), 1440–1446. <https://doi.org/10.1039/c7cp06856e>.
- (726) Barisik, M.; Atalay, S.; Beskok, A.; Qian, S. Size Dependent Surface Charge Properties of Silica Nanoparticles. *J. Phys. Chem. C* **2014**, *118* (4), 1836–1842. <https://doi.org/10.1021/jp410536n>.
- (727) Abbas, Z.; Labbez, C.; Nordholm, S.; Ahlberg, E. Size-Dependent Surface Charging of Nanoparticles. *J. Phys. Chem. C* **2008**, *112* (15), 5715–5723. <https://doi.org/10.1021/jp709667u>.

- (728) Brown, M. A.; Duyckaerts, N.; Redondo, A. B.; Jordan, I.; Nolting, F.; Kleibert, A.; Ammann, M.; Wörner, H. J.; Van Bokhoven, J. A.; Abbas, Z. Effect of Surface Charge Density on the Affinity of Oxide Nanoparticles for the Vapor-Water Interface. *Langmuir* **2013**, *29* (16), 5023–5029. <https://doi.org/10.1021/la4005054>.
- (729) Alvarez-Berrios, M. P.; Aponte-Reyes, L. M.; Aponte-Cruz, L. M.; Loman-Cortes, P.; Vivero-Escoto, J. L. Effect of the Surface Charge of Silica Nanoparticles on Oil Recovery: Wettability Alteration of Sandstone Cores and Imbibition Experiments. *Int. Nano Lett.* **2018**, *8* (3), 181–188. <https://doi.org/10.1007/s40089-018-0243-5>.
- (730) Andersson, M. P.; Hassenkam, T.; Matthiesen, J.; Nikolajsen, L. V.; Okhrimenko, D. V.; Dobberschütz, S.; Stipp, S. L. S. First-Principles Prediction of Surface Wetting. *Langmuir* **2020**, *36* (42), 12451–12459. <https://doi.org/10.1021/acs.langmuir.0c01241>.
- (731) De Gennes, P. G. Wetting: Statics and Dynamics. *Rev. Mod. Phys.* **1985**, *57* (3), 827–863. <https://doi.org/10.1103/RevModPhys.57.827>.
- (732) Wang, J.; Wu, Y.; Cao, Y.; Li, G.; Liao, Y. Influence of Surface Roughness on Contact Angle Hysteresis and Spreading Work. *Colloid Polym. Sci.* **2020**, *298* (8), 1107–1112. <https://doi.org/10.1007/S00396-020-04680-X>.
- (733) Janssen, D.; De Palma, R.; Verlaak, S.; Heremans, P.; Dehaen, W. Static Solvent Contact Angle Measurements, Surface Free Energy and Wettability Determination of Various Self-Assembled Monolayers on Silicon Dioxide. *Thin Solid Films* **2006**, *515* (4), 1433–1438. <https://doi.org/10.1016/j.tsf.2006.04.006>.
- (734) Matsubara, H.; Otsuka, J.; Law, B. M. Finite-Size and Solvent Dependent Line Tension Effects for Nanoparticles at the Air-Liquid Surface. *Langmuir* **2018**, *34* (1), 331–340. <https://doi.org/10.1021/acs.langmuir.7b03700>.
- (735) Yiapanis, G.; Makarucha, A. J.; Baldauf, J. S.; Downton, M. T. Simulations of Graphitic Nanoparticles at Air-Water Interfaces. *Nanoscale* **2016**, *8* (47), 19620–19628. <https://doi.org/10.1039/c6nr06475b>.
- (736) Fan, H.; Resasco, D. E.; Striolo, A. Amphiphilic Silica Nanoparticles at the Decane-Water Interface: Insights from Atomistic Simulations. *Langmuir*. 2011, pp 5264–5274. <https://doi.org/10.1021/la200428r>.
- (737) Hoorfar, M.; Neumann, A. W. Axisymmetric Drop Shape Analysis (ADSA). In *Applied Surface Thermodynamics*; Neumann, A. W., David, R., Zuo, Y., Eds.; CRC Press: Boca Raton, 2010; pp 107–174.
- (738) Nave, C.; Garman, E. F. Towards an Understanding of Radiation Damage in Cryocooled Macromolecular Crystals. *J. Synchrotron Radiat.* **2005**, *12* (3), 257–260. <https://doi.org/10.1107/S0909049505007132>.
- (739) Garman, E. F. Radiation Damage in Macromolecular Crystallography: What Is It and Why Should We Care? *Acta Cryst.* **2010**, *66* (4), 339–351. <https://doi.org/10.1107/S0907444910008656>.
- (740) Venturini, F.; Schöder, S.; Kuhs, W. F.; Honkimäki, V.; Melesi, L.; Reichert, H.; Schober, H.; Thomas, F. Synchrotron Radiation A Large-Volume Gas Cell for High-Energy X-Ray Reflectivity Investigations of Interfaces under Pressure. *J. Synchrotron Radiat.* **2011**, *18*, 251–256. <https://doi.org/10.1107/S0909049510052106>.
- (741) Scattering Length Density Calculator <http://www.refcalc.appspot.com/sld>.
- (742) Tiilikainen, J.; Bosund, V.; Mattila, M.; Hakkarainen, T.; Sormunen, J.; Lip-, H.; Lipsanen, H. Fitness Function and Nonunique Solutions in X-Ray Reflectivity Curve Fitting: Crosserror between Surface Roughness and Mass Density. *J. Phys. D. Appl. Phys.* **2007**, *40*, 4259–4263. <https://doi.org/10.1088/0022-3727/40/14/023>.
- (743) Danauskas, S. M.; Li, D.; Meron, M.; Lin, B.; Yee, K.; Lee, C. Stochastic Fitting of Specular X-Ray Reflectivity Data Using StochFit. *J. Appl. Cryst.* **2008**, *41*, 1187–1193. <https://doi.org/10.1107/S0021889808032445>.
- (744) Júnior, J. A. A.; Baldo, J. B. The Behavior of Zeta Potential of Silica Suspensions. *New J. Glas. Ceram.* **2014**, *4*, 29–37. <https://doi.org/10.4236/njgc.2014.42004>.
- (745) Azmi, W. H.; Sharma, K. V.; Sarma, P. K.; Mamat, R.; Anuar, S.; Dharma Rao, V. Experimental Determination of Turbulent Forced Convection Heat Transfer and Friction Factor with SiO₂ Nanofluid. *Exp. Therm. Fluid Sci.* **2013**, *51*, 103–111. <https://doi.org/10.1016/j.expthermflusci.2013.07.006>.
- (746) Tantra, R.; Schulze, P.; Quincey, P. Effect of Nanoparticle Concentration on Zeta-Potential Measurement Results and Reproducibility. *Particuology* **2010**, *8* (3), 279–285. <https://doi.org/10.1016/j.partic.2010.01.003>.
- (747) Carrique, F.; Arroyo, F. J.; Delgado, A. V. Electrokinetics of Concentrated Suspensions of Spherical Colloidal Particles with Surface Conductance, Arbitrary Zeta Potential, and Double-Layer Thickness in Static Electric Fields. *J. Colloid Interface Sci.* **2002**, *252* (1), 126–137. <https://doi.org/10.1006/jcis.2002.8418>.
- (748) Carrique, F.; Arroyo, F. J.; Jiménez, M. L.; Delgado, A. V. Influence of Double-Layer Overlap on the Electrophoretic Mobility and DC Conductivity of a Concentrated Suspension of Spherical Particles. *J. Phys. Chem. B* **2003**, *107* (14), 3199–3206. <https://doi.org/10.1021/jp027148k>.

- (749) Carrique, F.; Arroyo, F. J.; Delgado, A. V. Electrokinetics of Concentrated Suspensions of Spherical Colloidal Particles: Effect of a Dynamic Stern Layer on Electrophoresis and DC Conductivity. *J. Colloid Interface Sci.* **2001**, *243* (2), 351–361. <https://doi.org/10.1006/jcis.2001.7903>.
- (750) Loeb, A. L.; Overbeek, J. T. G.; Wiersema, P. H. *The Electrical Double Layer around a Spherical Colloid Particle - Computation of the Potential, Charge Density, and Free Energy of the Electrical Double Layer Around a Spherical Colloid Particle*; MIT press: Cambridge, MA: Cambridge, MA, 1960.
- (751) Ohshima, H.; Healy, T. W.; White, L. R. Accurate Analytic Expressions for the Surface Charge Density/Surface Potential Relationship and Double-Layer Potential Distribution for a Spherical Colloidal Particle. *J. Colloid Interface Sci.* **1982**, *90* (1), 17–26. [https://doi.org/10.1016/0021-9797\(82\)90393-9](https://doi.org/10.1016/0021-9797(82)90393-9).
- (752) Grahame, D. C. The Electrical Double Layer and the Theory of Electrocapillarity. *Chem. Rev.* **1947**, *41* (3), 441–501. <https://doi.org/10.1021/cr60130a002>.
- (753) Sonnefeld, J.; Göbel, A.; Vogelsberger, W. Surface Charge Density on Spherical Silica Particles in Aqueous Alkali Chloride Solutions - Part 1. Experimental Results. *Colloid Polym. Sci.* **1995**, *273* (10), 926–931. <https://doi.org/10.1007/BF00660369>.
- (754) Mobilio, S.; Boscherini, F.; Meneghini, C. *Synchrotron Radiation: Basics, Methods and Applications*; Springer Berlin Heidelberg, 2015. <https://doi.org/10.1007/978-3-642-55315-8>.

List of publications and oral presentations

Publications – Peer-reviewed

Smits, J., Giri, R. P., Chen, S., Mendonca, D., Murphy, B., Huber, P., Rezwan, K., Maas, M. Assessment of nanoparticle immersion depth at liquid interfaces from chemically equivalent macroscopic surfaces. In: *Journal of Colloid and Interface Science* **2022**, *611*, 670-683. DOI: [10.1016/j.jcis.2021.12.113](https://doi.org/10.1016/j.jcis.2021.12.113).

Smits, J., Giri, R. P., Chen, S., Mendonca, D., Murphy, B., Huber, P., Rezwan, K., Maas, M. Synergistic and Competitive Adsorption of Hydrophilic Nanoparticles and Oil-Soluble Surfactants at the Oil–Water Interface. In: *Langmuir* **2021**, *37* (18), 5659–5672. DOI: [10.1021/acs.langmuir.1c00559](https://doi.org/10.1021/acs.langmuir.1c00559).

Jiang, H., Zhang, T., , Smits, J., Maas, M., Huang, X., Yin, S. Ngai, T. Edible high internal phase Pickering emulsion with double-emulsion morphology. In: *Food Hydrocolloids* **2021**, *111*, 106405. DOI: [10.1016/j.foodhyd.2020.106405](https://doi.org/10.1016/j.foodhyd.2020.106405).

Smits, J.; Vieira, F.; Bisswurn, B.; Rezwan, K.; Maas, M. Reversible Adsorption of Nanoparticles at Surfactant-Laden Liquid-Liquid Interfaces. In: *Langmuir* **2019**, *35* (34), 11089–11098. DOI: [10.1021/acs.langmuir.9b01568](https://doi.org/10.1021/acs.langmuir.9b01568).

Poster/oral presentations

Poster: J. Smits, K. Rezwan, M. Maas. Interfacial rheology of mixed thin films of hydrophilic nanoparticles and lipids at the liquid interface. 16th Conference of the International Association of Colloid and Interface Scientists (IACIS), 2018, World Trade Center, Rotterdam, the Netherlands.

Oral presentation: J. Smits, K. Rezwan, M. Maas. Reversible adsorption of nanoparticles at a surfactant-laden liquid-liquid interface. 93rd ACS Colloid & Surface Science Symposium, 2019, Georgia Institute of Technology, Atlanta, USA.

Author contributions for the presented publications

Smits, J., Giri, R. P., Chen, S., Mendonca, D., Murphy, B., Huber, P., Rezwan, K., Maas, M. Assessment of nanoparticle immersion depth at liquid interfaces from chemically equivalent macroscopic surfaces. In: *Journal of Colloid and Interface Science* **2022**, *611*, 670-683. DOI: [10.1016/j.jcis.2021.12.113](https://doi.org/10.1016/j.jcis.2021.12.113). Contributions of this publication have been used in the Abstract and Chapters 1, 2, 3, 4, 7 and A.5.

Author	Contribution
Joeri Smits	Data Curation, Formal analysis, Investigation, Methodology, Validation, Visualization, Writing – Original Draft, Writing – Review & Editing
Rajendra Prasad Giri	Data Curation, Formal analysis, Investigation, Validation, Visualization, Writing – Review & Editing
Chen Shen	Data Curation, Formal analysis, Investigation, Validation, Visualization, Writing – Review & Editing
Diogo Mendonça	Data Curation, Formal analysis, Investigation, Validation, Visualization, Writing – Review & Editing
Bridget Murphy	Data Curation, Investigation, Resources, Supervision, Validation, Visualization, Writing – Review & Editing
Patrick Huber	Data Curation, Investigation, Resources, Supervision, Validation, Visualization, Writing – Review & Editing
Kurosch Rezwan	Resources, Supervision, Validation, Writing – Review & Editing
Michael Maas	Conceptualization, Data Curation, Investigation, Funding acquisition, Methodology, Project administration, Resources, Supervision, Validation, Visualization, Writing – Review & Editing

Smits, J., Giri, R. P., Chen, S., Mendonca, D., Murphy, B., Huber, P., Rezwan, K., Maas, M. Synergistic and Competitive Adsorption of Hydrophilic Nanoparticles and Oil-Soluble Surfactants at the Oil–Water Interface. In: *Langmuir* **2021**, *37* (18), 5659–5672. DOI: [10.1021/acs.langmuir.1c00559](https://doi.org/10.1021/acs.langmuir.1c00559). Contributions of this publication have been used in the Abstract and Chapters 1, 2, 3, 4, 6 and A.4.

Author	Contribution
Joeri Smits	Data Curation, Formal analysis, Investigation, Methodology, Validation, Visualization, Writing – Original Draft, Writing – Review & Editing
Rajendra Prasad Giri	Data Curation, Formal analysis, Investigation, Validation, Visualization, Writing – Review & Editing
Chen Shen	Data Curation, Formal analysis, Investigation, Validation, Visualization, Writing – Review & Editing
Diogo Mendonça	Data Curation, Formal analysis, Investigation, Validation, Visualization, Writing – Review & Editing
Bridget Murphy	Data Curation, Investigation, Resources, Supervision, Validation, Visualization, Writing – Review & Editing
Patrick Huber	Data Curation, Investigation, Resources, Supervision, Validation, Visualization, Writing – Review & Editing
Kurosch Rezwan	Resources, Supervision, Validation, Writing – Review & Editing
Michael Maas	Conceptualization, Data Curation, Investigation, Funding acquisition, Methodology, Project administration, Resources, Supervision, Validation, Visualization, Writing – Review & Editing

Smits, J.; Vieira, F.; Bisswurn, B.; Rezwan, K.; Maas, M. Reversible Adsorption of Nanoparticles at Surfactant-Laden Liquid-Liquid Interfaces. In: *Langmuir* **2019**, 35 (34), 11089–11098. DOI: 10.1021/acs.langmuir.9b01568. Contributions of this publication have been used in the Abstract and Chapters 1, 2, 3, 4, 5 and A.3.

Author	<i>Contribution</i>
Joeri Smits	Data Curation, Formal analysis, Investigation, Methodology, Validation, Visualization, Writing – Original Draft, Writing – Review & Editing
Felipi Vieira	Data Curation, Formal analysis, Investigation, Validation, Visualization, Writing – Review & Editing
Bianca Bisswurn	Data Curation, Formal analysis, Investigation, Validation, Visualization, Writing – Review & Editing
Kuroschi Rezwan	Resources, Supervision, Validation, Writing – Review & Editing
Michael Maas	Conceptualization, Data Curation, Investigation, Funding acquisition, Methodology, Project administration, Resources, Supervision, Validation, Visualization, Writing – Review & Editing

List of student projects

This thesis contains results that have been derived during the supervision of the following projects.

Felipi Vieira	Influence of film forming components at liquid-liquid interfaces
Bianca Bisswurn	Interfacial shear rheology of nanoparticle/surfactant films at the oil-water interface
Diogo Mendonca	Relating surface charge and wettability between inorganic thin films to the nanoscale roughness

